JOINT PERFORMANCE CHARACTERIZATION OF BONDED WHITETOPPING OVERLAYS

by

Manik Barman

Bachelor of Technology in Civil Engineering, North Eastern Regional Institute of Science and Technology, India, 2002

Master of Technology in Civil Engineering, Indian Institute of Technology (IIT) Kharagpur, India 2004

Submitted to the Graduate Faculty of

The Swanson School of Engineering in partial fulfillment

of the requirements for the degree of

Doctor of Philosophy

University of Pittsburgh

2014

UMI Number: 3582651

UMI

Dissertation Publishing

ProQuest

www.manaraa.com

UNIVERSITY OF PITTSBURGH

SWANSON SCHOOL OF ENGINEERING

This dissertation was presented

by

Manik Barman

It was defended on

November 8, 2013

and approved by

John Brigham, Ph.D., Assistant Professor

Department of Civil and Environmental Engineering

Donald J. Janssen, Ph.D., Associate Professor,

Civil and Environmental Engineering, University of Washington, Seattle

Luis E. Vallejo, Ph.D., Professor

Department of Civil and Environmental Engineering

Dissertation Director: Julie M. Vandenbossche, Assistant Professor

Department of Civil and Environmental Engineering

iii

JOINT PERFORMANCE CHARACTERIZATION OF BONDED WHITETOPPING OVERLAYS

Manik Barman, Ph.D.

University of Pittsburgh, 2014

Poor joint performance in whitetopping overlays increases the magnitude of the interlayer debonding stress and load related stress, which can result in corner and longitudinal cracks. However, currently available whitetopping design procedures do not account for the joint performance. Fiber reinforced concrete (FRC) is commonly used in constructing these overlays but the contribution of the fiber to load transfer has never been quantified either.

Under the scope of this dissertation, a new, economical, small-scale joint performance characterization procedure (B_{ALT}) was developed. The results from the B_{ALT} procedure were validated by comparing them to the results from large scale joint performance tests (S_{ALT}). The joint performances of one plain concrete (PC) and two FRC mixtures were characterized with respect to mixture type, crack width and number of load cycles. Load transfer efficiency (LTE) and dissipated energy ratio (DER) prediction models were developed for all the mixtures. It was found that FRC provides a 15 to 25 percent higher joint performance as compared to PC. The fiber plays a larger role in load transfer when the joint is fatigued. Interestingly fibers do not fatigue even after 10 million load cycles. Using finite element analysis, a relationship was developed for determining the joint stiffness ($AGG*$) for whitetopping overlay. It was found that the load-related stress can be reduced by 6 percent with application of FRC while the interface debonding stress can be reduced by 50 to 72 percent.

TABLE OF CONTENTS

LIST OF TABLES

LIST OF FIGURES

xiv

ACKNOWLEDGEMENTS

I sincerely acknowledge the motivation and endless support rendered by my advisor, Dr. Julie M. Vandenbossche during the entire period of my Ph. D. work. It was because of her proactive guidance I could successfully complete this dissertation.

I must thank Dr. Donald Janssen, one of the committee members, for his valuable suggestions throughout my doctoral study. His suggestions in the laboratory work were immensely helpful.

The time and cooperation of other committee members, Dr. John Brigham and Dr. Luis Vallejo are highly appreciated. I would also like to sincerely thank my colleagues, Kerri, Somayeh, Feng, Zichang, Luis, Matt and Tom for their cooperation during my stay at the University of Pittsburgh. A special thanks to Scooter for his help in my laboratory work as well as in my personal life.

The financial support by MnDOT and other state DOTs participated in this project is highly acknowledged. I also like to thank Frank Bryan Inc., Pittsburgh for providing the concrete used in the study.

I would like to thank my friends at Banaras Hindu University, India for their cooperation during my Ph. D. I also would like to thank my friends at the University of Oklahoma who have always inspired me to successfully accomplish this milestone. I would sincerely like to thank

Dr. Musharraf Zaman and Dr. Sesh Commuri, Professors at the University of Oklahoma for their valuable inputs and all the helps they rendered to me and my family during our needs.

My endless gratitude is extended to my friends in Pittsburgh, Ananda, Sreya, Aniruddha, Madhabi and many others who have always stood by me and my family in our good and bad times. Without their support my stay in this country would not have been possible.

My parents, my siblings and my in-laws deserve a lot more than thanks, I am grateful to of you all for being part of my life. My wife, who has sacrificed her own living style for making my life, is the one who has probably enjoyed less and suffered more. I apologize to her for not being a good and caring husband, but I will try my best to make it up in my post Ph. D. life. Lastly my beloved daughter, who is now our life, I apologize to her for not providing some quality time. Lastly, I started believing in God, and God is great.

THIS DISSERTATION IS DEDICATED TO MY FAMILY MEMBERS.

1.0 INTRODUCTION

1.1 PROBLEM STATEMENT

Whitetopping is a rehabilitation method for moderately distressed hot mix asphalt (HMA) pavements by plain concrete (PC) or fiber reinforced concrete (FRC) overlay. Whitetopping is constructed with thinner and shorter slabs. The structural stiffness of the existing HMA layer and the interface bonding between the concrete and HMA layers are accounted for in the mechanistic design procedure. This results in the need for a thinner concrete slab. The main advantage of this type of overlay over the traditional HMA overlays is the use of the underlying HMA layer to carry the traffic load, and thus reducing the thickness of the overlay.

The performance studies of different existing whitetopping projects available in the literature (Vandenbossche, 2003; Burnham, 2006 and Barman, et al., 2010) reveals that these overlays mainly fail by corner, transverse and longitudinal cracks. Also, it was observed that in most of the cases, cracks generally initiate at the edges of the slabs. When the repeated wheel loads on a critical location induces excessive stress, cracks initiate. The reasons for the increased stress could be (i) low load transfer between the adjacent concrete slabs, (ii) low load transfer through the HMA layer under the joint and (iii) debonding at the interface of concrete and HMA layers. All these reasons are directly or indirectly related to the joint condition. In this dissertation, the phrase 'joint performance' is used as an indicator of the joint condition.

1

The joint performance, conventionally expressed in terms of load transfer efficiency (LTE), is a function of the joint stiffness and support conditions. LTE depends on the type of the concrete material, width of the crack (cw), magnitude and repetitions of the wheel load, size of the slab and modulus of the subgrade reaction (k), etc. In bonded whitetopping, a major share of the wheel load can be transferred through the HMA layer, however, increasing the LTE between the adjacent slabs reduces the stress on the loaded slab, and more importantly reduces the potential for interface debonding. With a higher LTE, the differential deflection between the slabs remains low, which helps in reducing the debonding stress at the interface by protecting the HMA layer against peeling off from the concrete layer.

A higher LTE between the slabs can be achieved through (i) aggregate interlock and (ii) dowel action. A great contribution through aggregate interlock can be achieved by keeping the joints and cracks tight. Regarding the dowel action, conventional dowel bars are not used in whitetopping because of the weakness of the thin slab against the bearing stress under the dowel bar. FRC holds adjacent slabs in close proximity, resulting in an increase in effective aggregate interlock area. Structural fibers with sufficient stiffness might also provide dowel action that helps to transfer the load to the adjacent slab.

In the United States (US), FRC is commonly used in ultra-thin whitetopping. The results of a survey reported in the National Cooperative Highway Research Program (NCHRP) Synthesis 338 (Rasmussen & Rozycki, 2004) show that sixty-four percent of the responders have used FRC in ultra-thin whitetopping. However, it is unfortunate that even though the FRC has been used for years, the real benefits are not completely accounted for in bonded whitetopping design procedures. Bonded whitetopping design procedures do account for some of the benefits of the use of fibers in the performance of ultra-thin whitetopping (Roesler, et al.,

2

2006 and Roesler, et al., 2008). A 20 percent increase in the modulus of rupture (MOR) is proposed to account for the contribution of fibers. This was decided based on the experimental findings that the inclusion of an affordable quantity of fibers provides a 20 percent residual strength ratio (RSR). This might not be the sole contribution of the fibers.

1.2   RESEARCH SIGNIFICANCE AND OBJECTIVES

The reason behind the aversion to incorporating the joint performance benefit of FRC into the current design procedures is that the joint performance characterization itself is a challenging task. Moreover, no research has been performed to quantify the benefit of fibers in joint performance, especially in whitetopping overlays. Most of the research studies (Colley & Humphrey, 1967; Nowlen, 1968; Bruinsma, et al., 1995; Hansen, et al., 1998; Jensen & Hansen, 2001; Brink, et al., 2004) that characterize joint performance for conventional concrete pavements were carried out by casting large size slabs in laboratory conditions, which are expensive and generally cost-prohibitive when evaluating a large number of design parameters. The in-service joint performance evaluation through the use of a falling weight deflectometer (FWD) is also expensive.

Therefore, it is a dire necessity to develop a simple joint performance evaluation test procedure so that the joint performance characterization becomes easy, affordable and possible through the use of small scale specimens. This would provide researchers with a more affordable means for characterizing joint performance.

The present study includes the development of a small-scale joint performance test procedure. Beam specimens with a dimension of 24 in x 6 in x 6 in can be used in this small-

3

scale procedure. In this dissertation, this procedure is referred to as the Beam Accelerated Load Testing (B_{ALT}) procedure. This test procedure will be then correlated with the large-scale joint performance test procedure. In this dissertation, the large-scale procedure is referred to as Slab Accelerated Load Testing (S_{ALT}) procedure. The S_{ALT} will be conducted using an accelerated load testing facility (ALF) on full scale slabs. The correlation between the two procedures will facilitate the utilization of beam specimens in the B_{ALT} procedure in deriving the joint performance for slabs.

The other main objective of this research is to quantify the joint performance contribution of FRC in bonded whitetopping. In order to achieve this, joint performance testing on both plain concrete (PC) and FRC specimens will be conducted. The results will be compared to characterize the contribution of the FRC in joint performance.

Finally, through the use of the finite element method (FEM), a relationship between LTE and the non-dimensional joint stiffness (*AGG**) will be developed, specifically for bonded whitetopping overlays. *AGG** will be defined as a function of LTE and the design features of the whitetopping. This *AGG** can be used in the mechanistic design of bonded whitetopping. Also, the laboratory test results will be coupled with the FEM results to derive the debonding stresses for different whitetopping structures with and without the application of fibers.

These overall objectives will be accomplished by completing the following major tasks:

(i)   Design and fabricate the B_{ALT} test setup;

(ii)   Fabricate the S_{ALT} test setup;

(iii)   Develop the test specimen preparation techniques for both procedures;

(iv)   Develop test protocols for both procedures;

(v)   Investigate the joint performance of the PC and FRC concrete mixtures at different crack widths and load cycles using both procedures;

(vi)   Correlate the results of B_{ALT} and S_{ALT} procedures;

(vii)   Establish a relationship between LTE and *AGG** for bonded whitetopping;

(viii) Quantify the benefits of the inclusion of fibers in terms reducing the critical design stress;

(ix)   Quantify the benefits of the inclusion of fibers in terms of reducing debonding stress.

1.3   STRUCTURE OF THE DISSERTATION

This dissertation consists of seven chapters, each with a specific objective. The first chapter is the introductory chapter and consists of the problem statement, research significance and objectives of the study. This chapter also presents the structure of the dissertation.

The second chapter presents the background information. Introduction of bonded whitetopping, design procedures and failure modes are presented in this chapter. The literature related to the joint performance characterization, factors influencing the joints performance and different joint performance evaluation methodologies proposed by the previous researchers are also discussed in this chapter.

The third chapter presents the development of the joint performance test setups and evaluation procedures. The design principle, different components of B_{ALT} setup and their fabrications are discussed. The fabrication process and components of the S_{ALT} setup are also presented. Finally, the test specimen preparation, testing procedure and data analysis approach for both procedures is presented in this chapter.

5

The fourth chapter presents the material properties and detailed laboratory test plan. The total test matrices for both the B_{ALT} and S_{ALT} procedures are presented in this chapter as well.

The fifth chapter presents the main test results and discussions. Fresh and hardened properties for all three types of concretes used in the study are provided. Next, the joint performance test results obtained from both the B_{ALT} and S_{ALT} procedures are introduced and discussed in detail. Finally, the regression models developed from the test results are also presented.

Modeling of the joint performance for the bonded whitetopping using the finite element method is presented in the sixth chapter. The modeling approach, results and the developed relationship between the two joint performance components (LTE and AGG^*) are presented in this chapter. Debonding stresses are estimated and presented in this chapter as well.

The last chapter provides the conclusions drawn from the present study and recommendations for future studies.

6

2.0 LITERATURE REVIEWS AND BACKGROUND

Three types of whitetopping are common in practice, (i) conventional whitetopping, slab thickness (h_{PCC}) > 6 in; (ii) thin whitetopping (TWT), h_{PCC} = 4 to 6 in and (iii) ultra-thin whitetopping (UTW), $h_{PCC} \leq 4$ in. In ultra-thin and thin whitetopping, a bond between the concrete overlay and the underlying HMA layer is ensured so that the desired performance is achieved. This allows for a thinner concrete overlay, while still fulfilling the intended service life. The bond between the layers ensures that the two layers act like a single composite layer. This eventually reduces the tensile stress in the overlay, as shown in the schematic in Figure 2.1.
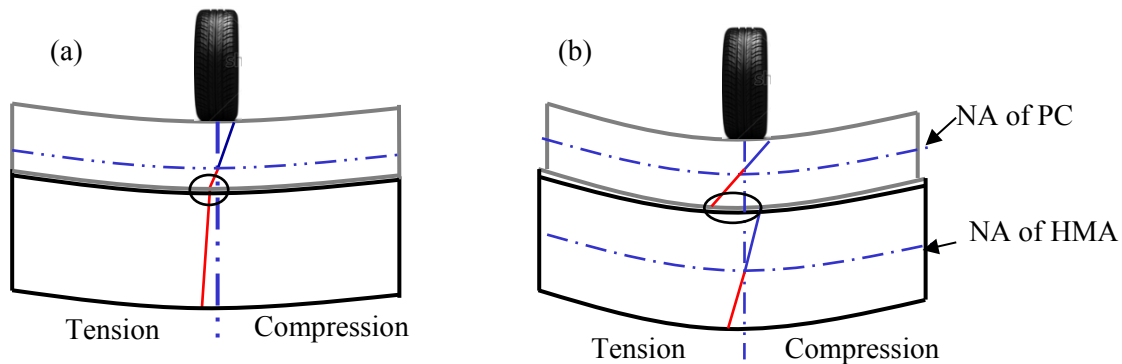
Lower tensile stress at the bottom of overlay   Higher tensile stress at the bottom of overlay

Figure 2.1. Stress distribution through the layers: (a) bonded and (b) unbonded whitetoppings.

2.1 WHITETOPPING DESIGN PROCEDURES

Whitetopping as a rehabilitation method was reported in the literature as early as 1918, though a very few projects were noted until the 1990s (Rasmussen & Rozycki, 2004). Since 1992, this rehabilitation method has gained momentum in the US. Several other countries, such as Canada, Chile, Brazil and Taiwan have also constructed whitetopping overlays (Roesler, et al., 2008). The increasing popularity of whitetopping has triggered many agencies to put effort towards the development of design procedures. Many agencies, namely the Portland Cement Association (PCA) (Wu, et al., 1998), the Colorado Department of Transportation (CDOT) (Tarr, et al., 1998; Sheehan, et al., 2004), the New Jersey Department of Transportation (NJDOT) (Gucunski, 1998), the American Concrete Pavement Association (ACPA) (ACPA, 1998 and Riley, et al., 2005), Illinois Center for Transportation (ICT) (Roesler, et al., 2008) and the University of Pittsburgh (Barman, et al., 2010, Mu & Vandenbossche, 2010, Barman, et al., 2011and Li, et al., 2013) have proposed their own design procedures. Each procedure has its own merits and demerits in comparison to the others and addresses different whitetopping types. The NCHRP Synthesis 338 (Rasmussen & Rozycki, 2004) indicates that the Arizona, Iowa, Illinois, Mississippi, Texas, Missouri, Kansas and Utah departments of transportation (DOT) adopted the ACPA design procedure, which was actually developed for UTW. Some states, including Colorado, use the CDOT design procedure, mainly developed for TWT. While others attempted to apply the 1993 American Association of State Highway Transportation Officials (AASHTO) Guide for the Design of Pavement Structures, which was actually not intended for the design of thin or ultra-thin whitetopping. The most recent whitetopping design procedure, BCOA-ME, which was developed at the University of Pittsburgh, was jointly funded by many states such as Iowa, Kansas, Minnesota, Mississippi, Missouri, North Carolina, Pennsylvania, South Dakota

and Texas. The main advantage of this procedure over the other available procedures is the consideration of influence of the climate into the performance as well as the recognition of variation in the failure based on the slab size.

In all of the procedures the basic design approach is same. The design input such as traffic, design life, concrete and existing HMA layer thicknesses, slab size, concrete and HMA layer material properties, base/subbase material properties are considered in the structural response model to estimate the critical stress and strain. Then, the estimated stress and strain are used in the fatigue damage prediction models to predict the fatigue accumulation over the design period. Multiple iterations are performed to select the design thickness. The thickness, which approximates 100 percent fatigue damage over the design period, is selected as the design thickness. The main disadvantage of the previously developed design procedures is that they do not consider the joint performance in determining the critical stress and strain. Since, the joint performance has an influence on the potential for debonding; consideration of the joint performance in the design procedure should influence the design life.

2.2   BONDED WHITETOPPING FAILURE MODES

The distress types in bonded whitetopping are primarily a function of the slab size and slab thickness, while the deterioration rate appears to be more related to the joint performance, HMA layer thickness, HMA materials stiffness, traffic, climate and more importantly the joint layout. When the longitudinal joints coincide with the wheelpath, the distresses progress more rapidly. The PCA (Wu, et al., 1998) and the ICT whitetopping design procedures (Roesler, et al., 2008) consider corner crack as the primary failure mode for UTW. The CDOT design procedure (

Tarr, et al., 1998; Sheehan, et al., 2004) considers transverse crack as the primary failure mode for TWT. A review of the performance of bonded whitetopping performed at the University of Pittsburgh (Barman, et al., 2010) examined the failure modes for bonded whitetopping projects constructed throughout the US. It was found that the primary mode of distress for the overlays with shorter slab size like 3 ft x 3 ft or 4 ft x 4 ft is corner cracking. Larger slab sizes, like 6 ft x 6 ft and 5 ft x 6 ft, exhibit longitudinal cracks. Examples of these three types of cracks, observed in Minnesota Road Research Project (MnROAD) whitetopping sections, can be seen in Figure 2.2. MnROAD is a full-scale pavement test facility consisting of a 3.5-mile section of interstate (I-94) and a 2.5-mile of low-volume roadway near Albertville, Minnesota, approximately 35 miles northwest of Minneapolis. This research facility includes many whitetopping test sections with different design features, along with other types of pavements.

An in depth analysis of the distress data for the MnROAD whitetopping cells further indicated that transverse cracks also develop but were not load related. They are typically either reflection or secondary cracks that developed off from the already initiated corner cracks (Vandenbossche & Barman, 2010). In Figure 2.2 (c), one such transverse crack is shown. It can be seen that this transverse crack has continued through from the HMA shoulder. Pre-overlay distress surveys revealed that the HMA layer underneath the whitetopping already had a crack, at this location.
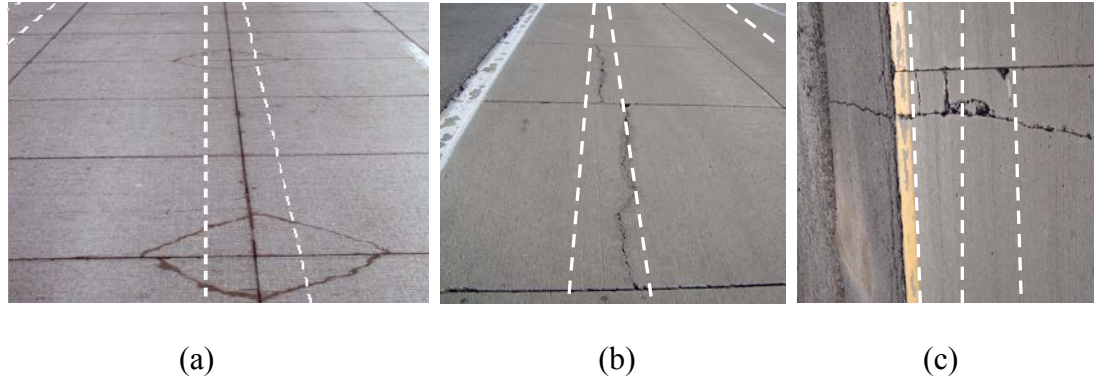
Figure 2.2. Common failure modes in whitetopping: (a) Corner crack in shorter slabs, (b) Longitudinal crack in larger slabs and (c) Reflected transverse crack
(Vandenbossche, 2003; Burnham, 2006; Barman, et al., 2010)

Therefore, it can be concluded that in 6-ft x 6-ft slabs when the wheelpath is away from the longitudinal joint, longitudinal cracks, or diagonal cracks that initiate like longitudinal cracks but then propagate towards the longitudinal joint, develop. In shorter slabs when the longitudinal joint lies at or near the wheelpath, corner cracks are the primary mode of distress.

The analysis of the distress data from the MnROAD projects also provides some insight regarding the locations of the crack initiation. In the larger slabs, longitudinal cracks generally initiate at the transverse joint in the wheelpath. In the shorter slabs, it is difficult to conclude whether the cracks initiate at the longitudinal edge or at the transverse edge of the slab. When the joint condition deteriorates, the presence of moisture coupled with higher deflections on both the slabs creates debonding of the HMA layer. This results in a higher stress at the loaded slab.

2.3   JOINT PERFORMANCE TERMINOLOGIES

Distress in bonded whitetopping tends to initiate at or near the joints. In other words, the long term performance of bonded whitetopping depends on the joint performance. Since the present

11

project focuses on the joint performance aspect, it has been thought to provide an introduction of the different parameters which are conventionally used to characterize the joint performance.

Load transfer efficiency

The deflection load transfer efficiency, or simply load transfer efficiency (LTE) in this dissertation, is defined as the ratio of the deflections on the unloaded slab to the deflection on the loaded slab, as given below, Equation (2.1)

$$LTE = \frac{\delta_U}{\delta_L} \times 100 \text{ percent} \tag{2.1}$$

where δ_U and δ_L are the deflections on the unloaded and loaded side of a joint, respectively. A schematic of a loaded concrete pavement joint explaining the poor and good joint performance is shown in Figure 2.3. At poor or no joint performance, theoretically no load is transferred to the unloaded side, therefore, the deflection on the unloaded side is zero ($\delta_U = 0$). In this case, LTE is obtained as 0 percent. At good load transfer, the deflection at the unloaded side is not zero, and the deflections at both the sides are equal ($\delta_L = \delta_U$); and the LTE is obtained as 100 percent.

δ_L= Deflection under the loaded slab; δ_U= Deflection under the unloaded slab
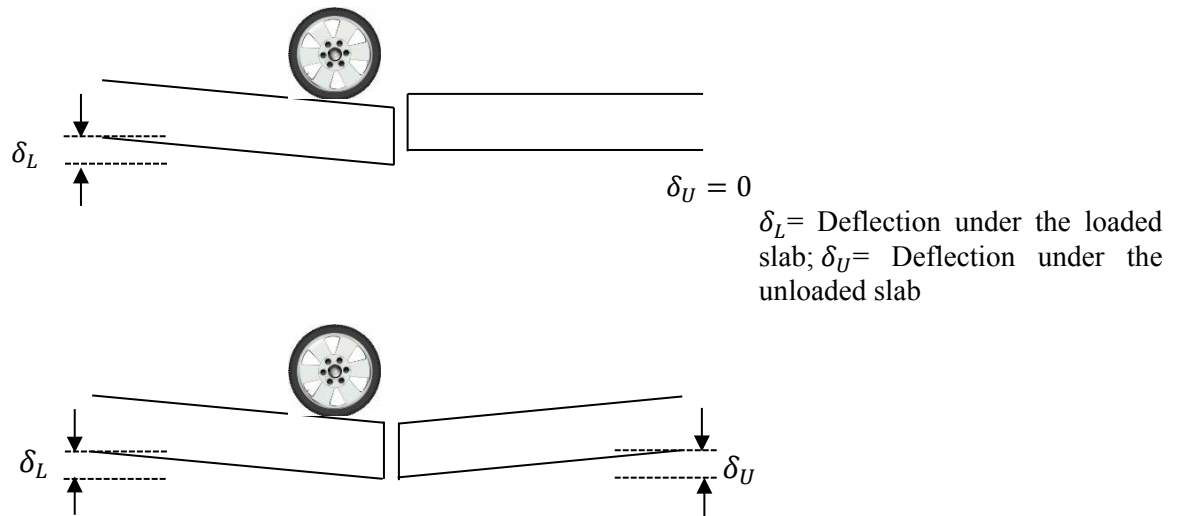
Figure 2.3. Joint performance demonstration (a) Poor joint performance (LTE = 0 percent), (b) Good joint performance (LTE = 100 percent).

Joint stiffness (AGG) and non-dimensional joint stiffness (AGG)*

Ioannides & Korovesis, 1990 characterized the joint performance of conventional concrete pavement in terms of the aggregate interlock shear stiffness, commonly known as *AGG*. The higher the shear stiffness, the higher the joint performance. They proposed a relationship between the non-dimensional joint stiffness (*AGG**), given in Equation (2.2), and LTE. The mathematical relationship can be seen in Equation (2.3).

$$AGG^* = AGG/kl \tag{2.2}$$

$$LTE = \cfrac{1}{1 + \log^{-1}\left[\cfrac{0.214 - 0.183\left(\dfrac{r}{l}\right) - \log\left(\dfrac{AGG}{kl}\right)}{1.180}\right]} \tag{2.3}$$

where r is the radius of the loaded area, k is the modulus of subgrade reaction and l is the radius of relative stiffness, which can be obtained by using the following equation.

$$l = \left(\frac{Eh^3}{12(1 - \mu^2)k}\right)^{\frac{1}{4}} \tag{2.4}$$

where E and μ are the modulus of elasticity and Poisson's ratio of the concrete, h is the thickness of the concrete slab and k is the modulus of subgrade reaction. The graphical relationship between the LTE and *AGG** is presented in Figure 2.4. It can be seen that the relationship between the LTE and *AGG** can be explained by a sigmoidal function. The relation is linear when the LTE is in between 20 to 80 percent. Outside this range *AGG** is highly sensitive to LTE.
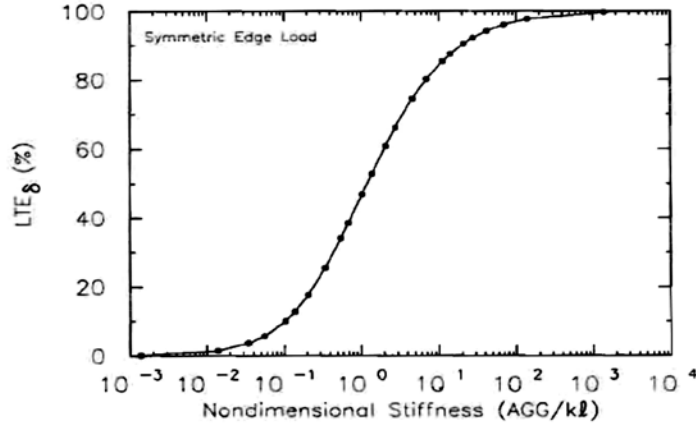
Figure 2.4. Relation between non-dimensional joint stiffness (*AGG**) and LTE
(Ioannides & Korovesis, 1990).

Differential energy dissipation (DED)

Differential energy dissipation (DED) is derived from the load vs deflection graph. When the

pavement system deflects under the wheel load, energy is dissipated out of the system. The

magnitude of the dissipated energy (DE) is proportional to the magnitude of the pavement

deflection. The dissipated energy is defined as the area under the load vs deflection curve. In a

concrete pavement, the magnitude of DE at the approach side differs from the leave side, based

on the joint performance. This difference is referred to as the differential energy dissipation

(DED) in this dissertation. The ratio between the DE of unloaded and loaded sides is referred as

the dissipated energy ratio (DER).

2.4   JOINT PERFORMANCE MEDIUM

In bonded whitetopping, the overlay remains bonded with the HMA layer. The HMA layer is

mostly a continuous layer underneath the overlay. Because of all these reasons, a larger portion

of the wheel load may be transferred through HMA layer. However, many researchers (

14

Nishizawa, et al., 2003 and Roesler & Wang, 2009) believe that the thin concrete overlay also transfers some amount of load. To determine which layer actually transfers a larger portion of the load, joint performance data from the MnROAD whitetopping sections was studied. The design features of three of the MnROAD whitetopping cells, namely Cell 94, 95 and 96 are given in Table 2.1. All of these three cells were constructed on a thick HMA layer. Joint performance data for these three cells for three consecutive years (1998 to 2000) are shown in Figure 2.5 through Figure 2.7. The variation in LTE with temperature for Cell 94 (4-ft x 4-ft slab, 3-in thick overlay on 10-in HMA layer) and Cell 96 (5-ft x 6-ft slab, 6-in thick overlay on 7-in HMA layer) reveals that LTE did increase with the increase in temperature.

Table 2.1. Summary of the design features for Cells 94, 95 and 96 in MnROAD
(Burnham, 2006; Vandenbossche, 2003; Barman, et al., 2010)

Cell No.	Age	Thickness of PCC slab (in)	Thickness of HMA layer (in)	Size of the slab (ft × ft)	Sealed joint (Y/N)	Doweled joint (Size/N)	Type of fiber reinforcement
94	Oct 97-Oct 04	3	10	4 × 4	Y	N	Polypropylene
95	Oct 97-Oct 04	3	10	5 x 6	Y	N	Polyolefin
96	Oct 97-current	6	7	5 x 6	Y	N	Polypropylene

15
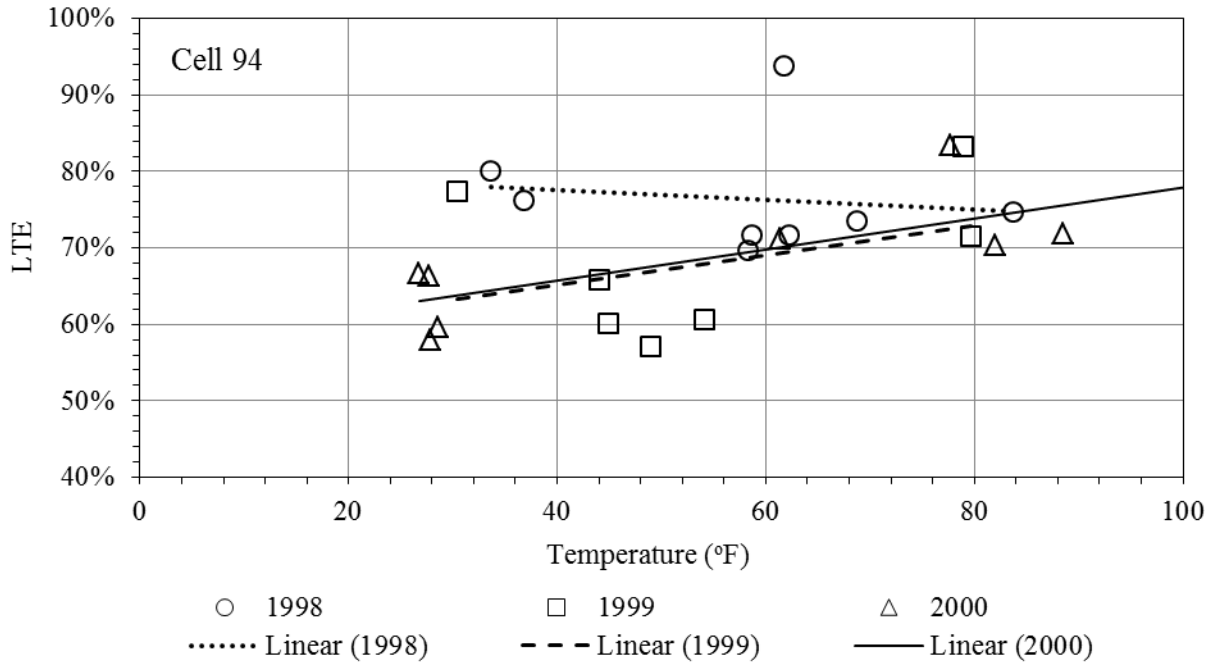
Figure 2.5. LTE vs pavement surface temperature for MnROAD Cell 94.
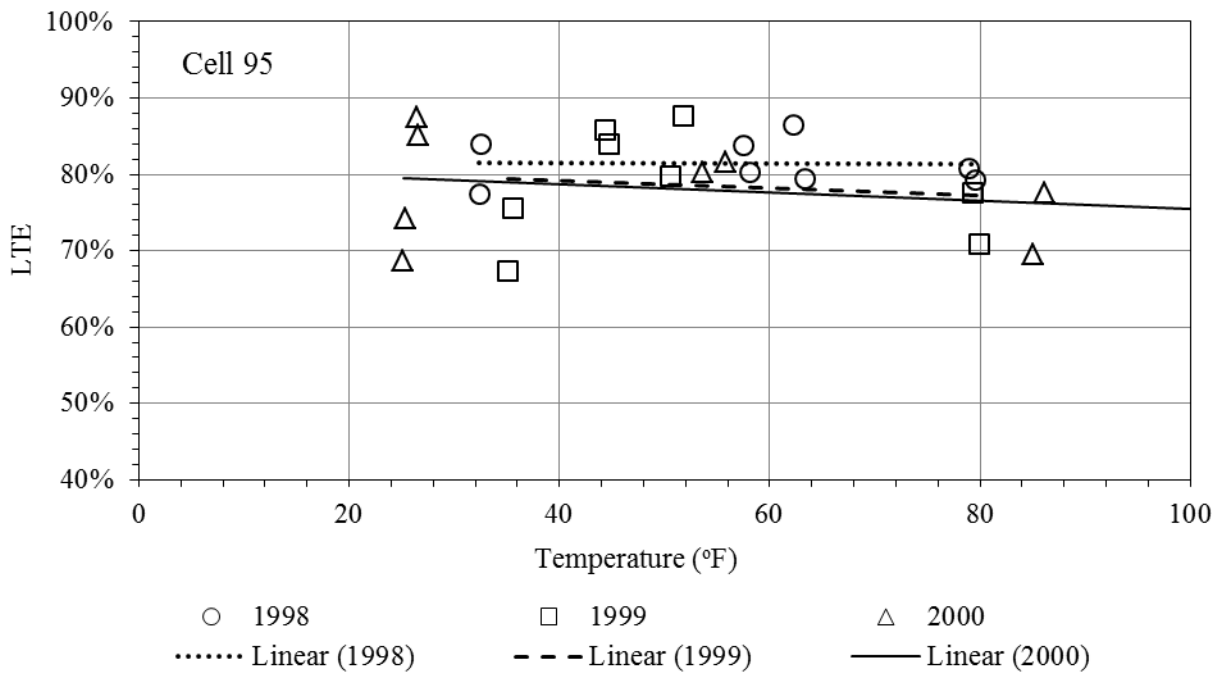
Figure 2.6. LTE vs pavement surface temperature for MnROAD Cell 95.

16
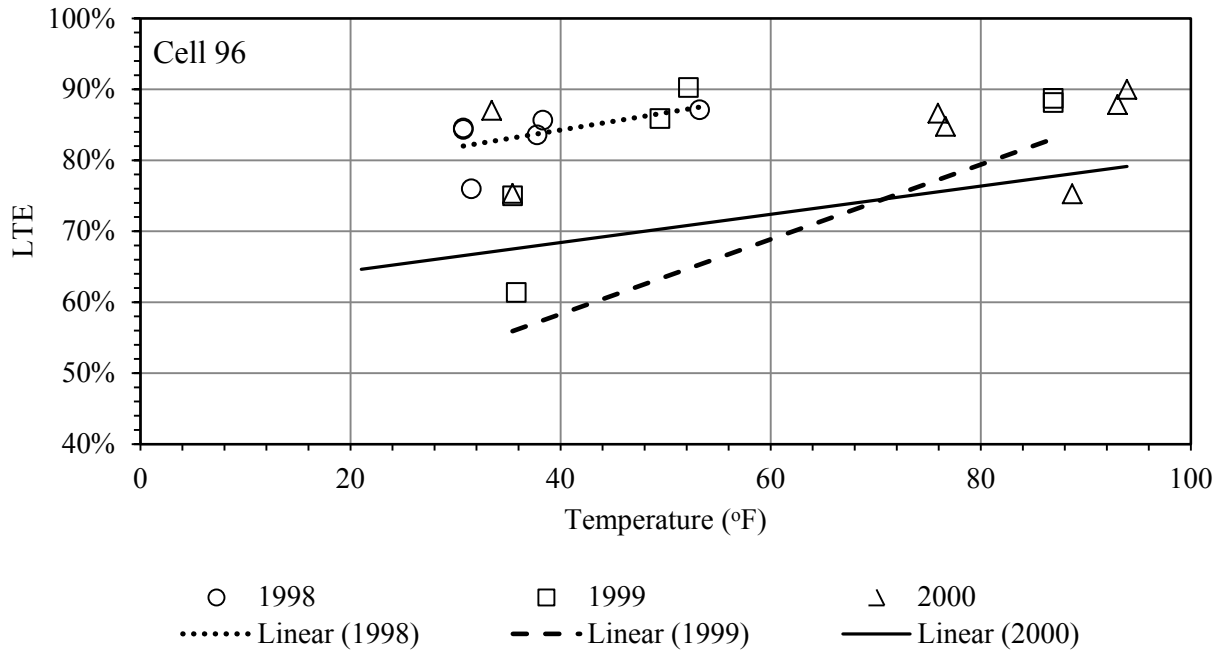
Figure 2.7. LTE vs pavement surface temperature for MnROAD Cell 96.

The LTE for Cell 95, which is a 5-ft x 6-ft and 3-in thick overlay on a 10-in HMA layer shows that LTE did not increase with temperature, but rather dropped by a marginal amount. Generally, when LTE is accomplished through aggregate interlock, LTE should increase with an increase in the temperature due to a decrease in crack width at higher temperatures. In all the cells, it can be assumed that the HMA layer underneath the PCC layer was a continuous layer, because, the stiffness of the HMA layer was higher than that of the PCC layer even during the hot summer. The potential for a crack propagating from one layer to the other layer is generally possible only when the later one experiences a lower stiffness at any time of the season (Vandenbossche & Barman, 2010). Therefore, it can be concluded that in all the cells, the HMA layer was able to transfer the load. Since, the LTE increased with the temperature in Cells 94 and 96, it can be concluded that a good amount of load was also being transferred through the concrete slabs. The opposite trend of the LTE vs temperature in Cell 95 can be explained by the

17

fact that the loss of load transfer through the HMA layer was larger than the increase in load transfer through the aggregate interlock when the temperature was higher during the summer. Moreover, Cell 95 was constructed with structural synthetic fibers, which might have helped in transferring load across the concrete slabs. LTE therefore always remained high for this cell, irrespective of the temperature variation. Therefore, it may be stated that when the HMA layer is thick, both the PC and HMA layers contribute to load transfer.

Roesler, et al., 2008 performed a study on the joint performance characteristics of an UTW constructed on a thin HMA layer. In that study, the frequency at which the joints propagated full depth was recorded. In a 4-ft x 4-ft UTW project constructed over a parking lot at the University of Illinois at Urbana-Champaign (UIUC) campus, during the Summer 2006, it was observed that every 5th to 8th joint cracked after approximately 24 hours. This UTW project was built with a 3.5- in FRC on a very thin, approximately 2-in thick HMA layer. FWD and ultrasonic testing was performed to evaluate joint load transfer after construction (in August 2006) and again after a couple of months (in October 2006). Figure 2.8 and Figure 2.9 present the LTEs measured at different stations in August 2006 and October 2006, respectively. In Figure 2.8, it can be seen that every 5th to 8th joints resulted in a lower LTE. A considerably low LTE at the joints as compared to the LTE at the center locations is an indication of the joints that cracked. Station numbers 5, 10 and 17 are assumed to have cracked after 24 hours post construction. In Figure 2.9, it can be seen that two months after construction, almost every other joint cracked. The other observation from the two figures is that the joints which cracked 24-hours after construction exhibited a lower LTE. Because of the longer effective length of the slab, the crack width became wider and a lower LTE was obtained as a result. This study

indicates that when both the HMA and PC layers are very thin, almost every other joint cracks and both the layers have an influence on the joint performance.
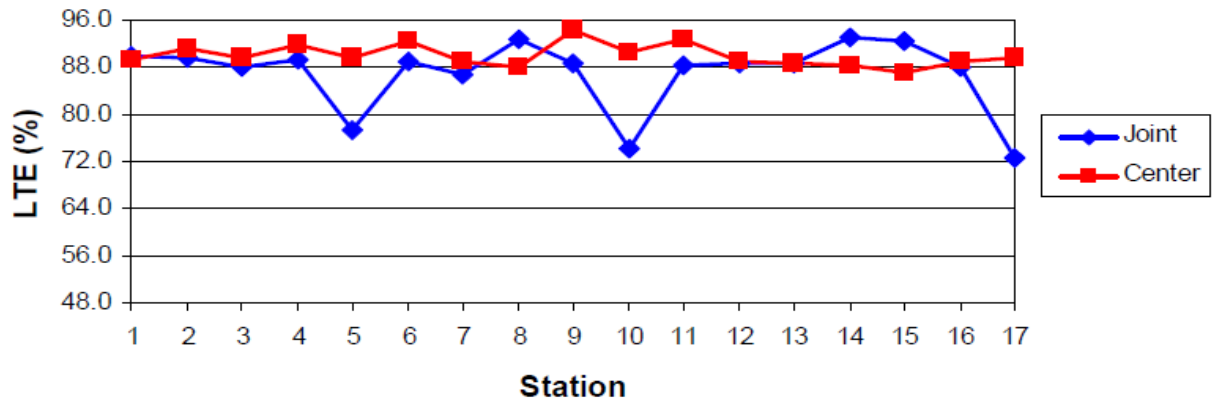
Figure 2.8. Load transfer efficiencies for UIUC E-15 Parking Lot – Parking Bay 1 (August 2006) (Roesler, et al., 2008).
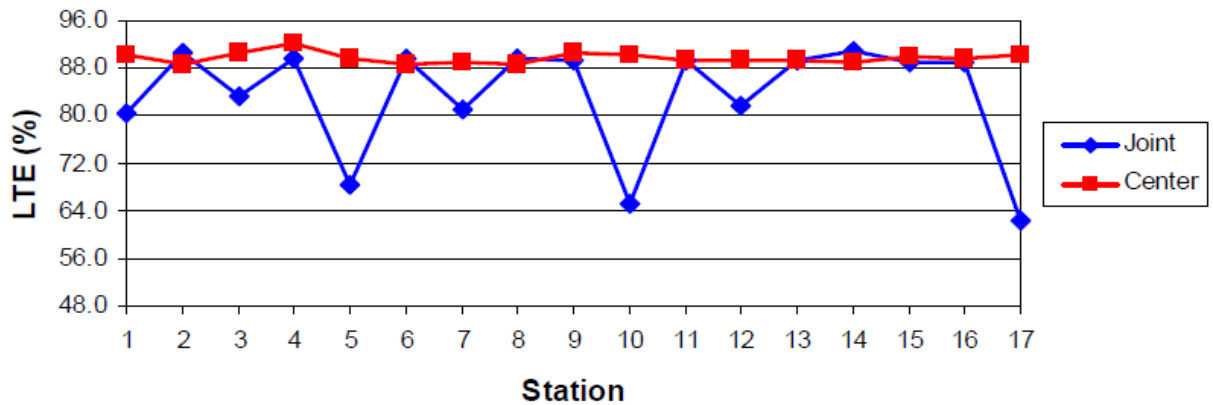
Figure 2.9. Load transfer efficiencies for UIUC E-15 Parking Lot – Parking Bay 1(October 2006) (Roesler, et al., 2008).

2.5   JOINT CRACK WIDTH RANGES

In another study (Roesler & Wang, 2009), it was shown that since smaller slab sizes are used in whitetopping, the joint opening remains narrow. Crack width data from MnROAD whitetopping

19

sections are studied to establish possible crack width range in different seasons. Figure 2.10 through Figure 2.12 present the crack widths for a few successive joints for Cells 93, 94 and 95, respectively, measured on different dates. The design features of Cells 94 and 95 were presented in Table 2.1 and the same information for Cell 93 is presented in Table 2.2. In Figure 2.10 (Cell 93), it can be seen that almost all of the joints actually cracked, and the crack width varies with season. Also, crack width variation is not same for all the joints. The maximum crack width (~ 0.030 in) was observed for Joint 3, in April 1998. In Figure 2.11 (Cell 94), it can be seen that every other joint exhibited a wider crack width. Joints 2 and 4 had the widest crack width, with the maximum occurring during the winter months (~ 0.042 to 0.068 in). In Figure 2.12 (Cell 95), Joints 2 and 5 exhibited wider crack widths, and again the widest crack width was observed during the winter months (~ 0.035 to 0.070 in).

Table 2.2. Summary of the design features for Cell 93 at MnROAD
(Barman, et al., 2010).

Cell No.	Age	Thickness of PCC slab (in)	Thickness of HMA layer (in)	Size of the slab (ft × ft)	Sealed joint (Y/N)	Doweled joint (Size/N)	Type of fiber reinforcement
93	Oct 97-Oct 04	4	9	4 × 4	Y	N	Polypropylene
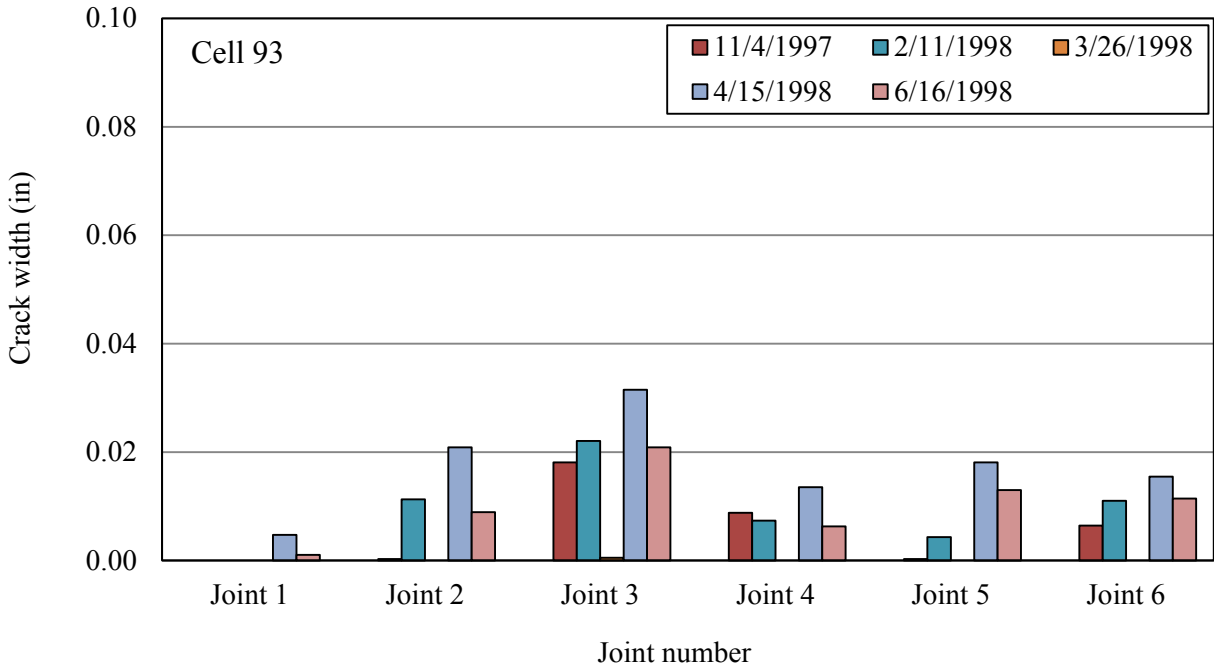
Figure 2.10. Crack width at different joints for MnROAD Cell 93.
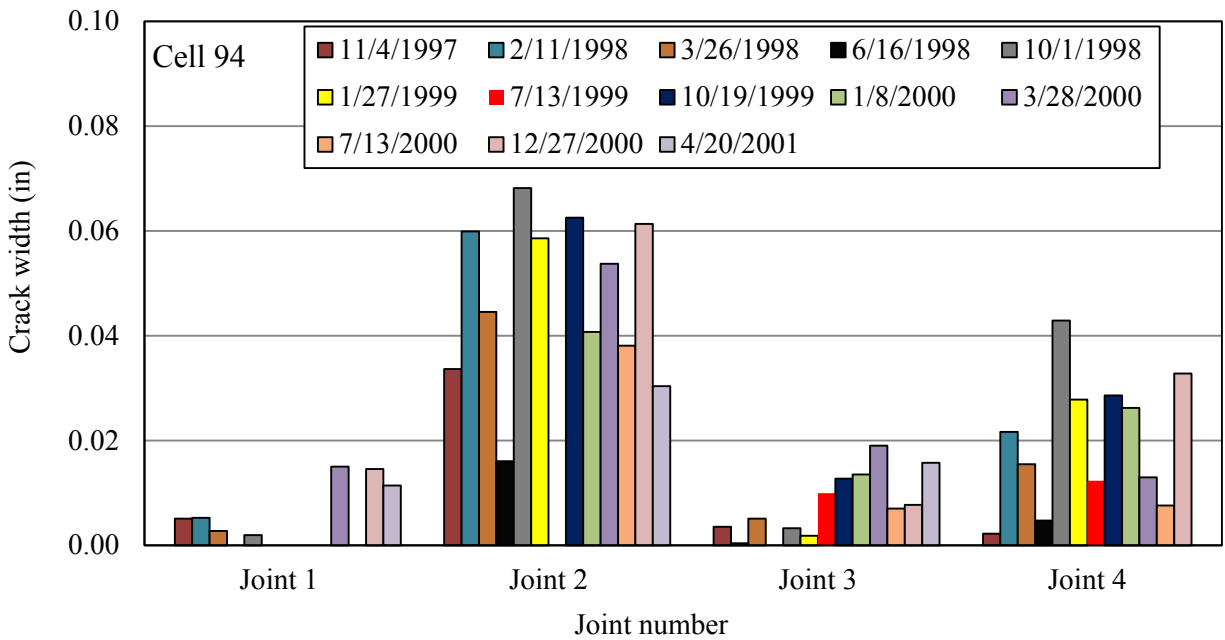
Figure 2.11. Crack width at different joints for MnROAD Cell 94.

21
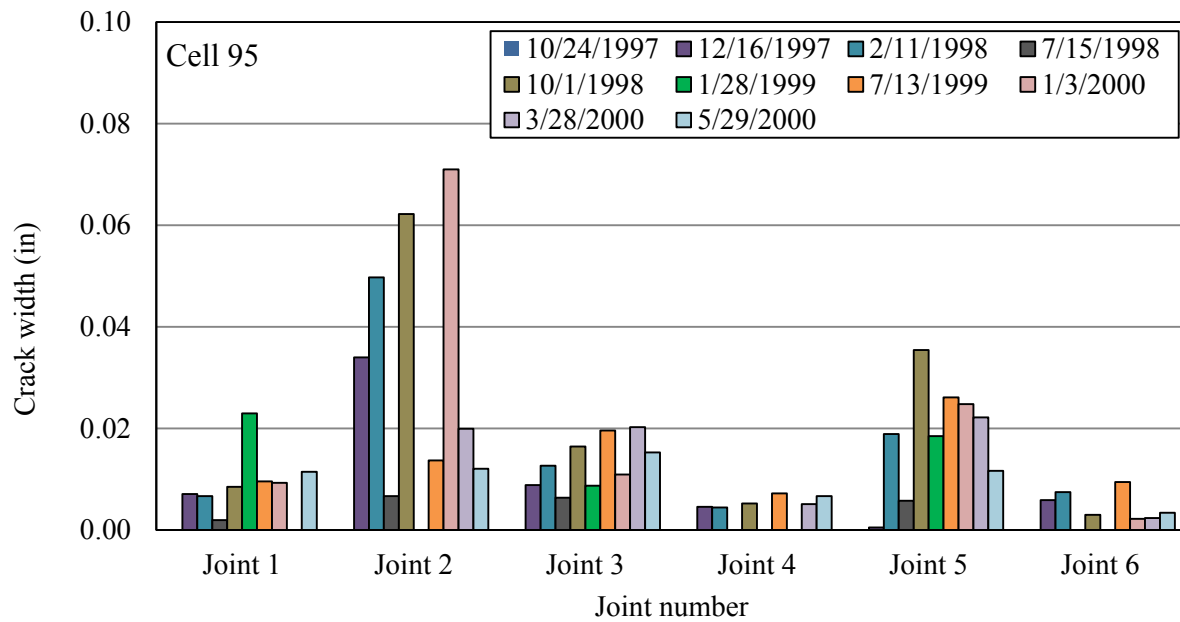
Figure 2.12. Crack width at different joints in MnROAD Cell 95.

2.6   INFLUENCE OF JOINT PERFORMANCE

The joint performance influences the integrity of the entire overlay system and contributes to the initiation of distresses. Poor joint performance mainly influences (i) debonding of the HMA layer from the UTW and (ii) the load related stress under the loaded slab. The following subsections describe the influence of joint performance with regards to both of the issues.

2.6.1   Debonding of HMA Layer

Differential deflections play an important role in debonding of the HMA layer from the concrete overlay. Normally, on the loaded side of the joint, the concrete slab and HMA layer are directly deflected under the compression exerted by the wheel load. The deflections exhibited by both the layers are same as a result. The stress at the interface (in the vertical direction) is compressive in nature. On the unloaded side, the nature and magnitude of the stress at the interface depend on the magnitude of differential deflection. In general, this stress would be tensile in nature in this case. In this dissertation this tensile stress is referred as the 'debonding stress.' Figure 2.13 shows the probable scenarios when the joint performance is high and low. At a high joint performance (Figure 2.13 a), the overlay and the HMA layer on the unloaded side exhibit a similar deflection to that of the loaded side layers exhibit. The debonding stress at the interface is lower in this case. At a low joint performance (Figure 2.13 b), the deflection on the unloaded slab is lower than the deflection on loaded slab. Since, the HMA layer is a continuous layer, the wheel load generated tensile stress tends to debond the HMA layer from the overlay, on the unloaded side. The tensile stress contributing to the debonding will be referred to as a 'peeling stress,' in this dissertation.

23

2.6.2 Stress in the Loaded Slab

For good joint performance, when the joint shear stiffness is higher, a larger percentage of the wheel load is transferred to the adjacent slab, or it can be said that the wheel load is distributed over a larger area. This reduces the stress on the loaded slab where the distress initiates. Figure 2.13 schematically shows the higher and lower load-related stress at the bottom of overlay at low and high joint performance conditions, respectively. It may also be added that at a good joint performance when the layers are properly bonded, the neutral axis of bending shifts downward resulting in lower tensile stress at the bottom of whitetopping.
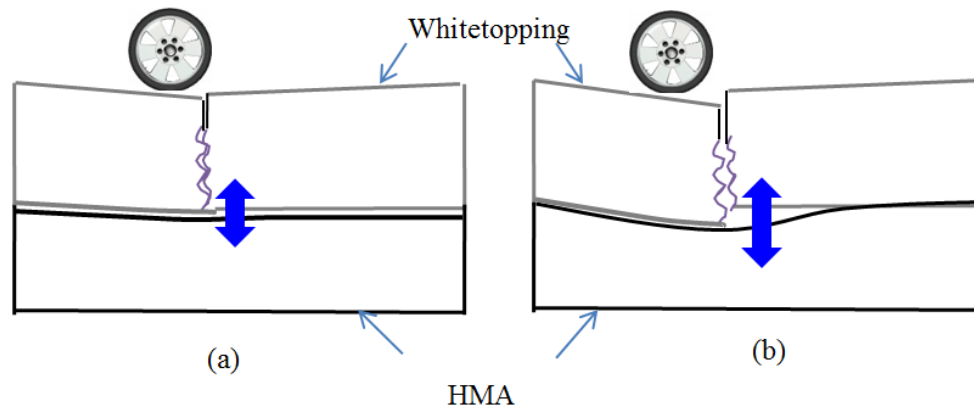
Figure 2.13. Schematic of debonding stress at the interface (a) Higher joint performance, (b) Lower joint performance.

2.7   JOINT PERFORMANCE EVALUATION PROCEDURES IN LITERATURE

The joint performance of an in-service pavement is typically evaluated by non-destructive methods. Usually falling weight deflectometer (FWD) testing is conducted to measure the deflections on both sides of the joint under a dynamic load. These deflections are used to

24

calculate the LTE. Such evaluations are very helpful in determining the structural condition of the joints for in-service pavements. However, this information does not become available during the design process. It would be a great opportunity if the joint performance behavior of the concrete to be used is known during the design process. The joint performance in regards to different variables, such as aggregate and concrete properties, crack width and crack face texture, will be great information to put into the design procedure. Different researchers thereby proposed different laboratory procedures to characterize the joint performance of concrete. This section describes a few laboratory joint performance testing setups developed by different researchers.

Colley & Humphrey, 1967, and Nowlen, 1968 developed a laboratory joint performance test setup, as shown in Figure 2.14. This setup was utilized to establish the effect of crack width on the joint performance through the aggregate interlock mechanism. Two types of subbase (i) 6-in thick sand gravel and (ii) 6-in thick cement treated gravel were considered. The schematic of the instrumentations on the test slabs is shown in Figure 2.15. Loading was applied through two actuators providing 9-kip loads, at a designed phase difference. The time difference between the two peak loads was 0.02 seconds, which was simulating a 30 mph vehicle speed. The applied load profiles and corresponding deflection profiles on the approach and leave slabs are shown in Figure 2.16.
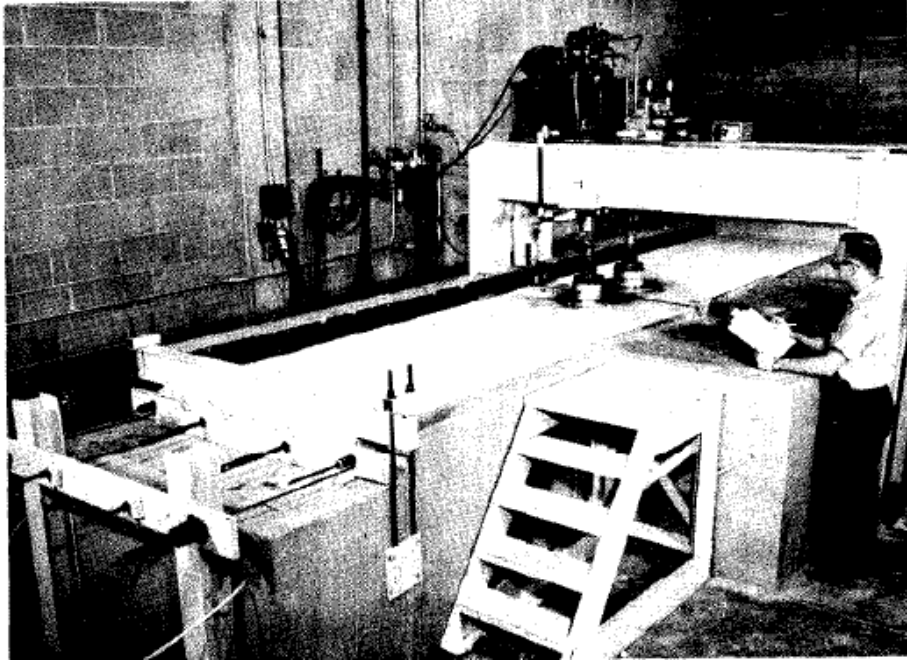
Figure 2.14. Joint performance evaluation setup (Colley & Humphrey, 1967 and Nowlen, 1968).
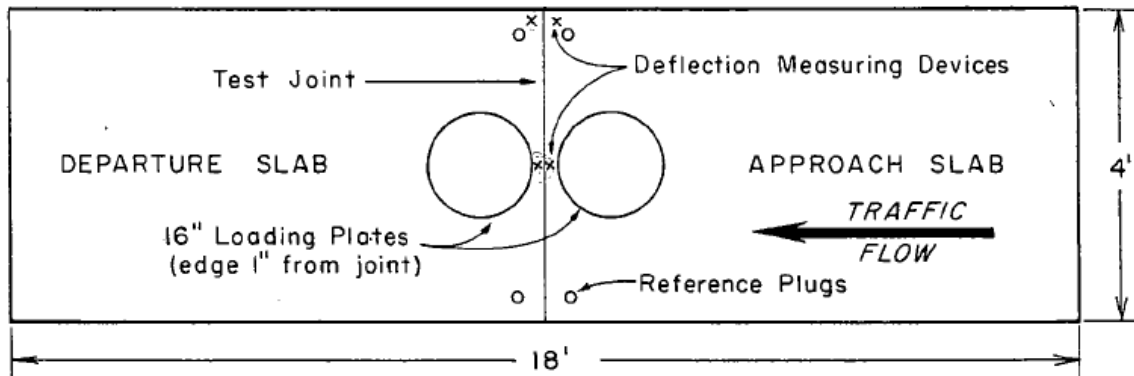
Figure 2.15. Schematic of the instrumentations on the test slabs (Colley & Humphrey, 1967 and Nowlen, 1968).

26
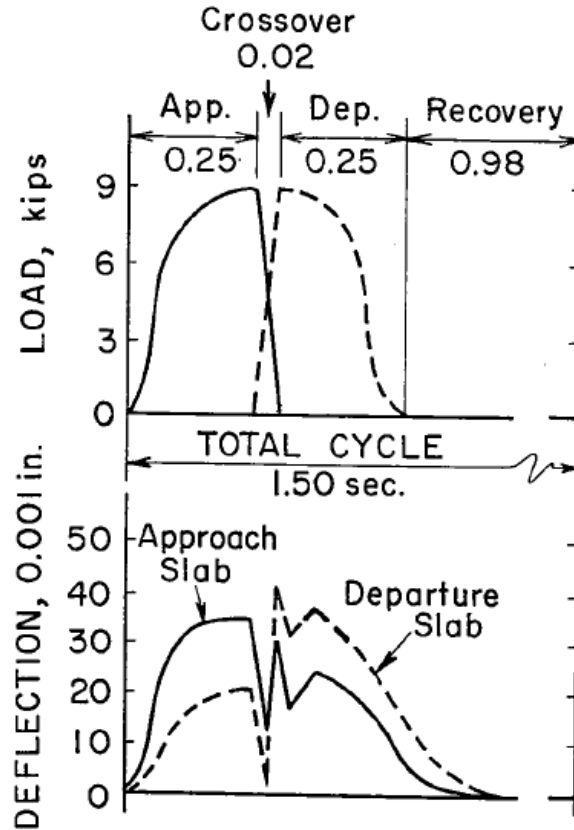
Figure 2.16. Load and deflection profiles (Colley & Humphrey, 1967 and Nowlen, 1968).

Raja & Snyder, 1995 studied the joint performance behavior of jointed reinforced concrete pavement (JRCP) slabs. In that study, joint performance of the slabs cast with different types of aggregates were investigated. Figure 2.17 is a schematic of the test stand used in their study. The foundation support under the test slab was provided by layers of semi rigid neoprene pads. The stiffness of the neoprene pad was equivalent to the composite stiffness of the granular layers beneath the slab. Two different moduli of subgrade reaction (k), 100- and 250-psi/in, were considered. The slabs were tested with a sinusoidal loading profile, as shown in Figure 2.18. The deflections of the loaded and unloaded slabs were measured to estimate the LTE at different crack widths and load repetitions.

27
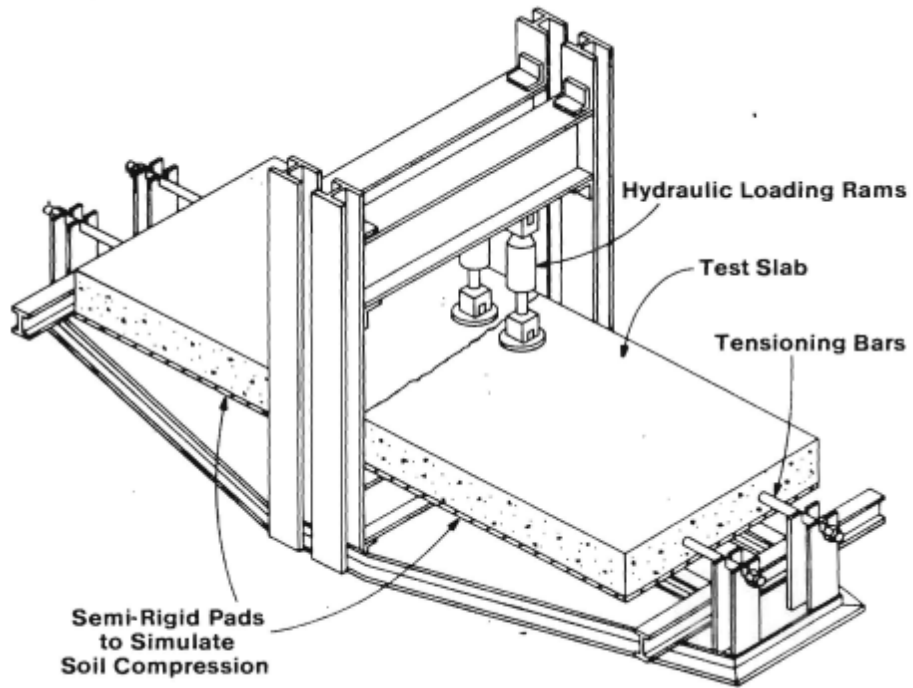
Figure 2.17. Schematic of the joint performance test frame in Raja & Snyder, 1995 study.
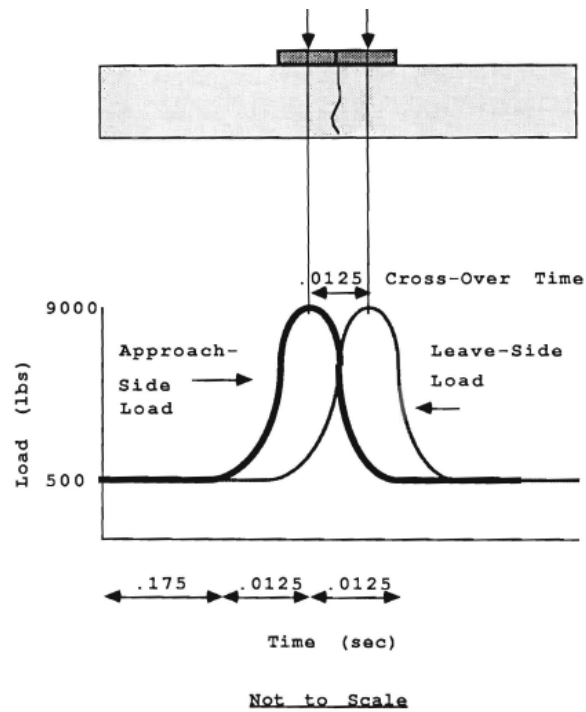
Figure 2.18. Load profile in Raja & Snyder, 1995 study.

28

A large-scale laboratory slab testing system was developed by Jensen & Hansen, 2001 as shown in Figure 2.19. The instrumentation on the test slabs is shown in Figure 2.20. In this study, the instrumented slab was placed on a 4-in open graded drainage course on a 16-in thick subbase. The vehicle wheel load was simulated by a single actuator. The magnitude and frequency of the applied load were 9-kip and 3 Hz, respectively. LTE was measured at different crack widths.

Figure 2.19. LTE test frame in Jensen & Hansen, 2001 study.

△ Schematic sensor layout along slab length
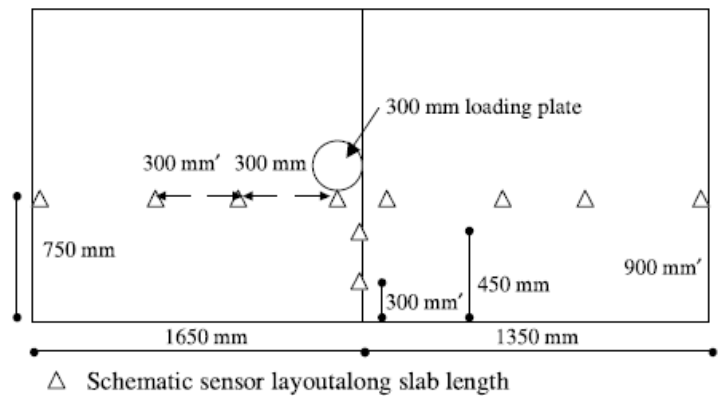
Figure 2.20. Slab instrumentation of joint performance test at Jensen & Hansen, 2001 study.

Brink, et al., 2004 conducted a joint performance study on 9-in thick slabs placed on an artificial foundation. The artificial foundation simulating the subbase support was prepared by

29

using a 2-in thick re-usable rubber layer. The rubber layer provided a composite modulus of subgrade reaction equal to 300 psi/in. A schematic of the test setup can be seen in Figure 2.21. Similar to the Colley & Humphrey, 1967 and Raja & Snyder, 1995 joint performance studies, the vehicle load was simulated using two actuators, with a 9-kip peak load applied by actuator. The peak loads on the actuators were applied in the form of a sinusoidal loading, with a phase difference, so that a 50 mph vehicle speed is attained. The dynamic load frequency was 3 Hz. Static and dynamic load transfers and the relative movement of the slabs were measured at different crack widths.

Arnold, et al., 2005 developed a small-scale laboratory joint performance test setup. Using this setup, a half-scale prism specimen was used for evaluating joint performance. In this procedure, 16-in x 4-in x 4-in beams were cracked at two locations, as shown in Figure 2.22. Upward and downward load cycles were applied at the center piece of the beam to create a mechanical action that simulates a vehicle passing the approach and leave slabs. The main disadvantage of this test setup is the avoidance of a foundation layer. The load magnitude was determined by simulating the equivalent mechanical action of an in-service pavement. Three different load magnitudes were considered, which includes $\pm$ 0.45 kip, $\pm$ 0.90 kip and $\pm$1.35 kip. This was to simulate $\pm$ 5.6 kip, $\pm$ 11.2 kip and 16.8 kip loads. The sinusoidal load profile that was used in the study can be seen in the Figure 2.23.
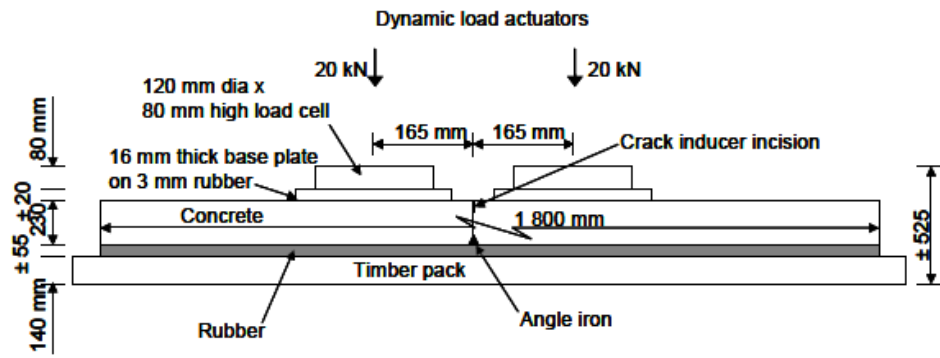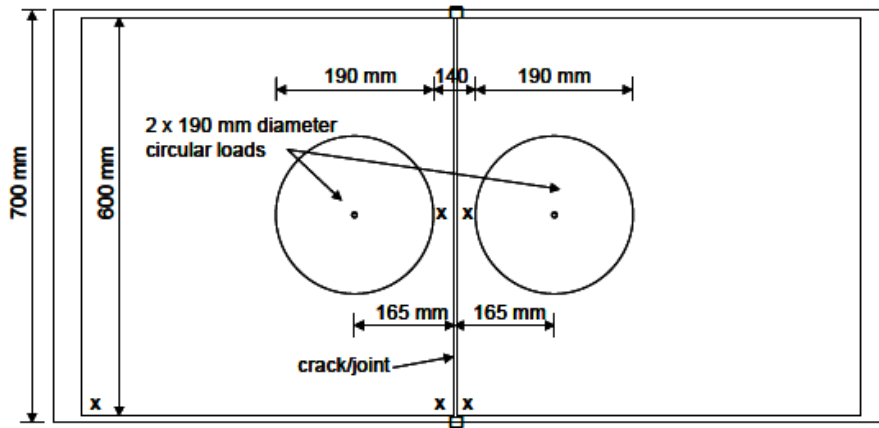
Figure 2.21. Schematic layout joint performance test setup in Brink, et al., 2004 study.
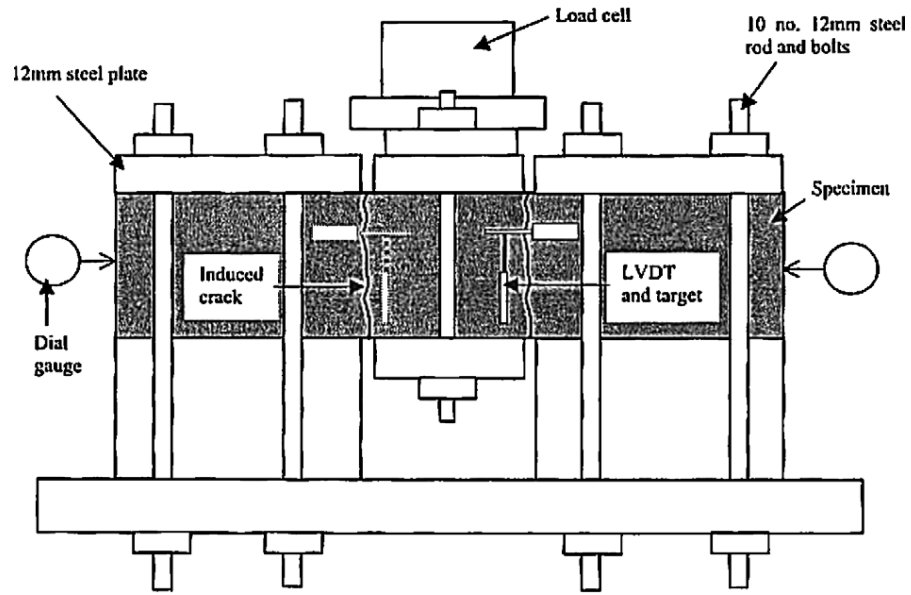
Figure 2.22. Joint performance test setup in Arnold, et al., 2005 study.
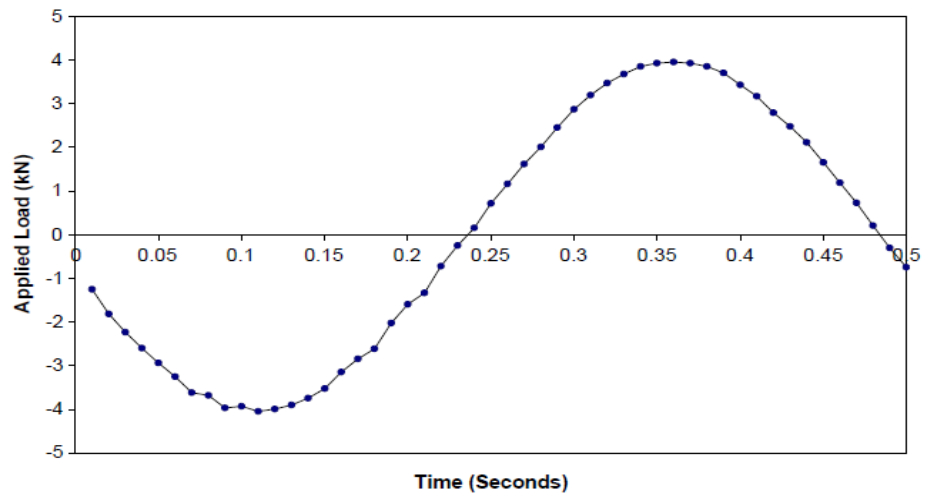
Figure 2.23. Load profile in Arnold, et al., 2005 study.

2.8   FACTORS INFLUENCING JOINT PERFORMANCE

The factors influencing the joint performance are discussed in this section. The main factor contributing to joint performance is the aggregate interlock, apart from the dowel action provided by the dowel bars or fibers, if any. The joint performance provided by aggregate interlock is a function of crack width and surface texture of the cracked face. The following subsection introduces the different factors that influence the aggregate interlock.

2.8.1   Volumetric Surface Texture

A larger amount of texture on the surface of the crack face of the slab results in a higher joint performance by engaging more aggregate particles in transferring the load. Vandenbossche, 1999 proposed a relationship to establish the joint performance based on surface texture and crack width (*cw*). Surface texture is quantified using the volumetric surface texture ratio (VSTR). It is the volume of texture per unit surface area of the crack face. In the volumetric surface texture (VST) test, the distance (d_i) of the crack surface from an arbitrarily selected datum is measured by using a probe or a laser profiler. Figure 2.24 shows a VST test setup used in the Vandenbossche, 1999 study. Generally, the crack face is divided into equal grids. Distance is measured at the center of each grid. A graphical representation of the VSTR measurements and calculations can be seen in Figure 2.25. The average distance (d_{avg}) of the individual distances (d_i) is calculated as follows:

$$d_{avg} = \frac{\sum_{1}^{n} d_i}{n} \qquad (2.5)$$

33

where n is the number of the grids on the crack surface. The residual (r_i), which is the difference between the average distance and distance of individual grids (d_i), is calculated by the following Equation.

$$r_i = d_i - d_{avg} \tag{2.6}$$

Then, the volume of each individual grid is calculated by using Equation (2.7).

$$V_i = r_i * A_i \tag{2.7}$$

where is V_i is the volume and A_i is the area of each grid on the crack surface. A positive value of V_i represents the volume of texture above the plane determined by d_{avg}. A negative value of V_i represents the volume of the texture below the plane. The algebraic sum of V_i obtained for each grid provides the volume of surface texture (VST) as given by the following Equation.

$$VST = \sum_{1}^{n} abs(r_i * A_i) \tag{2.8}$$
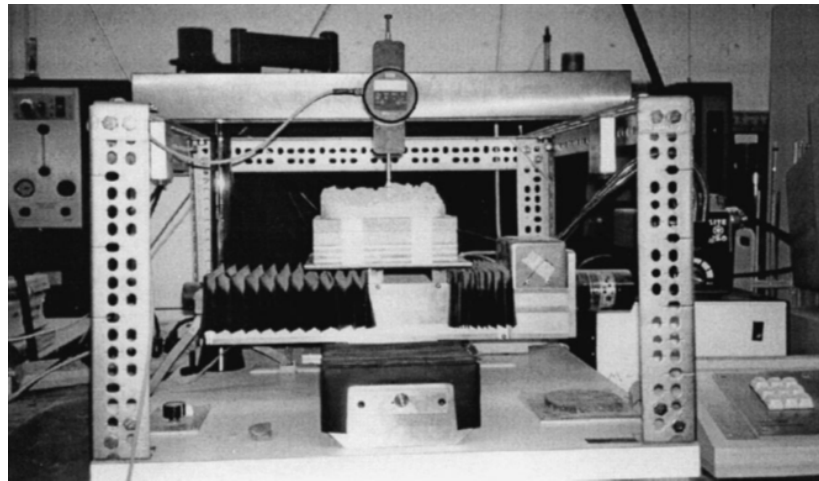
Figure 2.24. VST test setup in Vandenbossche, 1999 study

Test Area

$= i^{th}$ square where d_i is measured   A = Area of each square

$$VSTR = \{\Sigma abs[r_i A]\}/ab$$

Plan View

d_i

$r_i = d_i - d_{ave}$

Profile View
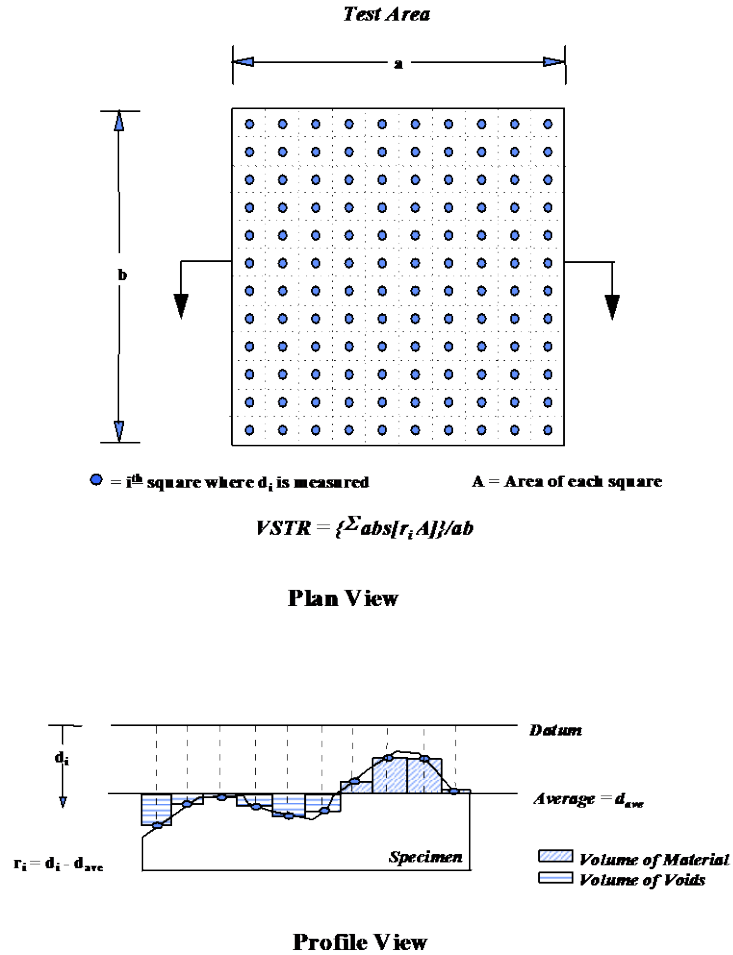
Figure 2.25. Graphical representation of VSTR measurements (Vandenbossche, 1999).

Vandenbossche, 1999 developed a relationship for the LTE as a function VST normalized by cw. Figure 2.26 presents the relationship that was developed with the laboratory test results. The proposed model is given by Equation (2.9).

$$LTE = 39.7 \cdot \log\left(\frac{VST}{cw}\right) + 5.6 \tag{2.9}$$

where *LTE* is the deflection load transfer efficiency in percent, VST is the volumetric surface texture in cm^3/cm^2 and *cw* is the crack width in cm.

Figure 2.27 presents the relationship between the *VST* and *AGG*. Laboratory test results were used to develop this model. The regression model is given in Equation (2.10).

35

$$AGG = 105.72e^{2.367\log(VST/cw)}$$

(2.10)

where *AGG* is the joint spring stiffness expressed in kPa/mm, the *VST* is the volumetric surface texture in cm^3/cm^2.
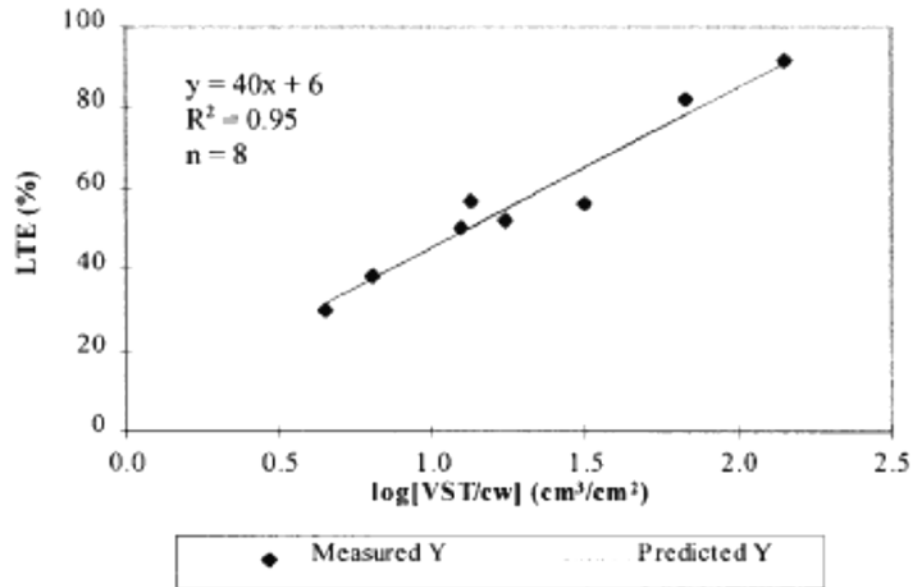
Figure 2.26. Regression model for LTE as a function of VST and *cw* (Vandenbossche, 1999)

36
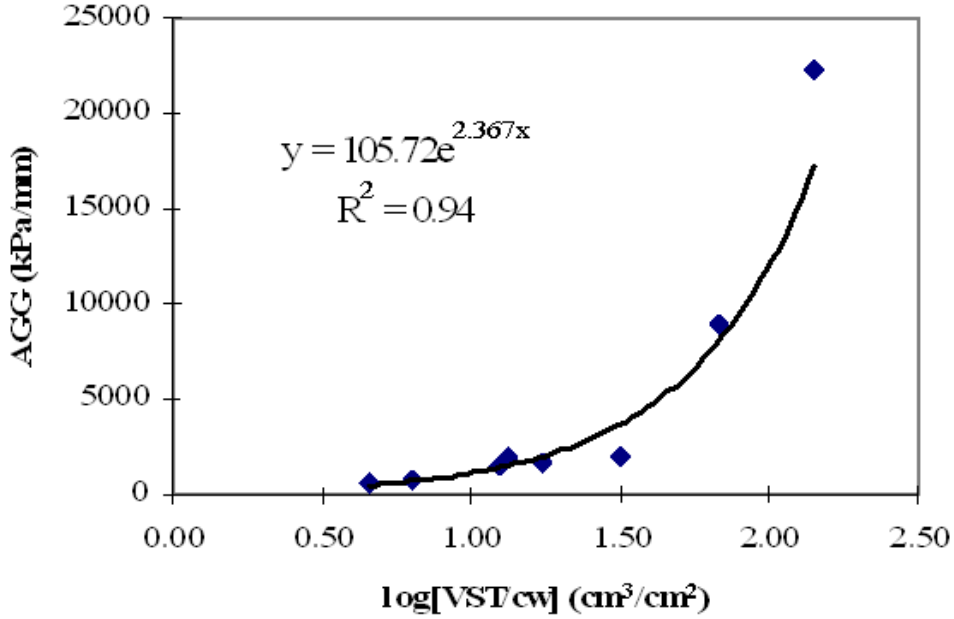
Figure 2.27. Regression model of *AGG* as a function of VST and *cw* (Vandenbossche, 1999).

Ramirez, 2010 modified the above model so that *AGG* could be estimated as a function of slab thickness, *VST* and *cw*. The modified model is given below.

$$AGG = \left[105.72 * e^{2.367 * \log\left(\frac{VSTR * a * ST}{cw}\right)} \right] * b \qquad (2.11)$$

where *a* and *b* are constants equal to 2.54 and 3.6838, respectively, for unit conversion (from US customary unit to SI unit), *ST* is the slab thickness in cm and *cw* is the crack width in cm.

The volumetric surface texture is a function of the type, shape, top size, and gradation of the coarse aggregate, and the water cement ratio. Since the *VST* influences the joint performance; a discussion on the factors that affects the *VST* are also included.

37

Aggregate type

The hardness of the aggregate, which is related to the abrasion resistance capability and toughness, influences the volumetric surface texture. With the presence of harder aggregates in the concrete, the crack meanders around the aggregates and produce a rougher fracture face (Vandenbossche, 1999; Chupanit & Roesler, 2008 and Ramirez, 2010). Figure 2.28 shows examples of fracture faces of concrete with a harder type aggregate, such as limestone, and a softer aggregate, such as slag. The study conducted by Vandenbossche, 1999 indicates that the concrete with the stronger aggregates (limestone in this case) possesses a higher VSTR than that of softer aggregates (gravel or slag in this case). See Figure 2.29. This graph shows the average VSTRs for eight specimens, for a coarse aggregate top size of 1.5 in. Since, the concrete prepared with harder aggregates as compared to softer aggregates exhibits a higher VSTR, the joint performance is also likely to be improved.
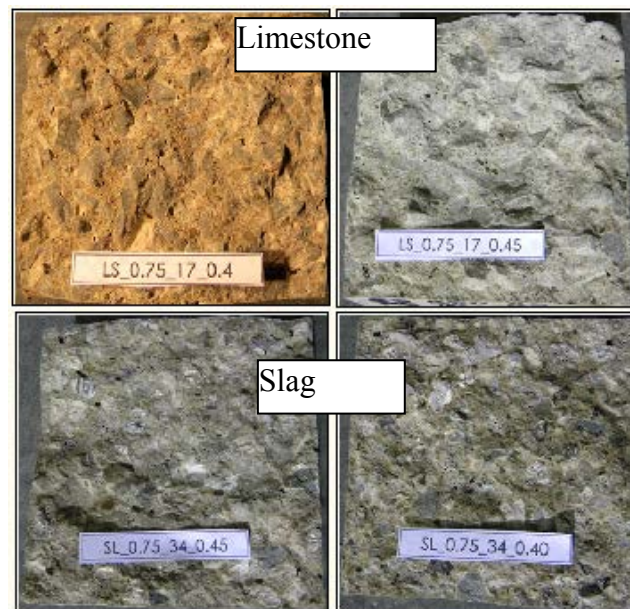
Figure 2.28. Example of fracture surface for two types of aggregates, (after Ramirez, 2010).
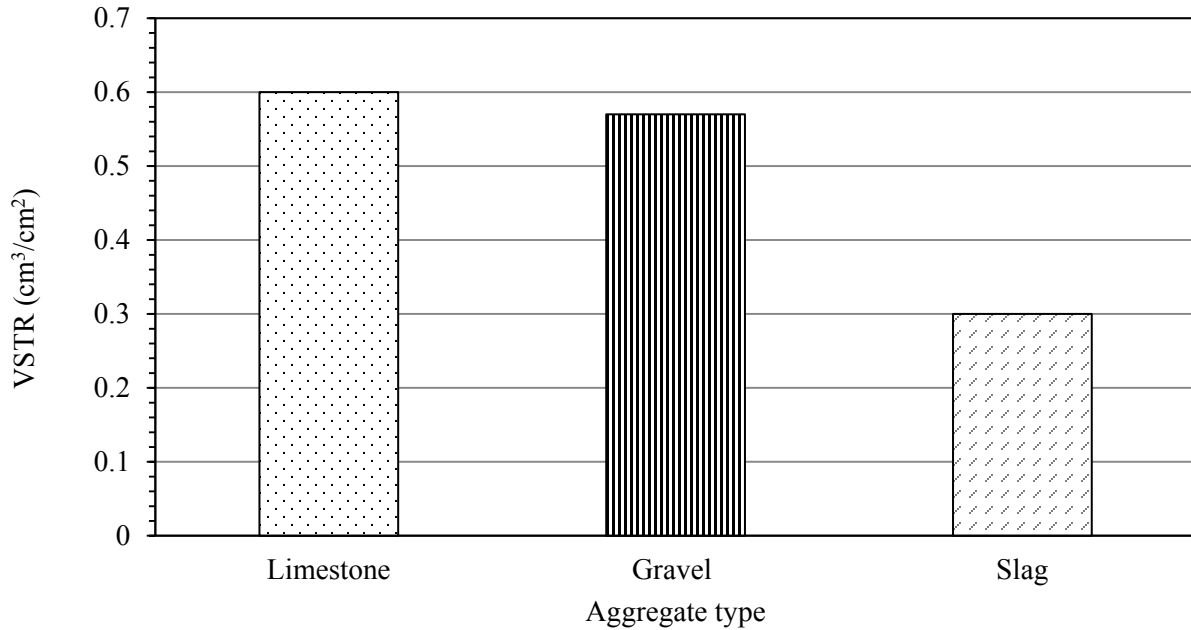
Figure 2.29. Effect of coarse aggregate type on VSTR (after Vandenbossche, 1999).

The study conducted by Raja & Snyder, 1995 also shows that harder aggregates exhibit lower abrasion under load cycles. Figure 2.30 is a comparison of the LTE obtained for virgin gravel, limestone and slag aggregates (Raja & Snyder, 1995). It can be seen that limestone aggregates not only exhibits a higher LTE but maintain a higher LTE for a larger number of load cycles. Similar findings were published by Colley & Humphrey, 1967. In Figure 2.31, it can be seen that aggregates with a lower Los Angeles Abrasion value result in a higher joint effectiveness. The joint effectiveness is given by the following equation.

$$E_j = \frac{2d'_u}{d'_u + d'_l} \tag{2.12}$$

where E_j is the joint effectiveness, d'_l and d'_u are the deflections of the loaded and unloaded slab, respectively.

39
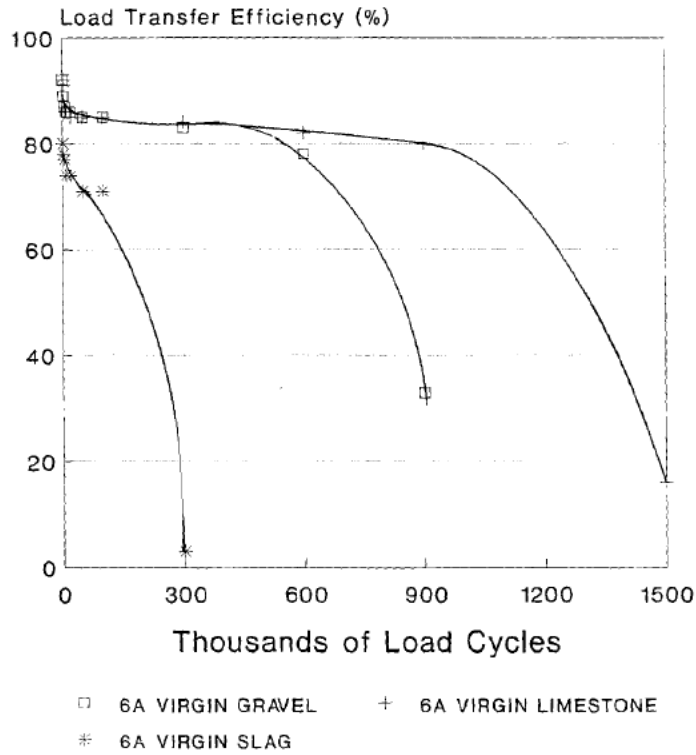
Figure 2.30. Effect of coarse aggregate type on LTE (Raja & Snyder, 1995).
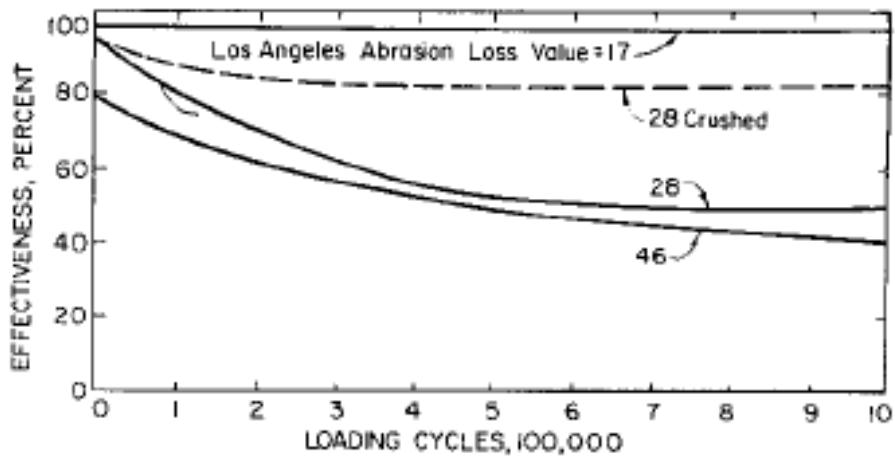
Figure 2.31. Effect of Los Angeles Abrasion value on LTE (Colley & Humphrey, 1967).

40

Coarse aggregate angularity

Several research studies have shown that the angularity of the aggregates also influences joint performance. Colley & Humphrey, 1967 compared the joint effectiveness of crushed gravel and natural gravel. Figure 2.32 shows that the angular crushed gravel mantians a higher joint effectiveness for a larger number of load cycles than that of the smoother natural gravel.
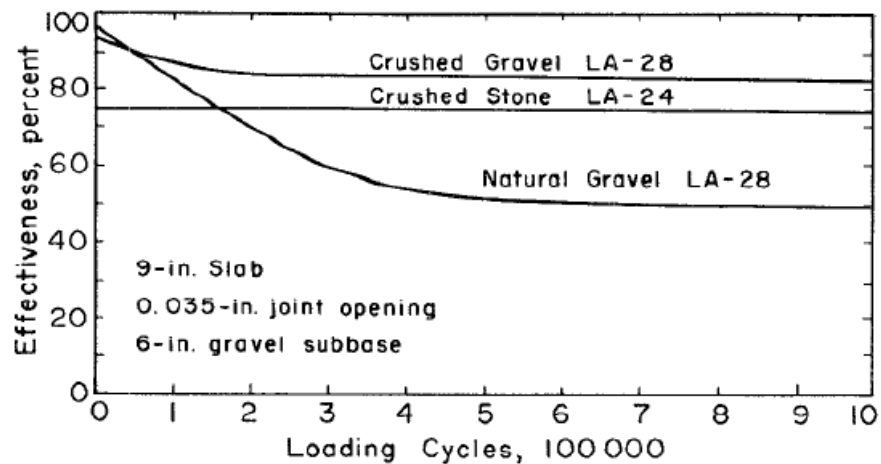
Figure 2.32. Influence of aggregate shape (angularity) on joint effectiveness (Colley & Humphrey, 1967).

Coarse aggregate top size

It is natural that when larger aggregates are used in the mix, the crack becomes more tortuous and results in a higher VSTR when compared to smaller size aggregates (Vandenbossche, 1999; Chupanit & Roesler, 2008; 2005 and Ramirez, 2010). Figure 2.33 shows concrete composed of 2.5-in top size aggregates results in a higher VSTR than the concrete with 1.5-in top size aggregate (Vandenbossche, 1999). Since, the VSTR of the concrete with coarser aggregates is higher, it is natural that joint performance will also be higher (Nowlen, 1968, Raja & Snyder, 1995, Jensen & Hansen, 2001).

Figure 2.34 shows that 1-in gravel (6 A virgin gravel) results in a higher LTE than a 0.75-in gravel aggregates (Raja & Snyder, 1995). The findings published by Colley & Humphrey, 1967 also support this fact. In Figure 2.35, it can be seen that the concrete composed of 2.5-in top size aggregates, as compared to 1.5- and 0.75-in top size aggregates, resulted in a higher joint effectiveness.
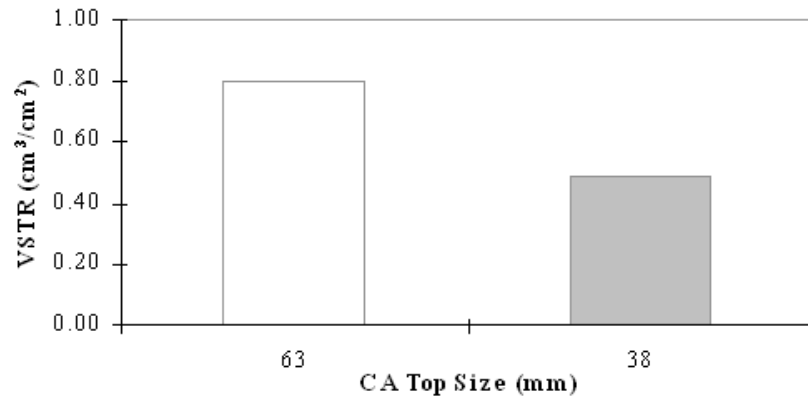
Figure 2.33. Influence of coarse aggregate top size on VSTR (Vandenbossche, 1999).
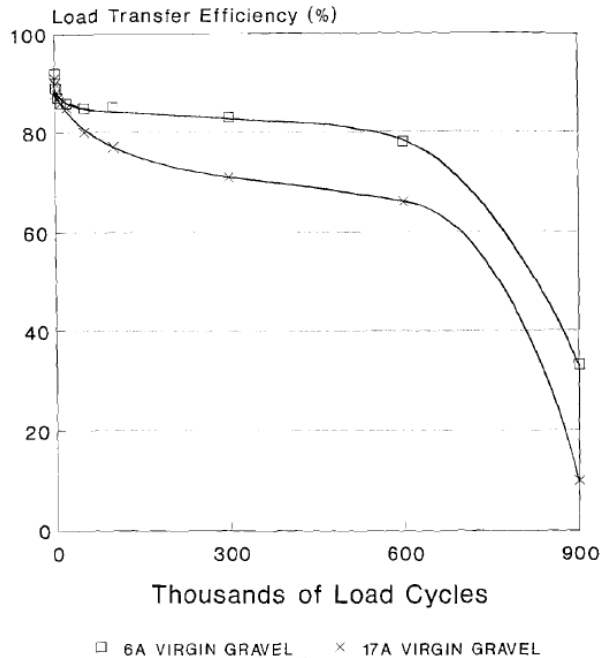
Figure 2.34. Influence of aggregate top size on LTE (Raja & Snyder, 1995).

42
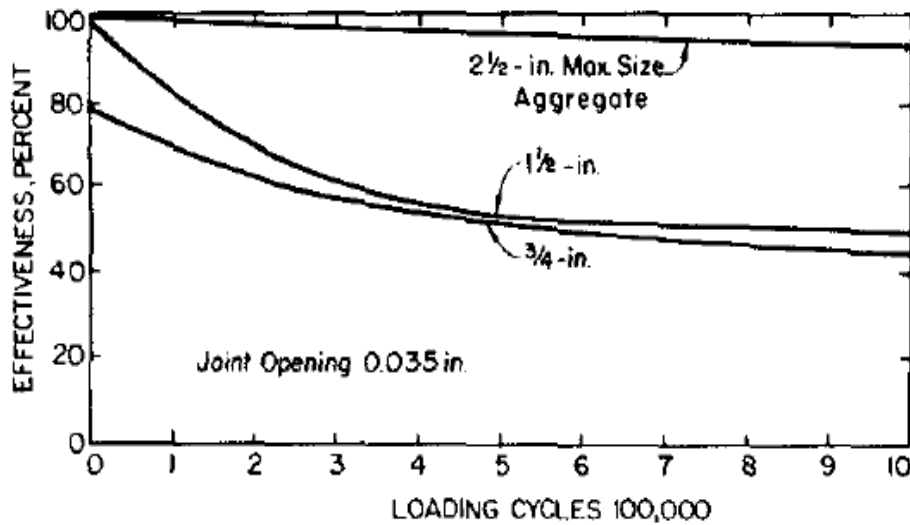
Figure 2.35. Influence of aggregate top size on joint effectiveness (Colley & Humphrey, 1967).

Coarse aggregate gradation

Aggregate gradation may also influence the surface texture of the fractured face. Unfortunately, only a very limited study is available to draw a sound conclusion about the sensitivity of the aggregate gradation. Chupanit & Roesler, 2008 conducted a study with a gap and dense graded aggregate. They concluded that the matrix with a gap gradation when compared to a dense gradation, exhibits slightly higher VSTR.

Age at crack initiation

The time of cracking of the specimen is an important factor, because, it influences the meandering of the crack. Nowlen, 1968 found that inducing cracks in the specimen at an early age results in a higher joint performance than when the specimen is cracked at a later age. At an early age, the strength of the matrix remains lower than that of the strength of the aggregates.

43

That is why when the concrete is cracked at an early age, cracks form around the aggregates and not through the aggregates. Figure 2.36 shows the joint effectiveness vs load cycle relationship for the concrete (with similar mix proportion) cracked at three different ages. This study was conducted on a 9-in concrete slab on top of a 6-in gravel subbase. The crack width was 0.035 in. It can be seen that the slab cracked after 7 days resulted in a lower load transfer when compared to the slabs cracked after 1- and 3-days.
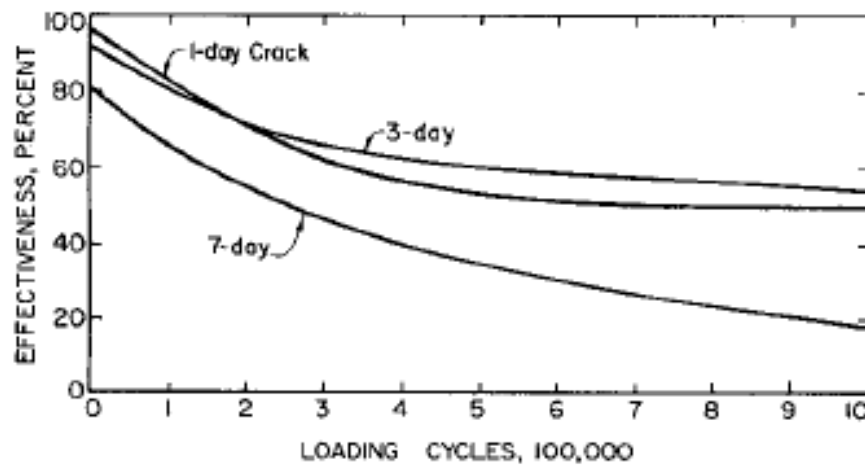
Figure 2.36. Influence of time of cracking on joint effectiveness (Nowlen, 1968).

2.8.2   Crack Width

Perhaps the most important variable that influences the joint performance is the crack width. Several studies have been conducted to establish the joint performance vs crack width relationship considering different pavement conditions, such as different support conditions, aggregate types and number of load cycle (Benkelman, 1933, Colley & Humphrey, 1967; Hansen, et al., 1998 and Jensen & Hansen, 2001).

44

In a study conducted by Hansen, et al., 1998, it was found that the joint performance starts decreasing at a crack width greater than 0.025 in (0.6 mm). See Figure 2.37. In the Jensen & Hansen, 2001 joint performance study (setup was discussed in Section 2.7), three significant stages of load transfer were identified, as shown in Figure 2.38. At stage I when the crack width remains lower than 0.02 in (0.5 mm), the LTE is near 100 percent. The load transfer at a crack width between 0.025 in (0.6 mm) and 0.10 in (2.5 mm) is referred as stage II. At this stage, the aggregate interlock is very important. Figure 2.38 and Figure 2.39 show the normalized deflection vs crack width and LTE vs crack width, respectively. The magnitudes of the loaded side deflection and the differential deflection increase with increases in crack width. However, the trends are not the same for different aggregate types (compare Figure 2.38 a and b) and aggregate top sizes (compare Figure 2.38 b and c). This study also compared the LTE vs *cw* relationship for two aggregate top sizes. The drop in LTE is lower in the case of 2-in glacial gravels as compared to 1-in glacial gravels. The load transfer at a crack width beyond 0.10 in is referred as stage III. At this stage, aggregate interaction basically diminishes and load is transferred primarily through the foundation.
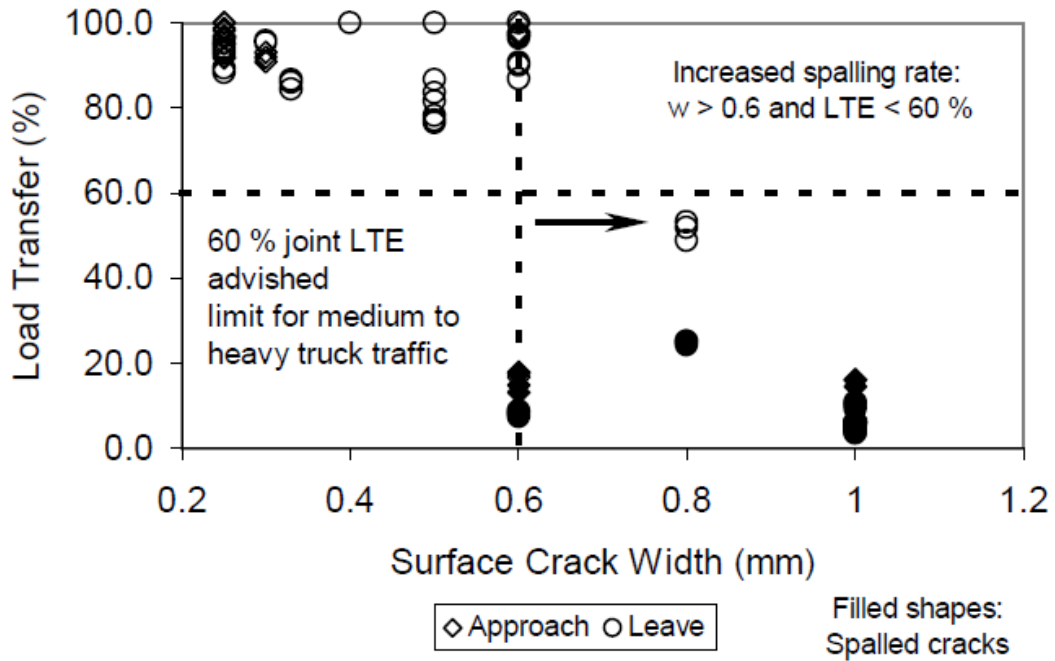
Figure 2.37. Load transfer vs crack width from the field observations from six different JRCPs (Hansen, et al., 1998).
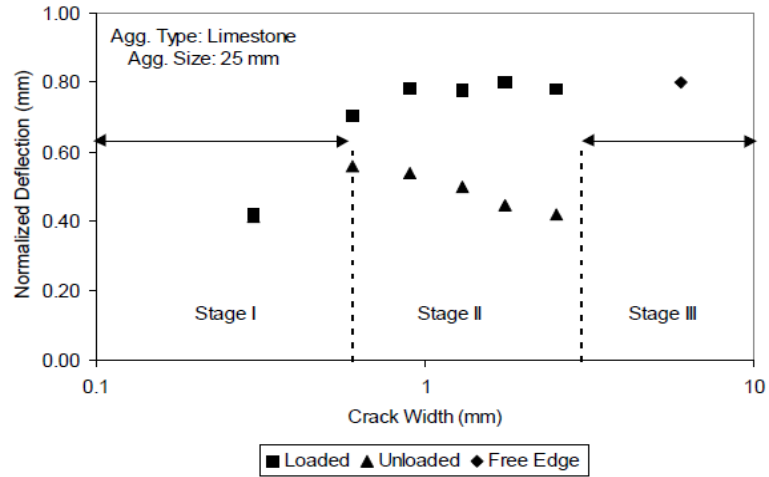
(a)
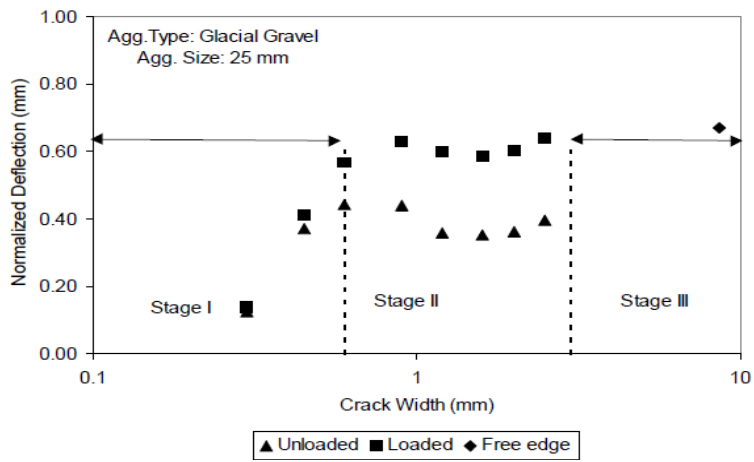
(b)
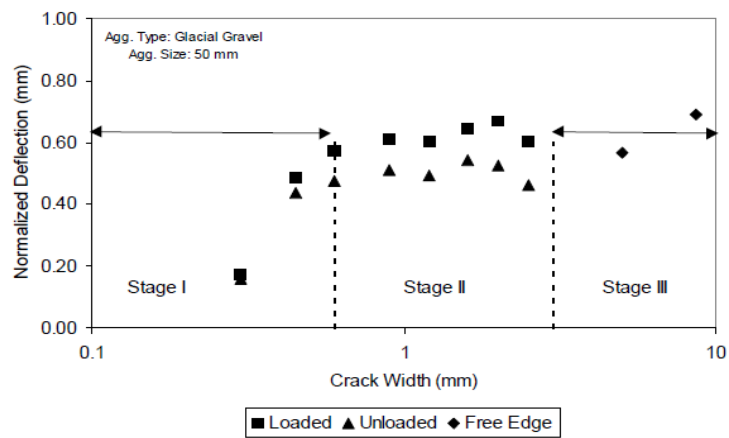
(c)

Figure 2.38. Normalized deflection vs crack width (a) 1- in limestone, (b) 1- in glacial gravel and (c) 2-in glacial gravel (Hansen, et al., 1998).
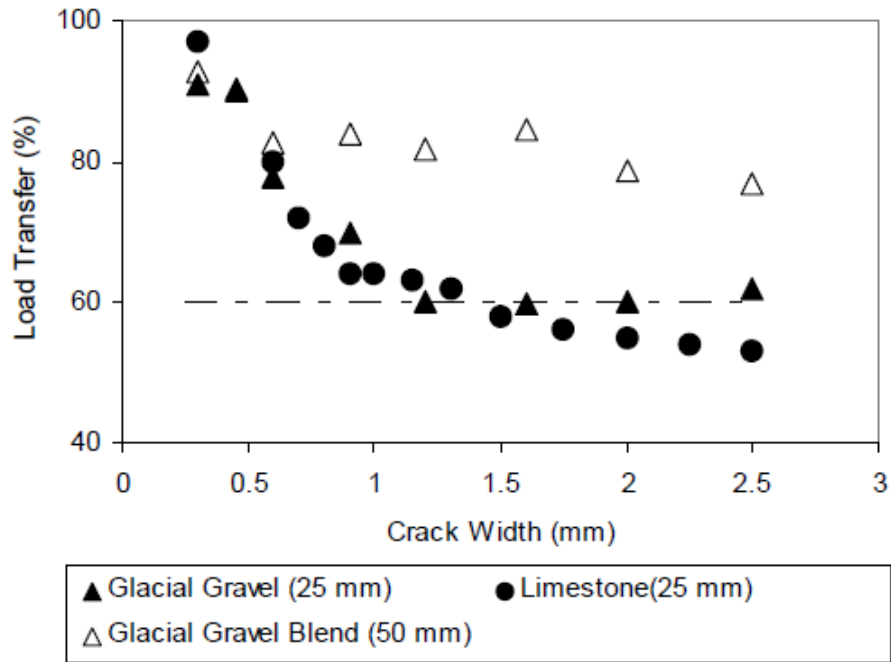
Figure 2.39. Load transfer vs crack width for different aggregate types (Jensen & Hansen, 2001).

The effect of crack width on the joint performance was also characterized by Nowlen, 1968, as shown in Figure 2.40. The laboratory test setup for that study was discussed in Section 2.7. The joint effectiveness was found to be 2 times more when the crack width was 0.035 in, as compared to 0.065 in, for a range of aggregate top sizes. Colley & Humphrey, 1967 and Nowlen, 1968 conducted tests on instrumented 7- and 9-in thick slabs. Figure 2.41 presents the relationship between the joint effectiveness, crack width and number of 9-kip load cycles for 7-in thick slabs. It can be seen that for a narrow crack width like, 0.015 in, the joint effectiveness does not drop with the number of load cycles. However, when the crack increases, the joint effectiveness rapidly declines.

48
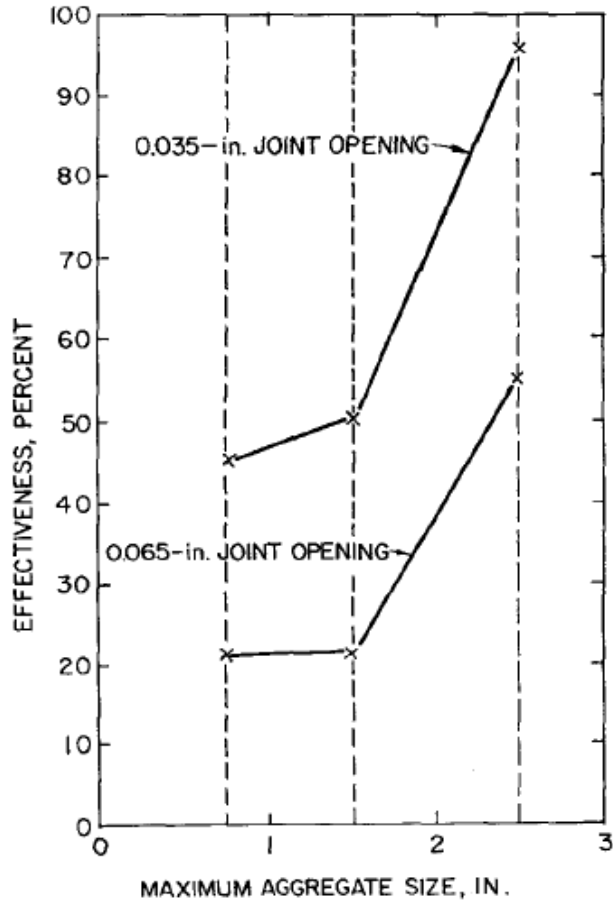
Figure 2.40. Joint effectiveness vs crack width for different aggregate top sizes (Nowlen, 1968).
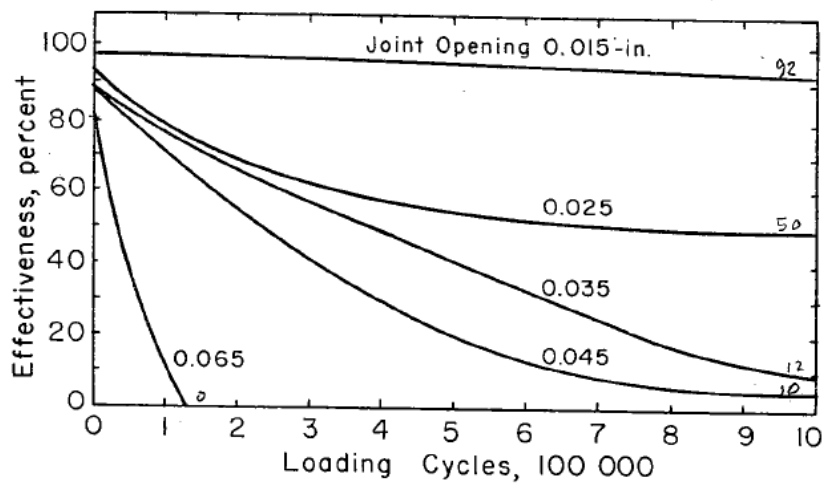
Figure 2.41. Joint effectiveness vs joint opening at different number of load cycles for 7- in slab (Colley & Humphrey, 1967).

49

In Brink, et al., 2004 study, the joint performance vs crack width relationship was investigated for two different aggregate top sizes and two aggregates types. The test setup was discussed in Section 2.6. The LTE vs crack width relationship was relatively different in this study as compared to the previously discussed studies. It can be seen in Figure 2.42 (1.5 in aggregate top size), that the dynamic LTE dropped only by approximately 4 percent when the crack width increased from 0.004 in to 0.100 in. Although the exact reason is not known, the low LTE drop could be due to the use of very small slab sizes (3 ft x 2 ft). See Figure 2.21. The far end unrestrained transverse edges of both the loaded and unloaded slabs most likely lifted up under the dynamic load. In this condition, the differential deflection, which is referred to as the relative movement by Brink, et al., 2004 is less dominated by the joint shear stiffness. This probably resulted in a very low variation in the relative movements regardless of the crack widths, as shown in Figure 2.43.
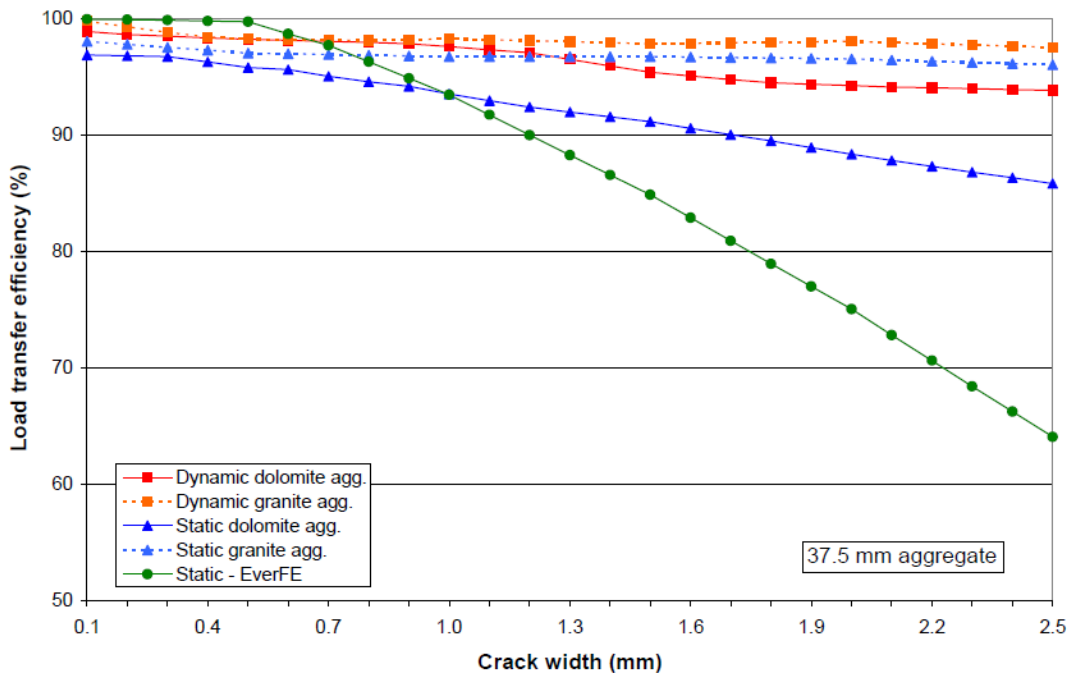
Figure 2.42. Load transfer vs crack width (Brink, et al., 2004).
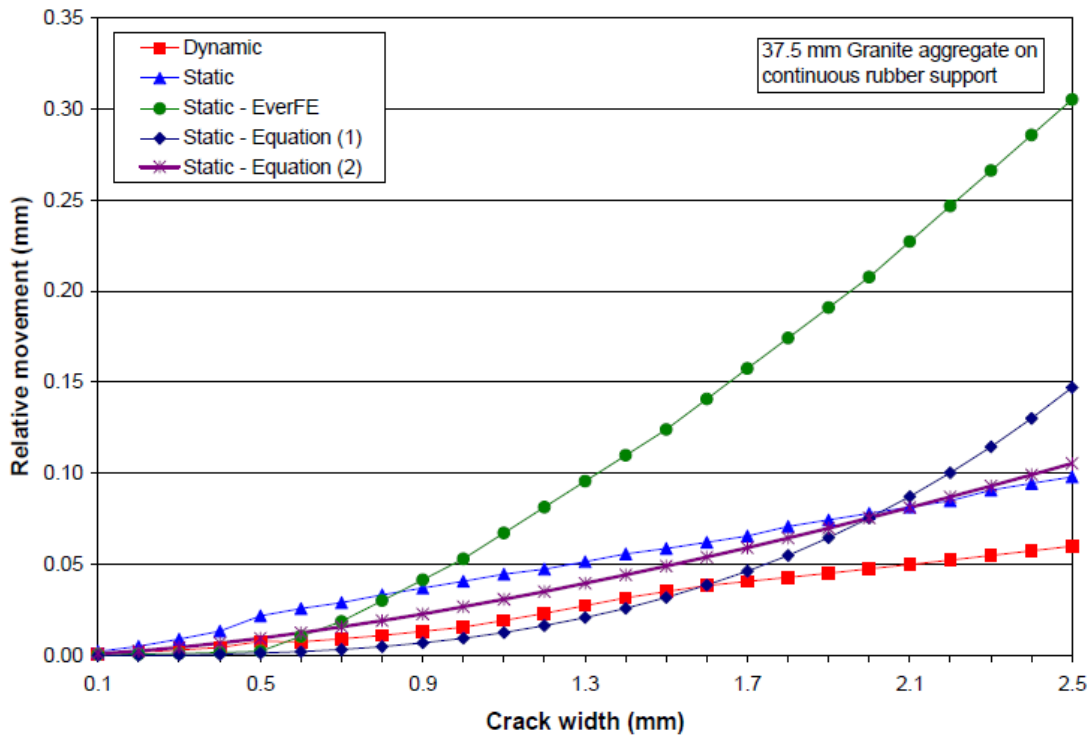
Figure 2.43. Relative movement vs crack width (Brink, et al., 2004).

2.8.3 Number of Load Applications

The aggregates at the joint abrade with accumulated load cycles (Colley & Humphrey, 1967 and Nowlen, 1968). The magnitude of the abrasion with respect to load cycle depends on the crack width and strength of the aggregates. As was shown in Figure 2.41, the joint effectiveness declination with respect to load cycle was large when the crack width was larger. At a 0.045-in crack width (Figure 2.41), the joint effectiveness dropped by 80 percent as compared to only 6 percent when the crack width was 0.015 in, after 100,000 load cycles. Brink, et al., 2004 reported that at a crack width less than 0.010 in, the load transfer drop was negligible even after

51

2 million load cycles. At a narrower crack width, the differential deflection remains very low.

The mechanical action on the aggregates is also low as a result.

2.8.4 Thickness of the Slab

Colley & Humphrey, 1967 and Nowlen, 1968 reported that the joint effectiveness is also a function of thickness of the slab. Figure 2.41 and Figure 2.44 show that the joint effectiveness vs. load cycles relationship for 7- and 9-in thick slabs, respectively. For both cases the slab was placed on a 6-in gravel subbase (Colley & Humphrey, 1967).   The joint effectiveness was observed to be higher for the thicker slab. A larger crack face area provided by the thicker slab results in a higher joint effectiveness.
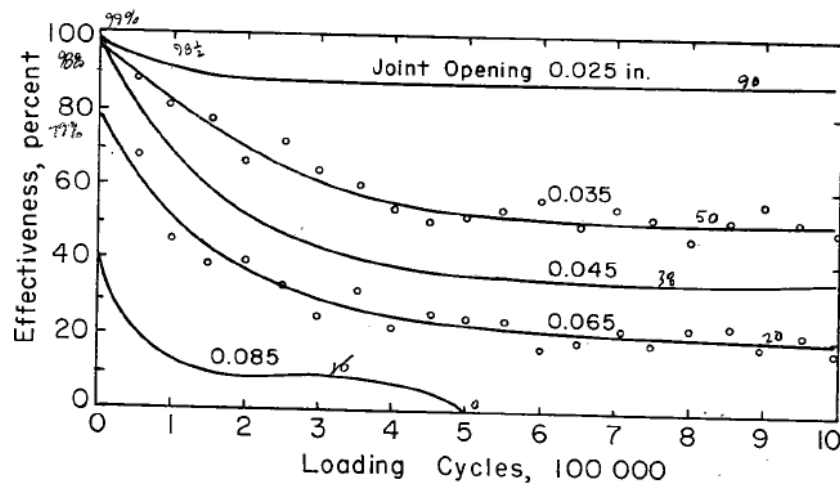
Figure 2.44. Joint effectiveness vs joint opening at different number of load cycles for 9-in slab
(Colley & Humphrey, 1967).

2.9 FIBER REINFORCED CONCRETE IN JOINT PERFORMANCE BENEFITS

The significant role of joint performance in the development of distress in whitetopping is the motivation for investigating feasible ways to increase the joint performance that can be maintained for a longer period of time. Since dowel bars are not used in ultra-thin whitetopping, structural fibers can be a potential alternative. Although many whitetopping projects with FRC have been constructed (Rasmussen, et al., 2002), the benefits of the applications of fibers in increasing the joint performance have actually not been properly investigated. A literature review on the applications of fibers in concrete revealed that both high and low elastic modulus fibers are used in the construction of UTW. High elastic modulus fibers are generally referred to as structural fibers. These fibers increase the toughness, residual strength, joint stiffness and flexural strength of the concrete (Boredelon, 2005; Roesler, et al., 2006; Roesler, et al., 2008 and Rodezno & Kaloush, 2010). The low elastic modulus fibers, known as non-structural fibers, reduce the plastic shrinkage cracking potential (Naaman, et al., 1984; Zollo & Ilter, 1986; Grzybowski & Shah, 1990; Bentur & Mindness, 1990 and Shah, et al., 1994). The primarily cracking resistance, impact, wear resistance and ductility of concrete also significantly increased with the addition of fibers (Zhang, et al., 2001). The benefit of the application of fibers in reducing the infiltration or permeability of the concrete through the cracks and joints has been reported by many researchers including Aldea, et al., 2000, Rapoport, et al., 2002, Lepech & Li, 2005 and Rajabipour & Akhavan, 2010.

Although both steel and synthetic fibers have been used in the construction of UTW, the use of a synthetic fiber is more common in the US (Rasmussen & Rozycki, 2004 and Barman, et al., 2010). The difficulties involved in dealing with the heavy weight steel fibers during mixing is probably the reason for the less frequent use of steel fibers as opposed to the synthetic fibers.

To evaluate the effect of fibers on the joint performance in whitetopping, the performance history of a couple of MnROAD whitetopping sections is reviewed. The performance of two whitetopping sections, one constructed with non-structural polypropylene fibers (Cell 94) and the other constructed with structural polyolefin fibers (Cell 95) are compared. Figure 2.45 shows a picture of the two types of fibers. Joint performance data for these two cells were compared to determine if the slabs in Cell 95 exhibit a higher LTE. It can be seen in Figure 2.46 that the LTEs in Cell 95 were always higher than the LTEs in Cell 94. Another observation is that the contribution of the fibers is more in the winter when the crack width is larger. The slabs with structural fibers had tighter joints than those with the non-structural fibers. The non-structural fibers cannot keep the crack width narrower because of their low stiffness and tensile strength. During the summer time, when thermal expansion forces the joints to be relatively tight, the LTE for the two cells does not differ significantly. Therefore, it can be concluded that structural fibers contribute in increasing LTE.

(a)   (b)
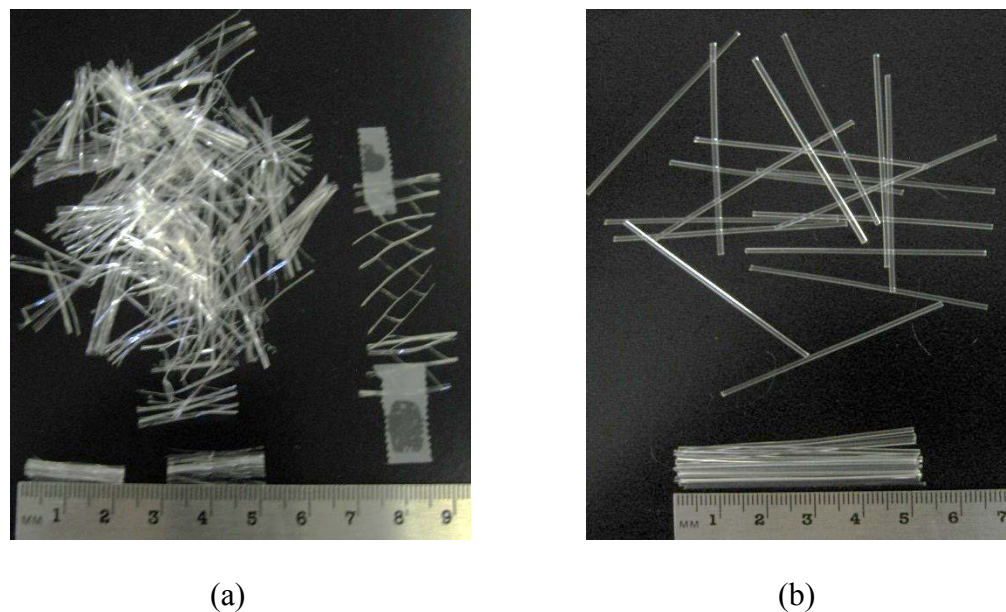
Figure 2.45. Picture of two types of synthetic fibers used in MnROAD Cells 94 and 95: (a) Polypropylene and (b) Polyolefin.

54
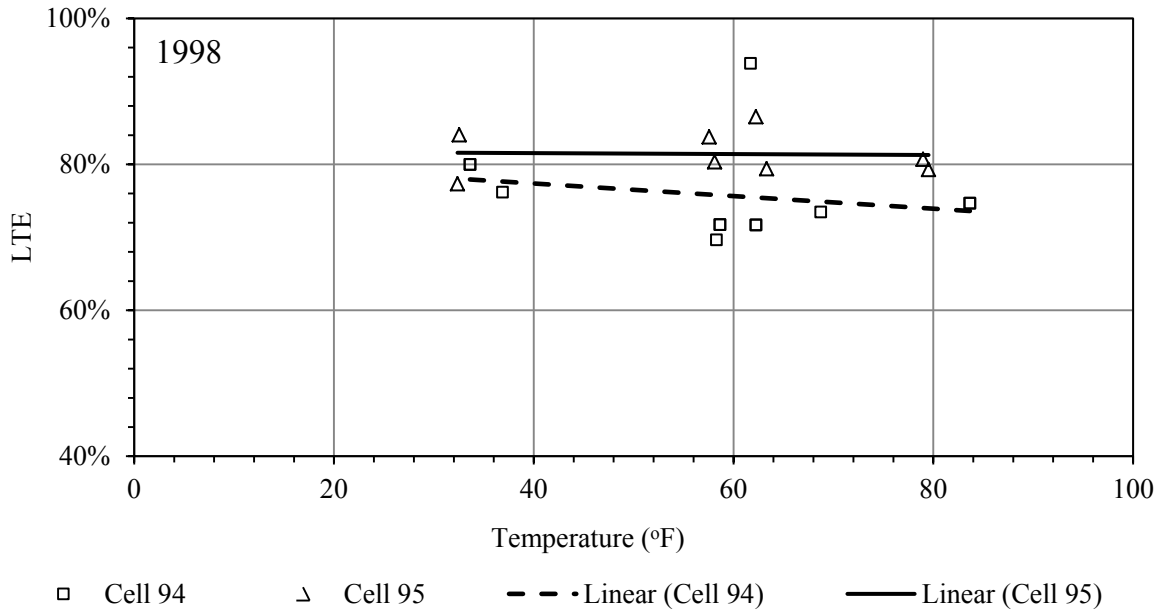
(a)
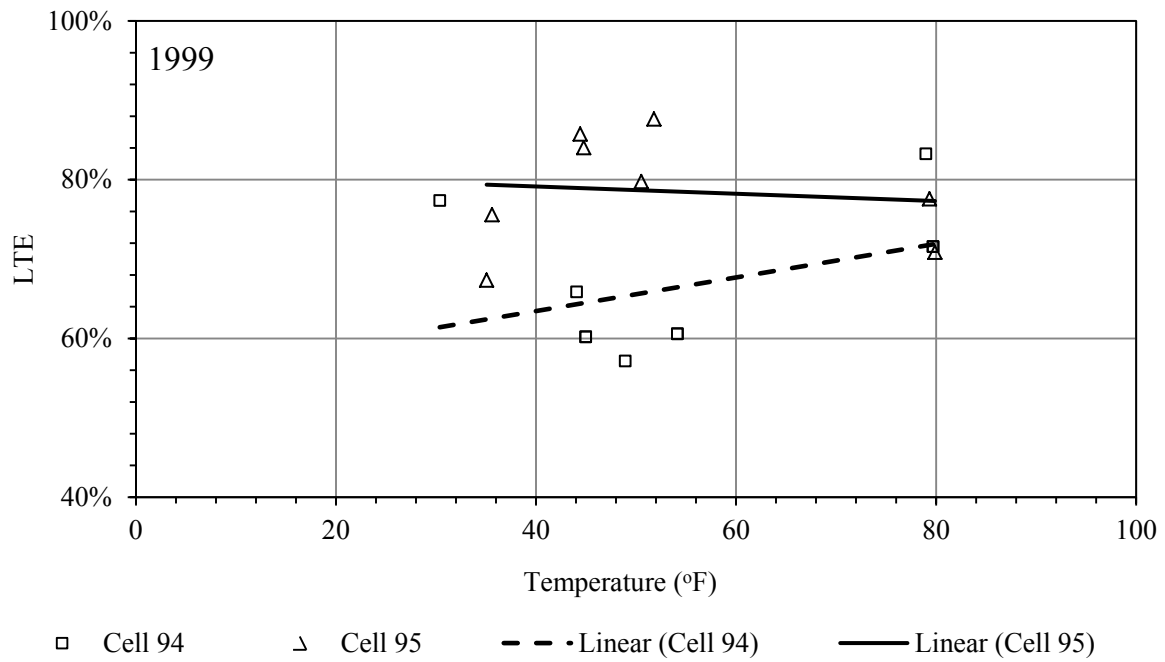
(b)
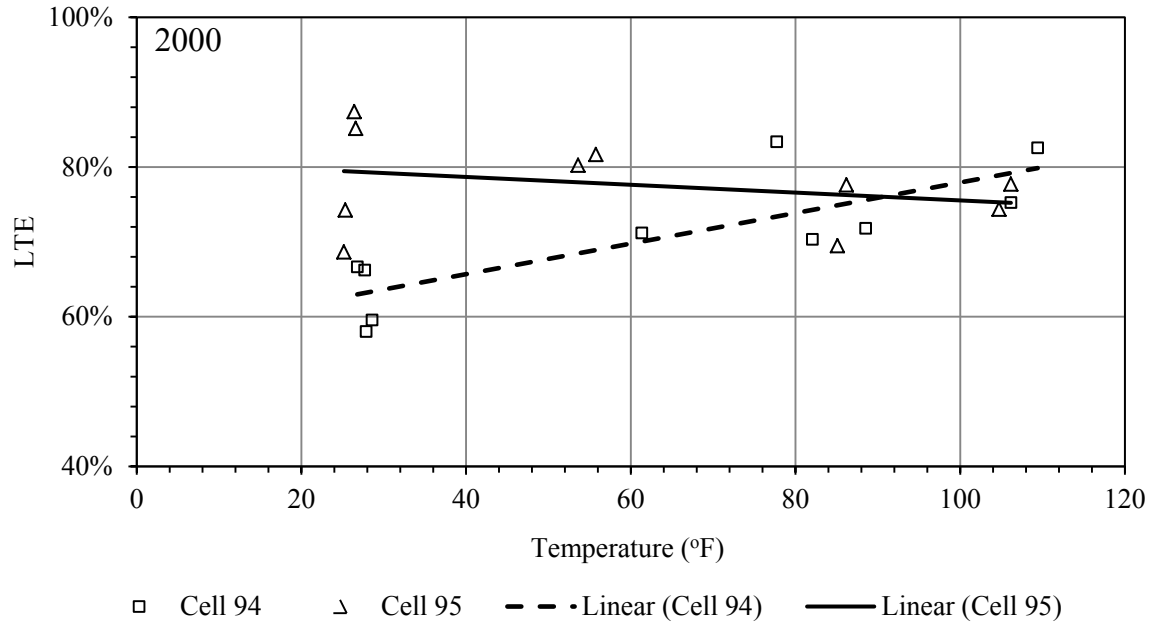
(c)

Figure 2.46. Load transfer efficiency of MnROAD Cells 94 and 95 in (a) 1998, (b) 1999, and (c) 2000.

The studies conducted by Boredelon, 2005 and Roesler, et al., 2008, utilized structural fibers with many shapes such as, straight, twisted and crimped. Both steel and synthetic fibers were considered. A number of factors that affect the performance of FRC including type, dosage, length, diameter and aspect ratio (AR) of the fibers were considered. AR is the ratio of the length of the fiber to its effective diameter. Table 2.3 presents the features of three different synthetic fibers utilized in the Roesler & Cervantes, 2008 study. The test results for the FRCs with each fiber are also presented in Table 2.3. It can be seen that the peak flexural load and modulus of rupture (MOR) vary with the dosage rate, shape and aspect ratio of the fiber. Dosage rates equal to 4.5 lb/yd^3 in the straight synthetic fiber category and 4.6 lb/yd^3 in the twisted synthetic fiber category seem to provide the highest peak flexural load and MOR. Boredelon, 2005 studied the residual strength ratio (RSR) vs. fiber volume fraction (V_f), as shown in Figure

56

2.47. The RSR of the FRC is determined by a four point bending test using beam specimens (ASTM-C1609/D1609M, 2010). RSR is expressed as shown below.

$$SR = 100 \frac{f_{e,3}}{\text{MOR}}$$ (2.13)

where $f_{e,3}$ is the residual strength at mid span for a deflection up to (span)/150 of a 24-in x 6-in x 6- in beam. The span equal to 18 in and therefore the residual strength is measured at 0.12-in deflection.

Bordelon, 2011 also studied the orientation of fibers in the concrete. This study investigated the orientation pattern of a few synthetic fibers with respect to the cast surface of the specimen. Figure 2.49 shows a graph for the structural synthetic fiber, which indicates that the average orientation is around 75 degrees from the vertical plane.

Table 2.3. Properties of a few structural synthetic fibers and FRC in the Roesler et al. 2008 study.

Fiber type	Straight synthetic						Twisted synthetic		Crimped synthetic
Cross section	Rectangular						Rectangular		Rectangular
Length (in)	1.57						2.13		2.00
Thickness (in)	0.004						NA		0.03
Width (in)	0.05						NA		0.05
Aspect ratio	90						NA		46
Specific gravity	0.92						0.91		0.91
Volume fraction in the mix (percent)	0.19	0.26	0.29	0.33	0.50	0.58	0.30	0.50	0.40
Dosages used (lb/yd³)	3.00	4.00	4.50	5.00	7.70	8.90	4.60	7.70	6.10
Peak flexural load (lb)	6623	5472	9276	8138	8088	8939	8101	6487	8160
Modulus of rupture (psi)	556	456	733	680	699	745	675	541	673
Testing age (days)	14	14	14	56	56	14	14	14	14
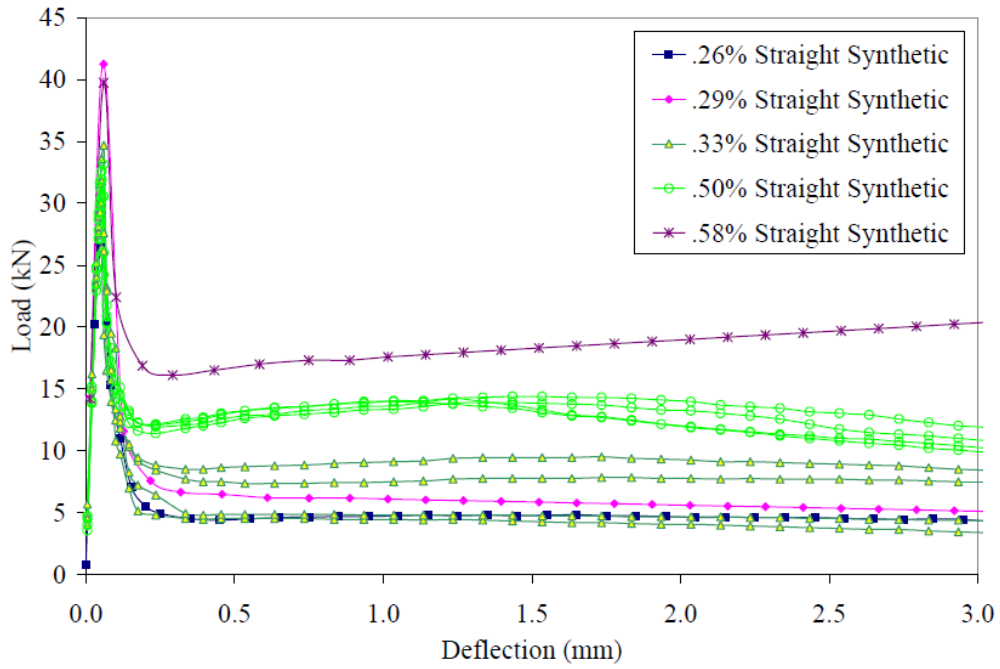
Figure 2.47. RSR vs. fiber volume fraction in Boredelon, 2005 study.
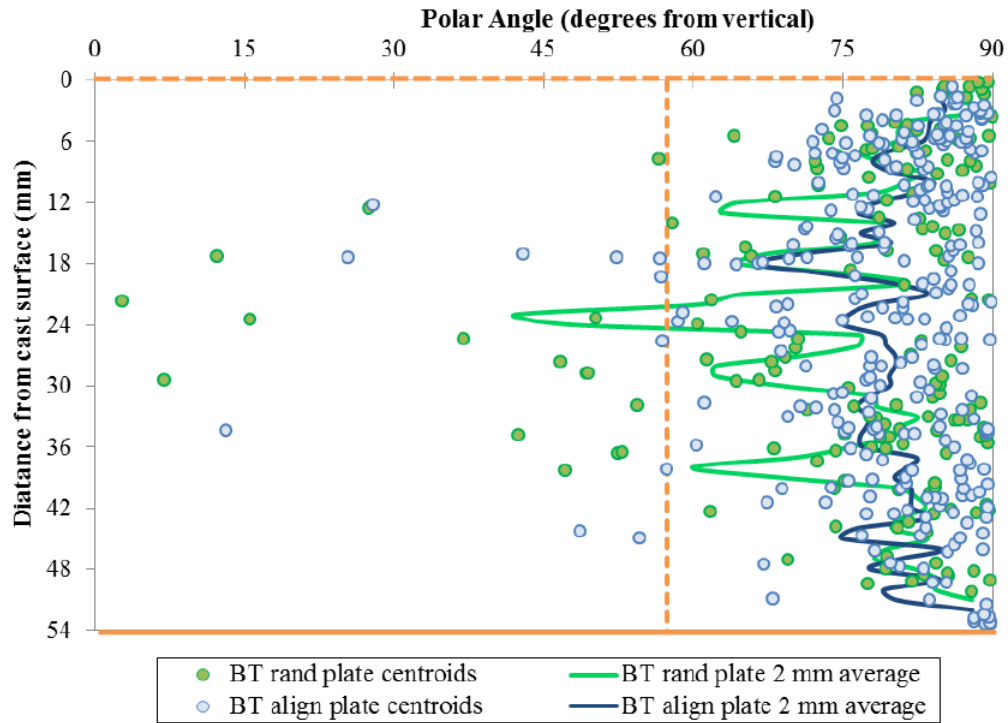
Figure 2.48. Polar angles and average orientation of fibers for each 2 mm with respect to cast surface (Bordelon, 2011).

58

This current literature about the application of fibers in whitetopping indicates that a substantial amount of research has been carried out to quantify the benefits of different types of fibers in the concrete. Most of this research investigated the benefit of fibers by looking at the change in drying shrinkage, toughness, and modulus of rupture or the residual strength of the concrete. Several experimental and analytical research studies were also carried out to model the crack bridging phenomenon of FRC (Kanda & Li, 1999, Zhang, et al., 2000 and Zhang, et al., 2001). The only study that was found in the literature, which considered the contribution of fibers in joint performance, is by Arnold, et al., 2005, as discussed in Section 2.7. In that work, the peak differential displacement as a function of dosages of hooked end steel fibers was studied. It can be seen in Figure 2.49 that an increase in fiber dosage resulted in a decrease in peak differential displacement. In that study, the failure criterion was established as when the differential displacement reaches 0.06 in. It can be seen that when the fiber was used in the concrete, failure occurs at a wider crack width.
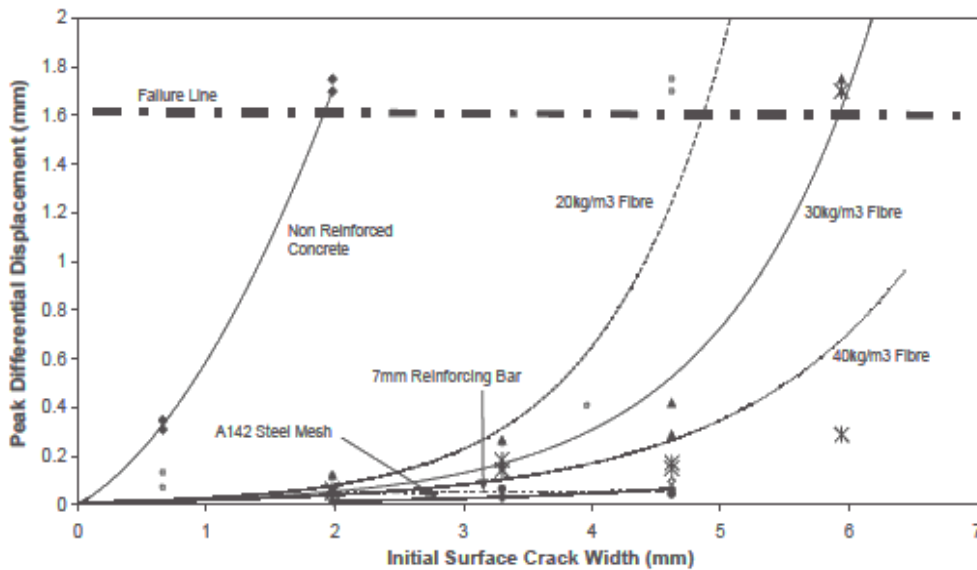
Figure 2.49. Effect of fiber reinforcement in peak differential displacement (Arnold, et al., 2005).

Unfortunately, no significant research has been conducted to characterize the effect of fibers on the load transfer across the cracks and joints. Also, only a limited number of studies investigated the benefits of the application of fibers for bonded whitetopping (Boredelon, 2005; Roesler, et al., 2008; and Rodezno & Kaloush, 2010).

2.10   CONCLUSIONS

This chapter provided an introduction of the whitetopping overlay. The literature survey reveals that the majority of the failures are related to the load induced stress along the wheelpath, which is a function of the joint performance. Higher load transfer efficiency is important in order to reduce the debonding of the HMA layer. A lower load transfer between the slabs coupled with the presence of moisture results in the development of the distresses in the overlay. Unfortunately, the current design procedures do not consider joint performance criteria. The reason for not considering the joint performance in the design process is because the effect of joint performance on the performance of a UTW has not been well established. The literature surveys related to the available joint performance evaluation procedures reveals that there is not a simplistic procedure that could be adopted to perform laboratory studies for investigating the joint performance of a bonded whitetopping. Therefore, it is necessary to develop a simple joint performance testing and evaluation procedure. Then it will be helpful to determine whether load transferring materials, such as fiber, can improve the load transfer between the thin slabs. Finally, joint performance shall be incorporated into the design procedure.

3.0   DEVELOPMENT OF JOINT PERFORMANCE SETUPS

3.1   INTRODUCTION

A joint performance component has not yet been incorporated in any of the currently available whitetopping design procedures. The complexity involved in its characterization is the reason for it being neglected. Most of the research studies (Colley & Humphrey, 1967; Nowlen, 1968; Bruinsma, et al., 1995; Raja & Snyder, 1995; Jensen & Hansen, 2001 and Brink, et al., 2004) that characterized the joint performance in conventional concrete pavements were carried out by casting large size slabs. Joint performance characterization with large size slabs is expensive and generally cost-prohibitive, when evaluating the joint performance with respect to a large number of variables. Therefore, development of a simple, economic and accurate joint performance test procedure is a dire necessity. The present study developed a small-scale joint performance test. As mentioned in Chapter 1.0 , this procedure is referred to as the 'beam accelerated load testing' (B_{ALT}) procedure.

The procedures for estimating the joint performance characterizing parameters such as LTE and DER are also established in this study. The results obtained from the B_{ALT} procedure is then compared and correlated with the results from a large-scale joint performance test. The large-scale procedure is referred as to the 'slab accelerated load testing' (S_{ALT}). Although the joint performance testing with a large size slab is not new, the setup used to conduct the tests in

61

the present study was fabricated under the scope of this study. This chapter includes a detailed description on the design and fabrication aspects associated with both the B_{ALT} and S_{ALT} procedures.

3.2 BEAM ACCELERATED LOAD TESTING (B_{ALT})

The B_{ALT} procedure has been developed with a vision to make the joint performance evaluation task very simple and economical so that the test can be conducted using readily available laboratory resources or with a marginal investment. In the B_{ALT} procedure, joint performance can be characterized by (i) using the conventional 24-in x 6-in x 6-in beam specimens that are actually cast for modulus of rupture testing, (ii) performing the test on a scaled down facility and (iii) using only one single low capacity (max. capacity ~2000 lbs) actuator. These objectives were achieved by (i) designing and fabricating the B_{ALT} in such a way that the mechanical action induced on the joints of an in-service concrete pavement can be replicated in the B_{ALT} procedure, (ii) determining magnitude of the scaled down load corresponding to an equivalent standard axle load (ESAL), (9000 lb), (iii) determining the location for the application of the scaled down load and (iv) establishing the specimen preparation, testing, data collection and data analysis procedures.

3.2.1 Setup Design Principle

The test setup was designed to replicate the abrasive action that occurs on the joints of an in-service concrete pavement. Both the conditions (i) when the wheel is on the approach slab (case

www.manaraa.com

I) and (ii) when the wheel is on the leave slab (case II) were considered. In the B_{ALT} procedure, unlike the in-service pavements, load is applied only on one side of the joint. In the in-service condition, when the load is applied on the approach slab, the approach slab directly deflects down, and the leave slab is indirectly pulled down by the approach slab because of the load transfer phenomenon. When the load is applied on the leave slab, the actions reverse. Figure 3.1 demonstrates these scenarios along with their corresponding simulations in the B_{ALT} procedure. In case I, when the approach slab moves down, an upward shearing resistance is generated on the fractured face of the leave slab (Figure 3.1 (a)). This upward shearing resistance was attained by applying an upward force on the right half of the beam (Figure 3.1 (b)). During the application of the load, the entire length of the beam was held under a constant restraint at the top and bottom. More details regarding the restraining are discussed in the following subsection. In case II, the direction of the shear resistance on the fractured face of the leave slab is downward (Figure 3.1 (c)). This downward shear force was simulated by a downward force on the right half of the beam (Figure 3.1 (d)). To simulate the repeated wheel loads for the in-service condition, loads were applied alternatively in upward and downward directions. The magnitudes of the loads in both the directions were kept similar.

63
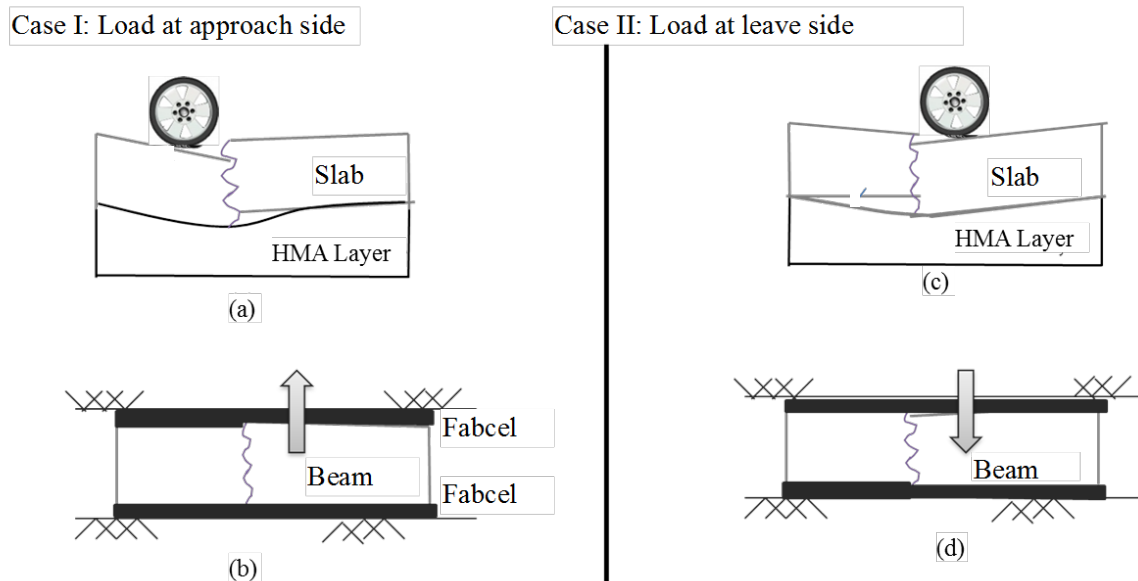
Figure 3.1. Loading scenarios in the in-service pavement and their simulation in the B_{ALT} procedure.

3.2.2   Components

Foundation and restraint

The foundation support provided by the lower layers under the concrete slab in an in-service pavement was replicated by an artificial foundation. Since, the load was applied in both upward and downward directions, an artificial foundation was provided at both the top and bottom of the specimen.   Two   layers   of   neoprene   pads,   known   as   Fabcel   25 (http://www.fabreeka.com/Products &productId=24), were used as the foundation. Figure 3.2 shows the Fabcel 25 waffle shaped neoprene pads.

The stiffness of the two combined Fabcel layers was determined by conducting plate load testing according to ASTM-D1195/D1195M, 2009, and was found as 200 psi/in. The specimen and Fabcel layers were vertically restrained so that the deflection under the load is only due to

64

the compression of the Fabcel layers. Figure 3.3 shows a picture of the B_{ALT} setup. Figure 3.4

shows the cross section of the test setup. Different components can be seen in these two figures.
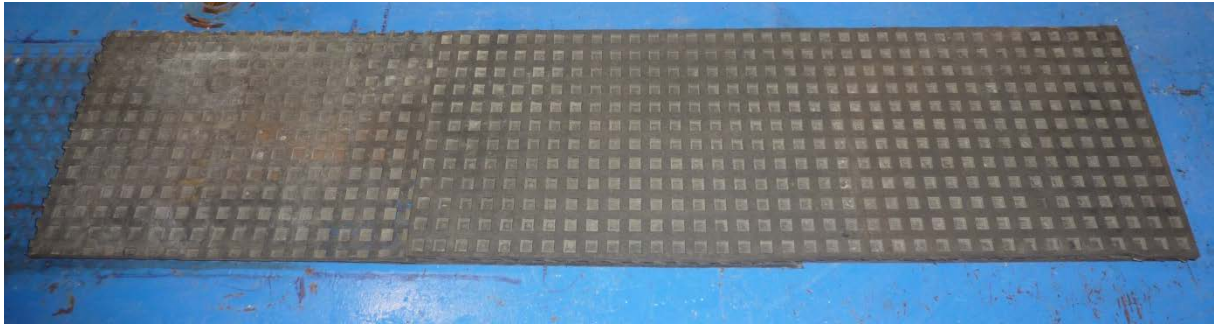
Figure 3.2. Picture of a waffle shape neoprene pad, Fabcel 25.

(a) Flange of base I-beam
(b) Fabcel
(c) Top I-beam
(d) Restraining rod
(e) Brace plate
(f) Horizontal load plates
(g) Vertical load plates
(h) Calibrated spring
(1) LVDT and its holder

F2-(BC3)
CW-0.05 inch

Unloaded side ← → Loaded side
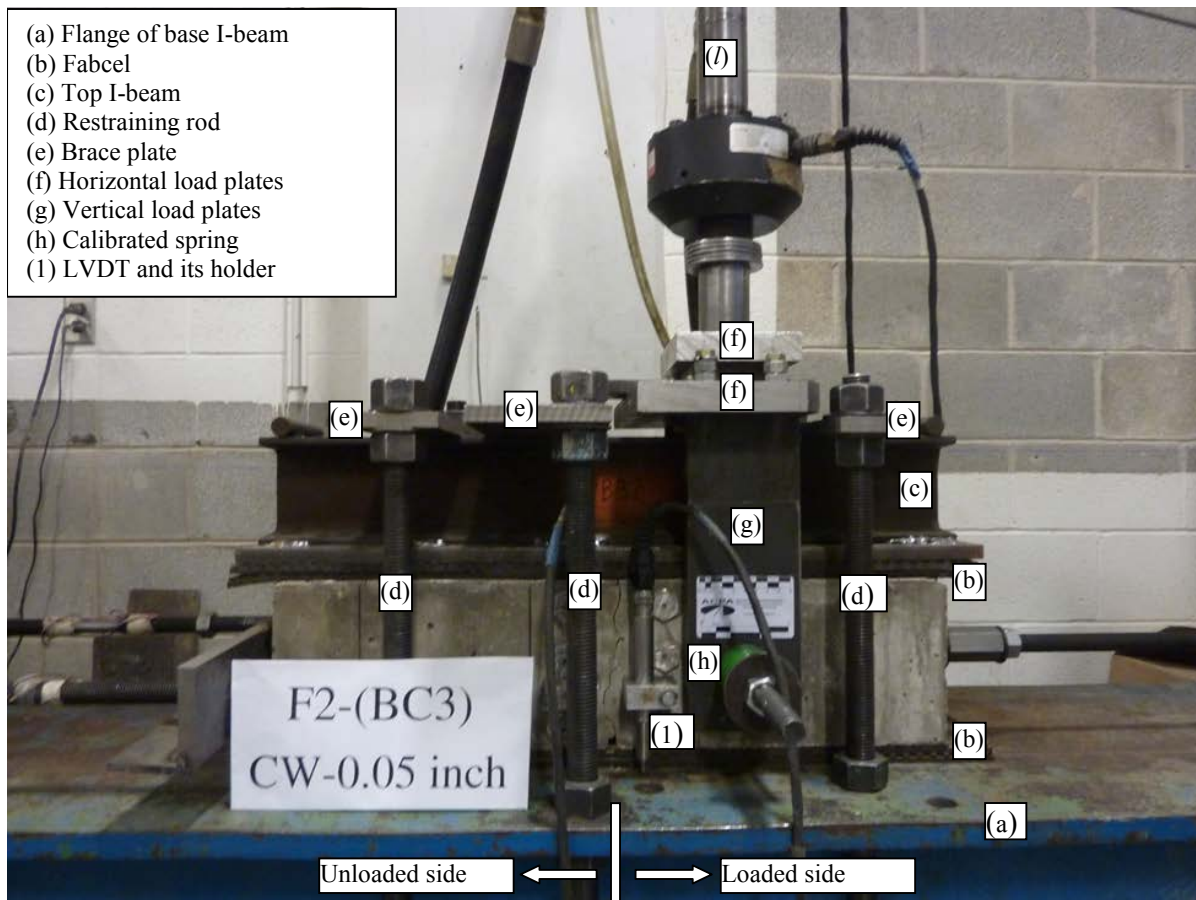
Figure 3.3. Photo of the B_{ALT} test setup.

65
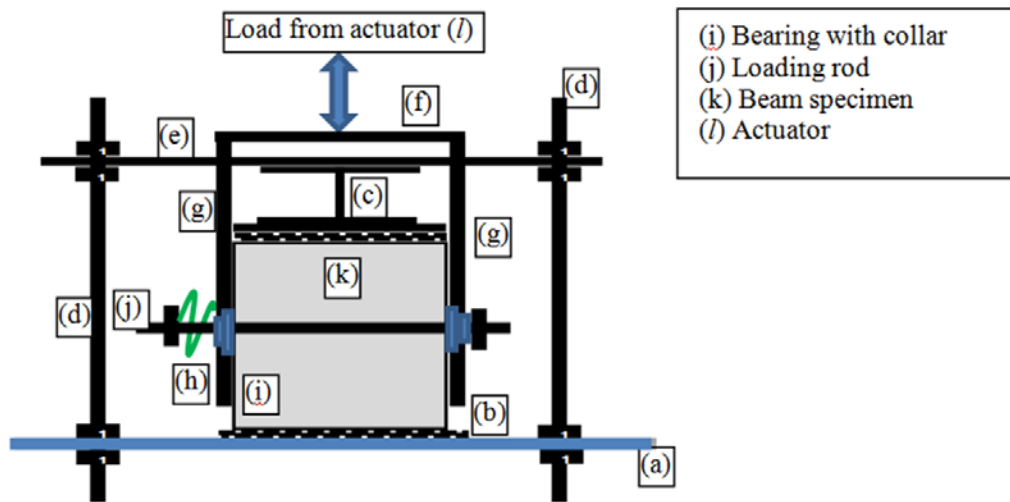
Figure 3.4. Schematic of the cross section of B_{ALT} setup.

A 17-in wide I-beam, to be referred as the base I-beam in this study, was used as the platform for the B_{ALT} setup. This base I-beam was situated on the concrete floor of the lab. The Fabcel layers were directly laid on the top flange of this base I-beam. At the top of the specimen, a built up I-beam with a 6-in wide bottom flange (equal to the width of the beam specimen), was placed on the Fabcel layer. This I-beam is referred as the top I-beam in this study, and is shown in Figure 3.5.

To secure the top I-beam with the base I-beam, six 1-in diameter threaded rods (referred to as restraining rods), three brace plates and twenty four hexagonal nuts were used in the assembly. The test specimen, covered with two layers of Fabcel at the top and bottom, rests in between the top I-beam and base I-beam. The brace plates, which run across the top flange of the top I-beam, were strategically placed, one at the mid-span (on top of the joint) and the other two near the edges. These brace plates were secured with the top flange of the base I-beam by a pair of restraining rods. Hexagonal nuts were used to tighten the assembly. A torque of 40 in-lb was applied to all the nuts located at the top of the brace plates that keep a uniform restraint

along and across the specimen. It was observed that with a 40-in-lb torque, the reproducibility of the results (deflections, LTE and DER) was better. The assembly was strong and sturdy with no or negligible movement of the top I-beam when the dynamic load was applied. A torque below 40 in-lb on the nuts provides a higher deflection under tension loading, and a higher torque produces lower deflection in both the tension and compression loads. However, the torque on the nuts creates a pre-compression in the Fabcel layers. The deflections measured, with the help of linear variable differential transformer (LVDT), before and after the application of the torque, showed that the Fabcel layers compress by 25 mils under this level of applied torque.

Figure 3.5. The top I-beam in B_{ALT} setup.

Load application and deflection measurement arrangement

Load on the beam specimen was applied with the help of an actuator capable of applying load in both upward and downward directions. A special arrangement, as was shown in Figure 3.3 and Figure 3.4, has been developed to transfer the load from the actuator to the beam. Load was applied to the right half of the beam in the form of a shear force.

A horizontal load plate was connected with the actuator. This horizontal load plate distributes the load equally on two vertical load plates. The load from the two vertical load

www.manaraa.com

plates to the beam is transferred through a specially designed bearing-collar assembly press fitted in each of the vertical load plates. See Figure 3.6. Each bearing has two collars attached, one at each side. The bearings transfer the load from the vertical load plates to the collars. The collar located at the inner face of each vertical load plate was partially projected out by 1/8 in. The projected surface of each inside collar was basically forced in surface to surface contact with the side walls of the beam, by a horizontal force. The horizontal force was applied through a ¾-in threaded rod, referred to as the loading rod. This rod runs through a calibrated spring, collars at the front vertical loading plate, a pre-made horizontally aligned hole located at the mid-depth of the specimen and collars at the rear vertical loading plate. Nuts on this loading rod on each side of the beam are tightened to apply the horizontal force. The pictures of the calibrated spring, loading rod, nut, bearing and collar assembly are shown in Figure 3.6. The load is quantified by the calibrated spring, which has a spring constant equal to 3000 lb/in. The magnitude of the required horizontal tensile force at the loading rod or the compression at the collar-beam interface is a function of the load magnitude on each vertical load plate and coefficient of friction between the steel and concrete surfaces. Sufficient horizontal force was applied to generate the required frictional resistance at the collar-beam interface so that the total vertical load from the actuator was transferred to the beam, without any sliding. The magnitude and location of the load used is discussed in Subsection 3.2.3. The purpose of the bearings in the loading assembly was to create a hinge along the axis of the loading rod so that no moment is transferred to the beam either from the load or from the restraint. The load induced deflection profile is therefore purely a function of the applied load magnitude, analogous to the in-service condition.

The deflections at both sides of the joint were measured by two LVDTs. One aluminum LVDT holder was glued on each side of the joint on the front side of the beam.

Crack width control arrangement

The crack width control assembly in the B_{ALT} setup can be seen in Figure 3.7 and Figure 3.8. Crack width was controlled by regulating a horizontal force along the length of the specimen. While casting the specimen, a ¾-in threaded rod was embedded in each end of the beam along the longitudinal axis. This rod is referred to as a tension rod. The embedded length of the tension rod was 4.5 in, while the exposed length was around 1.5 to 2 in. On the left hand side of the beam, the exposed end of the tension rod is connected to a horizontally aligned steel angle running across the width of the beam. Two more parallel ¾-in threaded rods (referred to as crack width (cw) control rods) coming out from this steel angle were connected to a vertical column through one more steel angel and a bracket, as shown in Figure 3.7.

On the right hand side, the tension rod was lengthened with the help of a coupler. The right end of the extended rod was directly attached to the vertical column through a bracket. The horizontal force could be adjusted by tightening and loosening the hexagonal nuts on the tension rod at the left hand side. The purpose of having two cw control rods on the left hand side was to facilitate an independent crack width tuning on facility on both sides (front and back) of the beam. Also, these rods could be moved up and down.
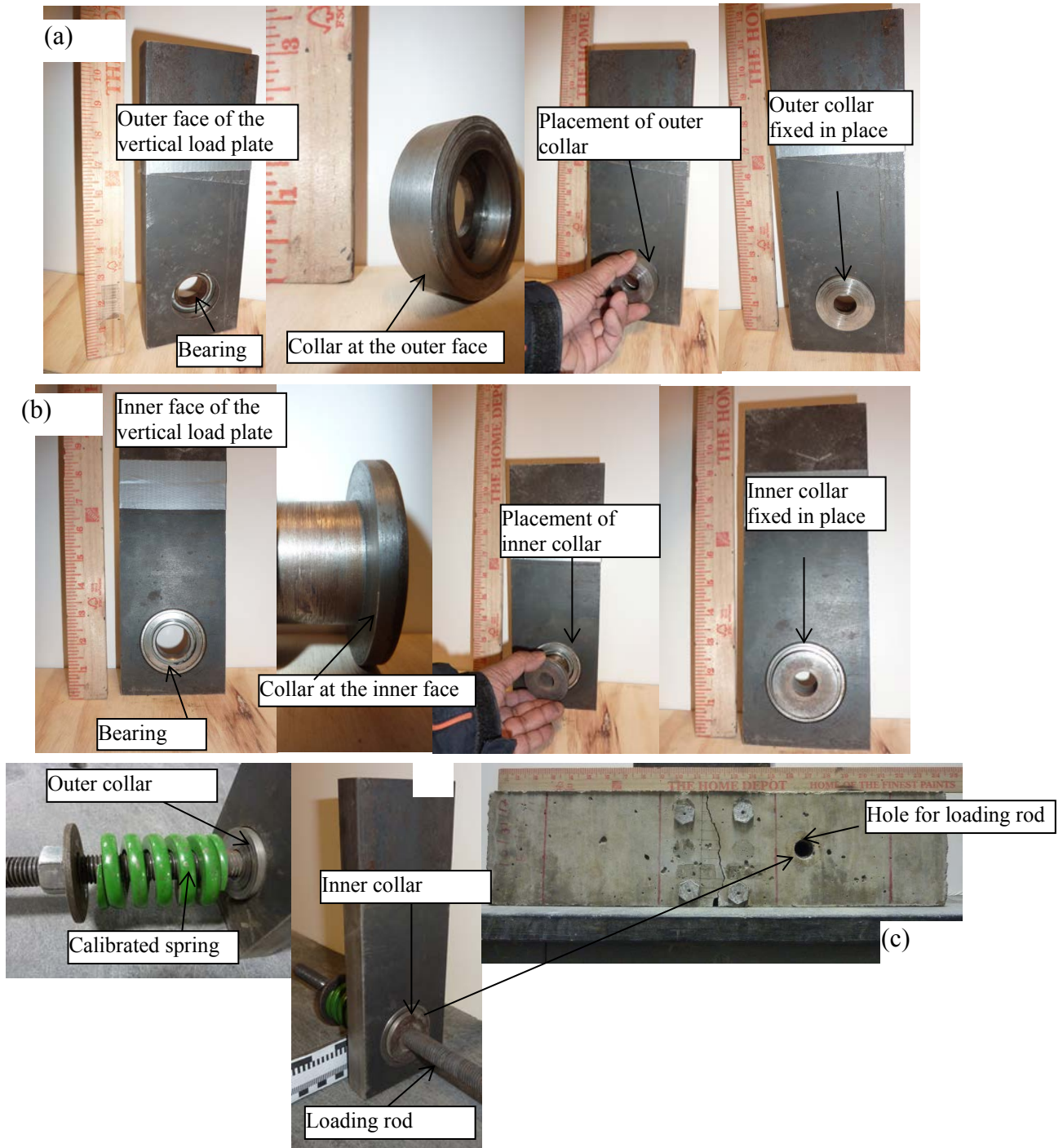
Figure 3.6. Load and deflection measuring assembly (a) bearing and collar at the outer face of the vertical load plate (b) bearing and collar at the inner face of the vertical load plate (c) calibrated spring, loading rod and the concrete face where the inner collar remains in contact.

These arrangements helped to keep a uniform crack width throughout the cross section of the specimen. Sometimes when fiber beams were tested, because of the non-uniform distribution of the fibers, a uniaxial horizontal force was unable to make a uniform crack width throughout the cross section. In this kind of situation, an extra moment was applied by adjusting the orientation of the cw control rods. This extra moment opens up the crack on the side where it was narrow when only a uniaxial horizontal force was applied. The right hand end was not disturbed during the test, partially because the actuator was connected to this side of the beam. Movement of this end could potentially misalign the actuator resulting in an oblique loading. The force on the cw control rods was measured using a strain gage attached to each cw control road. Threads on the cw control rods were locally machined off at the strain gage locations before they were mounted.
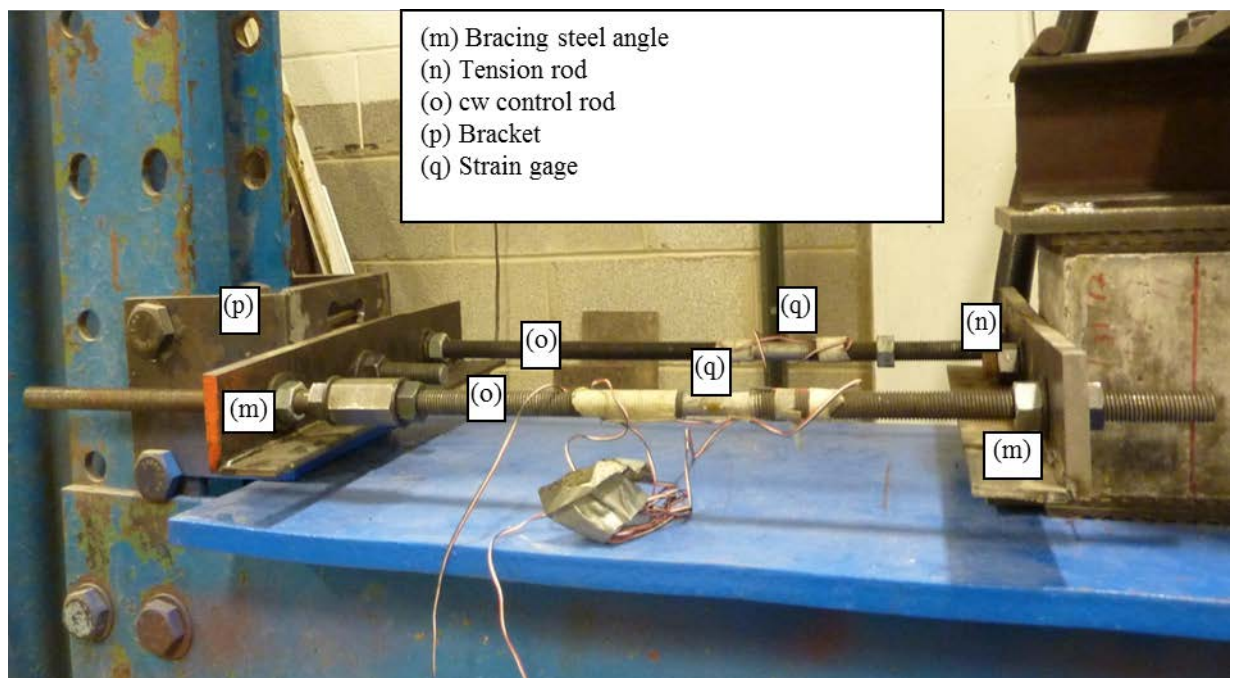
Figure 3.7. Crack width control assembly on the left hand side of the beam.

71
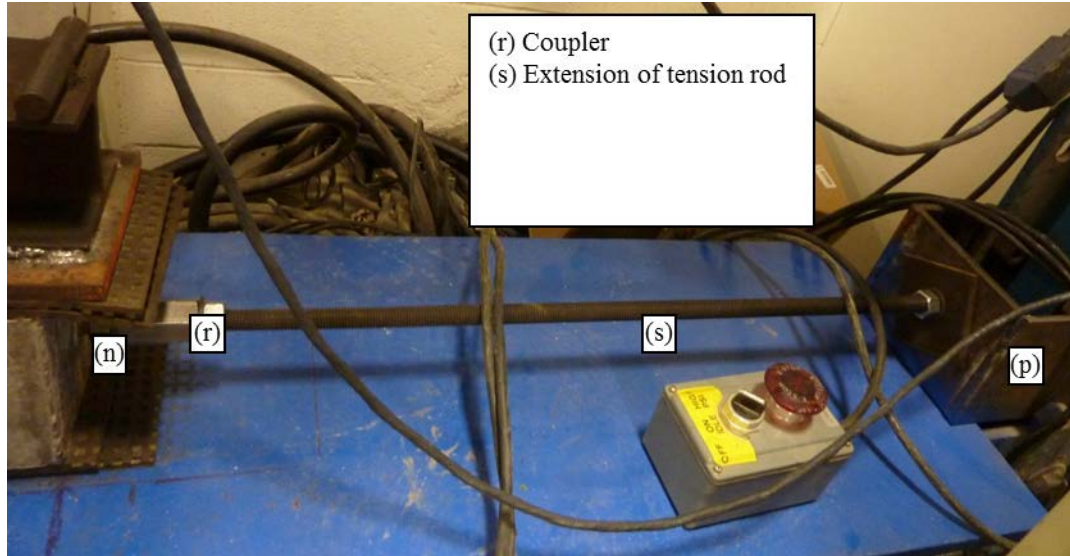
Figure 3.8. Crack width control assembly on the right hand side of the beam.

3.2.3 Load Magnitude and Location

The magnitude and location of the load in the B_{ALT} procedure were determined through an analysis using the finite element method (FEM). The finite element analysis software, Abaqus FEA (http://www.3ds.com/products/simulia/portfolio/abaqus/overview/) was utilized. The FEM analysis was performed in a linear solid mechanics platform with a static load application. Geometric, material and contact nonlinearities were not considered. In the finite element modeling of conventional rigid pavements and whitetopping overlays, it was found that consideration of a linear elastic material model can provide results with an acceptable accuracy (Nishiyama, et al., 2005; Hammons, 1998; Mitra, et al., 2010; Li, et al., 2013). The B_{ALT} procedure was modeled to capture the equivalent joint performance between the two adjacent 4-in thick, 5-ft x 6-ft whitetopping slabs. First a FEM model for the above mentioned slab was developed. Then, using similar material properties, a model for the beam specimen was developed. Deflection profiles for the 12-in x 6-in x 6-in beam specimen (half of a 24-in long

www.manaraa.com

beam) in the B_{ALT} procedure were matched with the deflection profiles for the 4-in slab in the S_{ALT} procedure. A detail of the modeling features for both the procedures is described below.

Table 3.1 presents the general features for the slab model. Figure 3.9 shows a screenshot of the slab model in Abaqus. A load of 9000 lbs was applied on a 10-in x 10-in square area on the right hand side of the slab. The center of the loading area is 18 in away from the left hand side longitudinal edge and 6 in away from the transverse joint, analogous to the Raja & Snyder, 1995 study. Both the adjacent slabs are rested on an elastic foundation with a 200 psi/in modulus of subgrade reaction. Two layers of Fabcel-25 pads provide such a foundation stiffness. The load transfer between the adjacent slabs was modeled using translational springs in the Z-direction. Each pair of nodes on the adjacent slab across the transverse and longitudinal joints was connected by one single spring.

Table 3.1. Input and FEM modeling features for the concrete slab model.

Slab size	60 in x 72 in x 4 in
Modulus of elasticity of concrete	4,000,000 psi
Poisson's ratio of concrete	0.15
Density of concrete	0.0026 slugs/in^3
Modulus of subgrade reaction	200 psi/in
Element type	27 noded brick
Element size	1 in x 1 in x 1 in
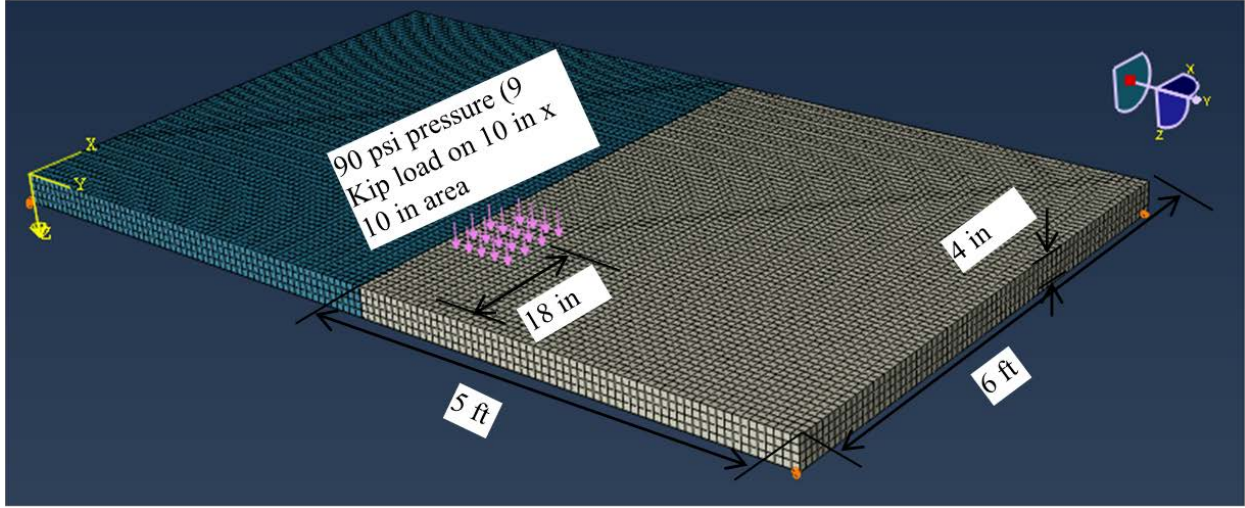
Figure 3.9. Screenshot of the slab model.

The joint stiffness (*AGG*) is a spring constant that relates to the non-dimensional joint stiffness (*AGG*= AGG/kl)*. Using the Ioannides & Korovesis, 1990 relationship for the *AGG** vs LTE, *AGG** for a given LTE can be determined. The stiffness (*K)* assigned to each node is determined based on the area contributing to the stiffness of that node. The ratio of the areas covered by the corner, edge and intermediate nodes is 1:2:4, therefore, for equally spaced nodes the spring constants can also be assigned in that ratio. The following equations (3.1), (3.2) and (3.3) (Hammons, 1998 and Feng & Ming, 2009) are used to determine the respective spring constants assuming uniformly spaced nodes.

$$K_{corner} = \frac{kLlAGG^*}{4(N_r - 1)(N_c - 1)} \qquad (3.1)$$

$$K_{edge} = 2K_{corner} \qquad (3.2)$$

$$K_{intermediate} = 4K_{corner} \qquad (3.3)$$

where K_{corner}, K_{edge} and $K_{intermediate}$ are the spring constants (lb/in) at the corner, edge and intermediate nodes on the joint faces, respectively; k is the modulus of subgrade reaction (psi/in); L is the width of the slab (in), 72-in in the present case; l is the radius of relative stiffness (in);

74

AGG^* is the non-dimensional joint stiffness; N_r and N_c and are the numbers of rows and columns of nodes on the joint face, which depend on the element size, type and area of the cross section of the slab.

Using the slab model, deflection profiles were generated for two different cases, one with an 85-percent LTE and the other with a 90-percent LTE. Relatively higher LTEs were chosen so that the influence of the joint performance is dominant in the generated deflection profiles, but not the foundation. The deflection profiles for the two cases are shown in Figure 3.10 and Figure 3.11. The maximum deflections obtained for the two cases are quite similar, 0.034 and 0.033 in for 85- and 90- percent LTEs, respectively. The slopes of the generated deflection profiles, calculated for a12-in length starting from the transverse joint, were -1/1350 and -1/1430 at 85- and 90-percent LTEs, respectively. The slopes on the loaded side of the slab were considered. The reason for determining the slope only up to a 12-in length is because the length of the loaded side of beam in the B_{ALT} procedure is also 12 in. It may be noted that the FEM model generated deflection values were compared with the test results in the Raja & Snyder, 1995 study. As discussed in Section 2.7, concrete slabs were tested for evaluating the joint performance in that study. Although comparatively large size slabs were tested in that study and the thickness of the tested slabs were higher, an engineering judgment was applied to compare the deflections values measured in that study with the generated deflection values in the FEM models presented in this chapter.
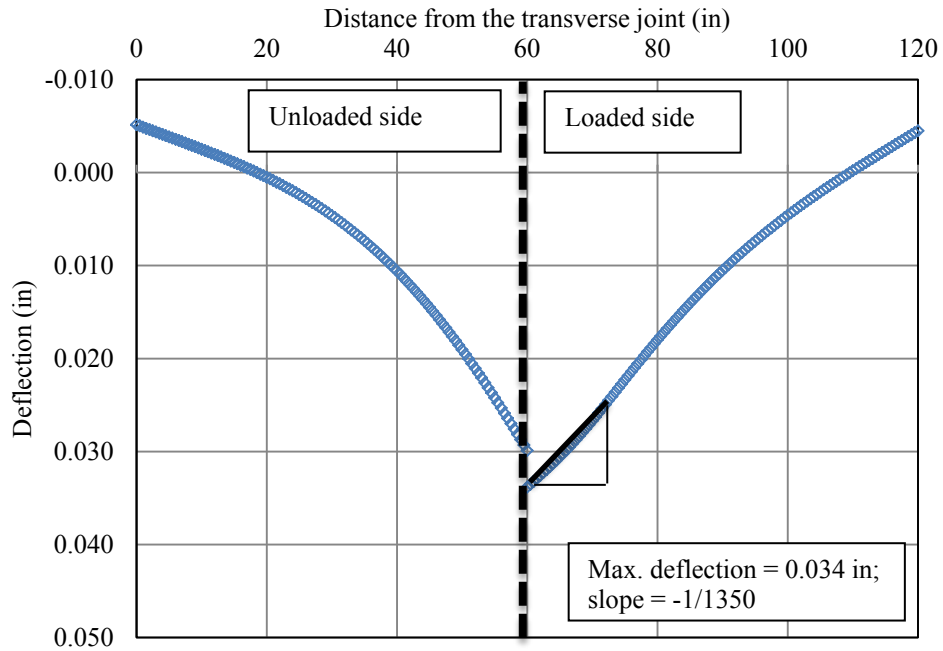
Figure 3.10. Deflection profile of slab at 85-percent LTE.
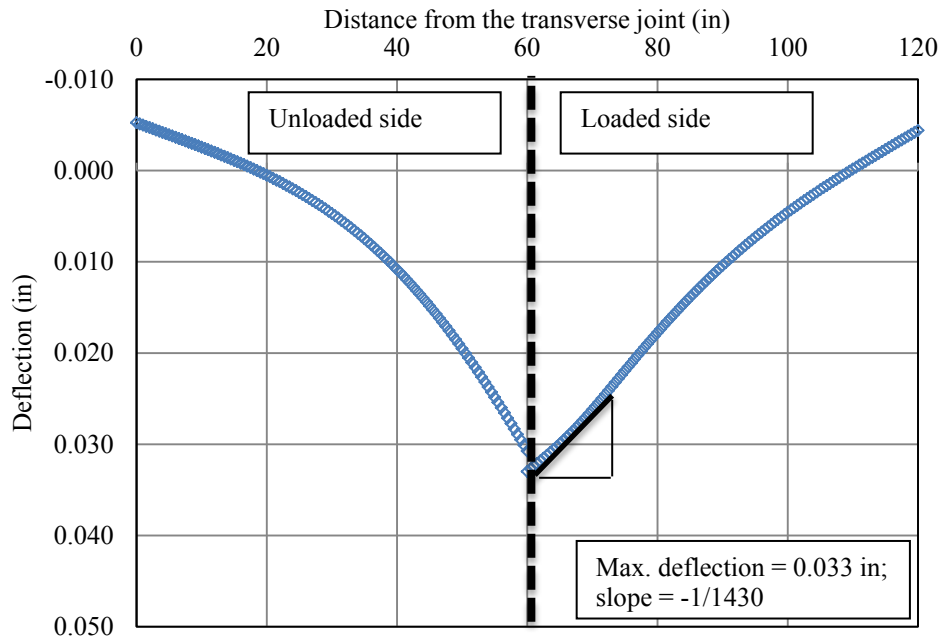
Figure 3.11. Deflection profile of slab at 90-percent LTE.

Next, the beam model was developed. The input related to foundation, materials and modeling features were kept similar to that of the slab model, as was given in Table 3.1. The

76

load in the beam model was applied in the form of surface traction on a 6 in^2 rectangular area, on both the front and back side walls. This loading scenario was chosen to simulate the applied force in the B$_{ALT}$. Figure 3.12 presents a screenshot of the beam model with the loading area shown at the front side of the beam. The ratio of the joint spring constants (K_{corner}, K_{edge} and $K_{intermediate}$) was 1:2:4. Figure 3.13 shows the transverse joint springs in the beam model and the modeled elastic foundations.
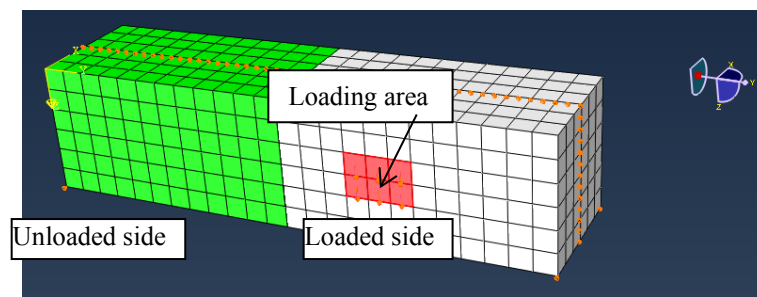
Figure 3.12. Beam model with the loading area depicted.
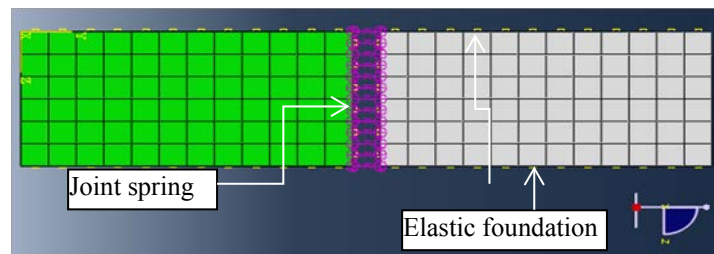
Figure 3.13. Side view of the beam model showing joint springs and foundations.

One important issue in calculation of the *AGG** for the beam model was determining the radius of relative stiffness for a beam. Since, the width of the beam is only 6 in, Ioannides & Korovesis, 1990 relationship, which was actually developed for the slab, is not directly applicable. And a similar kind of relationship is not available for a beam model. That is why an adjustment was required to be made to the radius of relative stiffness computed for a slab (using

77

Ioannides & Korovesis, 1990 relationship) to determine the equivalent radius of relative stiffness for a beam. As previously mentioned, the radius of relative stiffness for the slab is referred to as l and the same for the beam is referred to as l_{beam}. The spring constants, K_{corner}, K_{edge} and $K_{intermediate}$ for the beam model can be calculated using l_{beam}.

The adjustment factor for converting the slab l into the l_{beam} is referred to as *AF*. In order to derive the *AF*, Ioannides & Korovesis, 1990 relationship was used in conjunction with a finite element analysis of the beam model.

First three different LTEs, such as, 80, 85 and 90 percent were selected for this particular analysis. Relatively higher LTEs were selected to avoid the interference of the foundation. These are referred as the target LTEs. Using the Ioannides & Korovesis, 1990 relationship, the corresponding *AGG** values were determined. These are 7, 10 and 20 for 80, 85 and 90 percent LTEs, respectively. Next, these three *AGG** values were used in the beam model to generate deflection profiles for four assumed values of l_{beam} for each of the three selected LTEs. These are 2, 3, 4 and 6 in. Then, from the generated deflection profiles, the corresponding beam LTEs were calculated. The target slab LTEs were matched with the calculated beam LTEs. The magnitude of l_{beam} at which the calculated beam LTE matches with the target slab LTE was considered as the correct l_{beam}. Finally, *AF* was calculated as the ratio of correct l_{beam} to the slab l. The slab l for the 5-ft x 6-ft slab was calculated as 18 in.

In these FE analysis, the magnitude and location of the load were 1000 lb and 4.5 in, respectively, which were kept similar for all the cases. These were selected based on several preliminary analyses of the beam model. The location of the load is defined as the horizontal distance between the center of the applied surface traction and the transverse joint. Table 3.2 presents the comparison between the target LTEs (80, 85 and 90 percent) and calculated beam

78

LTEs for different values of l_{beam}. This table also presents the ratio of the l_{beam} to the l for all the combinations. It can be seen in Table 3.2 that when the value of l_{beam} is 3 in, the target LTE is very close to the calculated beam LTE for all three target LTEs. Therefore, the corresponding ratio of l_{beam} to the l was considered as the *AF*. The value of *AF* is hence established as 0.17. . Finally, the following equation can be used for calculating the beam *AGG** as a function of the slab *AGG* and *l*.

$$AGG^*_{Beam} = \frac{AGG_{slab}}{0.17lk} \tag{3.4}$$

where AGG^*_{Beam} is the beam AGG*; AGG_{slab} is the slab AGG.

Table 3.2. Target and calculated LTEs for determination of *AF*.

Target LTE (%)	l_{beam} (in)	l_{beam}/l^1	Calculated beam LTE (%)
80	2	0.11	72
80	3	0.17 (*AF*)	80
80	4	0.22	85
80	6	0.33	89
85	2	0.11	72
85	3	0.17 (*AF*)	83.5
85	4	0.22	92
85	6	0.33	91
90	2	0.11	95
90	3	0.17 (*AF*)	91
90	4	0.22	94
90	6	0.33	86

[1] the radius of relative stiffness for the slab, *l*, is 18 in.

It may be noted that this *AF* value was developed specifically for determining l_{beam} for a 12-in x 6-in x 6-in beam based on the *l* of a 5-ft x 6-ft x 4-in slab and, for other sizes of slabs and beams a similar approach can be followed. Henceforth, in all the beam analyses, *AF* was assumed as 0.17.

79

It was desired that the deflection and rotation of the beam and slab models are in well agreement. The load magnitude and location were selected to achieve this goal. Using the beam model, a number of analyses were performed with different combinations of magnitudes and locations of the load. The analysis was performed for LTEs of 85 and 90 percent. The generated deflection profiles for the beam were compared with deflection profiles for the slab (Figure 3.10 and Figure 3.11). An initial scanning of the beam deflections revealed that the magnitude of the load in the beam could be within the range of 1000 to 1100 lbs and the location between 4 to 5 in. Table 3.3 presents the values of maximum deflections and the slopes of deflection profiles for a few runs which were found to be closer to the slab deflection profiles at 85 and 90 percent LTEs. Figure 3.14 and Figure 3.15 provide the graphical comparison of the deflection profiles. It can be seen that in both cases (85 and 90 percent LTE) the maximum deflection and slope for the beam closely matches with the slab when the load magnitude and location are 1050 lbs and 4.5 in, respectively. Hence, the magnitude and location of the load in the beam test was selected as 1050 lbs and 4.5 in, respectively.

Table 3.3. Magnitude of the maximum deflection and the slope of the deflection profile for different load magnitudes and locations.

LTE (%)	Load (lb)	Distance from the transverse joint (in)	Maximum deflection (in)	Slope
85	1000	4.0	0.038	-1/543
85	1000	4.5	0.033	-1/1124
85	1000	5.0	0.028	1/155584
85	1050	4.5	0.035	-1/1070
85	1100	4.0	0.042	-1/495
85	1100	4.5	0.036	-1/1026
85	1100	5.0	0.031	1/14286
90	1000	4.0	0.036	-1/604
90	1000	4.5	0.032	-1/1379
90	1000	5.0	0.027	1/4881
90	1050	4.5	0.033	-1/1313
90	1100	4.0	0.040	-1/550
90	1100	4.5	0.035	-1/1253
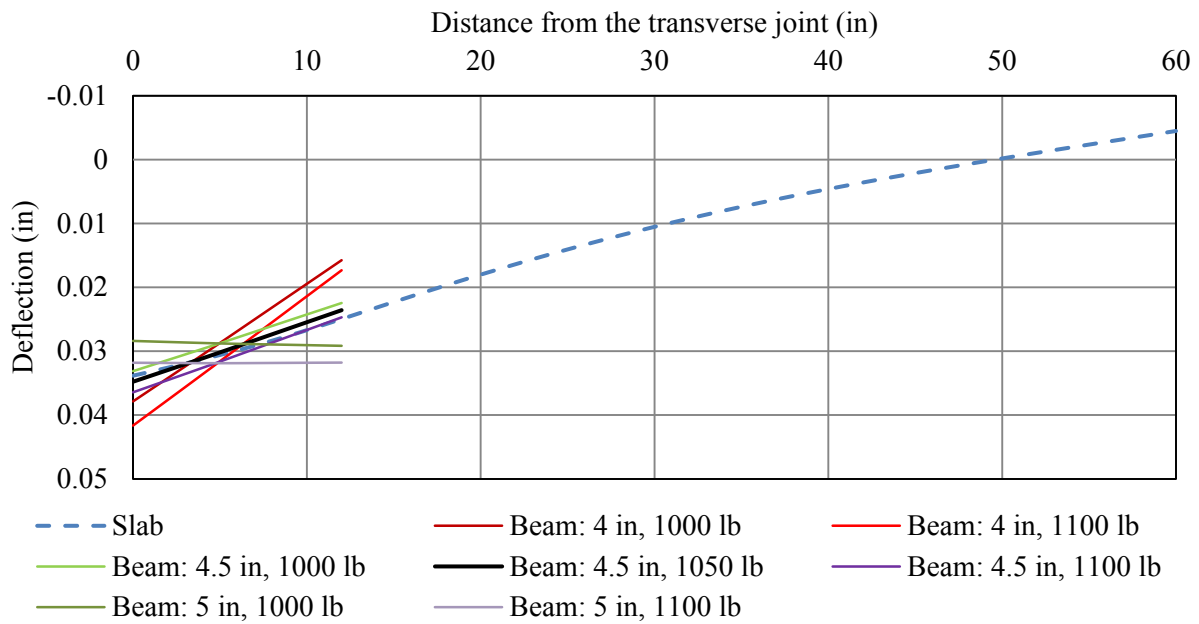
Figure 3.14. Comparison of the deflection profiles for the beam and slab at 85 percent LTE.
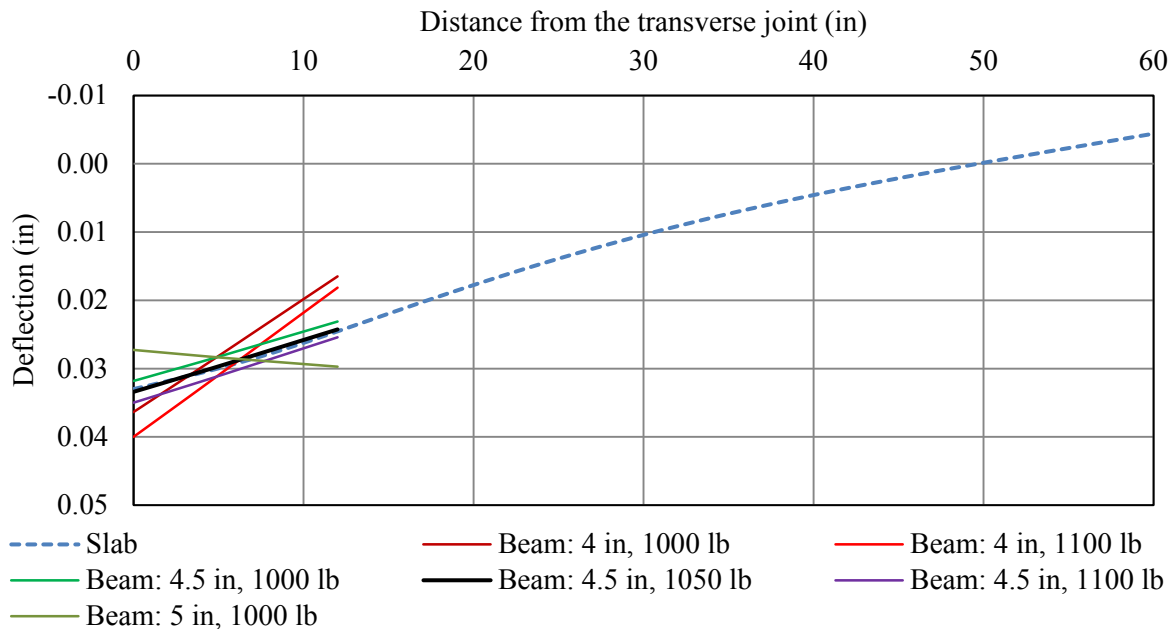
Figure 3.15. Comparison of the deflection profiles for the beam and slab at 90 percent LTE.

81

3.2.4 Specimen Preparation

One of the advantages of the B_{ALT} procedure is the utilization of the readily available 24-in x 6-in x 6-in steel beam molds for specimen preparation. These molds are generally utilized for making beams for testing the modulus of rupture of the concrete (ASTM-C78/C78M, 2010). Test specimens were prepared in a manner such that the specimen has one tension rod at each end along the longitudinal axis, and has a notched crack at the bottom at mid-span controlling the location of the fracture plane. In the present study, 24-in x 6-in x 6-in steel molds were used with some modification. To accommodate the tension rod at both of the ends, the steel end caps were replaced with wooden planks, as shown in Figure 3.16. The wooden planks were pressed fitted at the end of the longitudinal sides using the bolts available at the end of each longitudinal side. Holes were drilled through the center to accommodate the tension rods. A steel wire was looped around the all four sides to provide extra rigidity so that the end caps were held securely in place. Nuts were firmly tightened on both sides of the plank to secure the tension rods firmly in place. A ½-in x ¼-in x 6-in metal bar was glued at the center of the bottom plate to create a notch for crack initiation. A horizontally aligned hollow PVC pipe was attached in the mold to keep the space for the loading rod. Two plastic end caps were glued to the surface of the longitudinal walls of the mold to hold the pipe horizontal. The inside diameter of the pipe was ¾ in. The pipe was placed in a location such that the longitudinal axis of the pipe was 4.5 in away from the mid-span of the beam and 3 in above the bottom plate.
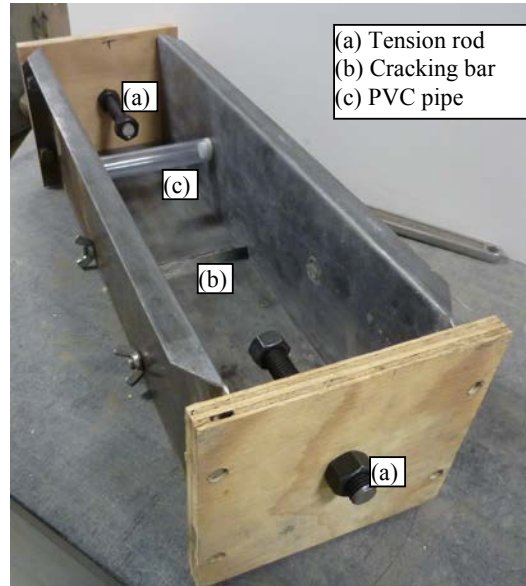
Figure 3.16. B_{ALT} test specimen mold.

The specimens were cast in accordance with ASTM-C1609/D1609M, 2010 and ASTM-C78/C78M, 2010. Extra care was required to keep the crack initiation bar and PVC pipe in place during the casting. The concrete was placed in two layers with the required vibration in each layer obtained with a table vibrator. Most of the time, a temping rod was used at the corners in addition to the vibration to avoid any honey combing. Figure 3.17 shows one example of a FRC beam preparation.

Figure 3.17. Preparation of an FRC beam specimen is in progress.

83

Specimens were demolded at 14 to 15 hours after casting. The crack initiation bar and the plastic end caps attached to the PVC pipe, were removed. A gentle tapping with a screw driver on one end of the crack initiation bar slides it out easily, as shown in Figure 3.18. The next task was to adhere three pairs of aluminum gage studs on each side of the specimen, as shown in Figure 3.19. These studs had a conical shaped slot on them. The distance between the slots in each pair of studs was measured in triplicate when recording the initial gage distance. The purpose of the gage studs was to monitor the crack width.

Figure 3.18. Removal of cracking bar from the concrete.

At 18 hours, the specimen was cracked at mid-span by applying a flexural load in the same manner used for a MOR test. Figure 3.20 shows cracking of an FRC beam. The loading rate, 15 to 45 lb/sec, was kept constant during the cracking process in accordance with ASTM-C78/C78M, 2010. During the cracking procedure, extra attention is required to ensure the beam is unloaded immediately after crack development. Initiation of the crack or just development of a very tight crack should be considered sufficient. Therefore, loading was stopped just after the appearance of a crack on the concrete surface. This is difficult to achieve for beams without

84

fibers. Putting the two separated halves of the beam back exactly in the same position, matching the crack surface textures, is really a challenging task. In the FRC beams, fibers bridge the crack, so the beam halves do not generally fall apart. See Figure 3.21. One notable point in this procedure of cracking the specimen is that the crack width at the bottom becomes wider than the top. This also simulates the non-uniform crack width pattern for an in-service pavement condition. In the present work, the cracked beams were transferred on a wooden plank right after the cracking procedure. Further handlings of specimens were performed on the plank so that the crack faces remain undisturbed until they were placed in the test setup. The cracked beams were cured for 28 days in a moist curing room at a relative humidity greater than 95 percent.

Figure 3.19. Aluminum gage studs for measuring crack width.

Figure 3.20. Cracking procedure for the beams used for B_{ALT}.
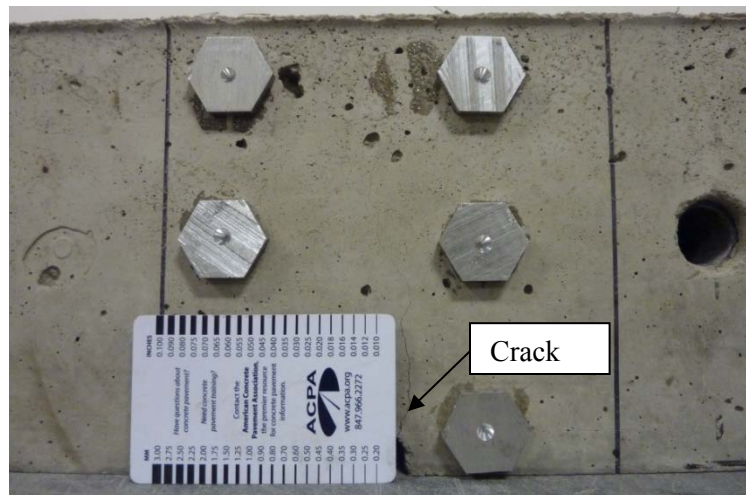
Crack

Figure 3.21. An FRC beam cracked at 18 hours.

3.2.5 Test Procedure

Now that a description of how the B_{ALT} specimen is prepared has been provided, a description of the B_{ALT} test will be provided. Before testing begins, the top surface of it must be inspected to verify the surface is smooth. If considerable undulations or irregularities are present on the beam surface, the surface is ground to obtain a smoother level surface. After the surface is checked (and smoothen if found undulated), the beam is carefully placed on the lower layer of Fabcel. The top Fabcel layers and the top I-beam are then placed on top of the beam. Care must be taken when handling the beam so the crack width is maintained. The restraining rods, bracing plates and the crack width control assembly are then set in place. The beam on the frame was positioned with care so that the axis of the vertically aligned actuator is directly above the loading location. Then, the loading components such as loading rod, vertical load plates assembled with bearing and collars, and the calibrated spring are put in their respective place, as discussed in Subsection 3.2.2. After that, the nuts on the restraint rods are tightened. The nuts on the bracing plates are tightened with a 40-in-lb torque. Then, while holding the vertical load plates aligned, the actuator in which the horizontal load plate is already attached is brought down in contact with the vertical load plates. A very minimal load, such as 5 to 10 lbs, is applied during this process so that the vertical plates come in contact with the horizontal load plate attached to the actuator. The horizontal force is then applied. The magnitude of the horizontal force is estimated based on the load on each vertical load plate, area of the surface of each inner collar that remains in contact with the concrete and coefficient of friction between the concrete and steel surfaces. The estimated horizontal force, which was 1500 lbs, was ensured by attaining a 0.5 in reduction in the length of the calibrated spring. The stiffness (spring constant) of the

87

calibrated spring was 3000 lbs/in. The vertical load plates were tightly fastened with the horizontal load plate by bolts.

Once the beam was successfully placed in the loading assembly, two LVDT holders were glued with epoxy to the vertical walls of the beam at front side. These holders were placed such that the deflections could be measured 1-in from crack on both sides of the crack. LVDTs were then mounted in the holders. Next, depending on the existing crack condition, the desired initial crack width was obtained using the cw control assembly. In the case of the plain concrete beams, obtaining the desired uniform initial crack width on all four sides of the beam was relatively easy as compared to FRC beams. Force and moment were applied through the tension rods to stabilize a uniform crack width, as previously discussed in Subsection 3.2.2. Also, a low magnitude, dynamic, vertical load (300 to 500 lb) with a low frequency (2 to 4 Hz) was sometimes applied in addition to the horizontal force through the tension rod, especially in the case of FRC beams. An average of the crack widths measured at the 3 locations (top, middle and bottom) on each side of the beam was used as the crack width of the joint.

Finally, when the setup was completely ready, a sinusoidal load cycle was applied through the actuator to obtain the load and deflection profiles. The magnitude of the peak load was 1050 lbs in both upward and downward directions. The loading frequency was 10 Hz. The typical load and deflection profiles are discussed in Subsection 3.4.1. The joint performance in the present study was evaluated at different crack widths and at different load cycles. The joint performance estimation procedures will be discussed in Section 3.4.

3.3   SLAB ACCELERATED LOAD TESTING (S_{ALT})

The large-scale test setup was developed to perform the joint performance test on full scale slabs. The developed setup simulates a wheel passing across a transverse joint between two adjacent slabs. This setup is capable of testing slabs with millions of load cycles in a relatively short period of time. The main purpose of the S_{ALT} was to investigate the validity of the joint performance results obtained with the B_{ALT} procedure. The following subsections briefly describe the details of the S_{ALT} setup.

3.3.1   Setup Design Principle

The S_{ALT} setup in the present study was developed in a similar manner to the setup developed in Raja & Snyder, 1995 study. The vehicle load was simulated using two actuators. These actuators provide sinusoidal loads on both sides of the joint. The peak loads on the approach and leave slabs were applied with a phase difference. The phase angle is established based on the desired vehicle speed.

3.3.2   Components

Foundation

A concrete foundation, 12-ft long, 6-ft wide and 2.75-ft deep, was used as the test platform. This was cast on a concrete reaction floor. Figure 3.22 shows a picture of the form-work built to cast the foundation. Concrete was poured in three separate and equal layers. To strengthen the

89

foundation at the mid-span, where the actuators would apply load during the joint performance test, a steel I-beam was embedded, as shown in Figure 3.22. Figure 3.23 presents a picture of the test setup showing platform for the S_{ALT}.
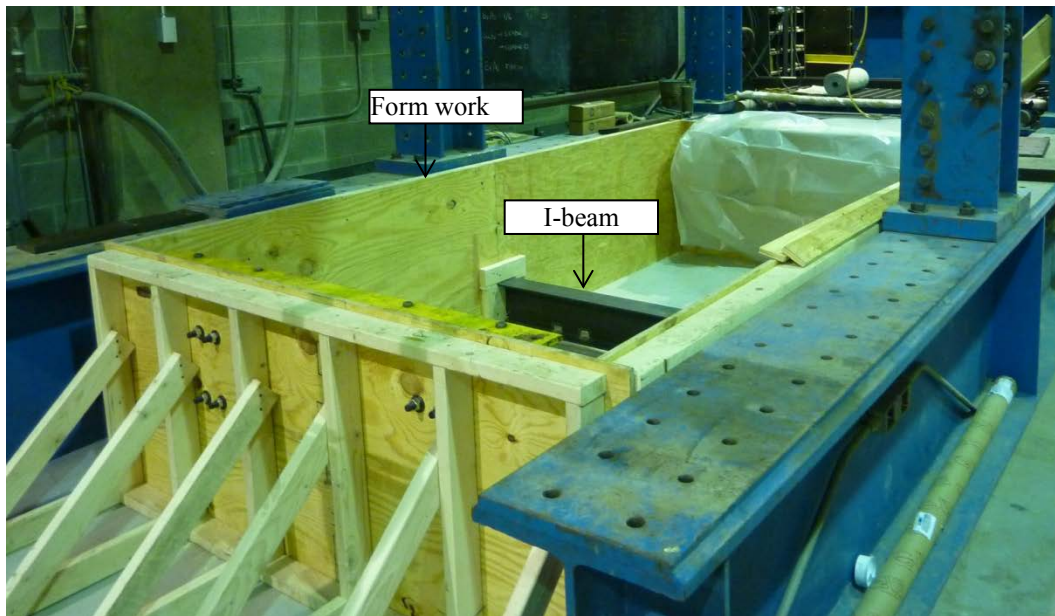
Figure 3.22. The form work used to cast the foundation.
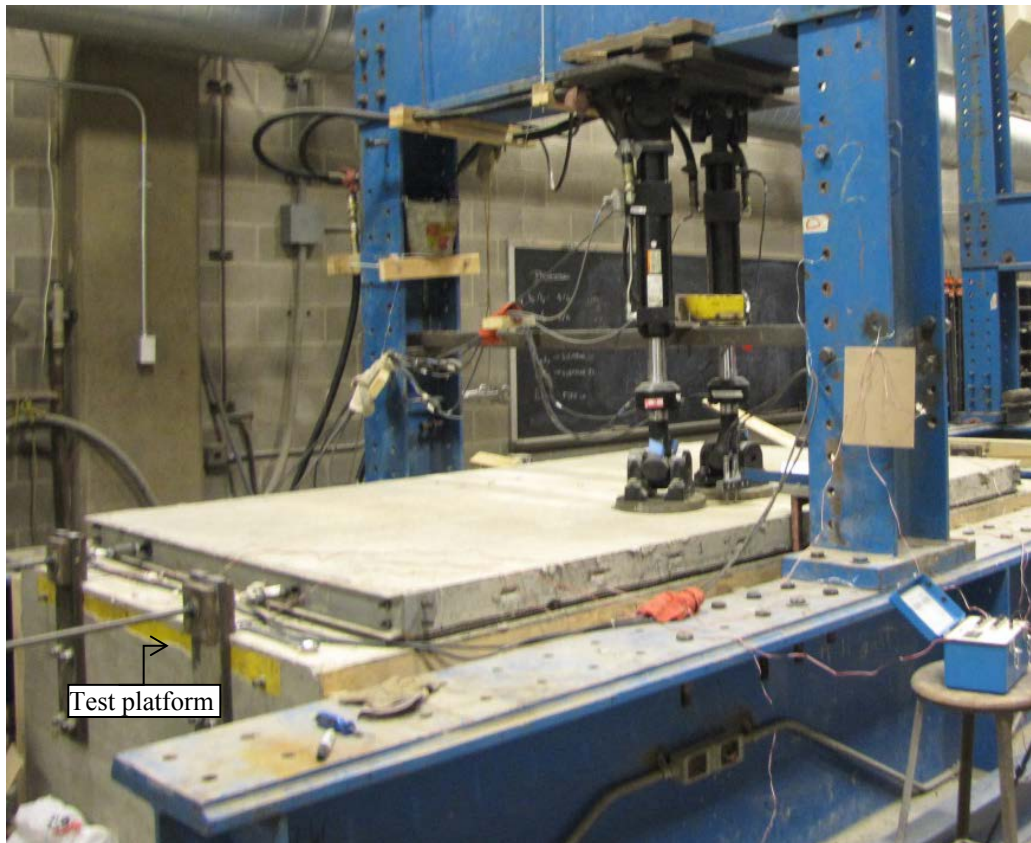
Figure 3.23. S_{ALT} setup.

Similar to the B_{ALT} setup, two layers of Fabcel 25 were used to simulate the subgrade with a modulus of subgrade reaction equal to 200 psi/in. Figure 3.24 presents a picture showing the two layers of Fabcel on top of the concrete foundation. Continuous vertical joints through the two Fabcel layers were avoided. Also, it was ensured that no joints between the pads coincide with the transverse joint of the test slab.

Figure 3.24. Two layers of Fabcel 25 laid on the concrete foundation.

Test Specimen

Different slabs sizes can be accommodated with this loading frame. In this study, 10-ft x 6-ft slabs, 4-in thick, were cast with a transverse crack initiated at the mid span (5-ft).

Casting Frame

An example of the frames used to cast the slab is shown in Figure 3.25. Four in deep steel channel sections were utilized for building the casting frame. The transverse sides were made with a single channel section whereas, the longitudinal sides are comprised of two separate channel sections, held together by a splice. See Figure 3.26. The longitudinal sides were tied by four equally spaced pencil rods which helped to attain a good rigidity in the transverse direction. Four I-bolts are placed on the two longitudinal sides of the frame so the crane can be used for lifting the specimen. See Figure 3.26. The other important components of the frame are the 26 shear keys. These are 2-in long steel rods welded on the inner side of the frame at an approximately equal spacing. These shear keys hold the slab from dropping out of the frame when it is lifted.

92
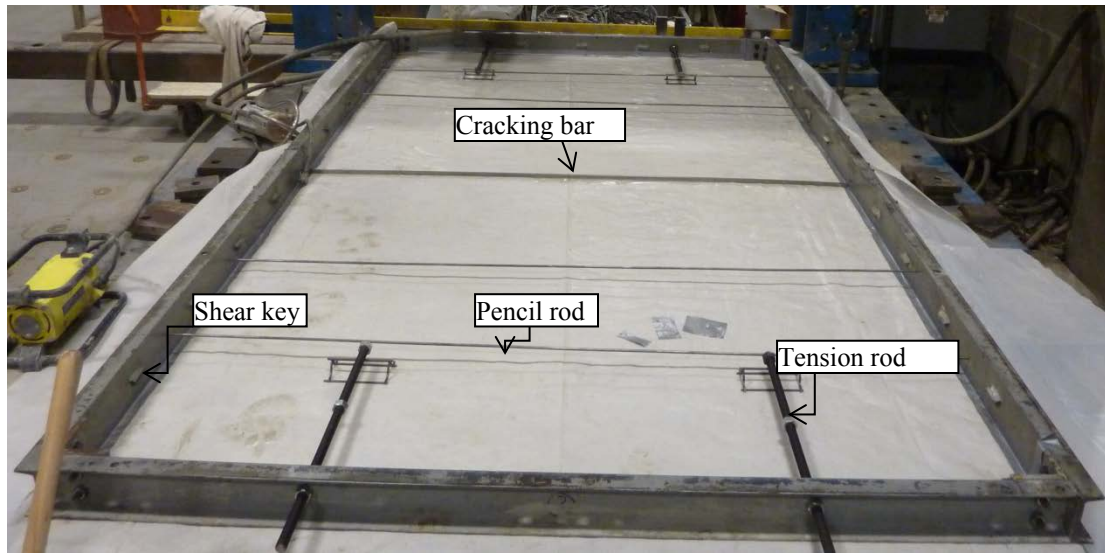
Figure 3.25. Test specimen frames for S_{ALT}.
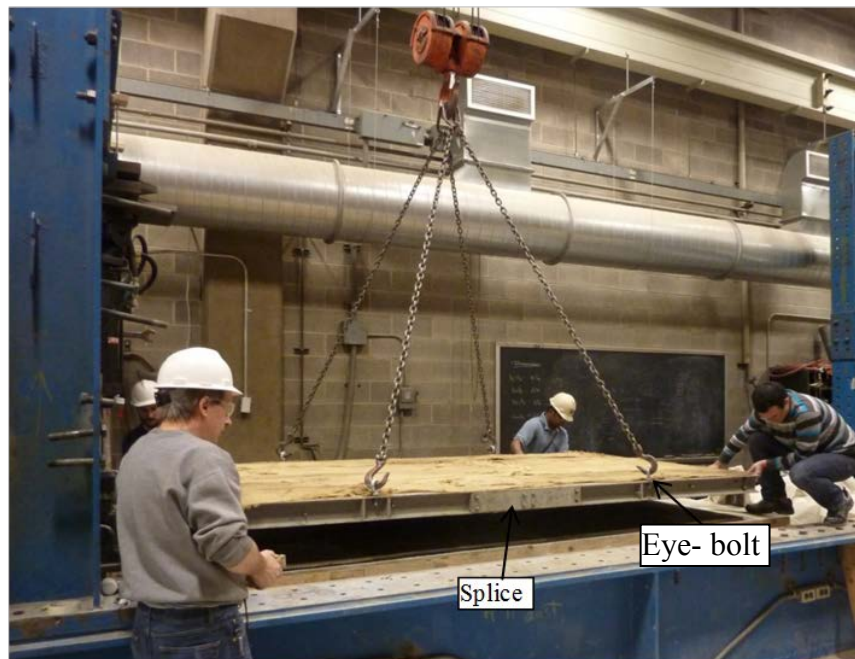
Figure 3.26. Slab is being placed after laying the Fabcel layers.

Crack Width Control Assembly

Similar to the B_{ALT}, a crack width control assembly is also required in the S_{ALT}. While casting the slabs, four threaded rods, to be referred to as tension rods, with three hexagonal nuts on each of them, were cast in the concrete in four locations, as was shown in Figure 3.25. The embedded and exposed length of the tension rods were 28 and 6 in, respectively. Each of the tension rods was extended by another threaded rod during the testing of the slab. This rod is referred to as cw rod. The cw rod is connected to the tension plate, as shown in Figure 3.27. Tension plates were mounted (vertically) on the transverse side of the foundation through bolts cast into the foundation. The tension plate has a rectangular slot at the top to allow the tension rod through it. The crack width was established by loosening and tightening the nuts on the cw rod. Two larger washers are also used on both sides of the tension plate. The strain on the tension rod was measured by using strain gages affixed to each of the cw rods.
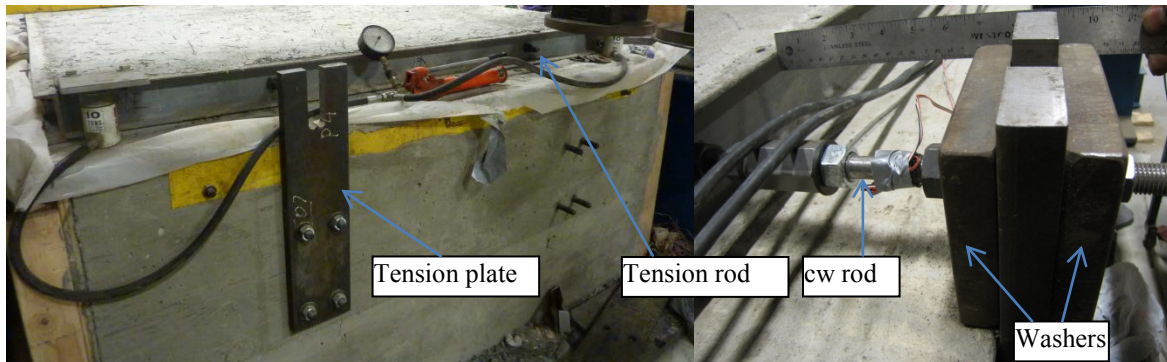
Figure 3.27. Crack width control assembly.

3.3.3   Specimen Preparation

The slabs were cast on the foundation itself so that the bottom surface of the test specimen mimics the shape of the top surface of the foundation. This proved to be immensely helpful to avoid any gaps between the artificial foundation and test slab. It may be mentioned here that a couple of shakedown slabs were initially cast on the laboratory floor but when they were transferred to the foundation for testing, gaps were noticed in many locations. Therefore, all test slabs were cast on a plastic sheet on the foundation. A properly oiled ½-in x ¼-in x 6-ft steel bar, known as crack initiation bar was cast into the slab at mid span (Figure 3.25). This crack initiation bar created a weak zone, which helped in initiating the crack at the desired location at the bottom mid-span.

Casting of the slab generally started at mid-span (Figure 3.28). Shaft vibrators were used to consolidate the concrete. Figure 3.29 shows a photograph taken right after finishing the surface. Gage studs for crack width measurement were inserted into the concrete right after finishing the surface. A pair of gage studs are installed 3 in off the longitudinal edge on each side of the slab. The gage studs consisted of small bolts with a conical slot drilled into the head, as shown in Figure 3.30.

www.manaraa.com

Figure 3.28. Casting of the slab.

Figure 3.29. Example of a finished slab.

Figure 3.30. Photograph of a pair gage studs inserted into the concrete.

The mid-slab transverse crack was initiated 18 hours after casting. A flexural load was applied to initiate the crack at the bottom of the slab and mid-span. One end of the 10-ft x 6-ft slab was jacked upward while restraining any upward movement on the other half of the slab. Figure 3.31 shows the slab cracking procedure. It can be seen that a 4-in x 4-in yellow steel angle was placed at the middle of the slab. The angle was placed such that it rests on the restrained half of the 10-ft long slab, while the upward force was applied at the corners at the other end. The upward force was applied by using a pair of 10-ton hydraulic jacks through the two steel plates connected to the frame at the corners along the end. The slab was cured with plastic covered wet burlap for at least 28 days before testing.

Figure 3.31. Slab cracking procedure.

3.3.4 Test Procedure

Before loading of the slab can begin, the slab must be lifted off the foundation so that the Fabcel layers can be placed. The slab is then placed on top of the two layers of Fabcel. Proper referencing work was performed before moving the slab so that it could be replaced back in the exact same location from where it was lifted. After laying the Fabcel layers and setting the slab in place, the crack width control assembly was installed along with the deflection measuring assembly. The deflection measuring assembly consists of a 6-in wide steel plates attached to the concrete foundation, an arm connected to the steel plate, two aluminum LVDT holders and two LVDTs. Figure 3.32 shows the two LVDTs mounted in the LVDT holders. Both of the LVDTs are placed 1in from the crack, one on the approach slab and the other one on the leave slab. Both are approximately 12 in from the longitudinal edge. The load was applied by two actuators with

www.manaraa.com

a 12-in diameter and 1-in thick circular load plates attached to each. A circular rubber pad was attached to each load plate to avoid any localized stress concentration on the slab. The location of the load plates and the LVDTs can be seen in the schematic presented in Figure 3.33.
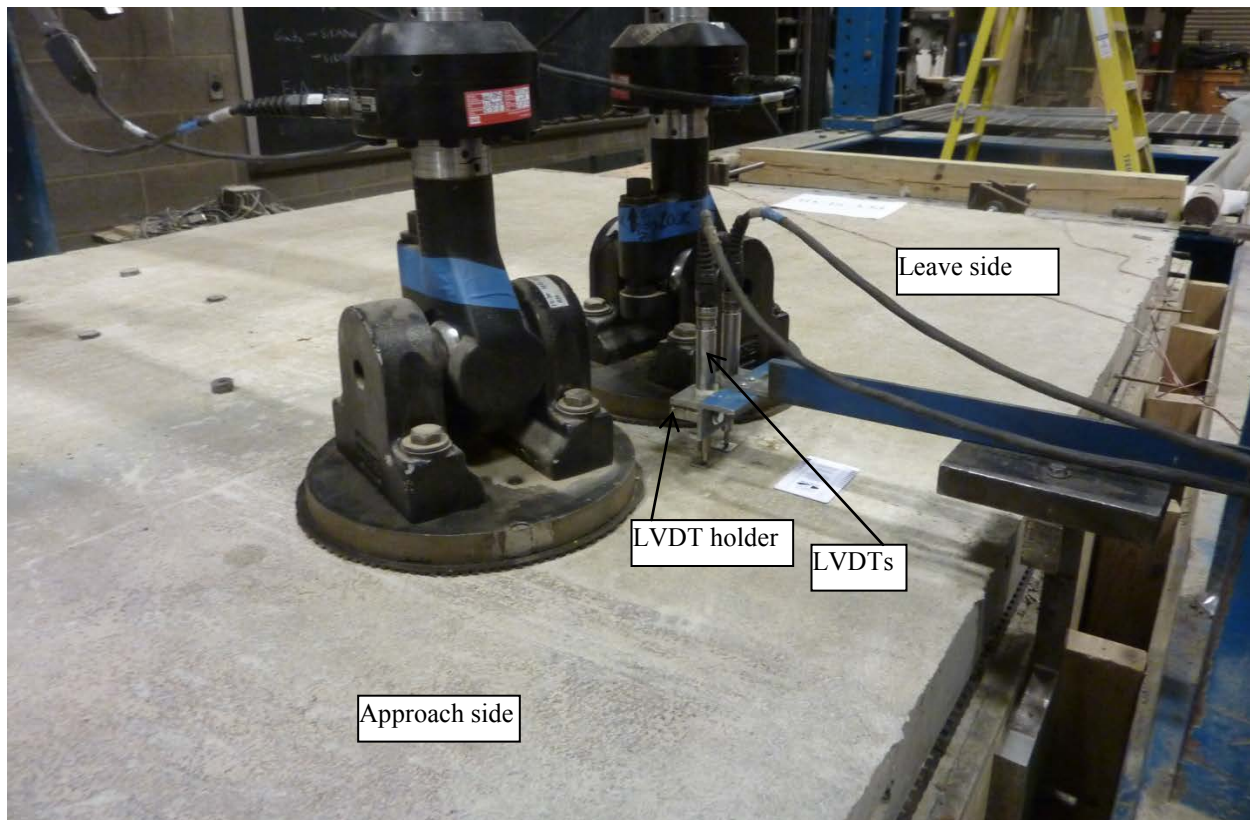
Figure 3.32. LVDTs and the LVDT holder for the S_{ALT}.
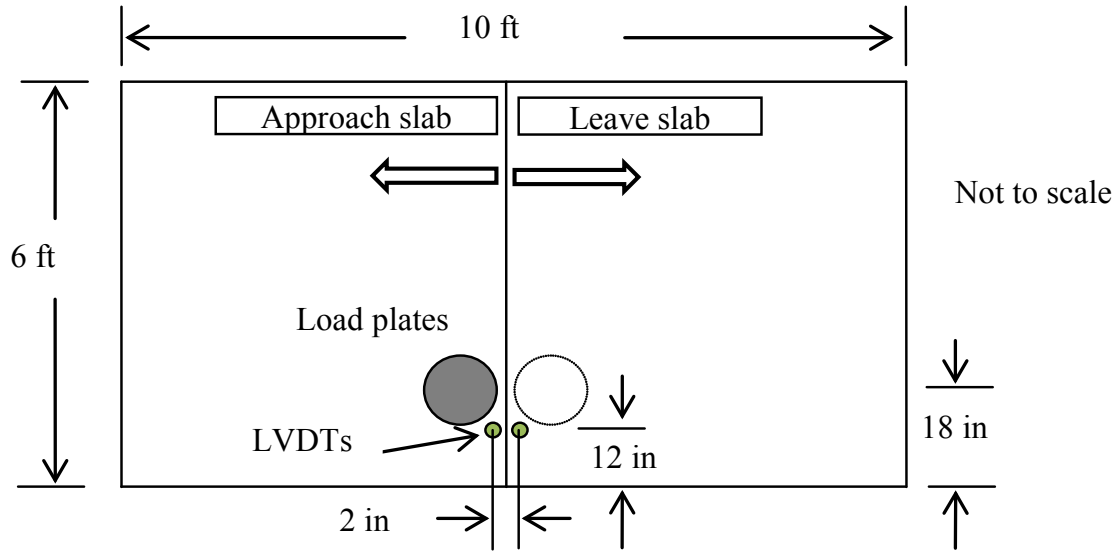
Figure 3.33. Location of load plates and LVDTs in S_{ALT} procedure.

The joint performance test was conducted by applying a composite sinusoidal load profile through each actuator. The load profile was designed in such a way that each slab was loaded for a period of 0.035 seconds with a 0.165 second rest period providing a time of 0.20 seconds to complete each cycle. Thus, the overall load cycle frequency is 5 Hz. During the actual loading period, the load rises from 500 to 9000 lbs in each actuator. In the rest period, a 500-lb load was maintained so that the actuator and slab remain in contact. The two actuators were operated with a 90-degree phase difference. The time difference between the two peaks was 0.032 seconds, which was equivalent to a vehicle speed of 30 to 35 mph. It was also ensured that when one actuator reaches its peak load, the other is applying the minimum 500-lb load. It may be noted that the magnitudes of the loading periods, rest periods, peak loads, loads at rest period and the phase difference between the peak loads of the two actuators may slightly vary with the joint condition. Similar to the B_{ALT}, the joint performance was evaluated at different crack widths and load applications. The joint performance evaluation concept followed in the S_{ALT} procedure is discussed in the next section.

100

3.4 JOINT PERFORMANCE EVALUATION PROCEDURE

The joint performance can be characterized in many ways, such as in terms of load transfer efficiency (LTE), differential deflection (DD), differential deflection ratio (DDR), differential energy dissipation (DED) and dissipated energy ratio (DER). In the present study, both the B_{ALT} and S_{ALT} procedures are able to produce any of the above mentioned joint performance characterization parameters. These parameters are derived either from the load and/or deflection profiles.

The following subsections describe the concepts of evaluating the joint performance through LTE and DER in both the B_{ALT} and S_{ALT} procedures.

3.4.1 Joint Performance through LTE

3.4.1.1 B_{ALT}

The deflection load transfer efficiency, LTE, was obtained by using the deflections corresponding to the time of the peak loads. As was mentioned in Subsection 3.2.2, load was applied in both upward and downward directions. Therefore, the LTE can be obtained in both these directions as well. Typical examples of the load and deflection profiles for the B_{ALT} procedure are shown in Figure 3.34. The negative sign represents the load and deflection in the upward direction when the actuator provides a tension load, whereas the positive sign represents the opposite. The presence of a very small phase difference between the peak load and peak deflection could be observed in Figure 3.34. This phase difference varies between 1 to 5 milliseconds and is a function of joint stiffness. This is due to the time dependent response of the Fabcel layers.

101
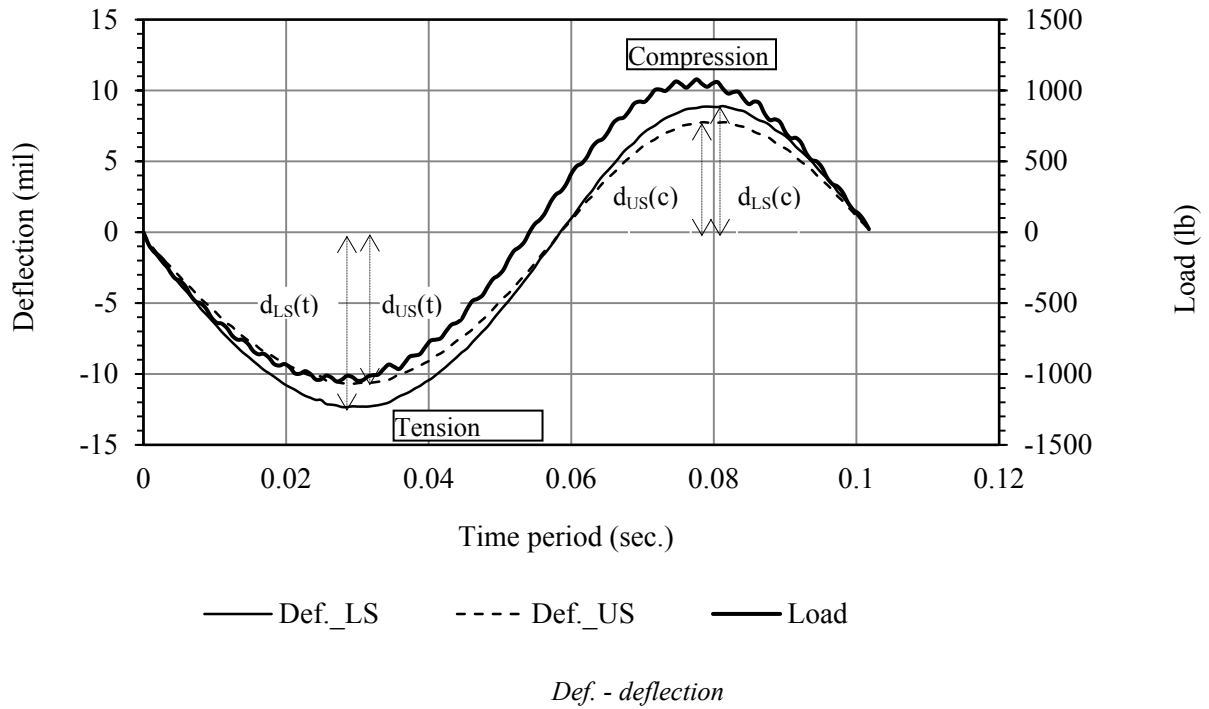
Def. - deflection

Figure 3.34. Load and deflection profiles for the B$_{ALT}$.

The LTE from B$_{ALT}$, LTE$_B$, is defined as the ratio of the unloaded side deflection to the loaded side deflection at the peak load. When the nature of the peak load is in tension, it is referred as the tension LTE, or LTE$_{B(t)}$, and when the nature of the load is compression, it is referred as the compression LTE, or LTE$_{B(c)}$. The LTE under both the tension and compression loads can be estimated by using the following equations.

$$\text{LTE}_{B(t)} = \frac{d_{US(t)}}{d_{LS(t)}} \tag{3.5}$$

$$\text{LTE}_{B(c)} = \frac{d_{US(c)}}{d_{LS(c)}} \tag{3.6}$$

102

where $d_{US(t)}$ and $d_{US(c)}$ are the unloaded side deflections under the tension and compression load, respectively; $d_{LS(t)}$ and $d_{LS(c)}$ are the loaded side deflections under the tension and compression load, respectively.

Ideally, the difference between $LTE_{B(t)}$ and $LTE_{B(c)}$ shall be zero when the surface areas of the aggregates engaged in load transfer in both the directions are equal. But in reality, the developed crack is not perfectly vertical, which results in a different quantity of aggregate engagement in one direction as compared with the other. Since the area of the crack face in a beam specimen is far lower than that of a slab specimen, a small difference in the area of the aggregate engaged in load transfer significantly influences the magnitude of the load transfer. Therefore, the average of $LTE_{B(t)}$ and $LTE_{B(c)}$ provides a more meaningful characterization. This average neutralizes the effect of macro texture to a certain extent.

3.4.1.2 S_{ALT}

The typical load and deflection profiles obtained in the S_{ALT} procedure are shown in Figure 3.35. It can be seen that when the approach slab load reaches the peak load, the leave slab load goes down to the minimum, and vice versa. It can be assumed that at the time when the load on a particular slab reaches the peak, the deflections on both the approach and leave slabs are due only to the load applied on that slab. It can be seen in Figure 3.35 that the time when the peak load is applied to the approach slab, peak deflection also occurs at about the same time the load peak is observed. The same occurs for the leave slab. In this procedure, a phase difference between the peak load and peak deflection can be observed, as was seen in the B_{ALT} due to the time-dependent response of the Fabcel.

103
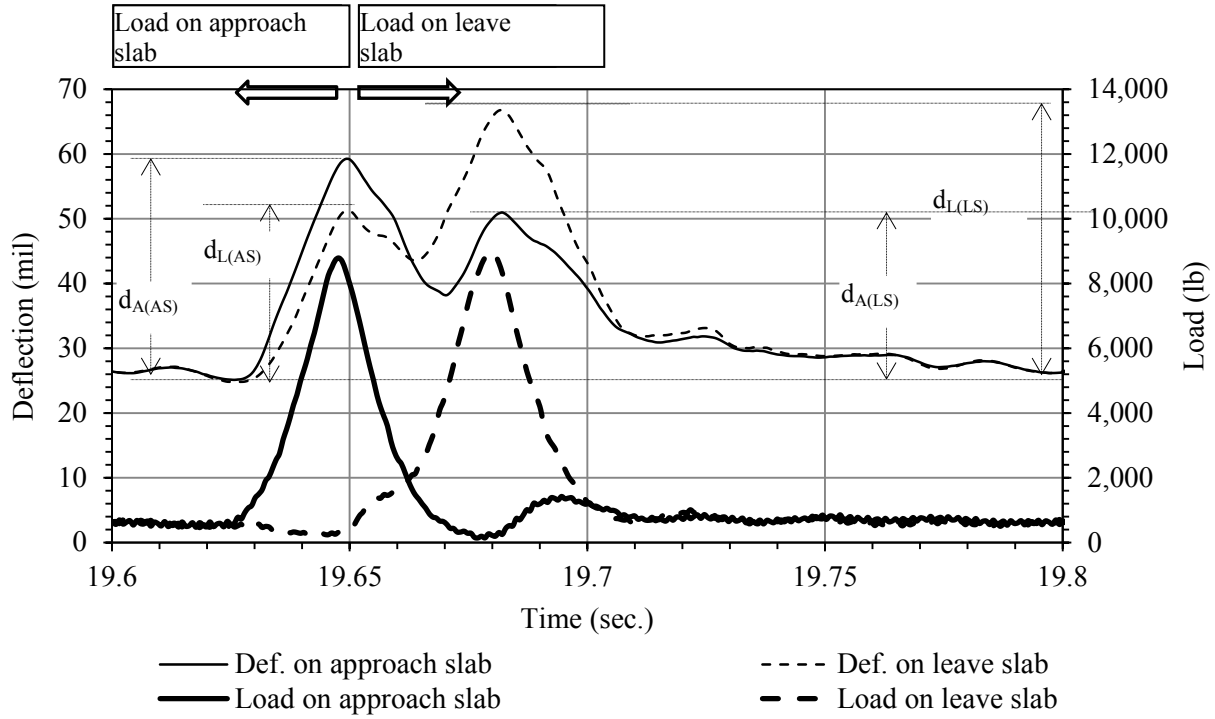
Figure 3.35. Typical load and deflection profiles for S_{ALT}.

In this case, LTE can be separately calculated for the approach and leave sides. These are calculated using the following equations.

$$LTE_{S(A)} = \frac{d_{L(AS)}}{d_{A(AS)}} \qquad (3.7)$$

$$LTE_{S(L)} = \frac{d_{A(LS)}}{d_{L(LS)}} \qquad (3.8)$$

where $LTE_{S(A)}$ and $LTE_{S(L)}$ are the approach and leave side LTEs; $d_{L(AS)}$ and $d_{A(AS)}$ are the deflections on the leave and approach sides, respectively, with the peak load on the approach slab; $d_{A(LS)}$ and $d_{L(LS)}$ are the deflections on the approach and leave sides, respectively, with the peak load on the leave slab. All these deflections are obtained by subtracting the deflections due to the load at rest period, as shown in Figure 3.35.

104

3.4.2 Joint Performance through DER

The concrete pavement system dissipates energy when it deflects under the wheel load. The magnitude of the dissipated energy (DE) is proportional to the magnitude of the pavement deflection. Conceptually, the DE is the area under the load vs deflection curve. The difference in magnitude of the DEs between the approach and leave sides is known as differential energy dissipation (DED), and the ratio between the leave side DE to the approach side DE is known as dissipated energy ratio (DER). For good joint performance, the magnitude of the DE on both sides is low with lower values of DED and DER.

3.4.2.1 B_{ALT}

In the B_{ALT}, as was shown in Figure 3.34, the total load cycle comprises of four individual loading segments, in order, (i) 0 to -1050 lbs, (ii) -1050 to 0 lb, (iii) 0 to +1050 lbs and (iv) +1050 to 0 lb. In this figure, it is seen that at the time when the load drops from -1050 to 0 lb (at the end of the second segment), the Fabcel layers still exhibit some amount of deflection. This results in a hysteresis in the load vs deflection curve. This means the areas of the load vs deflection curves for the 0 to maximum and maximum to 0 loads are not similar; the later one has a higher value. This can be seen in Figure 3.36. This figure includes load vs deflection profiles for all four segments, for deflections on both the loaded and unloaded sides. Because of the presence of the hysteresis, the areas under the load vs deflection curve for each segment are different and therefore computed separately.

105
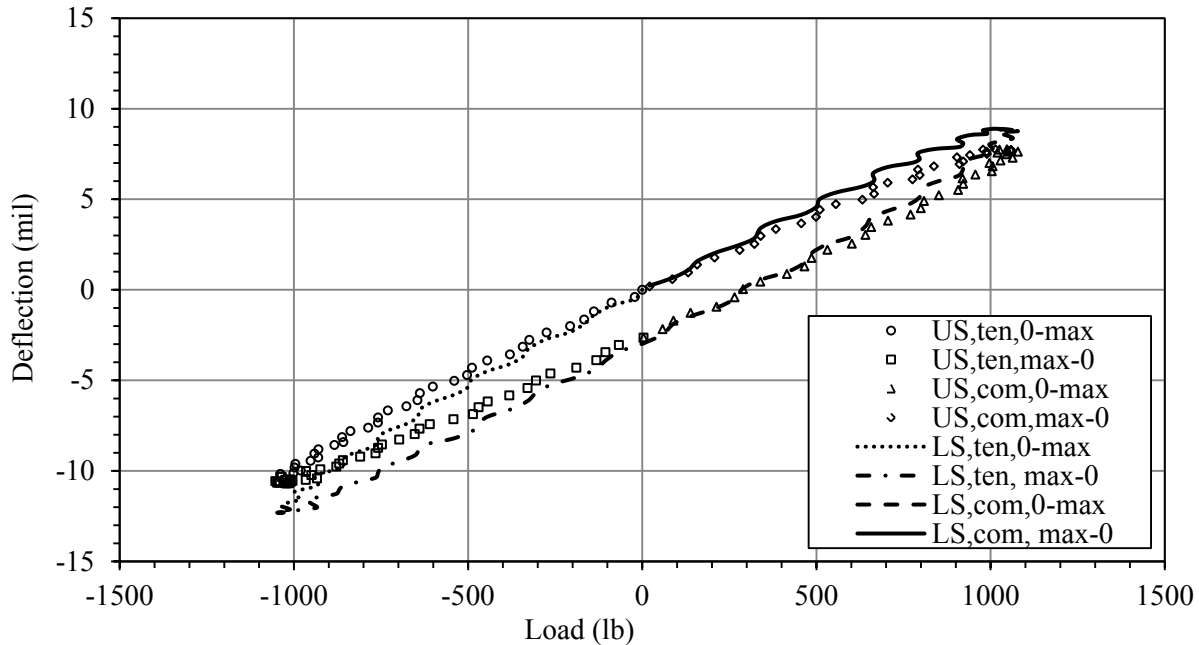
US- unloaded side; LS- loaded side; ten- tension; com- compression.

Figure 3.36. A typical load vs deflection curve for the B_{ALT}.

The total load vs deflection curve shown in Figure 3.36 is broken into eight separate segments, four each for the loaded and unloaded sides, as shown in Figure 3.37. The curves for the loaded side and unloaded side are presented in plots (i) to (iv) and (v) to (viii), respectively. The area in each plot, which represents the DE, is marked as A_n (n = 1 to 8). The DE computed separately for each segment facilitates the derivation of the DED and DER separately for the tension loading and compression loading. Under the tension loading, the sum of A_1 and A_2 represents the total DE under the loaded side, whereas the sum of A_5 and A_6 represents the total DE under the unloaded side. Similarly, A_3, A_4, A_7 and A_8 can be used to compute the corresponding DEs for the loaded and unloaded sides, when the compression load is applied.

106
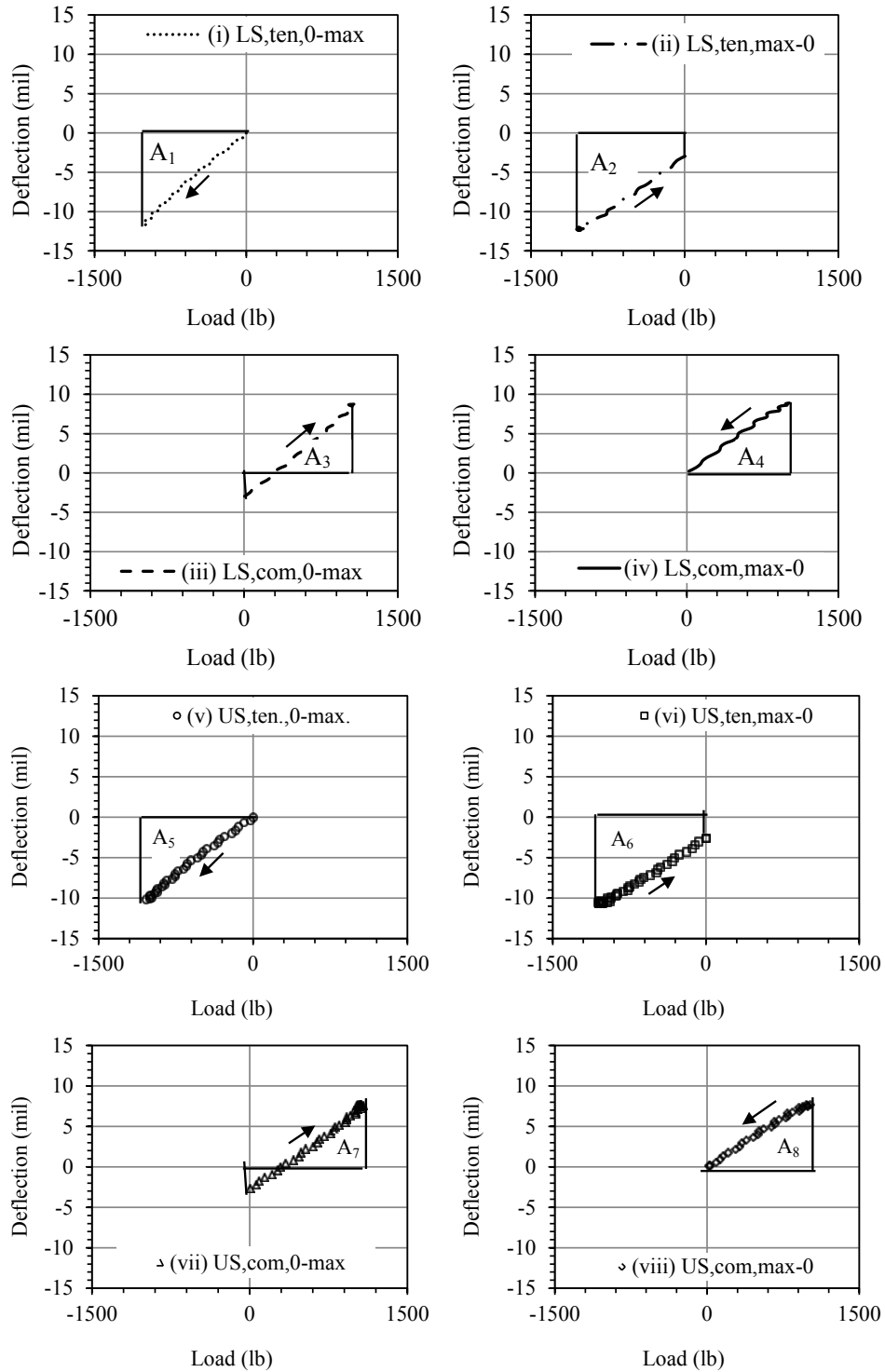
Figure 3.37. Individual segments in the load vs deflection curve: (i) to (iv) - loaded side and (v) to (viii) -unloaded side.

www.manaraa.com

The DED and DER in the B_{ALT} procedure can then be computed by using the following equations.

$$DED_{B(t)} = (A_1 + A_2) - (A_5 + A_6) \tag{3.9}$$

$$DED_{B(c)} = (A_3 + A_4) - (A_7 + A_8) \tag{3.10}$$

$$DER_{B(t)} = \frac{(A_5 + A_6)}{(A_1 + A_2)} \tag{3.11}$$

$$DER_{B(c)} = \frac{(A_7 + A_8)}{(A_3 + A_4)} \tag{3.12}$$

where $DED_{B(t)}$ and $DED_{B(c)}$ are the DED under the tension and compression loads, respectively; $DER_{B(t)}$ and $DER_{B(c)}$ are the DER under the tension and compression loads, respectively. Table 3.4 presents the values of A_1 to A_8 computed for the load and deflection profiles demonstrated in Figure 3.37. Table 3.5 presents values of DE, DED and DER for the same. A comprehensive detail of the DER calculated for all the B_{ALT} specimens tested under the scope of the present study are provided in Chapter 5.

Table 3.4. Values of A_1 to A_8 for the load and deflection profiles shown in Figure 3.36 and Figure 3.37.

Name of the segments	Energy or areas of load vs deflection curve
A_1	6576
A_2	10680
A_3	5386
A_4	5739
A_5	5682
A_6	9313
A_7	4701
A_8	5027

Table 3.5. DE, DED and DER for the load and deflection profiles demonstrated in Figure 3.36 and Figure 3.37.

Cumulative dissipation energy (DE) (lb-in)				Differential energy dissipation (DED) (lb-in)		Differential energy ratio (DER) (percent)	
Tension load		Compression load		$DED_{B(t)}$	$DED_{B(c)}$	$DER_{B(t)}$	$DER_{B(c)}$
LS	US	LS	US	2261	1396	87	87
17256	14996	11125	9728				

3.4.2.2 S_{ALT}

The load in the S_{ALT} is applied using two actuators so the derivation of DED and DER is different from the B_{ALT}. Figure 3.38 and Figure 3.39 show the load vs deflection curves for the approach and leave slabs, respectively, for the example demonstrated in Figure 3.35. The solid line in the graph represents the deflection when the load is applied on the approach slab, whereas, the dash line shows the deflection when load is applied on the leave slab. The presence of the hysteresis is visible in all the curves in both of the figures. The delayed response of the Fabcel is the reason for the hysteresis. Therefore, in the S_{ALT}, DEs are also calculated separately for each different segment in the total loading cycle.

The load vs deflection curves shown in Figure 3.38 and Figure 3.39 are broken in to eight separate segments, four for the approach and four the leave side slabs. These are shown in Figure 3.40. The area of each segment, marked as B_n (n = 1 to 8), represents the corresponding DE for that segment. B_1 and B_2 are the DEs for the approach slab, whereas B_5 and B_6 are the DEs for the leave slab with the load being applied on the approach slab. Similarly, B_3, B_4, B_7 and B_8 are the DEs corresponding to the load on the leave slab.
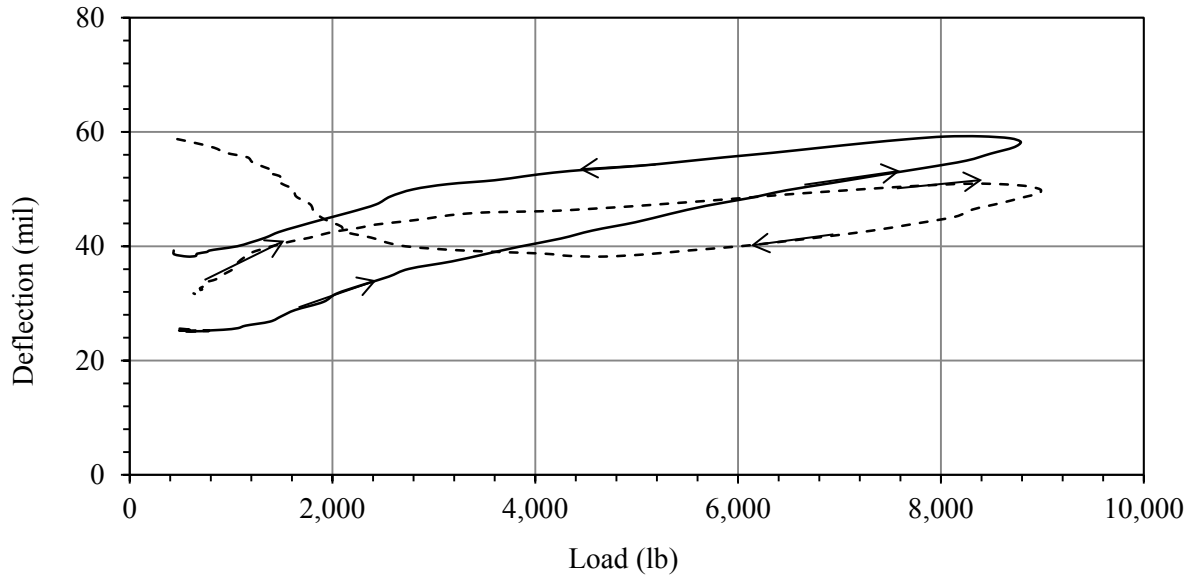
Figure 3.38. Load vs deflection curves for the approach slab.
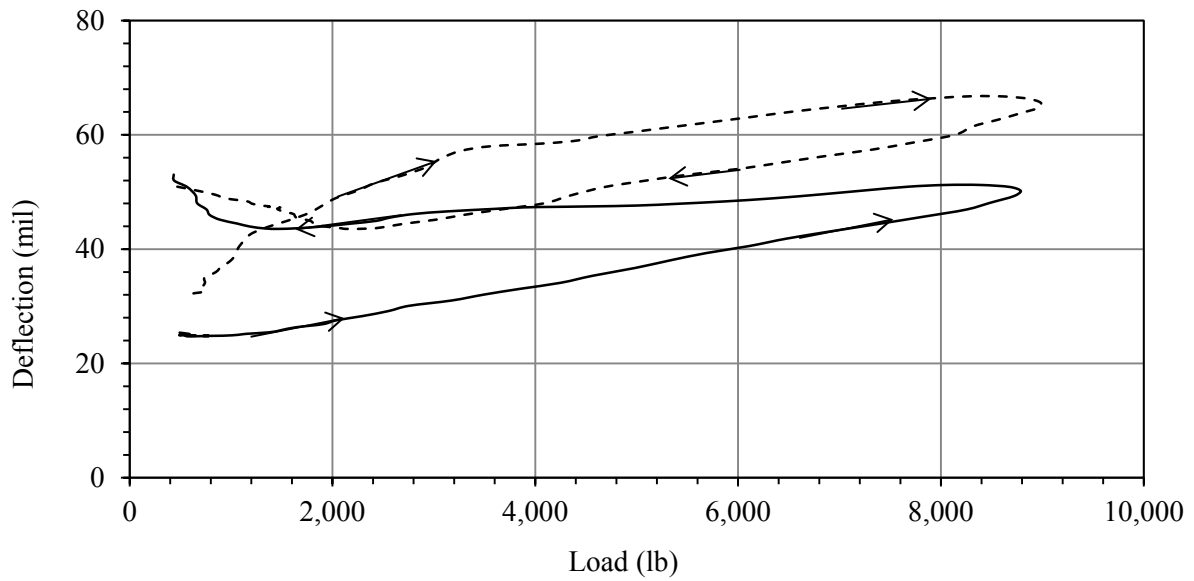
Figure 3.39. Load vs deflection curves for the leave slab.

110
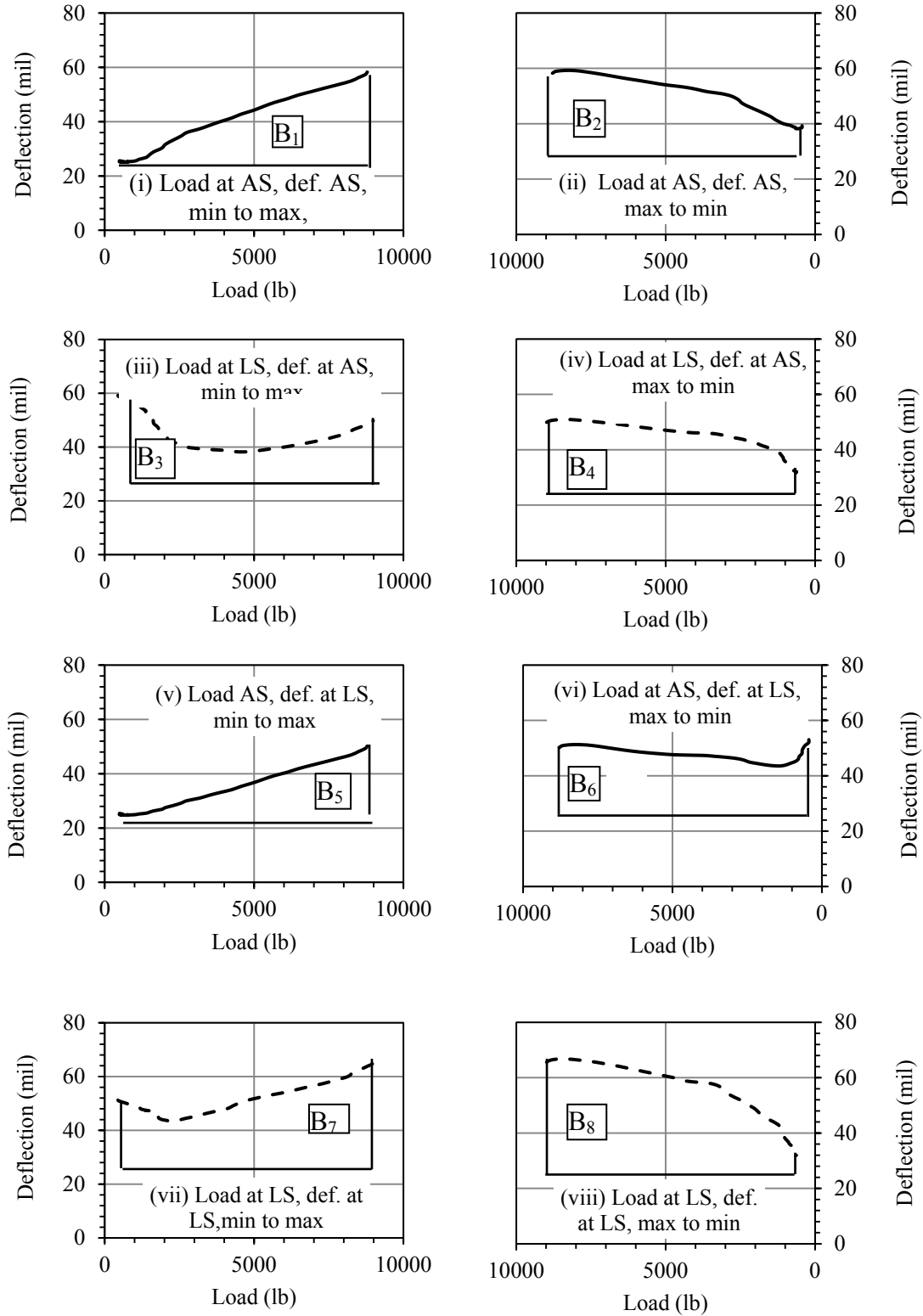
Figure 3.40. Individual segments in the S_{ALT} load vs deflection curve: (i) to (iv) – Deflection on the approach slab, (v) to (viii) – Deflection on the leave slab.

111

Using an approach similar to the B_{ALT} procedure, the DED and DER for the S_{ALT} can be determined using the following equations.

$$DED_{S(A)} = (B_1 + B_2) - (B_5 + B_6) \tag{3.13}$$

$$DED_{S(L)} = (B_7 + B_8) - (B_3 + B_4) \tag{3.14}$$

$$DER_{S(A)} = \frac{(B_5 + B_6)}{(B_1 + B_2)} \tag{3.15}$$

$$DER_{S(L)} = \frac{(B_3 + B_4)}{(B_7 + B_8)} \tag{3.16}$$

where $DED_{S(A)}$ and $DED_{S(L)}$ are the DED for the approach and leave slabs, respectively; $DER_{S(A)}$ and $DER_{S(L)}$ are the DER for the approach and leave slabs, respectively.

In the load profiles shown in Figure 3.35, it can be seen that there is an overlap for the approach and leave slab loads. This occurs in the middle of the loading cycle when the load applied on the approach slab is transferred to the leave slab. In this particular case (Figure 3.35), the overlapping of the load profiles starts when the load on the approach slabs drops below approximately 2000 lbs, and this overlapping remains until the load on the leave slab reaches 2000 lbs.

In Figure 3.38 and Figure 3.39, it can also be seen that the overlapping of the load profiles influences the magnitude of the defection at a lower load (below 2000 lbs in this case). Therefore, an adjustment is required to be made to minimize this influence. To investigate the influence of the overlapping of the load profiles on the magnitude of the DER_S, a sensitivity study was conducted. In the sensitivity study, the variation in the values of DER_S was investigated considering different cut-off loads (500, 750, 1000, 1500, 2000 and 2500 lbs). For example, when the cut-off load is 500 lbs, the energy computed for any load below 500 lbs was discarded. In addition to using different cut-off loads, one more option was considered, i.e.

112

utilization of the differential load. In this option, the difference in the magnitudes of loads between the two slabs (e.g. for approach slab: approach slab load minus leave slab load; for leave slab: leave slab load minus approach slab load) were determined. When the magnitude of the differential load is negative, the energy computed for that particular load was discarded. This approach provided a more meaningful solution as the energy estimated at the overlapping region was only adjusted. Whereas, when a cut-off load was used, energy estimated for any loads below that cut-off load was discarded.

Under the scope of the study, one PC and two FRC (FRC1 and FRC2) slabs were tested for evaluating joint performance. The joint performance was evaluated at different crack widths. Comprehensive details of the mixture properties for these slabs are presented in Chapter 4. The detailed joint performance results for these slabs are presented in Chapter 5. Using the load and deflection data, approach slab DER_S and leave slab DER_S were calculated. Figure 3.41 through Figure 3.43 present the averages of the approach and leave slab DER_S over the crack width for the PC slab, FRC1 and FRC2 slabs, respectively. In each plot, DER_S estimated considering different cut-off loads and also differential load are incorporated. The plots for the approach and leave slab DER_S over the crack width for all the three slabs are provided in Appendix A. It may be mentioned here that the deflection due to the rest period load was not deducted from the total deflection when calculating the DER_S in the sensitivity analysis. Since, this sensitivity analysis is performed only to find out a solution to avoid the interference of the overlapping of loads in the transition zone, utilizing the total deflection or total deflection minus deflection (net deflection) at rest load produces a similar variation in the DER_S results between the different cut-off loads or differential load. However, all the DER_S calculations in Chapter 5 are performed based on net deflection.

It can be seen that the sensitivity of the cut-off loads or the differential load increases with the crack width. On a closer investigation of the plots for the approach and leave slab DERs over the crack width, it was found that the difference between the approach slab DERs and leave slab DERs is relatively lower when the differential load is used as compared to the cut-off loads. Also, it may be mentioned that only one single load is used when joints are evaluated using the falling weight deflectometer (FWD) in the field. So, basically a cut-off load is not required for evaluation of the joints in the field. Considering all these points, it is decided to use the differential load for estimating the DER_S.

Table 3.6 presents the values of B_1 to B_8 and Table 3.7 presents the DED_S and DER_S for the approach and leave slabs for the load and deflection profiles demonstrated in Figure 3.35, Figure 3.38, Figure 3.39 and Figure 3.40. Net deflections are used in the example.
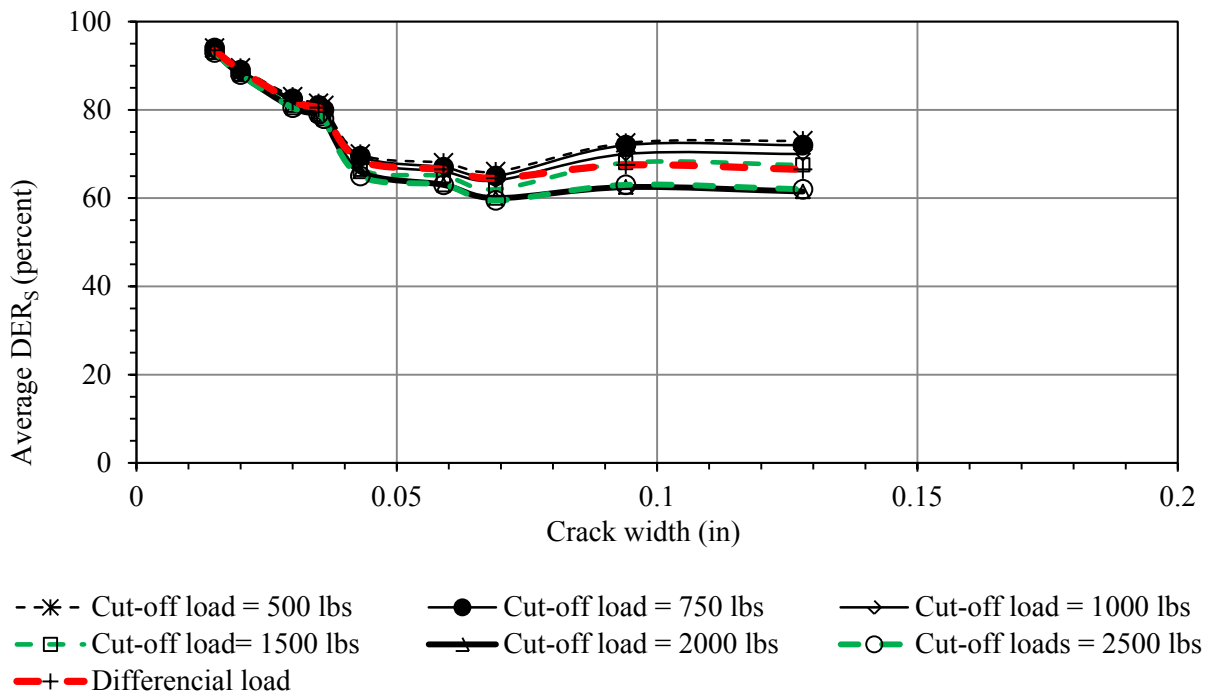
Figure 3.41. Average DER_S over the crack width for PC slab.
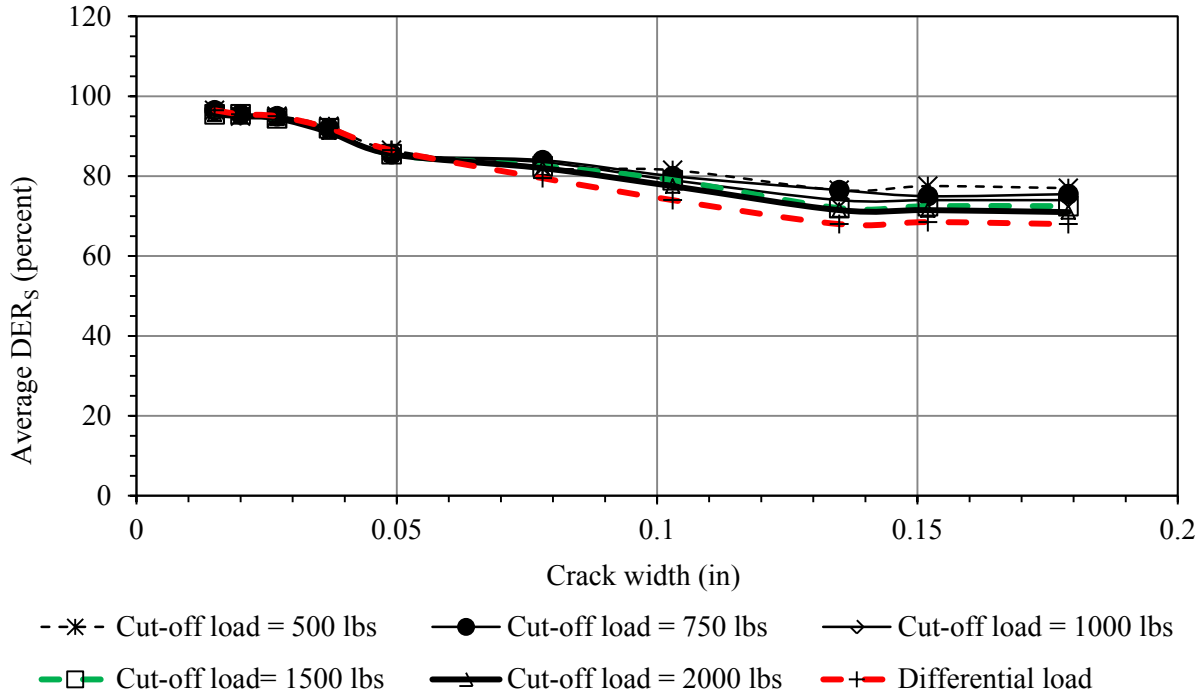
Figure 3.42. Average DER$_S$ over the crack width for FRC1 slab.
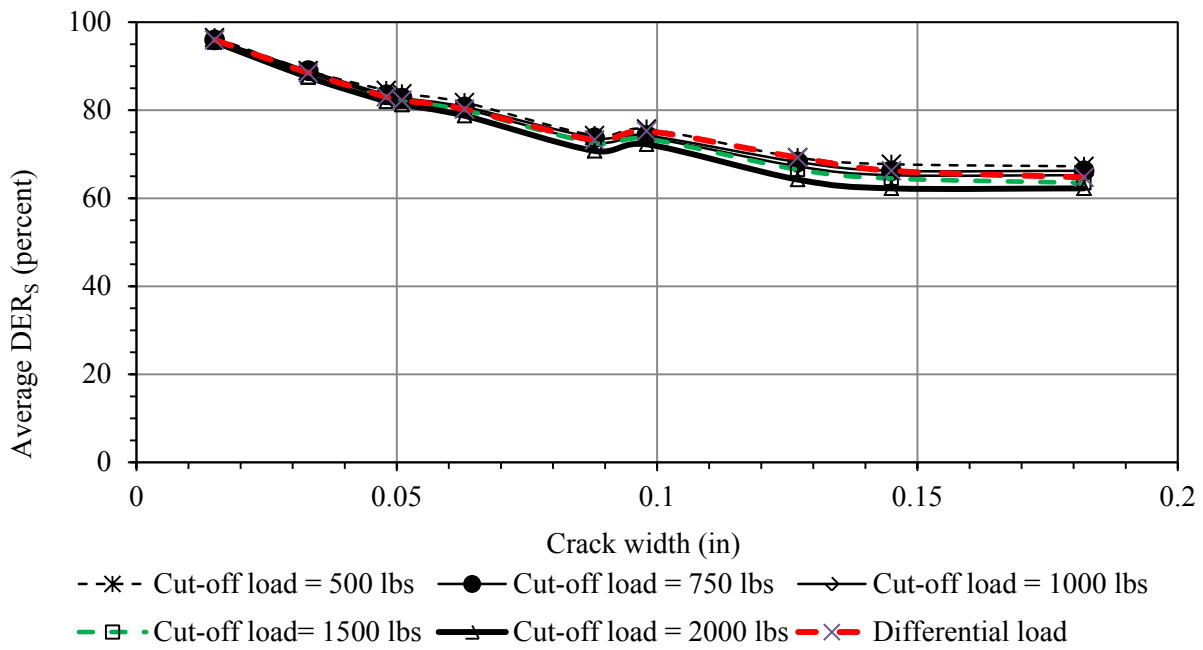
Figure 3.43. Average DER$_S$ over the crack width for FRC2 slab.

Table 3.6. Values of B_1 to B_8 for the example shown in Figure 3.40.

Name of the segments	Energy or areas of load vs deflection curve
B_1	159828
B_2	265511
B_3	159262
B_4	213307
B_5	107397
B_6	214214
B_7	248355
B_8	325124

Table 3.7. Cumulative DE, DED and DER for the example shown in Figure 3.40.

Cumulative dissipation energy (DE)				Differential energy dissipation (DED)		Differential energy ratio (DER) (percent)	
Load at AS		Load at LS		$DED_{S(A)}$	$DED_{S(L)}$	$DER_{S(A)}$	$DER_{S(L)}$
AS	LS	AS	LS				
425339	321611	372568	573479	103729	200910	76	65

3.5   CONCLUSIONS

This chapter presented a comprehensive description of the two joint performance test setups built under the scope of the present study. A discussion was presented on the design principle behind the development of the B_{ALT} procedure. This procedure was developed to simulate a slab LTE test with a beam LTE test. The magnitude and location of the load in the B_{ALT} was determined through an analysis using the finite element method.

Fabrication of the test setups and sample preparation techniques for both B_{ALT} and S_{ALT} were presented. The approaches for analyzing the data collected in order to characterize joint performance parameters are presented.

116

Although both of the methods were developed to evaluate the joint performance for a whitetopping overlay, the joint performance for any concrete pavement is also possible using either method. Evaluation of the joint performance with the B_{ALT} procedure is very economical faster, and provides an easy method to evaluate the other effects on the joint performance, such as provided fiber. This setup can be very helpful in characterizing joint performance when a large number of variables are to be considered. The S_{ALT} is more expensive but simulates the pavement joint condition in a more realistic manner.

4.0   MATERIAL PROPERTIES AND LABORATORY TEST PLAN

4.1   INTRODUCTION

A large-scale laboratory study was conducted to investigate the joint performance of the plain and fiber reinforced concretes through both the (i) B_{ALT} and (ii) S_{ALT} procedures. One PC and two FRC mixes were considered to evaluate the effect of the use of fibers has on joint performance. The relationship between LTE and number of load cycles (N) and cw were established for each concrete mixture. The majority of the testing consists of the $B_{ALT,}$ since it is more economical and faster than the S_{ALT}. This chapter presents the properties of the materials and the detailed plan for the laboratory study.

4.2   MATERIALS

4.2.1   Aggregates and Cement

In jointed plain concrete pavements,, the material that plays the most significant role in joint performance is the coarse aggregates. Therefore, only one aggregate source was used throughout the study. River gravel conforming to an AASHTO No. 57 gradation was used. The physical characteristics of the selected coarse aggregates are given in Table 4.1. The upper and lower

118

limits of the AASHTO No. 57 gradation and the actual gradation of the selected coarse aggregates are presented in Figure 4.1. One primary objective of this study is to investigate the contribution of fibers in joint performance. Therefore, an aggregate with a relatively high (34 percent) Los Angeles abrasion was selected so that the contribution of the fibers could be more prominently captured.

The fine aggregate used in casting all specimens is also from a single source. The fineness modulus, water absorption and saturated surface dry bulk specific gravity of the fine aggregate used are 2.86, 1.24 percent and 2.62, respectively. ASTM Type-I cement was used for casting all the specimens, except for a few trial specimens.

Table 4.1. Physical characteristics of the coarse aggregates.

Aggregate type	River gravel
Top size	1.0 in
Gradation	AASHTO No. 57
Bulk specific gravity (SSD)	2.50
Water absorption capacity	2.07 percent
Los Angeles abrasion value	34 percent

119
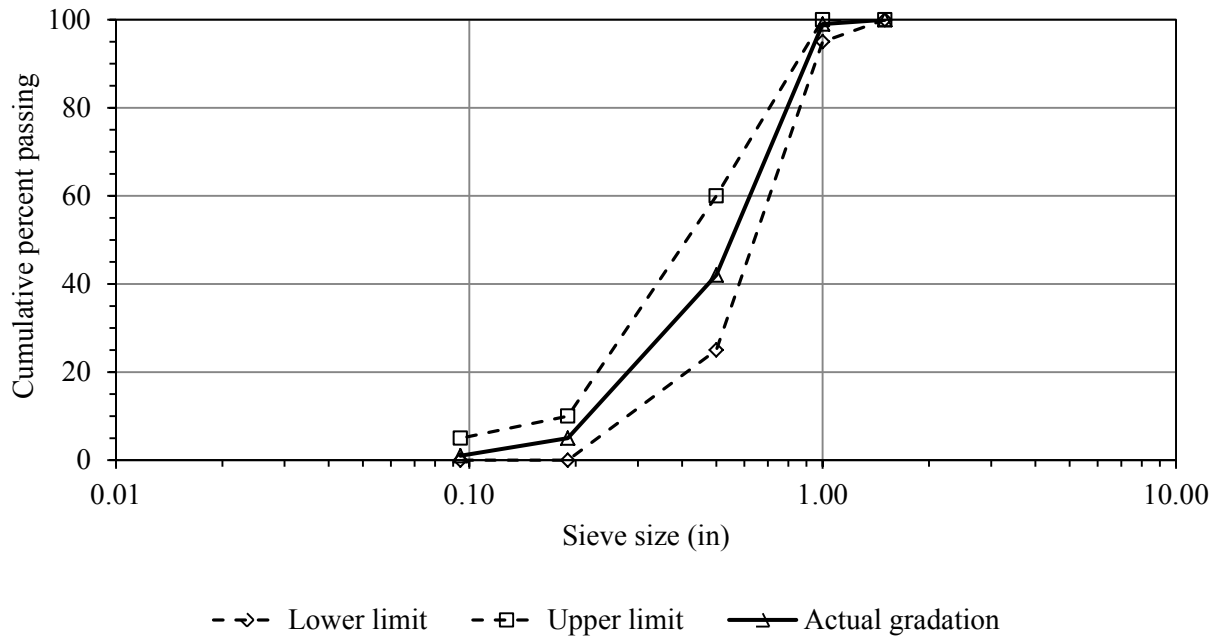
Figure 4.1. AASHTO No. 57 gradation and the actual gradation of the coarse aggregates used.

4.2.2 Fibers

A large variety of fibers are available with their primary differences being their raw material composition, shape, aspect ratio (*AR*) and stiffness. A review of the types of fibers commonly used in UTW was performed prior to the selection of the fibers to be included in this study (Barman, et al., 2010; Roesler, et al., 2008 and ACPA, 2009).

4.2.2.1 Types

A large number of whitetopping projects in the state of Illinois were constructed utilizing FRC. Some of those projects are summarized in Table 4.2. It can be seen that a large numbers of projects were constructed with structural synthetic fibers. In this project, straight synthetic (Figure 4.2a) and (ii) crimped synthetic (Figure 4.2b) structural fibers were selected. From this

120

point forward the straight synthetic fiber is referred to as Fiber 1 or F1 and the crimped synthetic

fiber as Fiber 2 or F2. The concrete mixtures produced with F1 and F2 are referred to as FRC1

and FRC2, respectively. While F1 is the most frequently used structural synthetic fiber for

whitetoppings constructed in the United States (ACPA, Illinois chapter, 2009), F2 provides the

highest bond strength (Won, et al., 2006). Table 4.3 presents the features of the two fibers

selected.

Table 4.2. Types of fibers used in whitetopping projects constructed in Illinois
(ACPA, Illinois chapter, 2009).

Project location	Year of construction	Concrete layer thickness (in)	Slab size (ft x ft)	Fiber type	Dosage (lb/cyd)
Stephenson county	1998	3	5.5 x 5.5	Synthetic	3
Mendota	1999	4.5	NA	Hybrid steel	50
Oak park	2001	4	5 x 6.5	structural steel	40
Peoria	2002	3	4 x 4	synthetic	3
Chicago/ cook co. Highway dept.	2003	4	3.5 x 4	structural synthetic	7.5
Schaumburg	2004	5	NA	structural synthetic	NA
Chicago, South Michigaan Ave.	2004	4	NA	structural synthetic	4
Kane county	2004	4.5	NA	structural synthetic	4
Cook county Highway	2004	4	NA	structural synthetic	7.5
Mundelein	2005	4	NA	structural synthetic	4
Olney	2008	3	4 x 4	synthetic	3
Macomb	2009	4	NA	structural synthetic	4
Logan County	2009	5.25	NA	structural synthetic	4
Henderson County	2010	5	NA	structural synthetic	4
Lombard	2010	4	4 x 4	structural synthetic	4
Shelby County	2010	4	NA	structural synthetic	4
Richland County	2010	5.5	5.5 x 5.5	structural synthetic	4
Clay County	2010	5.5	5.5 x 5.5	structural synthetic	4

Note: NA- Not available.
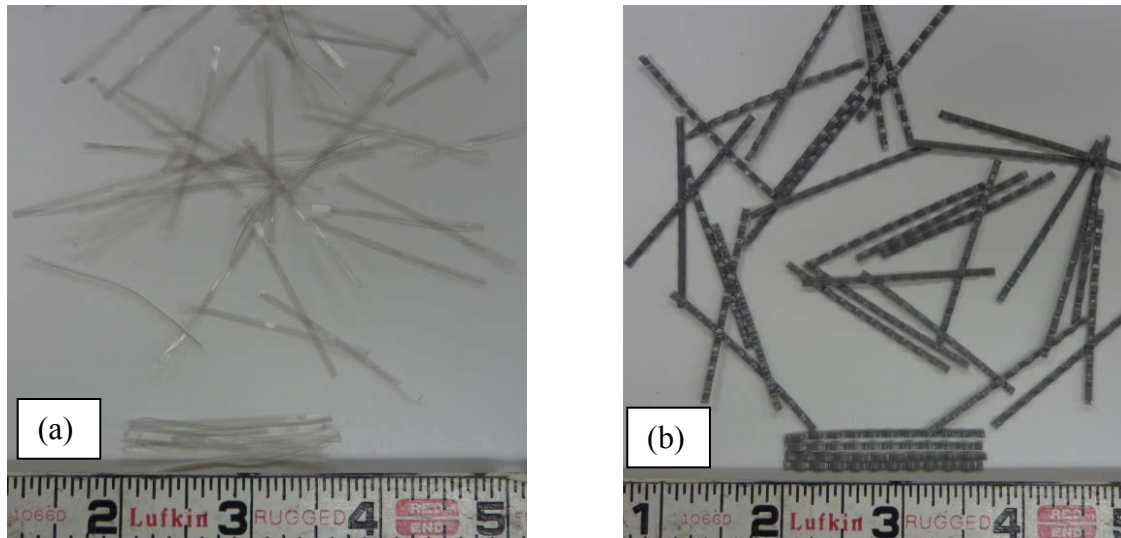
Figure 4.2. Picture of the selected fibers (a) Straight synthetic-Strux: 90/40,
(b) Crimped synthetic-Enduro 600.

Table 4.3. Features of the selected fibers for the present study.

Fiber category	Brand name	Length (in)	Shape	Cross section (in x in)	Specific gravity	Aspect ratio
Straight, synthetic	Strux: 90/40	1.57	Rectangular	0.05 x 0.004	0.92	90
Crimped, synthetic	Enduro 600	1.75	Rectangular	0.05 x 0.03	0.91	40

4.2.2.2 Volume fraction

The fiber volume fraction (V_f) may also play a significant role in the joint performance of whitetopping. However, at a given V_f, F1 and F2 may not necessarily provide an equal contribution to the joint performance due to their distinct features. Therefore, to select the most appropriate V_f for each fiber category, the literature was examined to investigate the influence of the shape and V_f on the strength of the concrete, especially on the residual strength ratio (RSR). Although FRC, as compared to the PC, has several other benefits, RSR is accounted for in design procedures. A 20 percent increase in the modulus of rupture (MOR) is assigned for a FRC with

122

a RSR of 20 percent. The RSR for the concrete with different types of structural synthetic fibers were studied by Boredelon, 2005 and Roesler, et al., 2008.

Hannant, 1978, and Thomas & Ramaswamy, 2007 studied the strength contribution of the fibers through the combined influence of V_f and AR. In their studies, a new parameter, known as the Reinforced Index (RI) was introduced. RI is expressed as below:

$$RI = V_f \, x \, AR \qquad\qquad\qquad (4.1)$$

Referring to this concept, the RSR test results from Boredelon, 2005 and Roesler, et al., 2008 were used to derive an approximation of the relationship between the RI and RSR, as shown in Figure 4.3. Three types of fibers are incorporated into this plot. A twisted synthetic fiber was included along with a straight and crimped synthetic fibers. Only one test result is available for the concrete with crimped synthetic fibers. The RI for each fiber was computed using the information provided in the above two studies and from the manufacturer's datasheets. It can be seen that all three types of structural synthetic fibers follow a similar trend. The RSR increases with an increase in the RI. The RI corresponding to a 20 percent RSR was determined to be 32 for straight fiber and 35 for the crimped fiber Equation 4-1. The dosages needed to obtain the V_f are provided in Table 4.4 for each fiber type.
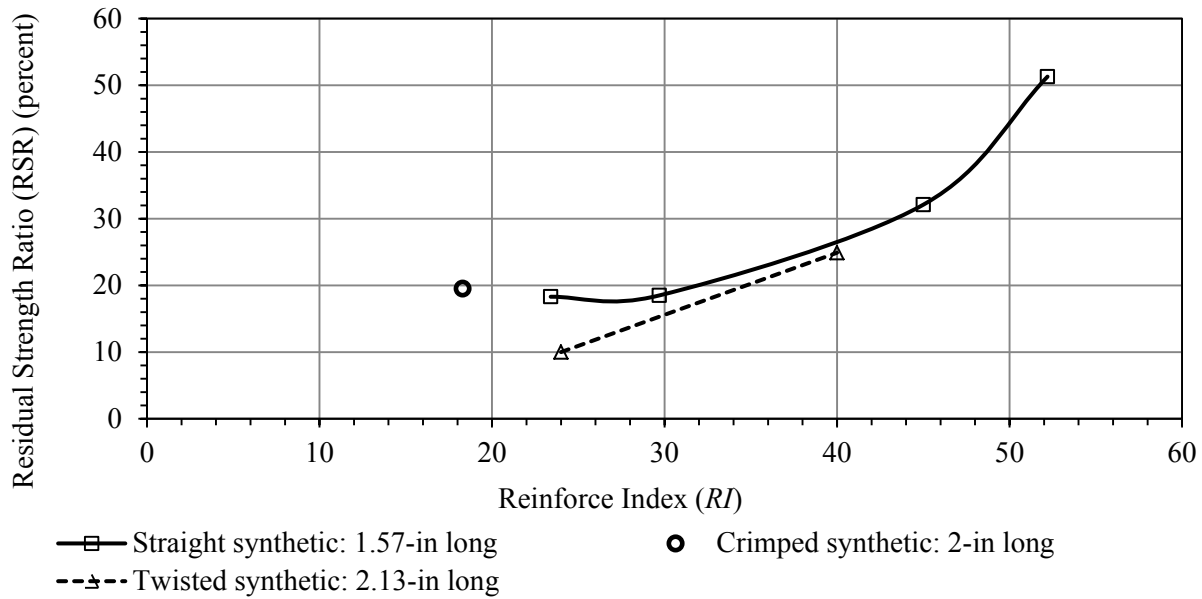
Figure 4.3. RI vs. RSR relationship for the structural synthetic FRC
(After Boredelon, 2005 and Roesler, et al., 2008).

Table 4.4. Volume fraction and dosages of two selected fibers
(After Boredelon, 2005 and Roesler, et al., 2008).

Straight synthetic. STRUX: 90/40		Crimped synthetic. Enduro 600	
Volume fraction (percent)	Dosage (lb/cy)	Volume fraction (percent)	Dosage (lb/cy)
0.36	5.25	0.43	6.20

4.2.3 Concrete Mixture Designs

The gravimetric and volumetric proportions for each concrete mixture are given in Table 4.5. The mixture designs were established based on typical mixes used for slip-form paving. A target water to cement ratio of 0.45 was used along with a target of 600 lbs of cement. A water reducer [CATEXOL 1000N (www.aximconcrete.com)] and air entrainer [CATEXOL AE 360 (www.aximconcrete.com)] were used to achieve the target slump of 2 ± 0.5 in and a 6 ± 1% air content.

124

Table 4.5. Target concrete mixture design.

Materials	Weight (lb/cy)	Volume (cft/cy)	Volume fraction
Coarse aggregates	1769	11.34	0.42
Fine aggregates	1089	6.66	0.25
Cement	600	3.05	0.11
Water	270	4.33	0.16
Air content	-	1.62	0.06
Water reducer, CATEXOL 1000N	0.75 oz per 100 lbs of cement		
Air entrainer, CATEXOL AE 360	1.5 oz per100 lbs of cement		

In normal practice, when fiber is added into a mix, the volume of fine aggregates is reduced to accommodate the fiber for a given workability. However, the volume fraction of the fibers in the present study is only about 0.36 percent for F1 and 0.43 percent for F2, both of which are far lower than the target air content, and are in fact within the tolerance of the target air content. Therefore, the same mix proportion for the PC and FRC presented in Table 4.5 was adopted. The water reducer was increased to 1.5 oz per 100 lbs of cement in both F1 and F2 mixtures to maintain the desired level of workability.

4.3   CONCRETE MATERIAL PROPERTIES

The compressive strength, modulus of elasticity, RSR and MOR were measured at 28 days after casting. The MOR was also measured at 18 hours after casting. This coincides with the time at which the transverse cracks were initiated into the S_{ALT} slabs and B_{ALT} beams. The VSTR for the B_{ALT} specimens was measured after fatiguing. A separate 24-in x 6-in x 6-in beam was also cast for each mixture for measuring the VSTR of the crack face. Each of these separate beams were fractured for measuring VSTR at 18 hours using a procedure similar to that adopted for initiating

125

the crack in the B_{ALT} specimens. The VSTR was also measured for the slab crack face after the S_{ALT} was performed by cutting a section of the slab face from the transverse joint.

The VSTR test was performed according to the procedure outlined in the Vandenbossche, 1999 study (Subsection 2.8.1). A photo of the equipment used for measuring the VSTR is provided in Figure 4.5. Using this equipment, the elevation of each grid from a datum surface is measured using a laser beam. A 5.5-in x 5.5-in area on the crack face of each B_{ALT} specimen was evaluated. The test procedure followed along with number of specimens tested for each mixture is summarized in Table 4.6.

Figure 4.4. Residual strength ratio testing.
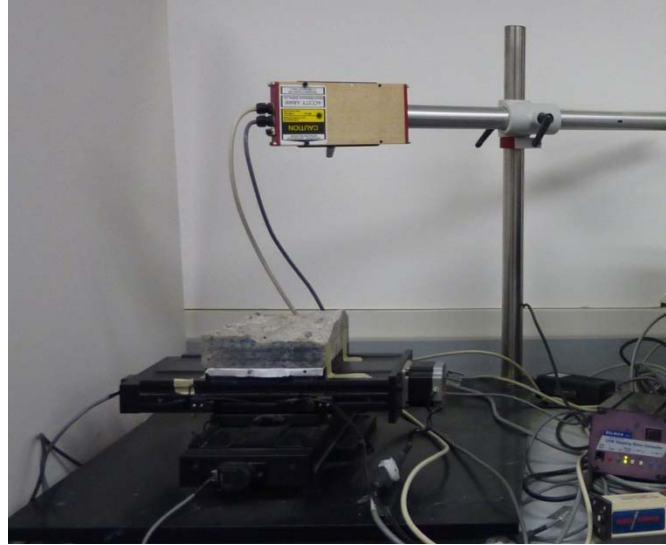
Figure 4.5. VSTR testing equipment.

Table 4.6. Test for characterizing concrete properties.

Test	Number of specimen	Age of specimen during testing	Specimen type/ size	Test procedure reference
Compressive strength	6	28 days	Cylinder/ 6in x 12 in	ASTM-C39/C39M-12a, 2010
Modulus of elasticity	3			ASTM-C469/C469M, 2010
Modulus of rupture	6	18 hours	Beam/ 24 in x 6 in x 6 in	ASTM-C78/C78M, 2010
	3	28 days		
Residual strength ratio	3	28 days		ASTM-C1609/D1609M, 2010
VSTR of B_{ALT} specimen, before fatiguing	1	NA	Crack face of B_{ALT} specimen/ 5.5 in x 6 in	Vandenbossche, 1999
VSTR of B_{ALT} specimen, after fatiguing	4			
VSTR of slab after fatiguing	3		Crack face of slab joint/ 3.5 in x 6 in	

127

4.4   TEST PLAN FOR THE B_{ALT} PROCEDURE

Before testing the specimens prepared with the three selected mixtures, a preliminary B_{ALT} was performed to establish the test protocol. This included establishing when and how data would be collected and what crack widths would be considered for fatiguing. Testing of the trial beams consisted of applying one million dynamic load cycles at a selected crack width to observe the fatiguing of the joint. Load and deflection profiles were recorded at different load cycles during the fatiguing process. After fatiguing, the crack width was opened in an approximately equal increment with the load and deflection profiles recorded at various crack widths. After each crack width change, 995 load cycles (seating load cycles) were applied before collecting the load and deflection profiles for the next five successive load cycles (total 1000 load cycles) to ensure the crack conditions at this crack width stabilized. Using the deflection profiles, LTE_B vs load cycles and LTE_B vs crack width relationships were established for each trial beam to investigate the drop in the LTE with increases in applied load cycles and crack width. These trends were then used to plan the final test matrix.

Although at least 10 trials beams were tested, the joint performance results from two PC and two FRC1 beams are incorporated in this chapter. The LTE_B vs load cycles and LTE_B vs crack width for these beams are presented in Figure 4.6 through Figure 4.13. The two PC beams are labeled PT1 and PT2, whereas, the two FRC1 beams are labeled F1T1 and F1T2; P, T and F1 stand for PC, trial and FRC 1, respectively. It may be mentioned that the test results from the trial beams are not included in the final analysis, performed in Chapter 5. The test setup during testing of these beams was slightly different than the finalized fabrication. The trial beams were tested with a flat steel plate on top of the Fabcel layers instead of the top I-beam.

128

The first reported PC trial beam, PT1, was fatigued at a 0.023-in crack width. It was observed that the LTE_B under both the tension and compression loads remained relatively similar for the entire range of load cycles (Figure 4.6). Again, the LTE under the tension and compression loads are referred as $LTE_{B(t)}$ and $LTE_{B(c)}$, respectively. There is a slight increase in the LTE_B at around 500,000 load cycles, which might have been a measurement error. The average decrease in the LTE_B at the end of 1 million load cycles was 3 percent. After fatiguing, when the crack width was opened, LTE_B was found to be initially maintaining the same trend for up to a 0.043-in crack width, followed by a sharp decrease with any further increases in crack width (Figure 4.7).

The second reported PC trial beam, PT2, was fatigued at a 0.028-in crack width (Figure 4.8). It can be seen that the LTE_B did not decrease even after 1 million load cycles. LTE_B under both the tension and the compression load remains 90 percent throughout the entire range of load cycles. However, a sharp decrease in the LTE_B was observed when the crack width was opened after fatiguing of the joint (Figure 4.9). A variation between the $LTE_{B(t)}$ and $LTE_{B(c)}$ was seen when the crack width was in between 0.05 and 0.10 in.
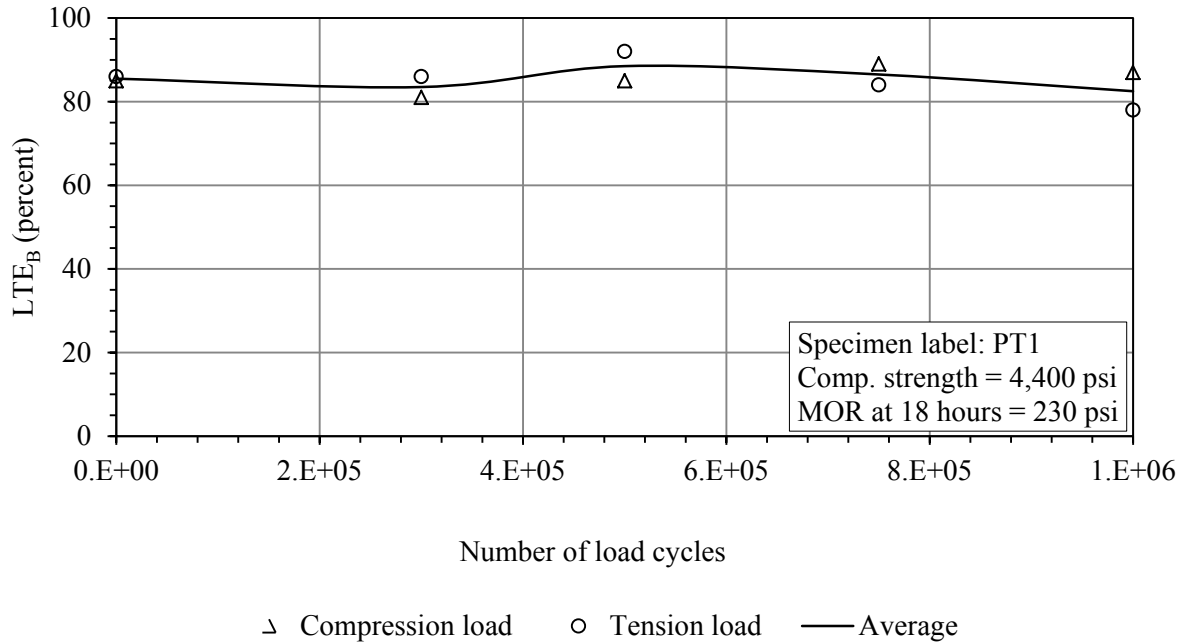
Figure 4.6. LTE vs number of load cycles for PC trial beam, PT1.
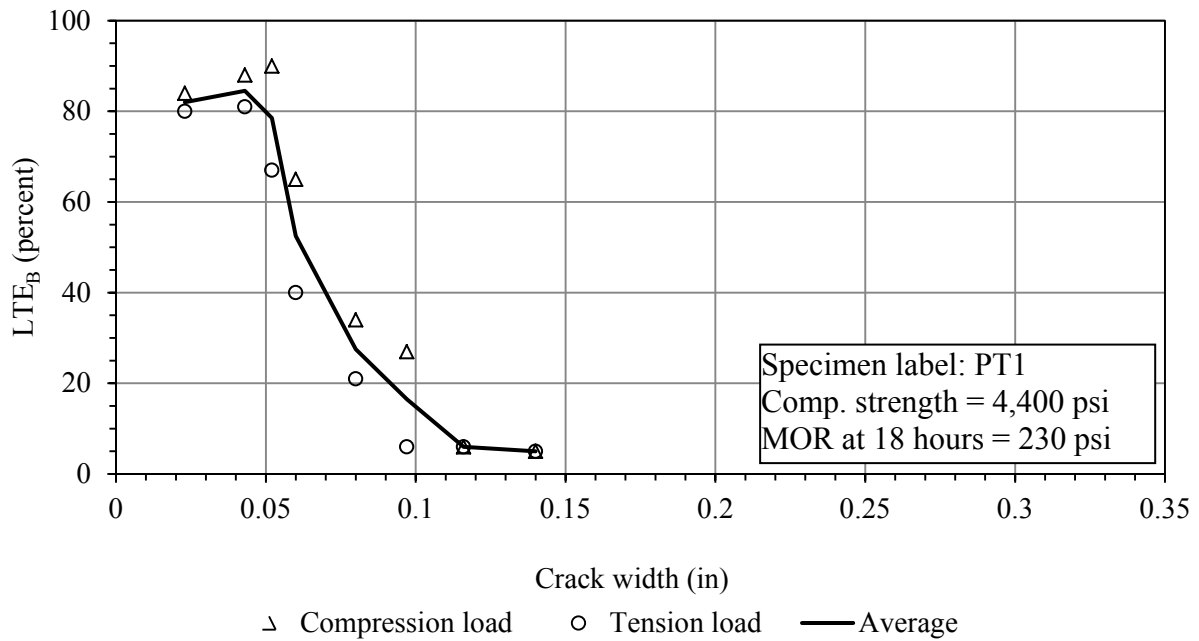
Figure 4.7. LTE vs crack width for PC trial beam, PT1.
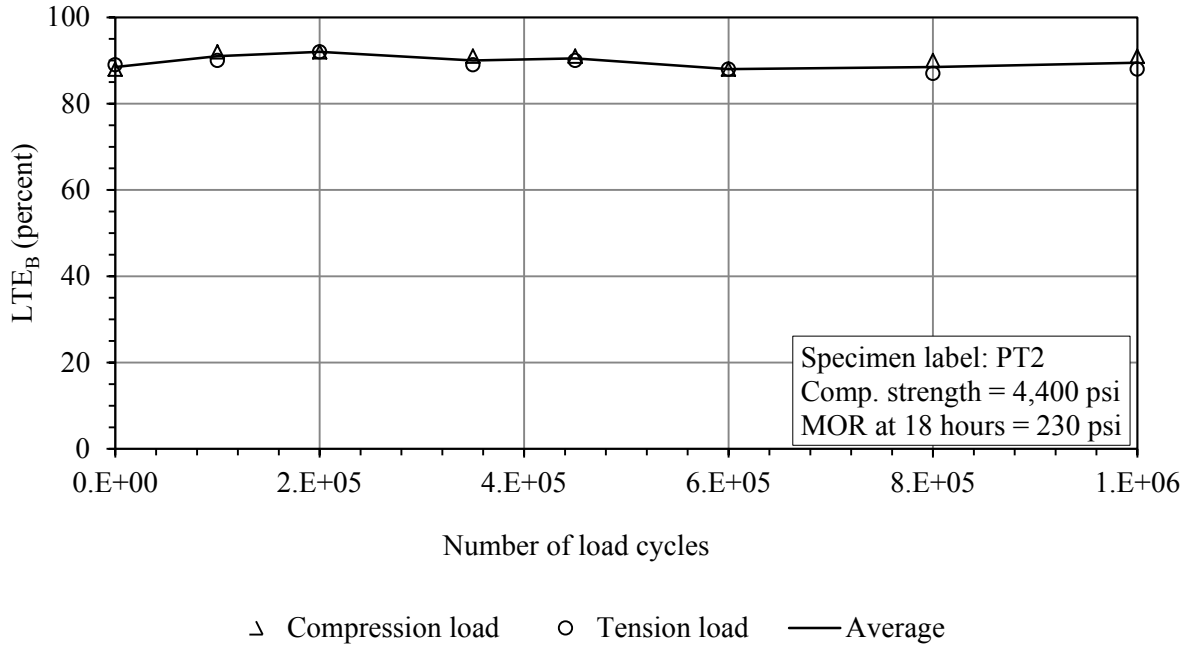
Figure 4.8. LTE vs number of load cycles for PC trial beam, PT2.
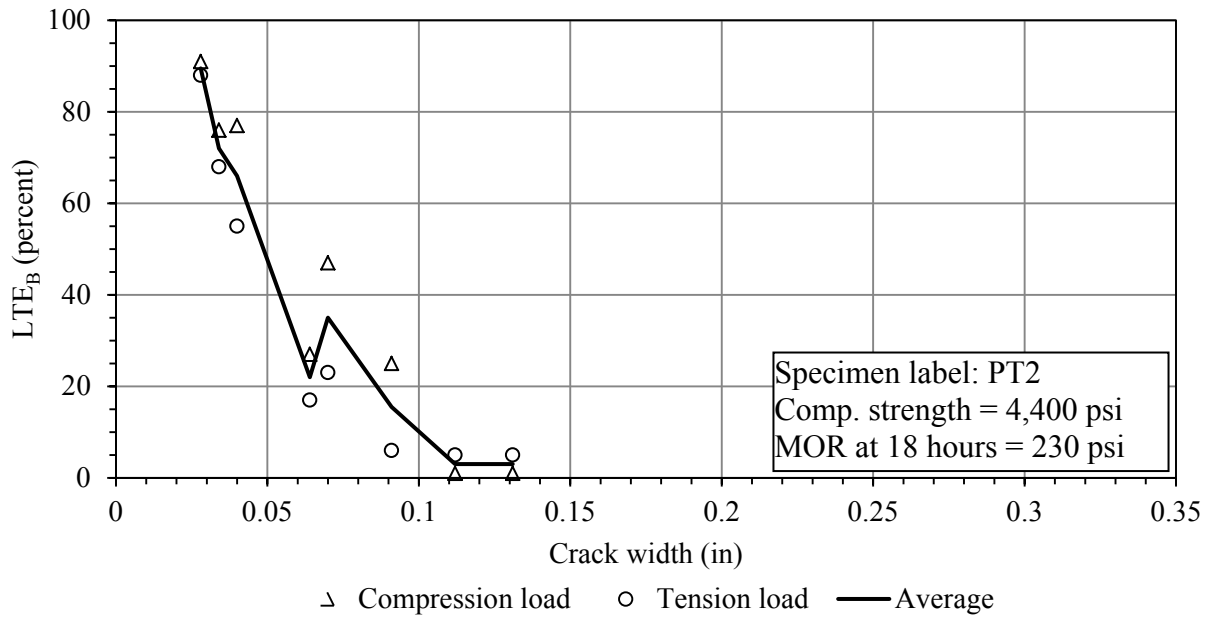
Figure 4.9. LTE vs crack width for PC trial beam, PT2.

131

The first reported FRC1 trial beam, F1T1 was fatigued at a 0.028-in crack width (Figure 4.10). It can be seen that the LTE_B decreased marginally (only by 1.5 percent) after 1 million load cycles. The difference between the $LTE_{B(t)}$ and $LTE_{B(c)}$ was negligible during the fatiguing. The interesting (and expected) observation was that the LTE_B did not sharply decrease when the crack width was increased, unlike with the PC beams.

The second reported FRC1 trial beam, F1T2, was fatigued at a considerably wider crack width, 0.05 inches. The average decrease in LTE_B was observed to be 6 percent. This beam was cast with a Type I cement. The compressive strength was only 1,500 psi at the time of testing (7 days after casting). Probably because of the lower concrete strength, the LTE_B quite sharply decreased when the crack width was increased.

One of the common observations when testing all four beams was that the difference between the $LTE_{B(t)}$ and $LTE_{B(c)}$ was larger when the crack width was between 0.05 to 0.10 in. This difference was the result of macrotexture of the crack. Most of the time, the crack does not propagate completely vertical and perpendicular to the surface of the beam. This results in more engagement of the two fractured crack faces in one loading direction compared to the other, and thus LTE_B becomes higher in the former. When the crack width is narrow, the influence of the slope or the macrotexture of the crack face is low. At a lower crack width, the difference in the effective interlocking areas between two the directions is negligible. Again when the crack width is extremely large (> 0.1 in), the aggregate interlock engagement in both the directions substantially decreases; thus LTE_B becomes insensitive to the side of the crack that is loaded.
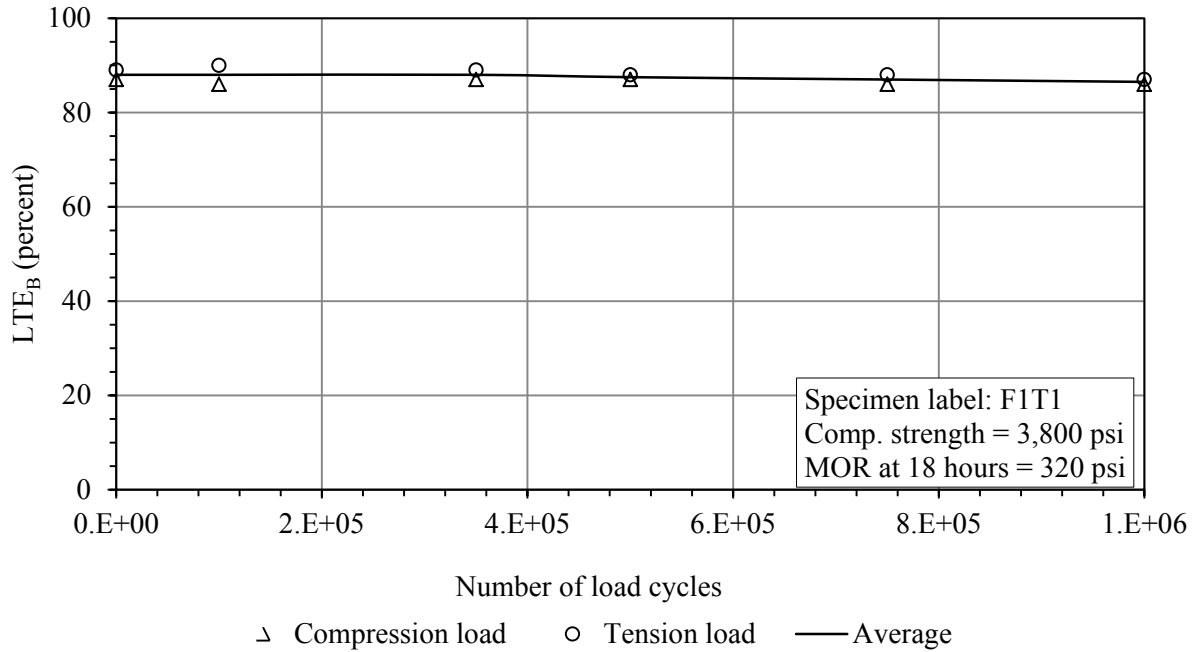
Figure 4.10. LTE vs number of load cycles for FRC1 trial beam, F1T1.
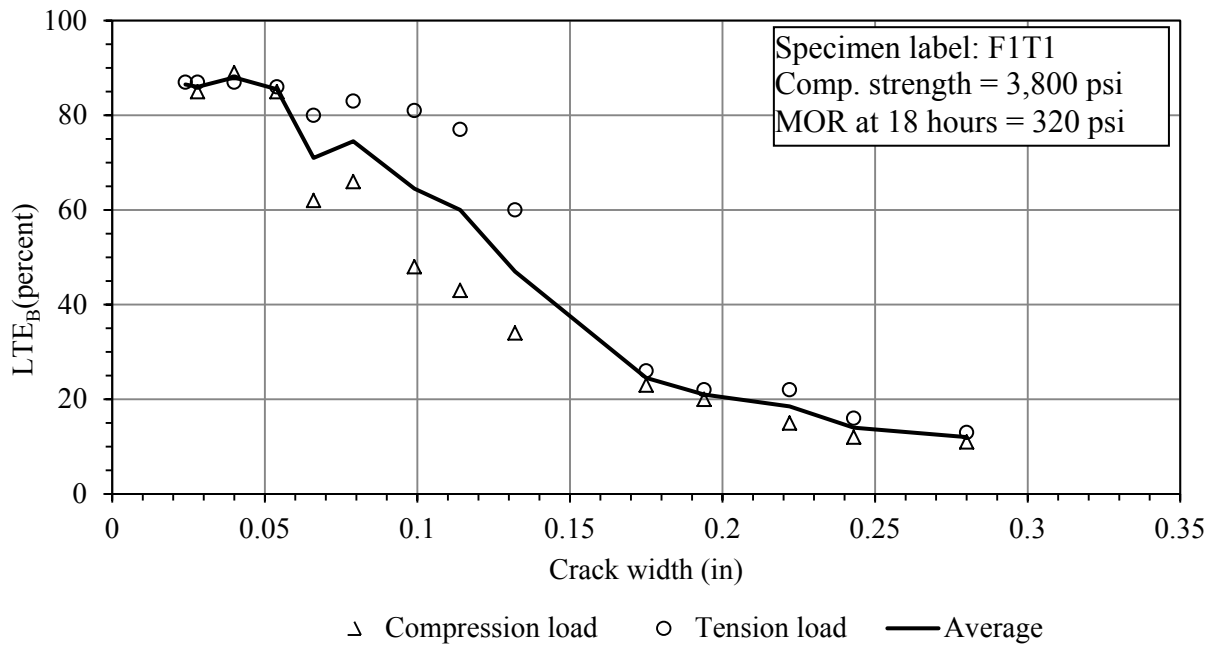
Figure 4.11. LTE vs crack width for FRC1 trial beam, F1T1.

133
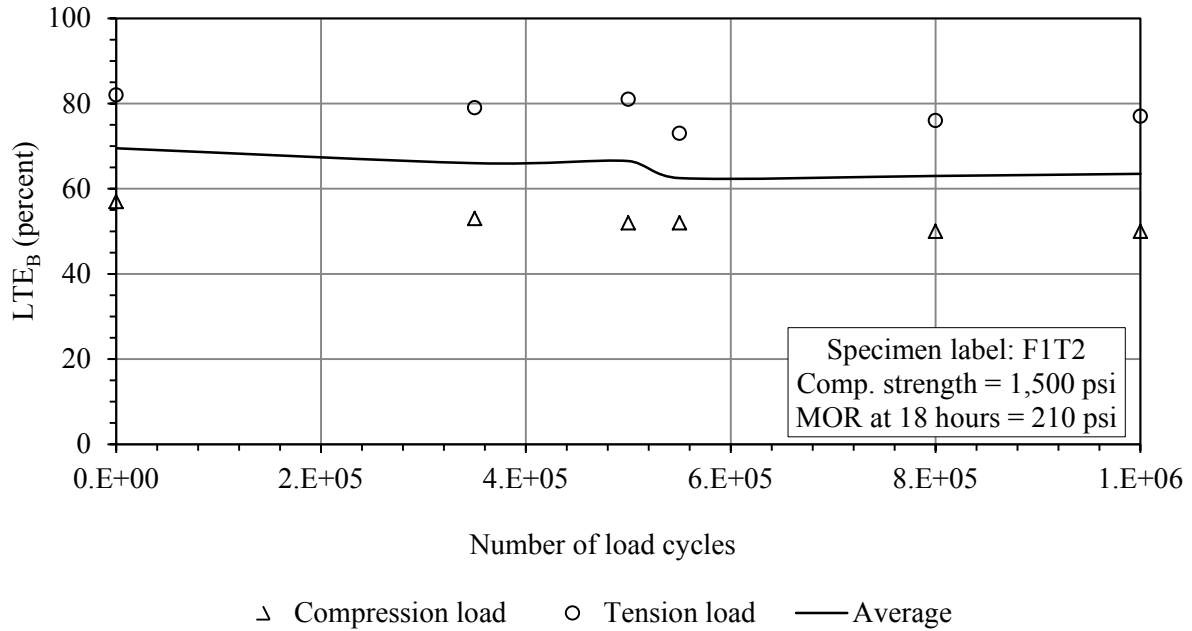
Figure 4.12. LTE vs number of load cycles for FRC1 trial beam, F1T2.
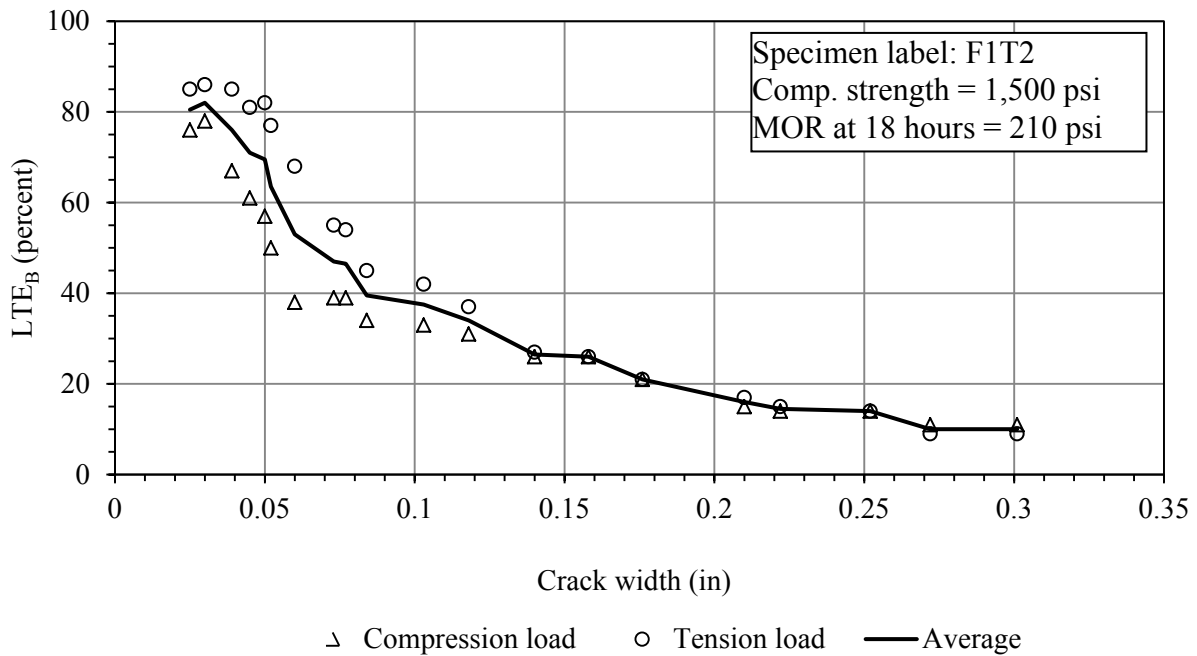
Figure 4.13. LTE vs crack width for FRC1 trial beam, F1T2.

134

A few beams were also tested at a very narrow crack width, such as 0.015 in. The problem associated with fatiguing at this crack width was the requirement of a higher horizontal compression force to maintain such a narrow crack width, especially in the case of the PC beams. This higher compression along the longitudinal axis compels the two halves of the beam to behave like a single unit. This deters any mechanical action, such as, sliding at the joint when loading. Both halves of the beam deflect with a single slope and do not rotate at the joint. The differential deflection thus becomes zero. In the case of the FRC beams, although a horizontal compression force is not necessary, the fibers probably transfer moment across the crack width when the crack width is very narrow. Therefore a similar response was observed for narrower crack widths, such as 0.015 in.

On the basis of these observations, it was decided that the beams would be fatigued at crack widths larger than 0.015 in. At a 0.025-in crack width, the LTE_B in both the PC and FRC beams is higher, whereas after a 0.060-in crack width, the LTE_B is quite lower. Therefore, it was decided that the actual test beams would be fatigued at two intermediate crack widths, 0.035 and 0.05 in. These two crack widths are also a good representation of the crack width range that the MnROAD whitetopping sections exhibited for a large period of the year (discussed in Chapter 2). Also, as suggested by Jensen & Hansen, 2001, the aggregate interlock load transfer phenomenon plays a more significant role in this crack width range.

The complete test matrix for the B_{ALT} procedure is given in Table 4.7. Four beams for each concrete mixture were tested to derive the LTE_B vs N relationship. Two of them were fatigued at 0.035-in and the other two were fatigued at 0.05-in crack widths. These crack widths will be referred to as the fatiguing crack width. In all four beams, before fatiguing, the crack width was incrementally increased from the initial existing crack width to the fatiguing crack

135

width. At each increment, load and deflection profiles were recorded for five successive load cycles, after applying 995 seating loading cycles. At the fatiguing crack width, one million load cycles were applied, except when a constant LTE_B was observed through a considerable range of cycles before reaching one million. For at least six consecutive load cycles, load and deflection profiles were recorded in the middle of the fatiguing process. The crack width was measured after every 50,000 load cycles to ensure a constant crack width was maintained. After fatiguing, the crack was again opened incrementally to record the load and deflection profiles at different crack widths. At each crack width, seating load cycles were again applied before recording the load and deflection profiles to ensure the system had stabilized.

The selection of one million as the number for load cycle applications was made based on the fact that most UTW projects are constructed for lower traffic volumes. Although one million load cycles do not represent the design life for all of the existing UTW projects, a significant number of projects in the country have a design life of around one million ESALs (Barman, et al., 2010). Therefore, investigating the joint condition for up to one million load cycle repetitions can be considered an appropriate amount for establishing a performance trend. Another consideration in making this choice for number of repetitions is the affordability of the resources and time for conducting each test. One beam was loaded to 10 million ESALs to establish the effects of fatigue on fiber performance. Apart from these above mentioned four beams, one separate beam was tested for each concrete mixture to evaluate the joint performance as a function of crack width when joints are not fatigued.

Table 4.7. Specimen matrix for B_{ALT} procedure.

Concrete category	Number of specimens	Fatiguing crack width (in)
PC	2	0.035
	2	0.050
	1	Not fatigued
FRC1	2	0.035
	2	0.050
	1	Not fatigued
FRC2	2	0.035
	2	0.050
	1	Not fatigued
	1	0.035, fatigued with 10 million load cycles

4.5   TEST PLAN FOR THE S_{ALT} PROCEDURE

The financially expensive component of the laboratory study was the casting and testing of the S_{ALT} specimens. Because of the financial and time constraints, only one slab for each concrete mixture was cast and tested.   The fatiguing crack width in each concrete category was established based on the joint performance results obtained in the corresponding B_{ALT} procedure. The PC slab was fatigued at a 0.035-in crack width. Fatiguing of the FRC1 slab was started at a 0.035-in crack width.   Unfortunately, this crack width did not remain constant during the fatiguing process. It increased to 0.049 in by the end of the fatiguing.   The FRC2 slab was fatigued at a 0.050-in crack width. A more comprehensive discussion regarding the selection of the fatiguing crack width in the S_{ALT} procedure is provided after the presentation of the B_{ALT} test results, in the next chapter.

137

4.6   CONCLUSIONS

This chapter presented the properties of the materials used in this study. One plain concrete and two fiber reinforced concrete mixes were included. The mixture proportions for both the PC and FRC were similar, except that two separate types of fibers were added in the two FRC mixes. The test description for the B_{ALT} and S_{ALT} joint performance test is presented in this chapter. Results of a few B_{ALT} trial beams were also discussed to support the selection criteria of the fatiguing crack widths for the B_{ALT} testing to be performed.

5.0   LABORATORY TEST RESULTS AND DISCUSSIONS

5.1   INTRODUCTION

This chapter presents the results of all the laboratory tests performed under the scope of the present study. First, the fresh and hardened concrete properties for the concrete mixtures used are presented. Then, the joint performances for the B_{ALT} and S_{ALT} procedures are presented in terms of LTE. The LTE vs number of load cycles and LTE vs crack width relationships are presented for each specimen. The results are compared with respect to the joint performance evaluation procedures and the mixture types. Regression models are then developed for estimating LTE as a function of crack width and mixture types. Correlations between the LTE values, based on the results from two joint performance evaluation procedures are developed for each concrete mixture. Also a general relationship was developed between the LTE values obtained by B_{ALT} and S_{ALT} procedures.

Next, DER results are presented. Comparisons of DER results between the specimens, mixture types and test procedures are presented. Regression relationships are developed for predicting DER as a function of crack width and mixture types. A relationship between the DERs obtained in B_{ALT} and S_{ALT} procedures are developed.

Finally, relationships between DER and LTE results obtained by both the methods are correlated and the best predictors for estimating the LTE_S and DER_S are established.

139

5.2 PROPERTIES OF CONCRETE MIXTURES

The concrete required for casting the specimens was provided by Frank Bryan, Inc., Pittsburgh, PA and was delivered to the laboratory in a ready-mix truck. There were four separate cast dates. The first plain concrete mix (PC1) was delivered on 04/16/2012 and the second one (PC2) was delivered on 10/31/2012. FRC1 mix was delivered on 05/04/2012 and FRC2 was delivered on 06/29/2012. All the specimens were to be tested after 28-days of wet curing at 75 to 80°F. As only one single B$_{ALT}$ setup was fabricated, the beams were stored in a constant temperature water bath at 40°F after 28 days of curing until testing could be performed. The hydration process of concrete generally remains dormant at or below this temperature. The properties of the all concrete mixes used in the study are presented in the following subsections.

5.2.1 PC Mixtures

As mentioned previously, the plain concrete specimens were cast on two separate days. Four B$_{ALT}$ beams were cast from the PC1 mix. The slump and air content for the PC1 mix were 2.5 in and 5 percent, respectively. The average 18-hours MOR, 28-days compressive strength, 28-days MOR, and 28-days modulus of elasticity for the PC1 mix were 278 psi, 4600 psi, 500 psi and 3.20 x 10^6 psi, respectively. The average VSTR for the B$_{ALT}$ specimens was 0.1742 in^3/in^2.

The second plain concrete (PC2) mix was supposed to be the same as PC1. However, the water content in the delivered concrete was 267 lb/cyd instead of 270 lb/cyd. This little difference in the water content did not affect the workability though. The air content was also within the acceptable range. The average 18-hours MOR, 28-days compressive strength, 28-days MOR, and 28-days modulus of elasticity for the PC1 mix were 255 psi, 4850 psi, 565 psi

140

and 3.37 x 10^6 psi, respectively. The PC slab and rest of the B_{ALT} beams were cast from PC2 mix. The average VSTR for the B_{ALT} beams was 0.1569 in^3/in^2, while it was 0.1669 in^3/in^2 for the slab. The complete list of fresh and hardened concrete properties for both of the PC mixtures is given in Table 5.1.

Table 5.1. Fresh and hardened concrete properties for the PC mixtures.

Parameters	PC1				PC2			
	Number of specimen	Average	Standard deviation	COV	Number of specimen	Average	Standard deviation	COV
Slump (in)	1	2.5	-	-	1	3.0	-	-
Air content (percent)	1	5	-	-	1	5.0	-	-
18-hours MOR (psi)	6	278	22	8	6	255	6	2
28-days compressive strength (psi)	6	4600	400	9	6	4850	200	4
28-days MOR (psi)	3	500	25	5	3	565	33	6
28-days modulus of elasticity (10^6 psi)	3	3.20	0.13	4	3	3.37	0.31	9
VSTR of beam specimens (in^3/in^2)**	4	0.1742	0.0370	21	2	0.1569	0.0088	6
VSTR of samples from slab (in^3/in^2)	-	-	-		3	0.1669	0.0283	17

**VSTR was measured on specimens fractured at 18-hours.
Note: COV- Coefficient of variation in percent.

5.2.2   FRC Mixtures

The fresh and hardened concrete properties for the FRC1 and FRC2 mixtures are summarized in Table 5.2. The FRC1 mixture was delivered in the morning hours. The workability was good (3-in slump) during the preparation of the specimens. The air content was 4.5 percent. The average 18-hours MOR, 28-days compressive strength, 28-days MOR, and 28-days modulus of elasticity for the FRC1 mix were 337 psi, 5140 psi, 611 psi and 3.48 x 10^6 psi, respectively.

141

Figure 5.1 shows the load vs deflection graph obtained in the RSR test for the FRC1 mixture. The average RSR of FRC1 was 24 percent.

The FRC2 mixture was delivered at noon when the ambient temperature was around 97^oF. This very high ambient temperature accelerated the rate of hydration. A high concrete temperature increases the water requirement and decreases the set time (Mindess, et al., 2002). When the concrete was delivered, the workability was good (3-in slump). But the workability dropped at a very fast rate. Finishing work of specimens had to be carried out in haste to avoid any unwanted undulation on the surface of the slab and beam specimens. The average 18-hours MOR, 28-days compressive strength, 28-days MOR, and 28-days modulus of elasticity for the FRC1 mixture were 361 psi, 5300 psi, 602 psi and 3.80 x 10^6 psi, respectively. The RSR for the FRC2 mixture, obtained by averaging the results from three samples, was 24 percent, as shown in Figure 5.2.

Table 5.2. Fresh and hardened concrete properties for the FRC mixtures.

Parameters	FRC1				FRC2			
	Number of specimen	Average	Standard deviation	COV	Number of specimen	Average	Standard deviation	COV
Slump (in)	1	3.0	-	-	1	3.0	-	-
Air content (percent)	1	4.5	-	-	1	5.5	-	-
18-hours MOR (psi)	6	336	19	6	6	361	37	10
28-day compressive strength (psi)	9	5140	470	9	8	5300	265	5
28-days MOR (psi)	3	611	10	2	3	602	14	2
28-day modulus of elasticity (10^6 psi)	3	3.48	0.60	17	3	3.8	0.23	6
VSTR of beam specimens (in^3/in^2)	6	0.1765	0.0628	36	6	0.1676	0.0279	17
VSTR of samples from slab (in^3/in^2)	3	0.1711	0.0205	12	3	0.1204	0.0093	8

142

Sample	RSR (percent)
FRC1-1	26
FRC1-2	28
FRC1-3	17
Average	24
Std. dev.	6
COV	25
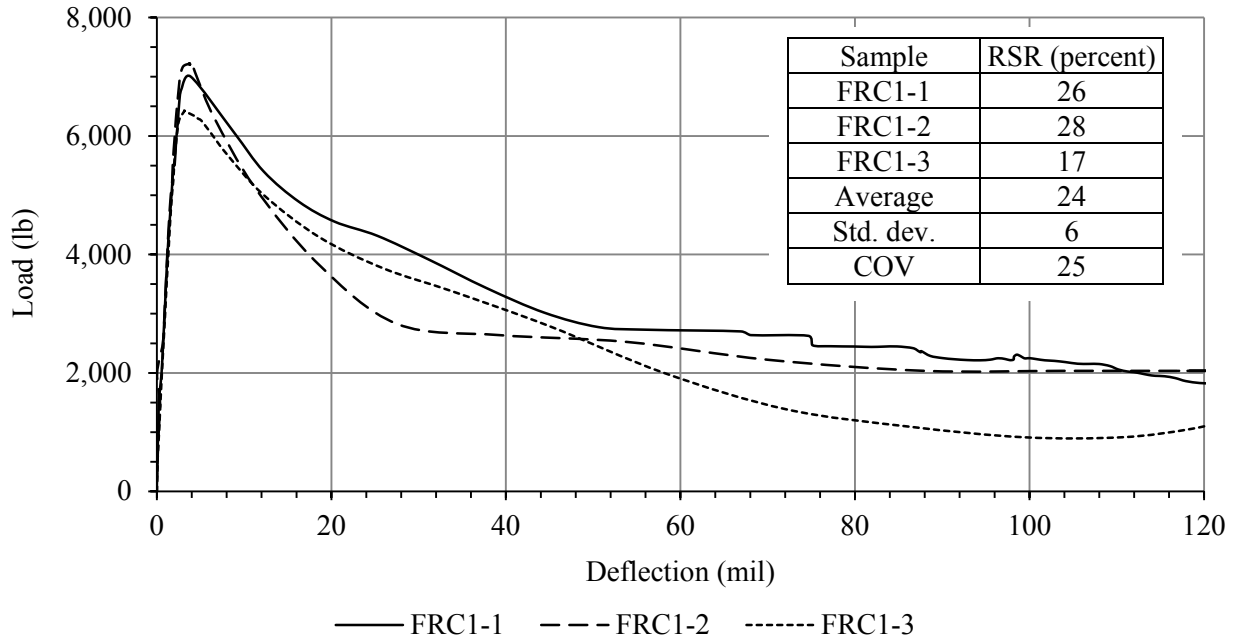
Figure 5.1. 28-days residual strength ratio for the FRC1 mixture.

Sample	RSR (percent)
FRC2-1	29
FRC2-2	22
FRC2-3	22
Average	24
Std. dev.	4
COV	17
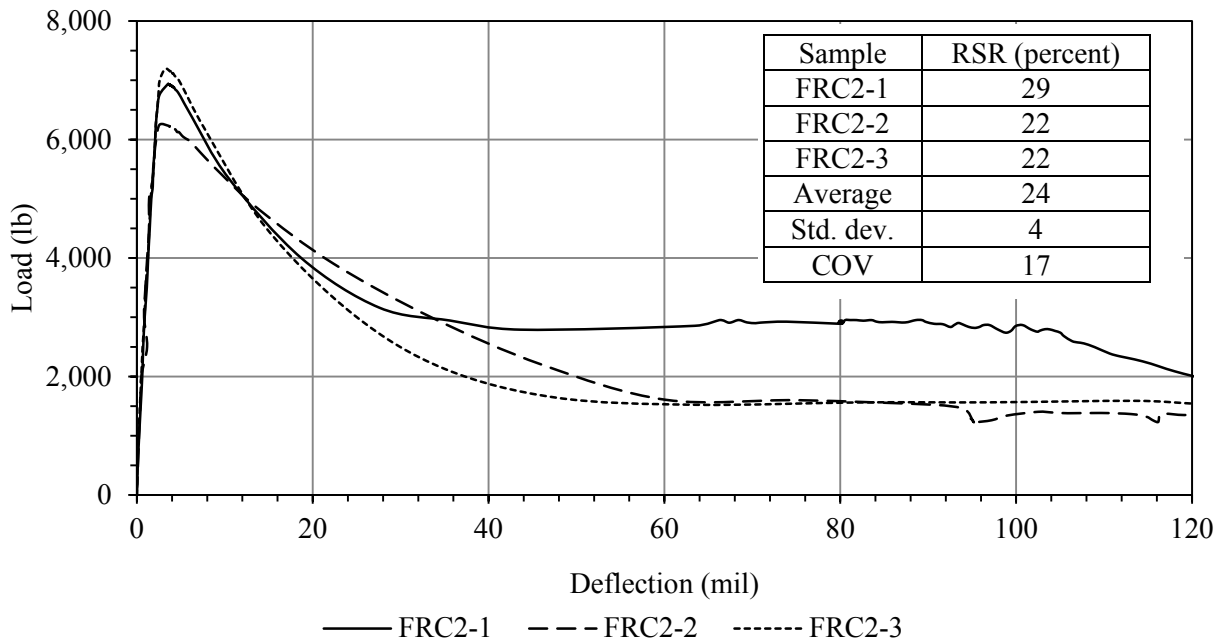
Figure 5.2. 28-days residual ratio for the FRC2 mixture.

143

5.2.3   Comparison between Mixtures

PC1 vs PC2

The 28-days compressive strength of PC2 was found to be slightly larger than that of PC1 (Table 5.1). To investigate the significance of the difference, a paired t-test was performed at a 95 percent confidence level. The results of the paired t-test can be seen in Table 5.3. It was found that the t-statistic (1.64) was lower than the t-critical (2.57), and the p-value for the test was 0.16 (>0.05). This indicates that the difference was not significant.

The 18-hours MOR was an important parameter because the beams were cracked at 18 hours. The paired t-test was also performed for the 18-hours MOR; the results are presented in Table 5.3. It can be seen that the difference between the 18-hours MORs of PC1 and PC2 is also not significant; the p-value is greater than 0.05. The volumetric surface texture ratio (VSTR) for both the PC1 and PC2 were found to be close as well. Therefore, the slight difference in the mixture designs between the two PC mixtures was determined to be insignificant.

Table 5.3. Paired t-test results for 18-hours MOR and 28-days compressive strength for PC mixtures.

t-test parameters	18-hours MOR		28-days compressive strength	
	PC1	PC2	PC1	PC2
Mean	278	255	4624	4888
Observations	3	3	6	6
Hypothesized mean difference	0		0	
Degree of freedom	2		5	
t-statistic	2.37		1.64	
P(T<=t) two-tail	0.14		0.16	
t critical two-tail	4.30		2.57	

FRC1 vs FRC2

Both the 18-hours MOR and 28-days compressive strength of the FRC2 were 7 percent higher than that of the FRC1. The 28-days MORs for both the fiber mixtures were similar. The larger value for 18-hour MOR for FRC2 mixture was most likely due to the accelerated rate of hydration in the hot ambient temperature. Then, when the specimens were fractured at 18 hours, cracks propagated through a larger percentage of the aggregates resulting in a reduced surface texture. Figure 5.3 presents a comparison for the VSTR results for the different mixtures. It can be seen that the FRC2 specimens exhibited a slightly lower VSTR when compared to that of FRC1 specimens.

The paired t-test, given in Table 5.4, confirms that the 18-hours MOR and 28-days compressive strength of FRC1 and FRC2 mixtures were not significantly different (p-value > 0.05). The RSR for both the FRC mixes were similar as well.

Table 5.4. Paired t-test results for 18-hours MOR and 28-days compressive strength for FRC1 and FRC2 mixtures.

t-test parameters	18-hours MOR		28-days compressive strength	
	FRC1	FRC2	FRC1	FRC2
Mean	336	361	4949	5312
Observations	6	6	6	6
Hypothesized mean difference	0		0	
Degree of freedom	5		5	
t-statistic	1.35		1.19	
P(T<=t) two-tail	0.23		0.29	
t critical two-tail	2.57		2.57	

145
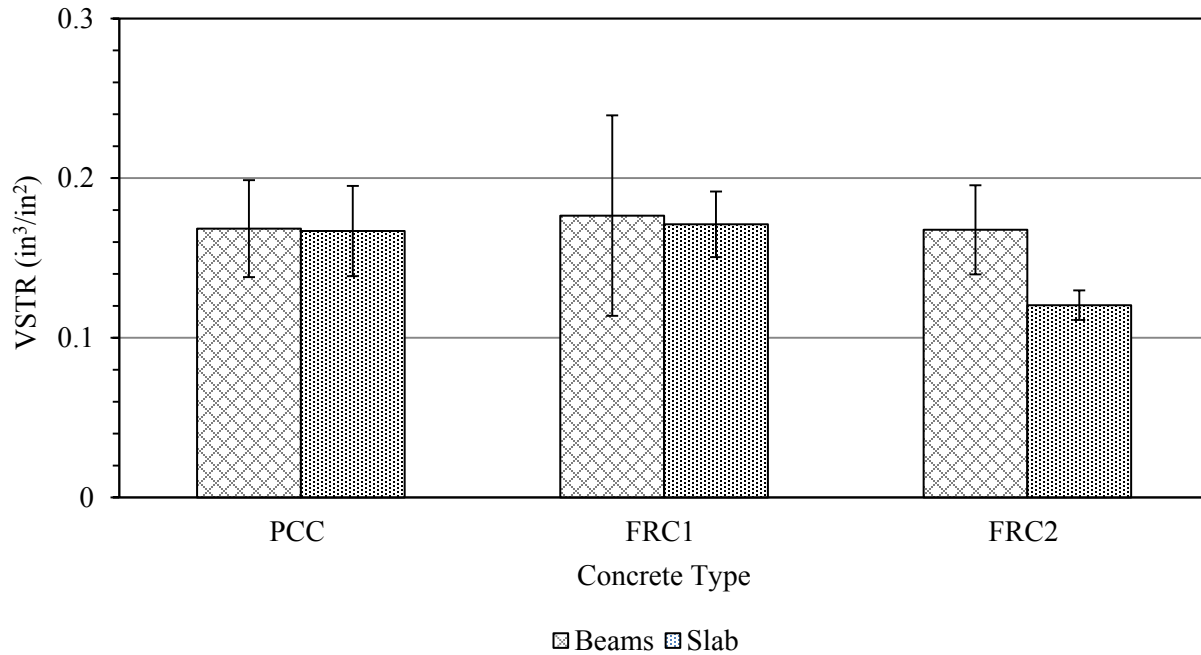
Figure 5.3. Comparison of VSTR results between the mixtures.

PC vs FRC

The hardened concrete properties for the FRC mixtures were slightly superior to that of the PC mixtures. The 18-hours MOR, 28-days compressive strength, 28-days MOR for the FRC1 mixture were respectively 14, 7 and 18 percent higher than that for the PC1 mixture. The paired t-test conducted for 18-hours MOR, 28-days compressive strength for the PC1 and FRC1 mixtures (Table 5.5) indicates that the difference is not significant (p-value > 0.05). The volumetric surface texture ratio for both FRC1 and PC1 mixtures also lie in a similar range. It can be observed that the strength properties for the FRC2 mixture were also slightly higher than that of the PC mixtures. However, as the concrete properties for both the FRC mixtures were similar, it can be concluded that FRC2 mixture is also not significantly different from the PC mixtures.

146

Finally, when comparing the VSTR results for all the beams and slabs in each concrete mixture type, it can be seen that they were similar as well (Figure 5.3). Only the FRC2 slab resulted in a slightly lower VSTR. When comparing the RSR values between the FRC mixtures, the average RSR values were similar for both the mixtures. Also, the load vs deflection trends (in RSR tests) for all the specimens tested for both the fiber mixtures, as shown in Figure 5.4, were similar.

Table 5.5. Paired t-test results for 18-hours MOR and 28-days compressive strength for PC1 and FRC1 mixtures.

t-test parameters	18-hours MOR		28-days compressive strength	
	PC1	FRC1	PC1	FRC1
Mean	290	336	4624	4949
Observations	3	3	6	6
Hypothesized mean difference	0		0	
Degree of freedom	2		2	
t-statistic	2.08		2.08	
P(T<=t) two-tail	0.17		0.17	
t critical two-tail	4.3		4.3	

147
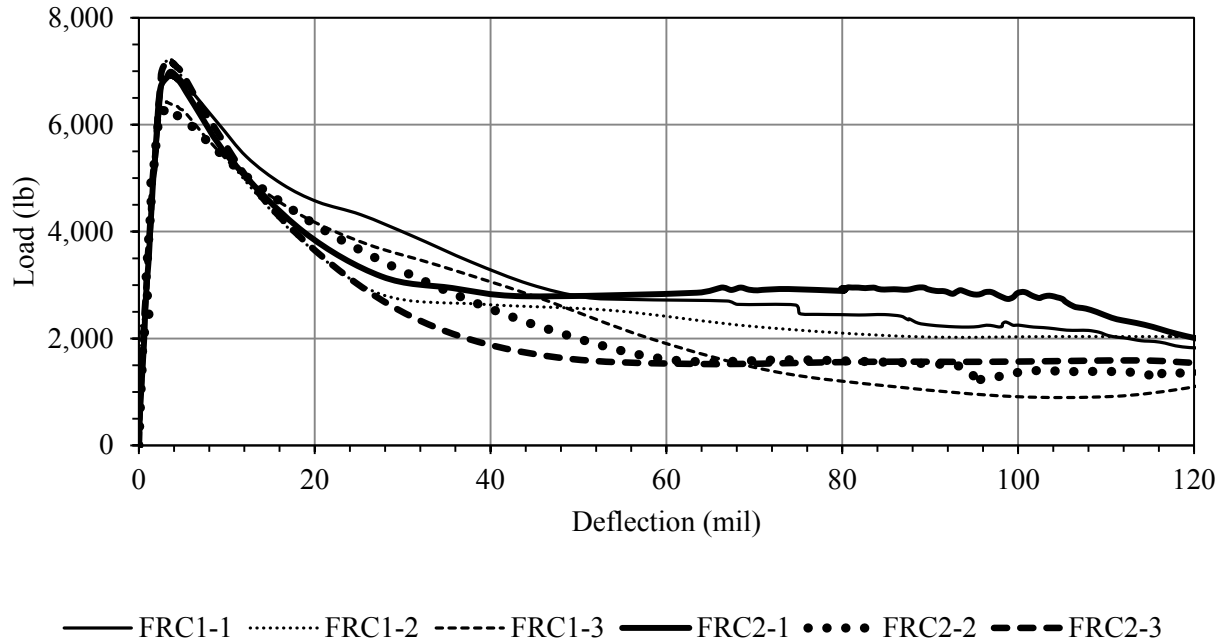
Figure 5.4. Comparison of RSR results for FRC1 and FRC2 mixtures.

5.3   JOINT PERFORMANCE IN TERMS OF LTE

The joint performance of five beams and one slab was evaluated for each concrete mixture. In addition to these, one separate FRC2 beam was tested with 10 million load cycles. The test for each beam and slab was started by evaluating joint performance at the minimum crack width. This crack width is the minimum possible crack width obtained after putting the specimen in the test setup and insuring the width of crack is uniform across the depth and width of the beam. This initial crack width for all the specimens lies in between 0.01 to 0.02 in. The crack width was then opened in approximately equal increments with the joint performance being evaluated at each crack width. Load cycles were applied to abrade the crack face, and deflection and load profiles were recorded. The effort was made to maintain a constant crack width during the

148

fatiguing process. However, the crack width did increase in some cases. Also, in some tests, the initial crack width prior to fatiguing was a couple mils off from the intended fatiguing crack width.

Table 5.6 shows the list of labels that were assigned to all of the beams and slabs. The labeling of the first specimen in the list is P-1, 0.049-0.050, 0.1834; where P stands for plain concrete mixture, 1 represents the specimen number, 0.049-0.050 is range of the crack widths (in) over which the specimen was fatigued and 0.1834 is the VSTR (in^3/in^2). F1 and F2 are the abbreviations for the FRC1 and FRC2 mixtures, respectively. First, the test results in the B_{ALT} procedure is presented followed by the test results of S_{ALT} procedure.

Table 5.6. Labeling of the B_{ALT} and S_{ALT} test specimens.

Concrete Mixture		Specimen label	Intended fatiguing crack width (in)
PC	Beam	P-1, 0.049-0.050, 0.1834	0.05
		P-2, 0.049-0.052, 0.1844	0.05
		P-3, 0.035, 0.1211	0.035
		P-4, 0.035, 0.2078	0.035
		P-5, NF*, 0.1631	n/a
	Slab	P, 0.035-0.036, 0.1669	0.035
FRC1	Beam	F1-1, 0.050-0.051, 0.1597	0.05
		F1-2, 0.05, 0.1680	0.05
		F1-3, 0.037-0.043, 0.1614	0.035
		F1-4, 0.036-0.039, 0.1500	0.035
		F1-5, NF*, 0.2026	n/a
	Slab	F1, 0.037-0.048, 0.1711	0.035
FRC2	Beam	F2-1, 0.048-0.053, 0.1771	0.05
		F2-2, 0.05-0.054, 0.1417	0.05
		F2-3, 0.034-0.035, 0.2027	0.035
		F2-4, 0.034-0.037, 0.1490	0.035
		F2-5, NF*, 0.1726	n/a
		F2-10M	0.05
	Slab	F2, 0.048-0.051, 0.1204	0.05

*NF indicates that the beam was not fatigued.
**10M indicates that the beam was fatigued with 10 million load cycles.*

149

5.3.1 Joint Performance through B_{ALT}

For each of the concrete mixtures, the load and deflection profiles at different stages of the test are presented only for one representative specimen. The general trends of load and deflection profiles for all of the specimens from a particular type of concrete mixture were found to be similar. The results of other specimens are presented for comparison purposes. The LTE for the B_{ALT} procedure is referred as LTE_B. The average of the compression and tension LTE_B values was used to define the measured LTE_B for the comparisons.

5.3.1.1 PC mixture

Figure 5.5 through Figure 5.7 present the load and deflection profiles at the initial crack width, the beginning of fatiguing and the end of fatiguing for the specimen, P-1, 0.049-0.050, 0.1834, respectively. It can be seen that when the crack width increased from 0.010 in (Figure 5.5) to 0.049 in (Figure 5.6), the difference in the deflection profiles between the loaded and unloaded sides increase, indicating a decrease in LTE_B. In this beam, fatiguing was initiated at a 0.049-in crack width, and 1 million load cycles were applied. One interesting observation was that at a wider crack width (Figure 5.6 and Figure 5.7) the unloaded side exhibited a discontinuity in the deflection profile. At a wider crack width, the effective area of aggregates that engage in load transfer, decreases, which results in a sliding between the two sections of the beam. This means when the actuator starts moving upward, the unloaded portion of the beam does not immediately move upward in response. This creates the abrasion in the crack face. The deflection profiles in Figure 5.7 are representative of the conditions after fatiguing. The increased difference in peak deflections between the loaded and unloaded sides, which is known as the differential deflection,

150

shows a more sliding effect or drop in load transfer with an increasing number of load cycles applied.

Def_LS = deflection on the loaded side; Def_US = deflection on the unloaded side
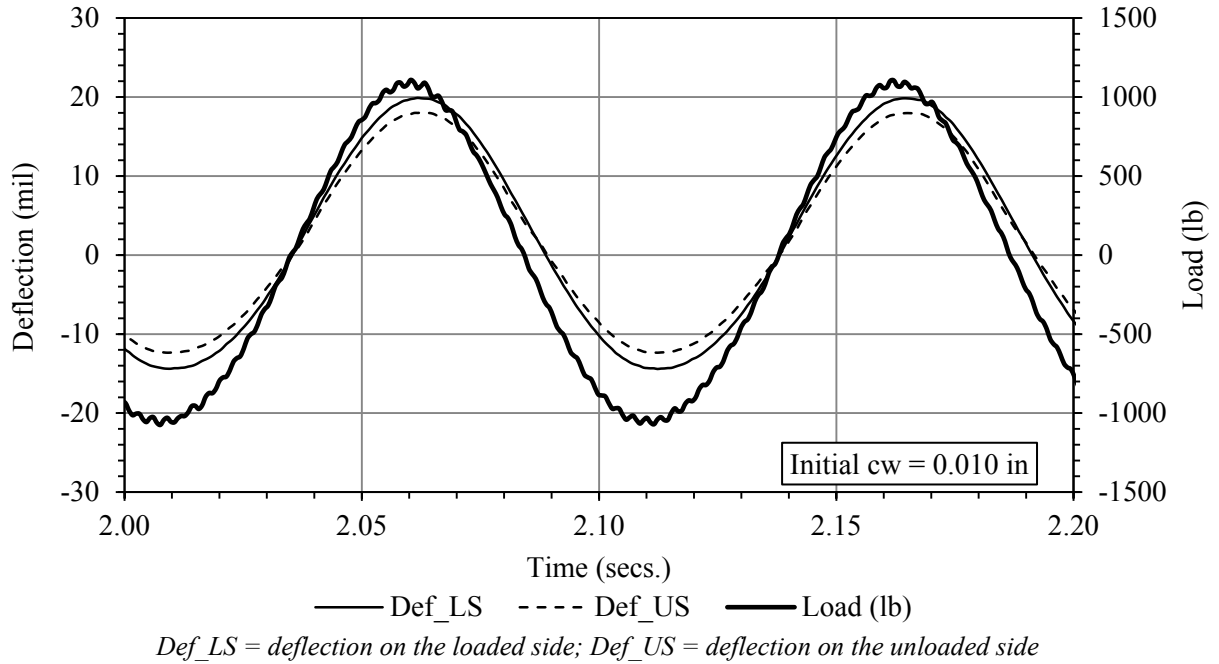
Figure 5.5. Load and deflection profiles at the initial crack width for P-1, 0.049-0.050, 0.1834.
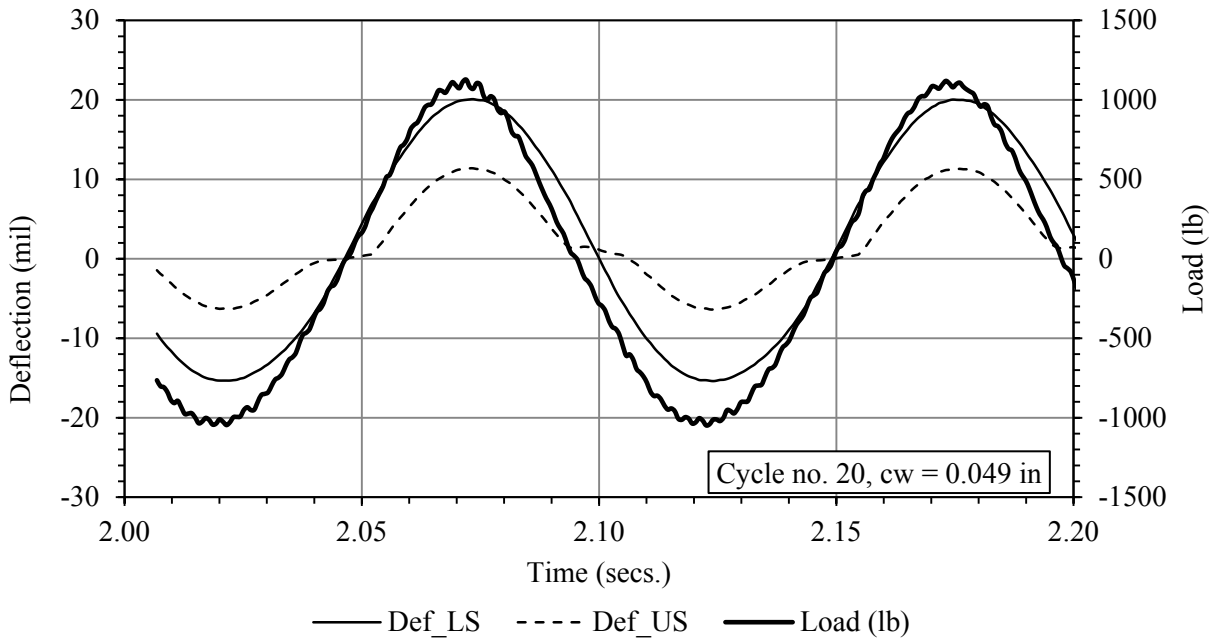
Figure 5.6. Load and deflection profiles at the beginning of fatiguing for P-1, 0.049-0.050, 0.1834.

151
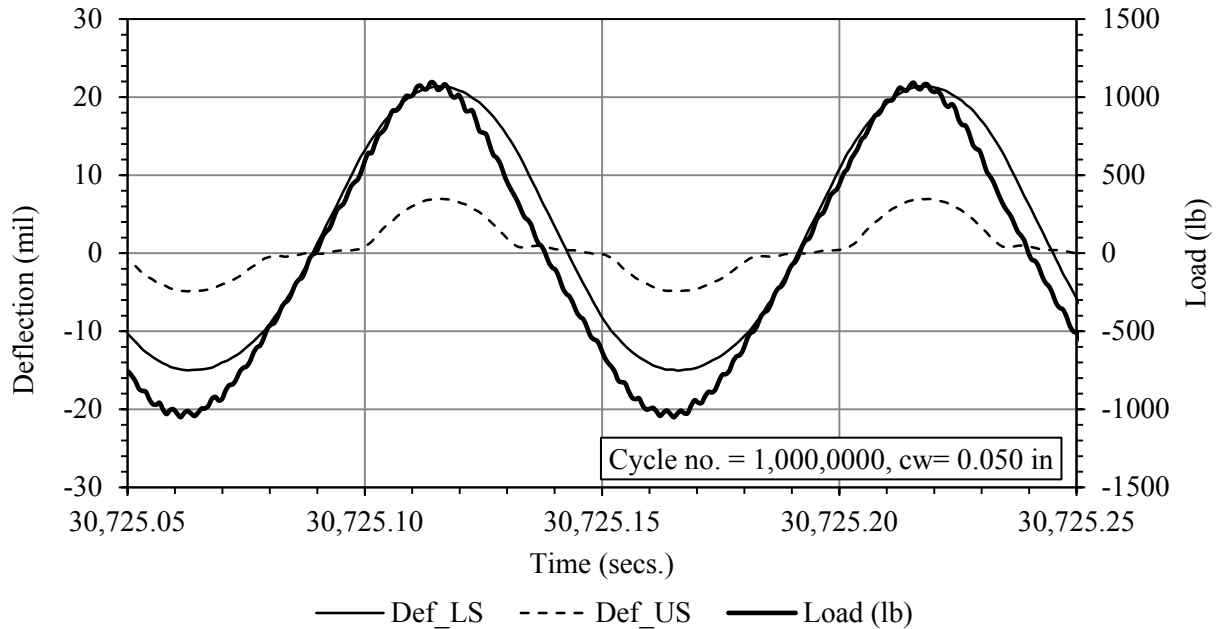
Figure 5.7. Load and deflection profiles at the end of fatiguing for P-1, 0.049-0.050, 0.1834.

Figure 5.8 shows the variation in tension, compression and average LTE_B values with respect to the load cycle applied. The difference is influenced by the macro-texture or the angle along which the crack propagated. The shape of the crack at the front and back sides of the beam, and surface texture at the crack face can be seen in Table 5.7. For the beam, P-1, 0.049-0.050, 0.1834, the difference between the tension and compression LTE_B values was low. The other notable observation was that the LTE_B dropped considerably initially and then after 500,000 load cycles were applied, it stabilized.

152
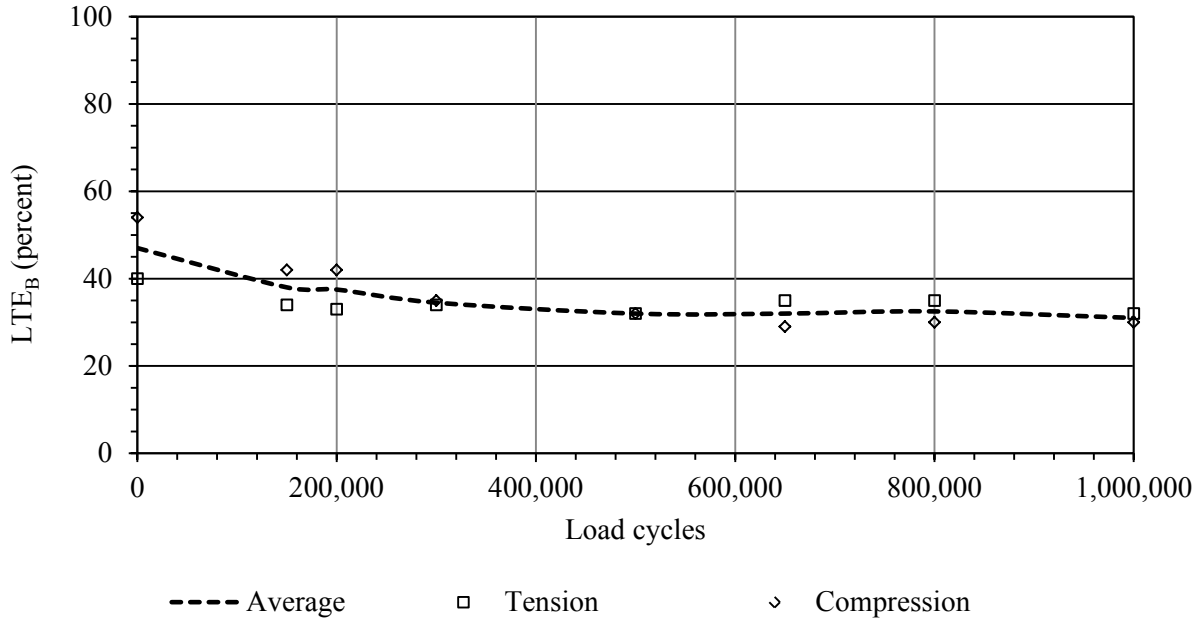
Figure 5.8. LTE$_B$ vs load cycle for P-1, 0.049-0.050, 0.1834.

The tension, compression and average LTE$_B$ values with respect to the crack width for the beam, P-1, 0.049-0.050, 0.1834 are shown in Figure 5.9. It can be seen that the tension and compression LTE$_B$ values remain relatively constant throughout the entire range of crack widths over which the beam was tested. The sudden drop in the LTE$_B$ at a 0.049-in to 0.050-in crack width indicates the drop produced by the fatiguing.

The average LTE$_B$ results with respect to load cycles for all four fatigued PC beams can be seen in Figure 5.10. Figure 5.11 shows the average LTE$_B$ with respect to crack width for five beams. The fifth beam was not fatigued. The crack profiles at the front and back sides of each specimen are shown in Table 5.7. This table also shows the micro texture for the crack faces on the loaded and unloaded sides.

153

Table 5.7. Crack shape and crack surface texture for PC beams.

Specimen	Front side Loaded side / Unloaded side	Back side Unloaded side / Loaded side	Surface texture
P-1			
P-2			
P-3			

154
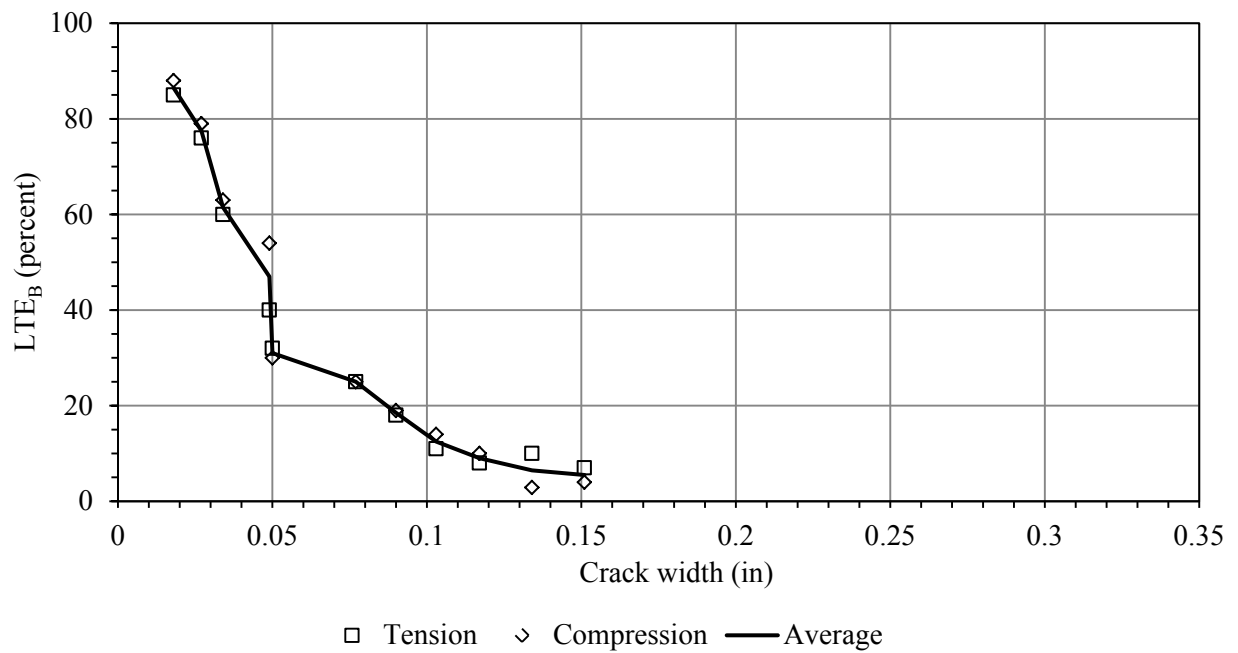
Figure 5.9. LTE$_B$ vs crack width for P-1, 0.049-0.050, 0.1834.

Figure 5.10 shows that for the LTE_B vs load cycle relationship, the LTE_B drops typically occur before 500,000 load cycles, and then LTE_B stabilizes. This may be due to the fact that when the joint is relatively fresh, the prominent microtexture abrades at a higher rate with load applications. After approximately 500,000 load cycles, the sharpness of the texture is lost due to abrasion. Therefore, further load cycles, at that specific crack width, produce less abrasion. Among the four beams, it can be observed that the two beams fatigued at a 0.05-in crack width exhibited a slightly higher drop in LTE_B (16 and 10 percent, average = 13 percent) as compared to the other two, which were fatigued at a 0.035-in crack width (8 and 10 percent, average = 9 percent). Between the two beams that were fatigued at a 0.05-in crack, the beam P-2, 0.049-0.052, 0.1844 exhibited a lower drop in LTE_B as compared to the other one. If the crack profile on the front side, for this beam, is carefully examined in Table 5.7, it can be seen that there are two distinct crack slopes, one opposite to the other. This particular crack profile might have resulted in a locking condition, and the differential deflection thereby remains low even at a wider crack width.

156
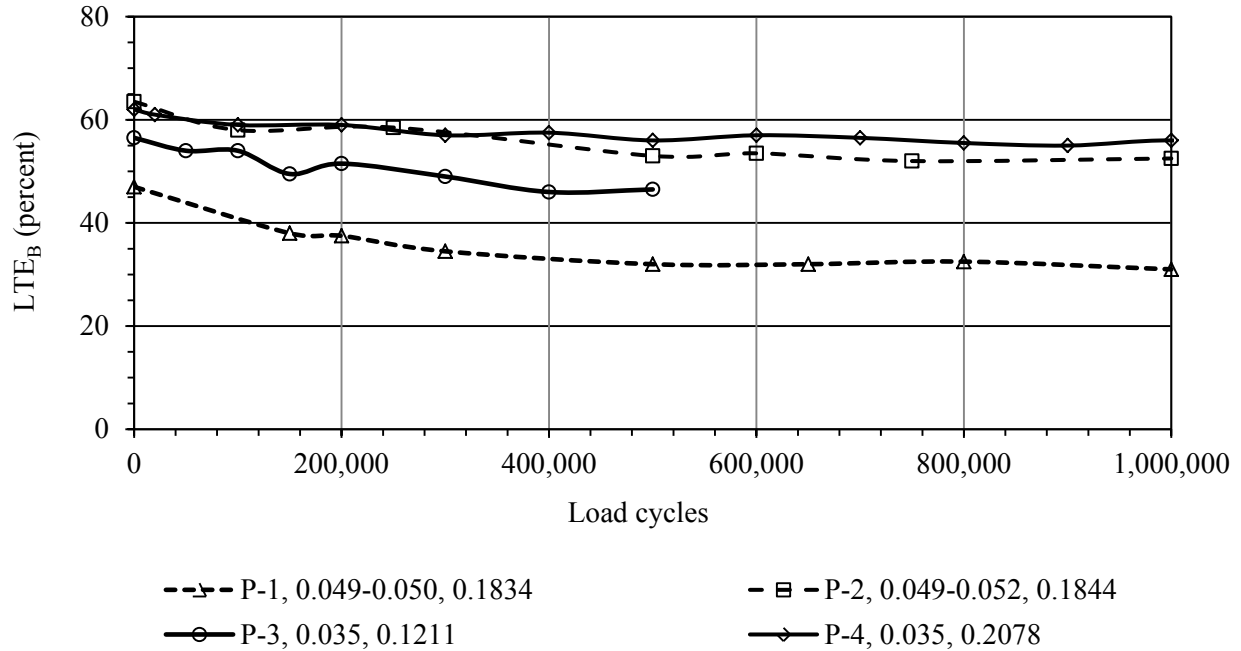
Figure 5.10. LTE$_B$ vs load cycle application for all four fatigued PC beams.

The trends for the LTE$_B$ vs crack width, depicted in Figure 5.11, for all the beams are similar. In Figure 5.11, hollow data markers present the LTE$_B$ values that were obtained before fatiguing. Beam P-5, NF, 0.1631, which was not fatigued, also does not show a significantly different trend. The largest rate of decrease in LTE$_B$ was exhibited in between 0.025-in to 0.050-in crack widths for all the beams. Similar trends were also observed in a few other studies (Hansen, et al., 1998 and Jensen & Hansen, 2001).

157
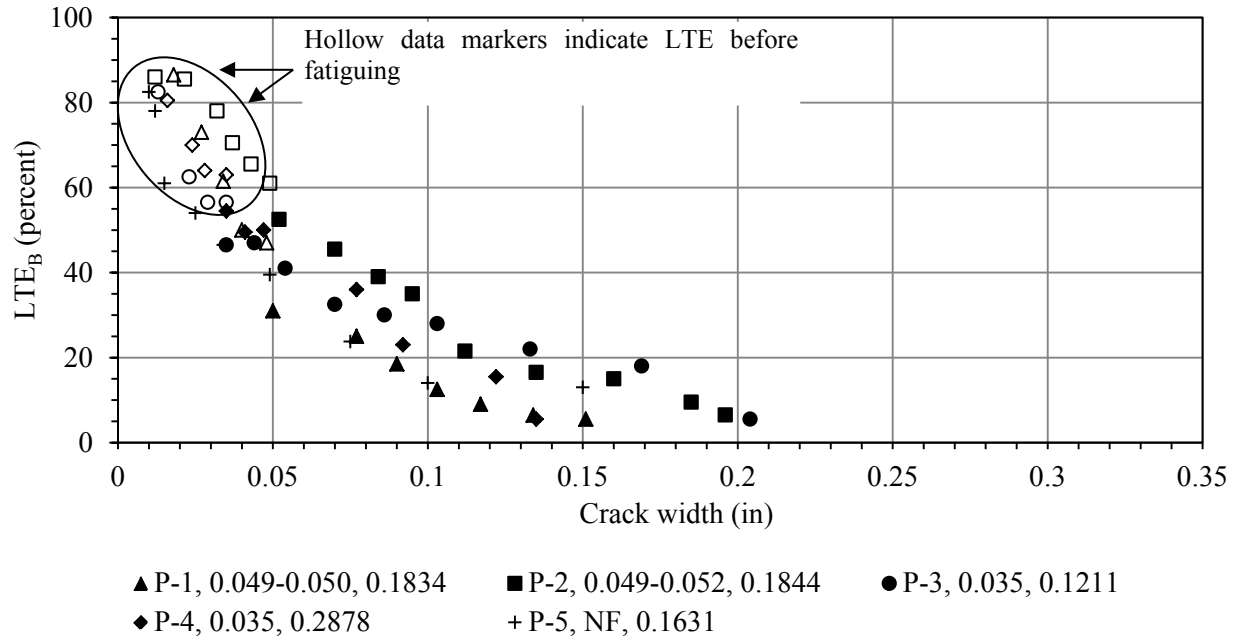
Figure 5.11. LTE$_B$ vs crack width for all five PC beams.

5.3.1.2 FRC1 mixture

Figure 5.12 through Figure 5.14 present the load and deflection profiles at the initial crack width, the beginning of fatiguing and the end of fatiguing, respectively for an FRC1 specimen, F1-1, 0.050-0.051, 0.1597. It can be seen that when the crack width increased from 0.020 to 0.050 in, the differential deflection increases, indicating a drop in LTE$_B$. This beam was fatigued at a 0.050-in crack width with 500,000 load cycles. The difference in the differential deflections was also slightly higher after fatiguing. In this beam, the discontinuity in the deflection profile did not occur when the crack width was increased to 0.050 in or even after fatiguing with 500,000 load cycles at a 0.050-in crack width, unlike the PC beams. The fiber most likely contributed to this. Since the differential deflection or the sliding of the beam sections against each other is comparatively lower than what was observed in PC beams, the drop in LTE$_B$ when fatiguing is also lower.

158
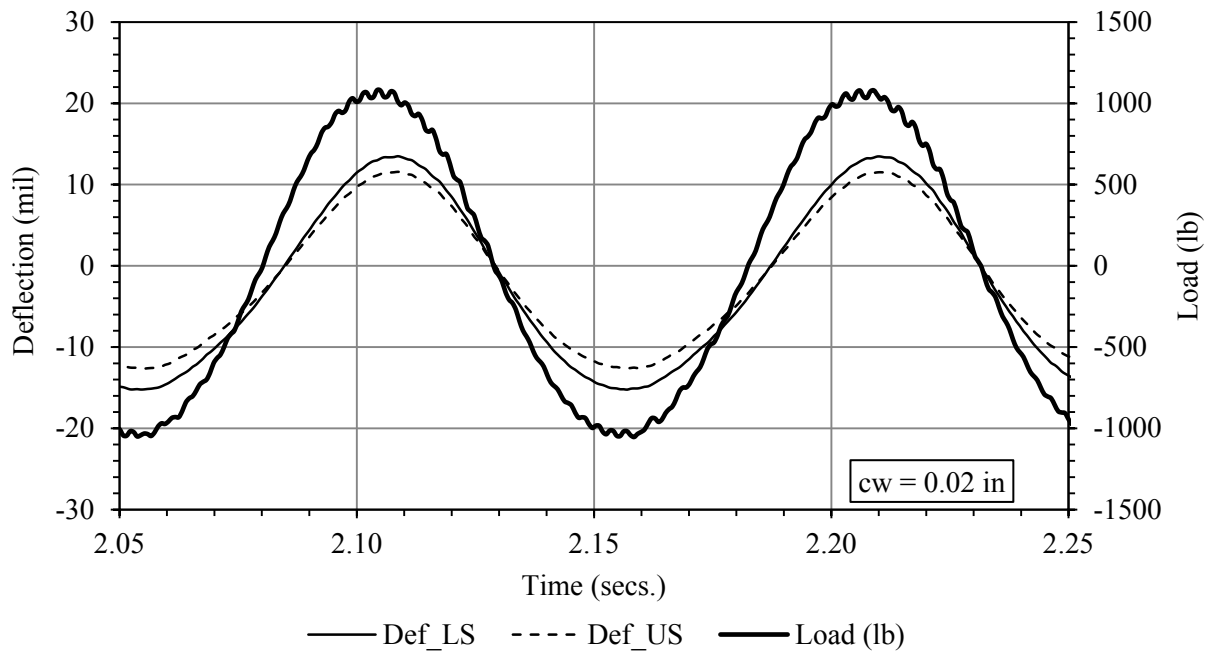
Figure 5.12. Load and deflection profiles at the initial crack width for F1-1, 0.050-0.051, 0.1597.
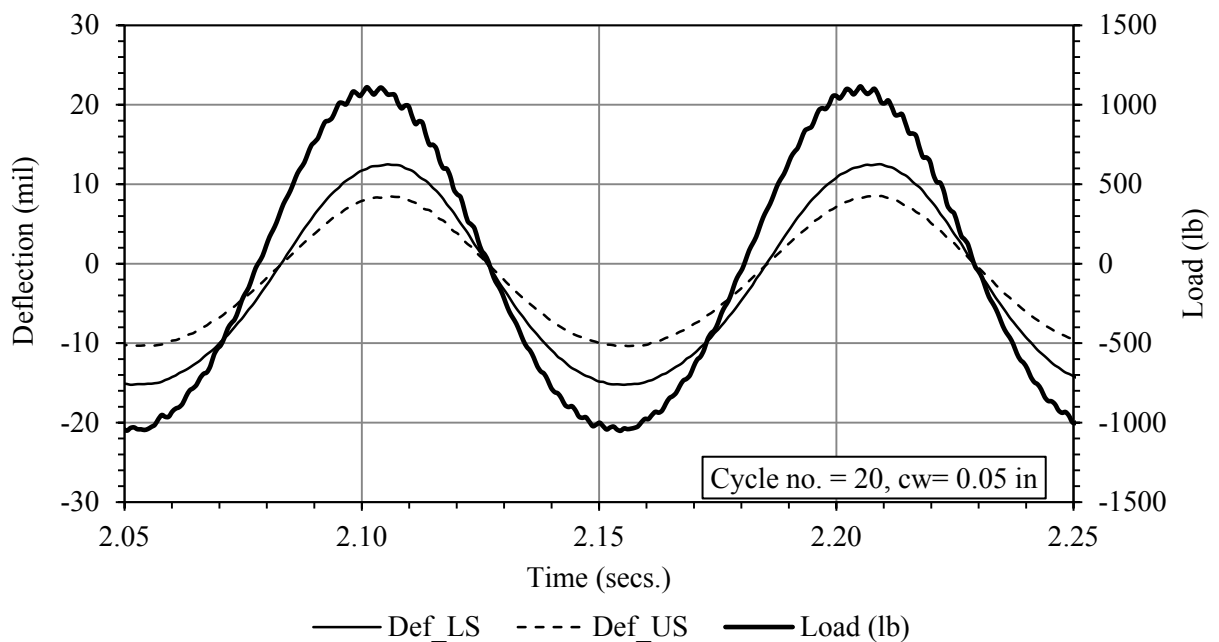
Figure 5.13. Load and deflection profiles at the beginning of fatiguing for F1-1, 0.050-0.051, 0.1597.

159
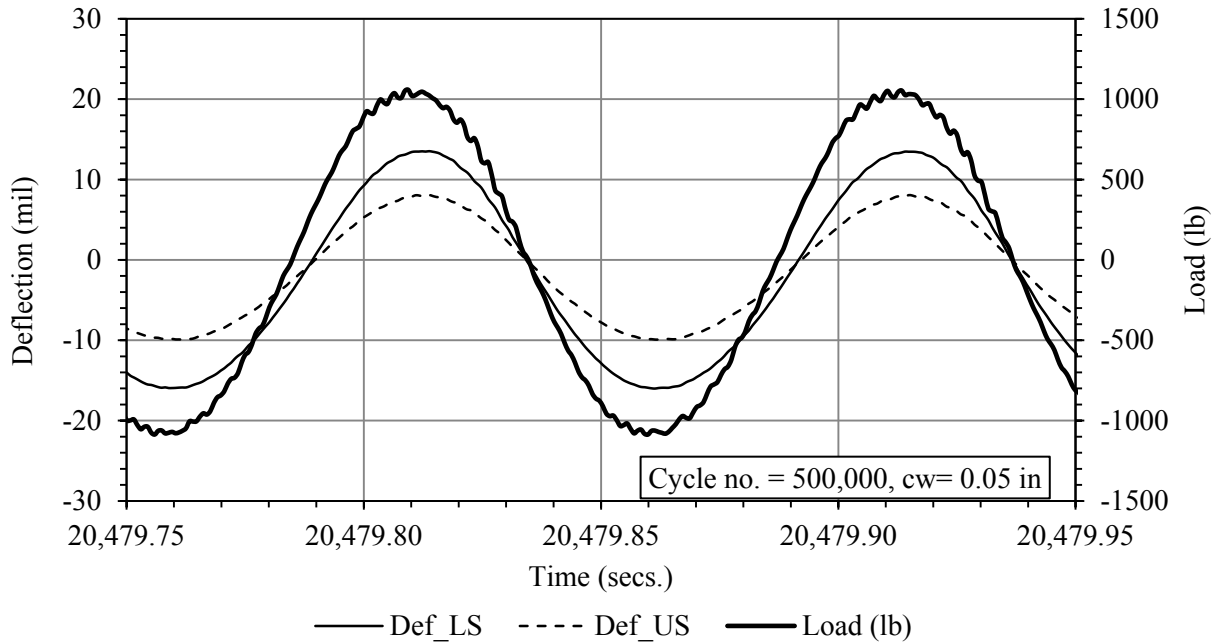
Figure 5.14. Load and deflection profiles at the end of fatiguing for F1-1, 0.050-0.051, 0.1597.

Figure 5.15 shows the variation in the tension, compression and average LTE_B values with respect to the load cycles. The difference between the tension and compression LTE_B values for this beam, as well as all the FRC beams, was comparatively lower with respect to the plain concrete beams. The fibers across the crack create a bridging action between the two beam sections, which reduces the sliding between the beam sections in both the upward and downward directions, and this reduces the difference between the tension and compression LTE_B values. The shape of the crack on the front and back sides, and surface microtexture of the crack face for this beam and for all other FRC1 beams are provided in Table 5.8. The crack shape or the macrotexture for this beam was quite irregular and also may be partially responsible for a lower difference between the tension and compression LTE_B values. The other notable observation is that the LTE_B dropped initially at around 20,000 load cycles (by 5 percent) and then after 50,000 load cycles, it stabilized.

160

The tension, compression and average LTE_B values with respect to crack width for beam F1-1, 0.050-0.051, 0.1597 are shown in Figure 5.16. It can be seen that the tension and compression LTE_B values are similar to each other throughout the entire range of crack widths. The sudden drop (7 percent) in LTE_B at 0.050 to 0.051 in reflects the drop due to fatiguing.
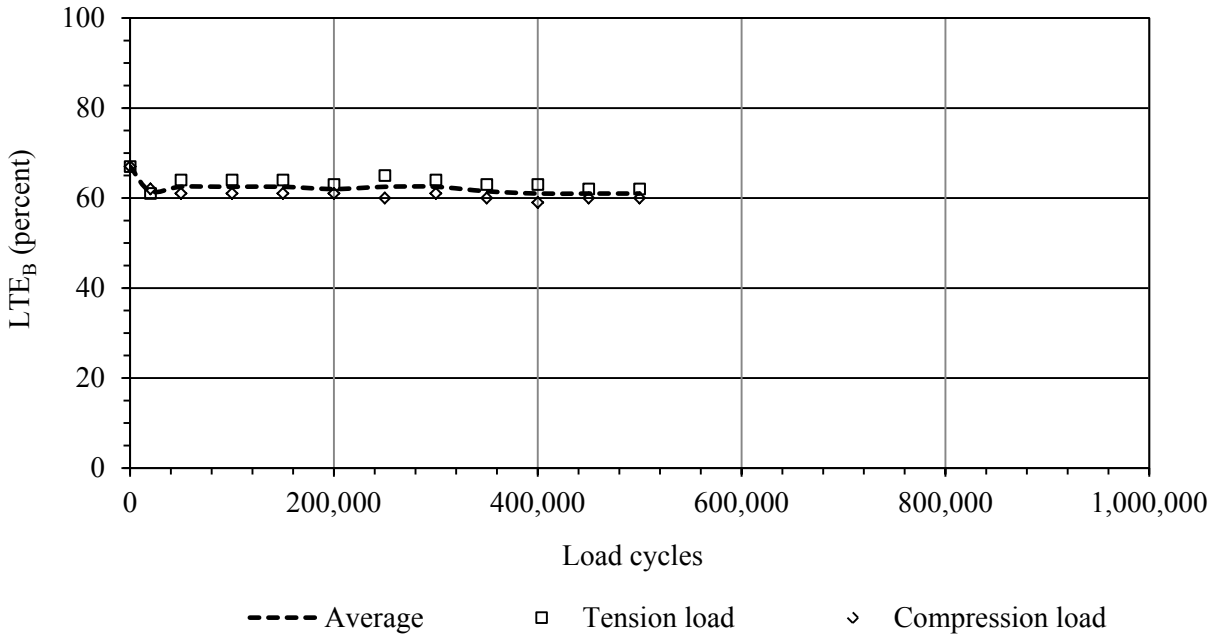
Figure 5.15. LTE_B vs load cycles for F1-1, 0.050-0.051, 0.1597.

Table 5.8. Crack shape and crack surface texture for FRC1 beams.

Specimen	Front side Loaded side / Unloaded side	Back side Unloaded side / Loaded side	Surface texture
F1-1			

F1-2			Not available
F1-3			
F1-4			
F1-5			
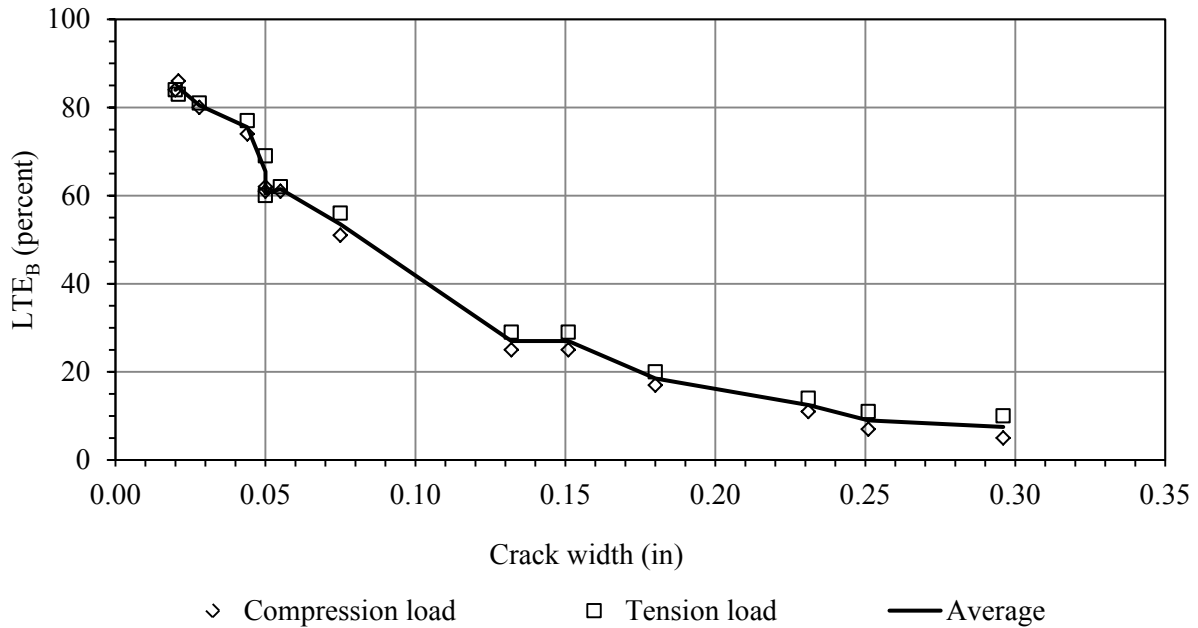
Figure 5.16. LTE_B vs crack width for F1-1, 0.050-0.051, 0.1597.

The average LTE_B with respect to load cycles for all four fatigued FRC1 beams can be seen in Figure 5.17. Figure 5.18 shows the average LTE_B with respect to crack width for all five FRC1 beams tested. Although the difference between the tension and compression LTE_B values is comparatively low for all FRC1 beams, the average LTE_B is chosen for comparison purposes to minimize the influences of crack slope or the macrotexture.

A decrease in LTE_B with increasing load cycles was observed for the first 400,000 load cycles for all FRC1 beams. The LTE_B then stabilized. This trend is similar to that observed for the PC beams. This also indicates that this fiber (Straight synthetic, Strux 90/40) does not fatigue by a noticeable amount after 0.5 to 1 million load cycles. Among the four beams, it can be observed that three of the beams exhibited a similar trend in LTE_B in that at the end of fatiguing it dropped 4 to 6 percent. The third beam, which was fatigued at a 0.037-in crack width, exhibited a 13 percent drop in LTE_B at the end of 1 million load cycles. This different

163

behavior for this beam can be attributed to the fact that the crack width during fatiguing increased from 0.037 to 0.043 in. It might have dropped by a similar magnitude (4 to 6 percent) had the crack been maintained at a constant width. The crack shapes for all four of the beams are comparable, as can be seen in Table 5.8, so a similar joint performance behavior would be expected.

It may be noted that in a couple of discarded specimens, crack width was found to be accidentally increasing by as much as 10 mils after approximately 200,000 to 400,000 load cycles. When the beam was further fatigued after reducing the crack width back to its intended fatigue crack width, the LTE_B vs load cycles curve followed a different trend than what was observed prior to the crack width adjustment. An example of one such beam is included here in Figure 5.19. The crack width was measured as 0.062 mils at the end of 300,000 load cycles. This crack width was 12 mils above the intended fatiguing crack width. When the crack width was reduced to 0.05 mils, the LTE_B was found to reduce by about 10 percent. This shows the reduction in the effectiveness of the fiber in transferring load when the crack width is below the maximum crack width experienced by the slabs. Plastic deformation occurs in the fiber to accommodate the increase in joint width. When the joint closes, the fiber is no longer taut and becomes less effective in transferring load.

However, in the warmer months when the joint width is narrow then both the aggregate interlock and fiber contribute in transferring the load, with the largest contribution occurring through the aggregate interlock. In the winter months, when the joint width is large, fibers contribute a larger share in load transfer. Moreover, the underlying support conditions are the stiffest during the winter months when the HMA is cold and the subgrade is frozen, at least in the

northern states, so more load is transferred through the underlying layer and less is needed from the fiber.
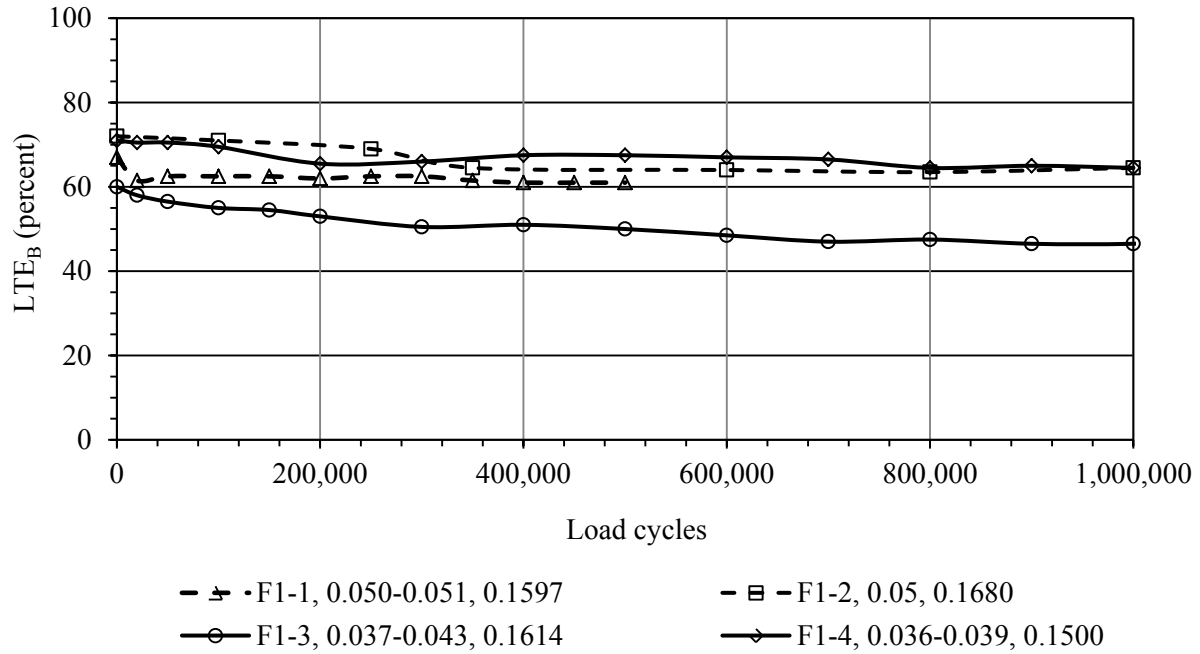
Figure 5.17. LTE_B vs load cycles for all four fatigued FRC1 beams.
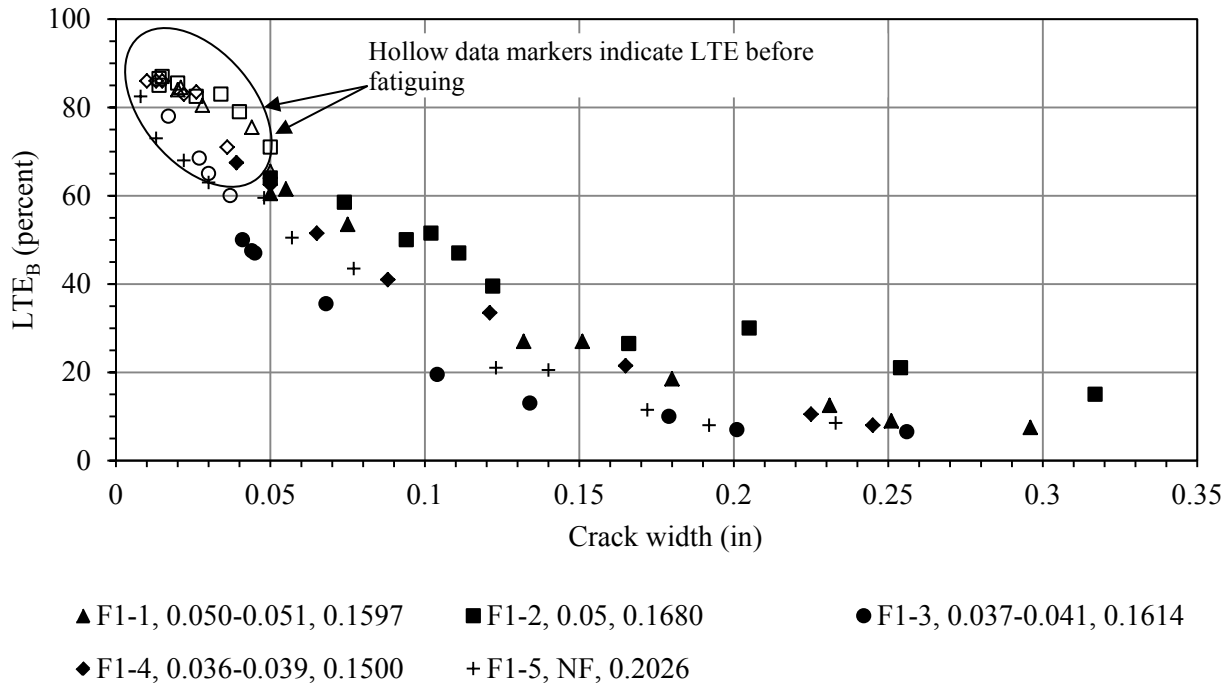
Figure 5.18. LTE_B vs crack width for all five FRC1 beams.
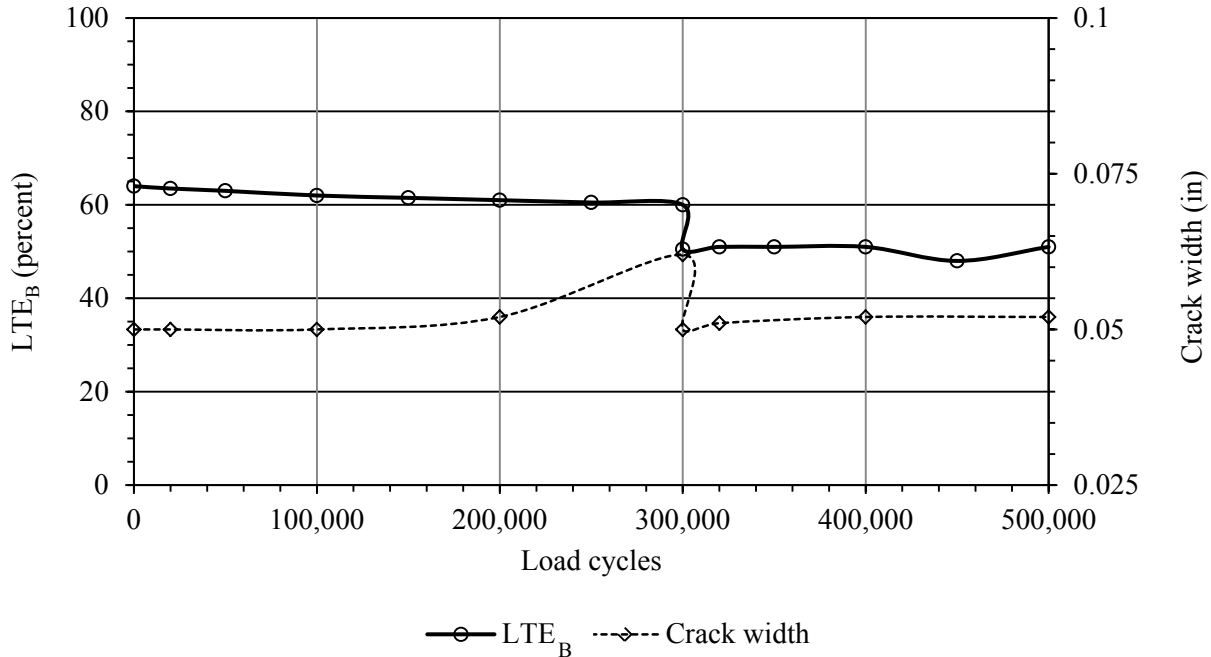
Figure 5.19. LTE$_B$ vs load cycles for a discarded beam; crack width increased by 12 mils during fatiguing.

The relationships between LTE$_B$ and crack width for all of the FRC1 beams are also consistent, as seen in Figure 5.18. The fifth beam, which was not fatigued, also does not show a significantly different trend, except that the tension LTE$_B$ for this beam was consistently 5 to 7 percent higher than the compression LTE$_B$. The reason for this is quite clear from the picture of the crack shape for this beam in the Table 5.8. The slope was slanted toward the loaded side, which means when tension is applied, the effective aggregate interlocking area is more as compared to that in compression load.

The LTE$_B$ decreased quite rapidly with an increase in crack width when the crack width was between 0.035 and 0.050 in. The rate of decrease in LTE$_B$ with increasing crack width then decreases. The LTE$_B$ stabilized at 5 to 10 percent when the crack increased to the point that the aggregate interlock was no longer effective.

166

5.3.1.3 FRC2 mixture

Figure 5.20 through Figure 5.22 present the load and deflection profiles at the initial crack width, the beginning of fatiguing and the end of fatiguing, respectively for the FRC2 beam F2-1, 0.048-0.053, 0.1771. It can be seen that when the crack increased from 0.017 to 0.048 in, the differential deflection increased. The trend is somewhat similar to that observed for the FRC1 beams but is significantly different from the PC beams. The beam was fatigued at a 0.048-in crack width for a total of 1 million load cycles. It can be seen that the differential deflection increased after fatiguing.
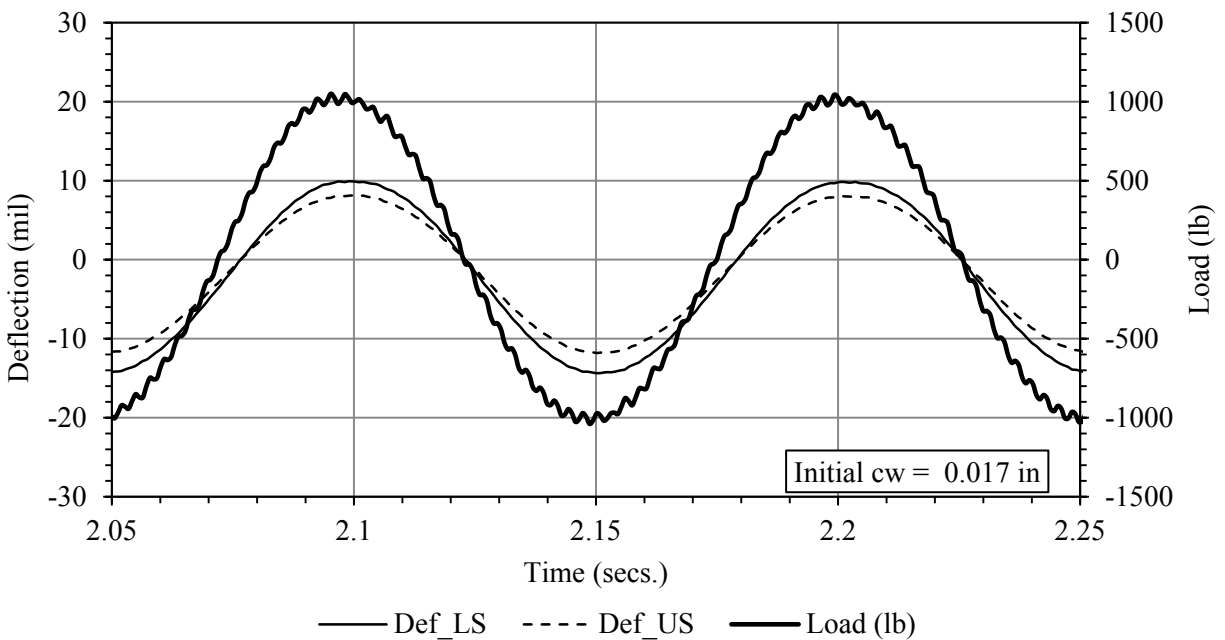
Figure 5.20. Load and deflection profiles at initial crack width for F2-1, 0.048-0.053, 0.1771.

167
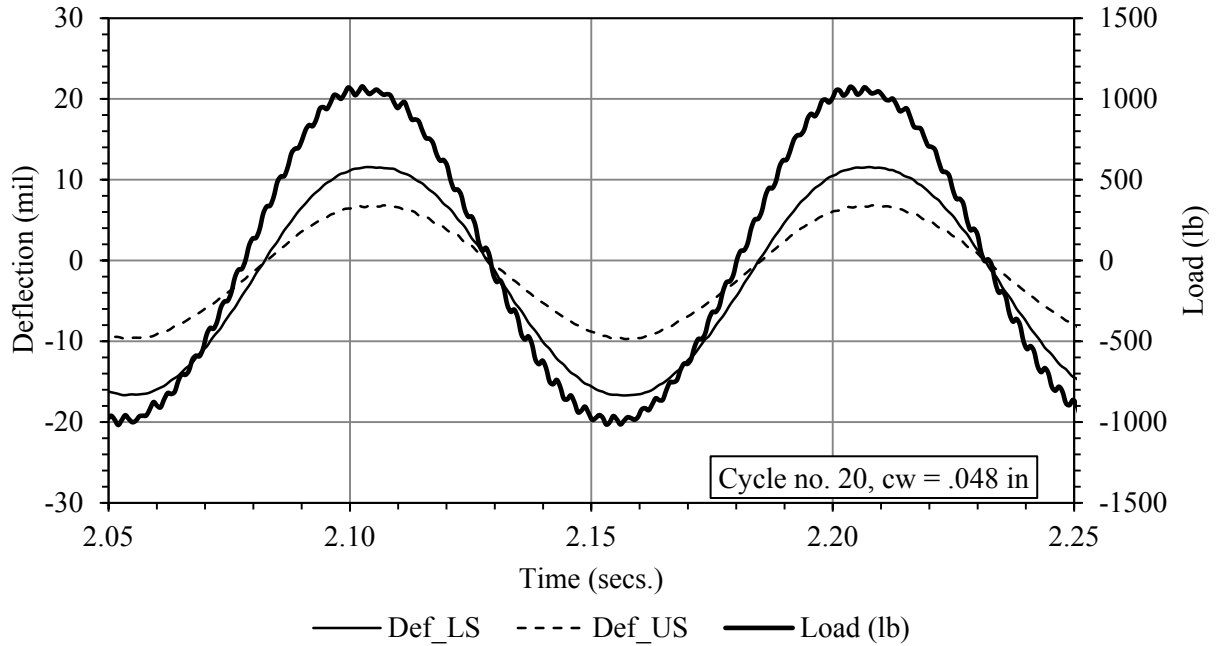
Figure 5.21. Load and deflection profiles at the beginning of fatiguing for F2-1, 0.048-0.053, 0.1771.
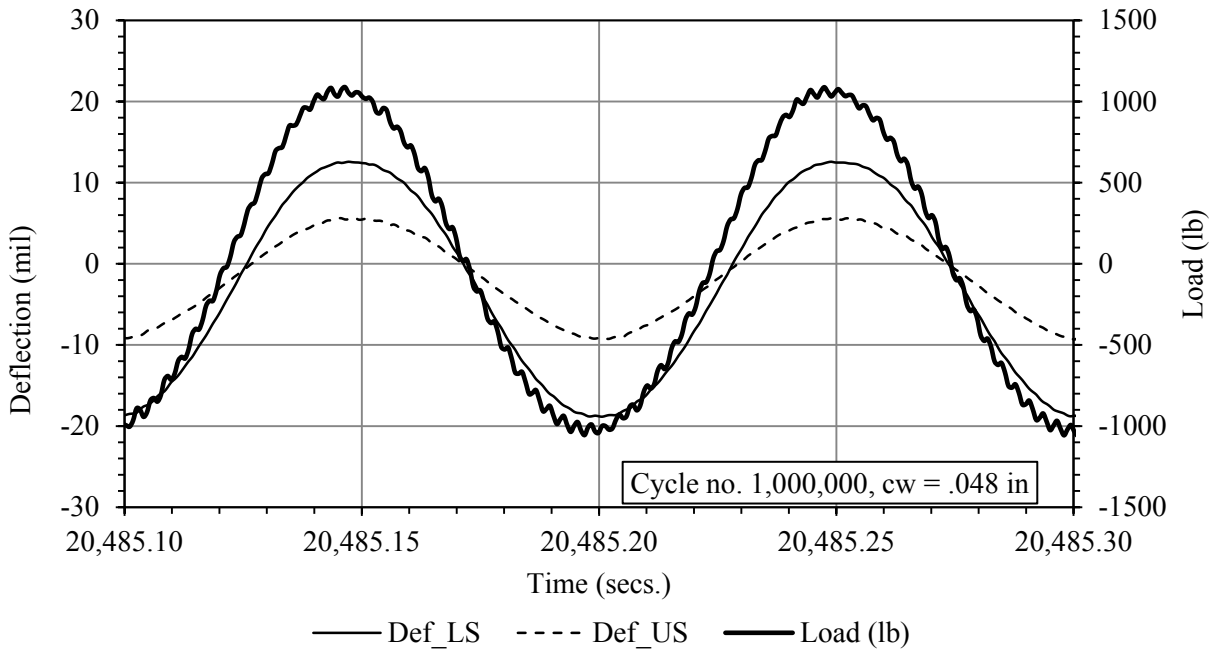
Figure 5.22. Load and deflection profiles at the end of fatiguing for F2-1, 0.048-0.053, 0.1771.

Figure 5.23 shows the variation between the tension, compression and average LTE_B values with respect to load cycles. This figure shows another example that FRC beams did not exhibit a significant difference between tension and compression LTE_B values. The strong fiber bridging effect, fairly rough crack surface texture and irregular crack meandering at the front and back sides might have created a greater interlocking that lead to similar tension and compression LTE_B values. The shape of the crack at the front and back sides, and surface microtexture of the crack face for this beam and for all other FRC2 beams can be seen Table 5.9. In this beam, the LTE_B initially dropped after around 20,000 load cycles by 4 percent and then again at 250,000 load cycles by another 6 percent followed by a very low decrease in LTE_B with the further load accumulation of load cycles. The initial drop in LTE_B after 20,000 load cycles was similar to what was observed in other beams, but the second drop at 250,000 was due to an increase in the crack width that occurred during fatiguing. The crack width measured at 250,000 was 0.052 in. This 4 mil difference in crack width most likely played a role in the large decrease in LTE_B.
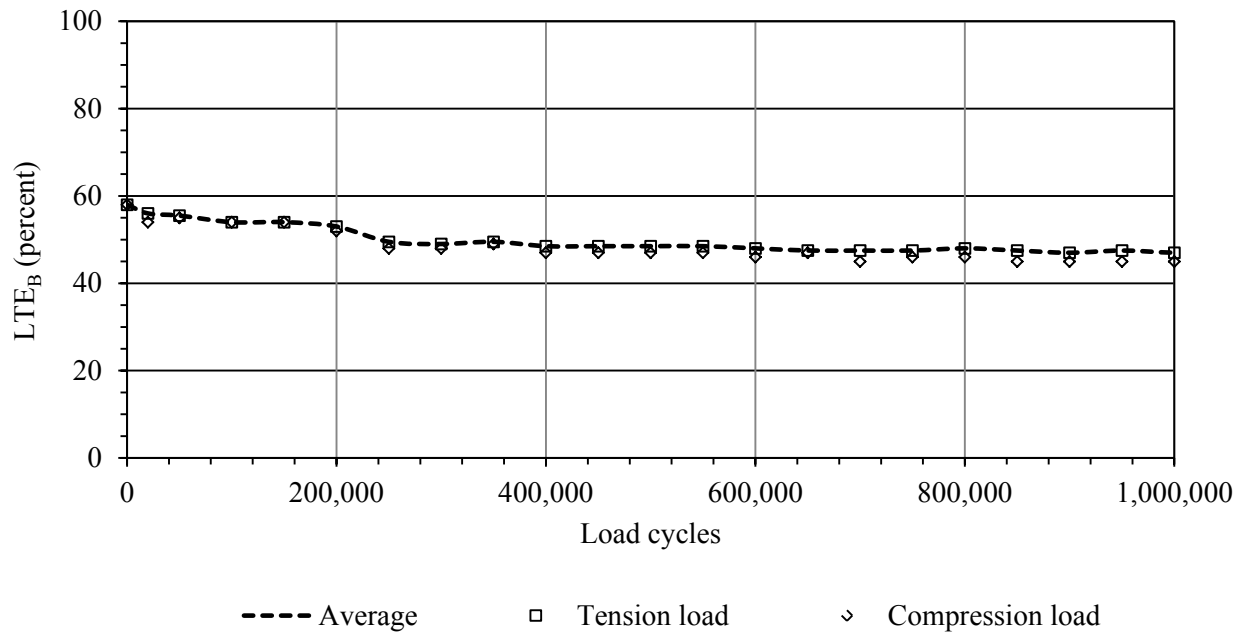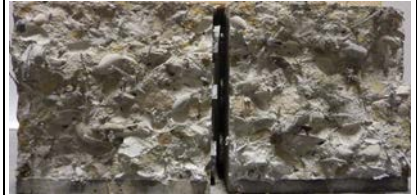
Figure 5.23. LTE_B vs load cycles for F2-1, 0.048-0.053, 0.1771.

Table 5.9. Crack shape and crack surface texture for FRC2 beams.

Specimen	Front side Loaded side / Unloaded side	Back side Unloaded / Loaded side	Surface texture
F2-1			
F2-2			
F2-3			
F2-4			
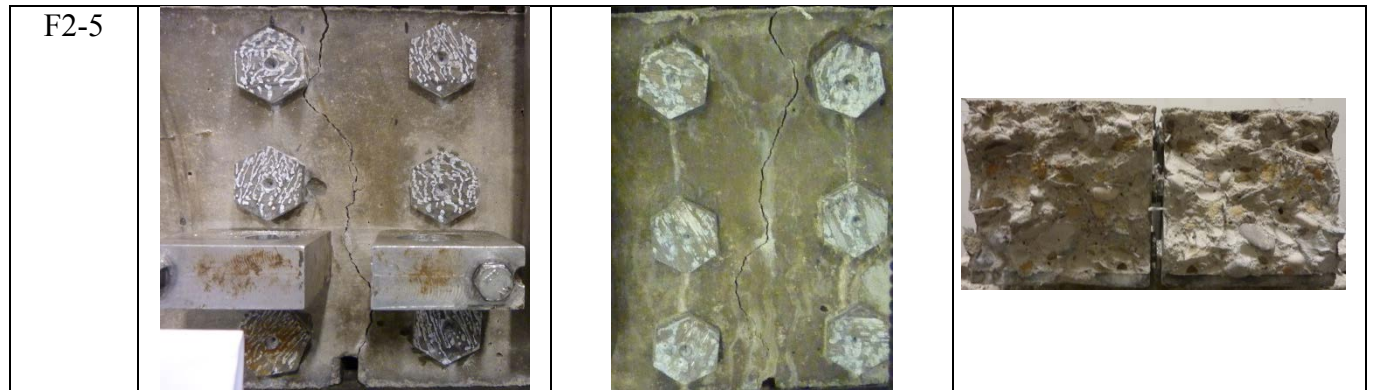
The tension, compression and average LTE_B values with respect to the crack width for the F2-1, 0.048-0.053, 0.1771 beam are shown in Figure 5.24. Similar to the FRC1 beams, the difference between the tension and compression LTE_B values remain constant throughout the entire range of crack widths. The sudden drop in LTE_B observed reflects the decrease due to fatiguing.
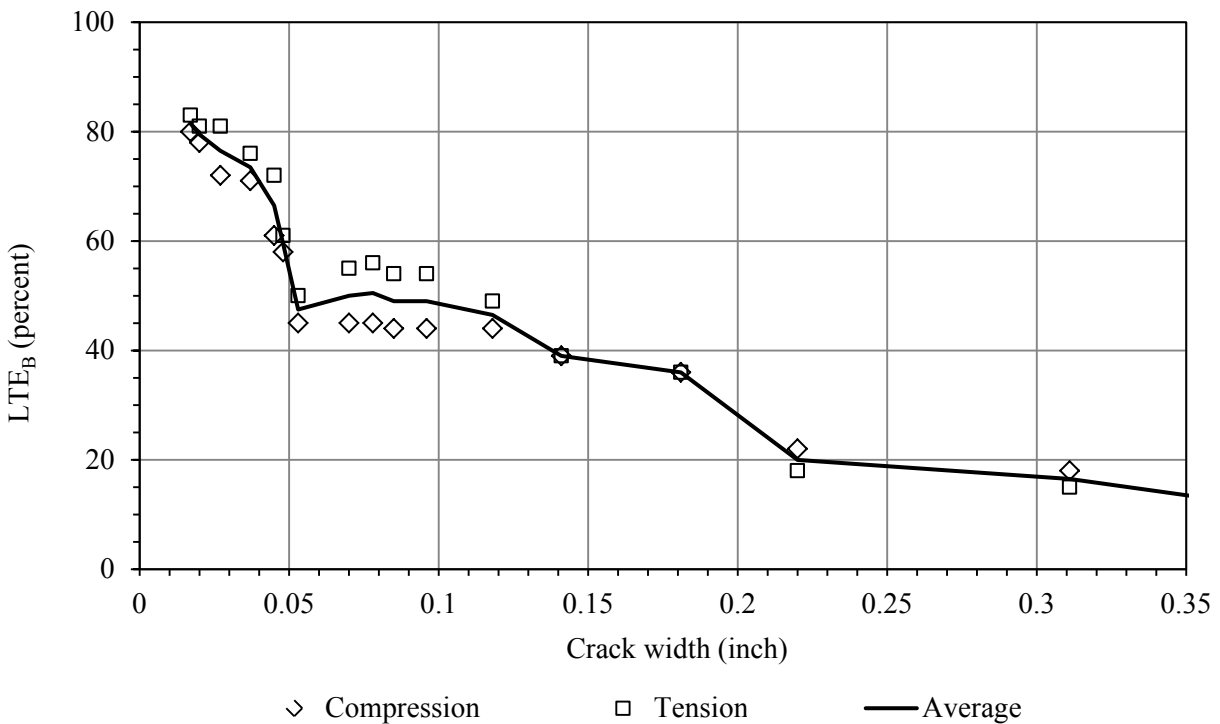
Figure 5.24. LTE_B vs crack width for F2-1, 0.048-0.053, 0.1771.

The average LTE_B with respect to load cycles for all four fatigued beams can be seen in Figure 5.25. It can be observed that all of the FRC2 beams exhibited a decrease in LTE_B after approximately 20,000 to 100,000 load cycles. This reflects the fact that the prominent texture of the crack face abrades at a higher rate initially, and then when the crack face becomes smoother the abrasion or fatiguing rate drops. Even though the crack width was constantly monitored, it was quite challenging to maintain a constant crack width. A few mils of variation (1 to 4 mils) occurred in the case of the FRC2 beam. More importantly, if an increase in the crack width was noticed, it was not reduced in the middle of fatiguing. The horizontal tension was marginally reduced so that a further increase in crack width is avoided while insuring that the beam remained in tension.
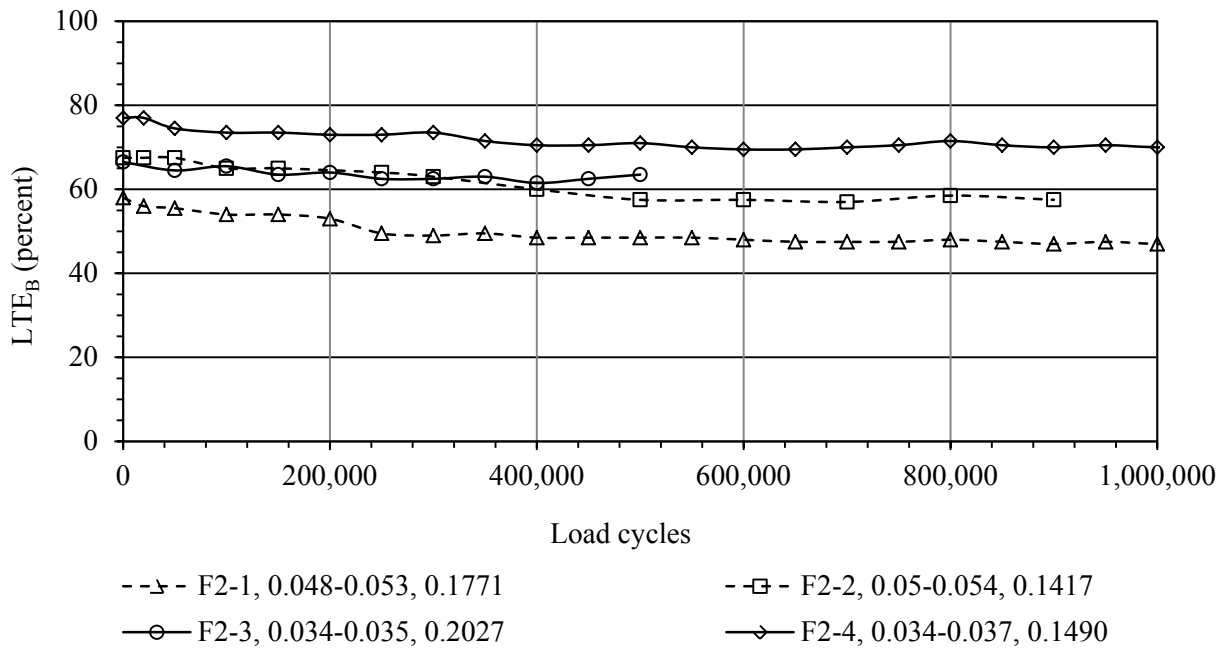
Figure 5.25. LTE_B vs load cycles for all four fatigued FRC2 beams.

Figure 5.26 shows the average LTE_B with respect to the crack width for all five FRC2 beams. The four beams which were fatigued show a similar LTE_B vs crack width relationship.

172

This is quite reasonable as the crack shape for all of these beams are similar, as was shown in Table 5.9. The fifth beam, which was not fatigued, shows a different trend. The crack shape of this beam actually contributed to the low average LTE_B with respect to crack width. The crack shape, as shown in Table 5.9, indicates that the effective area of the aggregate interlocking is relatively low under the tension load; therefore, the tension LTE_B was considerably low when the crack width was increased beyond 0.050 in. This brought the average LTE_B down.

In general, up to approximately a 0.035-in crack width, the decrease in LTE_B was slightly lower than what was observed for the crack widths between 0.035 and 0.050 in. This trend was similar to the FRC1 beams. Then, in between 0.05-in to 0.150- in crack widths, the decrease rate was relatively low. Finally, the LTE_B was stabilizing at 5 to 10 percent when contribution from aggregate interlock was negligible.
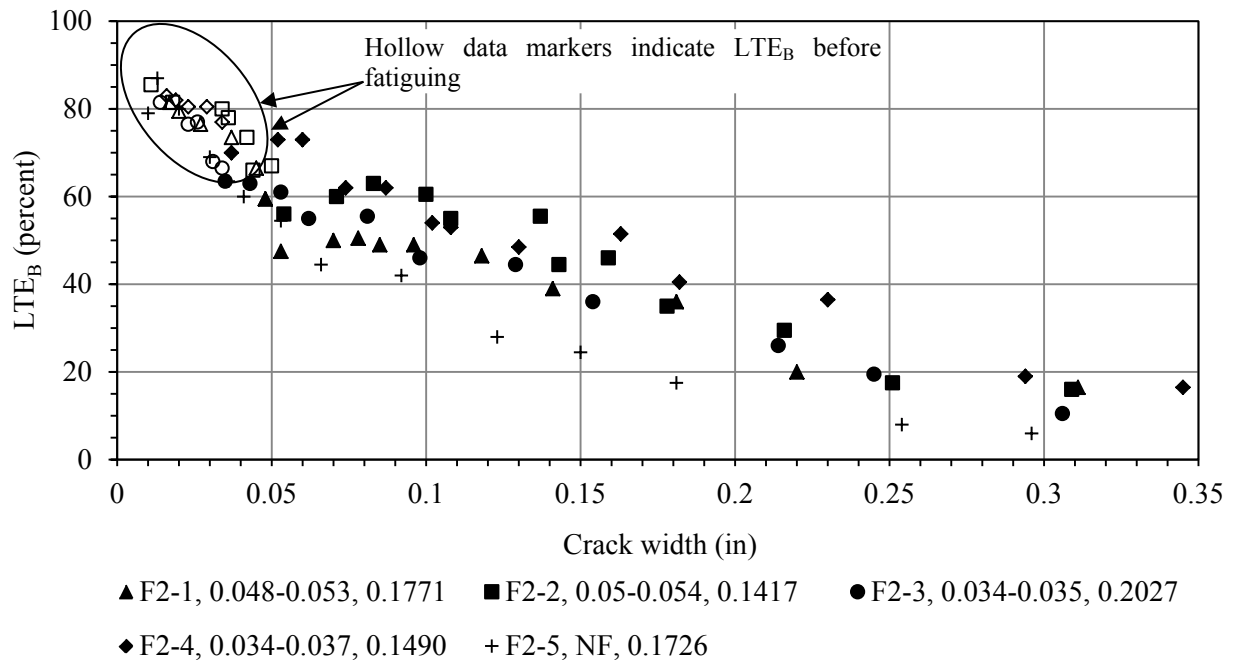
Figure 5.26. LTE_B vs crack width for all five FRC2 beams.

173

5.3.1.4 Comparison of LTE$_B$ results between the mixture types

A comparison in average LTE$_B$ vs load cycle trends between the different types of concrete mixtures are presented in Figure 5.27 and Figure 5.28. The first figure presents the comparison for the specimens that were fatigued at a 0.050-in crack width, while the second figure presents the comparison for the specimens fatigued at a 0.035-in crack width. The similarity in the general trends for all curves in both figures indicates that irrespective of the type of mixture and fatiguing crack widths, the decreasing rate in LTE$_B$ was larger between 0 to 500,000 load cycles when compared to the decreasing rate of LTE$_B$ that was observed after the application of the first 500,000 load cycles.

Among all the six beams in Figure 5.27, P-1, 0.049-0.050, 0.1834 exhibited the lowest LTE$_B$ throughout 1,000,000 load cycle applications. The other PC beam, P-2, 0.049-0.052, 0.1844, performed better with a relatively higher LTE$_B$. As previously mentioned, the crack shape or the macrotexture, for this particular beam was different, which contributed to the engagement of more interlocking action. The two FRC1 beams, F1-1, 0.050-0.051, 0.1597 and F1-2, 0.05, 0.1680 showed a similar performance. Both of them resulted in a higher LTE$_B$ when compared to the PC beams. The performance of the FRC1 beams was similar to that of FRC2 beams. In Figure 5.28, it can be seen that, in general, the PC beams resulted in a lower LTE$_B$ than the FRC beams. The FRC1 beam, F1-3, 0.037-0.043, 0.1614 exhibited a relatively lower LTE$_B$ among the FRC beams. In this beam, the crack width was found to increase by 5 mills during the fatiguing.
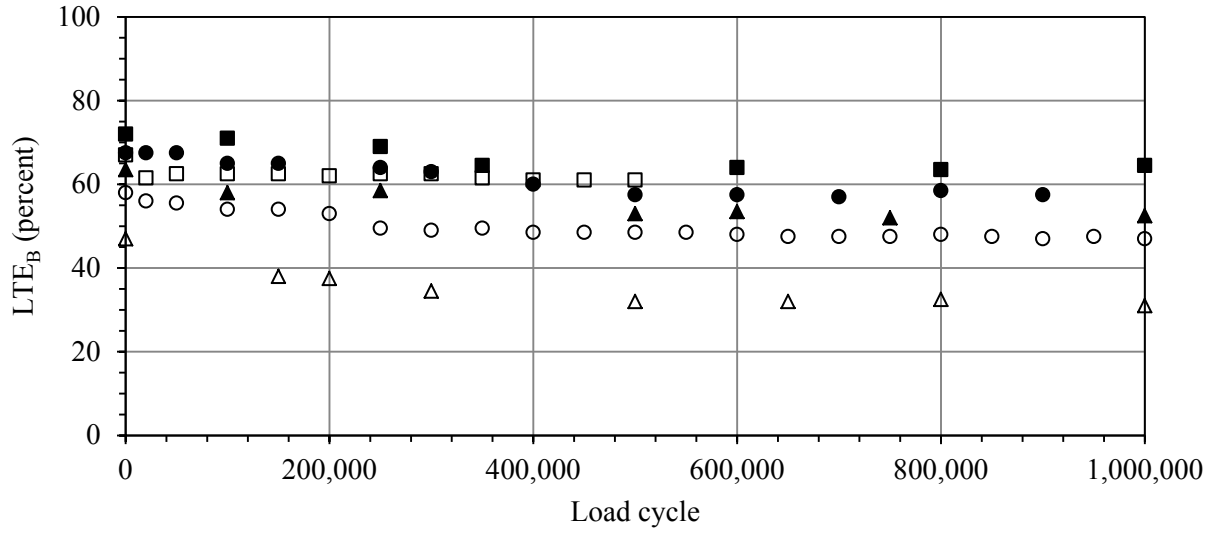
174

Figure 5.27. LTE$_B$ vs load cycle for the beams fatigued at a 0.050-in crack width.
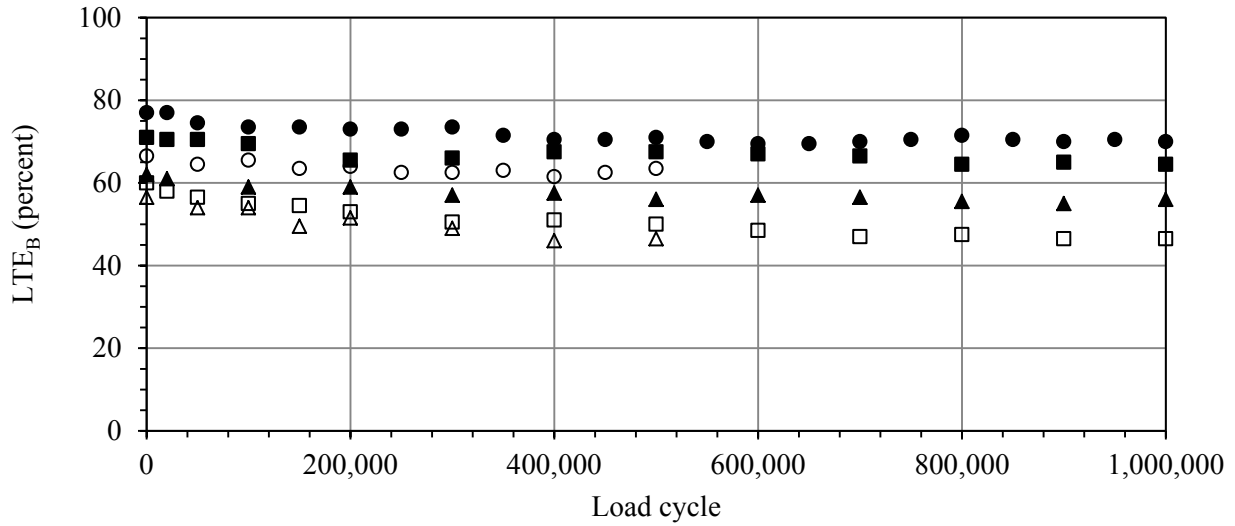
Figure 5.28. LTE$_B$ vs load cycle for the beams fatigued at a 0.035-in crack width.

175

The beam, F2-4, 0.034-0.037, 0.1490 resulted in the largest LTE_B among all the beams. A comparison of the decrease in LTE_B between the different mixture types can be seen in Figure 5.29 and Figure 5.30. The first figure presents the decrease in LTE_B after 0.5 million load cycle applications and the second figure presents the LTE_B after 1 million load cycle applications. It appears that the PC beams exhibited a higher decrease in the LTE_B both at the end of 0.5 and 1 million load cycle applications. At the end of 0.5 million load cycles, the average decrease in LTE_B for the PC beams fatigued at 0.050 and 0.035-in crack widths were 13 and 8 percent, respectively, whereas these were 6.5 and 7 percent for the FRC1 beams, and 9.5 and 4 percent for the FRC2 beams. In Figure 5.30, after 1 million load applications, it can be seen that LTE_B did not drop significantly from that observed after 0.5 million load cycles. This reiterates the fact that the LTE_B does not decrease significantly after 0.5 million load cycles if the crack width is held constant. To verify this fact, one FRC2 beam was fatigued by 10 million load cycles. The fatiguing crack width was maintained at 0.035 in. Figure 5.31 shows the LTE_B vs load cycles for that beam. It is interesting to note that LTE_B decreased only by 6 percent even after 10 million load cycles. This indicates that the fibers will not fail in fatigue throughout the expected life of the overlay and this is also clearly seen in Figure 5.32. This figure shows pictures of the fibers that were fatigued with 10 million load cycles. Between 0.3 to 1 million load cycles, a 4 percent drop was noticed. It may be noted that the results of this beam were not included in any additional analyses due to the late date at which it was tested.
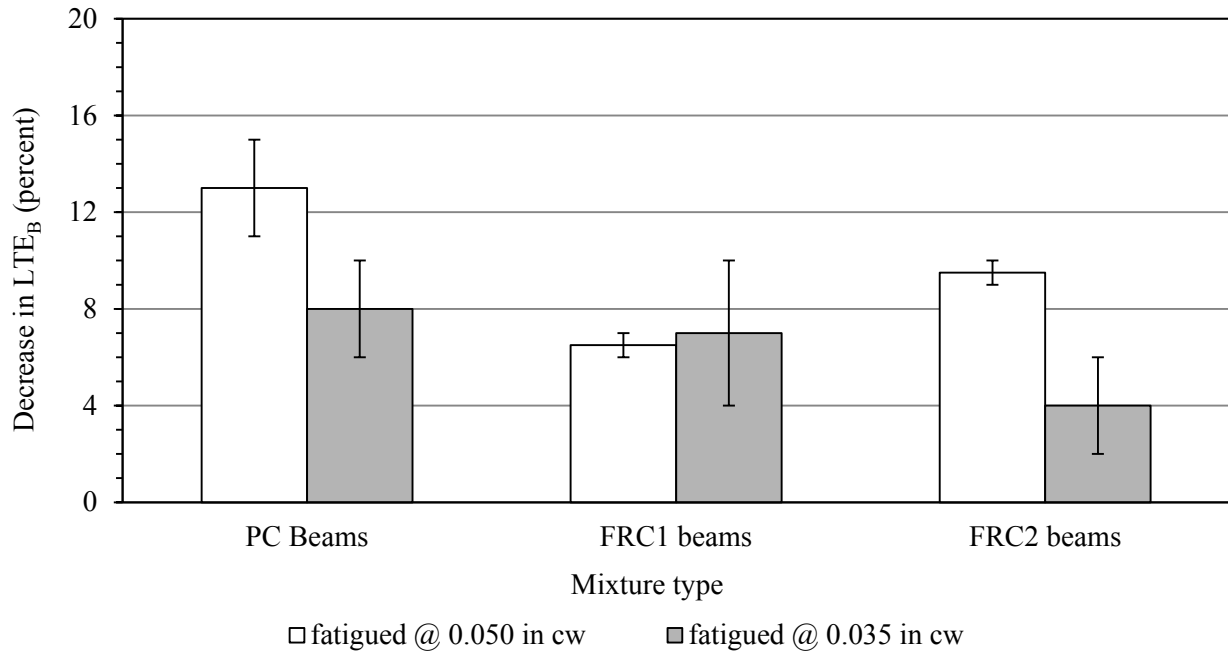
Figure 5.29. Comparison in the decreases in LTE$_B$ values between the mixture types after 0.5 million load cycles.
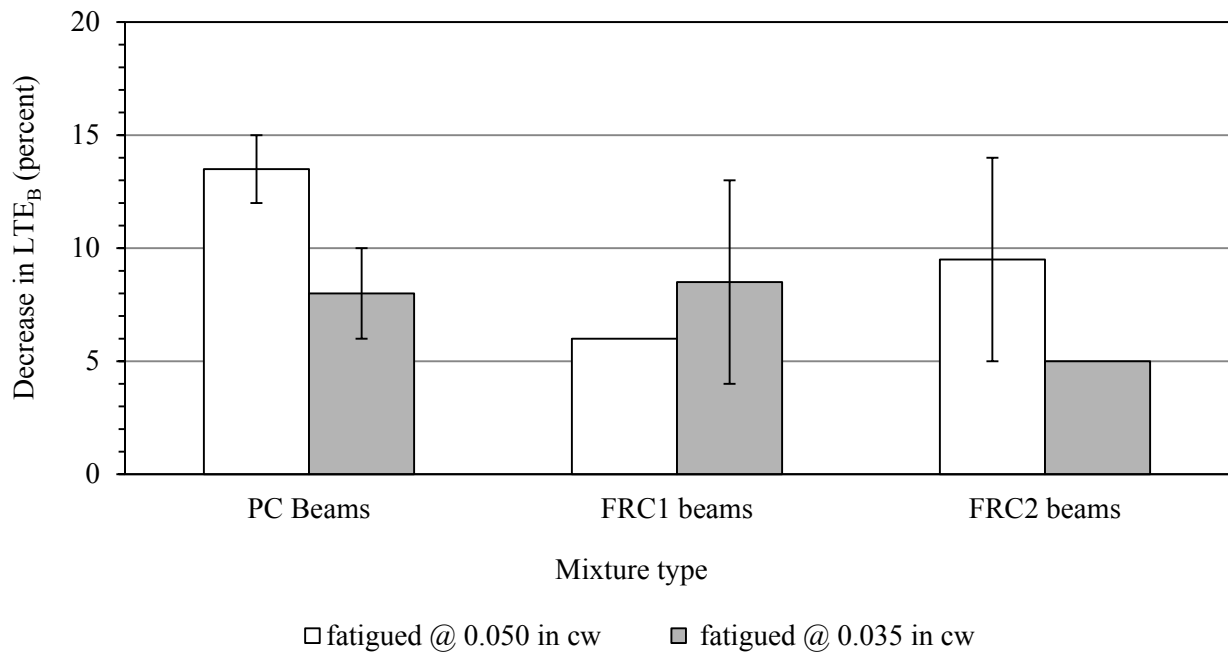
Figure 5.30. Comparison in the decreases in LTE$_B$ values between the mixture types after 1 million load cycles.

177
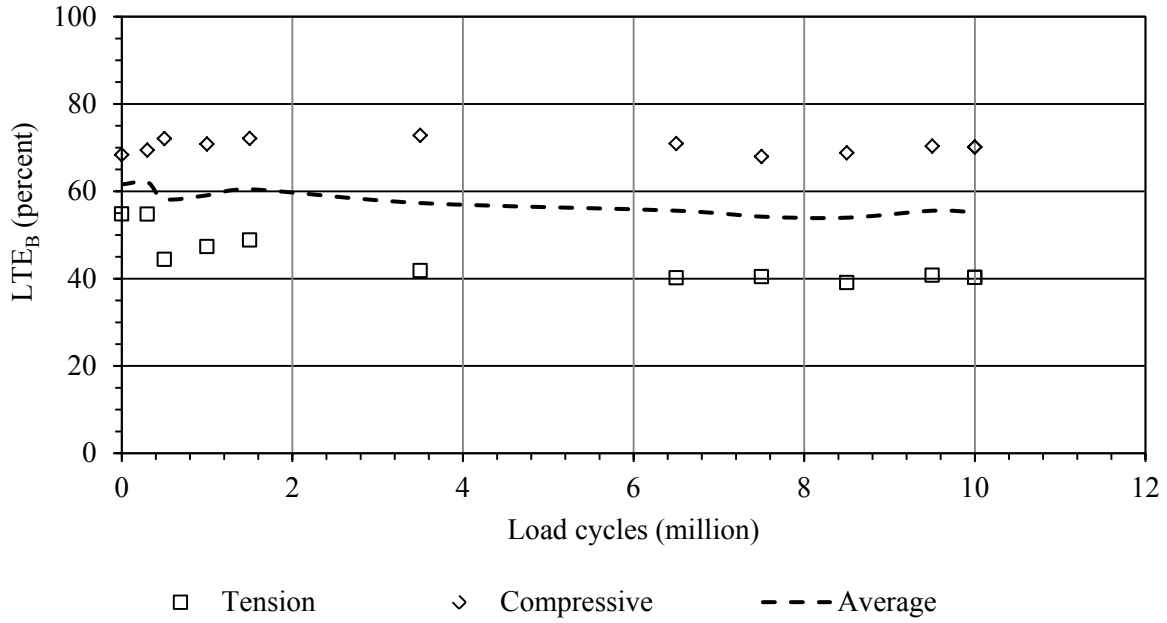
Figure 5.31. LTE_B vs load cycle for a beam fatigued at 0.035-in crack width for 10 million load cycles.

Figure 5.32. Pictures of F2 fiber (Enduro 600) after fatiguing with 10 million load cycles.

The comparison in the LTE_B vs crack width relationships between the mixture types is presented in Figure 5.33. Figure 5.33 contains the data for all the beams tested. This comparison is drawn on the basis of the measured LTE_B regardless to the fatiguing effect. It may be reminded that the LTE_B values were measured at a crack width below the fatiguing crack width represent the LTE_B without any fatiguing effect, and LTE_B measured beyond the fatiguing crack width represent the LTE_B with the fatiguing effect. The LTE_B test results obtained for the different mixtures are presented in this figure. For the purpose of comparisons, logarithmic trend lines have been drawn for each mixture. It can be seen that the FRC2 mixture provided the best performance, whereas, the PC mixture provided the worst performance. The difference in the LTE_B values among the mixtures is low when the crack width was very narrow (below 0.025 in). At approximately 0.100 in cracks width, the PC and FRC1 specimens exhibited 28 and 14 percent lower LTE_B values, respectively, than the FRC2 specimens.
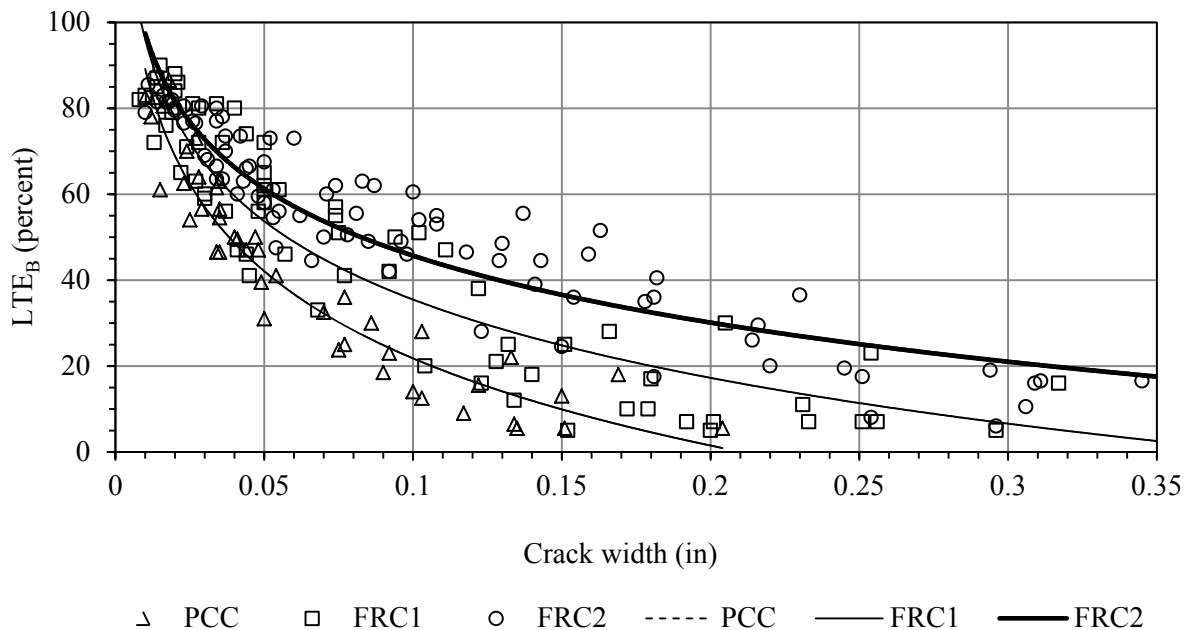
Figure 5.33. LTE_B vs crack width for different concrete mixtures.

5.3.1.5 Regression model for LTE$_B$

Regression models were developed for correlating the LTE$_B$ with the crack width. Separate regression models were developed for each mixture. As it was previously mentioned that the LTE$_B$ measurements were taken both before and after fatiguing, necessary adjustment was required to be made to the measured LTE$_B$ to convert them into a LTE$_B$ without the fatigue effect (referred to as non-fatigued LTE$_B$). This adjustment will help in developing the LTE$_B$ vs crack width relationship for the joint without a fatiguing effect. This condition simulates the joint of a newly constructed whitetopping overlay. More importantly, this adjustment will be very helpful in deriving the correlation between the LTE$_B$ and LTE$_S$ (LTE from S$_{ALT}$ procedure). A meaningful correlation between the LTE$_B$ and LTEs can be derived by avoiding the fatiguing effect in both the LTE$_B$ and LTE$_S$. However, it is recognized that this approach assumes that the effect of the loss in surface texture due to abrasion alone during fatiguing on LTE$_B$ does not vary with crack width. Although this is most likely not true, this approach does provide an approximation in the LTE$_B$ with changing crack width.

To determine non-fatigued LTE$_B$, the measured LTE$_B$ at all crack widths wider than the fatiguing crack width were raised by adding the corresponding drop in LTE$_B$ due to fatiguing. As was previously discussed, in some of the beams, crack width increased during the fatiguing, a necessary adjustment was made to exclude the drop in LTE$_B$ due to crack width increase alone during the fatiguing. In order to determine the drop in LTE$_B$ due to the crack width increase that occurred during fatiguing, the relationship between LTE$_B$ vs crack width before the fatiguing was examined. Based on the observed trends, the LTE$_B$ drop due to the crack width increase alone during fatiguing was determined. The fatigue adjustments for some of the beams which exhibited a considerable increase in crack width (> 4 mils) are presented in Appendix B. Table

5.10 presents the drop in LTE_B due to (i) fatiguing and crack width increase during fatiguing together (ii) due to crack width increase alone during fatiguing, and (iii) due to fatiguing alone. The third one was used to adjust the original LTE_B to determine the non-fatigued LTE_B.

A review of previous research was performed to identify relationship previously defined between the LTE_B and crack width. Vandenbossche, 1999, Ramirez, 2010 and Vandenbossche, et al., 2013 correlated LTE_B or AGG^* with crack width through logarithmic relationships. In this study, LTE_B was correlated with the crack width through logarithmic and as well as bi-linear fits. In both forms of the models, a stepwise progressive procedure was adopted to obtain the best fit. The coefficient of determination (R^2) and standard error (SE) were used as indicators for identifying the best fit. Initially a certain number of data point were considered. Then, in a stepwise progressive procedure, numbers of data points were progressively increased in order to achieve the best fit. Also, the bilinear split was obtained through this stepwise progressive procedure in the case of the bilinear regression models.

Table 5.10. LTE$_B$ drop during fatiguing and magnitude of increase in LTE$_B$ to adjust for fatiguing.

Concrete Mixture	Specimen label	LTE$_B$ drop due to fatiguing and crack width increase together (percent)	LTE$_B$ drop due to crack width increase alone (percent)	Magnitude of increase in LTE$_B$ to adjust for fatiguing (percent)
PC	P-1, 0.049-0.050, 0.1834	15	2	13
	P-2, 0.049-0.052, 0.1844	13	2.5	10.5
	P-3, 0.035, 0.1211	10	None	10
	P-4, 0.035, 0.2078	6	None	6
FRC1	F1-1, 0.050-0.051, 0.1597	4	1	3
	F1-2, 0.05, 0.1680	7	None	7
	F1-3, 0.037-0.043, 0.1614	10	3	7
	F1-4, 0.036-0.039, 0.1500	2.5	1	1.5
FRC2	F2-1, 0.048-0.053, 0.1771	12	3	9
	F2-2, 0.05-0.054, 0.1417	11	3	8
	F2-3, 0.034-0.035, 0.2027	3	0.5	2.5
	F2-4, 0.034-0.037, 0.1490	6	1.5	4.5

PC Beams

Logarithmic fit

Figure 5.34 and Figure 5.35 show the relationships developed for original and non-fatigued LTE$_B$, respectively. Here the measured LTE$_B$ is referred to as the "original" LTE$_B$. . Equations (5.1) and (5.2) present the developed regression models for original and non-fatigued LTE$_B$, respectively. In both the models, LTE$_B$ up to 0.151 in crack width were considered, and the regressions were performed through the stepwise progressive procedure. For the model with

original and non-fatigued LTE_B, the R^2 are 0.92 and 0.89, respectively, while the SE are 6.90 and 7.20, respectively.
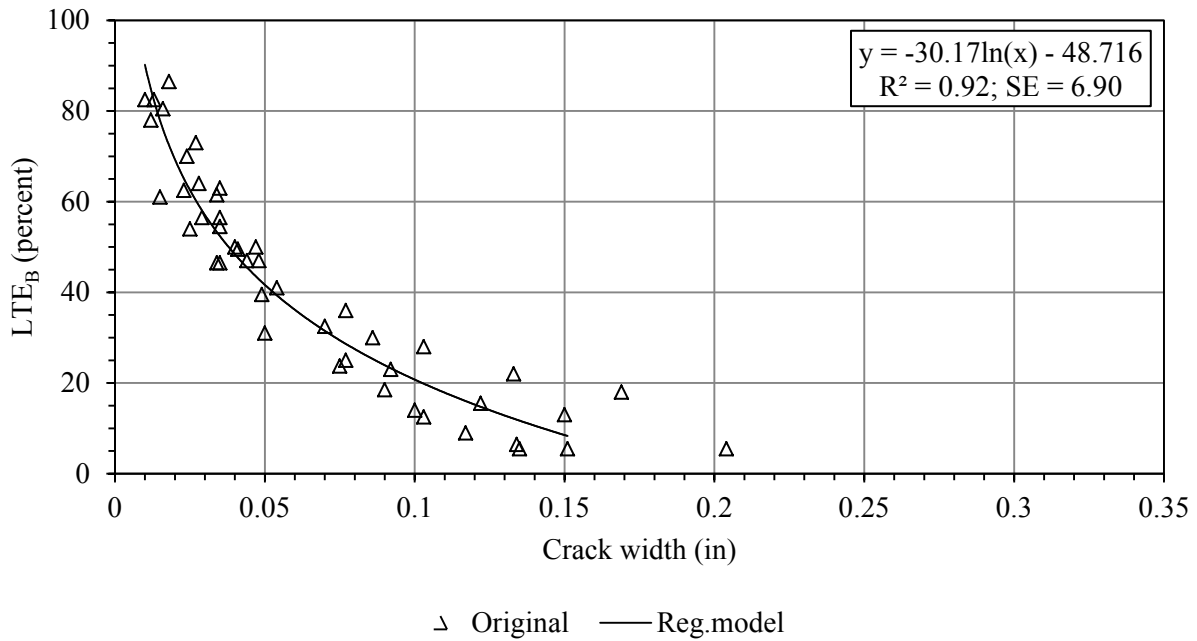
Figure 5.34. Relationship for original LTE_B for the PC beams, logarithmic fit.
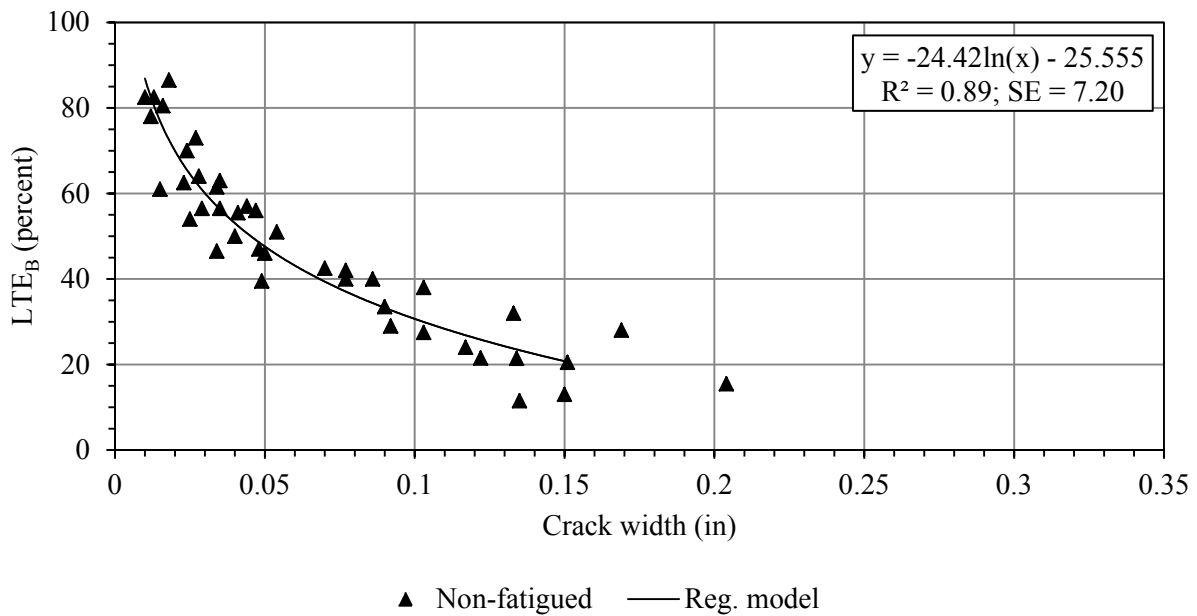
Figure 5.35. Relationship for non-fatigued LTE_B for the PC beams, logarithmic fit.

Original

$$LTE_B = -30.17 \ln (cw) - 48.716 \qquad (5.1)$$

Non-fatigued

$$LTE_B = -24.42 \ln (cw) - 25.555 \qquad (5.2)$$

Where LTE_B is the load transfer efficiency from B_{ALT} procedure in percentage and *cw* is the crack width in in.

Bi-linear fit

The bi-linear regressions developed for original and non-fatigued LTE_B are presented in Figure 5.36 and Figure 5.37, respectively. Based on the stepwise progressive regression procedure, the bi-linear splits were obtained at 0.068- and 0.06-in crack widths for the model with the original and non-fatigued LTE_B, respectively. Regression models are presented in Equations (5.3) through (5.6). For the model with original LTE_B, the R^2 for the first and second segments are 0.82 and 0.68, respectively, while the SE are 7.10 and 6.24, respectively. For the model with non-fatigued LTE_B, the R^2 for the first and second segments are 0.69 and 0.63, respectively, while the SE are 7.66 and 7.61, respectively.
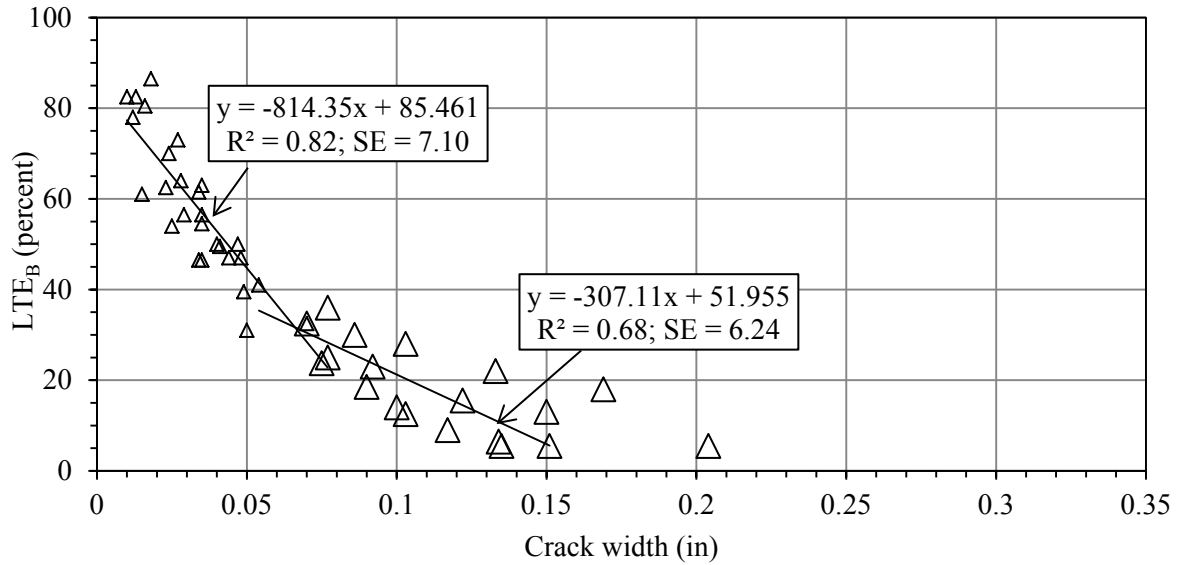
Figure 5.36. Relationship for original LTE_B for the PC beams, bi-linear fit.
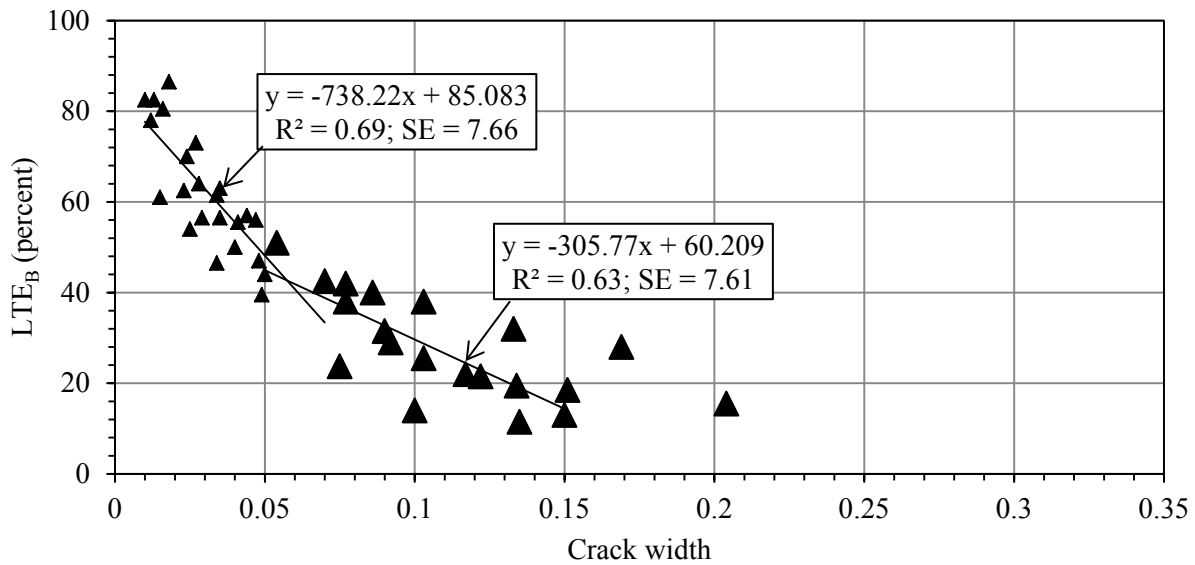
Figure 5.37. Relationship for non-fatigued LTE_B for the PC beams, bi-linear fit.

Original

$$\text{cw up to 0.068 in: } LTE_B = -814.35\ (cw) + 85.461 \qquad (5.3)$$

$$\text{cw beyond 0.068 in: } LTE_B = -307.11(cw) + 51.955 \qquad (5.4)$$

185

Non-fatigued

$$cw \text{ up to } 0.06 \text{ in: } LTE_B = -738.22 \ (cw) + 85.083 \tag{5.5}$$

$$cw \text{ beyond } 0.06 \text{ in: } LTE_B = -305.77 \ (cw) + 60.209 \tag{5.6}$$

FRC1 Beams

Logarithmic fit

Figure 5.38 and Figure 5.39 show the relationships developed for original and non-fatigued LTE_B, respectively.   Equations (5.7) to (5.8) present the regression models for original and non-fatigued LTE_B, respectively. In both models, LTE_B data were considered for up to 0.254 in crack width based on the stepwise progressive procedure. For the model with original and non-fatigued LTE_B, the R^2 are 0.89 and 0.86, respectively, while the SE are 9.10 and 9.46, respectively.

Original

$$LTE_B = -27.36 \ ln \ (cw) - 24.717 \tag{5.7}$$

Not fatigued

$$LTE_B = -24.86 \ ln \ (cw) - 16.858 \tag{5.8}$$

186
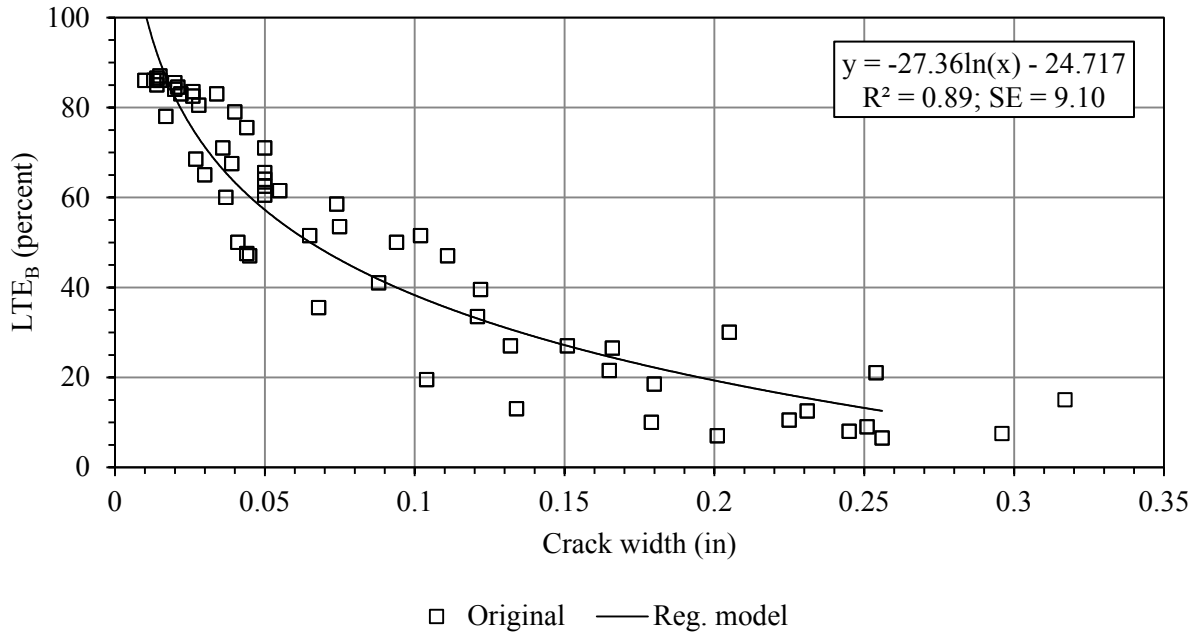
Figure 5.38. Relationship for original LTE$_B$ for the FRC1 beams, logarithmic fit.
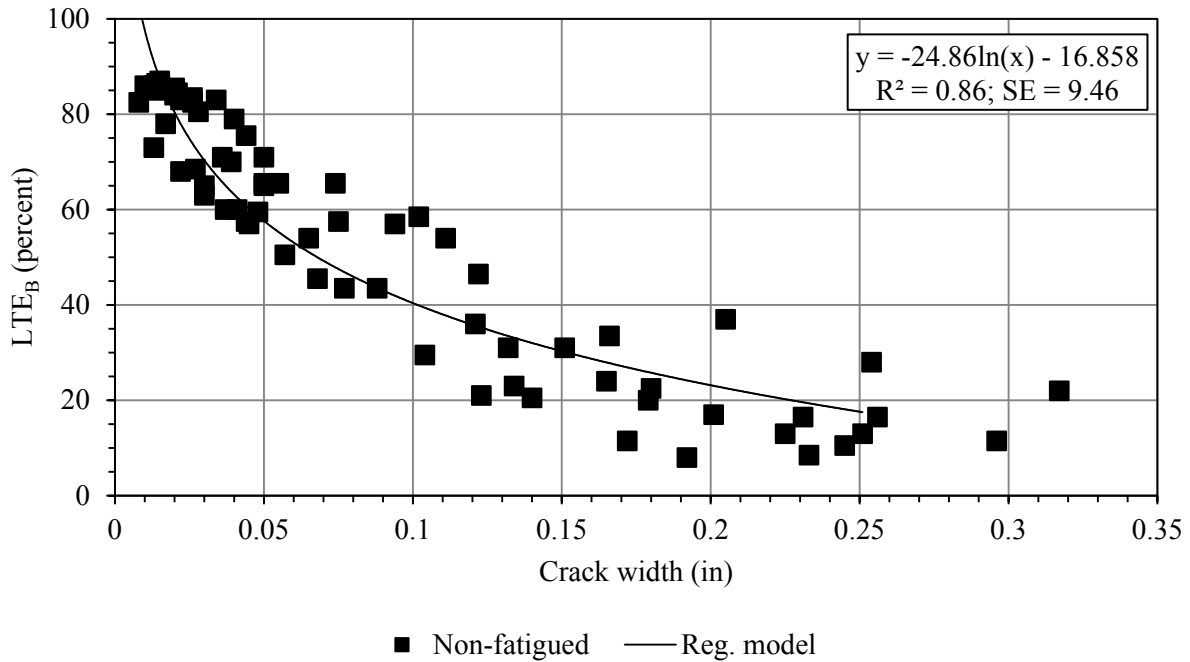
Figure 5.39. Relationship for non-fatigued LTE$_B$ for the FRC1 beams, logarithmic fit.

187

Bi-linear fit

The bi-linear relationships developed for original and non-fatigued LTE_B are presented in Figure 5.40 and Figure 5.41, respectively. Based on the stepwise progressive regression procedure, the bi-linear split was obtained at 0.09-in crack width for the model with the original LTE_B data, whereas, it is 0.102 in for the model with the non-fatigued LTE_B data. Regression models are presented in Equations (5.9) through (5.12). The maximum numbers of data points included was selected based on the stepwise progressive procedure. For the model with original LTE_B, the R^2 for the first and second segments are 0.73 and 0.59, respectively, while the SE are 8.97 and 9.52, respectively. For the model with non-fatigued LTE_B, the R^2 for the first and second segments are 0.65 and 0.53, respectively, while the SE are 7.88 and 9.83, respectively.
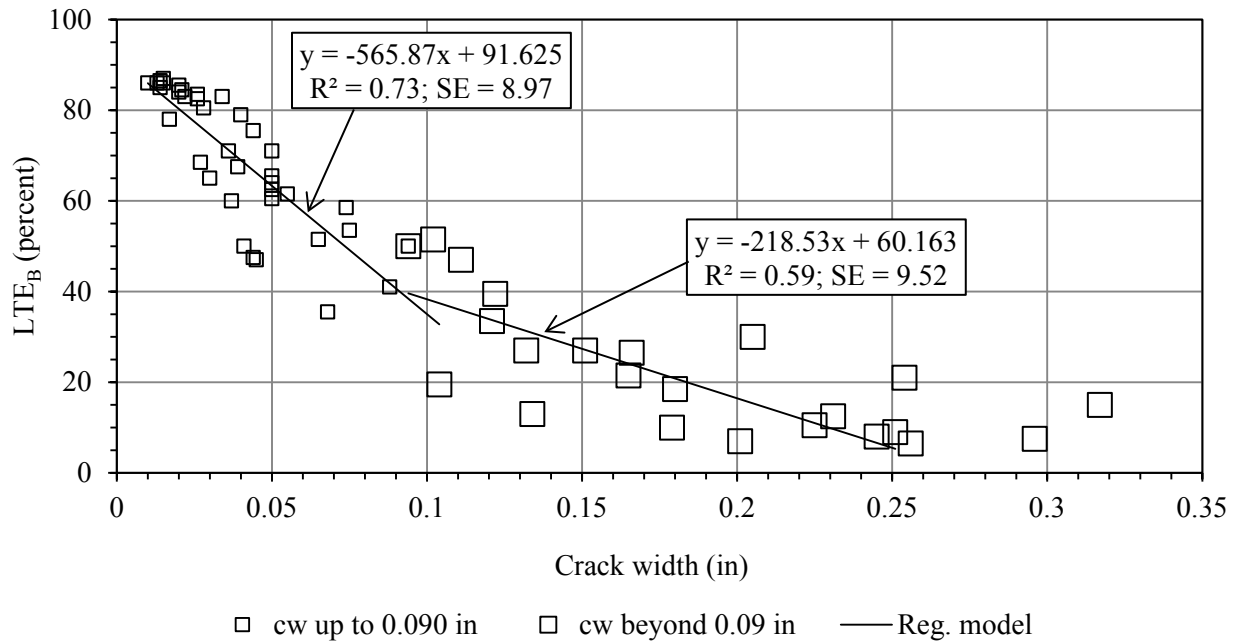
Figure 5.40. Relationship for original LTE_B for the FRC1 beams, bi-linear fit.
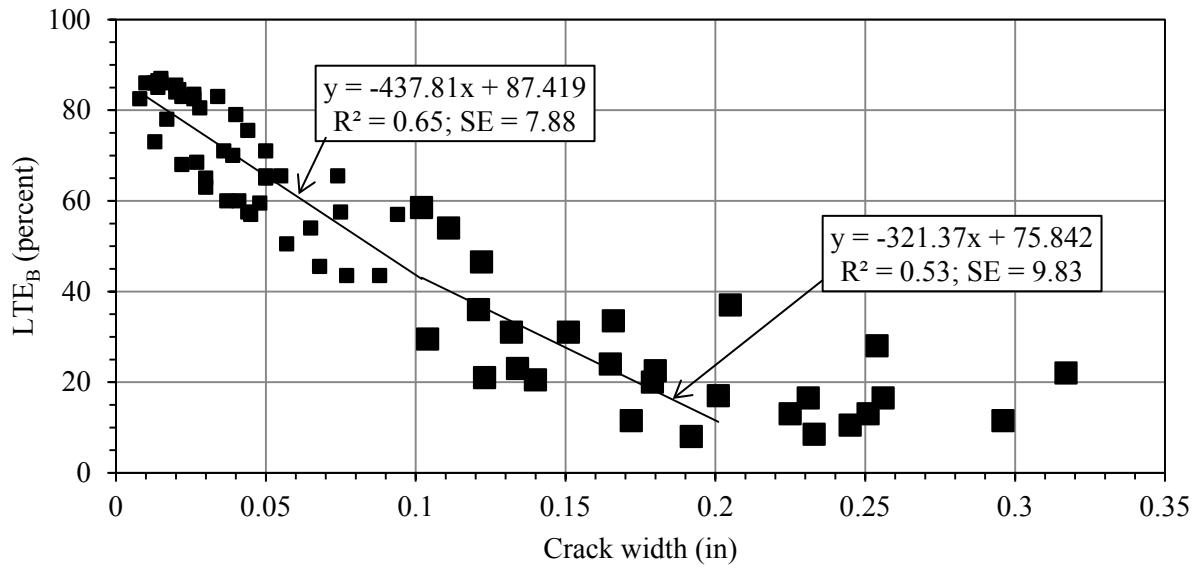
Figure 5.41. Relationship for non-fatigued LTE_B for the FRC1 beams, bi-linear fit.

Original

$$\text{cw up to 0.09 in: } LTE_B = -565.87\ (cw) + 91.625 \qquad (5.9)$$

$$\text{cw beyond 0.09 in: } LTE_B = = -218.53\ (cw) + 60.163 \qquad (5.10)$$

Non-fatigued

$$\text{cw up to 0.102 in: } LTE_B = -437.81\ (cw) + 87.419 \qquad (5.11)$$

$$\text{cw beyond 0.102 in: } LTE_B = -321.37\ (cw) + 75.842 \qquad (5.12)$$

FRC2 Beams

Logarithmic fit

Figure 5.42 and Figure 5.43 show the relationships developed for original and non-fatigued LTE_B, respectively, for FRC2 beams. An approach similar to that for the PC and FRC1 beams was followed in developing both the relationships. Equations (5.13) to (5.14) present the developed regression models for original and non-fatigued LTE_B, respectively. R^2 for the original and non-fatigued LTE_B models are 0.83 and 0.76, while the SE are 8.32 and 9.59, respectively.
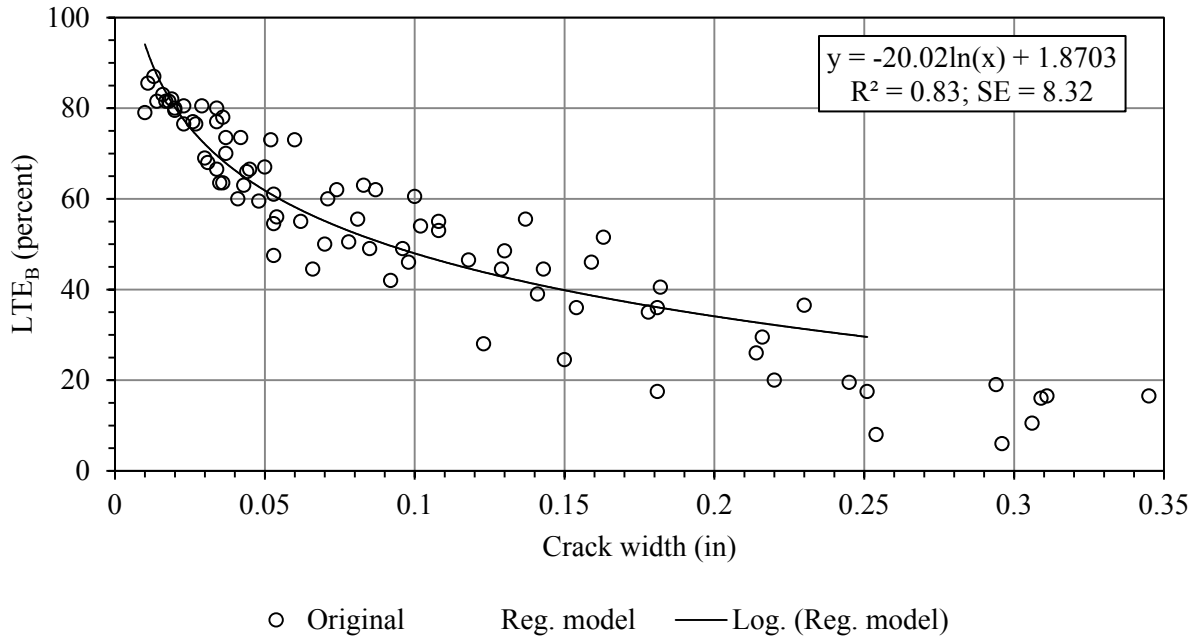
Figure 5.42. Relationship for original LTE$_B$ values for the FRC2 beams, logarithmic fit.

.
.
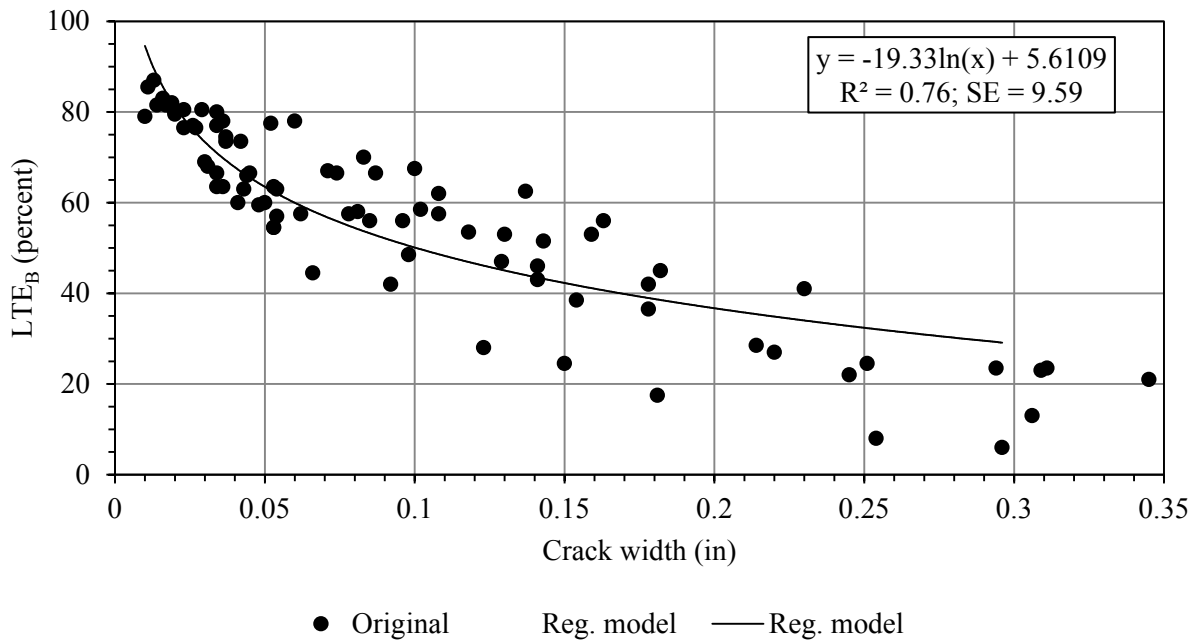
Figure 5.43. Relationship for non-fatigued LTE$_B$ values for the FRC2 beams, logarithmic fit.

191

Original

$$LTE_B = -20.02 \ln (cw) - 1.8703 \tag{5.13}$$

Not fatigued

$$LTE_B = -19.33 \ln (cw) + 5.6109 \tag{5.14}$$

Bi-linear fit

The bi-linear relationships developed for original and non-fatigued LTE_B are presented in Figure 5.44 and Figure 5.45, respectively. Based on the stepwise progressive regression procedure, the bi-linear split was obtained at a 0.054-in crack width for the model with the original LTE_B, whereas, it is 0.05 in for the model with non-fatigued LTE_B. Regression models are presented in Equations (5.15) through (5.18). For the model with original LTE_B, the R^2 for the first and second segments are 0.71 and 0.70, respectively, while the SE are 5.25 and 8.02, respectively. For the model with non-fatigued LTE_B, the R^2 for the first and second segments are 0.69 and 0.67, respectively, while the SE are 5.30 and 9.37, respectively.
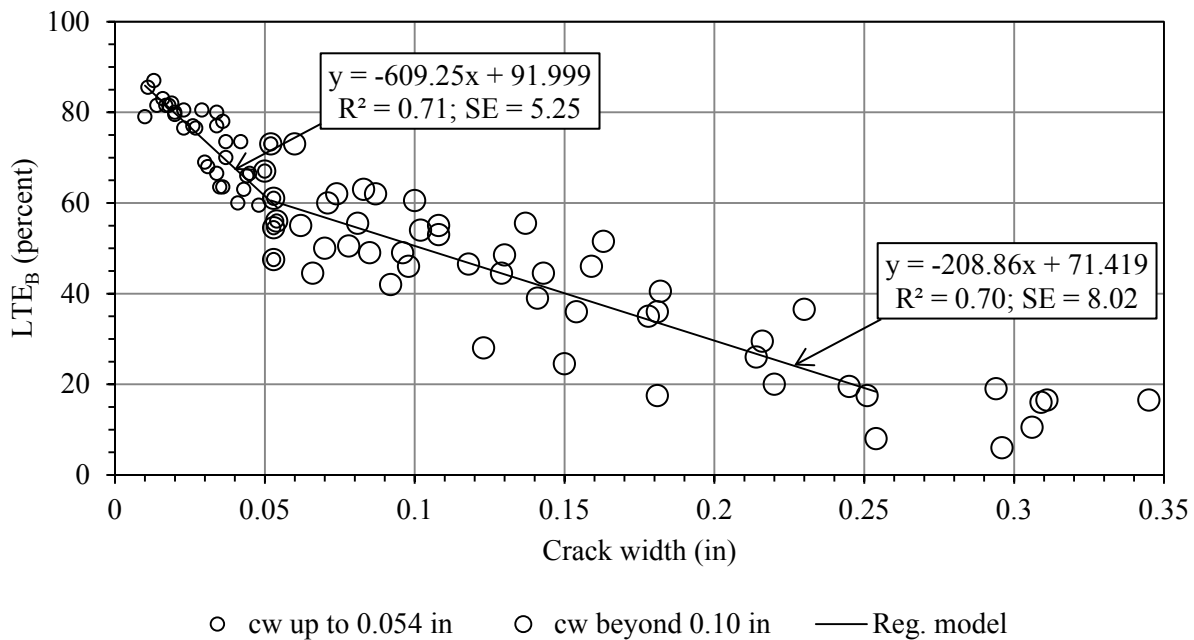
Figure 5.44. Relationship for original LTE_B values for the FRC2 beams, bi-linear fit.

192
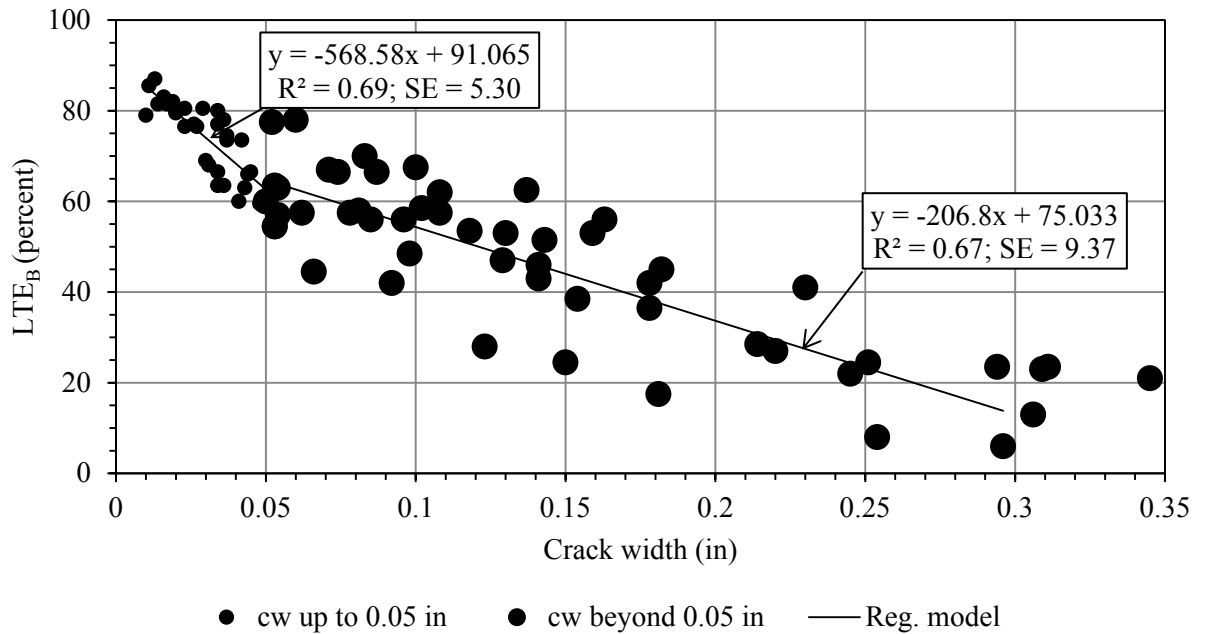
Figure 5.45. Relationship for non-fatigued LTE$_B$ values for the FRC2 beams, bi-linear fit.

Original

$$\text{cw up to 0.054 in: } LTE_B = -609.25(cw) + 91.999 \tag{5.15}$$

$$\text{cw beyond 0.054 in: } LTE_B = -208.86(cw) + 71.419 \tag{5.16}$$

Non-fatigued

$$\text{cw up to 0.050 in: } LTE_B = -568.58(cw) + 91.065 \tag{5.17}$$

$$\text{cw beyond 0.050 in: } LTE_B = -206.8 (cw) + 75.033 \tag{5.18}$$

Finally, a comparison of the SE between the two forms of regression fits reveals that the bi-linear fit provides slightly better prediction with a relatively lower SE. The SE of the first segment of each model was considered for the comparison purpose. Because, the crack width

ranges in the first segment are the ranges which are generally important from the field application point of view.

Comparison of LTE_B values predicted by the regression models between three mixtures

Table 5.11presents a comparison between the non-fatigued LTE_B for the three mixtures predicted by the best fit models (bi-linear models). Different crack widths ranging from 0.020 in to 0.10 in were considered for the comparison. The FRC1 and FRC2 mixtures show higher LTE_B for a given crack width as compared to PC mixture (Table 5.12). In general, the benefit of the fiber increases with the increase in crack width.

Table 5.11. Comparison of non-fatigued LTE_B between the different mixtures.

Crack width (in)	PC	FRC1	FRC2
0.02	71	79	80
0.03	63	74	74
0.04	55	70	68
0.05	47	66	63
0.06	40	61	63
0.07	39	57	61
0.08	36	52	58
0.09	33	48	56
0.10	30	44	54

Table 5.12. Percent increase in non-fatigued LTE_B for FRC mixtures as compared to PC mixture.

Crack width (in)	FRC1	FRC2
0.02	11	13
0.03	18	18
0.04	27	24
0.05	38	32
0.06	54	58
0.07	46	56
0.08	47	64
0.09	47	73
0.10	47	83

5.3.2 Joint Performance through S_{ALT}

5.3.2.1 PC mixture

Similar to the B_{ALT} procedure, load and deflection profiles at the initial crack width, the beginning of fatiguing and the end of fatiguing are presented in Figure 5.46 through Figure 5.48, respectively, for the PC slab. The PC slab was fatigued with 1 million load cycles at a 0.035-in crack width. From the PC beam test results, it was observed that the LTE_S (LTE in S_{ALT} procedure) at a 0.050-in crack width was very low and is less frequently encountered in the field, such as for the MnROAD whitetopping sections, as previously described. Therefore, the slab was fatigued at a 0.035-in crack width.

195

The initial crack width was quite narrow, approximately 0.01 in, as seen in Figure 5.49. The deflection profiles in all three figures (Figure 5.46, Figure 5.47 and Figure 5.48) show that the approach side exhibited a relatively lower deflection. The differential deflection was also low on the approach side. Although the exact reason is not known, it appears like the crack shape could have played a role. Figure 5.50 shows a photo of the crack profile on the side of the slab where the load was applied. This photo shows that the crack was slanted towards the leave slab. Therefore, when the approach slab was loaded, the effective area contributing to aggregate interlocking was more than when the leave slab was loaded.
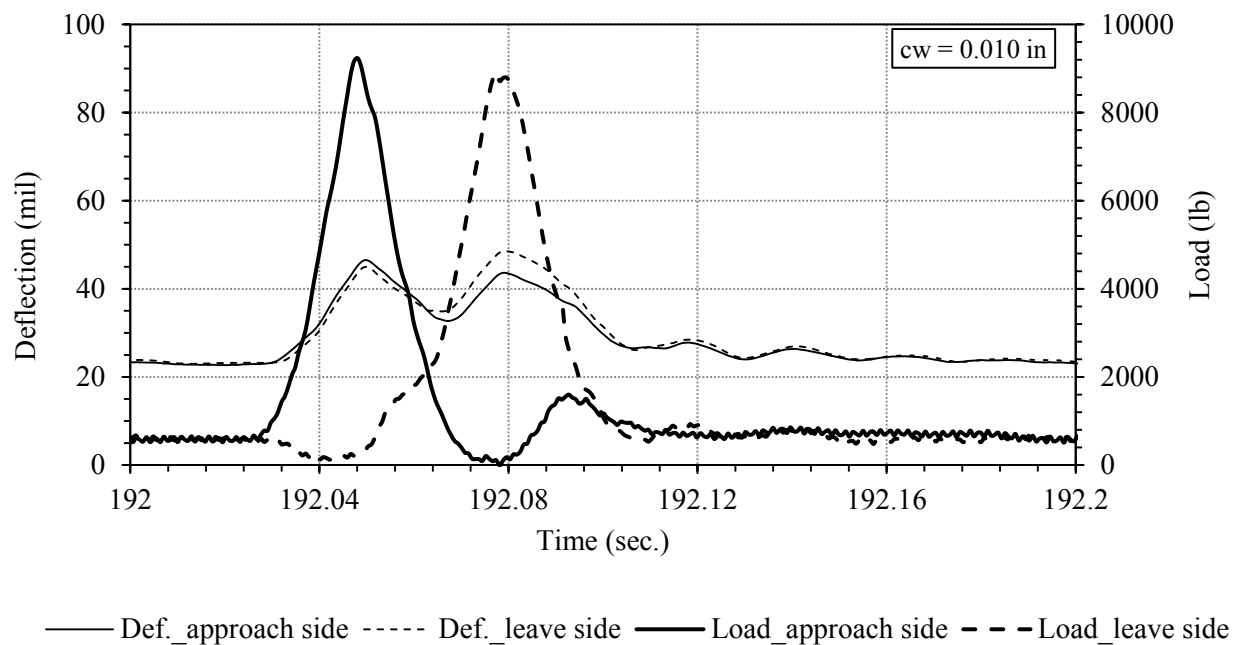
Figure 5.46. Load and deflection profiles at the initial crack width for the PC slab.
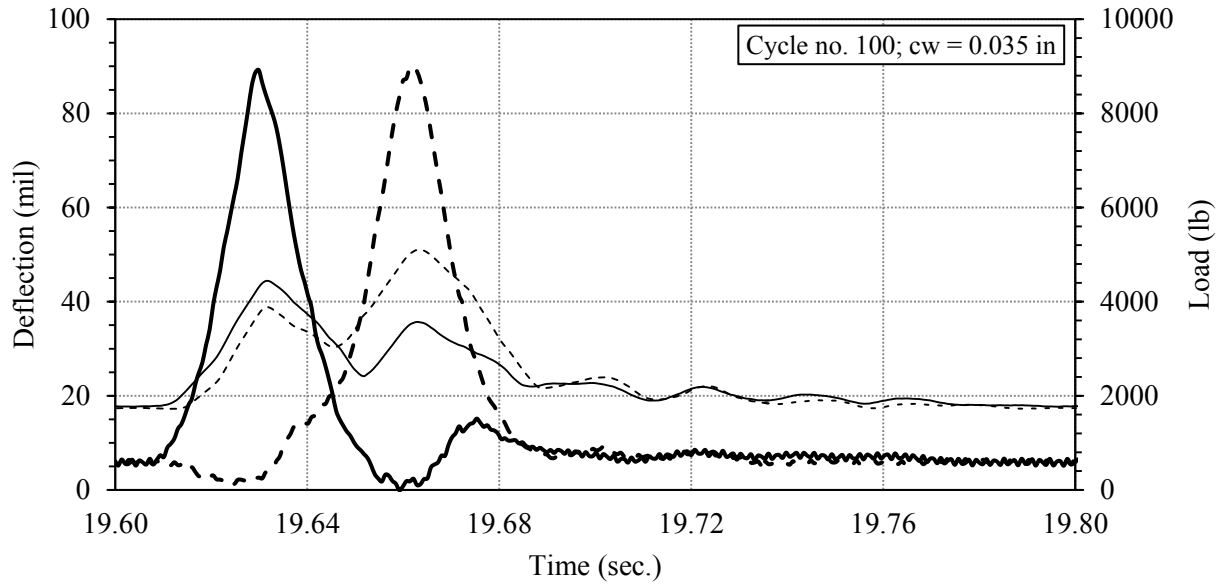
Figure 5.47. Load and deflection profiles at the beginning of fatiguing for the PC slab.
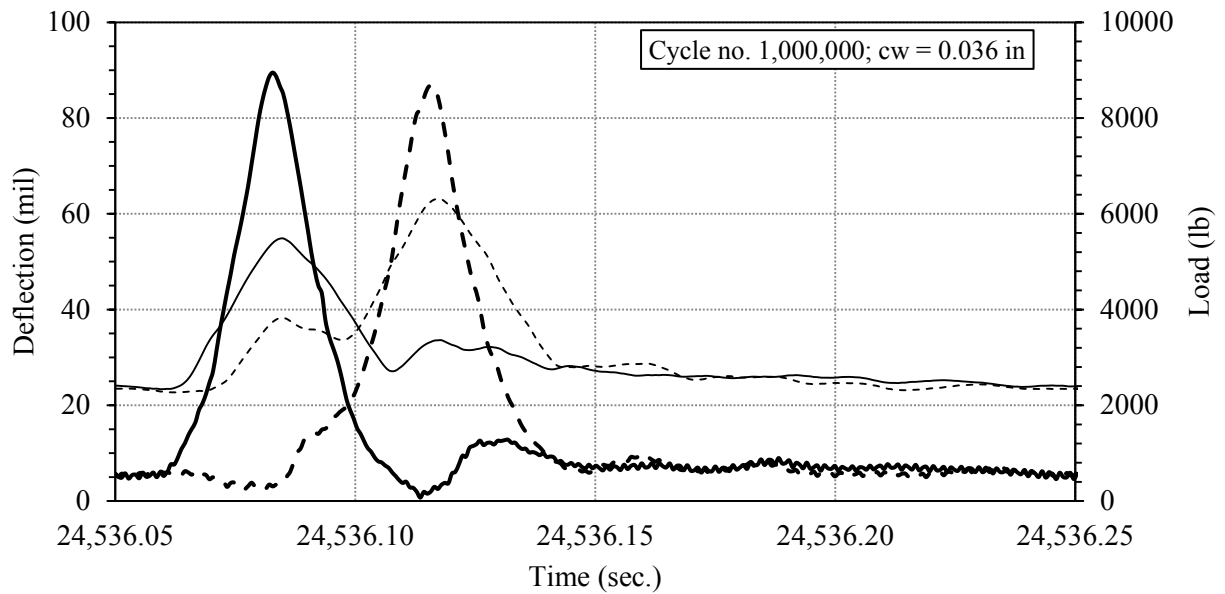
Figure 5.48. Load and deflection profiles at the end of fatiguing for the PC slab.

197
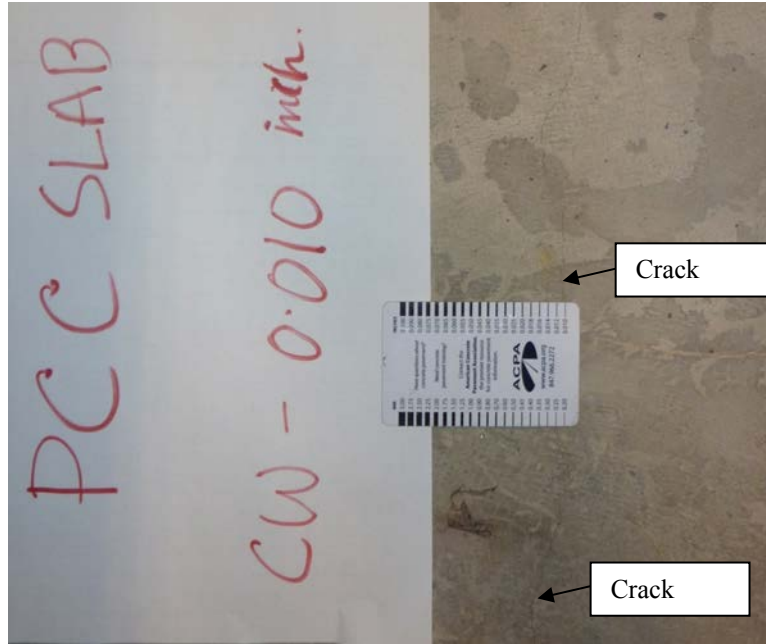
Figure 5.49. Initial crack width before the start of fatiguing, top view.

Figure 5.50. Crack profile near the loading location for the PC slab, side view.

A comparison of the three load and deflection profiles (Figure 5.46, Figure 5.47 and Figure 5.48) indicates that the joint performance decreased with increasing in crack width and number of load applications, as expected. Figure 5.51 presents the approach, leave and average

LTE_S after the application of 1 million load cycles. This figure shows that the approach LTE_S decreased from 80 to 47 percent (33 percent drop) and the leave LTE_S decreased from 55 to 26 percent (27 percent drop) after 1 million load cycles. Upon closer examination, it appears that most of the drop in LTE_S occurred between 175,000 to 800,000 load cycles. The fatiguing of the joint was quite noticeable and also spalling was observed after approximately 500,000 load cycles. Figure 5.52 and Figure 5.53 show the crack before and after the occurrence of spalling. The difference between the approach and leave LTE_S values remained consistent throughout the application of the 1 million load cycles.

Figure 5.54 shows the LTE_S vs crack width trend. It can be seen that LTE_S constantly decreased with the increase in crack width, before fatiguing. Then there is a large drop due to fatiguing. This was followed by a very low rate of decrease in LTE_S. The minimum average LTE_S obtained for this slab was 7 percent, whereas the lowest LTE_B for the beams was around 3 to 10 percent.
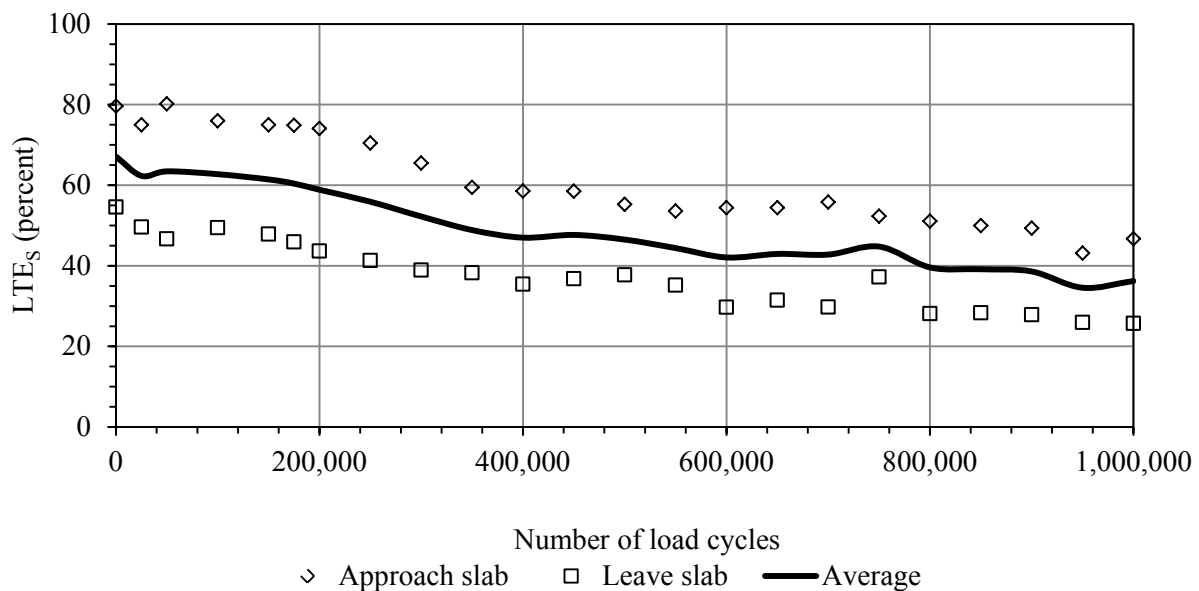
Figure 5.51. LTE_S vs load cycles for the PC slab.

199

Figure 5.52. Picture of the crack before fatiguing.

Figure 5.53. Picture of the crack after 600,000 load cycles.
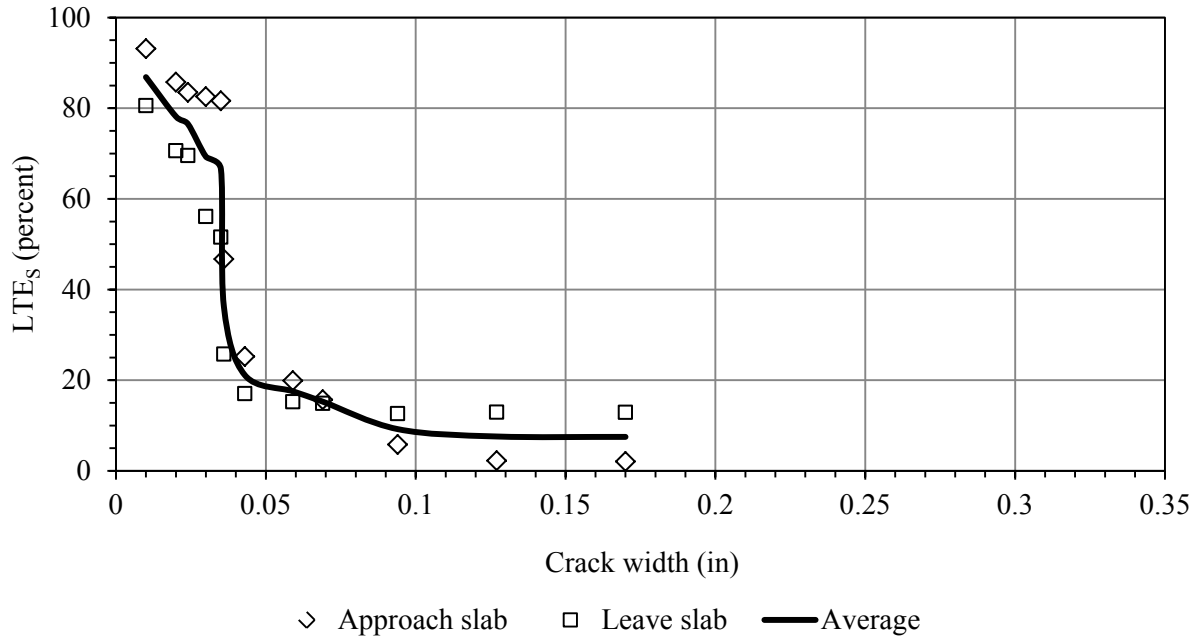
Figure 5.54. LTE$_S$ vs crack width for the PC slab.

5.3.2.2 FRC1 mixture

Load and deflection profiles for the FRC1 slab at the initial crack width, the beginning of fatiguing and the end of fatiguing are presented in Figure 5.55, Figure 5.56 and Figure 5.57, respectively. The FRC1 slab was fatigued with 0.5 million load cycles. The initial crack width was approximately 0.015 in, which can be seen in Figure 5.58. Fatiguing was started at a 0.035-in crack width. The fatiguing crack width was established with the intension that both the PC and FRC1 slab would be fatigued at a similar crack width so that a comparison between the joint performance results could be drawn. Similar to the FRC1 beams, a horizontal tensile force (along the length of the slabs) was applied to obtain the desired fatiguing crack width. The tension force was maintained during the fatiguing so that the crack would not close. During the fatiguing, the crack width kept increasing due to plastic deformation of the fibers. It was thought that manually adjusting the tension level in the middle of the test would invite unwanted error in

201

the crack width, so no adjustment was made in the middle of the fatiguing, which resulted in an increase in crack width from 0.037 in at the beginning of the fatiguing to 0.049 in at the end of the fatiguing.

The deflection profiles in all three figures (Figure 5.55, Figure 5.56 and Figure 5.57) show that the approach and leave sides exhibit quite similar deflection profiles, with marginally higher on the approach side. In the case of the PC slab, deflection of the leave side was higher than that observed on the approach slab. In the FRC1 slab, the fiber bridging phenomenon could have played a role in more similar slab joint performances between the leave and approach sides.

A comparison between the three load and deflections profiles (Figure 5.55, Figure 5.56 and Figure 5.57) indicates that the joint performance decreased with increase in crack width and number of load cycles. Figure 5.59 presents the approach, leave and average LTE_S over the 0.5 million load cycles. This figure shows that the approach LTE_S decreased from 89 to 71 percent (18 percent drop) and the leave LTE_S dropped from 83 to 65 percent (18 percent drop) at the end 400,000 load cycles and remained constant thereafter. It can be assumed that the LTE_S dropped more because of the increase in the crack width rather than due to the fatiguing. A similar incident was also noticed in case of the third FRC1 beam, F1-3, 0.037-0.043, 0.1614, discussed earlier. The fatiguing of the joint was not clearly noticeable, and also no spalling was observed. Figure 5.60 and Figure 5.61 shows pictures of the crack before and after the fatiguing. The difference between the approach and leave LTE_S values remained constant throughout the 500,000 load cycles.

202

—— Def._approach side ----- Def._leave side —— Load_approach side – – –Load_leave side
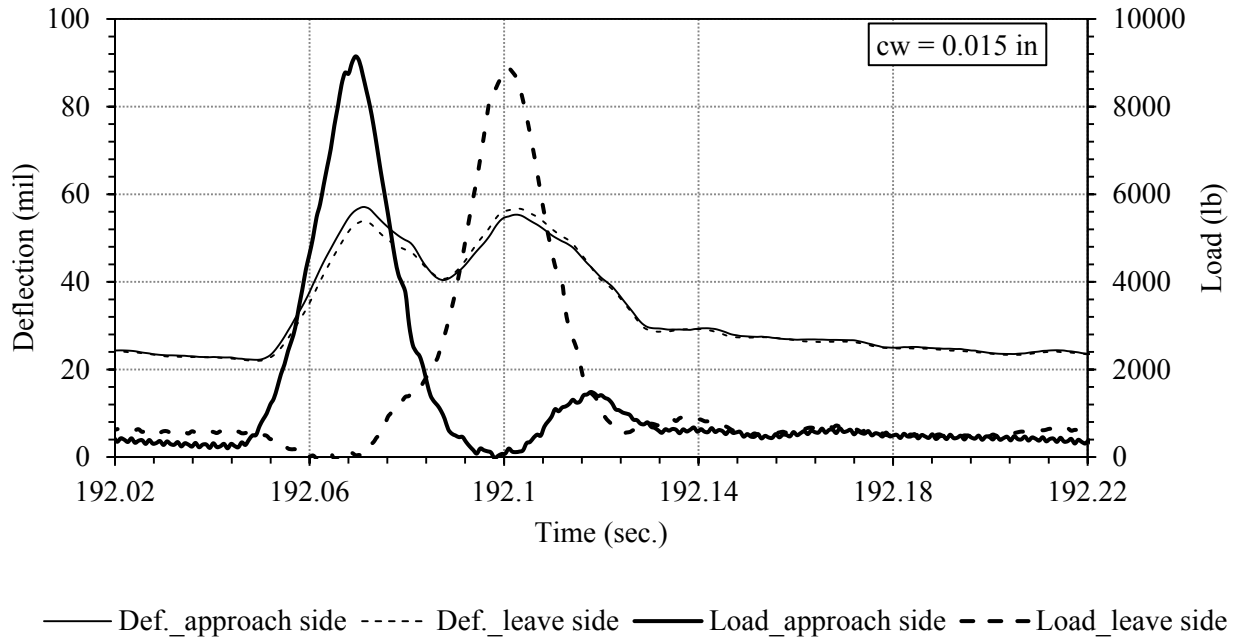
Figure 5.55. Load and deflection profiles at the initial crack width for the FRC1 slab.

—— Def._approach side ----- Def._leave side —— Load_approach side – – –Load_leave side
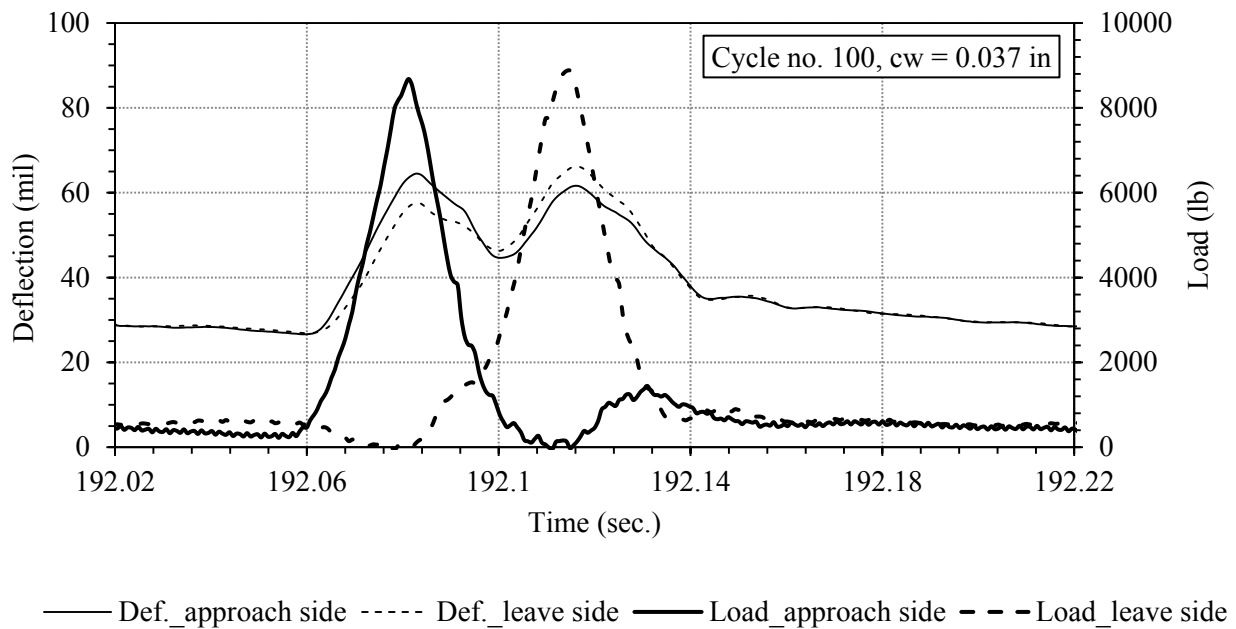
Figure 5.56. Load and deflection profiles at the beginning of the FRC1 slab.
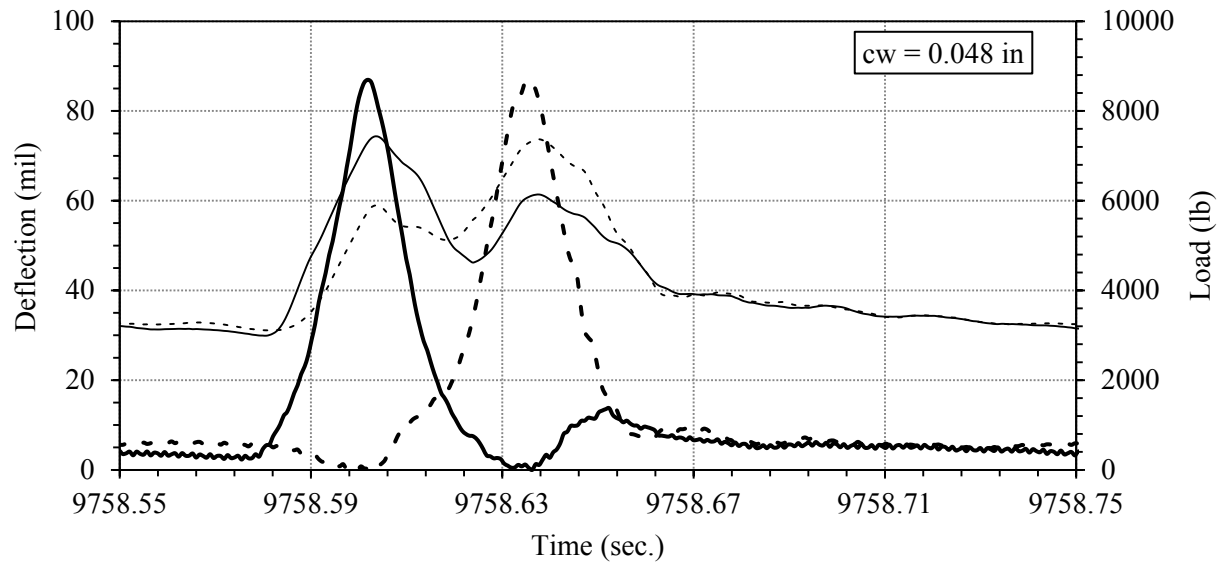
Figure 5.57. Load and deflection profiles at the end of fatiguing for the FRC1 slab.
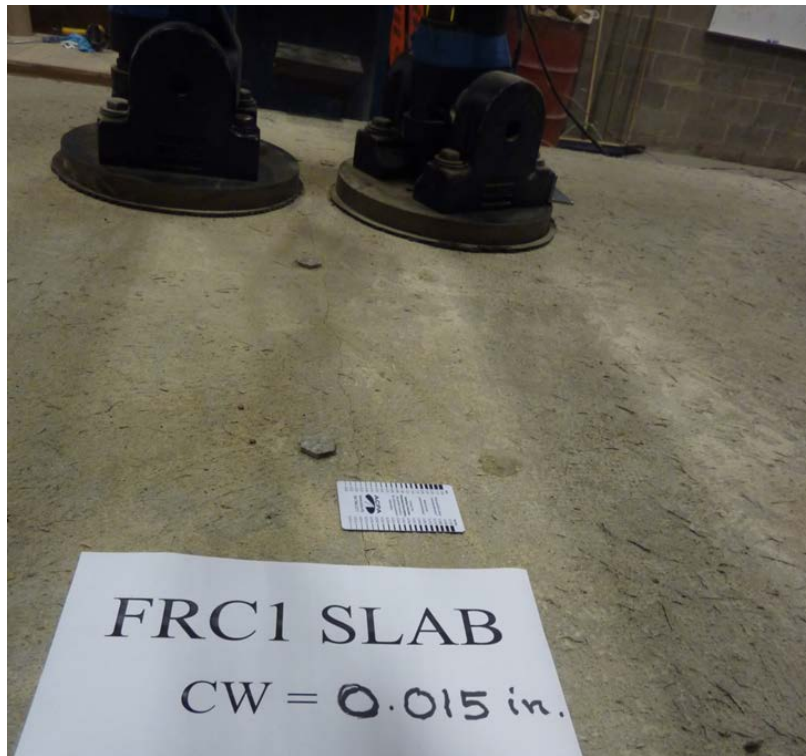
Figure 5.58. Initial crack for the FRC1 slab.
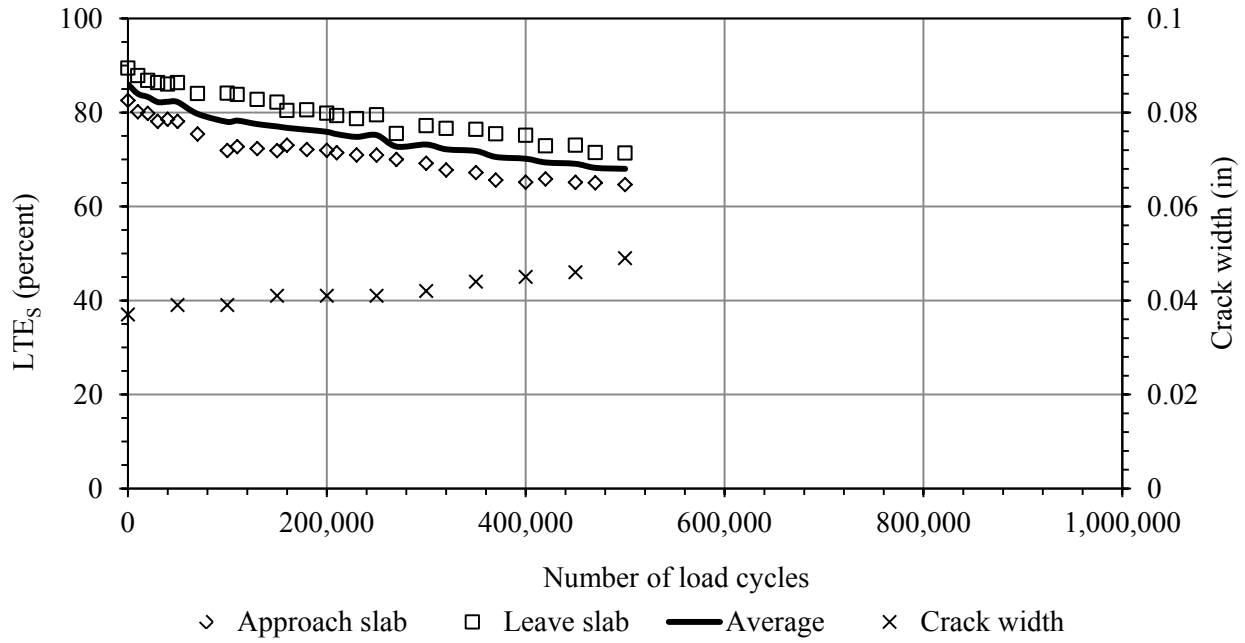
Figure 5.59. LTE$_S$ vs load cycles for the FRC1 slab.
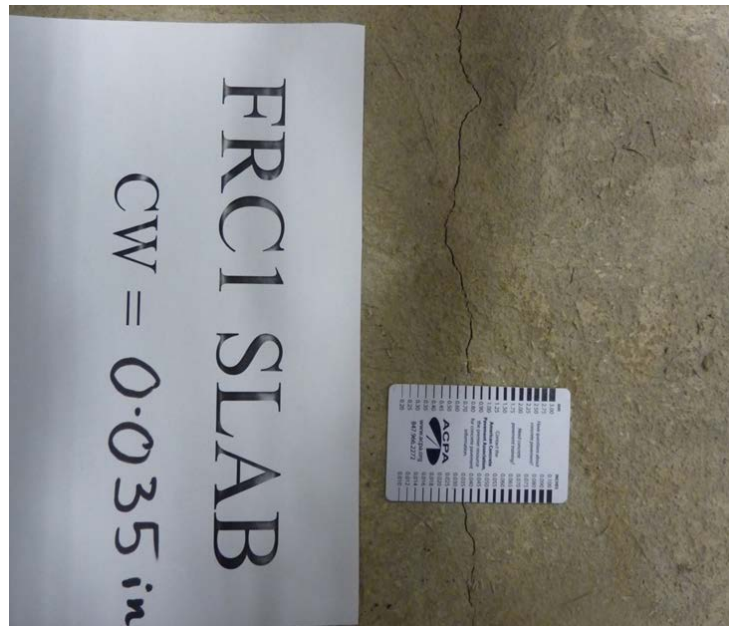
Figure 5.60. Crack before the beginning of fatiguing for FRC1 slab, top view.

Figure 5.61. Crack after fatiguing for FRC1 slab, top view.

Figure 5.62 shows the LTE$_S$ vs crack width trend. The LTE$_S$ constantly decreased with the increase in crack width, before fatiguing. When the crack was opened at the end of the fatiguing, the LTE$_S$ decreased following a similar slope that was observed before the fatiguing. This might be indicating that the joint does not fatigue with the accumulation of load cycles when fibers are mixed in the concrete mix. It was also observed in the B$_{ALT}$ procedure; even 1 million load cycles, did not significantly fatigue the joint. The integrity of the fibers at the joint can be seen in Figure 5.63. At a 0.250-in crack width, aggregate interlock is no longer effective so the load is being transferred purely through the foundation.

The minimum average LTE$_S$ that was obtained for this slab was approximately 8 percent, whereas the lowest LTE$_S$ for the beams was approximately 3 to10 percent.

206
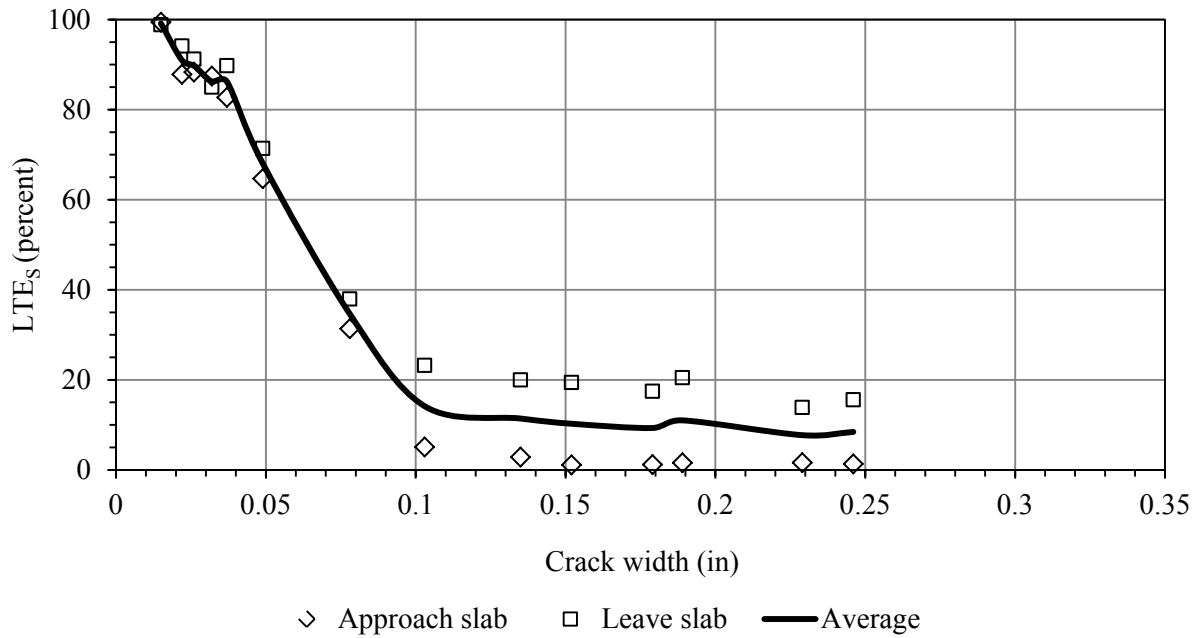
Figure 5.62. LTE$_S$ vs crack width for FRC1 slab.
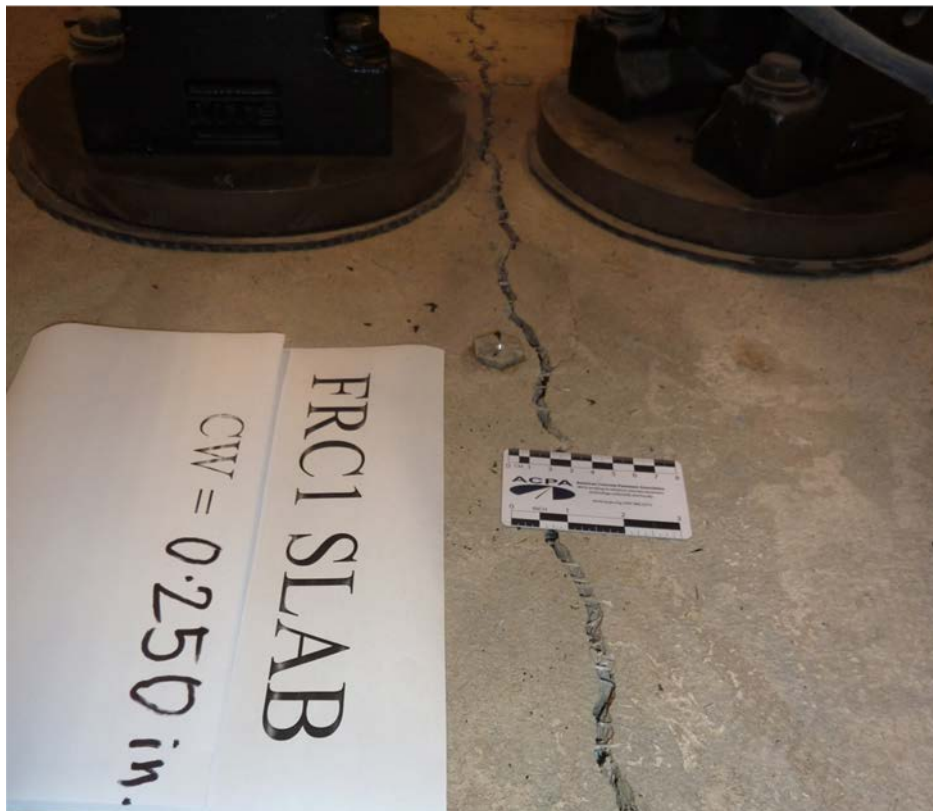
Figure 5.63. Fibers bridging the crack even at 0.250-in crack width, top view.

5.3.2.3 FRC2 mixture

Fatiguing of the FRC2 slab was started at a 0.048-in crack width. As in the case of the FRC1 slab, difficulties were faced in maintaining the crack width at 0.035 in, the FRC2 slab was fatigued at a higher crack width. Also, for the B_{ALT} specimens, when the FRC beams were fatigued at a 0.035-in crack width, no significant difference was observed between the LTE_S values before and after fatiguing. On the other hand, some amount of decrease in the LTE_S values was observed when the beams were fatigued at a 0.050-in crack width. Therefore, the FRC2 slab was fatigued at a 0.050-in crack width so that the fatiguing behavior at a wider crack width could be captured.

During the fatiguing of this slab, the crack width was closely monitored constantly throughout the loading so the loading could be stopped if a slight increase in the crack width was observed. When the crack width was found to be increasing beyond 0.5 mils, the horizontal tension was slightly released to restrict further increases in the crack width. This was performed several times. However, in spite of all efforts the crack width measured at the end of fatiguing was 3 mils higher than the crack width at which fatiguing was initiated.

Figure 5.64 through Figure 5.66 present the load and deflection profiles for the FRC2 slab at the initial crack width, the beginning of fatiguing and the end of fatiguing, respectively. The initial crack width was very tight, approximately 0.010 in, which can be seen in Figure 5.67. The deflection profiles in all three figures (Figure 5.64, Figure 5.65 and Figure 5.66) show that the leave slab exhibited a relatively higher overall and differential deflections when compared to the approach slab. The crack profile on the longitudinal side near the loading location can be seen in Figure 5.68. It appears that the aggregate areas that effectively contributed in interlocking was similar for both the approach and leave side slabs. But, the crack shape

208

throughout the length of the joint might not have been similar. The exact reason for the higher deflection on the leave side cannot be explained.

As expected, the joint performance decreased with increase in crack width and number of load cycles. Figure 5.69 shows that the approach LTE_S dropped from 77 to 70 percent (7 percent drop) and the leave LTE_S dropped from 62 to 52 percent (10 percent drop) at the end of 700,000 load cycles and remained constant thereafter. The behavior of the slab and beams with the FRC2 mixture were quite similar; the fatiguing of the joint after 1 million load cycles did not cause a significant decrease in the LTE_S.
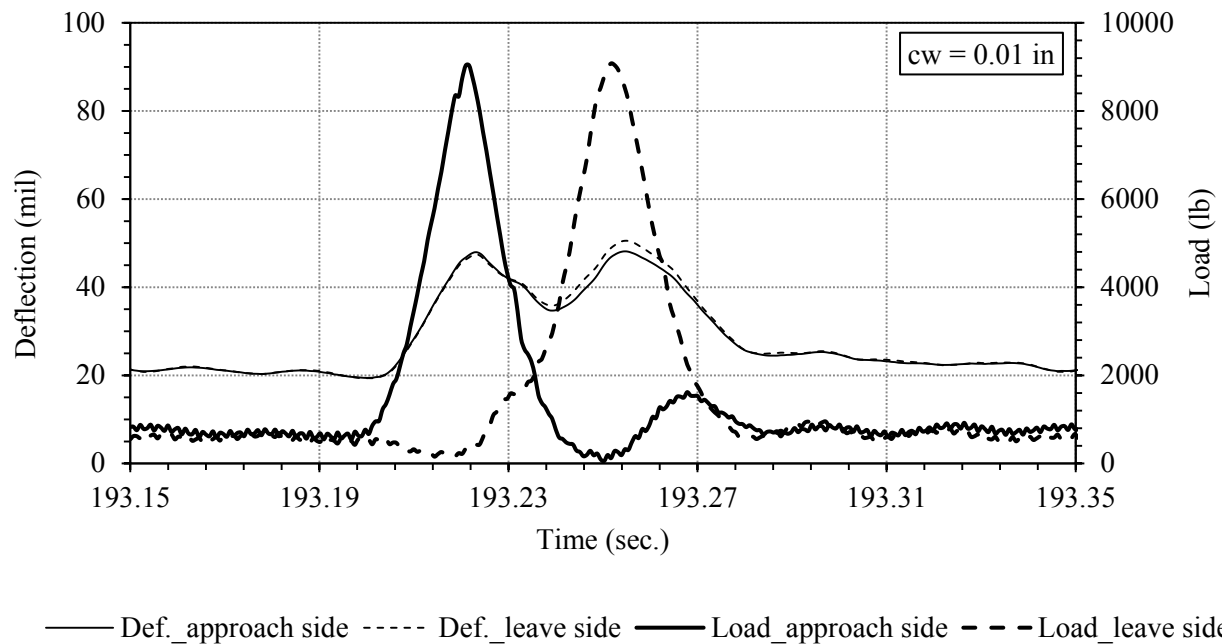
Figure 5.64. Load and deflection profiles at the initial crack width for the FRC2 slab.
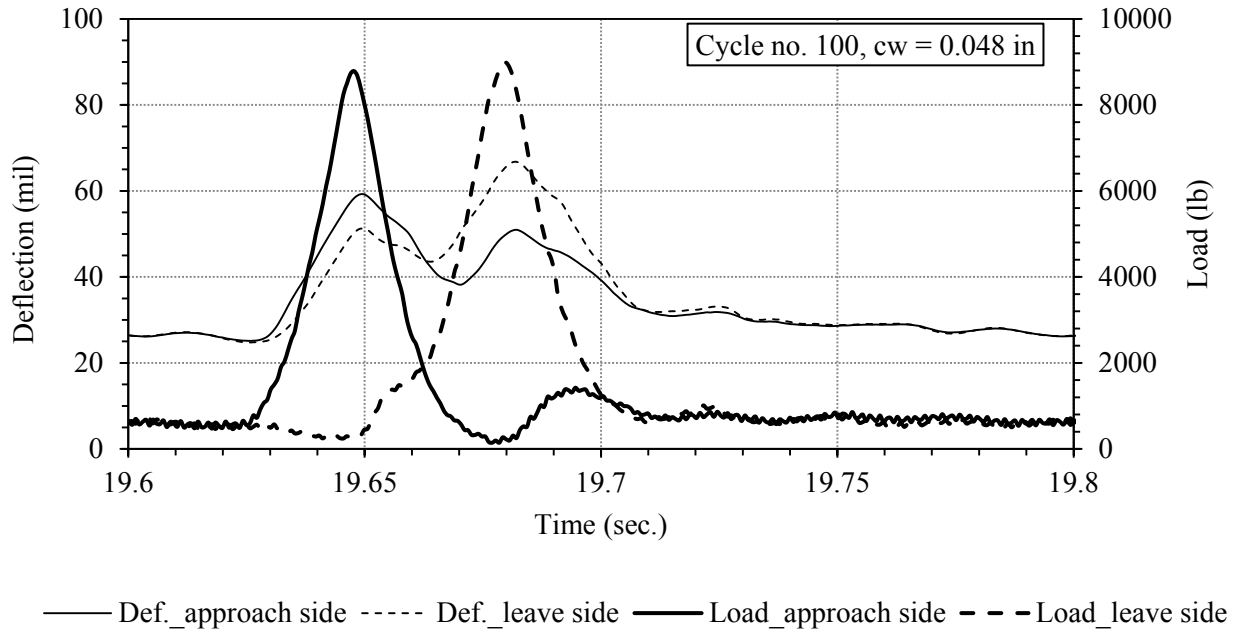
Figure 5.65. Load and deflection profiles at the beginning of fatigue for the FRC2 slab.
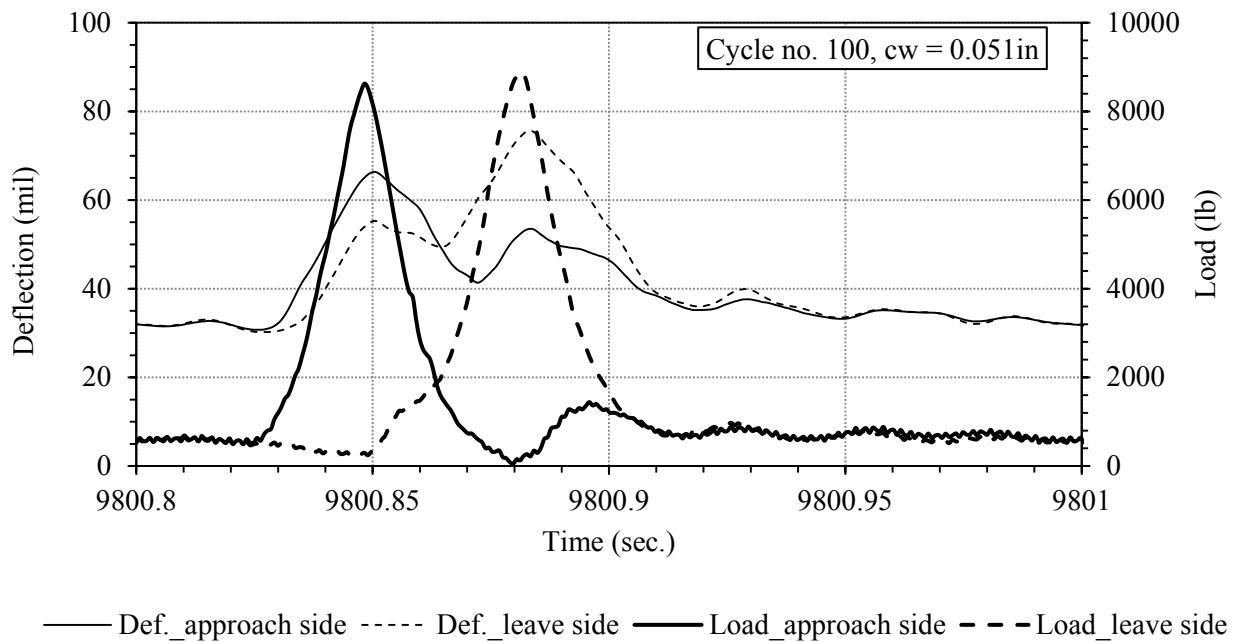
Figure 5.66. Load and deflection profiles at the end of fatigue for the FRC2 slab.

Figure 5.67. Initial crack width of FRC2 slab before the starting of the joint performance test, top view.

Figure 5.68. Crack profile near the loading location for the FRC2 slab, side view.
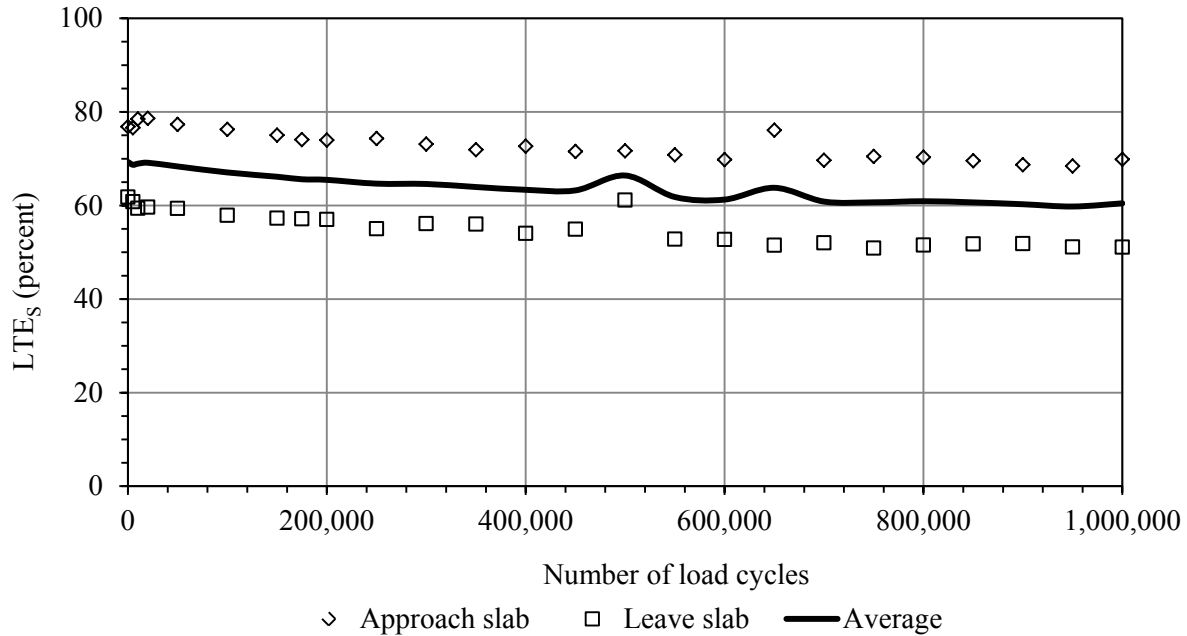
Figure 5.69. LTE$_S$ vs load cycles for the FRC2 slab.

Figure 5.70 shows the LTE$_S$ vs crack width trend for the FRC2 slab. It can be seen that the LTE$_S$ constantly dropped with the increase in crack width. When the crack was opened at the end of fatiguing, the decreasing rate in LTE$_S$ was found to be similar to that observed before fatiguing for up to a crack width of 0.10 in. After a 0.10-in crack width, the decreasing rate in the LTE$_S$ was lower until it reached a minimum at approximately 0.20 in. It can be concluded that the fiber does not fatigue after 1 million load cycles. It was also observed in the B$_{ALT}$ procedure; 1 million or even 10 million load cycles (Figure 5.31) did not significantly fatigue the joint. The minimum average LTE$_S$ for this slab was around 12 percent. Again, the Enduro 600 fiber appears to transfer approximately 10 to 15 percent of the load when the crack width is sufficiently wide that aggregate interlock is no longer effective.

212
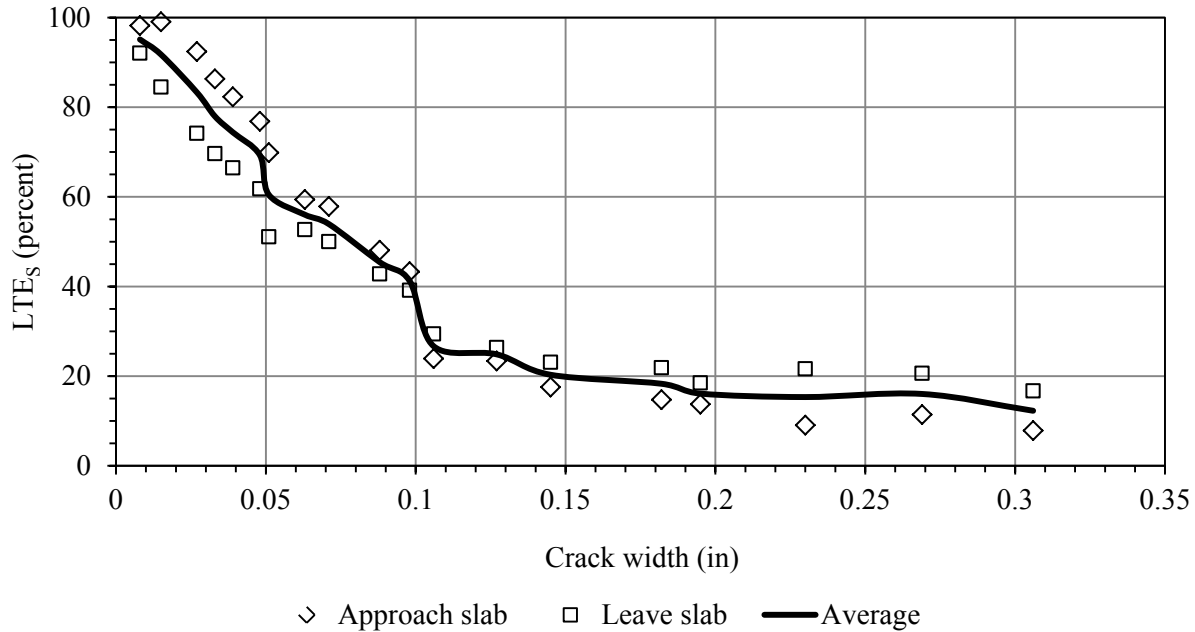
Figure 5.70. LTE$_S$ vs crack width for FRC2 slab.

5.3.2.4 Comparison of LTE$_S$ results between the mixture types

A comparison between the average LTE$_S$ vs load cycle trends observed in the three slabs is presented in Figure 5.71. The total decrease in LTE$_S$ due to fatiguing for the different mixtures are shown in the bar chart diagram in Figure 5.72. The contribution from the fibers is evident. Both the FRC1 slab with the Strux 90/40 fiber and FRC2 slab with the Enduro 600 fiber resulted in higher LTE$_S$ than for the slab without fibers. Even though the PC slab was fatigued at a lower crack width, 0.035 in to 0.036 in, as compared to 0.037 in to 0.049 in for FRC1 and 0.048 to 0.051 in for FRC2, the observed LTE$_S$ for the PC slab were lower. Also, the rate of decrease in the LTE$_S$ was higher for the PC slab. An intersesting observation in Figure 5.71 is that at the end of 0.4 million load cycles, the LTE$_S$ for the FRC1 and FRC2 slabs were similar. Coinsidently, the fatiguing crack widths for both the slabs were quite close, 0.048 and 0.049 in for the FRC1 and FRC2 slabs, respectively. The LTE$_S$ for the FRC2 slab decreased by 7 percent after 0.4

213

million load cycles were applied and thereafter, it remained constant. On the other hand, the LTE$_S$ for the FRC1 slab decreased by 18 percent after same number of load cycles, but the crack width for the FRC1 slab increased from 0.037 to 0.049 in. Therefore, it can be said that the 21 percent decrease in LTE$_S$ for the FRC1 slab, at 0.5 million load cycles, was due to both the increased crack width and fatiguing. Appendix B presents the decrease in LTE$_S$ due to crack witdth increase (8 percent) and fatiguing (10 percent) separately.
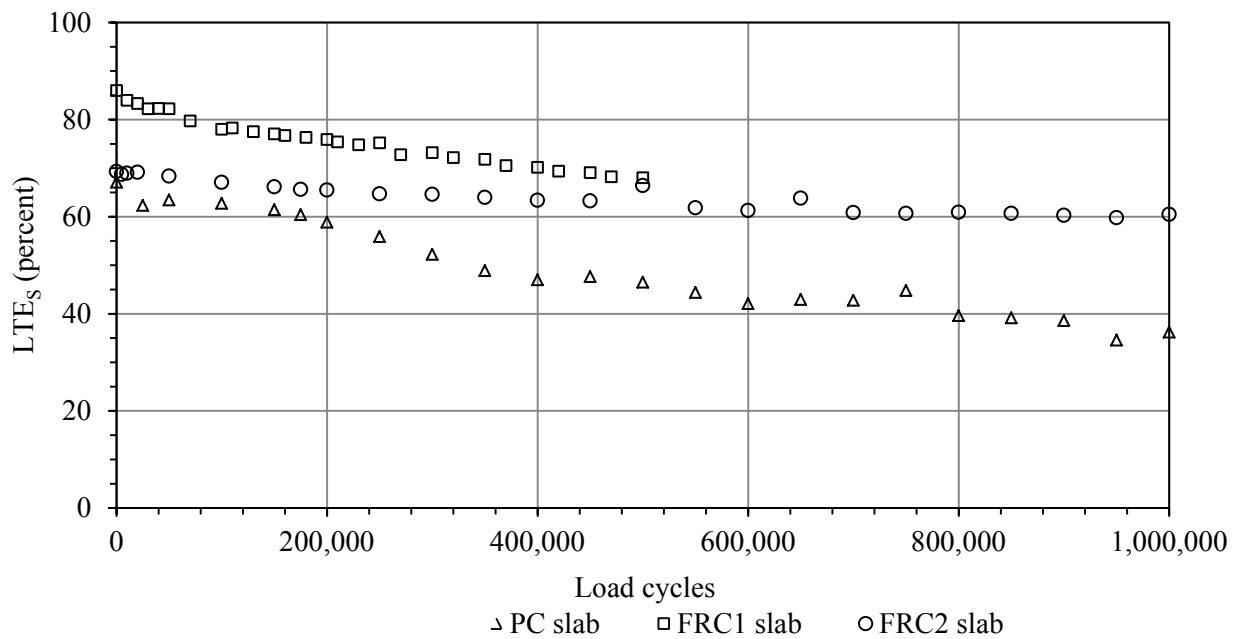
Figure 5.71. LTE$_S$ vs load cycle for different mixes.
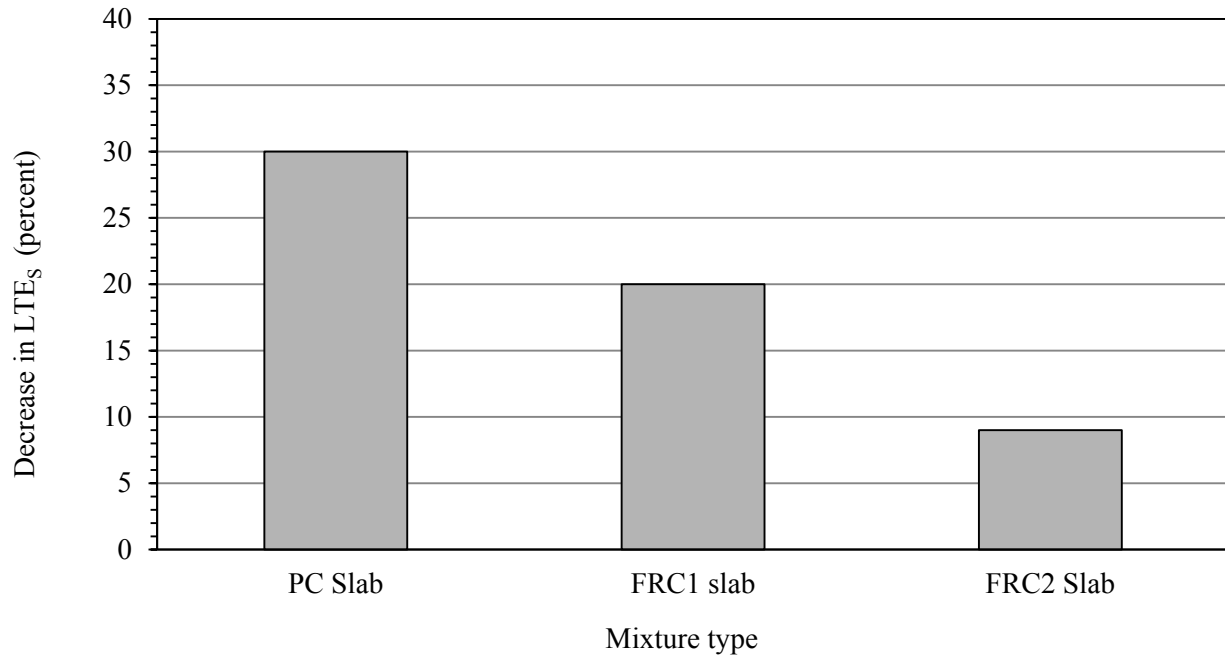
Figure 5.72. Decrease in LTE$_S$ during fatiguing of the joint.

Figure 5.73 presents the comparison of the LTE$_S$ vs crack width relationships for the three mixtures. Similar to the B$_{ALT}$ procedure, the differences in LTE$_S$ among the three mixtures were relatively low when the crack width was narrow (below 0.025 in). At low crack width, aggregate interaction played a key role for joint performance. But contribution of fiber was also noticed at low crack width. It can be seen that FRC1 and FRC2 slabs exhibited a similar LTE$_S$ vs crack width trend at a crack width below 0.050 in, and then FRC2 slab did perform slightly better than the FRC1 slab. The PC slab consistently exhibited the lowest LTE$_S$.

215
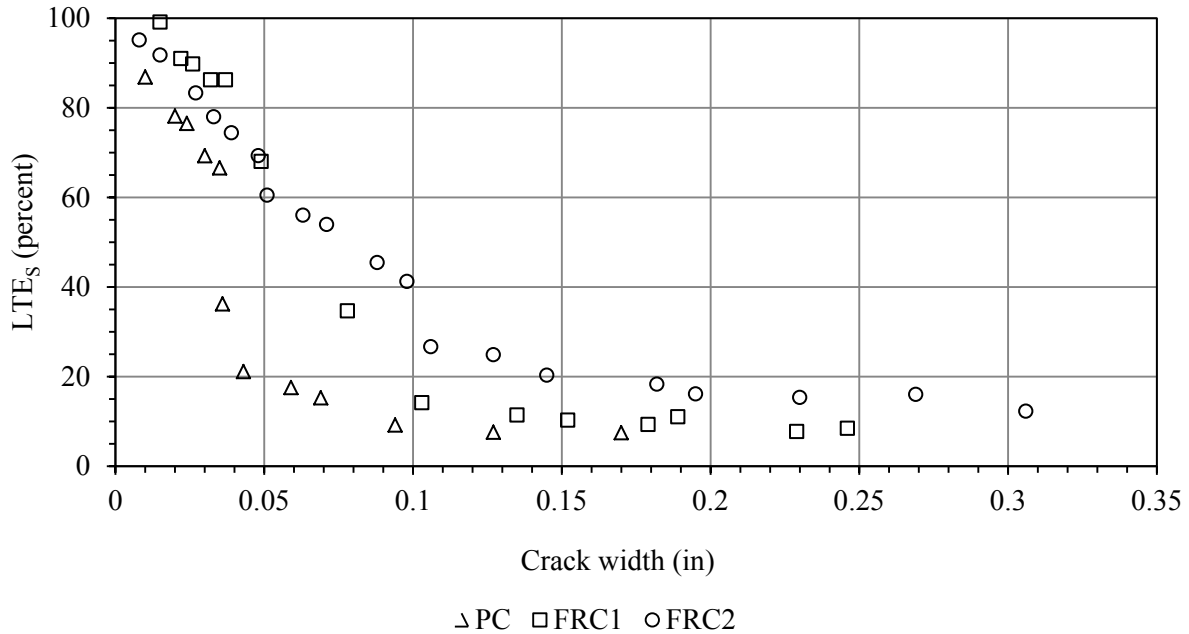
Figure 5.73. LTE$_S$ vs crack width for different mixtures.

5.3.2.5 Regression model for LTE$_S$

Regression models were developed for correlating the LTE$_S$ with the crack width. Separate regression models were developed for each slab. As previously mentioned, the LTE$_S$ were measured both before and after fatiguing. Adjustments were made to the measured LTE$_S$ to convert them into LTE$_S$ without fatigue effects (referred as non-fatigued LTE$_S$). To do this, the LTE$_S$ measured at a crack width wider than the fatiguing crack width were raised by adding the corresponding drop in LTE$_S$ due to fatiguing. The drops in LTE$_S$ due to fatigue or the magnitude of adjustment for converting the measured LTE$_S$ into non-fatigued LTE$_S$ for the three slabs are given in Table 5.13. LTE$_S$ drop due to crack width increase during fatiguing was determined by following a similar procedure which was adopted for the B$_{ALT}$ specimens. The crack width increase during fatiguing was 12 mils for the FRC1 slab; the adjustment in LTE$_S$ for this increase

in crack width is presented in Appendix B. The original and non-fatigued LTE_S are correlated with the crack width by logarithmic and bilinear relationships.

Table 5.13. Drop in LTE_S due to fatigue, crack width increase during fatiguing and magnitude of LTE_S for determining non-fatigued LTE_S for the three slabs.

Slab type	LTE_S drop due to fatiguing and crack width increase during fatiguing (total) (percent)	LTE_S drop due to crack width increase alone during fatiguing (percent)	Magnitude of increase in LTE_S to adjust for fatiguing (percent)
PC slab	30	2	28
FRC1 slab	18	8	10
FRC2 slab	9	2	7

PC slab

Logarithmic fit

Figure 5.74 and Figure 5.75 present the logarithmic relationships developed for the original and non-fatigued LTE_S, respectively. To obtain the non-fatigued LTE_S at a crack width beyond the fatiguing crack width, a 28 percent LTE_S was added for the PC slab. This 28 percent LTE_S is equivalent to the LTE_S drop due to fatiguing alone (Table 5.13).

Equations (5.19) and (5.20) present the regression models developed with the original and non-fatigued LTE_S, respectively. In the regressions for both the original and non-fatigued LTE_S, data was considered for up to 0.128 in crack width, based on the stepwise progressive procedure. The R^2 for the model with the original and non-fatigued LTE_S are 0.83 and 0.93, respectively, while the SE are 13.51 and 4.87, respectively.

217

Original

$$LTE_S = -39.33 \ln (cw) - 82.893 \qquad (5.19)$$

Non-fatigued

$$LTE_S = -23.68 \ln (cw) - 17.096 \qquad (5.20)$$
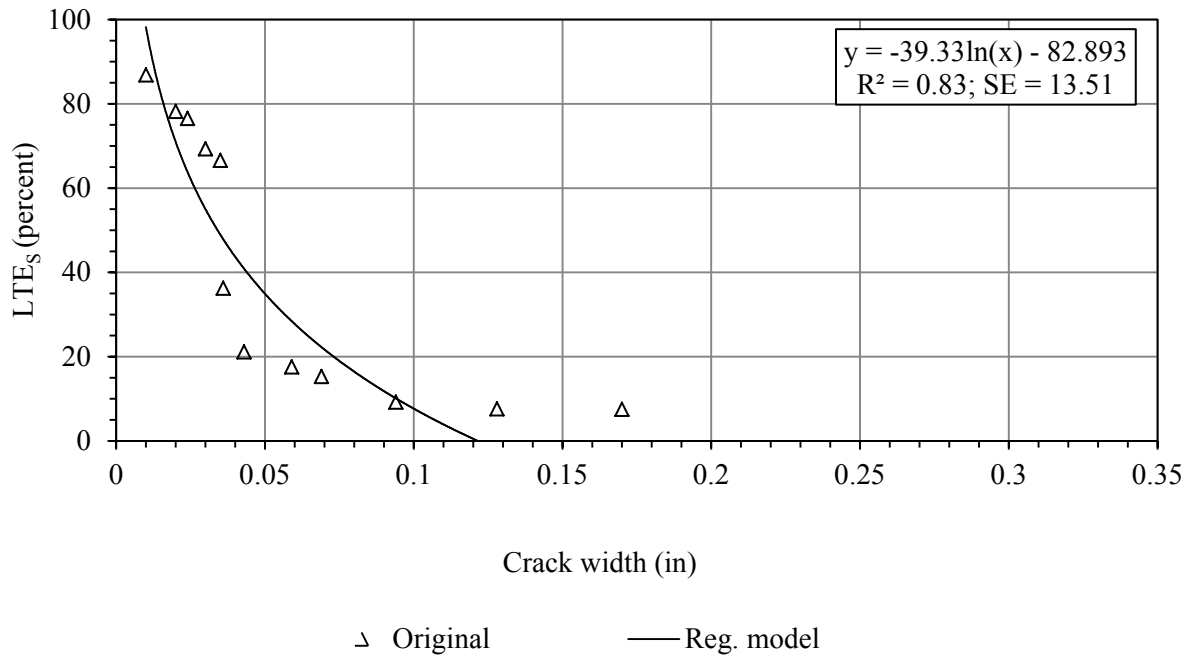
Figure 5.74. Relationship for original measured LTE$_S$ for the PC slab, logarithmic fit.
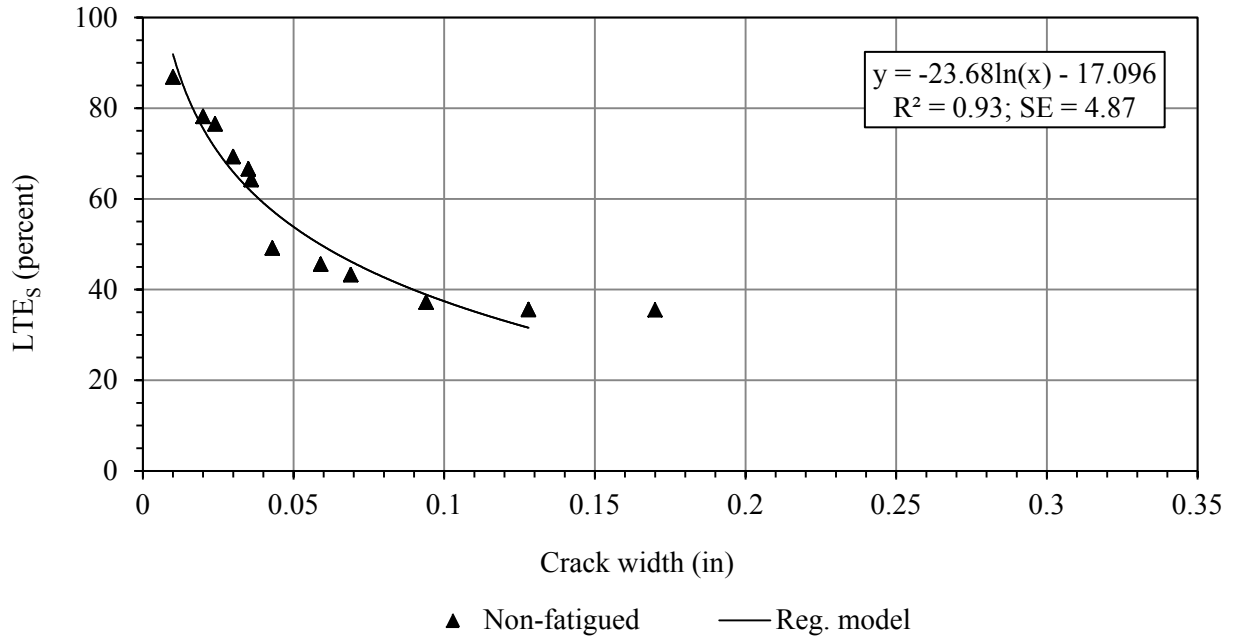
Figure 5.75. Relationship for non-fatigued LTE$_S$ for the PC slab, logarithmic fit.

Bi-linear fit

The bi-linear relationships developed for original and non-fatigued LTE$_S$ are presented in Figure 5.76 and Figure 5.77, respectively. The bi-linear split and the maximum number of data points were obtained through a stepwise progressive regression. In both the original and non-fatigued LTE$_S$ models, bi-linear split was obtained at 0.060-in crack width. Regression models are presented in Equations (5.21) through (5.24). For the model with original LTE$_S$, the R^2 for the first and second segments are 0.83 and 0.89, respectively, while the SE are 12.36 and 1.90, respectively. For the model with non-fatigued LTE$_B$, the R^2 for the first and second segments are 0.94 and 0.89, respectively, while the SE are 3.72 and 1.90, respectively.

219
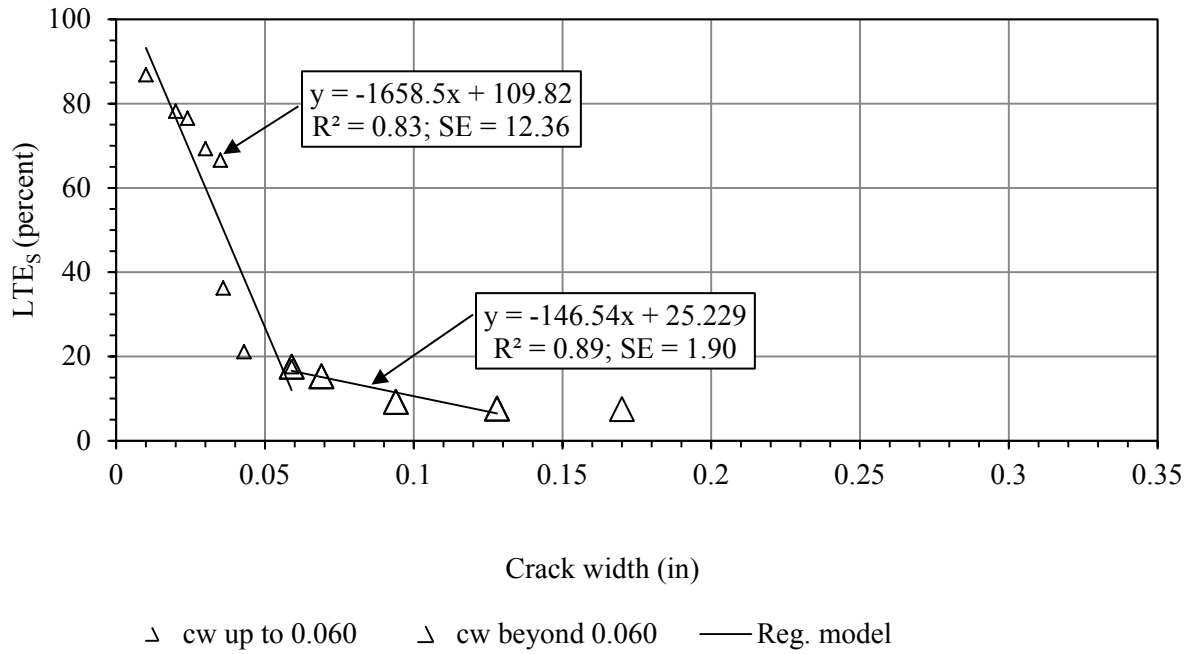
Figure 5.76. Relationship for original LTE$_S$ for the PC slab, bi linear fit.
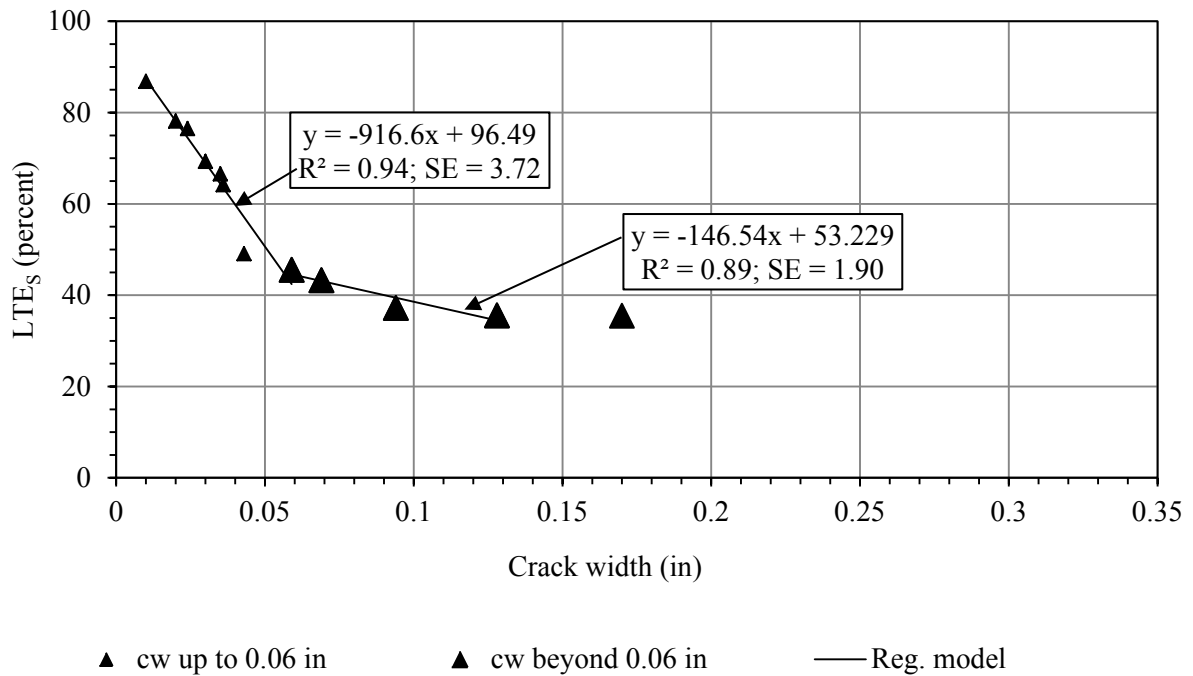
Figure 5.77. Relationship for non-fatigued LTE$_S$ for the PC slab, bi-linear fit.

Original

$$LTE_S = -1658.5 \ (cw) \ + 109.82 \qquad (5.21)$$

cw up to 0.06 in: $LTE_S = -1658.5 \ (cw) \ + 109.82$ (5.21)

cw beyond 0.06 in: $LTE_S = -146.54 \ (cw) \ + 25.229$ (5.22)

Non-fatigued

cw up to 0.06 in: $LTE_B = -916.6 \ (cw) \ + 96.49$ (5.23)

cw beyond 0.06 in: $LTE_S = -146.54 \ (cw) + 53.229$ (5.24)

FRC1 slab

Logarithmic fit

Figure 5.78 and Figure 5.79 show the regression relationships developed for the original and non-fatigued LTE$_S$ for the FRC1 slab. To obtain the non-fatigued LTE$_S$ at the crack widths beyond the fatiguing crack width, a 10 percent LTE$_S$ was added. This 10 percent LTE$_S$ is assumed to be equivalent to the LTE$_S$ drop only due to fatiguing. Equations (5.25) and (5.26) present the regression models developed with the original and non-fatigued LTE$_S$, respectively. The R^2 for both the model with the original and non-fatigued LTE$_S$ are 0.95, while the SE are 9.12 and 9.04, respectively.

Original

$$LTE_S = -42.3 \ ln \ (cw) - 67.229 \qquad (5.25)$$

Non-fatigued

$$LTE_S = -37.19 \ ln \ (cw) - 47.121 \qquad (5.26)$$

221
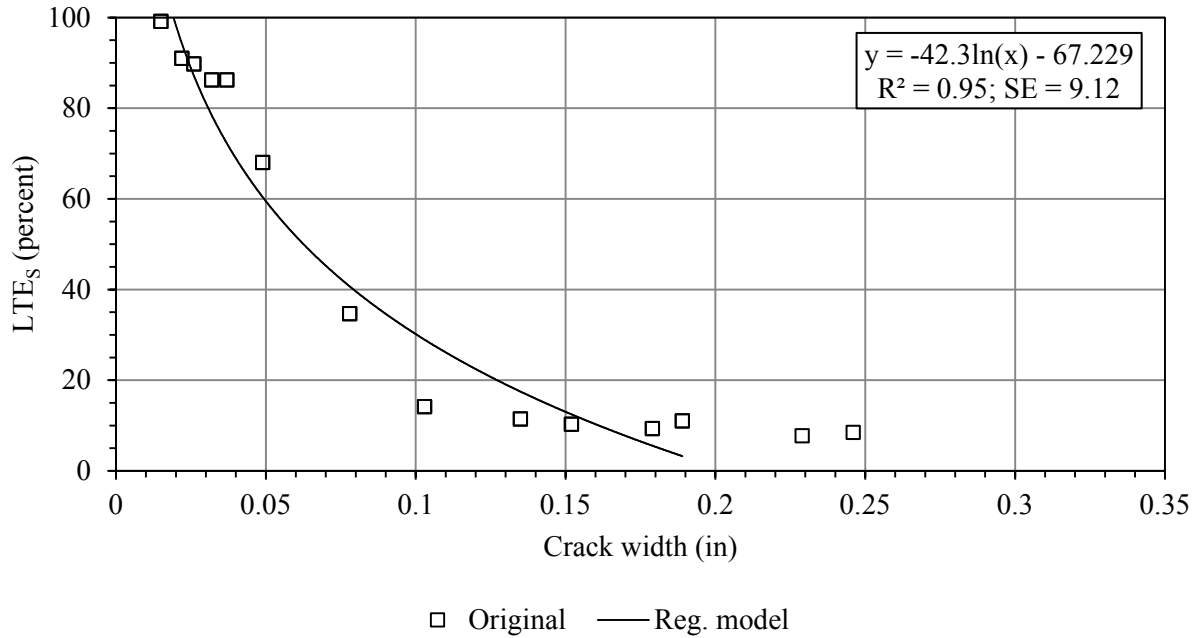
Figure 5.78. Relationship for original LTE$_S$ for the FRC1 slab, logarithmic fit.
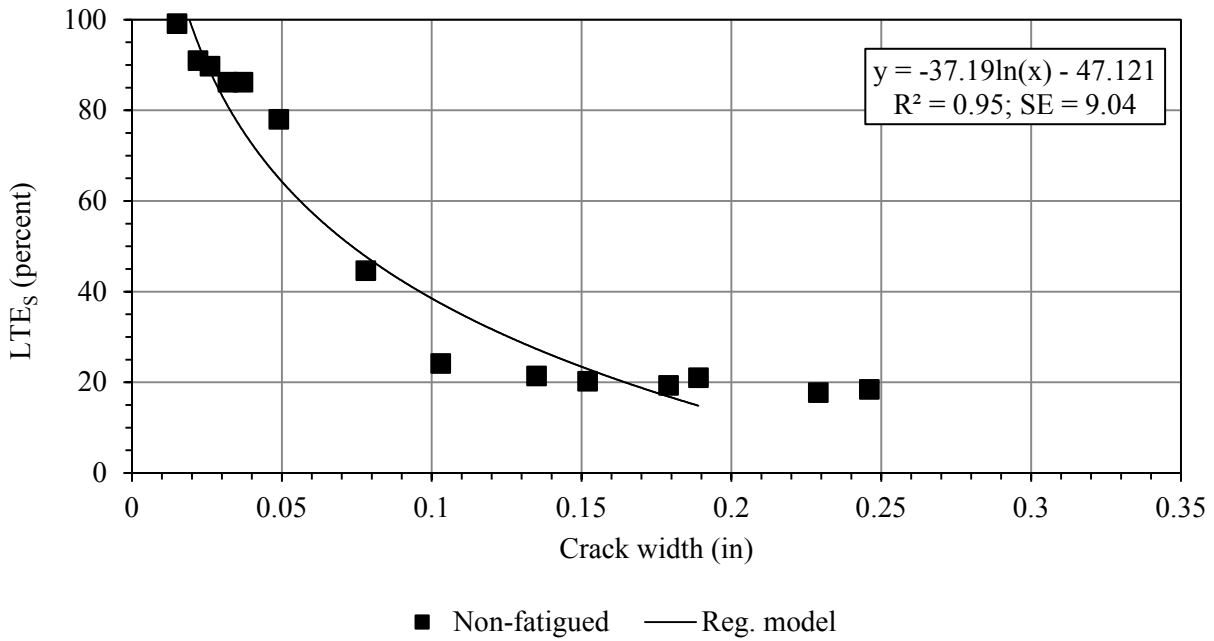
Figure 5.79: Relationship for non-fatigued LTE$_S$ for the FRC1 slab, logarithmic fit.

222

Bi-linear fit

The bi-linear relationships developed for the original and non-fatigued LTE_S are presented in Figure 5.80 and Figure 5.81, respectively. The bi-linear spilt was obtained at 0.10-in crack width for both the models. In both the models, data beyond 0.150-in crack width were not considered. Regression models are presented in Equations (5.27) through (5.30). For the model with original LTE_B, the R^2 for the first and second segments are 0.99 and 0.96, respectively, while the SE are 3.7 and 0.52, respectively. For the model with non-fatigued LTE_B, the R^2 for the first and second segments are 0.98 and 0.96, respectively, while the SE are 3.76 and 2.66, respectively.
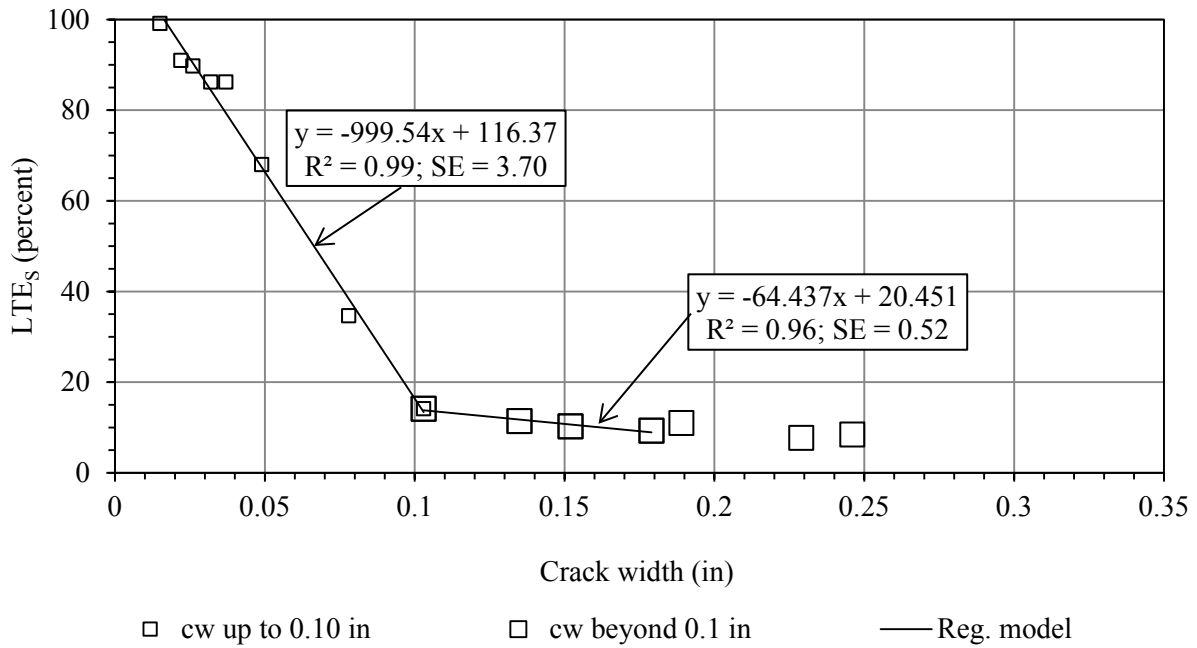
Figure 5.80. Relationship for original LTE_S for the FRC1 slab, bi-linear fit.
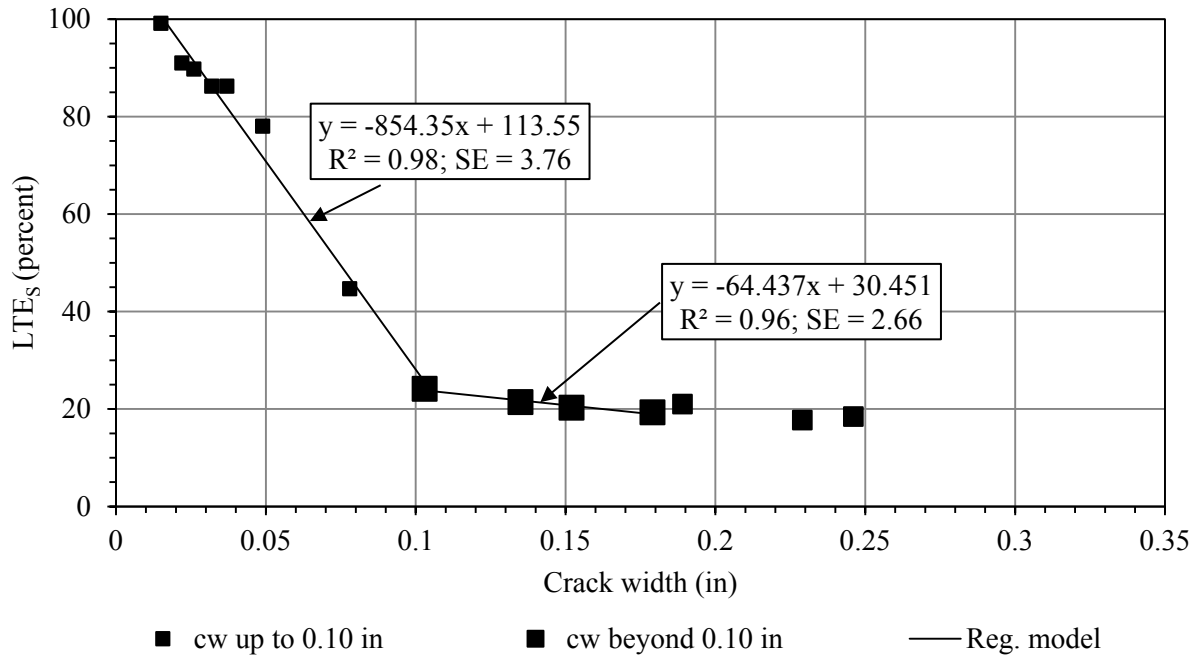
Figure 5.81. Relationship for non-fatigued LTE$_S$ for the FRC1 slab, bi-linear fit.

Original

$$\text{cw up to 0.10 in: } LTE_S = -999.54 \ (cw) + 116.37 \qquad (5.27)$$

$$\text{cw beyond 0.10 in: } LTE_S = -64.437 \ (cw) + 20.451 \qquad (5.28)$$

Non-fatigued

$$\text{cw up to 0.10 in: } LTE_B = -854.35 \ (cw) \ + 113.55 \qquad (5.29)$$

$$\text{cw beyond 0.10 in: } LTE_S = -64.437(cw) \ + 30.451 \qquad (5.30)$$

FRC2 slab

Logarithmic fit

Figure 5.82 and Figure 5.83 show the regression relationships developed for the original and non-fatigued LTE$_S$ for the FRC2 slab. To obtain the non-fatigued LTE$_S$ at the crack widths beyond the fatiguing crack width, a 7 percent LTE$_S$ was added. This 7 percent LTE$_S$ is

224

equivalent to the LTE_S drop due to fatiguing alone (Table 5.13). Equations (5.31) and (5.32) present the regression models developed with the original and non-fatigued LTE_S, respectively. The R^2 for the model with the original and non-fatigued LTE_S are 0.94 and 0.92, respectively, while the SE for the two models are 7.22 and 7.50, respectively.

Original

$$LTE_S = -28.44 \ln (cw) - 26.339 \qquad (5.31)$$

Non-fatigued

$$LTE_S = -25.87 \ln (cw) - 15.057 \qquad (5.32)$$
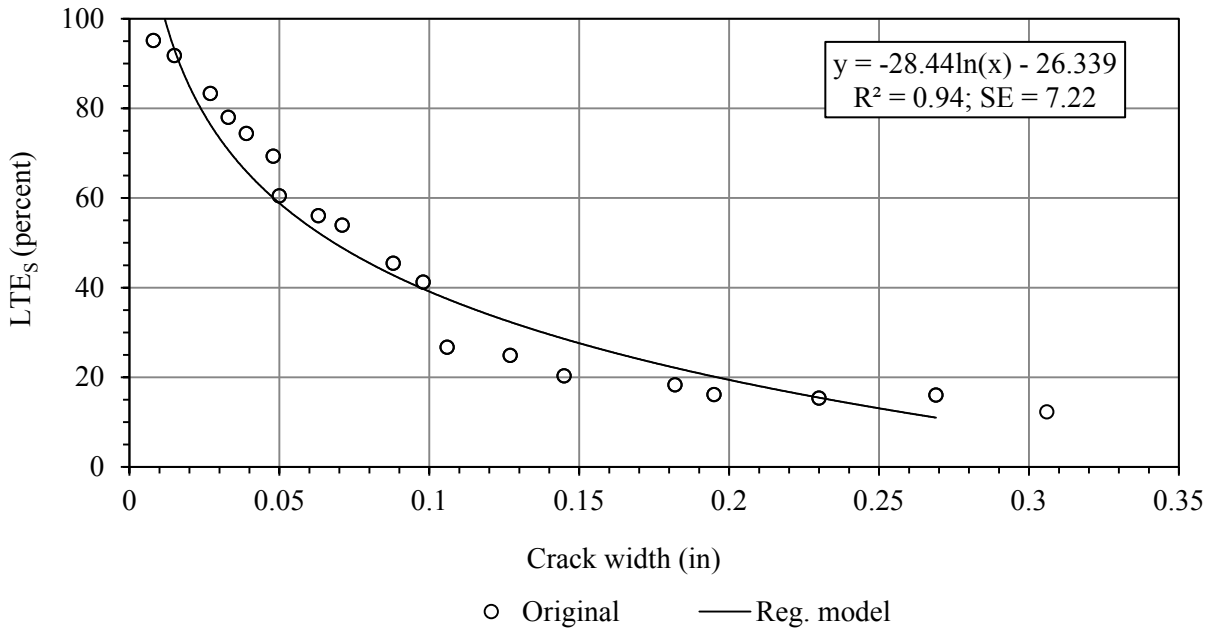
Figure 5.82. Relationship for original LTE_S for the FRC2 slab, logarithmic fit.

225
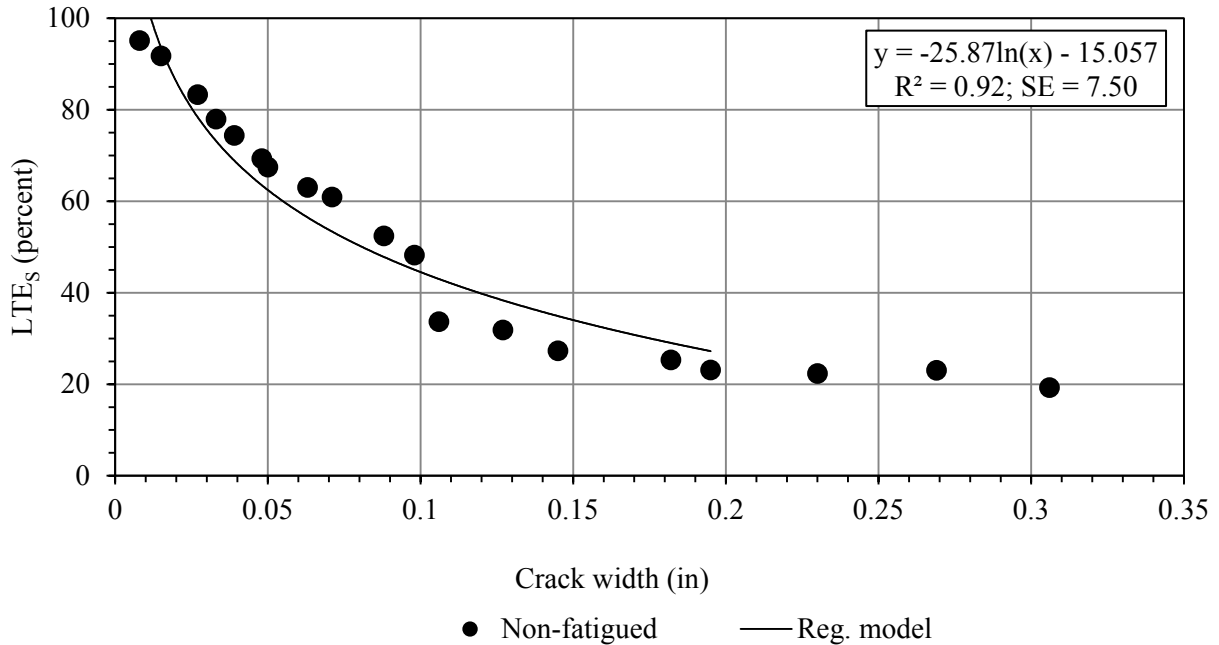
Figure 5.83. Relationship for non-fatigued LTE_S for the FRC2 slab, logarithmic fit.

Bi-linear fit

The bi-linear relationships developed for original and non-fatigued LTE_S are presented in Figure 5.84 and Figure 5.85, respectively. The bi-linear split was obtained at 0.10-in crack width. Regression models are presented in Equations (5.33) through (5.36). For the model with original LTE_S, the R^2 for the first and second segments are 0.98 and 0.72, respectively, while the SE are 3.25 and 5.37, respectively. For the model with non-fatigued LTE_S, the R^2 for the first and second segments are 0.97 and 0.95, respectively, while the SE are 2.65 and 5.46, respectively.

226
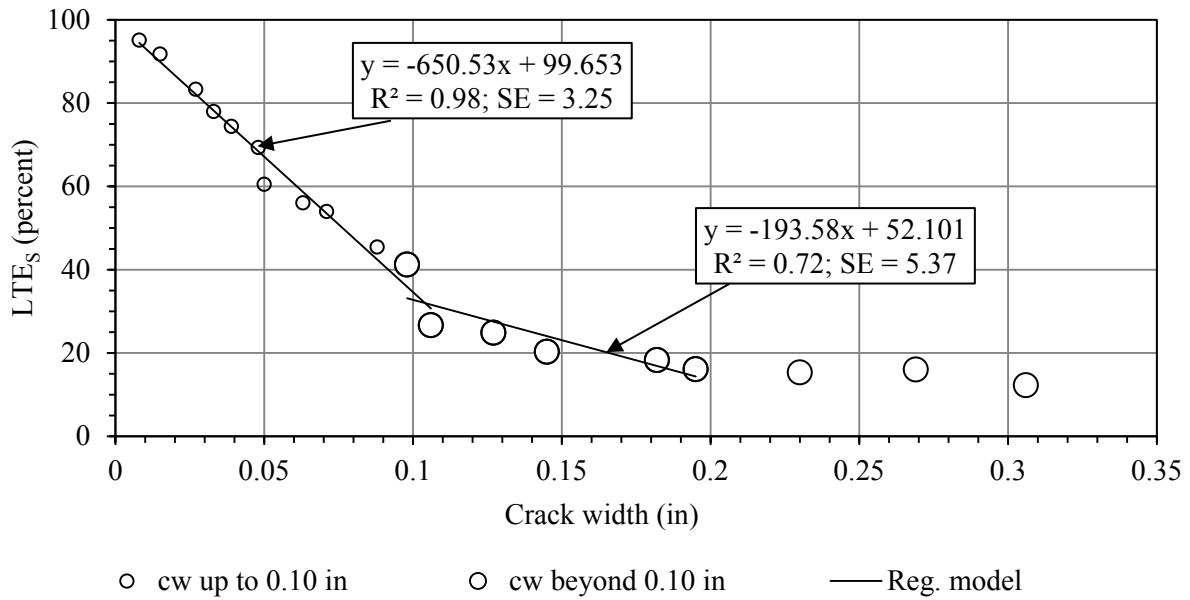
Figure 5.84. Relationship for original LTE$_S$ for the FRC2 slab, bi-linear fit.
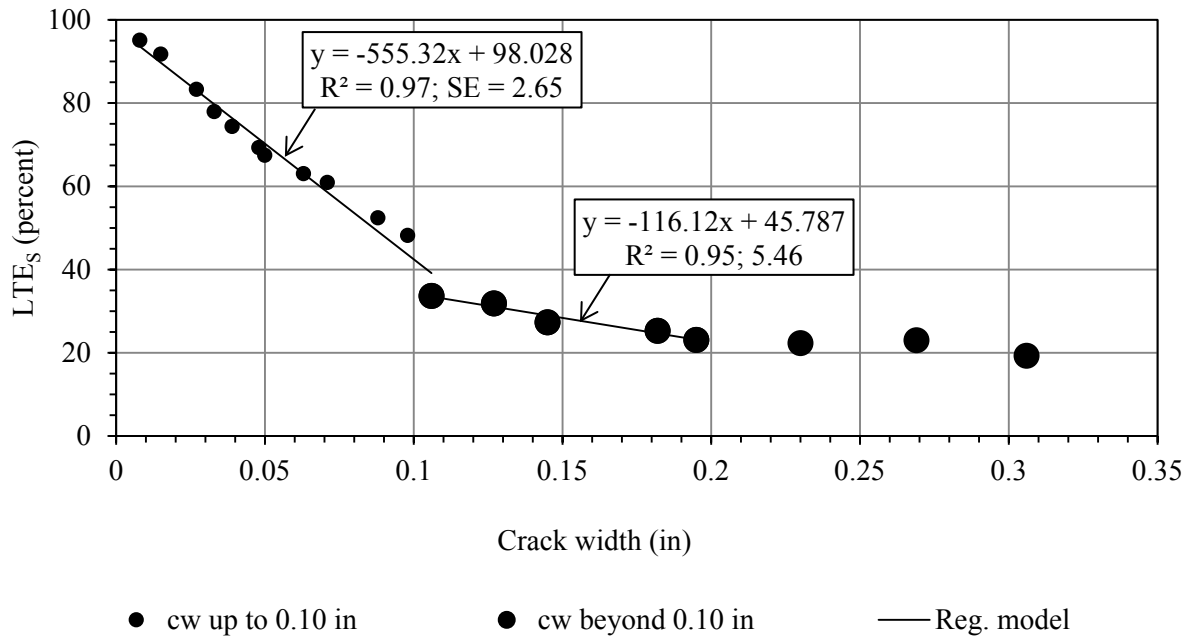
Figure 5.85. Relationship for non-fatigued LTE$_S$ for the FRC2 slab, bi-linear fit.

227

Original

$$\text{cw up to 0.10 in: } LTE_S = -650.53 \, (cw) + 99.653 \qquad (5.33)$$

$$\text{cw beyond 0.10 in: } LTE_S = -193.58 \, (cw) + 52.101 \qquad (5.34)$$

Non-fatigued

$$\text{cw up to 0.10 in: } LTE_B = -555.32 \, (cw) + 98.028 \qquad (5.35)$$

$$\text{cw beyond 0.10 in: } LTE_S = -116.12 \, (cw) + 45.787 \qquad (5.36)$$

Finally, a general comparison SE between the two forms of regression fits reveals that the bi-linear fit provides better prediction with a relatively lower SE. The SE for the bi-linear regression models for the first segments for each concrete mixture was compared with the SE for the logarithmic regression models.

Comparison of LTE$_S$ values predicted by the regression models between three mixtures

Figure 5.86 shows the comparison of non-fatigued LTE$_S$ between the three mixtures. Both the FRC1 and FRC2 mixtures provide a higher LTE$_S$ than the PC mixture. Initially, up to 0.05-in crack width, LTE$_S$ of the FRC1 mixture is higher than the FRC2 mixture. However, the decreasing rate of LTE$_S$ for FRC1 (as a function of crack width) is steeper than of the FRC2 mixture, which brings the LTE$_S$ of FRC1 and FRC2 mixtures equal at 0.05 in crack width. One of the most interesting observations is that the decreasing rate of LTEs for PC and FRC1 mixtures are the same up to about 0.06 in crack width. The shallower LTE$_S$ decreasing slope for FRC2 indicates a greater contribution of the Enduro 600 fiber (F2). This is probably due to the higher stiffness of the F2 fiber. The other important observation is that the FRC mixtures have a linear relationship with the crack width for up to a crack width as much as twice that the PC

228

mixture has. One thing that should be noted is that the LTE_S of the PC slab was adjusted for fatiguing by a considerably large amount (28 percent), so the LTE_S of the PC slab after fatiguing might be superficially increased. In general, it can be said that when the crack width is narrow, the contribution of the fiber is low (Comparing FRC2 and PC mixture) and aggregate interlock plays the dominant role in transferring the load. The contribution of fiber is quite significant when the crack width is in the range of 0.03 to 0.06 in.

Table 5.14 presents a comparison between the non-fatigued LTE_S values for the three mixtures predicted by the bi-linear models. Different crack widths ranging from 0.020 to 0.10 in are considered for the comparison. Table 5.15 presents the benefits of FRC mixtures as compared to the PC mixture. Although the non-fatigued LTE_S for the FRC mixtures are higher, the increase in LTE_S is not consistent over the crack widths.

Figure 5.86. Comparison of the non-fatigued LTE$_S$ between the three concrete mixtures.

Table 5.14. Comparison of non-fatigued LTE$_S$ between the different mixtures.

Crack width (in)	PC	FRC1	FRC2
0.02	78	96	87
0.03	69	88	81
0.04	60	79	76
0.05	51	71	70
0.06	44	62	65
0.07	43	54	59
0.08	42	45	54
0.09	40	37	48
0.10	39	28	42

230

Table 5.15. Percent increase in non-fatigued LTE_S when using FRC mixtures.

Crack width (in)	FRC1	FRC2
0.02	23	11
0.03	27	18
0.04	33	27
0.05	40	39
0.06	40	46
0.07	25	38
0.08	9	29
0.09	0	20
0.10	0	10

5.3.3   Comparison between LTE_B vs LTE_S

A comparison between the LTE obtained with the B_{ALT} and S_{ALT} is presented in this subsection. The decrease in the LTE_B for all the beams and the LTE_S for all the slabs due to fatiguing after 0.5 and 1 million load cycles are presented in Figure 5.87 and Figure 5.88, respectively. In the B_{ALT} procedure, the average of LTE_B results from the two beams fatigued at a similar crack width is presented in each column. Also, the difference between the results can be determined by the error bars associated with each column. For the S_{ALT} procedure, the average of the approach and leave slab LTE_S are presented. For the B_{ALT} specimens, the decrease in the LTE_B mostly occurred within the first 0.5 million load cycle applications. For the S_{ALT} specimens, the PC slab exhibited some decrease after 0.5 to 1 million load cycles, while the FRC2 did not exhibit any drop after 0.5 million load cycles. Between the PC beams and PC slab, which were fatigued at a 0.035-in crack width, the slab exhibited a 20 percent greater decrease in the load transfer efficiency. The FRC1 beams and FRC1 slab exhibited a similar LTE drop after 0.5 million load cycles. Also, the decrease in the LTE_B for the FRC2 beams and LTE_S for FRC2 slab were in a similar range.

231
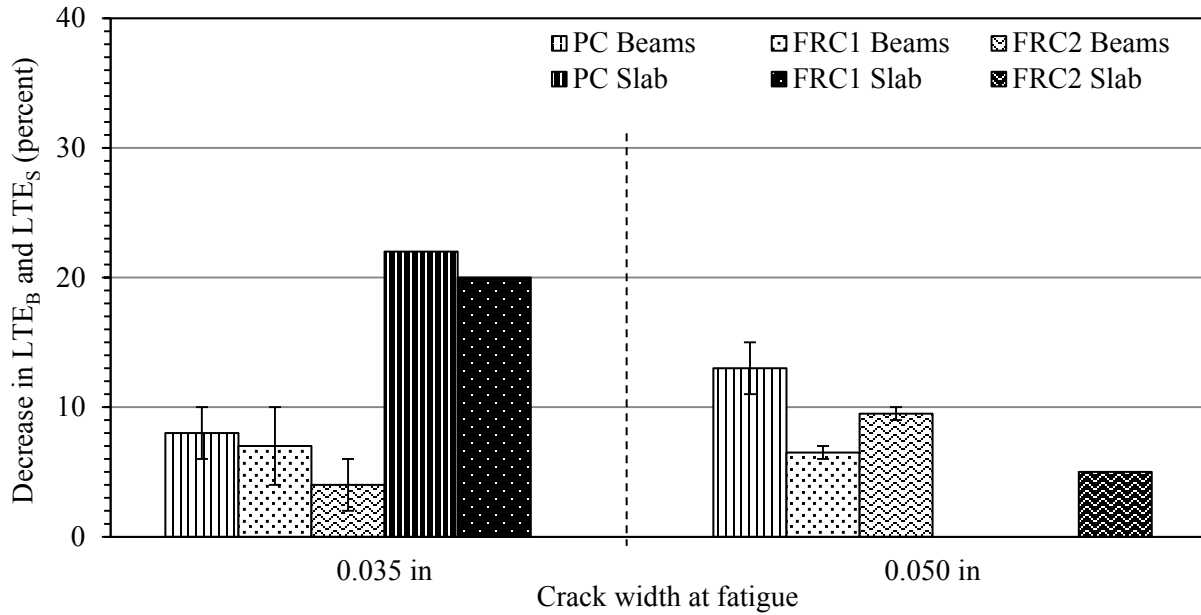
Figure 5.87. Comparison between decreases in the LTE_B and LTE_S after 0.5 million load cycles.
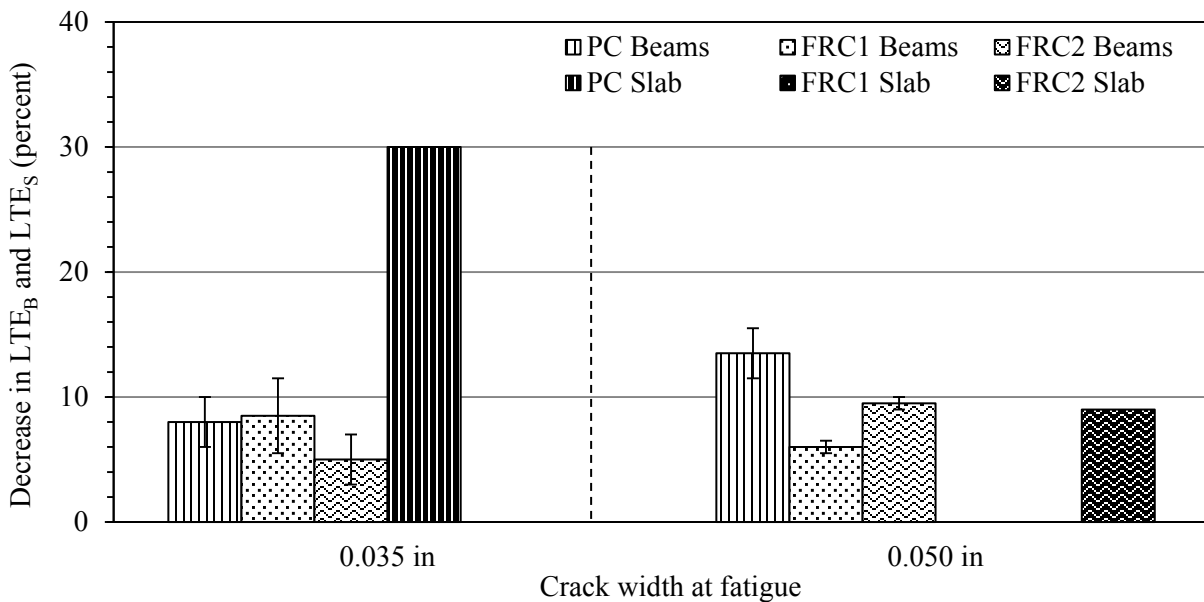
Figure 5.88. Comparison between decreases in the LTE_B and LTE_S after 1 million load cycles.

A comparison of the original LTE_B and LTE_S vs crack width relationships between the two procedures for all the mixtures is shown in Figure 5.89. For all of the mixtures, the LTE_B were higher than the corresponding LTE_S. The difference between the LTE_B and LTE_S results

232

increased with increasing the crack width. For the S$_{ALT}$ specimens, the FRC2 mixture performed better than the other two mixtures. For the B$_{ALT}$ specimens, the FRC2 beams provided a higher LTE$_B$ when compared to the FRC1 beams. The most interesting observation from this figure is that the trends in the LTE$_B$ vs crack width and LTE$_S$ vs crack width relationships for a given mixture were quite similar. This similarity in trends indicates that the B$_{ALT}$ procedure, developed under the scope of this study, can be a useful joint performance evaluation technique and the LTE$_B$ and LTE$_S$ can be correlated.
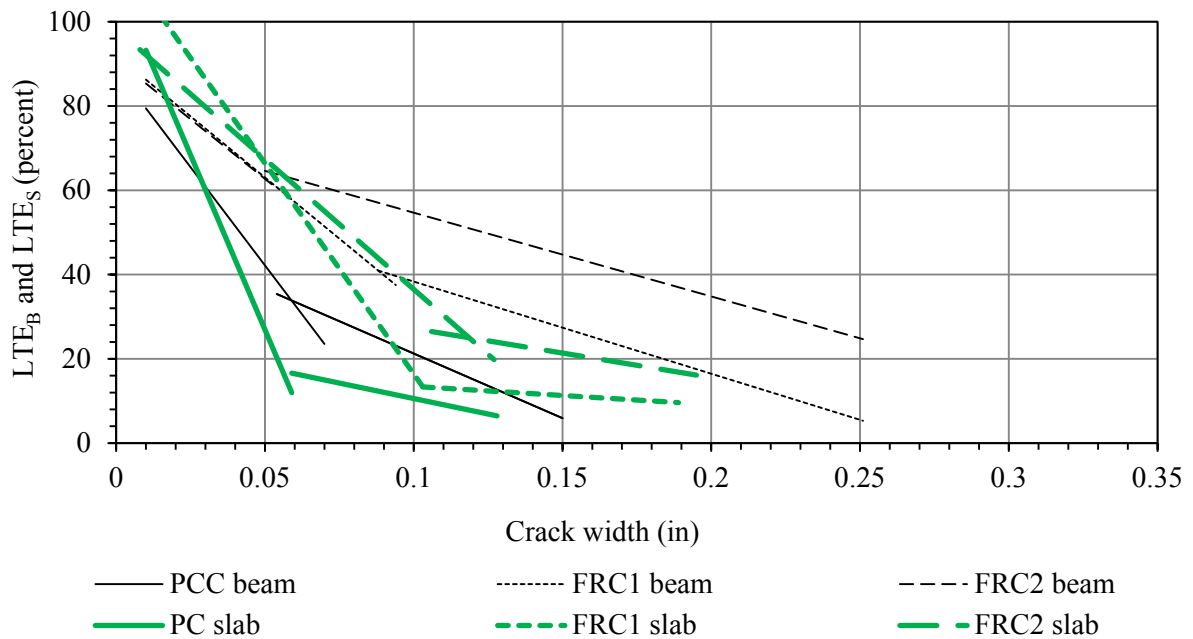
Figure 5.89. Comparison of LTE$_B$ and LTE$_S$ vs crack width relationships between all the mixtures.

To develop the correlation between the LTE$_B$ and LTE$_S$, the non-fatigued LTE$_B$ and LTE$_S$ values predicted by the developed models are correlated. It was seen that bi-linear fit provided better prediction for both LTE$_B$ and LTE$_S$. Therefore, LTE$_B$ values predicted by the bi-linear models are correlated with bi-linear LTE$_S$ values. Three separate relationships were developed for three concrete mixtures. Figure 5.90 through Figure 5.92 and Equations (5.37) through (5.39) present regression models for the three mixture types. In each of the figures, the

233

trend line for the LTE_B vs LTE_S relationship is presented along with the upper and lower error lines. Since these regression models were developed using the LTE_B and LTE_S values predicted by the models developed for predicting LTE_B and LTE_S as a function of crack width, the corresponding standard error in the LTE_B predicting model was added to determine the upper and lower error limits. The R^2 for the models with PC, FRC1 and FRC2 mixtures are 0.97, 1.0 and 0.91, respectively. The SE for the models with PC, FRC1 and FRC2 mixtures are 10.11, 7.88 and 10.27, respectively. Next a common relationship was developed for all the mixtures as shown in Figure 5.93 ($R^2 = 0.83$ and SE = 14.58). This relationship can be used for determining LTE_S from LTE_B, irrespective of any mixture type.

PC mixture

$$LTE_S = 0.9913\ LTE_B + 5.8971 \tag{5.37}$$

FRC1 mixture

$$LTE_S = 1.9514\ LTE_B - 57.041 \tag{5.38}$$

FRC1 mixture

$$LTE_S = 1.7174\ LTE_B - 45.103 \tag{5.39}$$

All mixtures

$$LTE_S = 1.2096\ LTE_B - 9.5007 \tag{5.40}$$

234
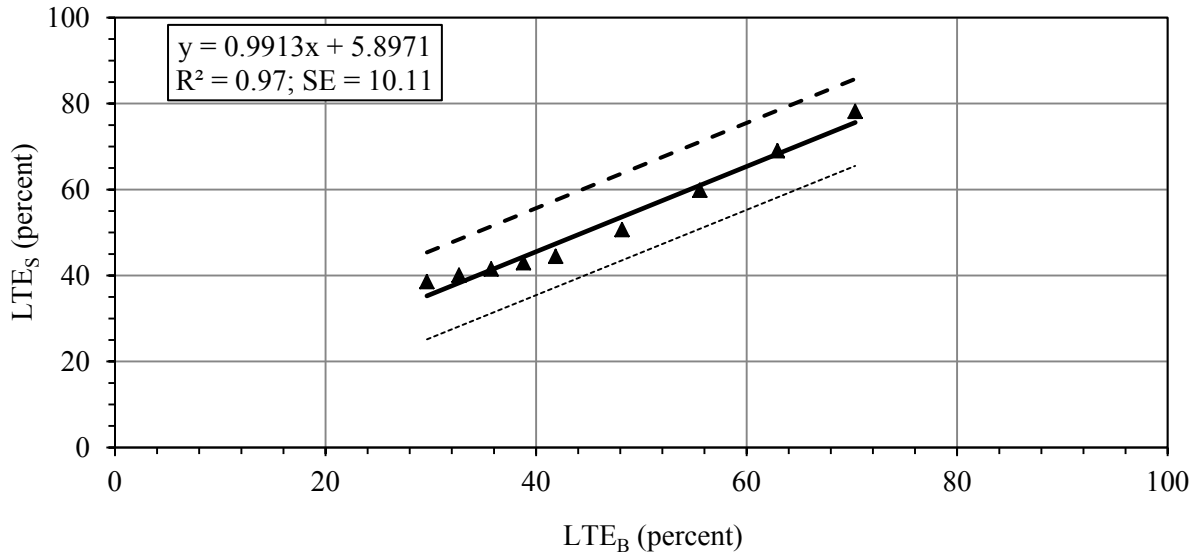
Figure 5.90. Relationship between Non-fatigued LTE$_S$ and non-fatigued LTE$_B$ for PC mixture.

Figure 5.91. Relationship between Non-fatigued LTE$_S$ and non-fatigued LTE$_B$ for FRC1 mixture.

235

$$y = 1.7174x - 45.103$$
$$R^2 = 0.91; SE = 10.27$$
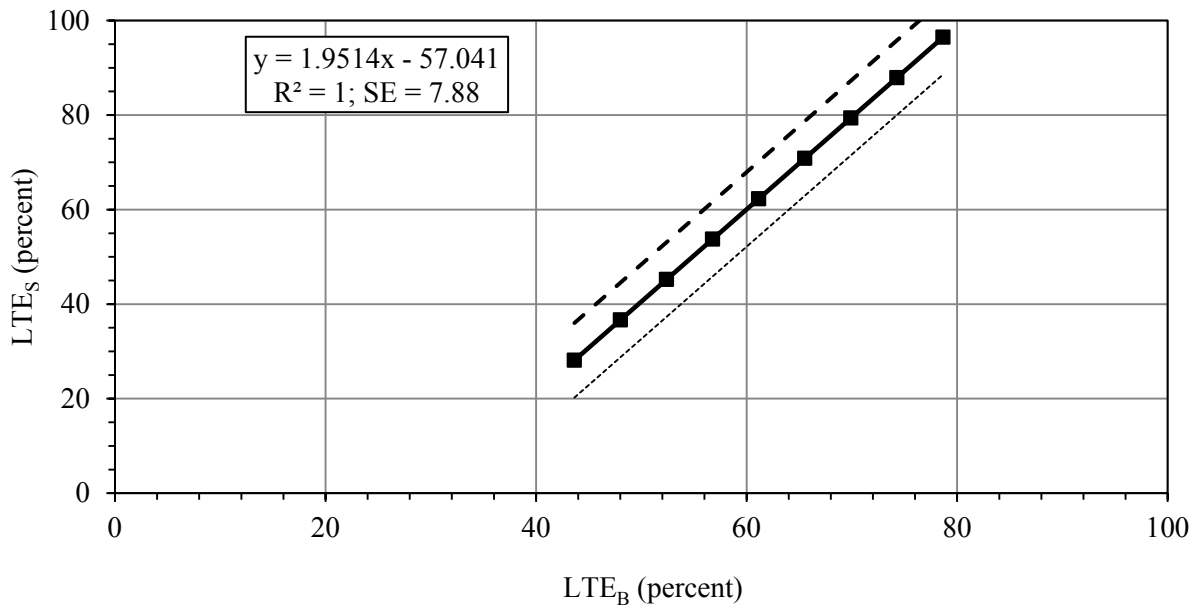
● Non-fatigued ——— Reg. model – – –Upper error line -------- Lower error line
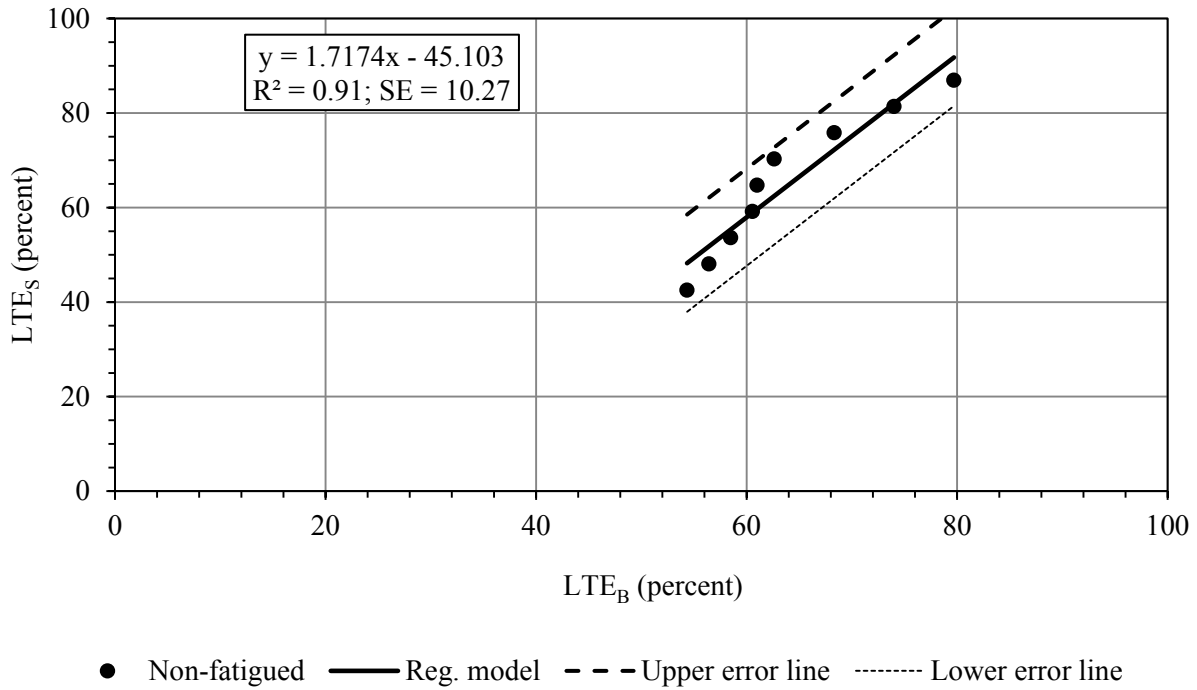
Figure 5.92. Relationship between Non-fatigued LTE_S and non-fatigued LTE_B for FRC2 mixture.

$$y = 1.2096x - 9.5007$$
$$R^2 = 0.83; 14.58$$

▲ PCC ■ FRC1 ● FRC2

– – –Upper error line -------- Lower error line ——— Reg. model
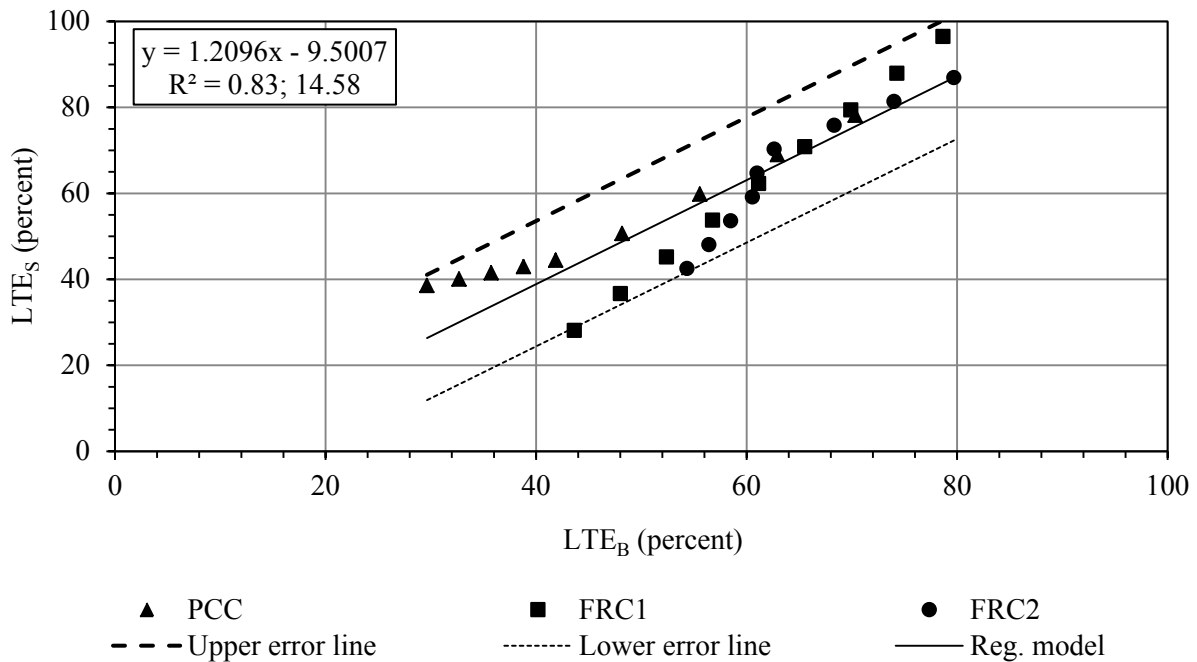
Figure 5.93. Relationship between Non-fatigued LTE_S and non-fatigued LTE_B for all the mixtures combined.

236

5.4 JOINT PERFORMANCE IN TERMS OF DER

5.4.1 B_{ALT}

DERs for all of the B_{ALT} specimens (DER_B) were calculated as per the procedure outlined in Chapter 3.0 . Figure 5.94 though Figure 5.96 present DER_B vs crack width relationships for one beam from each of the three mixtures considered in this study. All other DER_B results are presented together for comparison purposes. Figure 5.97 shows the DER_B vs crack width relationships for all the PC beams. The hollow data markers present the DER_B measured at the crack widths below the fatiguing crack width, while the solid data markers present the DER_B measured at the crack widths beyond the fatiguing crack width. It can be seen that the declining trend of DER_B over the crack width is similar for all of the PC beams. A similar trend was also observed in the case of the LTE_B vs crack width relationships. Figure 5.98 and Figure 5.99 present the DER_B vs crack width relationships for the FRC1 and FRC2 beams. Again, all the beams for each FRC mixture type show a similar trend. Figure 5.100 shows the comparison of the DER_B results for all the beams tested. It can be seen that the FRC beams performed better than the PC beams with the best performance provided by the FRC2 beams.

The drop in the DER_B due to fatigue was also studied. Table 5.16 presents the drop in DER_B due to fatigue alone, crack width increase during fatiguing and the magnitude of DER_B that is required to add to obtain no-fatigued DER_B for all the beams. On average, the PC beams exhibited a larger amount of fatigue than the FRC beams, while the FRC2 beams experienced the lowest drop in DER_B as compared to the other two mixtures.
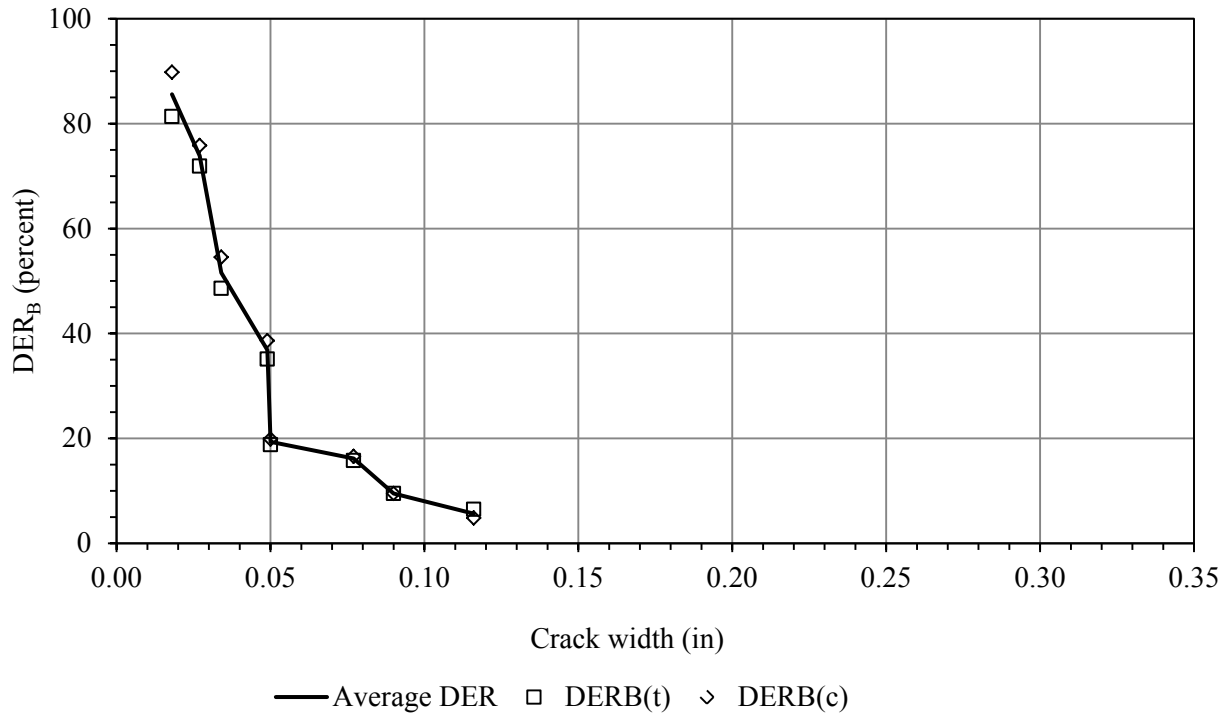
Figure 5.94. DER$_B$ vs crack width for P-1, 0.049-0.050, 0.1834 beam.
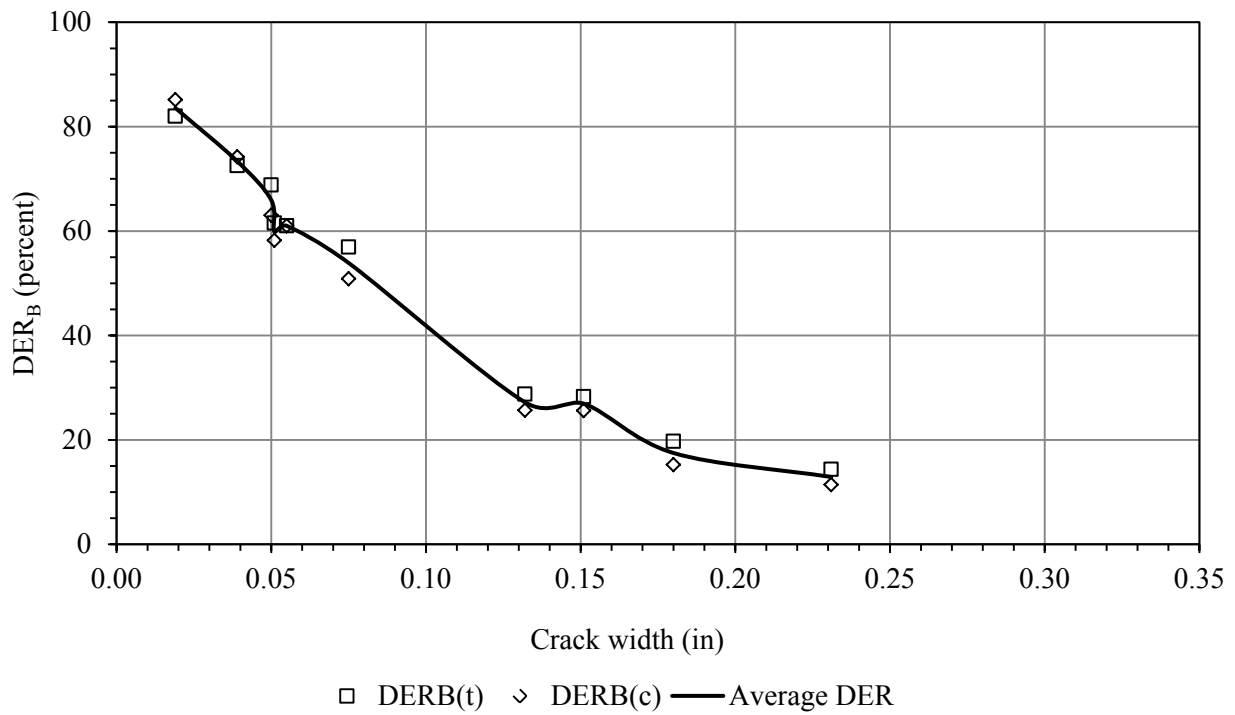
Figure 5.95. DER$_B$ vs crack width for F1-1, 0.050-0.051, 0.1597 beam.
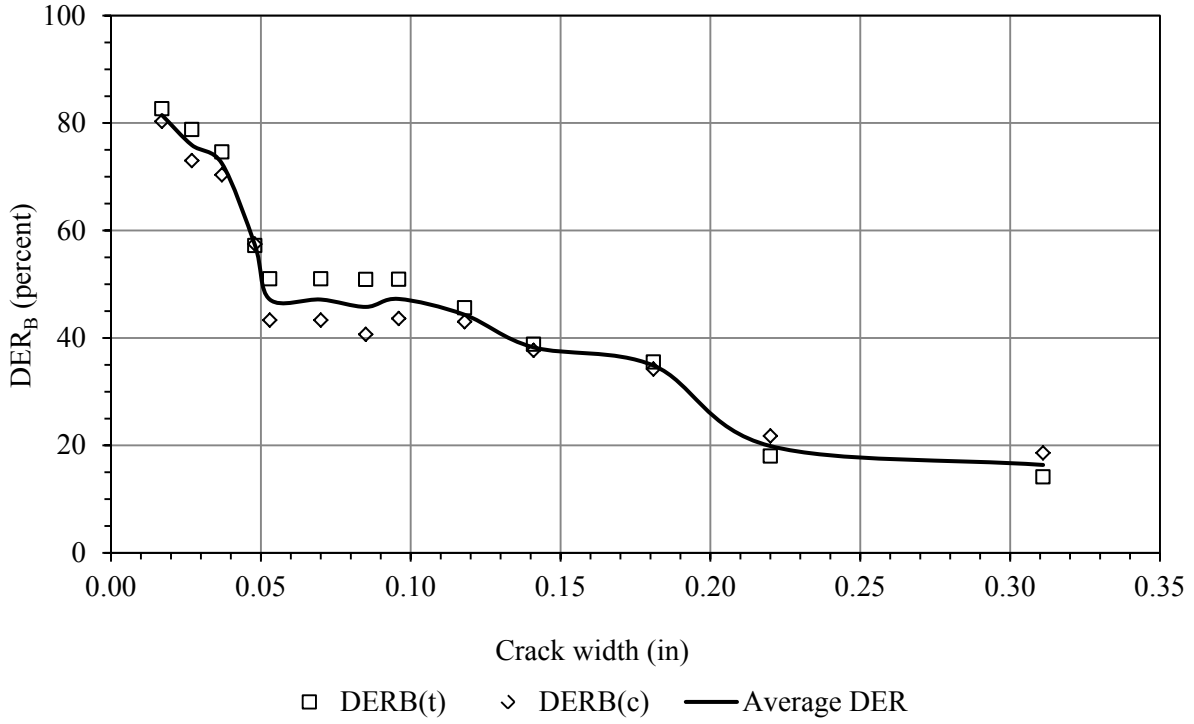
Figure 5.96. DER$_B$ vs crack width for F2-1, 0.048-0.053, 0.1771 beam.

▲ P-1, 0.049-0.050, 0.1834   ■ P-2, 0.049-0.052, 0.1844   ● P-3, 0.035, 0.1211

◆ P-4, 0.035, 0.2878   + F1-5, NF, 0.2026
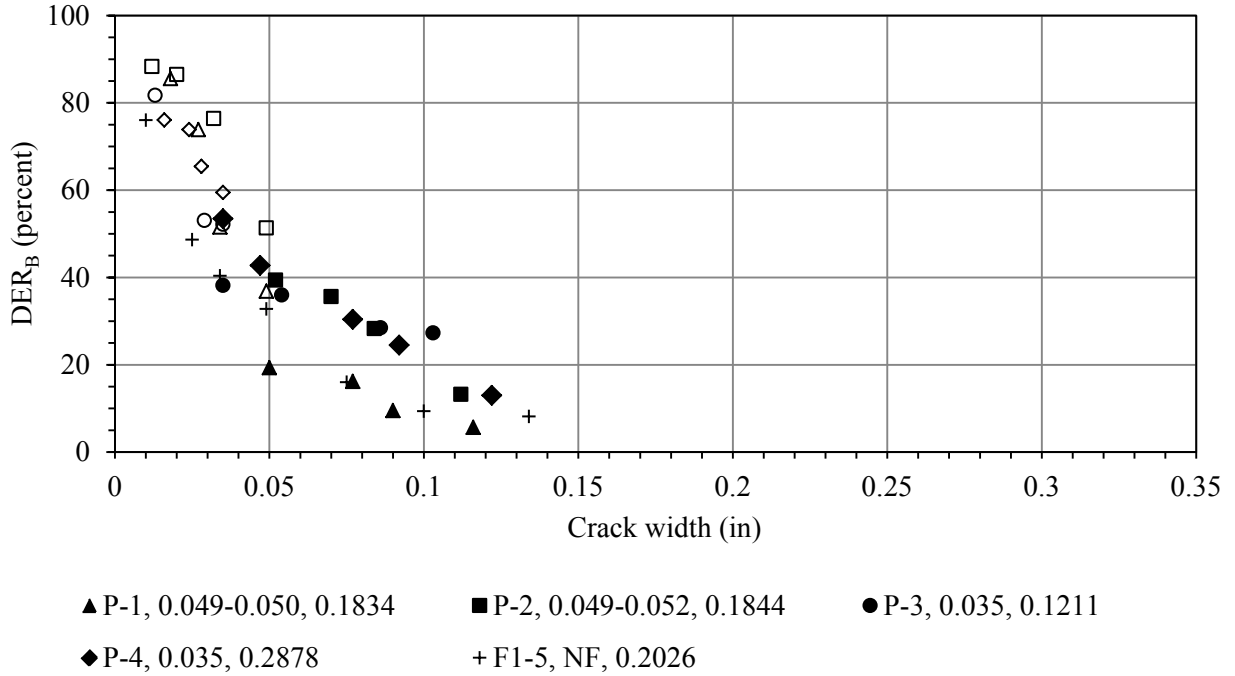
Figure 5.97. DER$_B$ vs crack width for all the PC beams
(hollow markers present DER$_B$ measured before fatiguing).

239
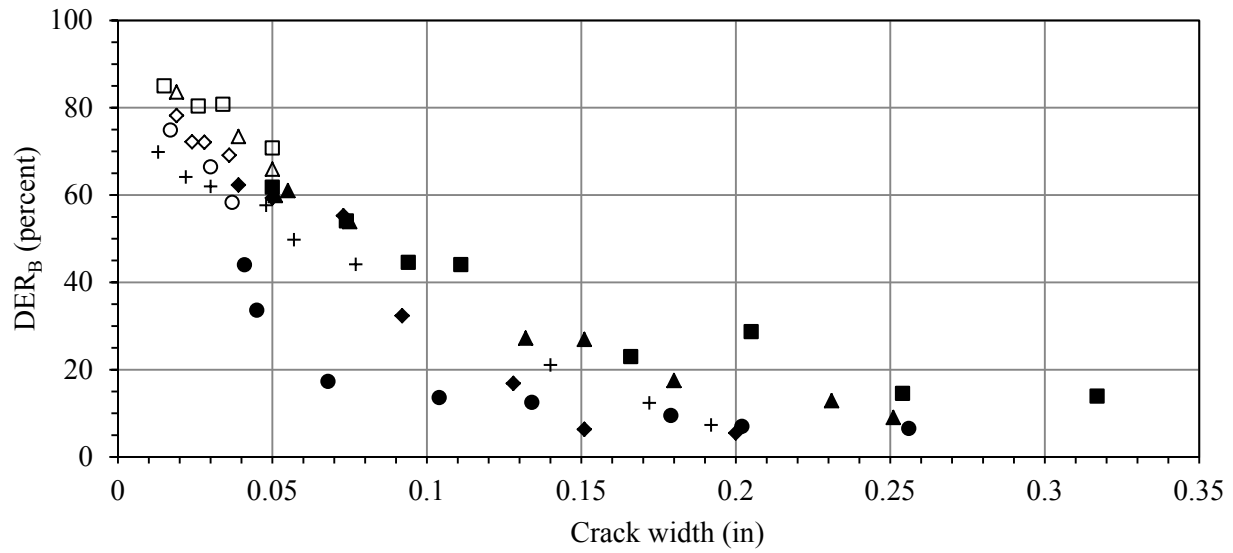
▲ F1-1, 0.050-0.051, 0.1597   ■ F1-2, 0.05, 0.1680   ● F1-3, 0.037-0.041, 0.1614

◆ F1-4, 0.036-0.039, 0.1500   + F1-5, NF, 0.2026

Figure 5.98. DER_B vs crack width for all the FRC1 beams.
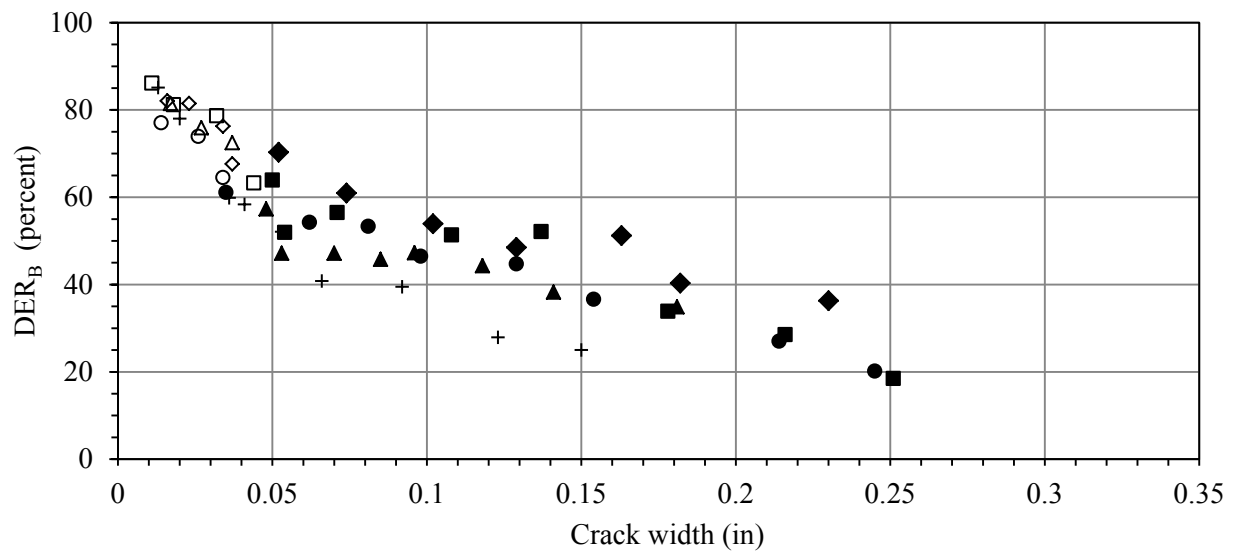
▲ F2-1, 0.048-0.053, 0.1771   ■ F2-2, 0.05-0.054, 0.1417   ● F2-3, 0.034-0.035, 0.2027

◆ F2-4, 0.034-0.037, 0.1490   + F1-5, NF, 0.2026

Figure 5.99. DER_B vs crack width for all the FRC2 beams.

240
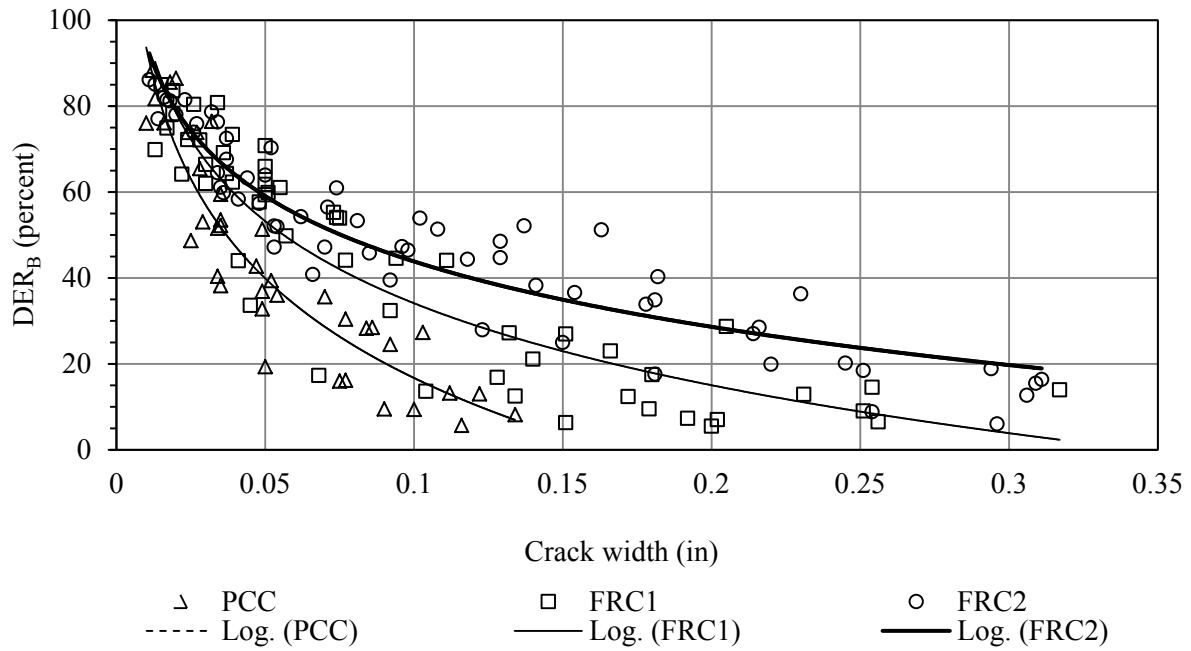
Figure 5.100. Comparison of DER_B results for all the beams for each of the three mixture types.

241

Table 5.16. Drop in DER$_B$ for B$_{ALT}$ specimens due to fatiguing.

Concrete Mixture	Specimen label	DER$_B$ drop due to fatiguing and crack width increase during fatiguing (total) (percent)	DER$_B$ drop due to crack width increase alone during fatiguing (percent)	Magnitude of increase in DER$_B$ to adjust for fatiguing (percent)
PC	P-1, 0.049-0.050, 0.1834	18	2	16
	P-2, 0.049-0.052, 0.1844	12	3	9
	P-3, 0.035, 0.1211	14	0	14
	P-4, 0.035, 0.2078	6	0	6
	P-5, NF, 0.1631	Not fatigued		
FRC1	F1-1, 0.050-0.051, 0.1597	6	1	5
	F1-2, 0.05, 0.1680	9	0	9
	F1-3, 0.037-0.043, 0.1614	14	4	10
	F1-4, 0.036-0.039, 0.1500	7	2	5
	F1-5, NF, 0.2026	Not fatigued		
FRC2	F2-1, 0.048-0.053, 0.1771	10	3	7
	F2-2, 0.05-0.054, 0.1417	12	4	8
	F2-3, 0.034-0.035, 0.2027	3	0	3
	F2-4, 0.034-0.037, 0.1490	8	1.5	6.5
	F2-5, NF, 0.1726	Not fatigued		

5.4.1.1 Regression models for DER$_B$

Similar to the regression models developed for the LTE$_B$ as a function of crack width in the B$_{ALT}$ procedure, regression models were also developed for the DER$_B$. The measured DER$_B$ values were adjusted for determining the corresponding non-fatigued DER$_B$. The measured DER$_B$ values were adjusted using the drop in DER$_B$ due to fatigue alone, as provided in Table 5.16.

242

PC beams

Logarithmic fit

Figure 5.101 and Figure 5.102 present the regression models developed with the original and non-fatigued DER_B, respectively, for the PC beams. Equations (5.41) and (5.42) present the developed regression models for original and non-fatigued DER_B, respectively. The R^2 for the models with the original and non-fatigued DER_B are 0.88 and 0.81, respectively, while the SE are 8.87 and 9.64, respectively.

Original

$$DER_B = -35.43 \ln (cw) - 64.349 \qquad (5.41)$$

Non-fatigued

$$DER_B = -28.44 \ln (cw) - 39.553 \qquad (5.42)$$
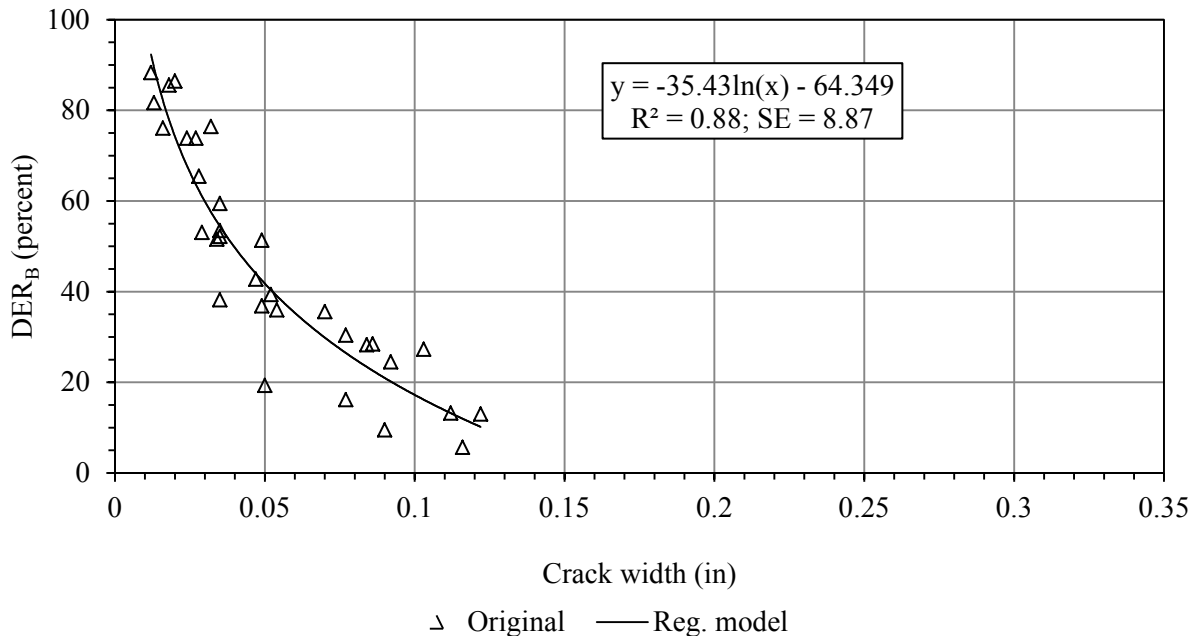
Figure 5.101. Relationship for original DER_B for the PC beams.

$$y = -28.44\ln(x) - 39.553$$
$$R^2 = 0.81; \; SE = 9.64$$

▲ Non-fatigued   —— Reg. model
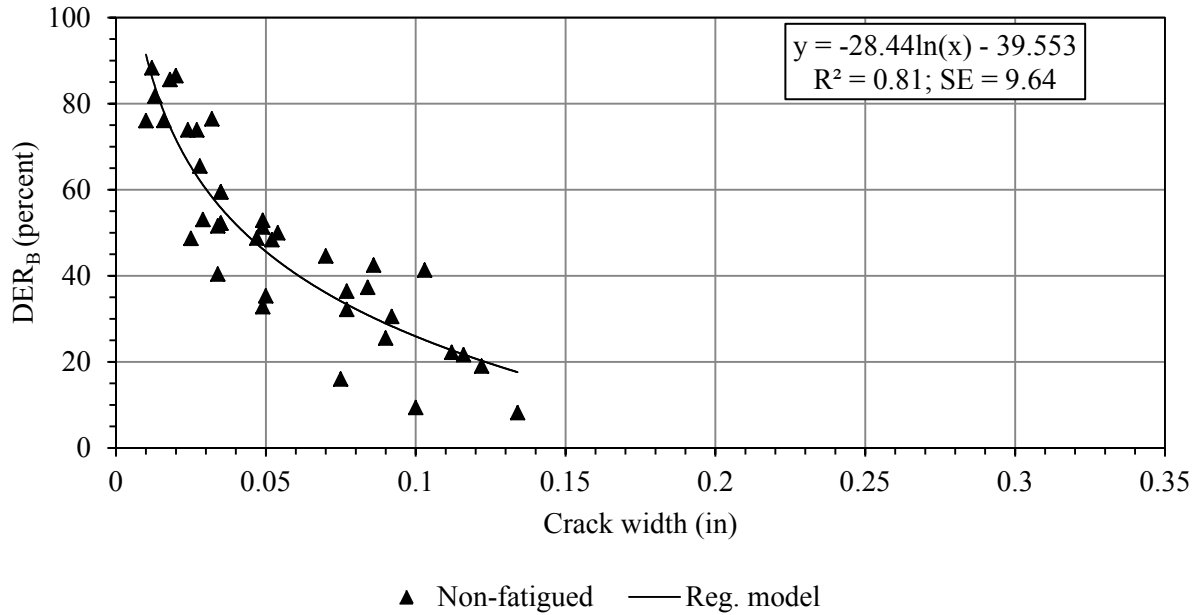
Figure 5.102. Relationship for non-fatigued DER_B for the PC beams.

Bi-linear fit

The bi-linear relationships developed for original and non-fatigued DER_B are presented in Figure 5.103 and Figure 5.104, respectively, for the PC beams. Based on the stepwise progressive regression procedure, the bi-linear split was obtained at 0.05-in crack width for both the models with original and non-fatigued DER_B. Regression models are presented in Equations (5.43) through (5.46). For the model with original DER_B, the R^2 for the first and second segments are 0.80 and 0.45, respectively, while the SE are 9.11 and 8.21, respectively. For the model with non-fatigued DER_B, the R^2 for the first and second segments are 0.68 and 0.51, respectively, while the SE are 9.70 and 9.40, respectively.

244
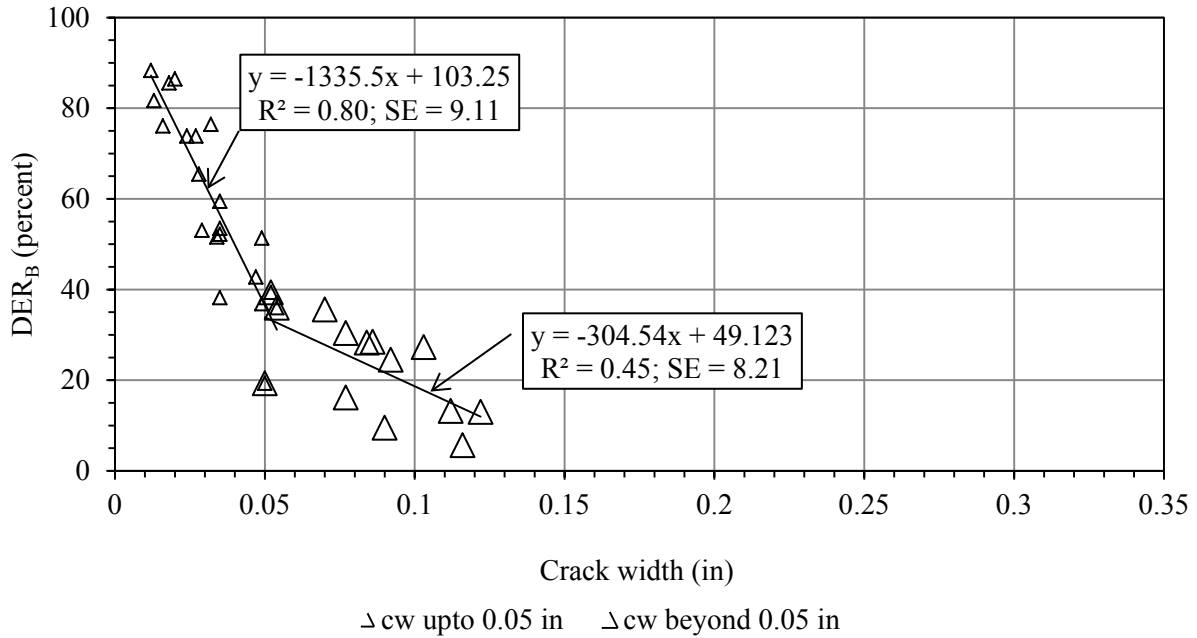
Figure 5.103. Relationship for original DER_B for the PC beams, bi-linear fit.
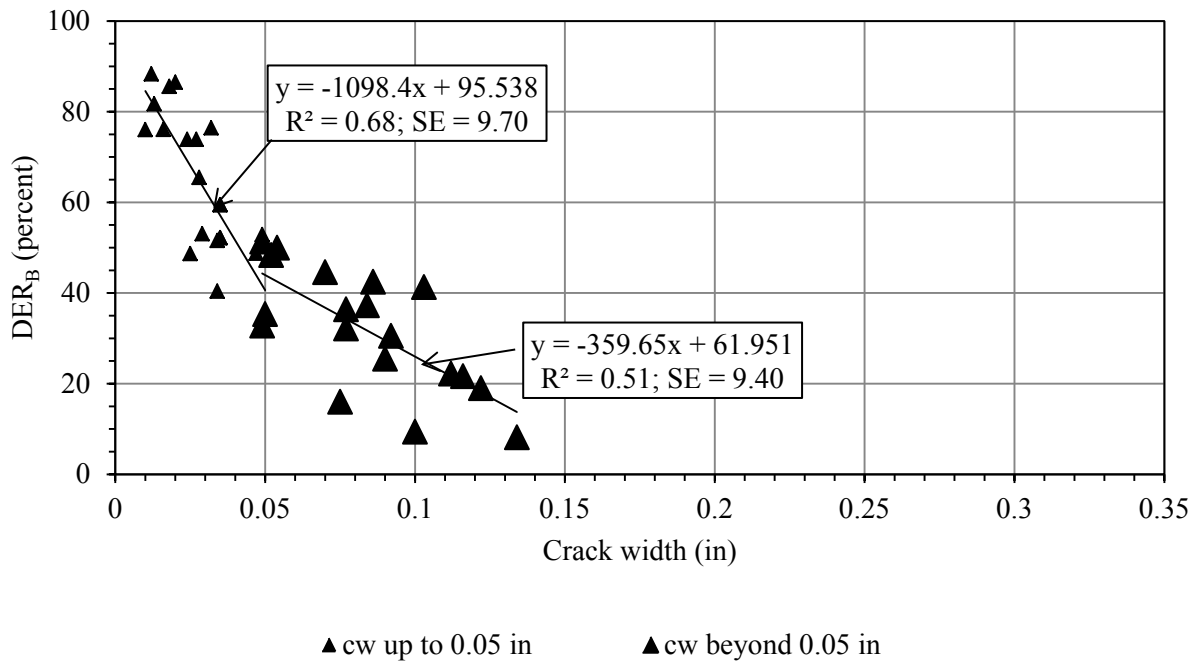
Figure 5.104. Relationship for non-fatigued DER_B for the PC beams, bi-linear fit.

245

Original

$$\text{cw up to 0.05 in: } DER_B = -1335.5 \ (cw) + 103.25 \qquad (5.43)$$

$$\text{cw beyond 0.05 in: } DER_B = -304.54 \ (cw) + 49.123 \qquad (5.44)$$

Non-fatigued

$$\text{cw up to 0.05 in: } DER_B = -1098.4 \ (cw) + 95.538 \qquad (5.45)$$

$$\text{cw beyond 0.05 in: } DER_B = -359.65 \ (cw) + 61.951 \qquad (5.46)$$

FRC1 beams

Logarithmic fit

Figure 5.105 and Figure 5.106 present the regression models for original and non-fatigued DER_B, respectively, for FRC1 beams. Equations (5.47) and (5.48) present the regression models for original and non-fatigued DER_B, respectively. The R^2 for the models with original and non-fatigued DER_B are 0.82 and 0.79, respectively, while the SE are 10.98 and 10.73, respectively.

Original

$$DER_B = -29.04ln(cw) - 34.317 \qquad (5.47)$$

Non-fatigued

$$DER_B = -26.32ln(cw) - 22.922 \qquad (5.48)$$

246

Figure 5.105. Relationship for original DER$_B$ for the FRC1 beams, logarithmic fit.

Figure 5.106. Relationship for non-fatigued DER$_B$ for the FRC1 beams, logarithmic fit.

247

Bi-linear fit

The bi-linear relationships developed for original and non-fatigued DER_B are presented in Figure 5.107 and Figure 5.108, respectively, for the FRC2 beams. Based on the stepwise progressive regression procedure, the bi-linear split was obtained at a 0.095-in crack width for the model with original DER_B and at a 0.134-in crack width for the model with non-fatigued DER_B. Regression models are presented in Equations (5.49) through (5.52). For the model with original DER_B, the R^2 for the first and second segments are 0.62 and 0.48, respectively, while the SE are 10.82 and 9.47, respectively. For the model with non-fatigued DER_B, the R^2 for the first and second segments are 0.69 and 0.21, respectively, while the SE are 9.74 and 8.08, respectively.
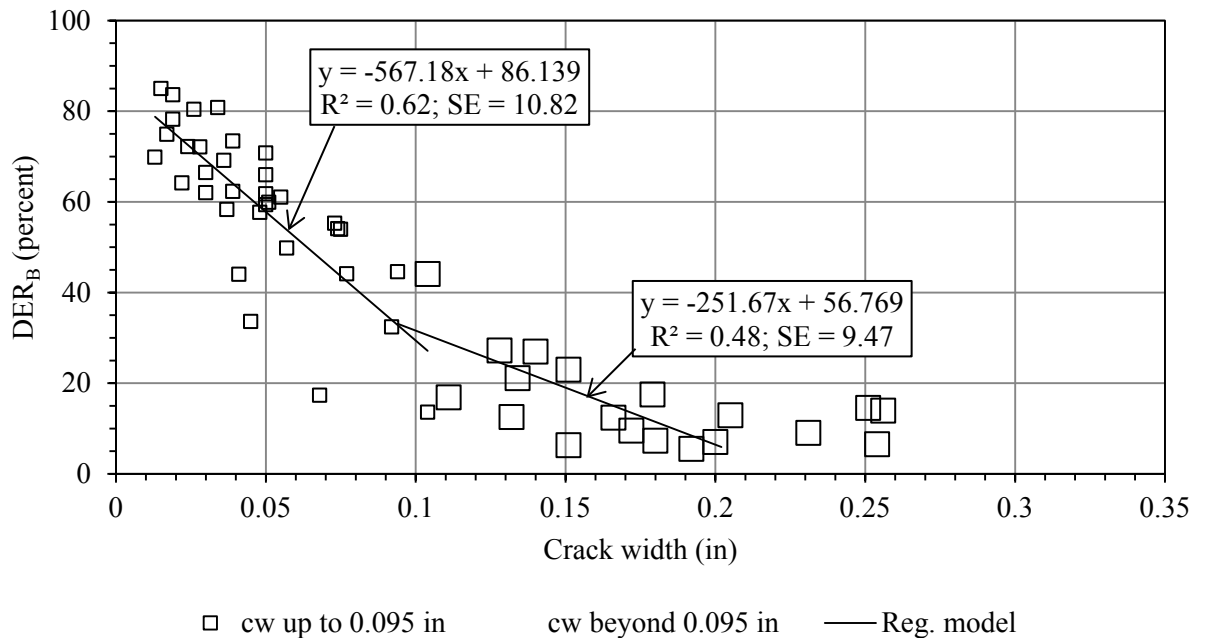
Figure 5.107. Relationship for original DER_B for the FRC1 beams, bi-linear fit.

248
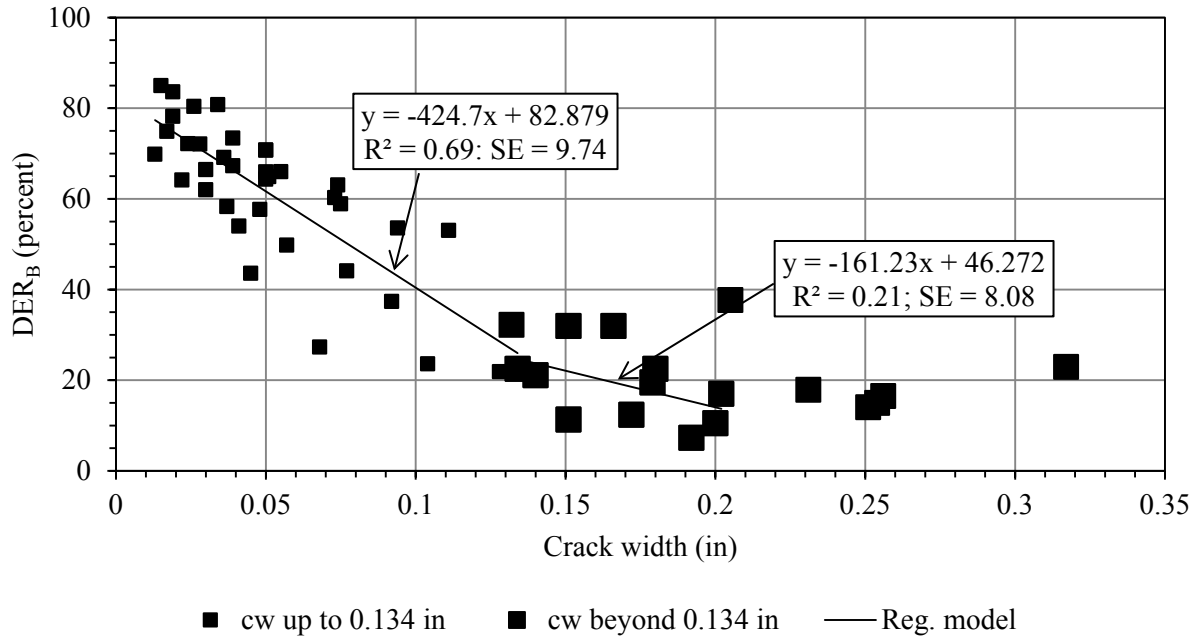
Figure 5.108. Relationship for non-fatigued DER_B for the FRC1 beams, bi-linear fit.

Original

$$\text{cw up to 0.10 in: } DER_B = -567.18\ (cw) +\ 86.139 \tag{5.49}$$

$$\text{cw beyond 0.10 in: } DER_B = -251.67\ (cw) + 56.769 \tag{5.50}$$

Non-fatigued

$$\text{cw up to 0.134 in: } DER_B = -424.7\ (cw)\ + 82.879 \tag{5.51}$$

$$\text{cw beyond 0.134 in: } DER_B = -161.23\ (cw)\ \ + 46.272 \tag{5.52}$$

FRC2 beams

Logarithmic fit

Figure 5.109 and Figure 5.110 present the regression models for original and non-fatigued DER_B, respectively, for FRC2 beams. Equations (5.53) and (5.54) present the developed

249

regression models for original and non-fatigued DER_B, respectively. The R^2 for the models with original and non-fatigued DER_B are 0.86 and 0.79, respectively. The R^2 was obtained as the highest when all the data were considered in both the models. The SE for the models with original and non-fatigued DER_B are 7.71and 8.81, respectively.

Original

$$DER_B = -21.42 \ln (cw)-6.2188 \qquad (5.53)$$

Non-fatigued

$$DER_B = 20.08 \ln (cw)+ 1.2093 \qquad (5.54)$$
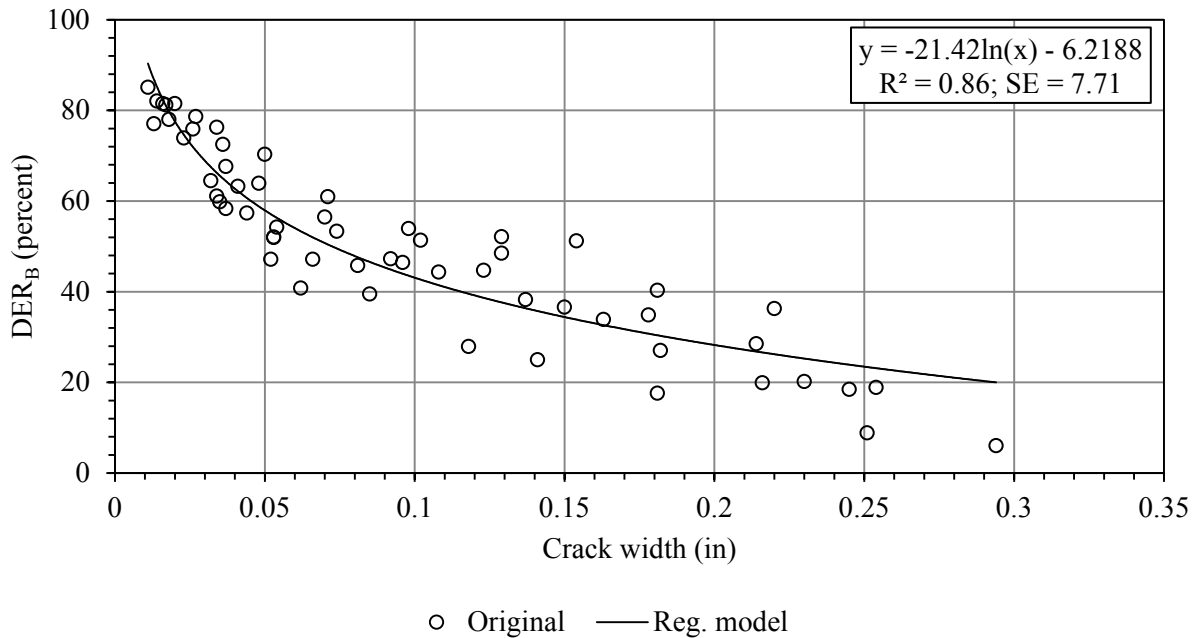
Figure 5.109. Relationship for original DER_B for FRC2 beams, logarithmic fit.

$$y = -20.08\ln(x) + 1.2093$$
$$R^2 = 0.79; \ SE = 8.81$$

● Non-fatigued — Reg. model
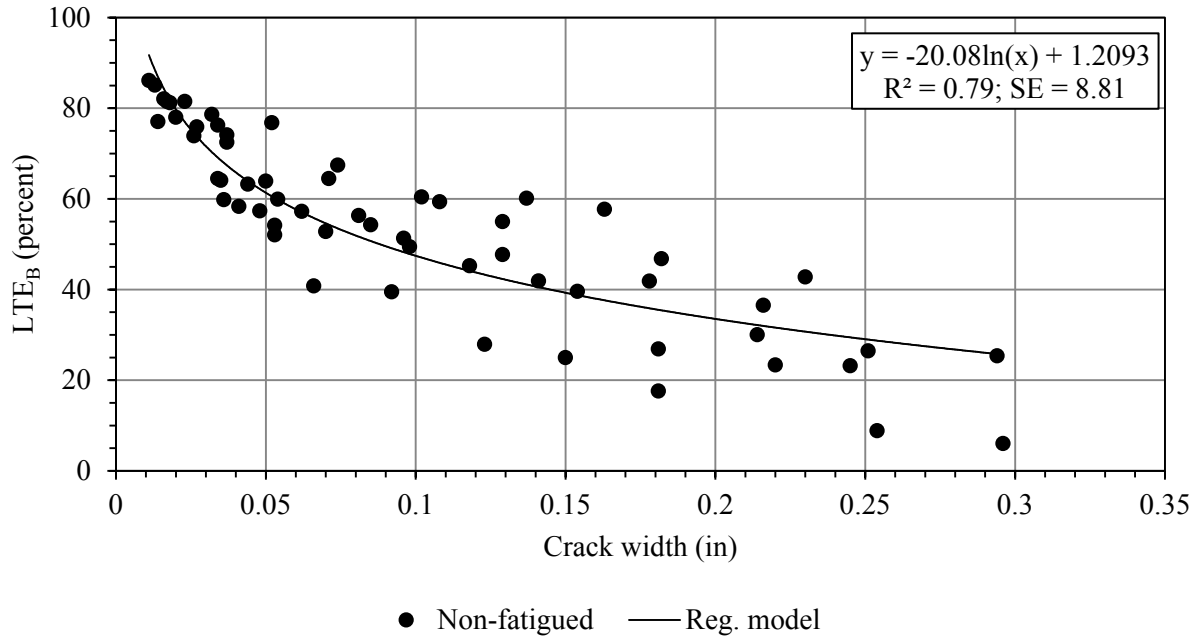
Figure 5.110. Relationship for non-fatigued DER_B for FRC2 beams, logarithmic fit.

Bi-linear fit

The bi-linear relationships developed for original and non-fatigued DER_B are presented in Figure 5.111 and Figure 5.112, respectively, for the FRC2 beams. Based on the stepwise progressive regression procedure, the bi-linear split was obtained at 0.055-in crack width for the model with original DER_B and at 0.060-in crack width for the model with non-fatigued DER_B. Regression models are presented in Equations (5.55) through (5.58). For the model with original DER_B, the R^2 for the first and second segments are 0.81 and 0.72, respectively, while the SE are 7.91 and 8.0, respectively. For the model with non-fatigued DER_B, the R^2 for the first and second segments are 0.83 and 0.72, respectively, while the SE are 7.68 and 7.85, respectively.

251
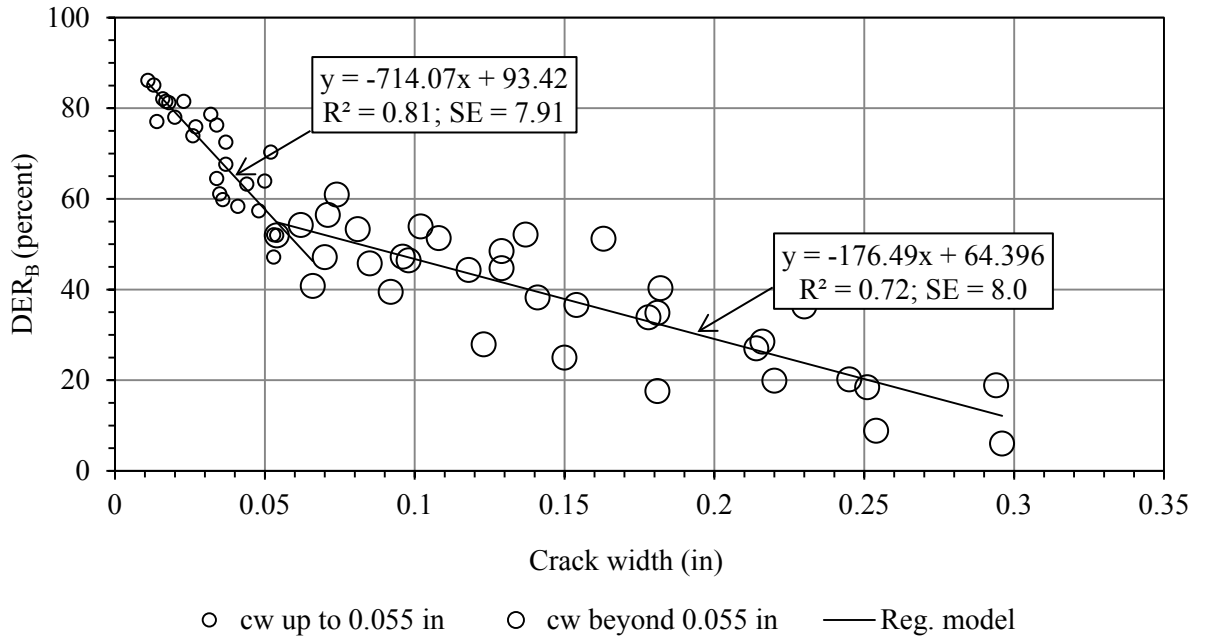
Figure 5.111. Relationship for original DERB for FRC2 beams, bi-linear fit.
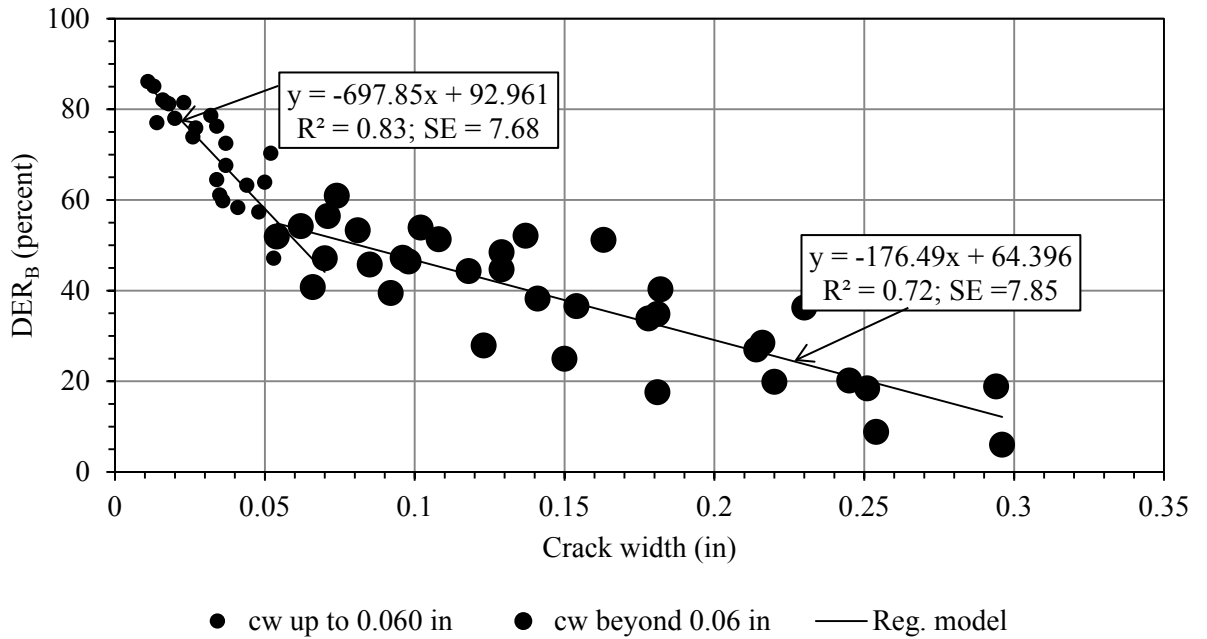
Figure 5.112. Relationship for non-fatigued DERB for FRC2 beams, bi-linear fit.

Original

$$\text{cw up to 0.055 in: } DER_B = -714.07 \ (cw) + 93.42 \qquad (5.55)$$

$$\text{cw beyond 0. 055 in: } DER_B = -176.49 \ (cw) + 64.396 \qquad (5.56)$$

Non-fatigued

$$\text{cw up to 0.060 in: } DER_B = -697.85 \ (cw) + 92.961 \qquad (5.57)$$

$$\text{cw beyond 0.060 in: } DER_B = -176.49(cw) + 64.396 \qquad (5.58)$$

Finally, the comparison between all the regression models reveal that the bi-linear fit provides better prediction for all the mixtures with a relatively lower standard deviation.

Comparison of DER_B predicted by the regression models between the three mixtures

Table 5.17 presents a comparison between the non-fatigued DER_B values for the three mixtures predicted by the bi-linear models. Different crack widths ranging from 0.020 to 0.10 in are considered for the comparison. Table 5.18 presents the benefits in DER_B that can be achieved by using FRC mixtures. While the benefits are apparent, but not consistent over the crack widths.

Table 5.17. Comparison of non-fatigued DER_B between different mixtures.

Crack width (in)	PC	FRC1	FRC2
0.02	74	74	79
0.03	63	70	72
0.04	52	66	65
0.05	41	62	58
0.06	40	57	55
0.07	37	53	53
0.08	33	49	51
0.09	30	45	49
0.10	26	40	48

253

Table 5.18. Percent increase in non-fatigued DER$_B$ when using FRC mixtures as compared to PC mixture.

Crack width (in)	FRC1	FRC2
0.02	1	7
0.03	12	15
0.04	28	26
0.05	52	43
0.06	42	35
0.07	45	44
0.08	47	54
0.09	51	67
0.10	1	7

5.4.2 S$_{ALT}$

The values of DER for the S$_{ALT}$ (DER$_S$) for the three slab specimens are presented in this subsection. The procedure outlined in Chapter 3.0 is referred to for calculating DER$_S$. Figure 5.113 through Figure 5.115 show the original DER$_S$ vs crack for PC, FRC1 and FRC2 slabs respectively. The averages of the original DER$_S$ for all the three slabs are compared in Figure 5.116. Similar to the LTEs vs cw relationships in the S$_{ALT}$, the PC slab exhibited lower DER$_S$ as compared to the other two slabs. FRC1 and FRC2 exhibits a similar DER$_S$ vs crack width relationship. The difference in the DER$_S$ between the PC and FRC mixtures slightly increases with the crack width. For example, at 0.05-in crack width, the difference is 25 to 28 percent and at 0.10-in crack width, this difference increases to 26 to 30 percent.

Table 5.19 presents the drop in DER$_S$ due to fatigue alone, crack width increase during fatiguing and the magnitude of DER$_S$ that is required to add to obtain no-fatigued DER$_S$ for all the slabs. PC slab experienced the highest drop in DER$_S$ due to fatiguing.

254
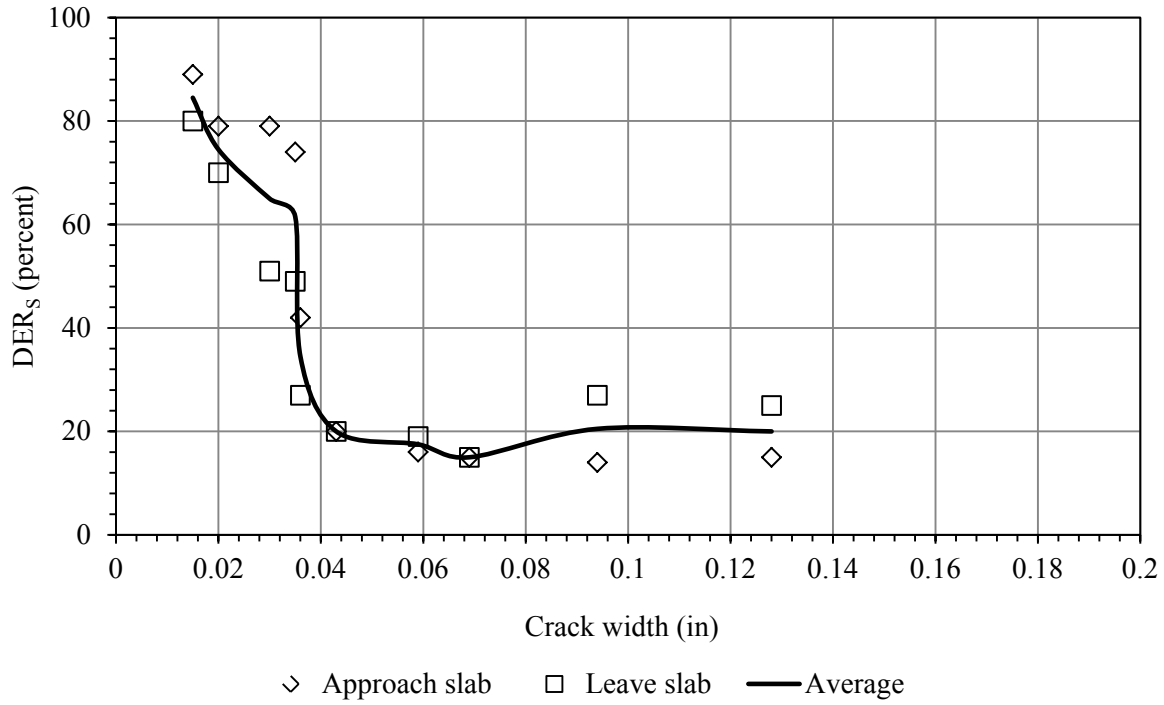
Figure 5.113: Original DER$_S$ vs crack width for PC slab.
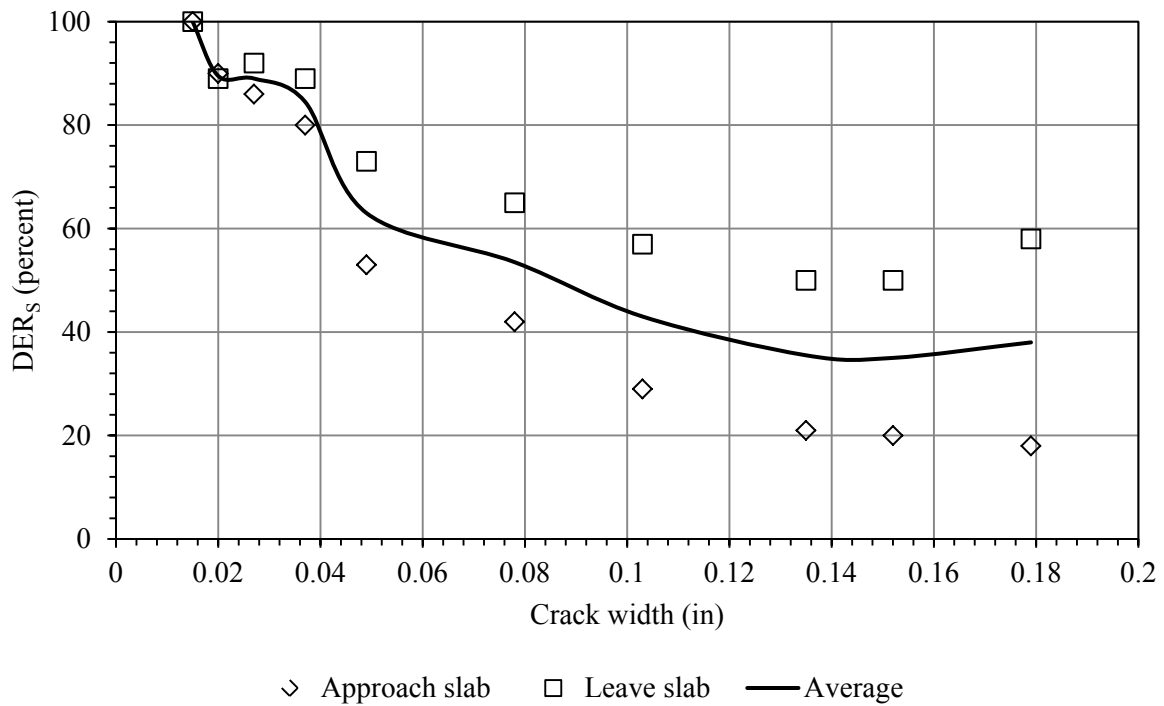
Figure 5.114: Original DER$_S$ vs crack width for FRC1 slab.
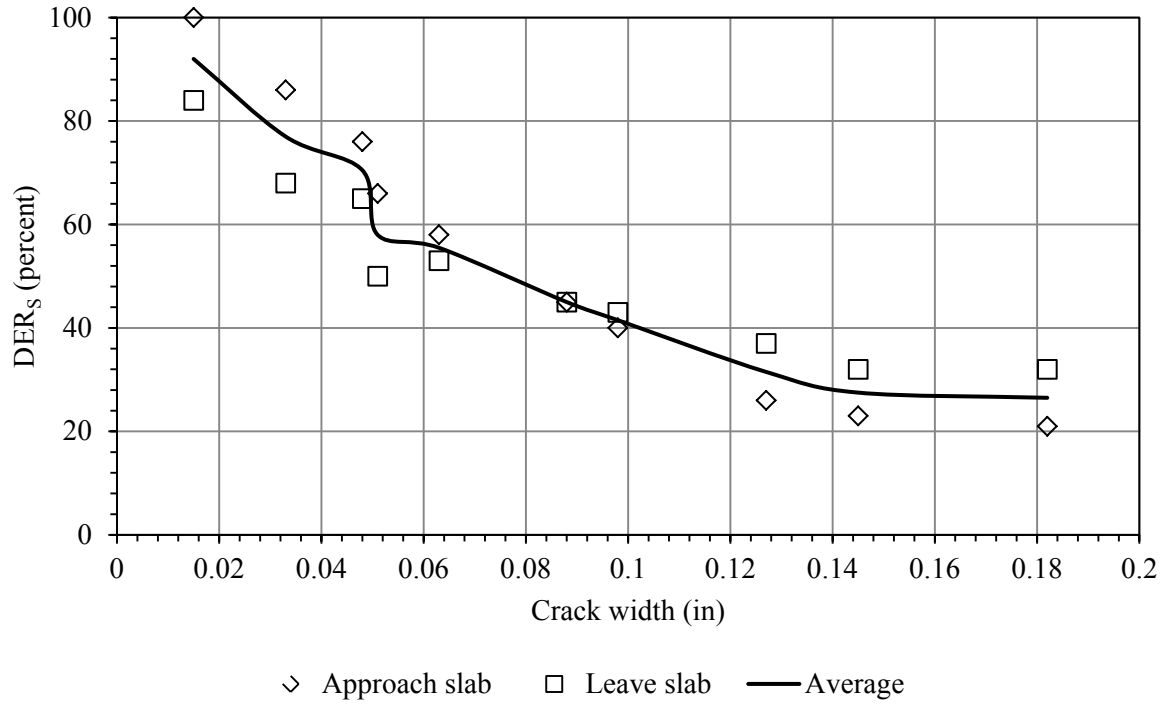
Figure 5.115: Original DERS vs crack width for FRC2 slab.
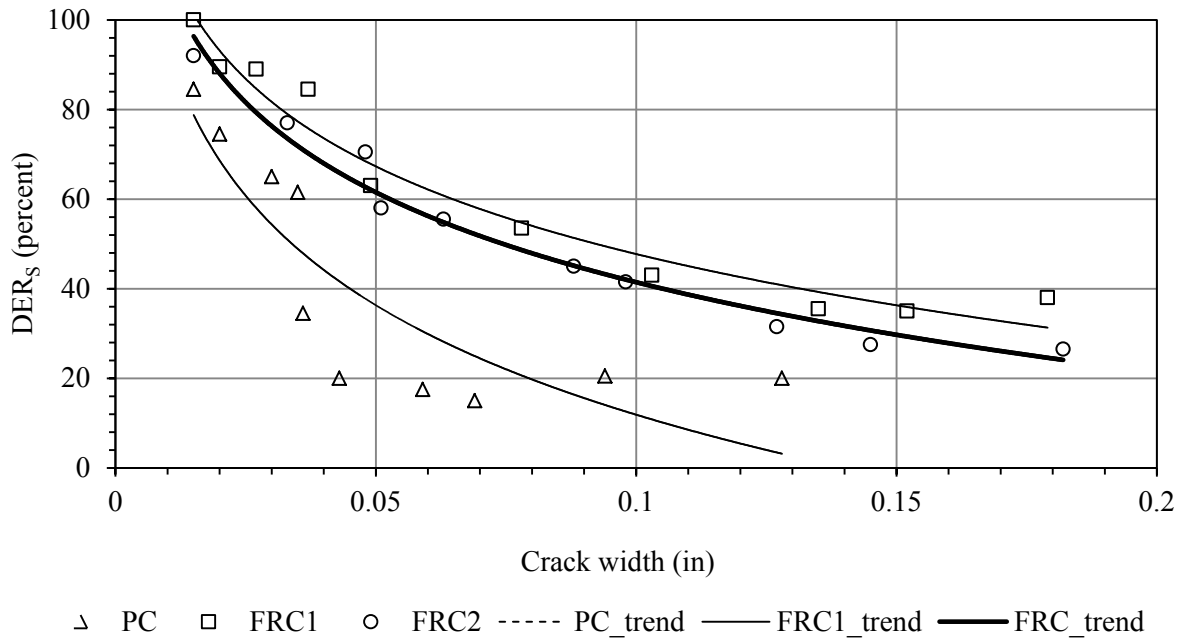
Figure 5.116: Comparison of the averages of the original DER_S vs crack width between the three slabs.

256

Table 5.19. Drop in DER$_S$ due to fatigue for the three slabs.

Slab type	DER$_S$ drop due to fatiguing and crack width increase during fatiguing (total) (percent)	DER$_S$ drop due to crack width increase alone during fatiguing (percent)	Magnitude of increase in DER$_S$ to adjust for fatiguing (percent)
PC slab	28	2	26
FRC1 slab	22	9	13
FRC2 slab	13	2	11

5.4.2.1 Regression models for DER$_S$

PC slab

Logarithmic fit

Figure 5.117 and Figure 5.118 show the regression relationships developed for the original and non-fatigued DERs, respectively, for the PC slab. To obtain the non-fatigued DER$_S$ at the crack widths beyond the fatiguing crack width, a 12 percent DER$_S$ was added. This 12 percent DER$_S$ is equivalent to the DER$_S$ drop due to fatiguing alone. Equations (5.59) and (5.60) present the regression models developed with the original and non-fatigued DER$_S$, respectively. The R^2 for the original and non-fatigued models are 0.76 to 0.79, respectively, while the SE are 14.05 and 7.3, respectively.

Original
$$DERs = -35.26 \ln (cw) - 69.305 \tag{5.59}$$

Non-fatigued
$$DERs = -20.2 \ln (cw) - 7.0471 \tag{5.60}$$

257
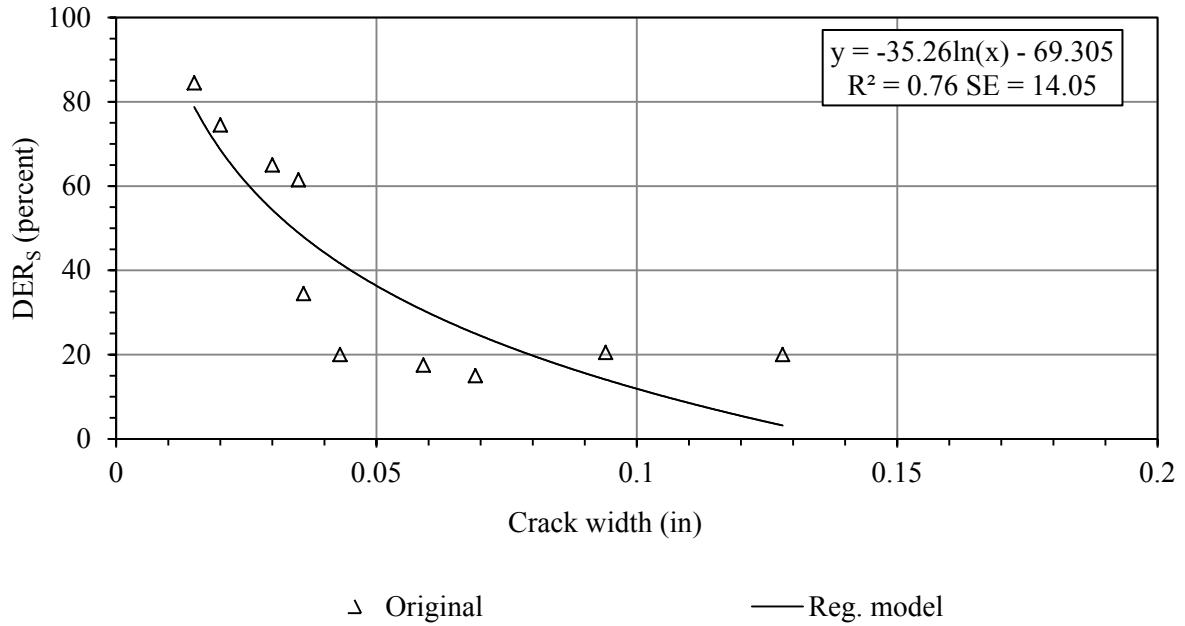
Figure 5.117. Relationship for original DER_S for the PC slab, logarithmic fit.
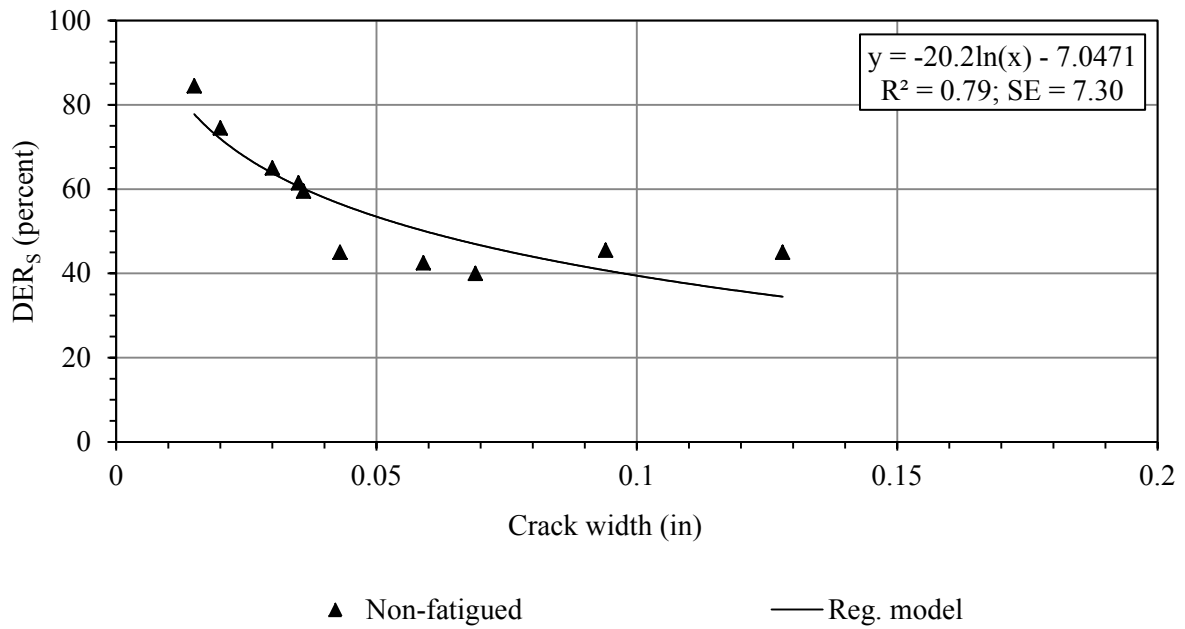
Figure 5.118. Relationship for non-fatigued DER_S for the PC slab, logarithmic fit.

258

Bi-linear fit

The bi-linear relationships developed for the original and non-fatigued DER$_S$ are presented in

Figure 5.119 and Figure 5.120, respectively. The bi-linear split was obtained through a stepwise

progressive regression. In both the original and non-fatigued DER$_S$ models, bi-linear split was

obtained at 0.050-in crack width. Regression models are presented in Equations (5.61) through

(5.64). For the model with original DER$_S$, the R^2 for the first and second segments are 0.84 and

0.15, respectively, while the SE are 11.84 and 7.01, respectively. For the model with non-

fatigued DER$_S$, the R^2 for the first and second segments are 0.92 and 0.15, respectively, while the

SE are 6.68 and 7.23, respectively.
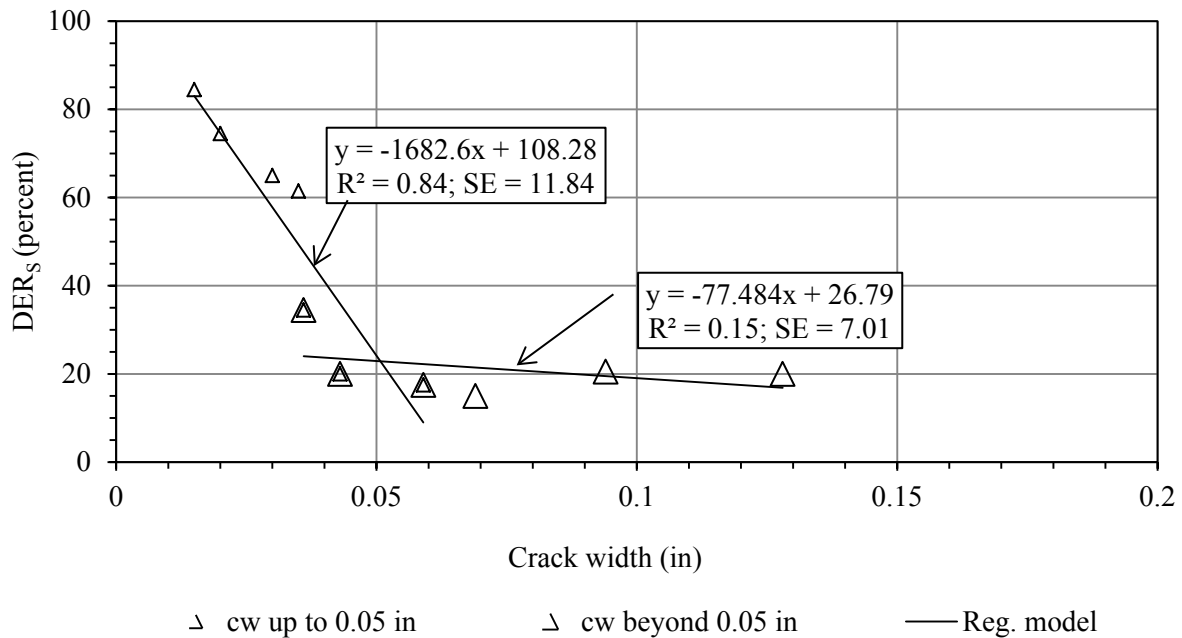
Figure 5.119. Relationship for original DER$_S$ for the PC slab, bi-linear fit.
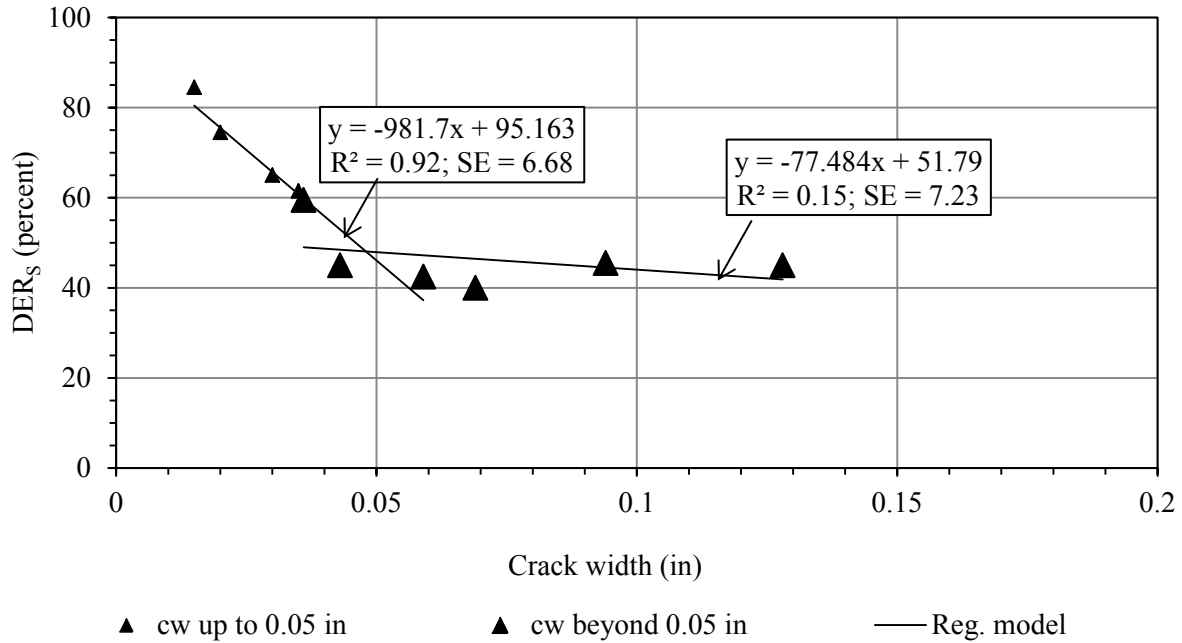
Figure 5.120. Relationship for non-fatigued DER$_S$ for the PC slab, bi-linear fit.

Original

$$\text{cw up to 0.05 in: } DER_S = -1682.6 \ (cw) + 108.28 \tag{5.61}$$

$$\text{cw beyond 0. 05 in: } DER_S = -77.484 \ (cw) + 26.79 \tag{5.62}$$

Non-fatigued

$$\text{cw up to 0.05 in: } DER_S = -981.7 \ (cw) + 95.163 \tag{5.63}$$

$$\text{cw beyond 0.05 in: } DER_S = -77.484 \ (cw) + 51.79 \tag{5.64}$$

FRC1 slab

Logarithmic fit

Figure 5.121 and Figure 5.122 show the regression relationships developed for the original and non-fatigued DER$_S$, respectively. To obtain the non-fatigued DER$_S$ at the crack widths beyond the fatiguing crack width, a 13 percent DER$_S$ was added. This 13 percent DER$_S$ is assumed to be

260

equivalent to the DER_S drop only due to fatiguing. Equations (5.65) and (5.66) present the regression models developed with the original and non-fatigued DERs, respectively. The R^2 for models with original and non-fatigued DER_S are 0.97 and 0.98, respectively, while SE for the two models are 4.59 and 3.02.

Original

$$DER_S = -29.67ln\ (cw) - 22.297 \tag{5.65}$$

Non-fatigued

$$DER_S = -22.53ln\ (cw) + 6.169 \tag{5.66}$$
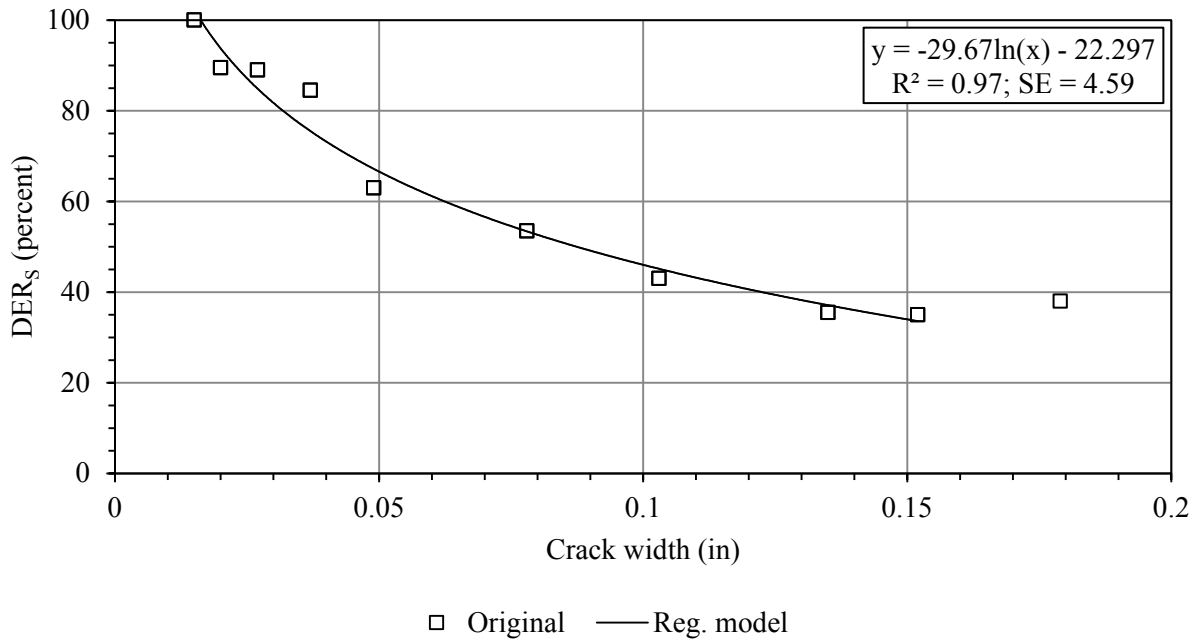
Figure 5.121. Relationship for original DER_S for the FRC1 slab, logarithmic fit.
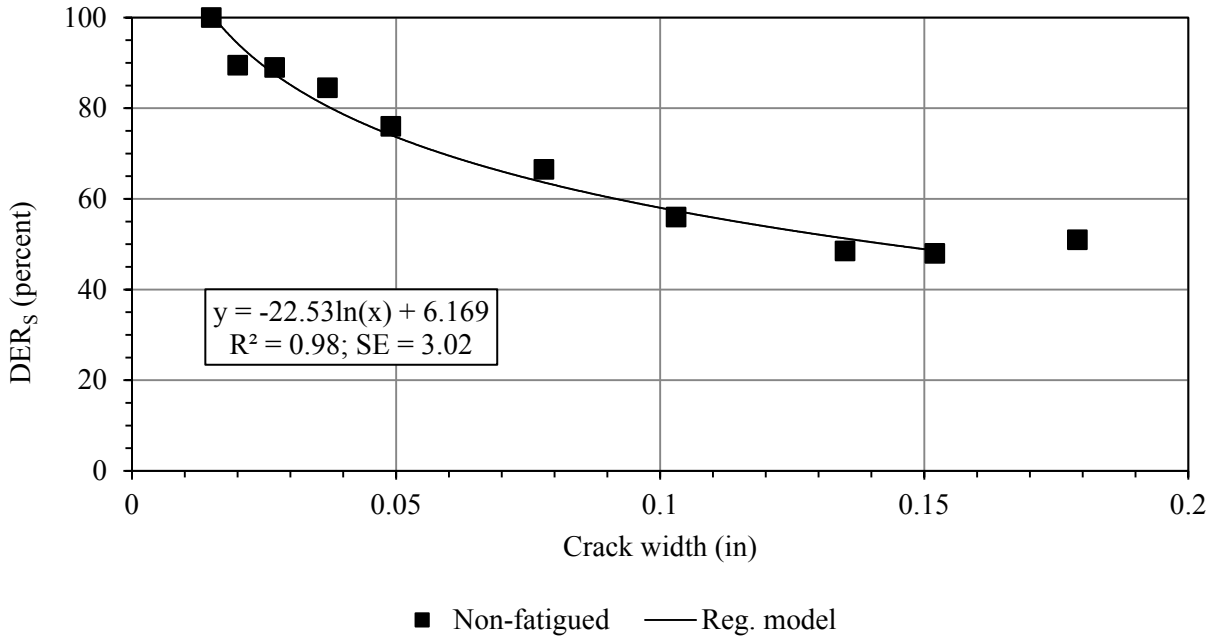
Figure 5.122. Relationship for non-fatigued DER_S for the FRC1 slab, logarithmic fit.

Bi-linear fit

The bi-linear relationships developed for the original and non-fatigued DER_S are presented in Figure 5.123 and Figure 5.124, respectively. In both the original and non-fatigued DER_S models, bi-linear split was obtained at 0.10-in crack width. Regression models are presented in Equations (5.67) through (5.70). For the model with original DER_S, the R^2 for the first and second segments are 0.94 and 0.92, respectively, while the SE are 5.84 and 1.82, respectively. For the model with non-fatigued DER_S, the R^2 for the first and second segments are 0.96 and 0.92, respectively, while the SE are 4.44 and 1.83, respectively.

262
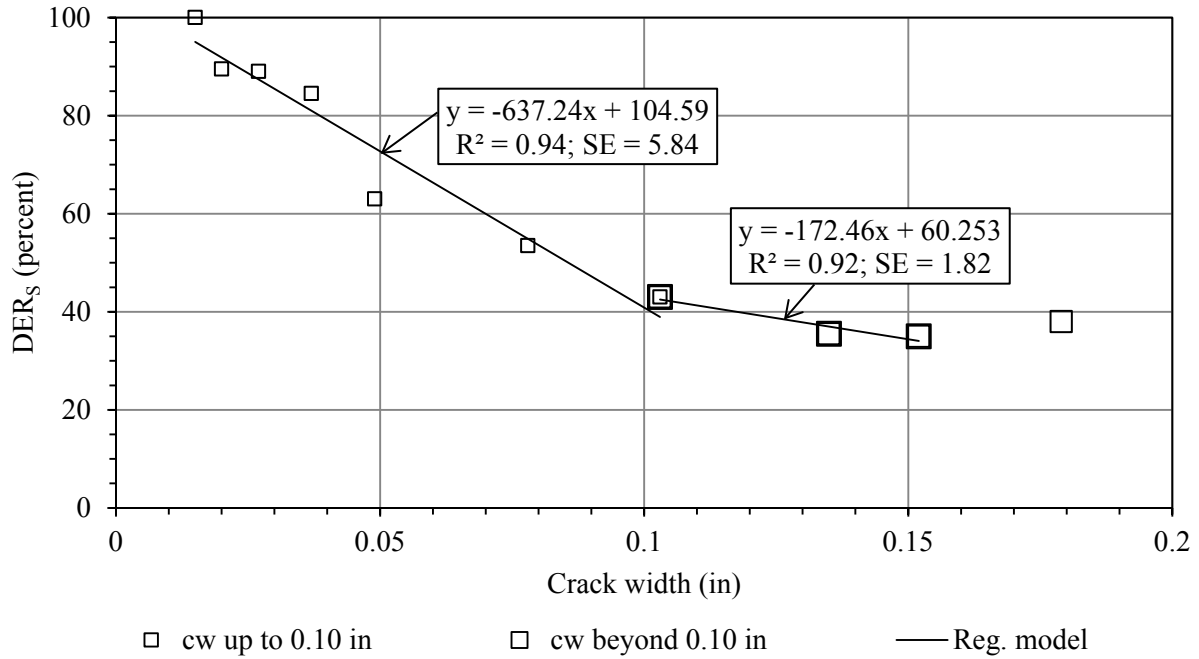
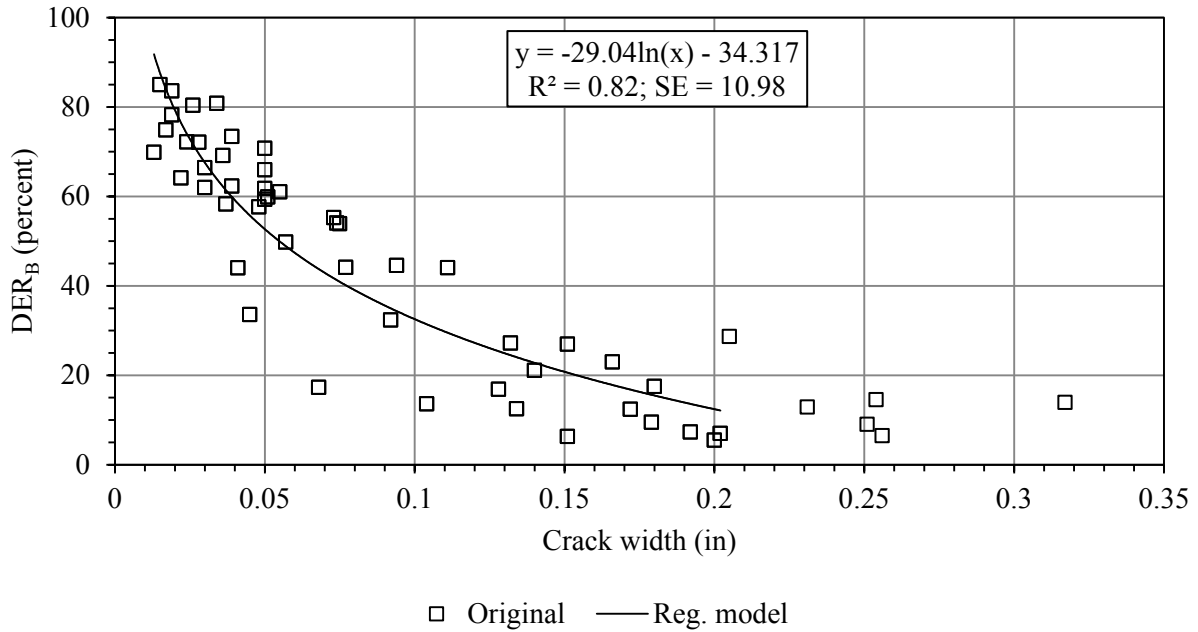Figure 5.123. Relationship for original DER_S for the FRC1 slab, bi-linear fit.
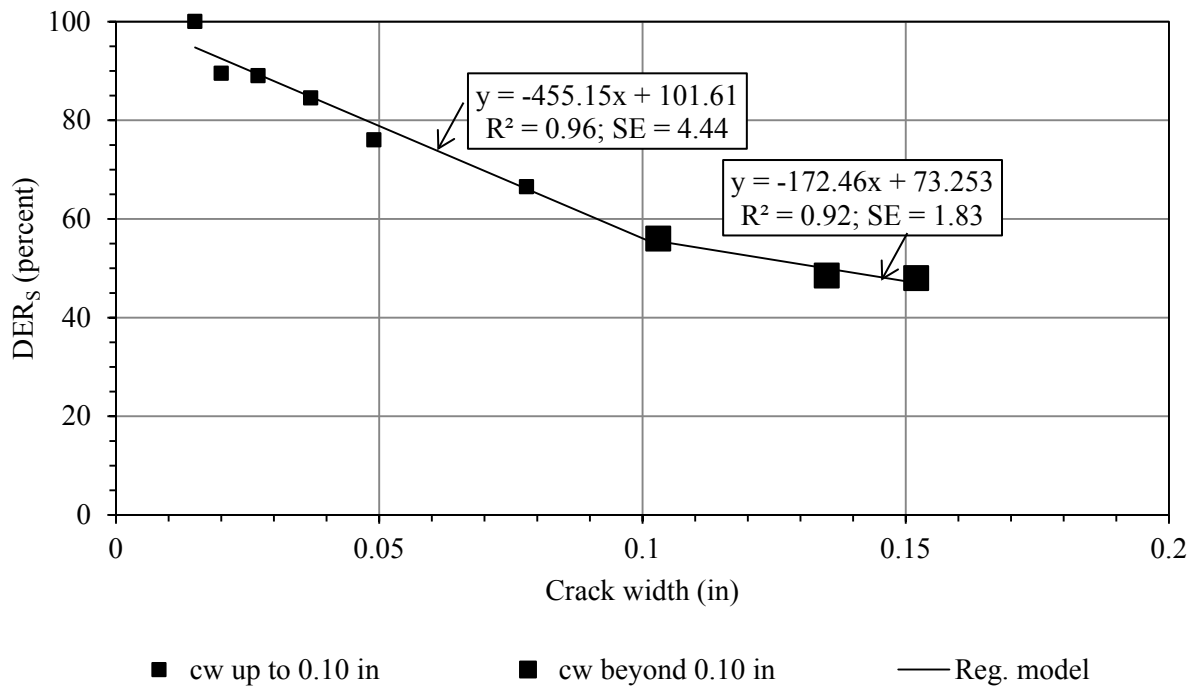
Figure 5.124. Relationship for non-fatigued DER_S for the FRC1 slab, bi-linear fit.

263

Original

$$\text{cw up to 0.10 in: } DER_S = -637.24 \ (cw) \ + 104.59 \tag{5.67}$$

$$\text{cw beyond 0. 10 in: } DER_S = -172.46(cw) \ + 60.253 \tag{5.68}$$

Non-fatigued

$$\text{cw up to 0.10 in: } DER_S = -455.15 \ (cw) \ + 101.61 \tag{5.69}$$

$$\text{cw beyond 0.10 in: } DER_S = -172.46(cw) \ + 73.253 \tag{5.70}$$

FRC2 slab

Logarithmic fit

Figure 5.125 and Figure 5.126 show the regression relationships developed for the original and non-fatigued DERs, respectively. To obtain the non-fatigued DERs at the crack widths beyond the fatiguing crack width, a 3 percent DERs was added. This 3 percent DERs is equivalent to the DERs drop due to fatiguing alone. Equations (5.71) and (5.72) present the regression models developed with the original DERs and non-fatigued DERs, respectively. The R^2 for both the original and non-fatigued DER_S models are 0.97 and 0.98, respectively, while the SE are 4.02 and 2.99, respectively.

Original

$$DERs = -29.59ln \ (cw) - 27.242 \tag{5.71}$$

Non-fatigued

$$DERs = -23.41ln \ (cw) - 2.6246 \tag{5.72}$$

264
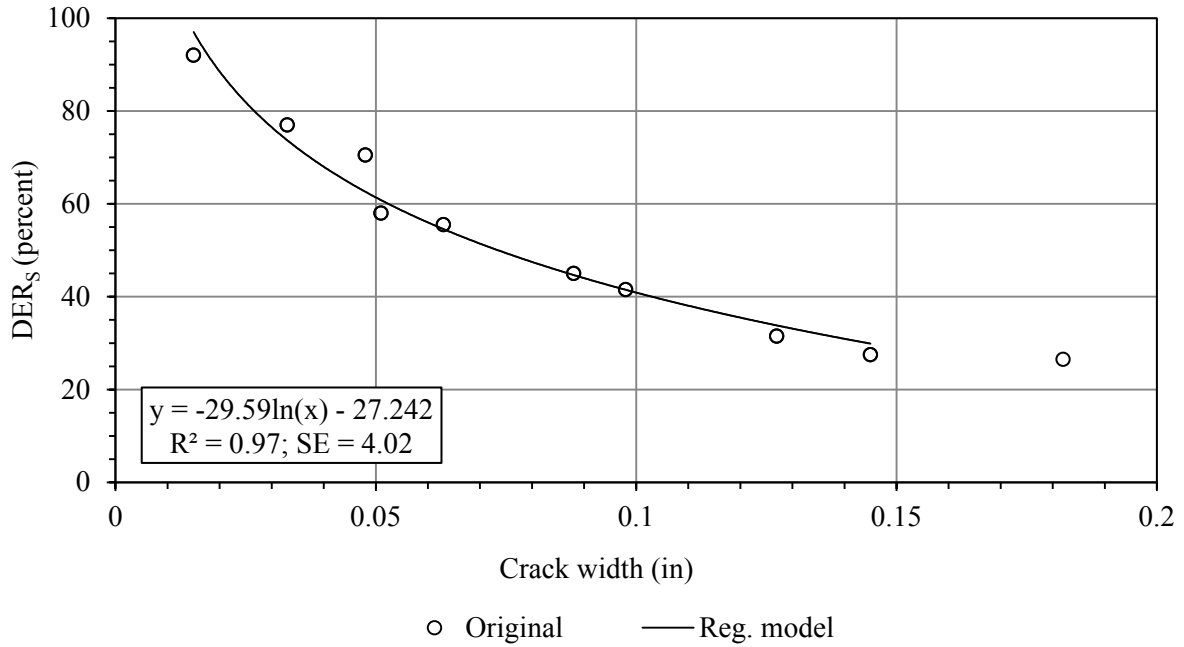
Figure 5.125. Relationship for original DER$_S$ and crack width for the FRC2 slab, logarithmic fit.
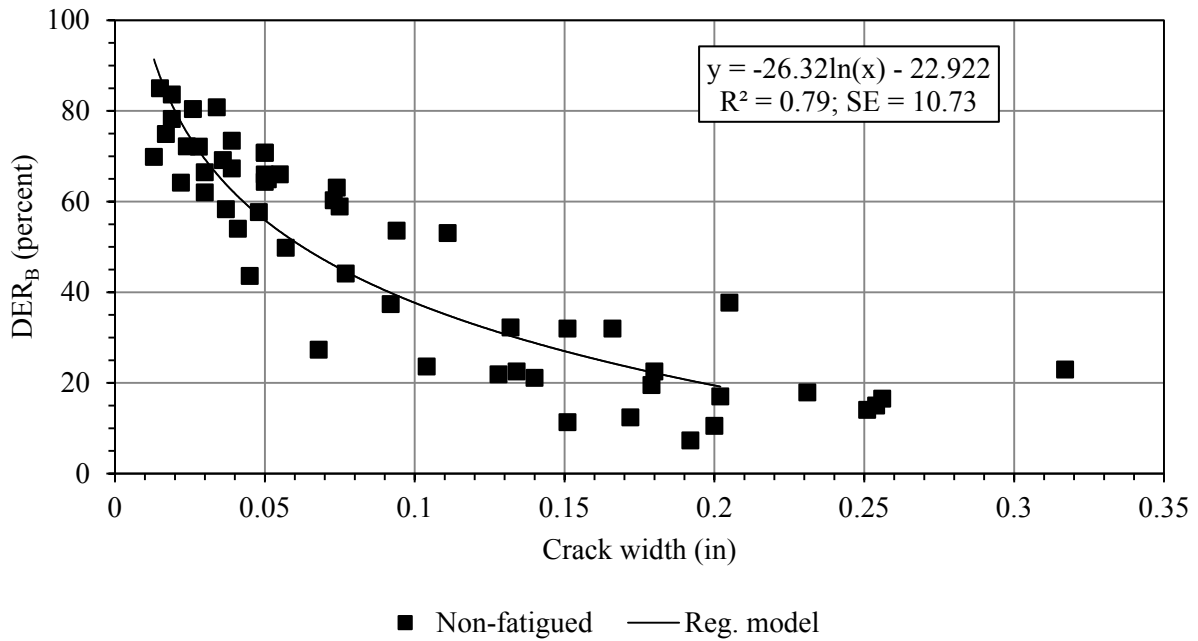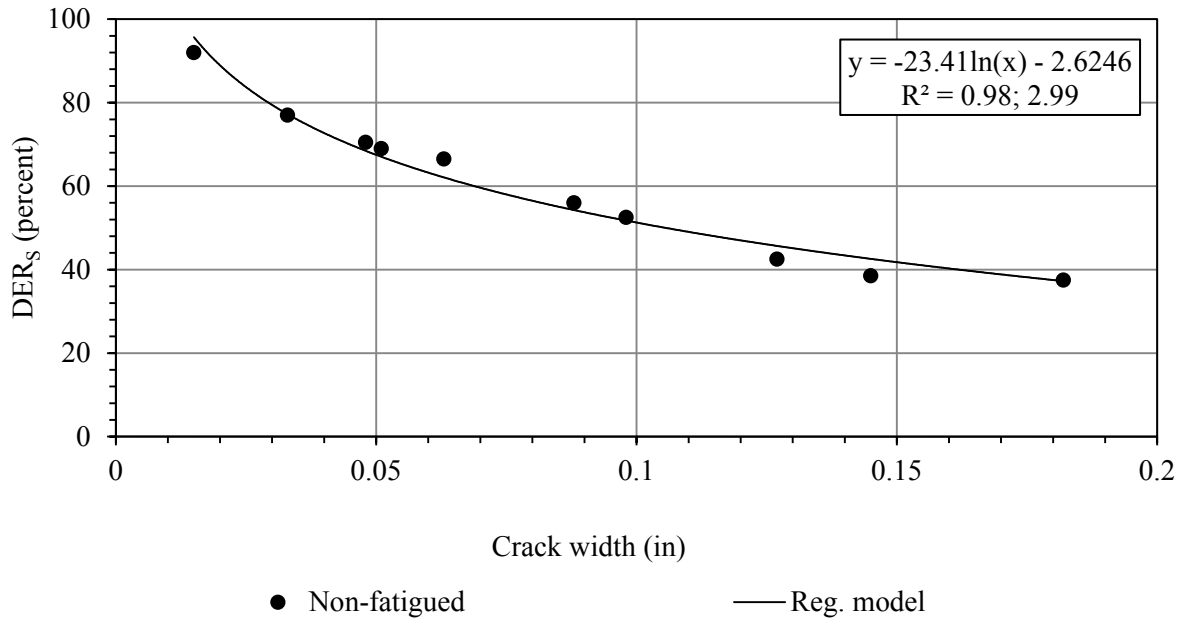

Figure 5.126. Relationship for non-fatigued DER$_S$ for the FRC2 slab, logarithmic fit.

265

Bi-linear fit

The bi-linear relationships developed for the original and non-fatigued DER_S are presented in Figure 5.127 and Figure 5.128, respectively. In both the original and non-fatigued DER_S models, bi-linear split was obtained at 0.10-in crack width. Regression models are presented in Equations (5.73) through (5.76). For the model with original DER_S, the R^2 for the first and second segments are 0.94 and 0.81, respectively, while the SE are 4.83 and 3.7, respectively. For the model with non-fatigued DER_S, the R^2 for the first and second segments are 0.96 and 0.81, respectively, while the SE are 2.92 and 3.70, respectively.
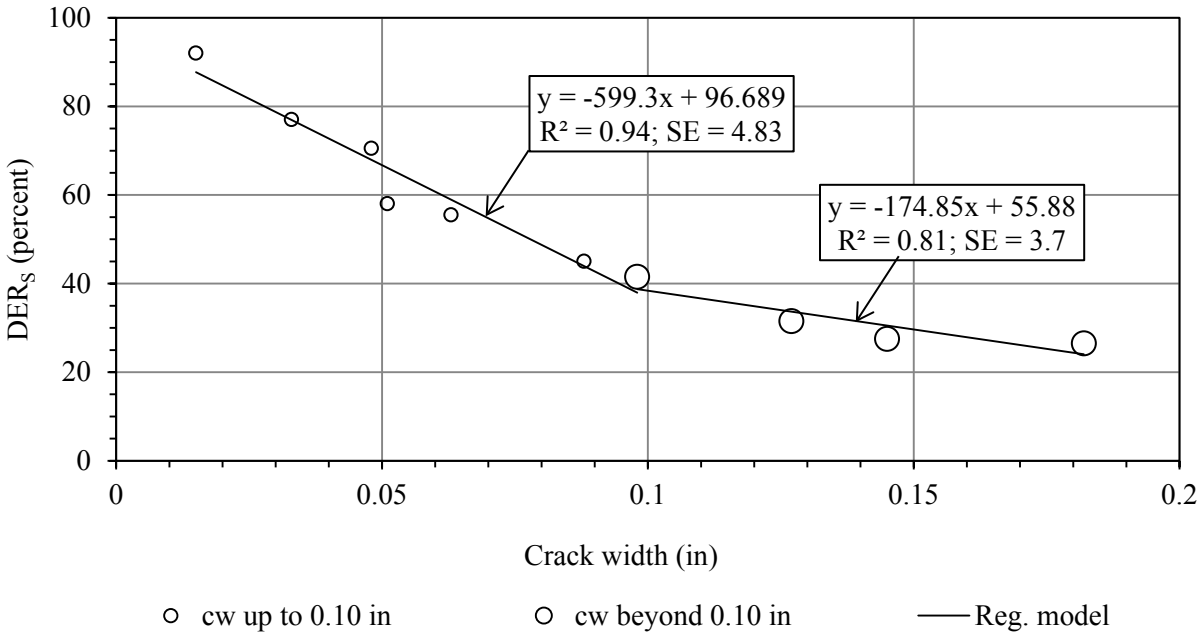
Figure 5.127. Relationship for original DER_S and crack width for the FRC2 slab, bi-linear fit.
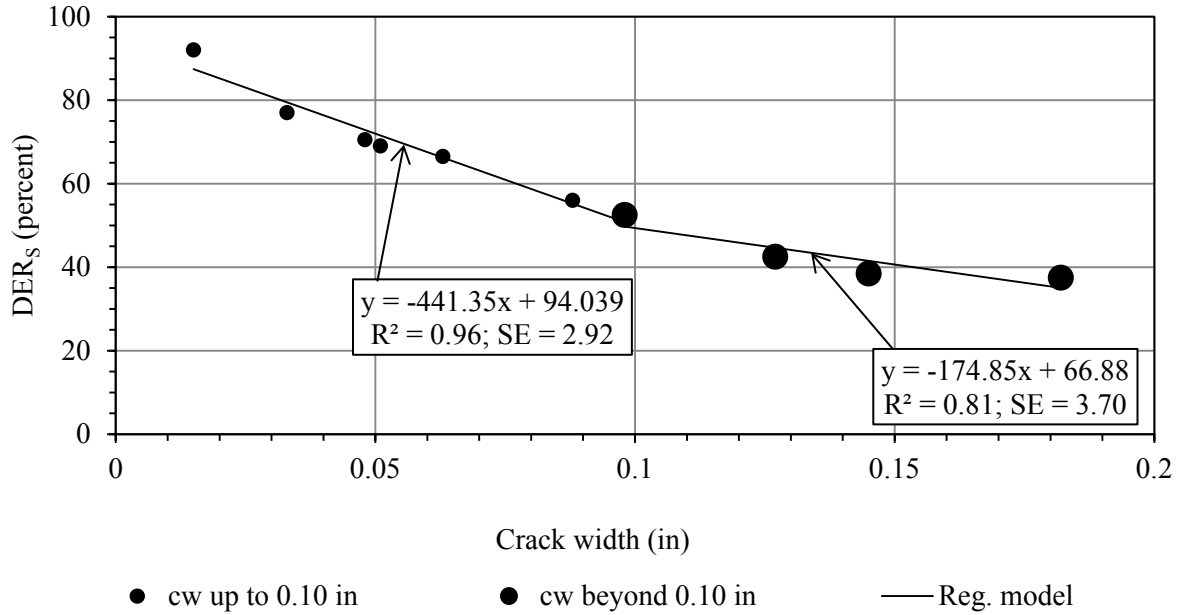
Figure 5.128. Relationship for non-fatigued DER_S and crack width for the FRC2 slab, bi-linear fit.

Original

$$\text{cw up to 0.10 in: } DER_S = -599.3 \, (cw) + 96.689 \tag{5.73}$$

$$\text{cw beyond 0.10 in: } DER_S = -174.85 \, (cw) + 55.88 \tag{5.74}$$

Non-fatigued

$$\text{cw up to 0.10 in: } DER_S = -441.35 \, (cw) + 94.039 \tag{5.75}$$

$$\text{cw beyond 0.10 in: } DER_S = -174.85 \, (cw) + 66.88 \tag{5.76}$$

Finally, the general comparison between all the models for DER_S reveals that the best fit between the DER_S and crack width for FRC1 mixture was obtained using logarithmic fit and bi-linear models provides the best fit for the other two mixtures.

267

Comparison of DERs predicted by the regression models between the three mixtures

Table 5.20 presents a comparison between the non-fatigued DER_S for the three mixtures predicted by the logarithmic models. Different crack widths ranging from 0.020 to 0.10 in are considered for the comparison.   Table 5.21 presents the benefits in non-fatigued DER_S achieved by using FRC mixtures. Even though the DER_S of PC slab was increased by 25 percent as opposed to 13 and 11 percent for the other two slabs, contribution of FRC mixtures are apparent in Table 5.21, but the benefit is not consistent over the crack widths.

Table 5.20. Comparison of non-fatigued DER_S obtained by regression models between the different mixtures.

Crack width (in)	PC	FRC1	FRC2
0.02	76	94	85
0.03	66	85	81
0.04	56	79	76
0.05	48	74	72
0.06	47	70	68
0.07	46	66	63
0.08	46	63	59
0.09	45	60	54
0.10	44	58	50

Table 5.21. Percentage increase in non-fatigued DER_S in using FRC.

Crack width (in)	FRC1	FRC2
0.02	25	13
0.03	30	23
0.04	41	37
0.05	54	50
0.06	48	43
0.07	43	36
0.08	38	29
0.09	35	21
0.10	25	13

268

5.4.3   Relationship between DER_S vs DER_B

As the bi-linear models for DER_B shown good predictability, DER_B predicted by the bi-linear models were used for developing the DER_S vs DER_B relationship.   For the DER_S, bi-linear models for PC and FRC2 provide the best predictability, whereas, logarithmic model provided the best fit for FRC1.   Three separate models were developed for PC, FRC1 and FRC2 mixtures. Figure 5.129 through Figure 5.131 and Equations (5.77) through (5.79) present regression models for the three mixtures.   The R^2 and SE for the model for the PC mixture are 0.95 and 12.26; these are equal to 0.95 and 10.73 for the FRC1 mixture, and, 0.90 and 11.71 for the FRC2 mixture. It may be noted that the SE presented for each of the models are the sum of the corresponding SE in the DER_B prediction model (as function of crack width) and SE obtained in the DER_S and DER_B relationship itself.   Since, these models are developed using the regression model predicted data, the SE obtained in concerned models are added together in order to understand the real accuracy of the prediction.   Equation 5.80 and Figure 5.132 provides relationship for developed for all the mixtures combined ($R^2 = 0.88$; SE = 13.98).

PC mixture

$$DER_S = 0.6836\,DER_B + 22.61 \tag{5.77}$$

FRC1 mixture

$$DER_S = \; = 1.0129\,DER_B + 13.974 \tag{5.78}$$

FRC2 mixture

$$DER_S = 1.0553\,DER_B + 5.4335 \tag{5.79}$$

All mixtures

$$DER_S = 0.9329\,DER_B + 14.295 \tag{5.80}$$

$y = 0.6836x + 22.61$
$R^2 = 0.95$; $SE = 12.26$
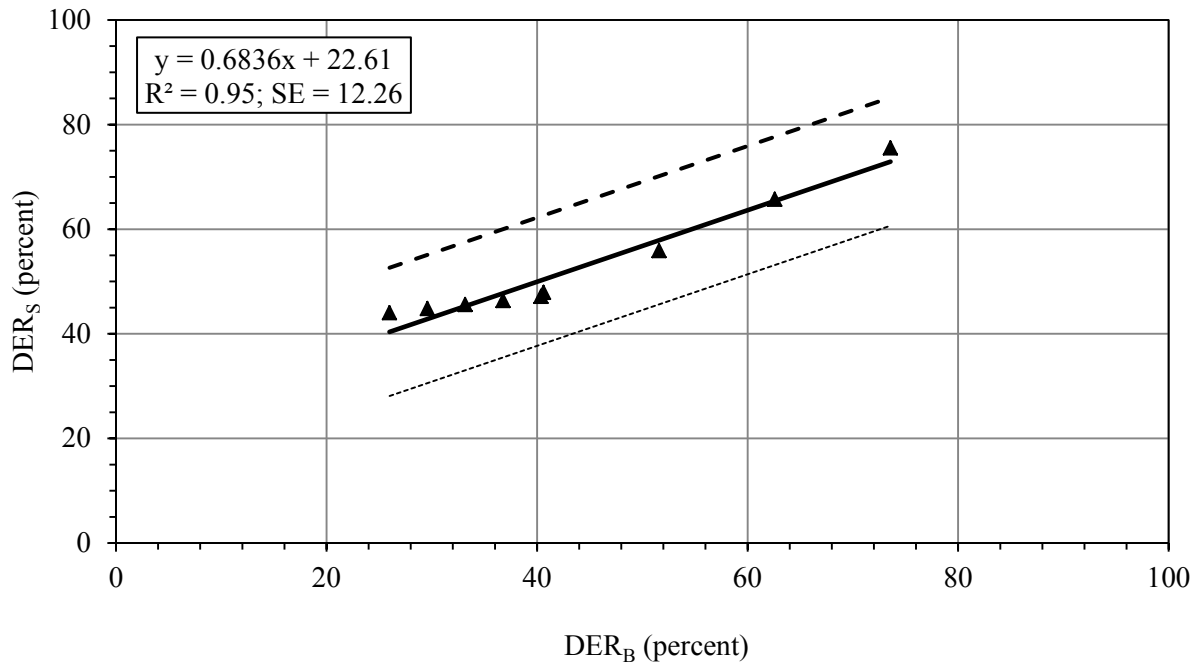
▲ Non-fatigued ⎯⎯ Reg. model − − − Upper error line ------- Lower error line

Figure 5.129. Relationship between non-fatigued DER_S and non-fatigued DER_B for PC mixture.

270

$y = 1.0129x + 13.974$
$R^2 = 0.95$; SE = 10.73

■ Non-fatigued ——— Reg. model – – – Upper error line -------- Lower error line
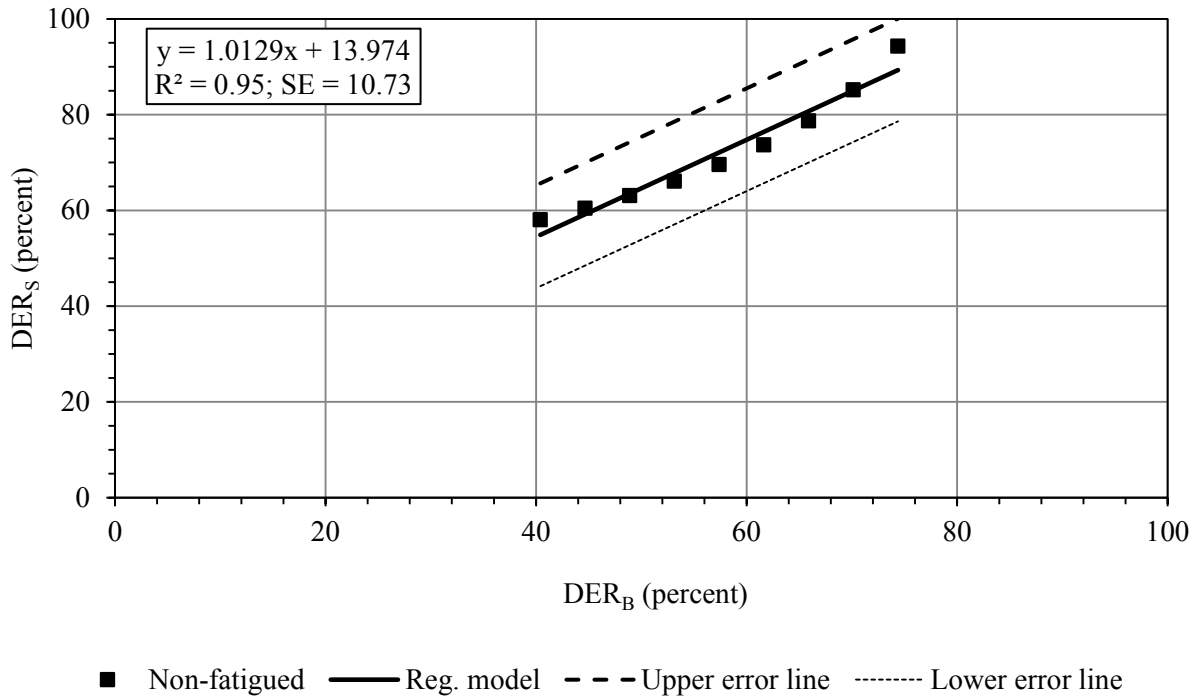
Figure 5.130. Relationship between non-fatigued DER_S and non-fatigued DER_B for FRC1 mixture.

$y = 1.0553x + 5.4335$
$R^2 = 0.90$; SE = 11.71

● Non-fatigued ——— Reg. model – – – Upper error line -------- Lower error line
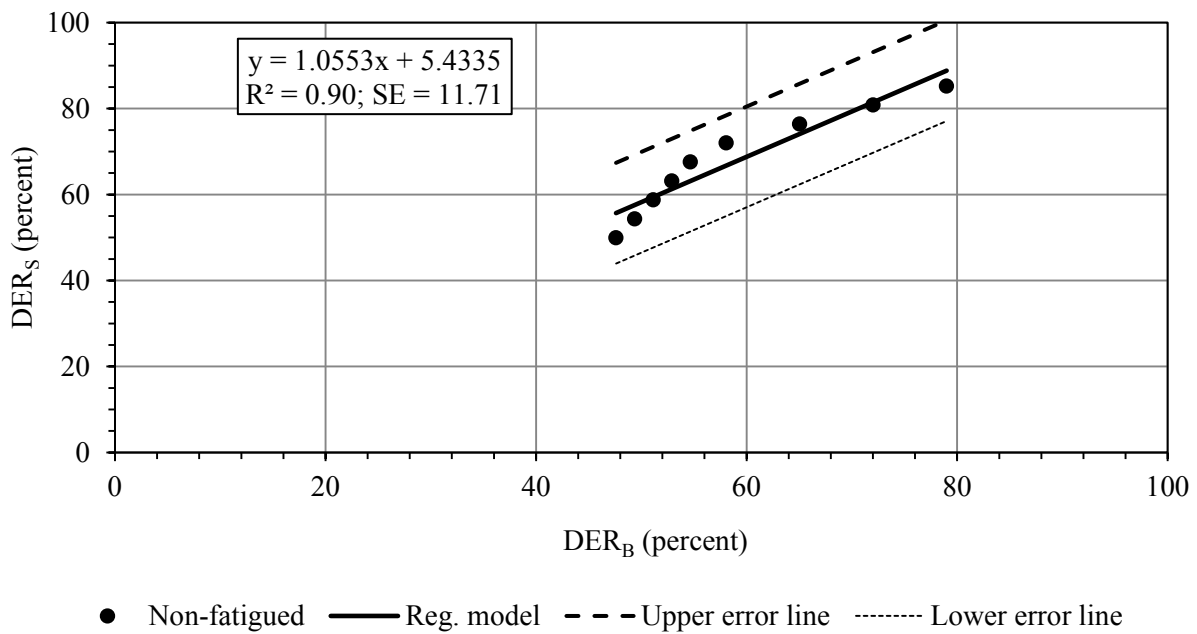
Figure 5.131. Relationship between non-fatigued DER_S and non-fatigued DER_B for FRC2 mixture.

271
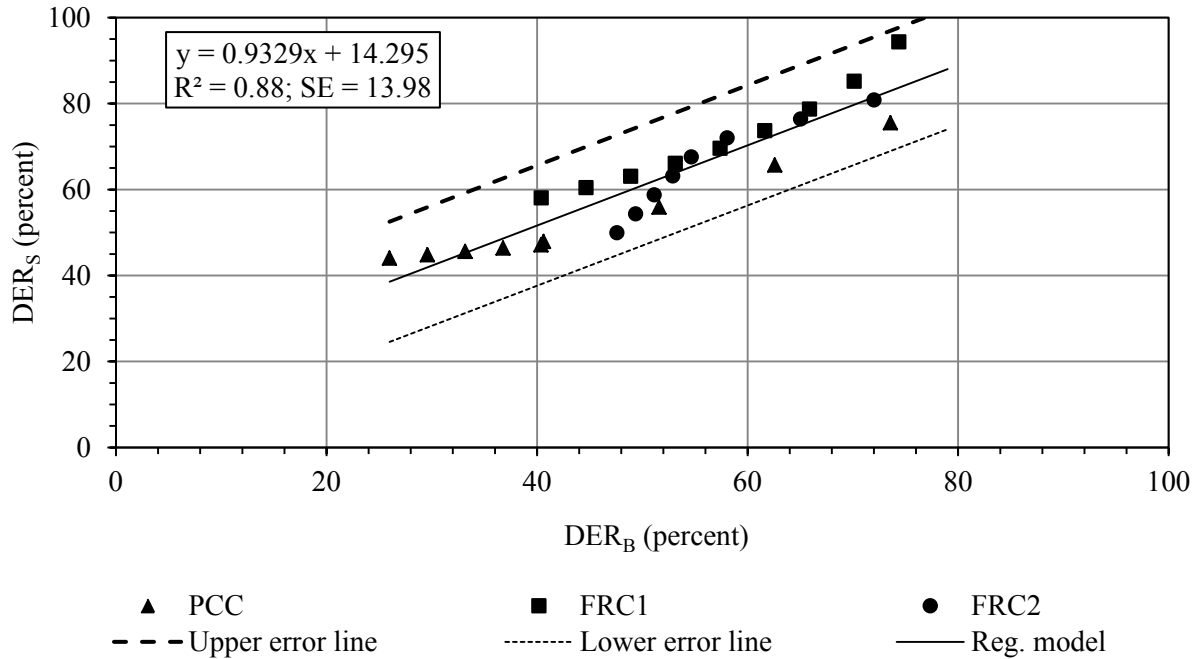
Figure 5.132. Relationship between non-fatigued DER_S and non-fatigued DER_B for all mixtures combined.

5.5   RELATIONSHIP BETWEEN LTE_S AND DER_B

Based on the goodness of fit, LTE_S and DER_B predicted by bi-linear models are correlated. Three separate models were developed for PC, FRC1 and FRC2 mixtures. Figure 5.133 through Figure 5.135 and Equations (5.81) through (5.83) present regression models for the three mixtures. The R^2 and SE for the model for the PC mixture are 0.95 and 12.26; these are equal to 1.0 and 9.74 for the FRC1 mixture; and these are 0.90 and 11.71 for the FRC2 mixture. Here also, the SE presented for each of models are the sum of the corresponding SE in the DER_B prediction model (as function of crack width) and SE obtained in the LTE_S and DER_B relationship itself. Figure 5.136 presents the relationship developed for all the mixtures together.

272
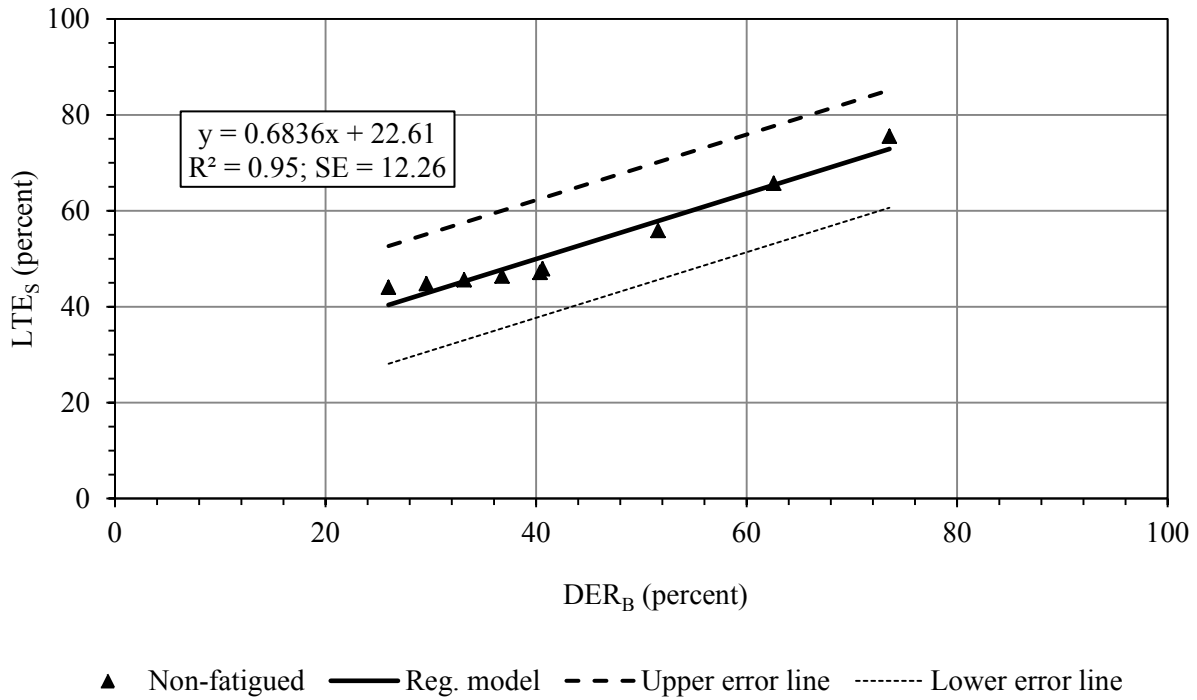
Figure 5.133. Relationship between non-fatigued LTE$_S$ and non-fatigued DER$_B$ for PC mixture.
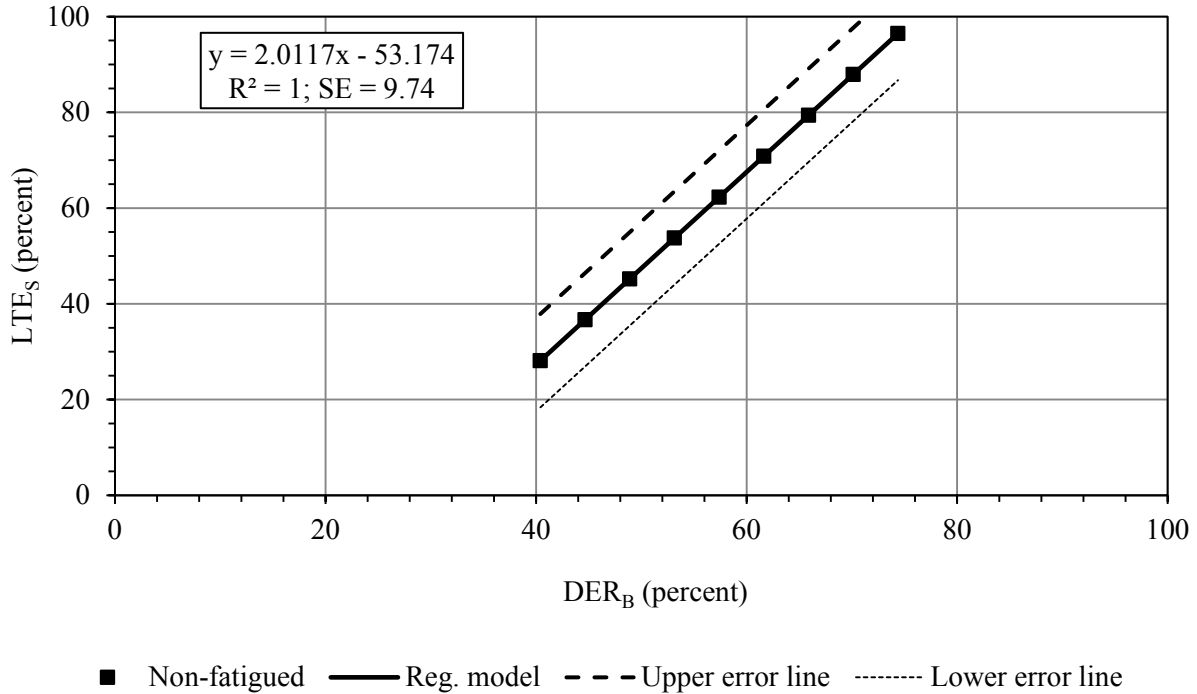
Figure 5.134. Relationship between non-fatigued LTE$_S$ and non-fatigued DER$_B$ for FRC1 mixture.

273
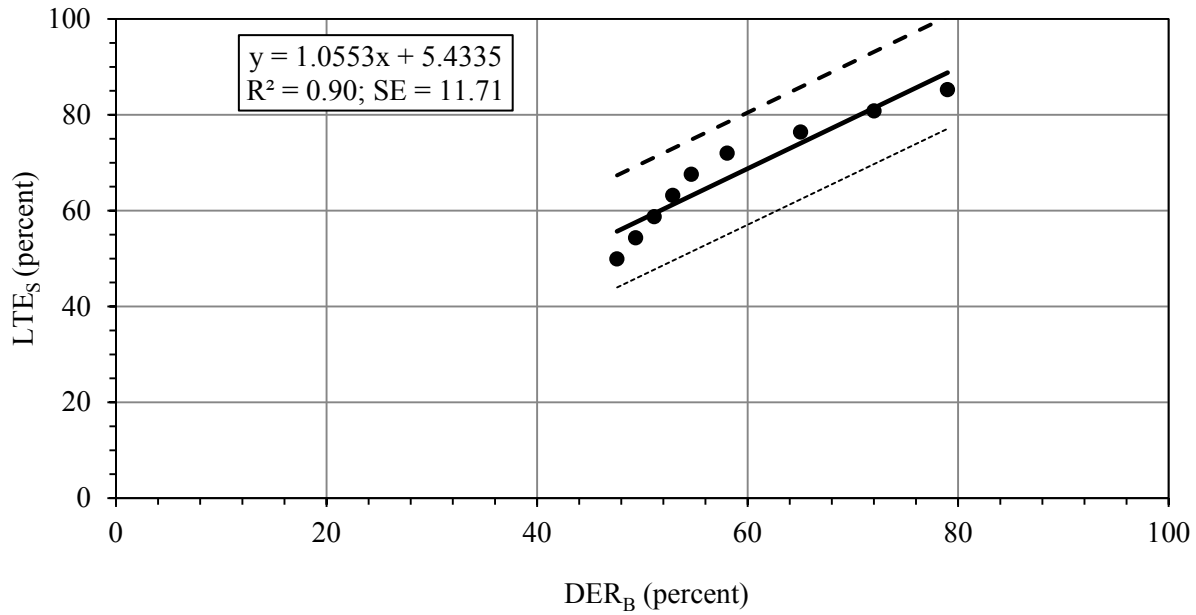
Figure 5.135. Relationship between non-fatigued LTE_S and non-fatigued DER_B for FRC2 mixture.

PC mixture

$$LTE_S = = 0.6836 \, DER_B + 22.61 \qquad (5.81)$$

FRC1 mixture

$$LTE_S = 2.0117 \, DER_B - 53.174 \qquad (5.82)$$

FRC2 mixture

$$LTE_S = 1.0553 \, DER_B + 5.4335 \qquad (5.83)$$

All mixtures

$$LTE_S = 1.0702 \, DER_B + 3.6987 \qquad (5.84)$$

274
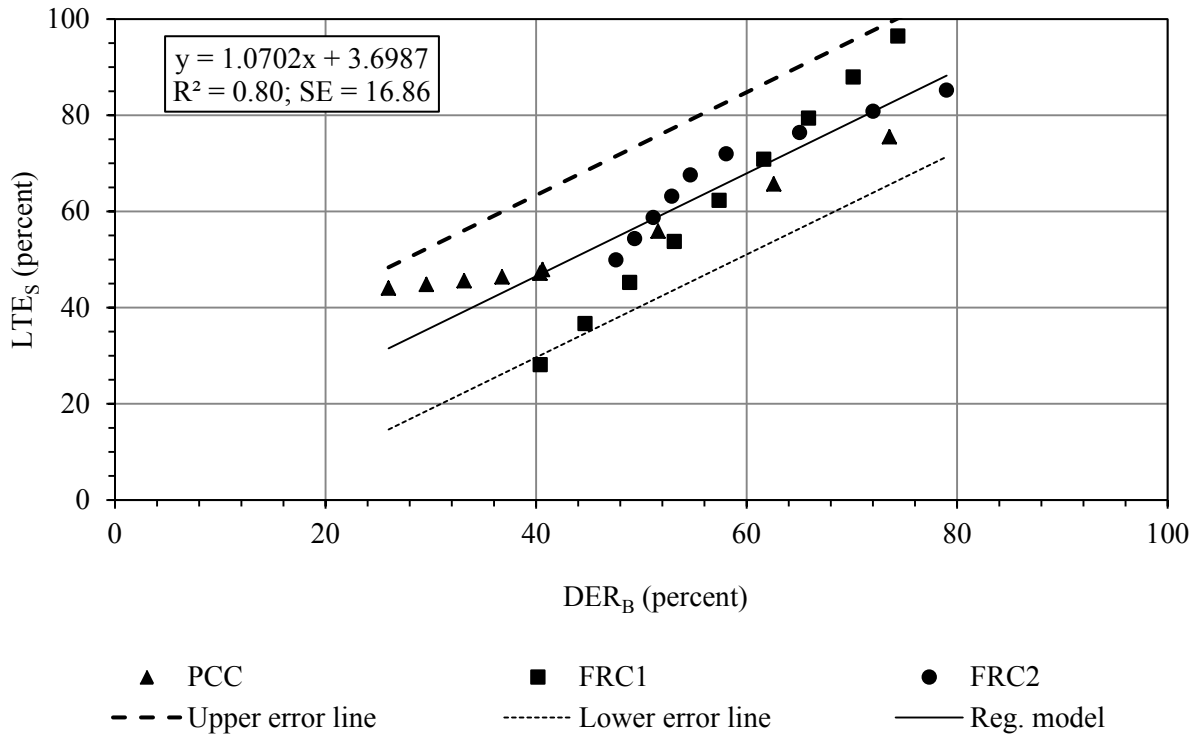
Figure 5.136. Relationship between non-fatigued LTE_S and non-fatigued DER_B for all mixtures combined.

5.6   RELATIONSHIP BETWEEN DER_S AND LTE_B

In this case also, DER_S and LTE_B predicted by the best fit models are used. Figure 5.137 through Figure 5.139 and Equations (5.85) through (5.87) present regression models for the three mixtures. The R^2 and SE for the model for the PC mixture are 0.90 and 13.52; these are equal to 0.95 and 12.61 for the FRC1 mixture; and these are 0.91 and 11.63 for the FRC2 mixture. Here also, the SE presented for each of models are the sum of the corresponding SE in the LTE_B prediction model (as function of crack width) and SE obtained in the LTE_B and DER_S relationship itself.   Figure 5.140 provides the relationship developed for all the mixtures combined ($R^2 = 0.87$ and SE = 14.27).

275

PC mixture

$$DER_S = 0.7433\ LTE_B + 18.224 \qquad (5.85)$$

FRC1 mixture

$$DER_S = 0.9826\ LTE_B + 12.027 \qquad (5.86)$$

FRC2 mixture

$$DER_S = 1.3649\ LTE_B - 19.717 \qquad (5.87)$$

All mixtures

$$DER_S = 0.9549\ LTE_B + 9.554 \qquad (5.88)$$
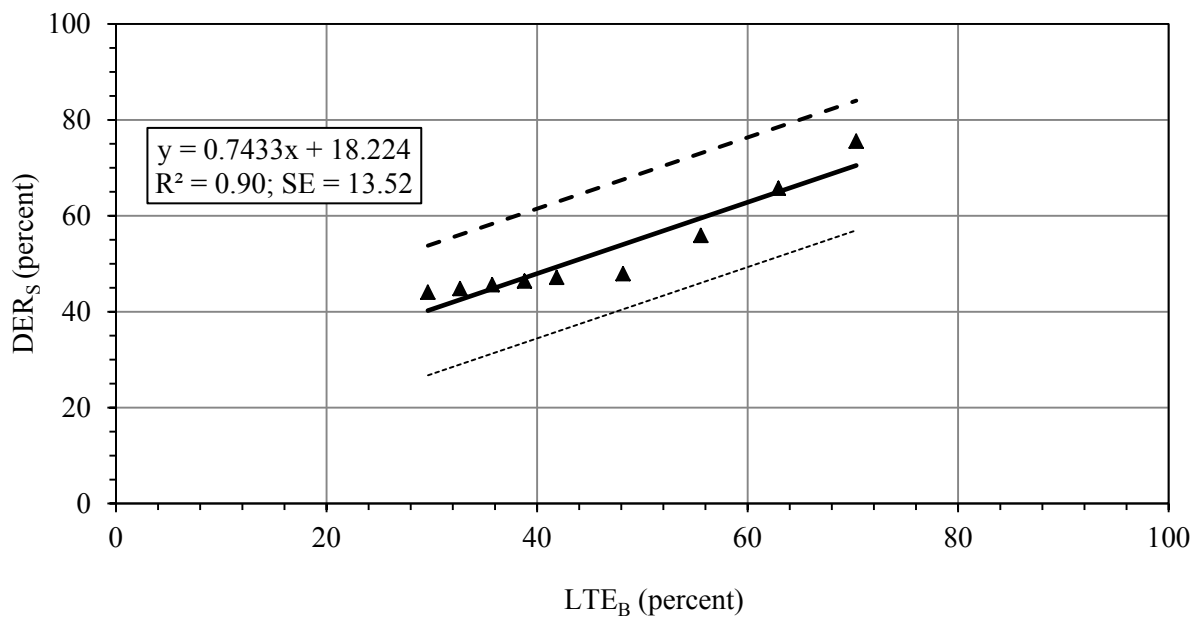
Figure 5.137. Relationship between non-fatigued DER_S and non-fatigued LTE_B for PC mixture.
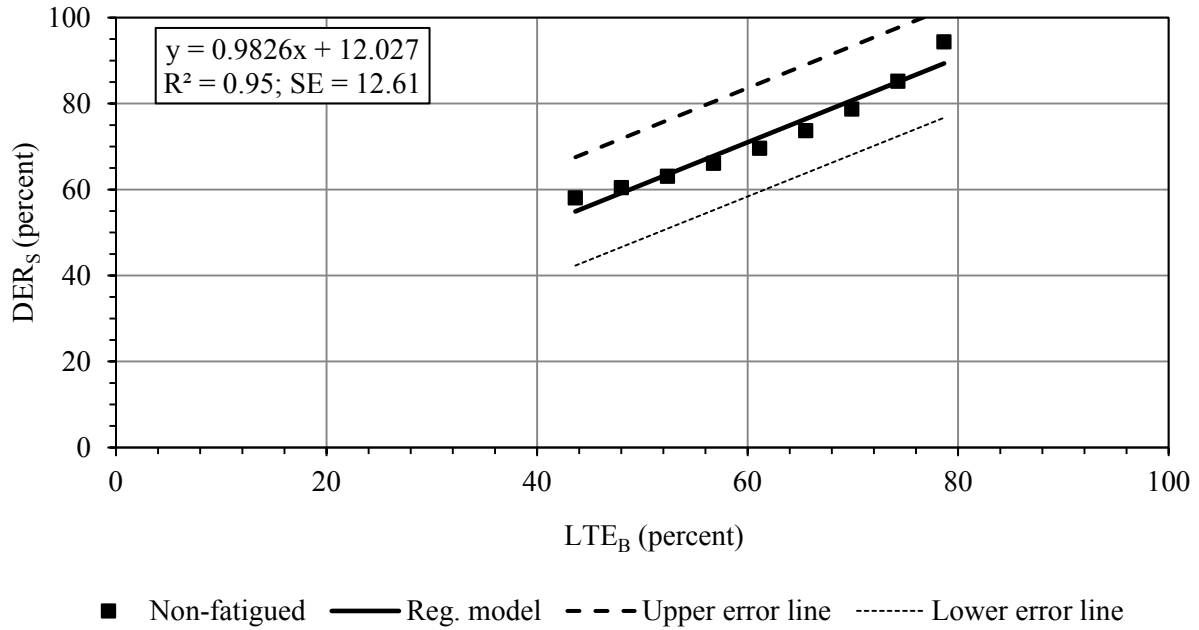
Figure 5.138. Relationship between non-fatigued DER$_S$ and non-fatigued LTE$_B$ for FRC1 mixture.
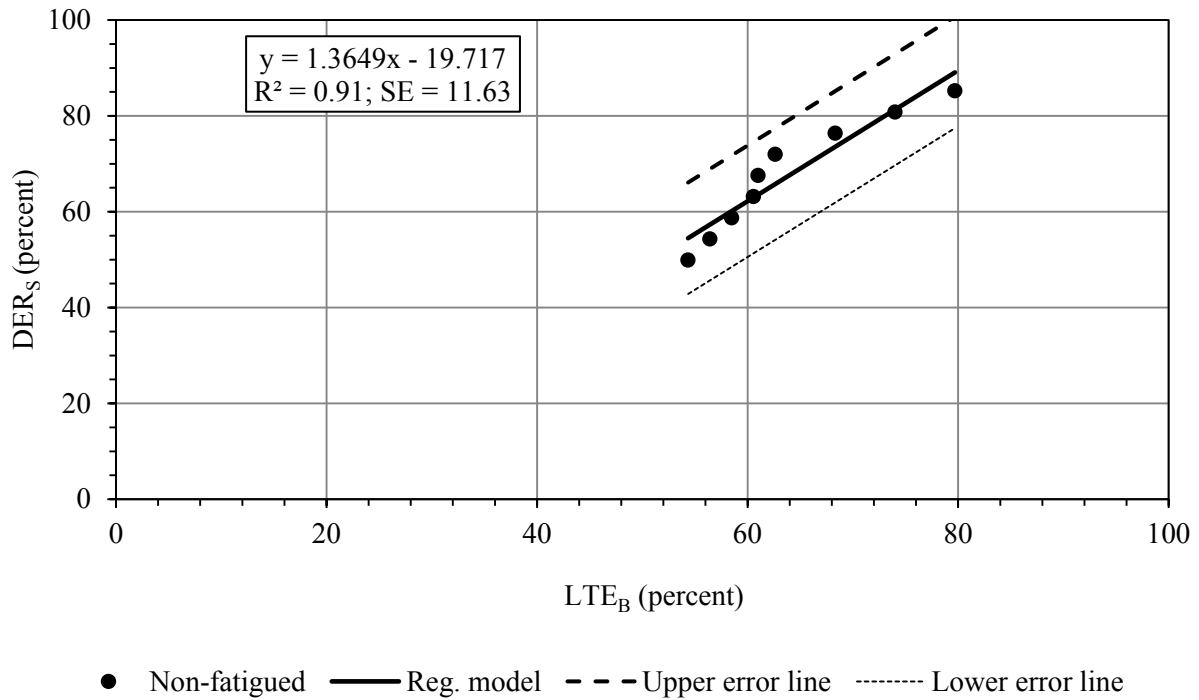
Figure 5.139. Relationship between non-fatigued DER$_S$ and non-fatigued LTE$_B$ for FRC2 mixture.

277

$$y = 0.9549x + 9.554$$
$$R^2 = 0.87; SE = 14.27$$
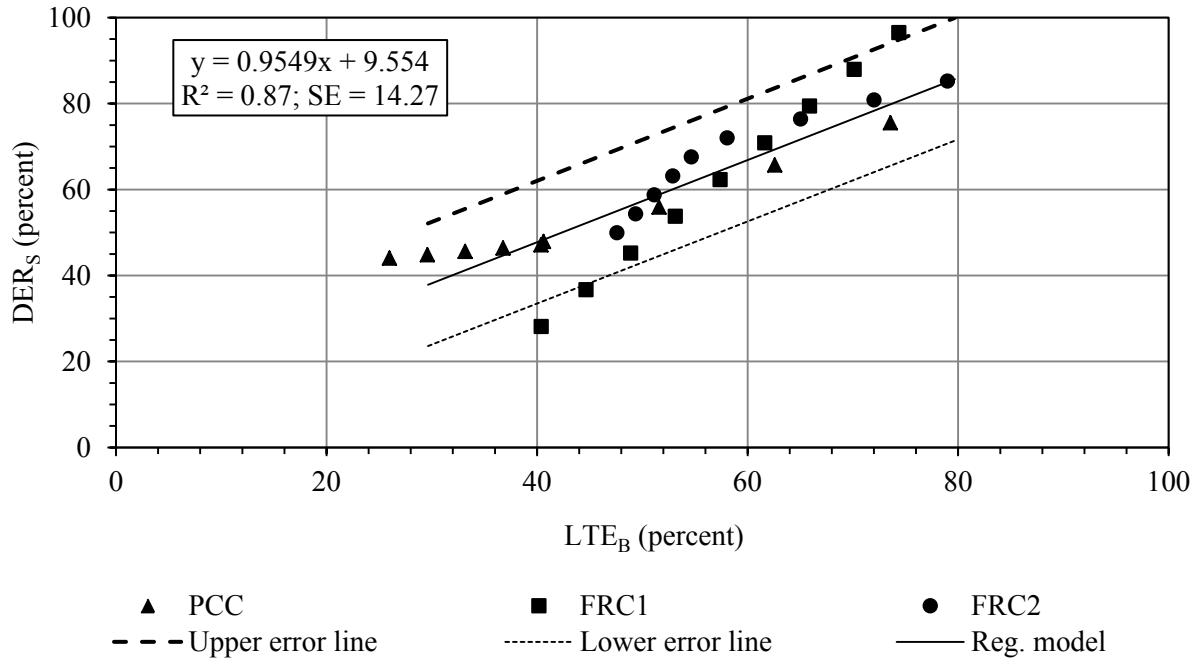
Figure 5.140. Relationship between non-fatigued DER_S and non-fatigued LTE_B for all mixtures combined.

5.7   SELECTION OF BEST PROCEDURE TO ESTIMATE LTE_S

Now that the relationships for the two joint performance parameters (LTE and DER) between the B_{ALT} and S_{ALT} are established, the best relationships are to be selected. These relationships can be used to predict the LTE_S and DER_S using test results from the beam test. LTE_S is the required input for determining the joint stiffness and design stress discussed in Chapter 6.0 . Whereas, the best relationship between LTE_S vs LTE_B, LTE_S vs DER_B, DER_S vs LTE_B or DER_S vs DER_B can be used to compare the joint performances between the mixture types. The best relationships for estimating the LTE_S and DER_S were selected on the basis of the R^2 and SE.

Table 5.22 presents a comparison of the R^2 and SE obtained for different relationships between the joint performance parameters in B_{ALT} and S_{ALT} procedures. It can be seen that

278

between the two relationships that predict the LTE_S, better correlation were obtained in the LTE_S vs LTE_B relationship. Comparing the two relationships that predict DER_S, the DER_S vs DER_B relationship has the lowest SE and highest R^2. Therefore, it can be concluded that the best predictor of the DER_S is the DER_B.

Lastly, comparing all the four relationships, it appears that the DER_S vs DER_B relationship has better predictability than the rest of the three. So, when comparing the joint performance of different concrete mixtures by using the B_{ALT} method, DER_B can be determined and the DER_S can be estimated for the purpose of comparison. It may be stated that the methodology for determining DER_S has been proposed in this study. It has many advantages over the traditionally used LTE_S such as (i) entire deflection profile is used for computing DER_S as opposed to only peak deflections for LTE_S, (ii) the method is more mechanistic and (iii) the DER_S vs crack width relationships have shown better correlations than the LTE_S vs crack width relationship.

Also, even though the R^2 and SE for DER_S relationships are only slightly better than for LTE_S, almost all the DER_S values fall within the SE bars, and appears to be less mixture biased. So, it can be concluded that DER_S relationships would be generally preferred over the LTE_S relationships for comparison of joint performance between the mixture types.

Table 5.22. Comparison of R^2 and SE obtained in different relationships correlating joint performance parameters by B_{ALT} and S_{ALT}.

Relationships	R^2	SE
LTE_S vs LTE_B	0.83	14.58
LTE_S vs DER_B	0.80	16.86
DER_S vs LTE_B	0.87	14.27
DER_S vs DER_B	0.88	13.98

5.8 RECOMMENDATION FOR NUMBERS OF SPECIMENS IN B_{ALT} TEST

Since the B_{ALT} test procedure is very new and only proposed in this study, it is necessary to recommend the required number of specimens to be tested in order obtain the joint performance. A literature review was performed to investigate the variation in LTE results in different research works. As DER is also proposed in this study, no literature data could be found for variation in DER.

The study conducted by Brink, et al., 2004 reported the coefficient of variation (COV) for LTE for three different projects (conventional rigid pavement); these are 13, 44 and 49 percent. Byrum, et al., 2011 reported a COV for LTE for two different projects (conventional rigid pavement), these are 13 to 41 percent in the first project and 10 to 36 percent in the second project. Roesler, et al., 2008 reported LTE results for two whitetopping projects located in Illinois. The COV for the LTE for the project at Highway-4 in Pitt county is 1 percent and it is 16 percent for the project on US Highway 36 in Tuscola county. Lev & Gotlif, 2002 reported a COV for LTE vs cumulative percentage of pavements in the LTPP database. In this study it was found that the COV for LTE is around 22 percent when 95 percent pavements are considered. So, it can be concluded that there is a possibility for a considerable variation of the LTE results in the field projects.

In this study, 5 beams were tested for each of the three concrete mixture types. From the non-fatigued LTE_B vs crack width plot for each specimen, LTE_B were determined at seven different crack widths between 0.02 and 0.10 in. For each concrete mixture design, the COV (considering all the 5 specimens) was determined at each of the seven crack widths. Then an average of the seven COVs were determined for the three mixture types. Table 5.23 presents the average COVs for all three mixture designs.

280

The COV for the three mixtures varies between 13 to 21 percent, with the average being 18 percent, which is close to 22 percent that was observed in the Lev & Gotlif, 2002 study (for 95 percent of the pavements). So, indirectly, it can be stated that when 5 beams are tested, the number of the beams can represent the variability in the field conditions. Moreover, in the present study, a considerable variation in the LTE_B or DER_B could be noticed. So, under the circumstance and considering the variability observed LTE_B or DER_B in the present project, it is recommended that a minimum of 5 beam specimens be tested in order to obtain a representative joint performance evaluation.

Table 5.23. Average coefficient of variation for the LTE_B results for 5 specimens.

Mixture	COV (percent)
PC	21
FRC1	19
FRC2	13
Average	18

5.9   CONCLUSIONS

A summary of the results from the laboratory experiment has been presented. Comparisons between the joint performance results with respect to the mixture types and test procedures are presented. The fresh and hardened concrete properties of all three mixtures used in the study were comparable, with a marginally higher strength for the two FRC mixtures. The surface textures of the fractured slab and beam crack faces were also similar. The addition of the fibers did not change the surface microtexture significantly.

In both the B_{ALT} and S_{ALT} procedures, it was found that the joint performance of the FRC specimens was different from that of the PC specimens when crack widths were larger. The joint performance at narrow crack widths (< 0.025 in), when the aggregate interlock is engaged, was high for both the fiber and the plain concrete specimens. The benefit of the fiber in load transfer is primarily exhibited at larger crack widths when aggregate interlock is ineffective.

The rate in decrease in the LTE with load cycle applications was higher for the PC specimens. The drop in joint performance was larger when fatigued at a 0.050-in crack width than a 0.035-in crack width. Between the two FRC mixtures, the FRC2 beam specimens with the Enduro 600 fiber exhibited a slightly better joint performance than the beams with the Strux 90/40 fibers. However, the performance of the slabs with these fibers performed in a similar manner. Even though the shapes, sizes and aspect ratios of the two fibers were different, performances were quite similar. This might indicate that a similar improvement in joint performance due to the use of a fiber can be achieved if the RSR is similar. It was also seen that the fibers did not fail in fatigue even after 10 million load cycles.

Regression models have been developed to determine the LTE and DER as a function of crack width for both the B_{ALT} and S_{ALT} procedures. Regression models were developed for original and non-fatigued LTE and DER values. Correlations have been developed between the LTE and DER results of B_{ALT} and S_{ALT} procedures which will be helpful for the designers in establishing the LTE or DER for a slab if the LTE or DER is established with beam. Lastly, it was found that the LTE_B provides the best estimate of LTE_S. And either of the DER_B or LTE_B provides a good estimate of DER_S. However, the best relationship was obtained between the DER_B and DER_S, so it is recommended that for the comparison of the joint performance between the mixture types, this can relationship can be used.

Lastly, it was found that if 5 beams are tested, it can represent the variability in the joint performance in the field conditions. Also, since a considerable variation in the B_{ALT} test results were noticed, so testing a minimum 5 beams is highly recommended.

6.0   MODELING OF JOINTS IN BONDED WHITETOPPING

6.1   INTRODUCTION

This chapter presents a comprehensive detail of the joint modeling. The joint of bonded whitetopping was modeled utilizing the finite element method (FEM). One of the main objectives of this FEM modeling was to establish a correlation between the two joint performance quantifying parameters, LTE and $AGG*$, exclusively for the whitetopping. An established relationship between these two parameters coupled with the crack width (cw) vs joint performance relationships, established in the previous chapter, is useful in estimating the design stresses while accounting for the influence of joint performance. These stresses can be used in the mechanistic design of whitetopping.

The relationship between the LTE and $AGG*$ developed for conventional rigid concrete pavements (Ioannides & Korovesis, 1990), discussed in Chapter 2.0 , is not applicable for whitetopping. In the conventional rigid pavements, the majority of the load transfer between the adjacent slabs occurs through aggregate interlock. Also, most of the time, no interlayer bonding is ensured. However, for bonded whitetopping, a considerable amount of load is transferred through the HMA layer, and it is necessary to keep the HMA layer bonded with the overlay. Therefore, the LTE vs $AGG*$ relationship for whitetopping is different than that for a conventional rigid concrete pavement.

284

In whitetopping, the bonding between the concrete and the underlying HMA layer is essential throughout the design life. The rate of bond degradation can be controlled with a better joint performance by minimizing the debonding stress at the interface. Therefore, it is very important to account for the joint performance in whitetopping design. An accurate estimation of the stresses can be more easily obtained if relationship between the LTE and $AGG*$ is established for bonded whitetopping. The other two objectives of this analytical study are to investigate the influence of joint performance on the magnitude of the design stress at the critical location on the loaded slab and the debonding stress (σ_{db}) at the interface. If the benefits of increased joint performance on these two issues are verified, a conclusion can then be drawn about whether the FRC mix over the PC mix is more beneficial for whitetopping bonded overlay.

6.2   LTE VS *AGG** RELATIONSHIP

In bonded whitetopping, 5-ft x 6-ft and 4-ft x 4-ft slabs are more common (Barman, et al., 2010). The critical stress location varies with slab size or joint spacing. For example, in whitetopping with 4-ft x 4-ft slabs, the inner wheelpath coincides with the longitudinal joints; however, in whitetopping with 5 ft x 6 ft slabs, the wheelpath remains 1.5 to 2 ft away from the longitudinal joints. Therefore, in the present analysis two separate models have been developed for these two slab sizes, covering the two different loading conditions observed in the field. The general purpose finite element code, Abaqus FEA (http://www.3ds.com/products/simulia/portfolio/abaqus/overview/) was used to build the models.

The first model consisted of a total of six 5-ft x 6-ft whitetopping slabs. The second model included twelve 4-ft x 4-ft slabs. In both of the models, slabs were placed on a continuous

285

HMA layer. Figure 6.1 and Figure 6.2 show the assembly of the different parts in the two models. All the parts in both the models were built with 27 node isoparametric brick elements (C3D27). In the rigid pavement FEM modeling work, this element type was found to provide sufficiently accurate results at an acceptable computational cost (Kou, 1994 and Vandenbossche & Li, 2013). The mesh size for the concrete and HMA layer was selected based on the convergence analysis performed in the Vandenbossche & Li, 2013 study. In that study, for a similar type of whitetopping model (with 6-ft x 6-ft slabs), it was observed that the difference in the maximum deflections between the two separate models built with 4-in x 4-in x 4-in and 2-in x 2-in x 2-in elements is less than 0.5 percent. In those two models, the difference in terms of critical stresses at the top and bottom of the whitetopping were 0.5 and 4.4 percent, respectively, which are acceptable considering the variation in the structural composition of the overlay in the in-service condition (Vandenbossche & Li, 2013). Therefore, it can be understood that both the above mentioned element sizes are actually reasonable in the whitetopping modeling. However, a combination of both the element sizes can judiciously be made in a single model to optimize the accuracy and the computational time.

As shown in Figure 6.1, in the model with 5-ft x 6-ft slabs, a finer mesh (2 in x 2 in x 2 in) was used in the three slabs (Slab 1, 6 and 5) adjacent to the shoulder, amongst which, load was applied on the middle slab (Slab 6). The load transfer through the transverse joint between Slabs 6 and 5 was studied. These three slabs were given importance because Slab 6 was the one on which load was applied and Slabs 1 and 5 form the transverse joints with Slab 6. The other slabs (Slab 2, 3 and 4) are adopted in the model for simulating a closely matching boundary condition that exits in the field. These slabs were modeled with a 4-in x 4-in x 4-in mesh size.

286
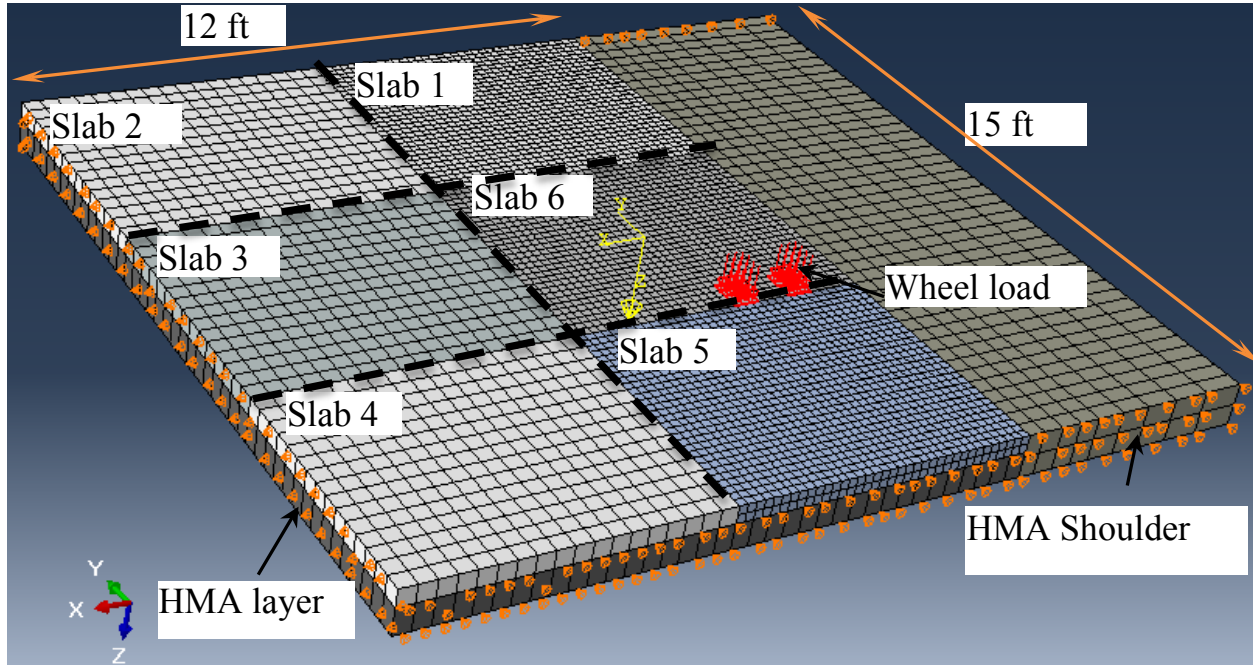
Figure 6.1. FEM model for 5-ft x 6-ft joint spacing.

Similarly, in the model with the 4-ft x 4-ft slabs, as shown Figure 6.2, the three slabs (Slab 10, 11 and 12) were meshed with 2-in x 2-in x 2-in elements and the remaining nine slabs were meshed with 4-in x 4-in x 4-in elements. Wheel loads were applied on Slab 11. The load transfer through the transverse joint from Slab 11 to 10 was studied for the 4-ft x 4-ft slabs.

In both the models, the HMA layer under the slabs was continuous and tied with a 5-ft wide asphalt shoulder. Both the HMA layer and the shoulder were placed on an elastic foundation.
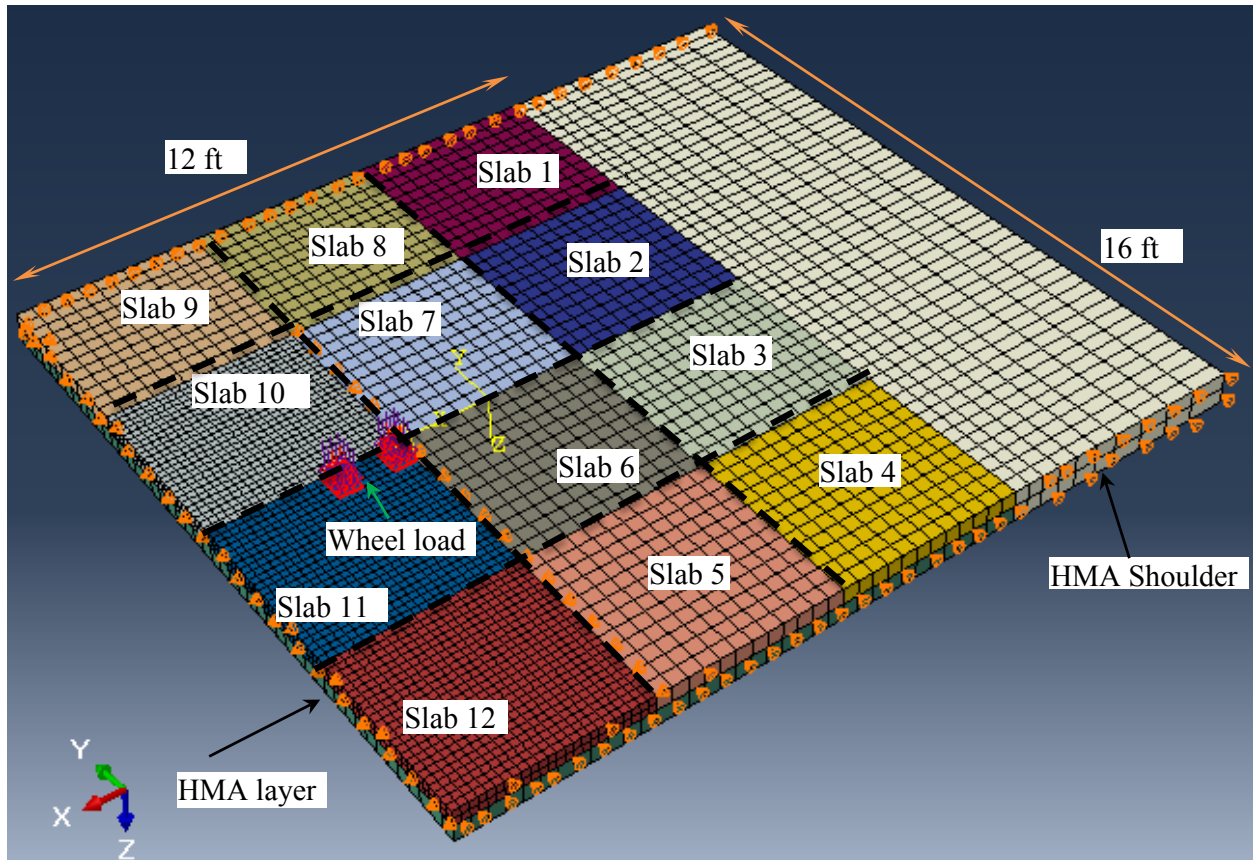
Figure 6.2. FEM model for 4-ft x 4-ft joint spacing.

The wheel load was applied on two identical 6-in x 8-in size rectangular areas, simulating the imprint areas equivalent to the area under the two wheels of a truck axle. Although the actual tire imprint is an elliptical area, a rectangular loading area was selected due to the discrete nature of the model, where the load is applied on top of the surface of a few cubical elements.

In both the models, the loading area was positioned in such a way that the load could be applied at the critical location from the load transfer point of view. According to the Mechanistic-Empirical Pavement Design Guide (MEPDG) (ARA, 2004), typically the mean outer wheelpath location is 1.5 ft away from the lane marking. When the location of the loading area is nearest to the transverse joint, it creates the critical condition. Based on these two assumptions, in the model with 5-ft x 6-ft slabs, the loading areas were placed adjacent to the

288

transverse joint and in the outer wheelpath, as shown in Figure 6.1. In the model with 4-ft x 4-ft slabs, since the inner wheelpath coincides with the longitudinal joints, to simulate the worst case scenario, loading areas were placed on the corner of Slab 11 (Figure 6.2). In both the models, the magnitude of the load was assumed to be equivalent to that of an 18-kip standard axle load, with 9 kip being applied to the dual wheels on each side, and was applied in the form of an evenly distributed pressure (93.75 psi) over the entire loading area.

The load transfer between the adjacent slabs was modeled using translational springs in the Z- direction that connected the nodes of the adjacent slabs across the transverse and longitudinal joints. An equal joint stiffness (AGG^*) was considered in both the transverse and longitudinal joints. A more comprehensive description of this type of spring element was presented in Section 3.2.3. Using an approach similar to that discussed in that section, the spring constants K_{corner}, K_{edge} and $K_{intermediate}$ were determined. As described in Section 3.2.3 (Equations (3.1), (3.2) and (3.3)), the magnitude of the spring constant is related to AGG^*, number of nodes on the joint face, modulus of subgrade reaction (k), and radius of relative stiffness (l). Because the number of the nodes on joint faces of those slabs meshed with 2-in x 2-in x-2 in elements and those meshed with 4-in x 4-in x 4-in elements was not the same, each node from the coarse meshed slab and every alternate node from the fine meshed slab were connected. The same spring stiffness assigned to the transverse joints was also assigned to the longitudinal joints.

The computational procedure to determine l for the bonded whitetopping overlay is different from the conventional rigid pavement. This is because the stiffness of the underlying HMA layer has an influence on the l for this type of composite structure. The effective radius of

289

relative stiffness, l_e, was therefore utilized instead of l. The following equations (6-1 and 6-2) were used to estimate the l_e (Khazanovich, 1994).

$$l_e = \frac{E_{wt} h_{wt}^3}{12} + E_{wt} h_{wt} \left(NA - \frac{h_{wt}}{2} \right)^2 + \frac{E_{HMA} h_{HMA}^3}{12} + E_{HMA} h_{HMA} \left(h_{wt} - NA + \frac{h_{HMA}}{2} \right)^2 \tag{6.1}$$

$$NA = \frac{\frac{E_{wt} h_{wt}^2}{2} + E_{HMA} h_{HMA} \left(h_{wt} + \frac{h_{HMA}}{2} \right)}{E_{wt} h_{wt} + E_{HMA} h_{HMA}} \tag{6.2}$$

Where E_{wt} and h_{wt} are the modulus of elasticity and thickness of the whitetopping; E_{HMA} and h_{HMA} are the modulus of elasticity and thickness of the HMA layer; and NA is the depth of the neutral axis from the top surface of the whitetopping.

To investigate the nature of the LTE vs $AGG*$ relationship under different bonding conditions, both fully and partially bonded conditions were considered in the analysis. In the fully bonded case, the nodes at the interface between the whitetopping and the HMA layer were rigidly connected by a feature called the 'Tie' constraint in the Abaqus CAE. In the partially bonded case, translational springs were used in the X, Y and Z directions to connect the pair of nodes at the bottom of the whitetopping and at the top of the HMA layer. The Vandenbossche & Li, 2013 study also utilized the 'Tie' and translational springs, respectively, at the interface for modeling the fully and partially bonded cases, whereas the studies conducted by Gucunski, 1998 and Nishiyama, et al., 2005 only utilized translational springs for modeling the interface bonding. The interface spring constant for the partially bonded case was assumed as 20,000 lbf/in, corresponding to a 50 percent interface bonding level as per Nishiyama, et al., 2005 study.

290

In both the fully and partially bonded cases, 'hard contact' properties were assigned to the whitetopping and HMA surfaces at the interface to avoid any interlayer penetration effect. A similar 'hard contact' property was also assigned to the joint faces at all the transverse and longitudinal joints.

A partial factorial parametric study was conducted with different design features, including h_{wt}, h_{HMA} and E_{HMA}. The values of k and the elastic modulus of the concrete, E_{wt} were kept constant. The range for the different variables, for both the models containing 5-ft x 6-ft and 4-ft x 4-ft slabs, are given in Table 6.1. For each set of design variables and E_{HMA} (example of one such set: h_{wt}= 4 in, h_{HMA} = 4 in, E_{HMA} = 100,000 ksi), the FEM model was run for six different assumed values of $AGG*$ (0.0, 0.1, 1.0, 10.0, 100.0 and 1000.0). Among these six, one case was run with a joint stiffness of zero ($AGG* = 0$). In this case, no springs were used at the joints. The remaining five runs represented different joint stiffnesses.

Table 6.1. Range of variables considered within the parametric study.

Slab size (ft x ft)	5 x 6 and 4 x 4
Whitetopping thickness (in)	3, 4, 5 and 6
HMA thickness (in)	3, 4, 5, 6, 8
Modulus of elasticity of concrete (ksi)	4,000
Modulus of elasticity of HMA (ksi)	100, 350, 700 and 1,000
Poisson's ratio of concrete	0.15
Poisson's ratio of HMA	0.35
Modulus of subgrade reaction (psi/in)	150
Non-dimensional joint stiffness, $AGG*$	0, 0.1, 1.0, 10.0, 100.0, 1000.0

6.2.1 Fully Bonded Cases

Figure 6.3 and Figure 6.4 present the LTE vs $AGG*$ bar chart for the models with 5-ft x 6-ft and 4-ft x 4-ft slabs, respectively, for the fully bonded cases. The average LTEs for all the runs for a value of $AGG*$ is presented in each bar. It may be noted that the LTE obtained from the FEM modeling is the sum of the LTEs contributed by both the aggregate interlock and the HMA layer. Henceforth, LTE from the FEM model is denoted as LTE$_{total}$.

In the model with 5-ft x 6-ft slabs, the deflections along the center of two loading areas were used to calculate the LTE$_{total}$; and for the model with 4-ft x 4-ft slabs, the deflections at the longitudinal edge of the slab adjacent to the transverse joint were considered, such that the load transfer along the wheelpath could be obtained. In both models, deflections were noted right at the transverse joint. It was observed that the deflection magnitude remained the same for up to a couple of inches on either side of the joint. As anticipated, the influence of $AGG*$ on the LTE$_{total}$ was negligible. It can be seen in Figure 6.3 and Figure 6.4 that the LTE$_{total}$ was always close 100 percent, irrespective of the magnitude of the $AGG*$.

This finding verifies that when the whitetopping and HMA layers are fully bonded, the contribution of the joint performance is low, but probably only at that instant. However, these findings do not rule out the contribution of a better joint performance in holding the fully bonded condition for a longer period of time by reducing the debonding stress.

292
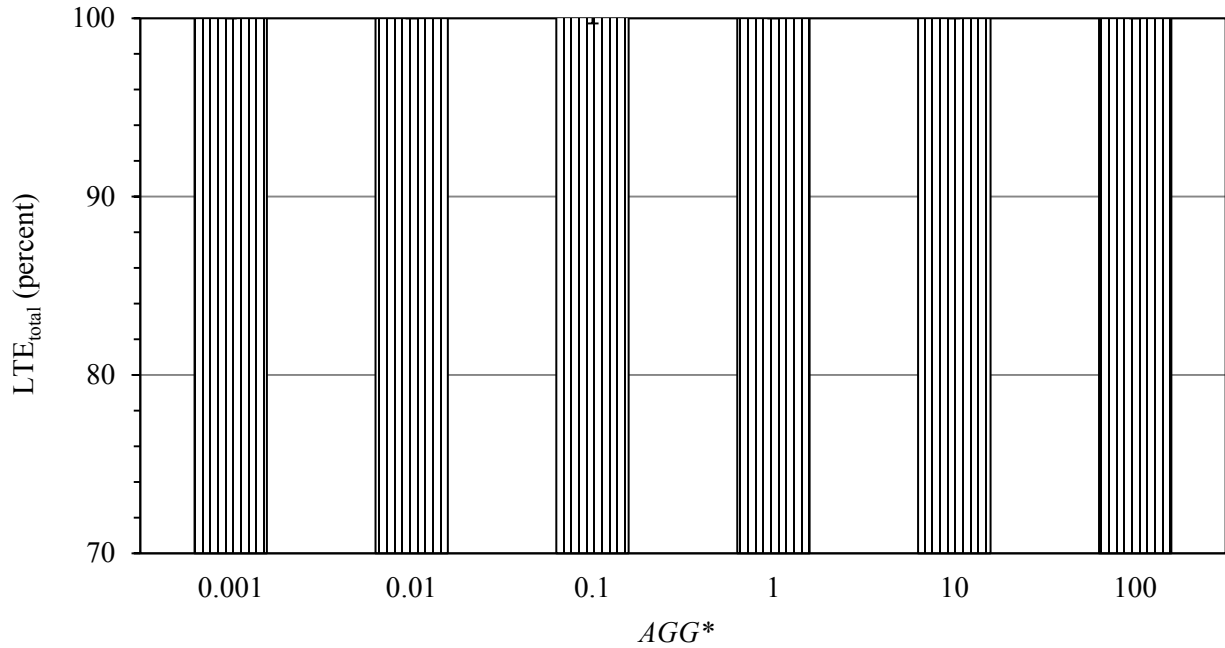
Figure 6.3. LTE$_{total}$ vs $AGG*$ for fully bonded cases in model with 5-ft x 6-ft joint spacing.
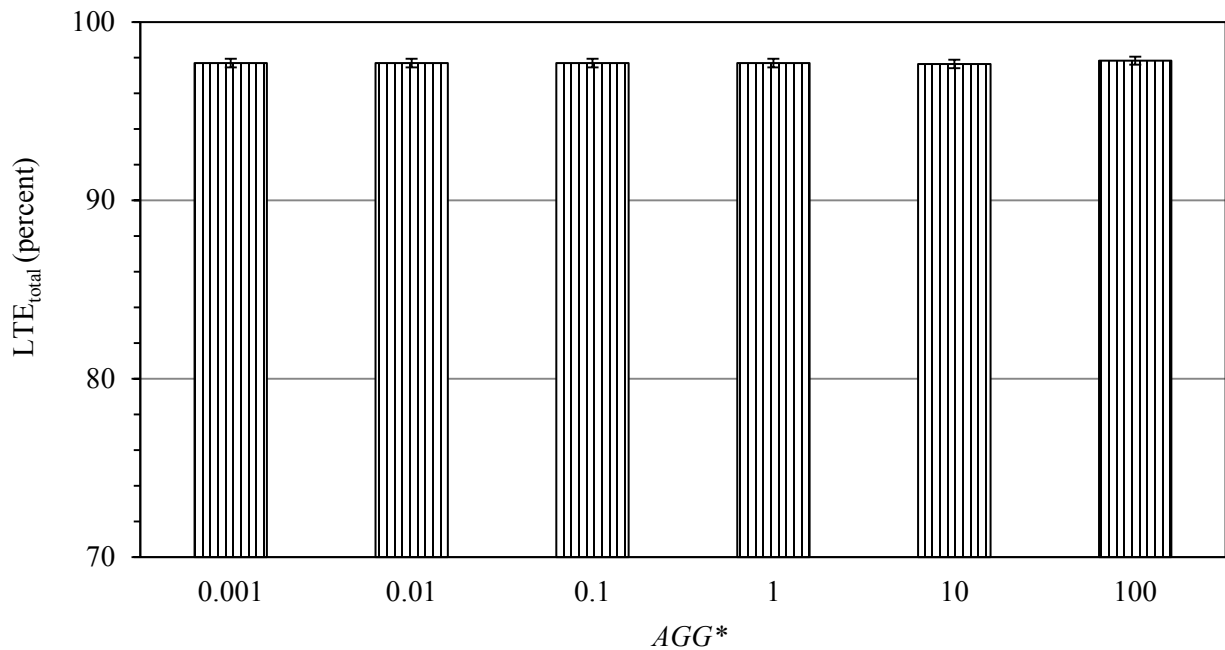
Figure 6.4. LTE$_{total}$ vs $AGG*$ for fully bonded cases in model with 4-ft x 4-ft joint spacing.

293

6.2.2 Partially Bonded Cases

Figure 6.5 and Figure 6.6 show the typical deflection contour in the models with 5-ft x 6-ft and 4-ft x 4-ft joint spacings, respectively, for the partially bonded cases. Slabs are flipped upside down in these figures to show the deflection contour at the bottom of the slabs. Both these figures present the deflection contour for the same design; the thickness of both the concrete overlay and HMA layers is 4 in; E_{HMA} and AGG^* are equal to 100 ksi and 100, respectively.
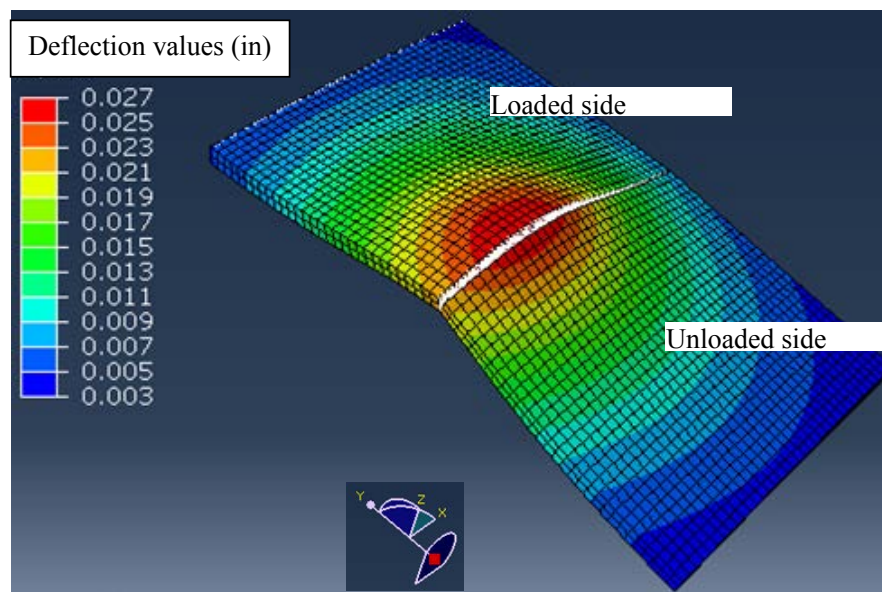
Figure 6.5. Deflection contour at the bottom of a 4-in whitetopping over a 4-in HMA layer in the model with the 5-ft x 6-ft joint spacing; E_{HMA} =100 ksi, AGG^* = 100.
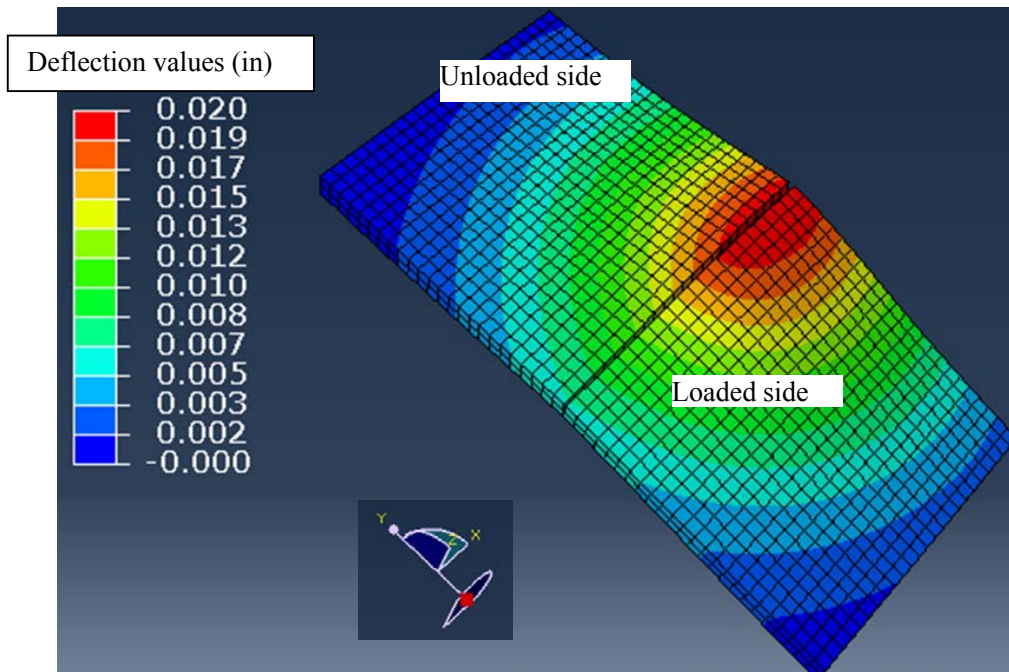
Figure 6.6. Deflection contour at the bottom of a 4-in whitetopping over a 4-in HMA layer in the model with the 4-ft x 4-ft joint spacing; E_{HMA} =100 ksi, AGG^* = 100.

Figure 6.7 through Figure 6.18 present the trends of LTE_{total} vs AGG^* for different designs, in both the models. Unlike in the fully bonded cases, the influence of the joint performance can be observed in this case. The first six figures (Figure 6.7 through Figure 6.12) present the relationships for the 4-in whitetopping over three different HMA layer thicknesses (4, 6 and 8 in). A 4-in whitetopping is a design thickness commonly used in the field (Barman, et al., 2010). The thickness of the slab in the laboratory study was also 4 in.

295
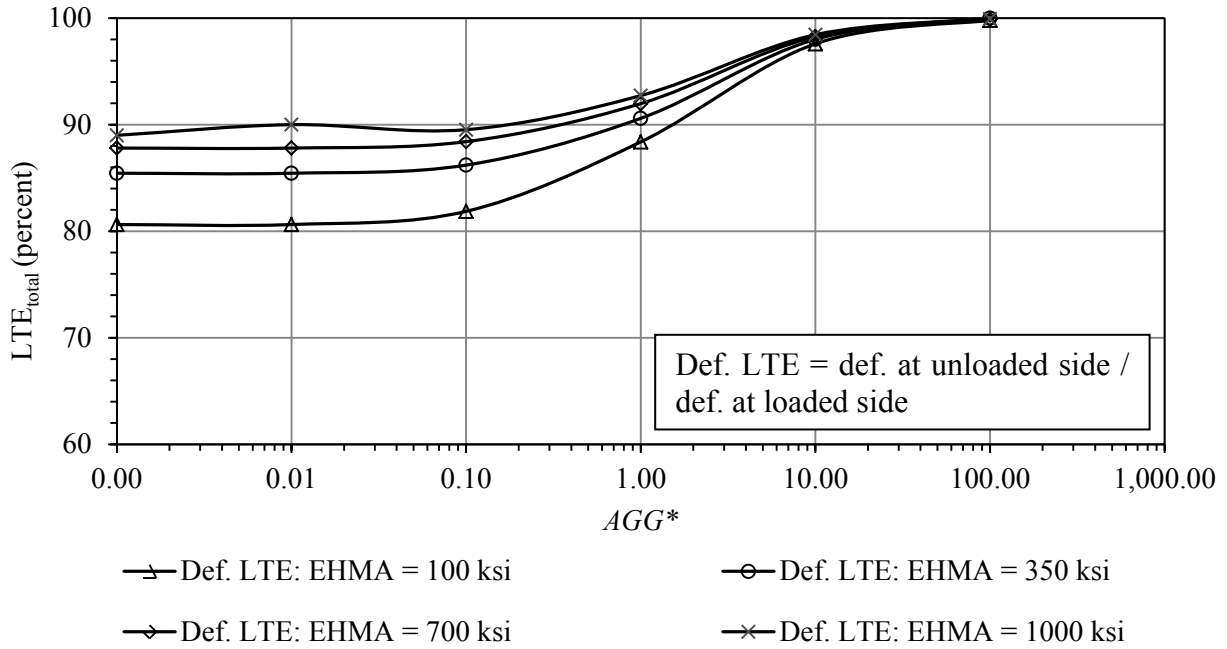
Figure 6.7. LTE_total vs *AGG** relationship for a 4-in whitetopping over a 4-in HMA layer in the model with 5-ft x 6-ft joint spacing.
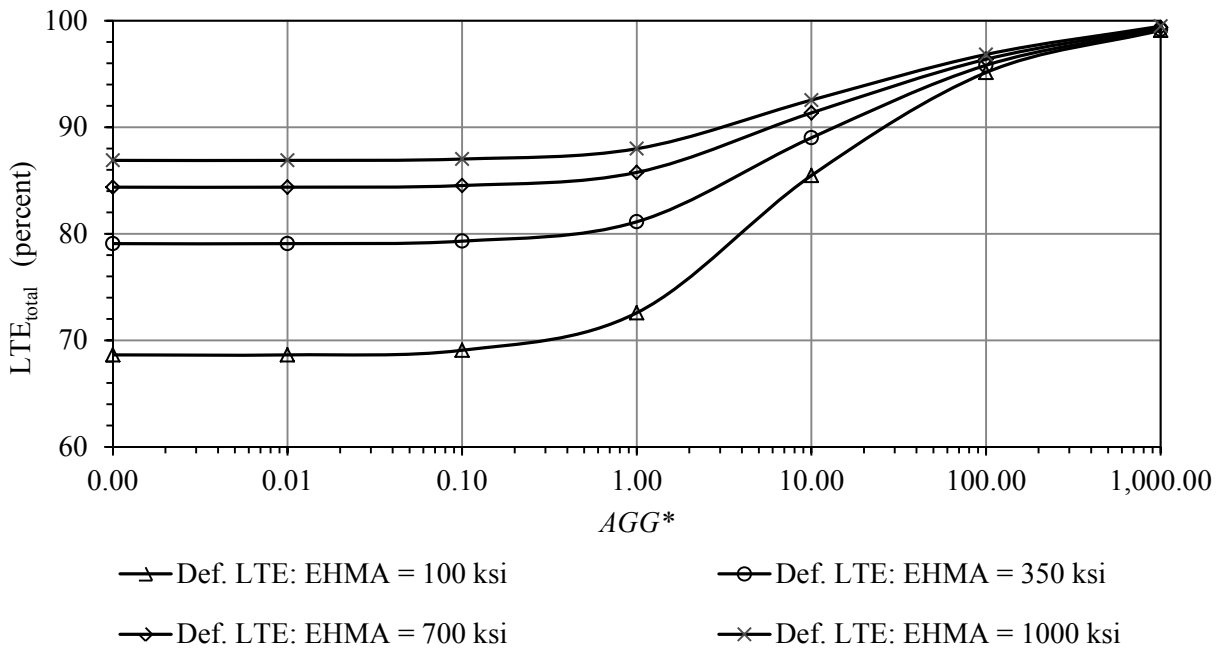
Figure 6.8. LTE_total vs *AGG** relationship for a 4-in whitetopping over a 4-in HMA layer in the model with 4-ft x 4-ft joint spacing.
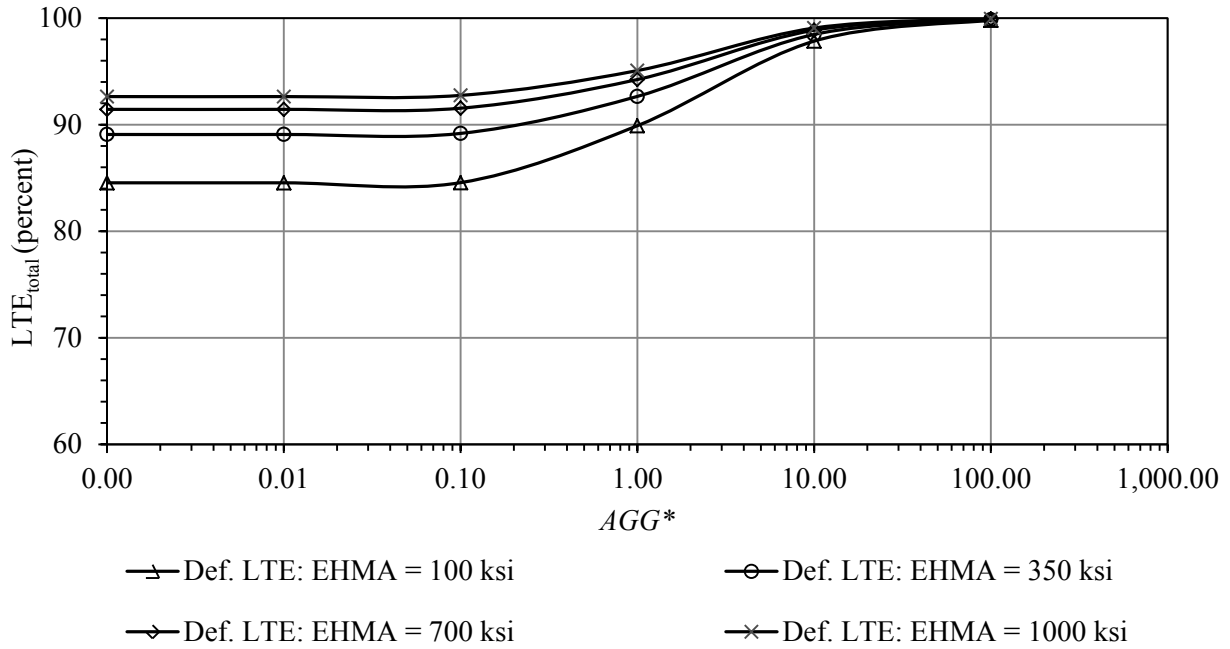
Figure 6.9. LTE$_{total}$ vs $AGG*$ relationship for a 4-in whitetopping over a 6-in HMA layer in the model with 5-ft x 6-ft joint spacing.
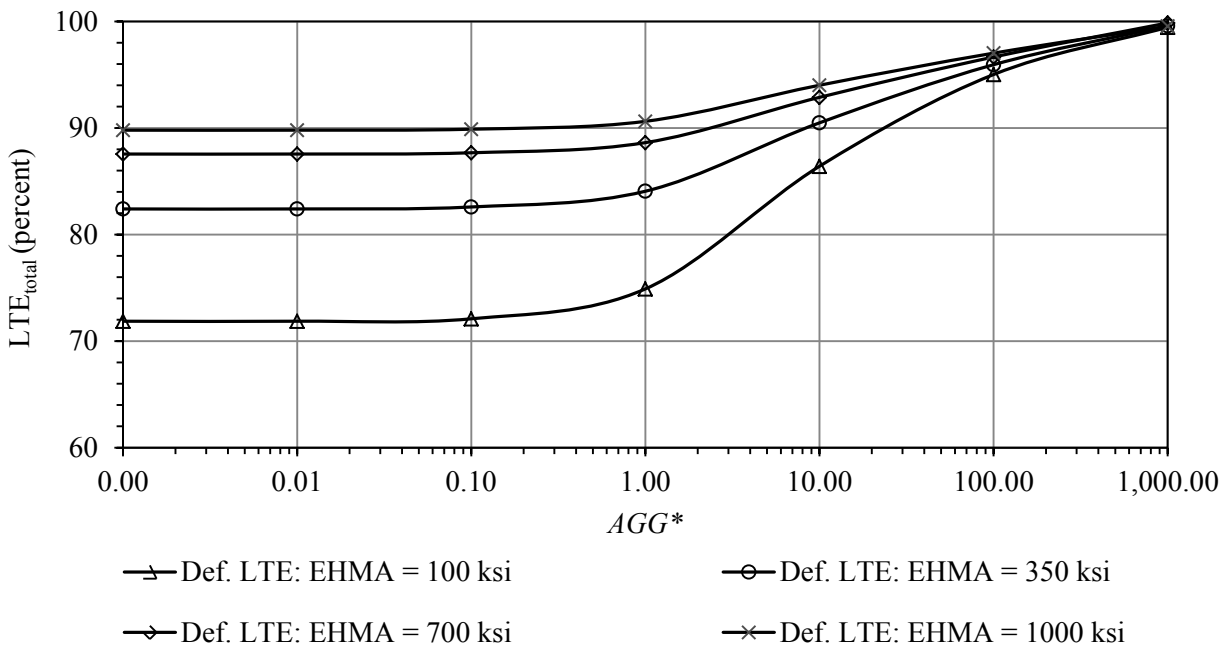
Figure 6.10. LTE$_{total}$ vs $AGG*$ relationship for a 4-in whitetopping over a 6-in HMA layer in the model with 4-ft x 4-ft joint spacing.

297
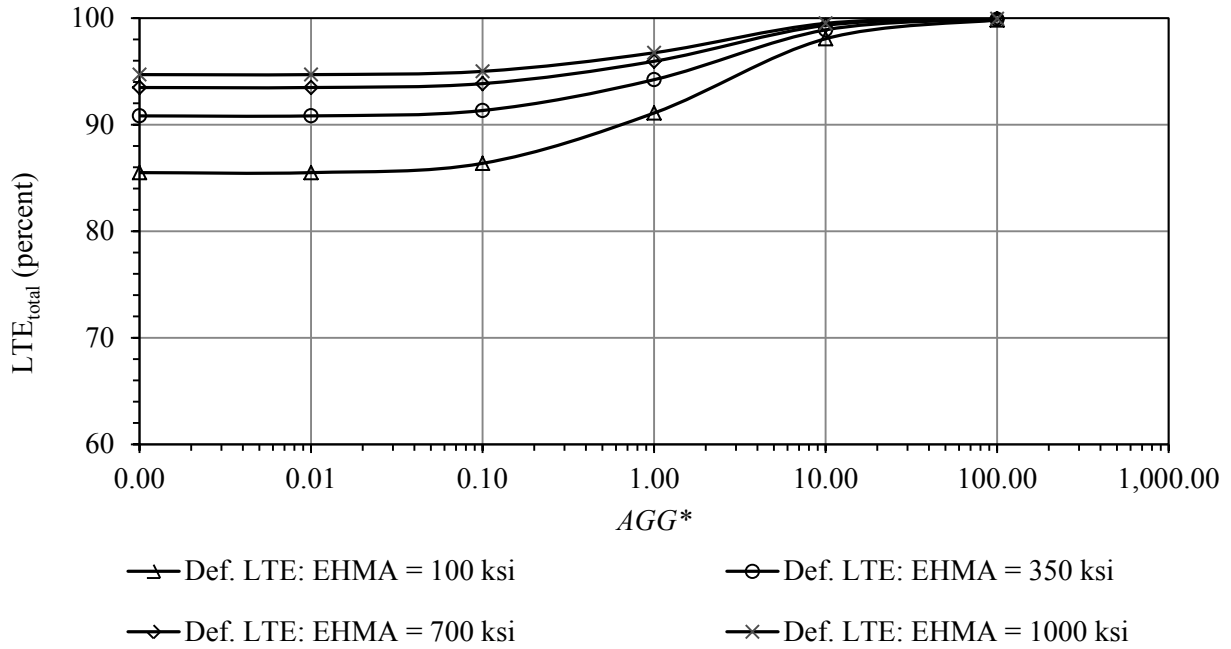
Figure 6.11. LTE_total vs *AGG** relationship for a 4-in whitetopping over an 8-in HMA layer in the model with 5-ft x 6-ft joint spacing.
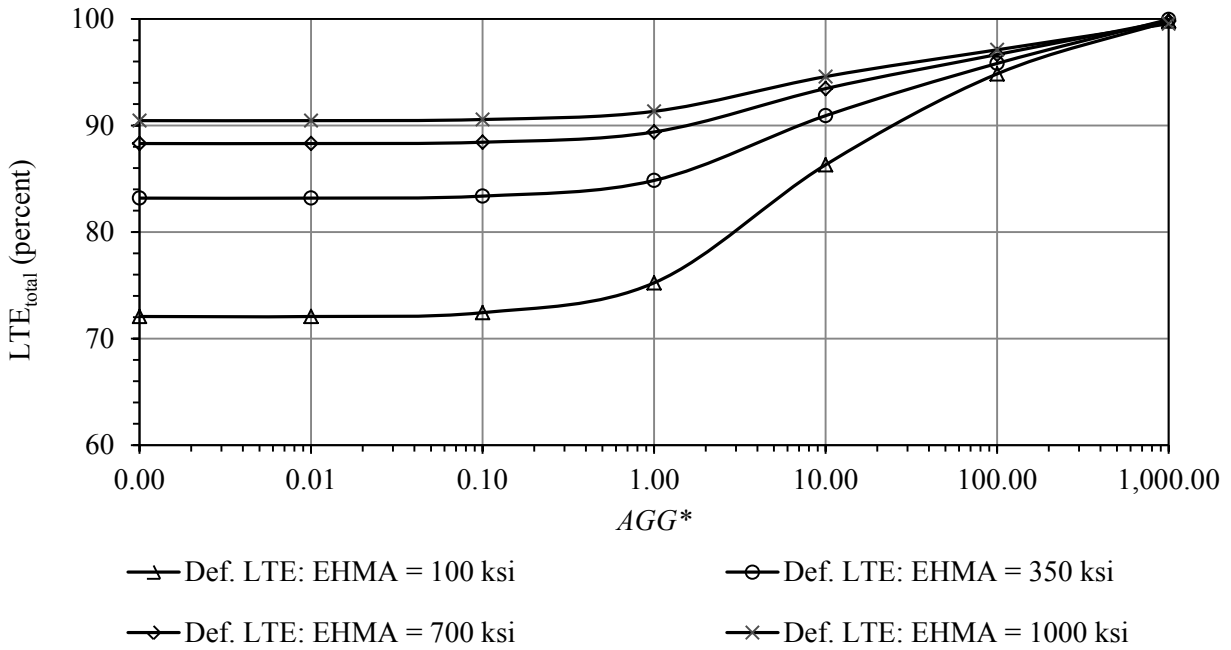
Figure 6.12. LTE_total vs *AGG** relationship for a 4-in whitetopping over an 8-in HMA layer in the model with 4-ft x 4-ft joint spacing.

298

In practice, UTW are typically constructed with 4-ft x 4-ft or smaller slab sizes. Therefore, 3-in UTWs were considered; two cases, such as a 3-in whitetopping over a 4-in HMA and a 3-in whitetopping over a 6-in HMA were considered in the model with 4-ft x 4-ft slabs. In addition to the 4-in thick UTW, a UTW consisting of a 3-in whitetopping over a 4-in HMA with 5-ft x 6-ft slabs is also considered. Also, three TWTs (a 5-in whitetopping over a 4-in HMA, a 6-in whitetopping over a 4-in HMA and a 6-in whitetopping over a 3-in HMA) were added as well. Generally, TWTs are not constructed with 4-ft x 4-ft slabs and were therefore not included. The LTE_{total} vs AGG^* relationship for the above mentioned designs are presented in Figure 6.13 through Figure 6.18.

In the model with 5-ft x 6-ft slabs, the LTE_{total} was found to be increasing up to 100 percent (approx.) when the AGG^* was increased to 100. In the model with 4-ft x 4-ft slabs, LTE_{total} did not reach to 100 percent when the AGG^* was increased to 100; that is why in this case, load transfer was computed even at an AGG^* equal to 1000.

299
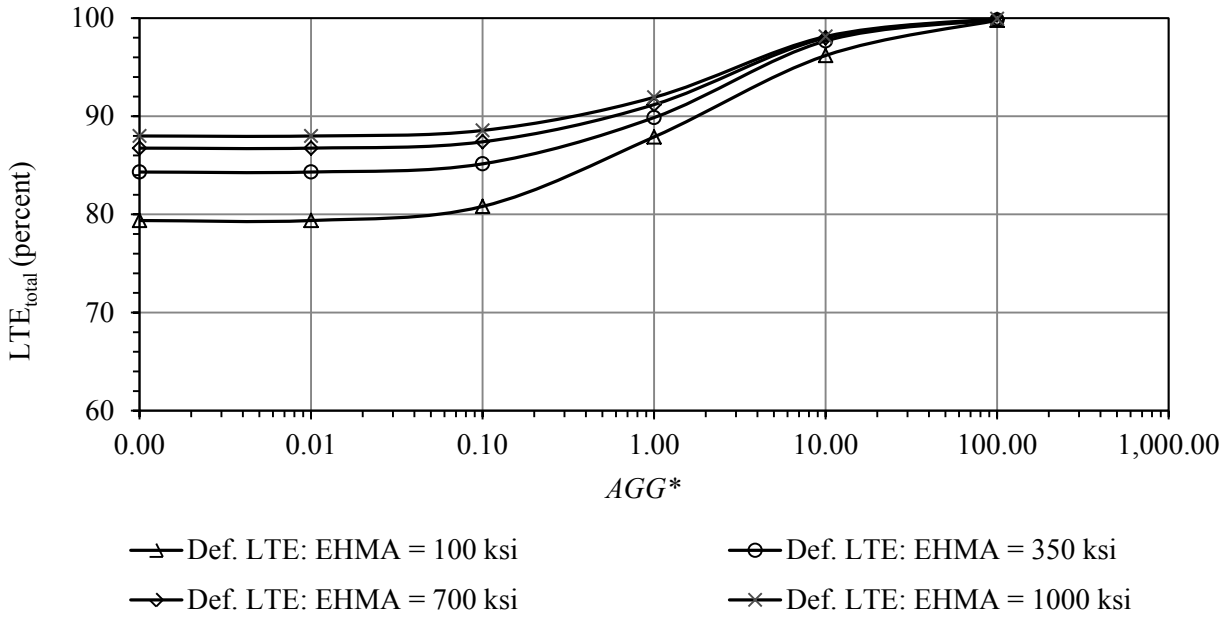
Figure 6.13. LTE$_{total}$ vs AGG^* relationship for a 5-in whitetopping over a 4-in HMA layer in the model with 5-ft x 6-ft joint spacing.
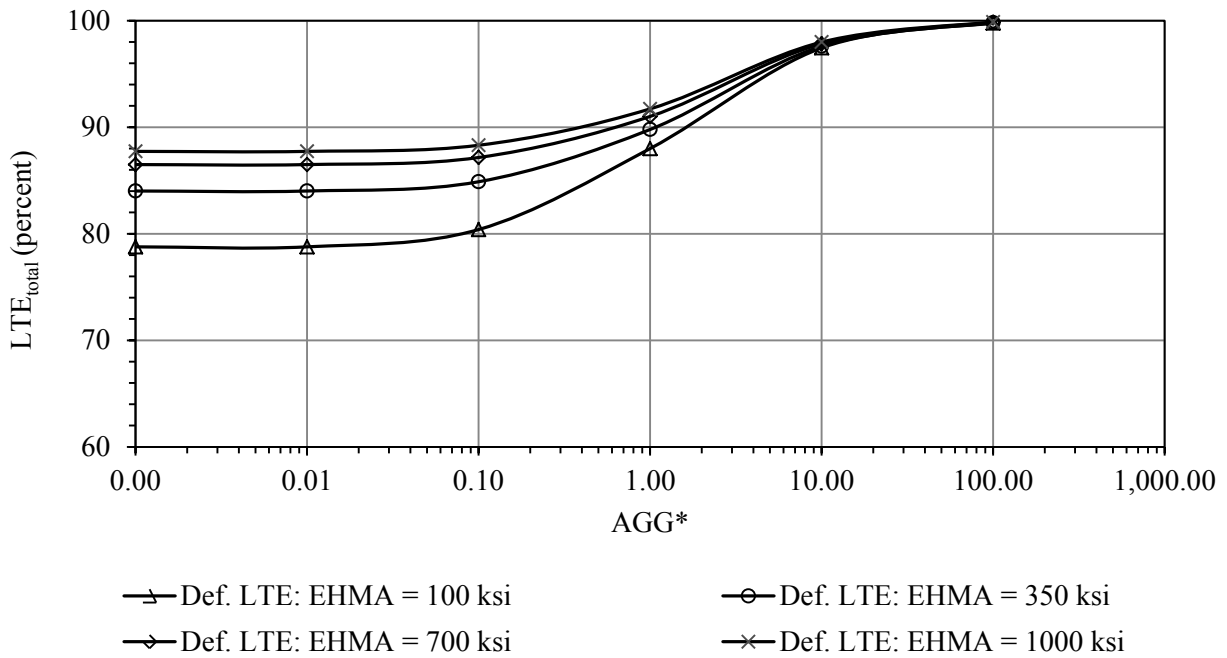
Figure 6.14. LTE$_{total}$ vs AGG^* relationship for a 6-in whitetopping over a 4-in HMA layer in the model with 5-ft x 6-ft joint spacing.

300
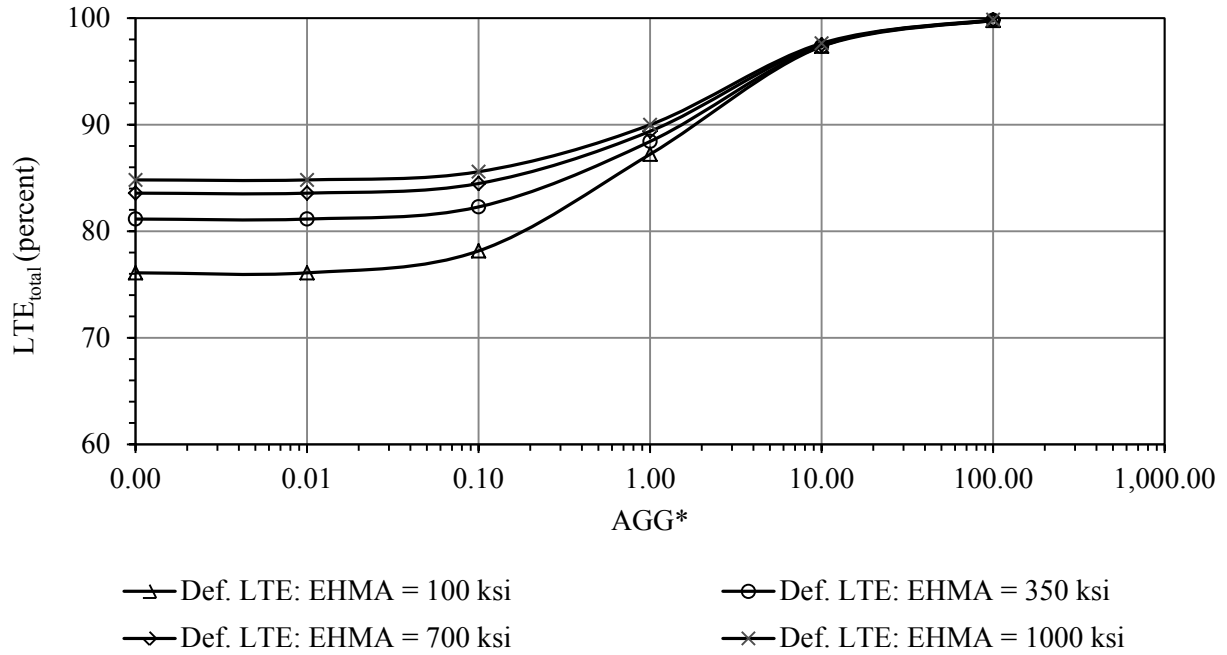
Figure 6.15. LTE$_{total}$ vs AGG^* relationship for a 6-in whitetopping over a 3-in HMA layer in the model with 5-ft x 6-ft joint spacing.
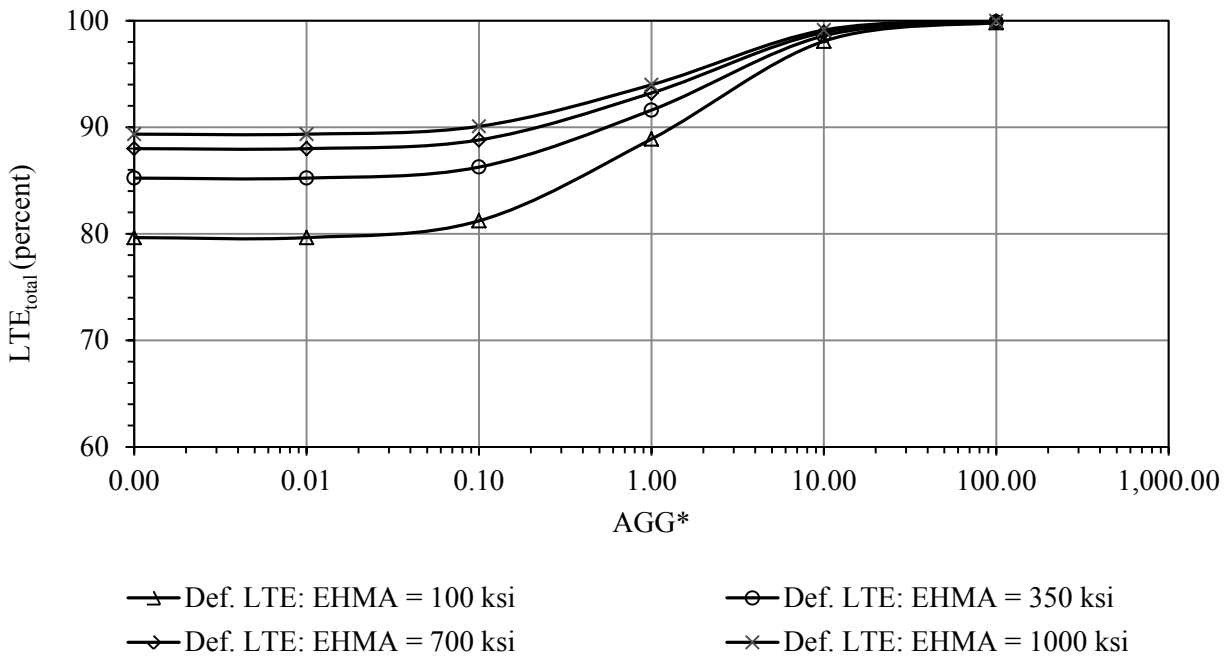
Figure 6.16. LTE$_{total}$ vs AGG^* relationship for a 3-in whitetopping over a 4-in HMA layer in the model with 5-ft x 6-ft joint spacing.

301
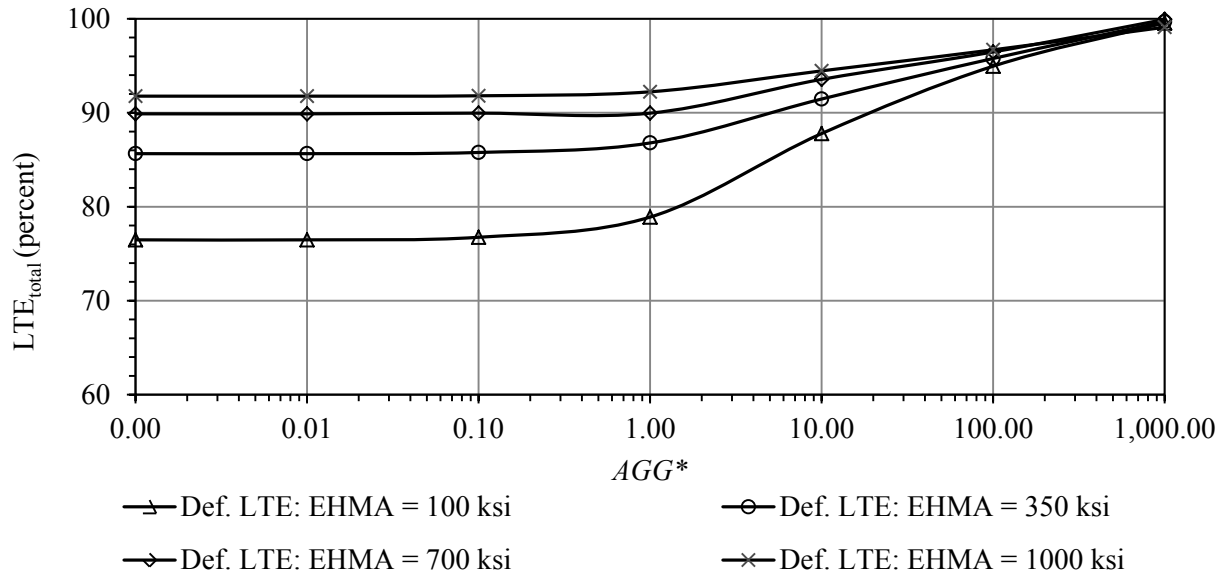
Figure 6.17. LTE$_{total}$ vs AGG^* relationship for a 3-in whitetopping over a 4-in HMA layer in the model with 4-ft x 4-ft joint spacing.
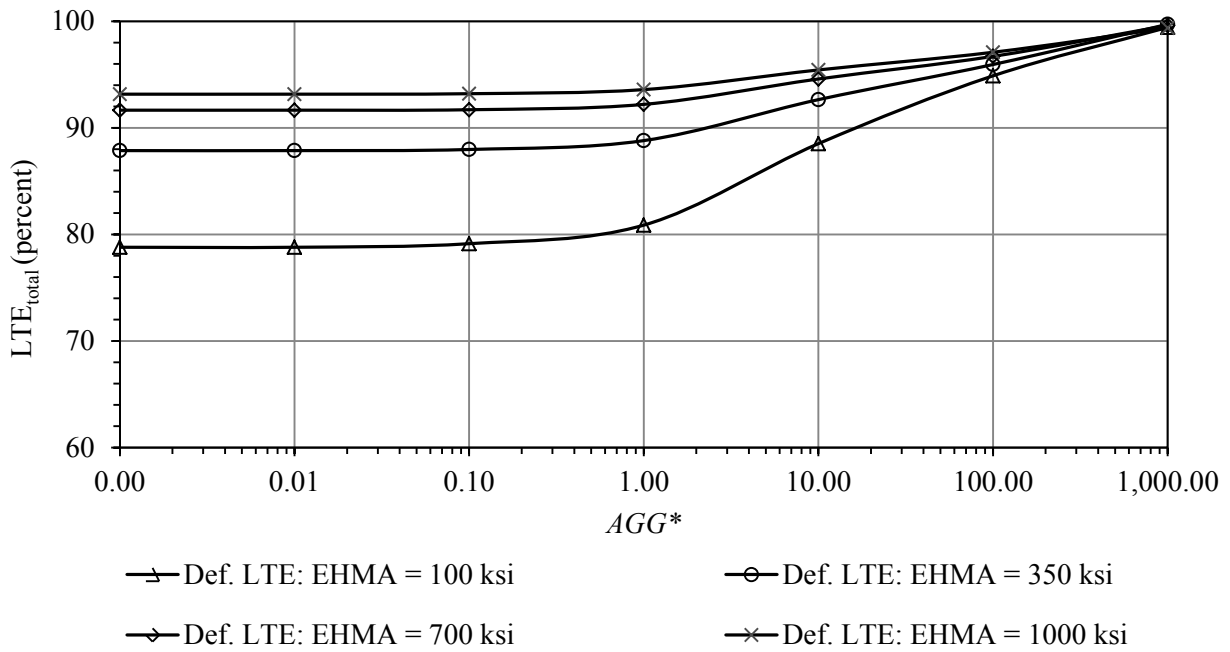
Figure 6.18. LTE$_{total}$ vs AGG^* relationship for a 3-in whitetopping over a 6-in HMA layer in the model with 4-ft x 4-ft joint spacing.

302

6.2.2.1 Load transfer contribution by the HMA layer

In all the figures (Figure 6.6 through Figure 6.18), it can be seen that even when the AGG^* was equal to 0, the LTE_{total} was from 68 to 95 percent. No load is transferred through aggregate interlock when $AGG^* = 0$ and therefore the contribution to the LTE is provided solely by the HMA layer. Therefore, LTE_{total} is equal to the load transfer contributed by the HMA layer (LTE_{HMA}). In the FEM models, this condition was simulated by avoiding any spring at the joints.

A closer look at all the graphs confirms that an increase in the E_{HMA} and h_{HMA} increases the LTE_{HMA}, indicating an increased contribution of the HMA layer in load transfer. For example, in the 4-in whitetopping over a 4-in HMA layer with a 5-ft x 6-ft joint spacing (Figure 6.7), the LTE_{HMA} increased from 80 to 89 percent when the E_{HMA} was increased from 100 to and 1000 ksi. For the same 4-in thick whitetopping with an $E_{HMA} = 100$ ksi, the LTE_{HMA} increased from 80 to 86 percent when the h_{HMA} was increased from 4 (Figure 6.7) to 8 in (Figure 6.11). It is also interesting to see that when the HMA layer stiffness was low, the difference in the LTE_{HMA} between models with 5-ft x 6-ft slabs and 4-ft x 4-ft slabs was greater. In the TWT cases, it can be seen that when $E_{HMA} = 100$ ksi, the difference in LTE_{total} among the design combinations is between 12 to 14 percent, whereas when E_{HMA} is 1,000 ksi, this difference is reduced to 3 to 4 percent. In the UTW cases, the HMA layer exhibits a greater contribution to load transfer for both 5-ft x 6-ft and 4-ft x 4-ft joint spacings (compare Figure 6.16 and Figure 6.17).

As it was seen that the LTE_{HMA} increases with increasing E_{HMA} and h_{HMA}, it was thought LTE_{HMA} can have a correlation with the flexural stiffness of the HMA layer. The flexural stiffness of HMA layer can be calculated by using the following equation.

303

$$FS_{HMA} = \frac{E_{HMA}h_{HMA}^3}{12(1 - \mu_{HMA}^2)} \qquad (6.3)$$

Where FS_{HMA} is the flexural stiffness of HMA layer, E_{HMA}, h_{HMA} and μ_{HMA} are the modulus of elasticity, thickness and poison's ratio of HMA layer, respectively.

Figure 6.19 presents the LTE$_{HMA}$ vs FS_{HMA} relationship for 3- and 4-in thick UTW for both 4-ft x 4-ft and 5-ft x 6-ft slabs. It can be seen that a correlation exists between the LTE$_{HMA}$ and SR_{HMA}. A logarithmic relationship could be established between the LTE$_{HMA}$ and SR_{HMA} for all four cases. As anticipated, the 3-in UTW shows more dependence on LTE$_{HMA}$ as compared to the 4-in thick UTW. However, a clear difference of LTE$_{HMA}$ vs SR_{HMA} relationship between the slab sizes is not observed. To verify the dependence of LTE$_{HMA}$ on the flexural stiffness of the HMA layer, LTE data for the MnROAD whitetopping sections was reviewed. The LTE$_{total}$ vs surface temperature relationships for two MnROAD Cells were presented in Chapter 2.0 . Figure 2.5 and Figure 2.6 presented 3 years (1998, 1999 and 2000) of load transfer data for Cells 95 and 96, respectively. In the winter, when the temperature is low, the crack width between the slabs reaches its widest. It can be assumed that during the winter, contribution of the HMA layer is the highest.

Cells 95 was constructed with a 3-in overlay over a 10-in HMA layer and Cell 96 was constructed with a 6-in overlay over a 7-in HMA layer. The joint spacing for both the cells was 5ft x 6ft. From Figure 2.5 and Figure 2.6, the LTE$_{total}$ at the minimum temperature was collected and presented in Table 6.2. Flexural stiffness was calculated using 0.35 as the poison's ratio and 722,700 psi as the modulus of elasticity of the HMA layer, at the minimum temperature, 30°F (Barman, et al., 2010). It is very interesting to see that even though Cell 95 was constructed with a 3-in overlay as compared to a 6-in overlay for Cell 96, the LTE$_{total}$ for Cell 95 was higher. This means the higher HMA layer flexural stiffness in Cell 95 had a contribution in load transfer.

This again proves that a good amount load is transferred through the HMA in a whitetopping overlay.

Table 6.2. Design features and Minimum LTEtotal data for MnROAD Cells 95 and 96.

Cell No.	Thickness of PCC slab (in)	Thickness of HMA layer (in)	Size of the slab (ft × ft)	Flexural stiffness (lb-in)	Minimum LTE$_{total}$ (observed at ~ 30°F)		
					1998	1999	2000
95	3	10	5 x 6	68,632,479	84	80	80
96	6	7	5 x 6	23,540,940	84	55	65
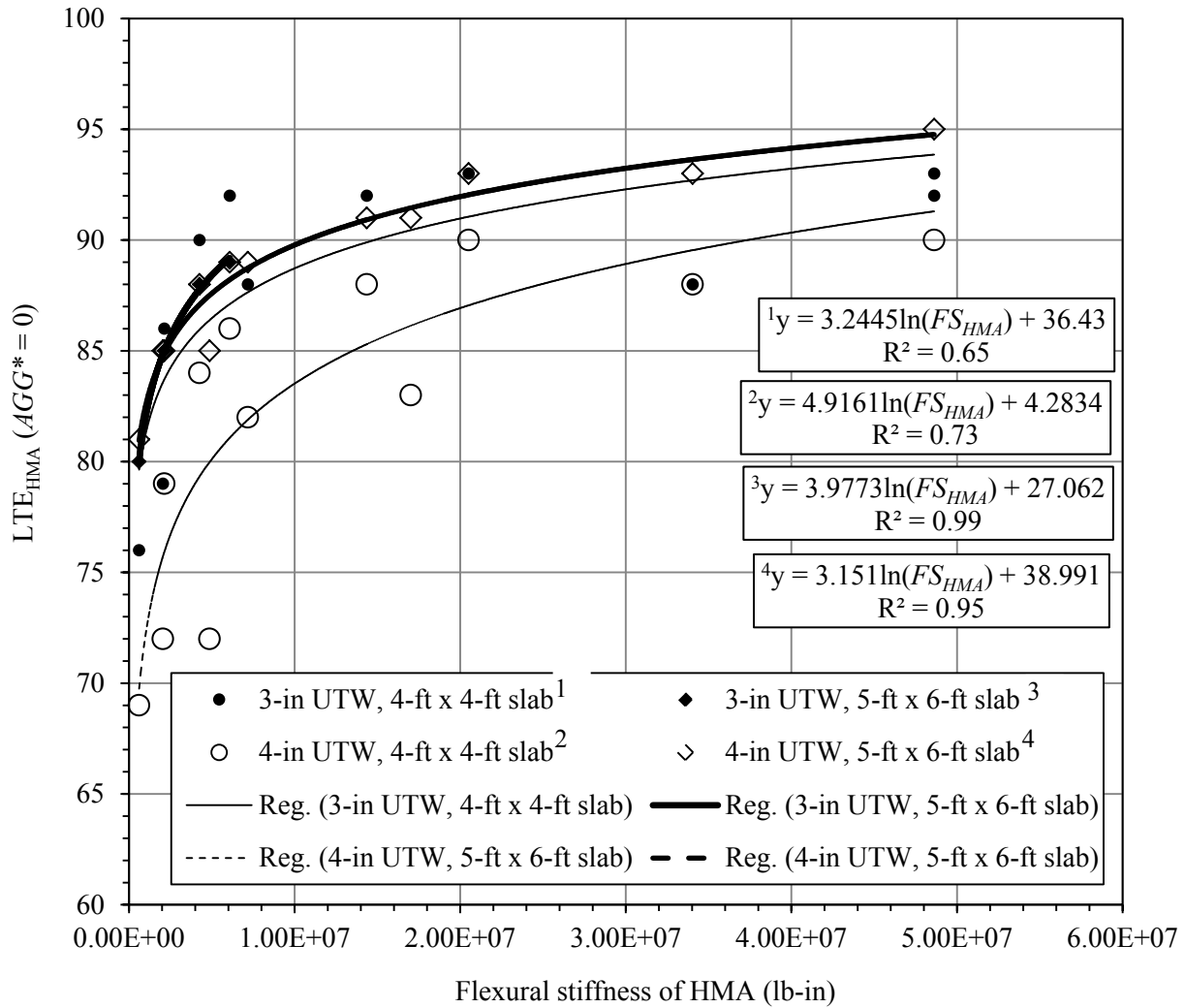
Figure 6.19. LTE$_{HMA}$ vs flexural stiffness of HMA layer.

[1]y = 3.2445ln(FS_{HMA}) + 36.43
R² = 0.65

[2]y = 4.9161ln(FS_{HMA}) + 4.2834
R² = 0.73

[3]y = 3.9773ln(FS_{HMA}) + 27.062
R² = 0.99

[4]y = 3.151ln(FS_{HMA}) + 38.991
R² = 0.95

305

6.2.2.2 LTE$_{total}$ vs AGG^* for different whitetopping designs

In the 5-ft x 6-ft slabs, the comparison the between 4-, 5-, 6- and 3-in whitetoppings over a given h$_{HMA}$ thickness shows that the LTE$_{total}$ vs AGG^* relationship is similar. This indicates a low sensitivity of the LTE$_{total}$ vs AGG^* relationship to overlay thickness. However, in the 4-ft x 4-ft slabs, it is found that the LTE$_{total}$ vs AGG^* relationship is sensitive to the overlay thickness (compare Figure 6.8 and Figure 6.17). These results are reasonable because, in the shorter slabs, the dominance of the joint stiffness is greater because the load location is influenced by both the transverse and longitudinal joints and the spring constants assigned to each were the same. In Figure 6.15, where the relationship for the 6-in whitetopping over a 3-in HMA layer is presented, the slightly lower LTE$_{total}$ for the entire range of AGG^* is more a function of the thinner HMA layer than a thicker overlays.

It was observed that the LTE_{total} vs AGG^* relationship varies with respect to the E_{HMA} and h_{HMA}. Also the relationship is different for different slab sizes, mainly because of the location of the wheel load. The most interesting finding in this analysis is that the LTE$_{total}$ vs AGG^* relationship has a good correlation with the flexural stiffness ratio (FSR) of the whitetopping and HMA layers. The FSR is the ratio of the whitetopping stiffness to the HMA layer stiffness and is given by the Equation (6.4) (Vandenbossche & Barman, 2010).

$$FSR = \frac{E_{wt}h_{wt}^3(1-\mu_{HMA}^2)}{E_{HMA}h_{HMA}^3(1-\mu_{wt}^2)} \tag{6.4}$$

Where FSR is the flexural stiffness ratio of the whitetopping and HMA layer; E_{wt}, E_{HMA}, h_{wt}, $h_{HMA,}$ μ_{wt} and μ_{HMA} are previously defined.

306

Figure 6.20 (for a 5-ft x 6-ft joint spacing) and Figure 6.21 (for a 4-ft x 4-ft joint spacing) present the LTE$_{total}$ vs AGG^* for different structures classified in terms of FSR. For both the 5-ft x 6-ft and 4-ft x 4-ft joint spacings, it can be seen that as the FSR increases, the LTE$_{total}$ decreases for any given value of AGG^*. This is because with a decrease in the HMA layer stiffness or increase in the FSR, the contribution of the HMA layer is reduced and the whitetopping joint stiffness becomes more influential. Also, at a given FSR, a 5-ft x 6-ft as compared to 4-ft x 4-ft joint design has a higher LTE$_{HMA}$. The LTE$_{total}$ vs AGG^* relationship as a function of FSR will be very helpful in the whitetopping design procedure to account for the joint stiffness when estimating the critical stresses.
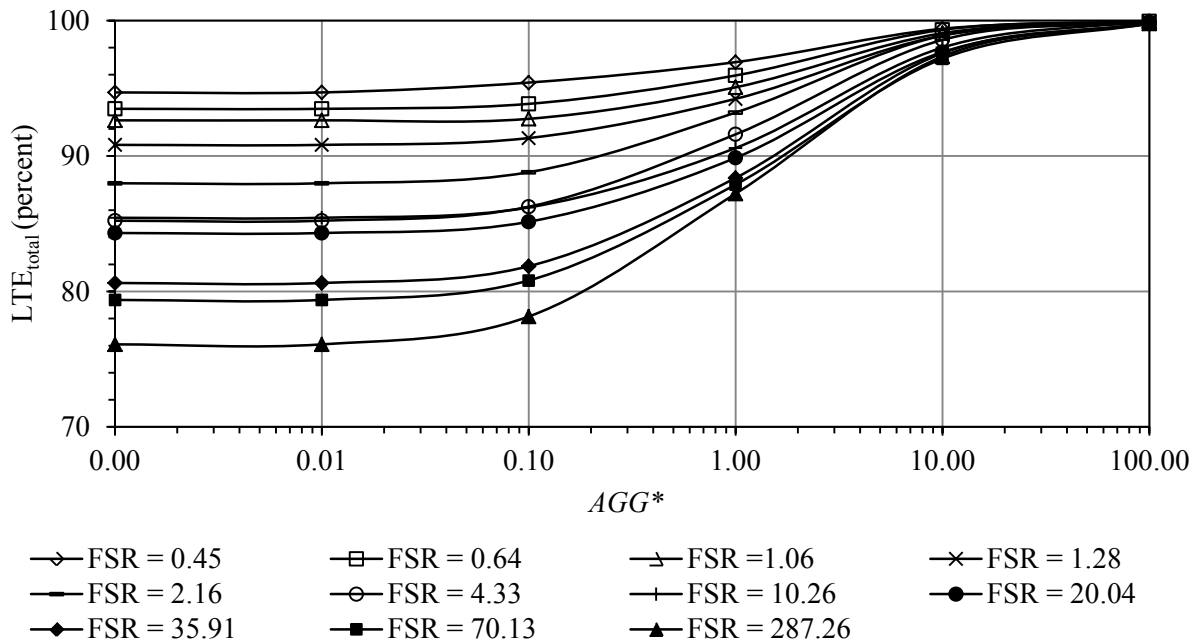
Figure 6.20. LTE$_{total}$ vs AGG^* relationship as a function flexural stiffness ratio (FSR) for 5-ft x 6-ft joint spacing.
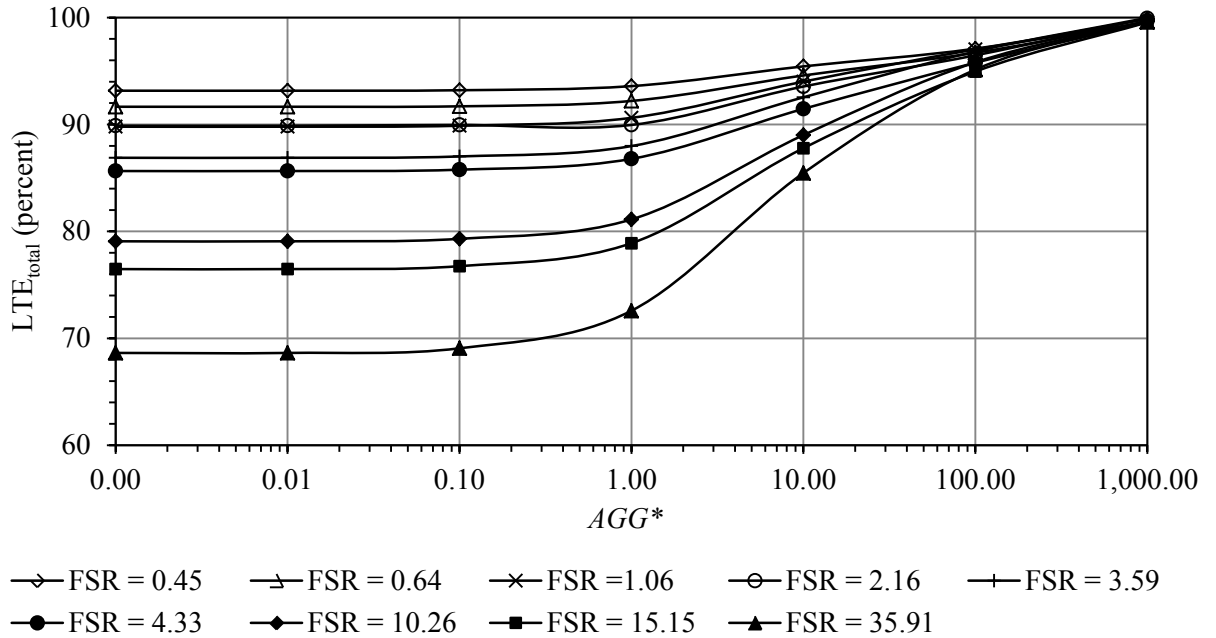
Figure 6.21. LTE$_{total}$ vs AGG^* relationship as a function flexural stiffness ratio (FSR) for 4-ft x 4-ft joint spacing.

6.2.2.3 Proposed method for determining AGG^* for whitetopping design

In the previous chapter, the deflection load transfer characteristics of the PC and two types of FRC mixes were established from the laboratory test results. The LTE contribution through aggregate interlock for the PC and FRC mixes were related to crack width. This LTE contribution by the concrete, through aggregate interlock, obtained from the laboratory experiments, is denoted as LTE$_{conc}$. It may be mentioned that the LTE$_{conc}$ is a function of concrete mixture type and crack width regardless of its application in whitetopping or any other conventional rigid pavements. LTE$_{conc}$ can be directly determined from the laboratory test or by using the regression models developed in Chapter 5.0 .

In whitetopping, LTE$_{total}$ is the sum of the LTEs contributed by the whitetopping and the HMA layers, and LTE$_{total}$ can be expressed as Equation (6.5).

308

$$LTE_{total} = LTE_{wt} + LTE_{HMA} \qquad (6.5)$$

Where LTE_{wt} and LTE_{HMA} are the LTE (percent) contributed by whitetopping and the HMA layer, respectively. The difference between LTE_{conc} and LTE_{wt} is that the LTE_{conc} represents the load transfer contribution by a concrete mixture through the aggregate interlock at any given crack width regardless to its application in whitetopping or any other rigid pavements, whereas, LTE_{wt} is the LTE contribution by the whitetopping (concrete layer) in a whitetopping overlay. LTE_{wt} is established in this chapter using the FEM.

The combination of the LTE_{conc} vs crack width relationship, and LTE_{total} vs AGG^* relationship as a function of FSR (Figure 6.20 and Figure 6.21) can provide the value of AGG^* at any crack width for different types of concrete mixes. The magnitude of LTE_{HMA}, as a function of the FSR, can be found in the Figure 6.20 and Figure 6.21. The LTE_{total} at $AGG^* = 0$ is equal to the LTE_{HMA}. The LTE_{wt} can be determined using the following equations.

$$LTE_{wt} = LTE_{total} - LTE_{HMA} \qquad (6.6)$$

In an ideal case, when $cw = 0$, the $LTE_{total} = 100$ percent, considering no crack propagation through the HMA layer. So, LTE_{wt} can be expressed by the following Equation.

$$LTE_{wt} = 100 - LTE_{HMA} \qquad (6.7)$$

In reality, $cw > 0$, then,

$$LTE_{wt} < 100 - LTE_{HMA} = (100 - LTE_{HMA}) \ x \ \frac{LTE_{conc}}{LTE_{conc_{cw=0}}} \qquad (6.8)$$

Here, LTE_{conc} is basically used as a measure of the joint condition. $LTE_{conc_{cw=0}}$ is the LTE through aggregate interlock at $cw = 0$, which is basically 100 percent (the ideal case). Based on the crack width and type of concrete mixture, LTE_{conc} can be determined. Thus, the expression for the LTE_{wt} can be simplified as below.

309

$$LTE_{wt} = (1 - \frac{LTE_{HMA}}{100}) \, LTE_{conc}$$

<div align="right">(6.9)</div>

Finally, after determining the LTE$_{total}$, the *AGG** can be determined from the Figure 6.20 and Figure 6.21 as a function of *FSR*.

6.3   JOINT PERFORMANCE VS DESIGN STRESS

The magnitude of stress in the loaded slab is influenced by the LTE$_{total}$ or *AGG**. The design stress (σ_d) was computed at the critical location, along the wheelpath. The maximum principal stress was considered as the design stress. In the model with the 5-ft x 6-ft joint spacing, the σ_d was obtained along the center of the outer loading area (Figure 6.22) as the stress was found to be larger under the outer loading area. In the model with the 4-ft x 4-ft joint spacing, the σ_p was obtained along the center of the inner loading (Figure 6.23); in some cases, stress was higher under the inner wheel path area, but the difference between the stress under the inner and outer wheel path was marginal. Figure 6.24 through Figure 6.34 present the trends in the change in the σ_d ($\Delta\sigma_d$) with the change in LTE$_{total}$, for different designs and slab sizes. Each figure includes $\Delta\sigma_d$ vs LTE$_{total}$ relationships for 4 different *E$_{HMA}$* values for a particular design. For each curve in these figures, the σ_d corresponding to the minimum LTE$_{total}$ (at *AGG** = 0), denoted as σ_{dmax}, is assumed to be 100 percent. The left and right ends of each curve correspondence to minimum *AGG** (0) and maximum *AGG** (100 or 1000), respectively. The influence of the increased LTE$_{total}$ on the $\Delta\sigma_d$ is quite noticeable. With the increase in the LTE$_{total}$, a higher magnitude of

load from the loaded side was transferred to the unloaded side, reducing the σ_d on the loaded

side.
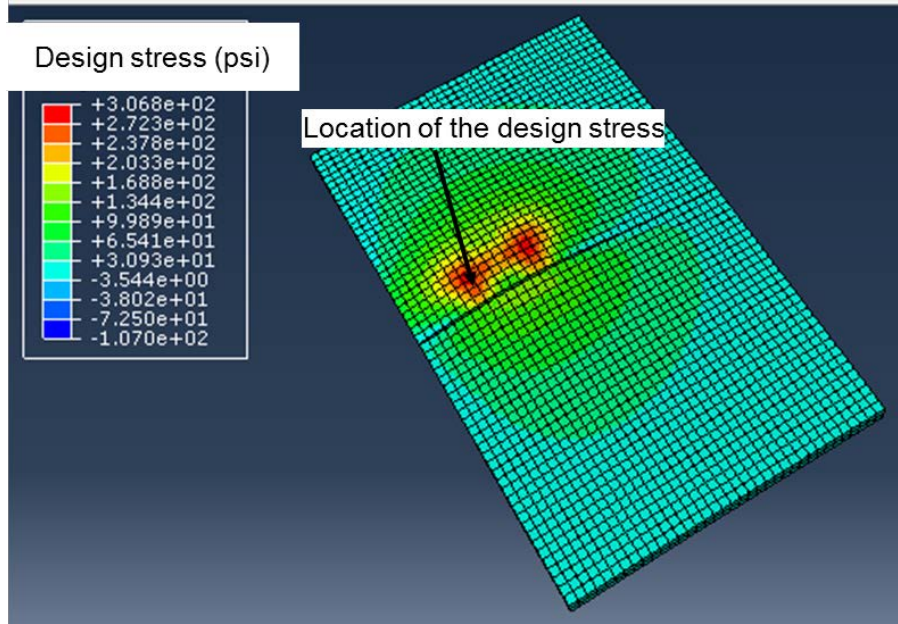
Figure 6.22. Location of the design stress in model with the 5-ft x 6-ft joint spacing.
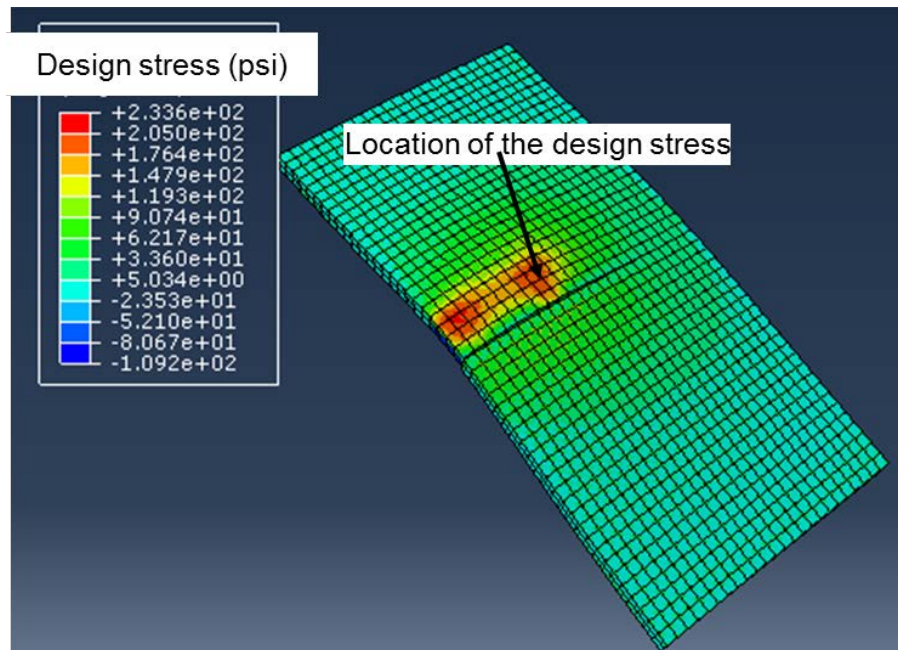
Figure 6.23. Location of the design stress in model with the 4-ft x 4-ft joint spacing.

311

When comparing the 5-ft x 6-ft slabs to the 4-ft x 4-ft slabs, the influence of the LTE$_{total}$ on σ_d was reduced. For example, in the 4-in whitetopping over a 4-in HMA layer (Figure 6.24), at an LTE$_{total}$ equal to 90 percent, the magnitudes of $\Delta\sigma_d$ were 93 and 98 percent for E_{HMA} equal to 100 and 1000 ksi, respectively. For the 4-ft x 4-ft slabs, these $\Delta\sigma_d$ values were 96 and 98 percent, respectively.

The h_{HMA} showed only a small influence on the $\Delta\sigma_d$ vs LTE$_{total}$ relationship for both slab sizes (between 2 to 6 percent). For the 5-ft x 6-ft slabs, Figure 6.24, Figure 6.26 and Figure 6.28 can be compared. For 4-ft x 4-ft slabs, Figure 6.25, Figure 6.27 and Figure 6.29 can be compared. However, this does not rule out the influence of h_{HMA} to the magnitude of the σ_d or on LTE$_{total}$. This finding is only indicating that change in the h_{HMA} does not have a significantly large influence the $\Delta\sigma_d$ vs joint performance relationship by a large extent.
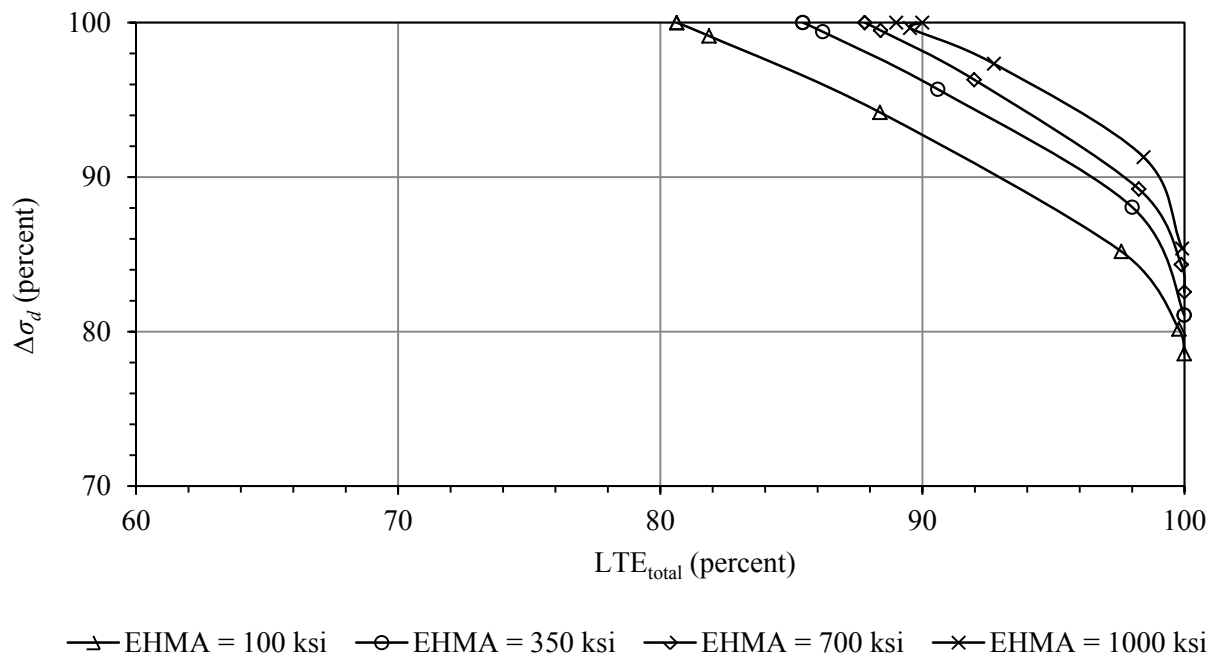
Figure 6.24. LTE$_{total}$ vs $\Delta\sigma_d$ for the 4-in whitetopping over a 4-in HMA with 5-ft x 6-ft joint spacing.

312
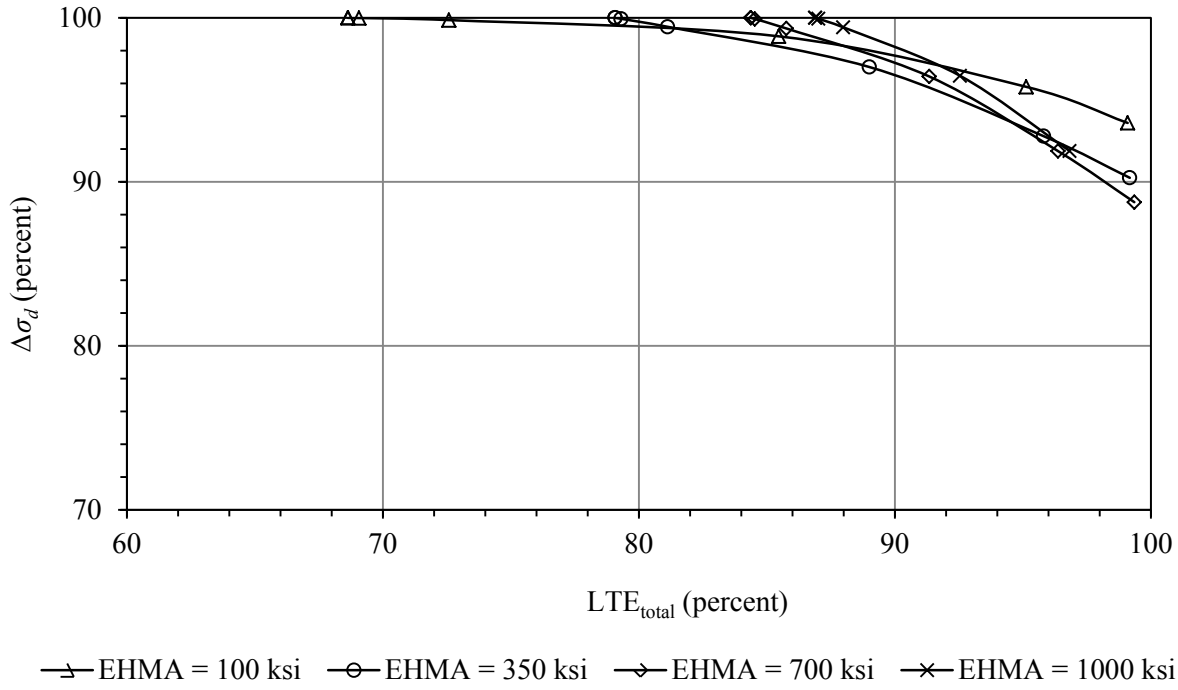
Figure 6.25. LTE$_{total}$ vs $\Delta\sigma_d$ for the 4-in whitetopping over a 4-in HMA with 4-ft x 4-ft joint spacing.
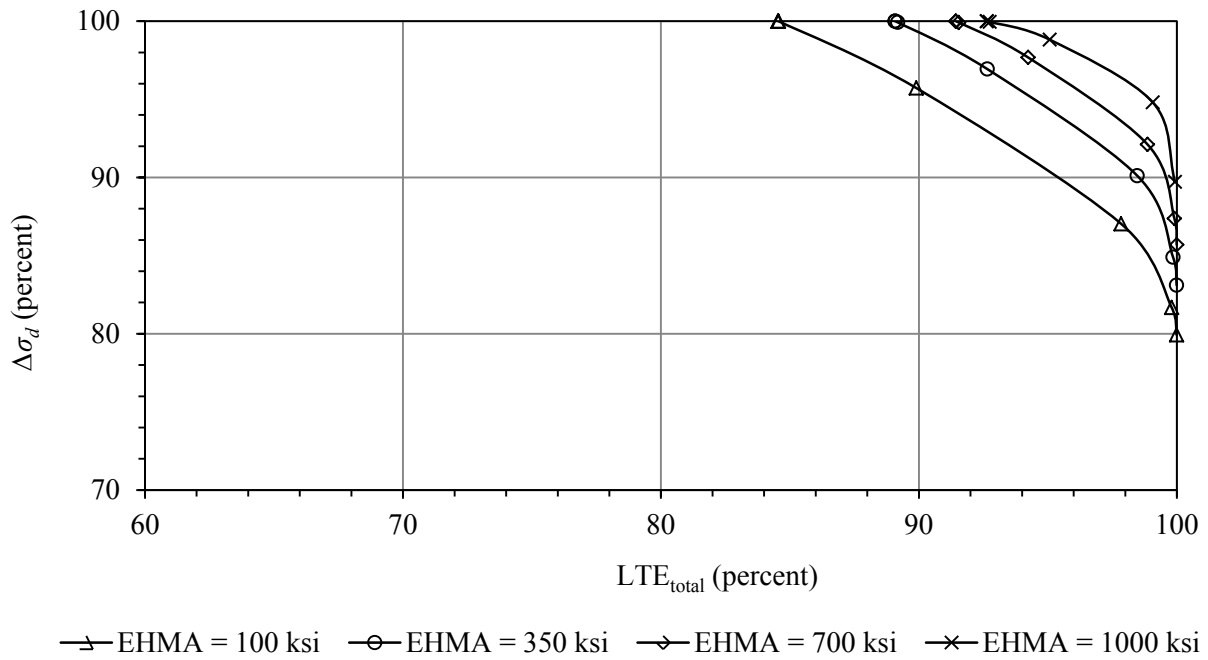
Figure 6.26. LTE$_{total}$ vs $\Delta\sigma_d$ for the 4-in whitetopping over a 6-in HMA with 5-ft x 6-ft slabs.

313
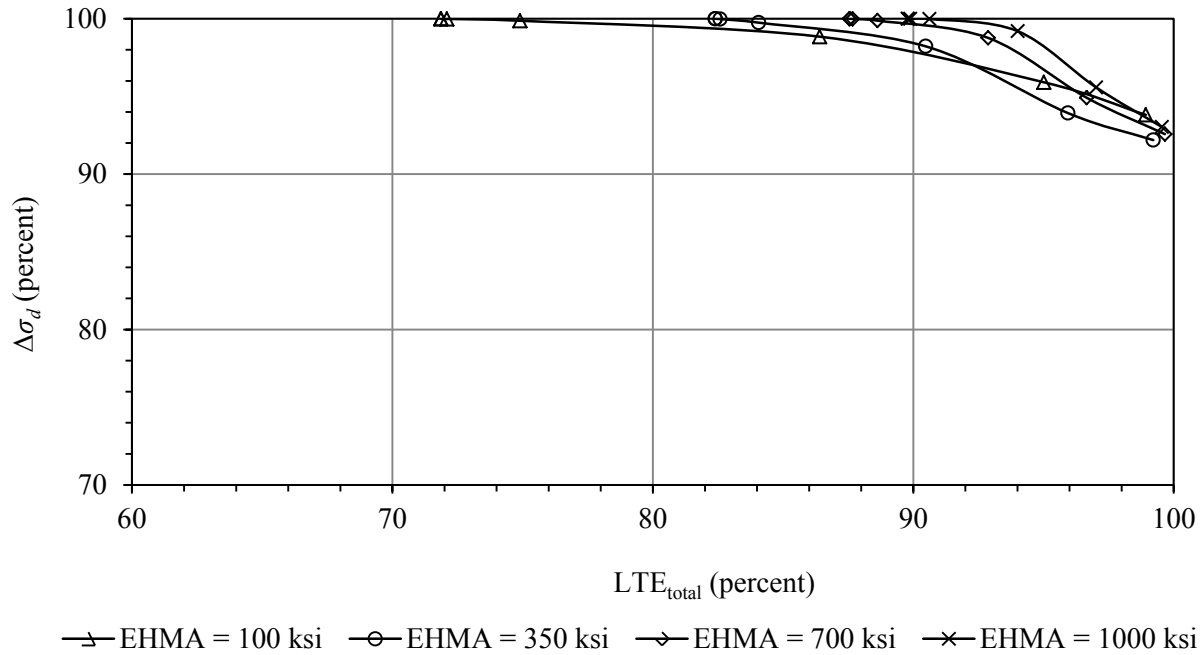
Figure 6.27. LTE$_{total}$ vs $\Delta\sigma_d$ for the 4-in whitetopping over a 6-in HMA with 4-ft x 4-ft slabs.
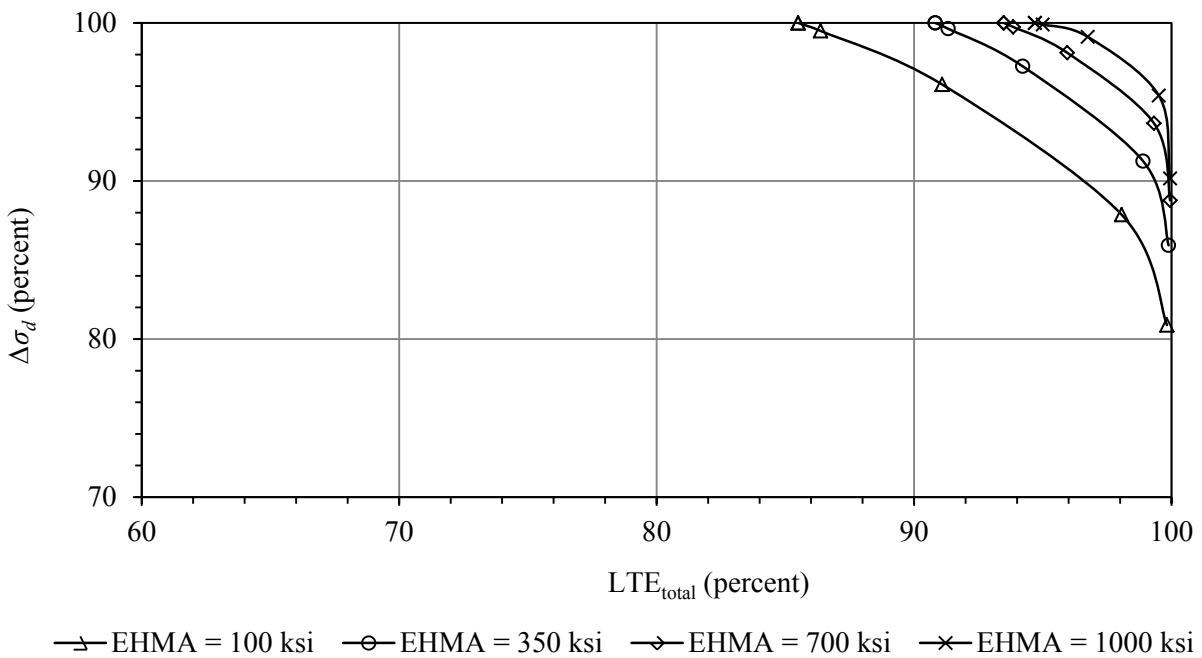
Figure 6.28. LTE$_{total}$ vs $\Delta\sigma_d$ for the 4-in whitetopping over 8-in HMA with 5-ft x 6-ft slabs.

314
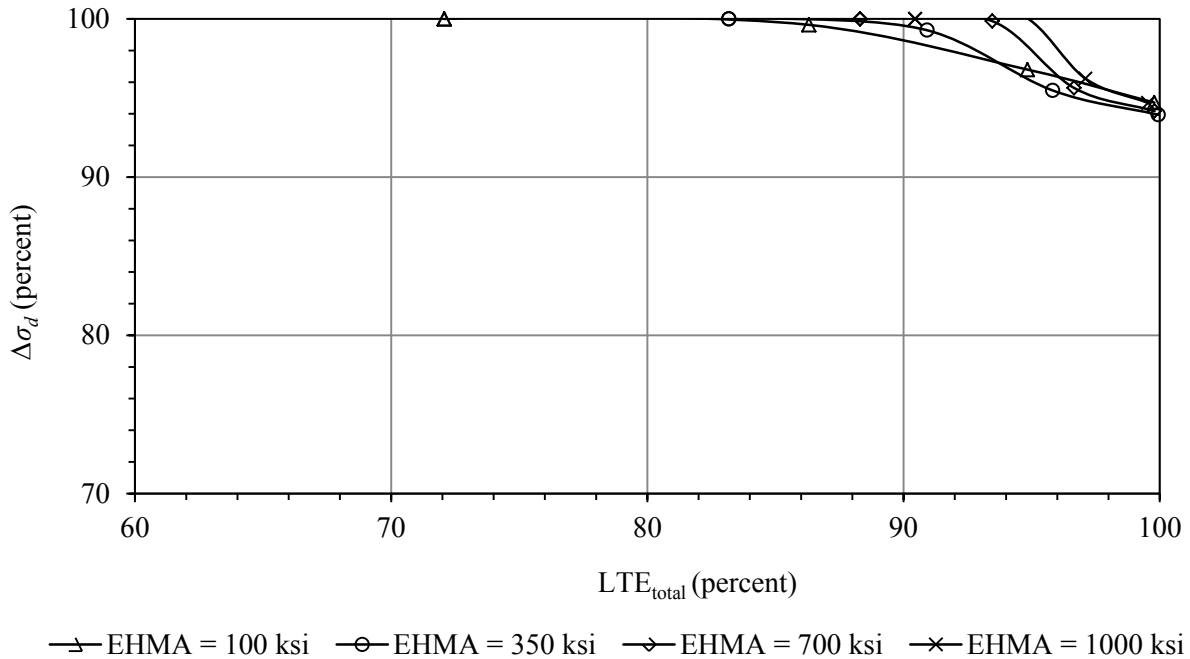
Figure 6.29. LTE$_{total}$ vs $\Delta\sigma_d$ for the 4-in whitetopping over a 8-in HMA with 4-ft x 4-ft slabs.

The influence of the h_{wt} on the $\Delta\sigma_d$ vs LTE$_{total}$ relationship was also not observed in this analysis (between 3 to 6 percent) to be significantly large. For the 5-ft x 6-ft slabs, Figure 6.24 (h_{wt} = 4 in), Figure 6.30 (h_{wt} = 5 in), Figure 6.31 (h_{wt} = 6 in) and Figure 6.33 (h_{wt} = 3 in) can be compared to see the influence of h_{wt} on $\Delta\sigma_d$ vs LTE$_{total}$ relationship. All of these whitetopping overlays had a 4-in HMA layer and 5-ft x 6-ft joint spacing. For the 4-ft x 4-ft slabs, Figure 6.25 (h_{wt} = 4 in) and Figure 6.34 (h_{wt} = 3 in) can be compared. The thickness of the HMA layer was 4 in for these two designs. Again, this finding only indicating that $\Delta\sigma_d$ vs LTE$_{total}$ relationship is not significantly sensitive to $h_{wt,}$ at a given LTE$_{total}$. The magnitude of the σ_d is obviously a function of h_{wt}. Moreover, LTE$_{total}$ itself increases with the increase in h_{wt} at a given crack width.

Figure 6.32 shows the $\Delta\sigma_d$ variation for a with 6-in whitetopping over a 3-in HMA. This design is included to see if a different trend is observed when the HMA layer is too thin. However, the σ_d variation is somewhat similar to the 6-in whitetopping over 4-in HMA structure.

315

Overall, a general comparison among all of figures (Figure 6.24 through Figure 6.34) shows that the influence of the E_{HMA} reduces with an increase in the h_{HMA}. It was seen that there is a considerable influence of LTE$_{total}$ on the $\Delta\sigma_d$ as well as σ_d. In the 5-ft x 6-ft slabs, the influence was larger when compared to the 4-ft x 4-ft slabs.
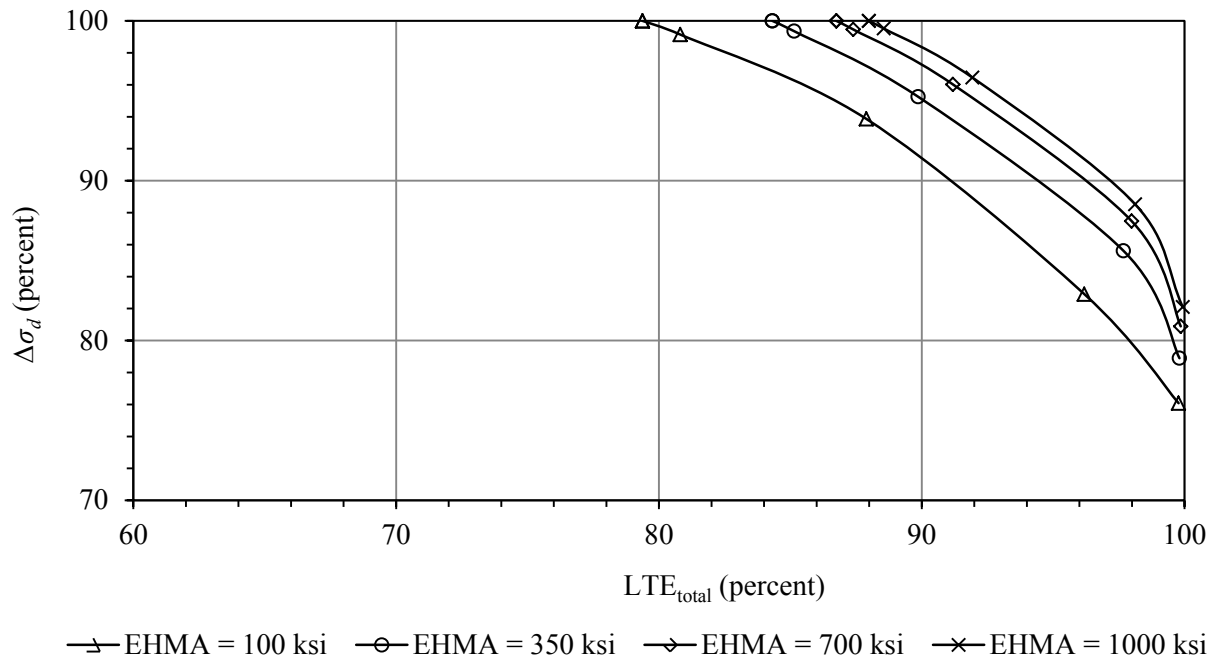
Figure 6.30. LTE$_{total}$ vs $\Delta\sigma_d$ for a 5-in whitetopping over a 4-in HMA with 5-ft x 6-ft slabs.
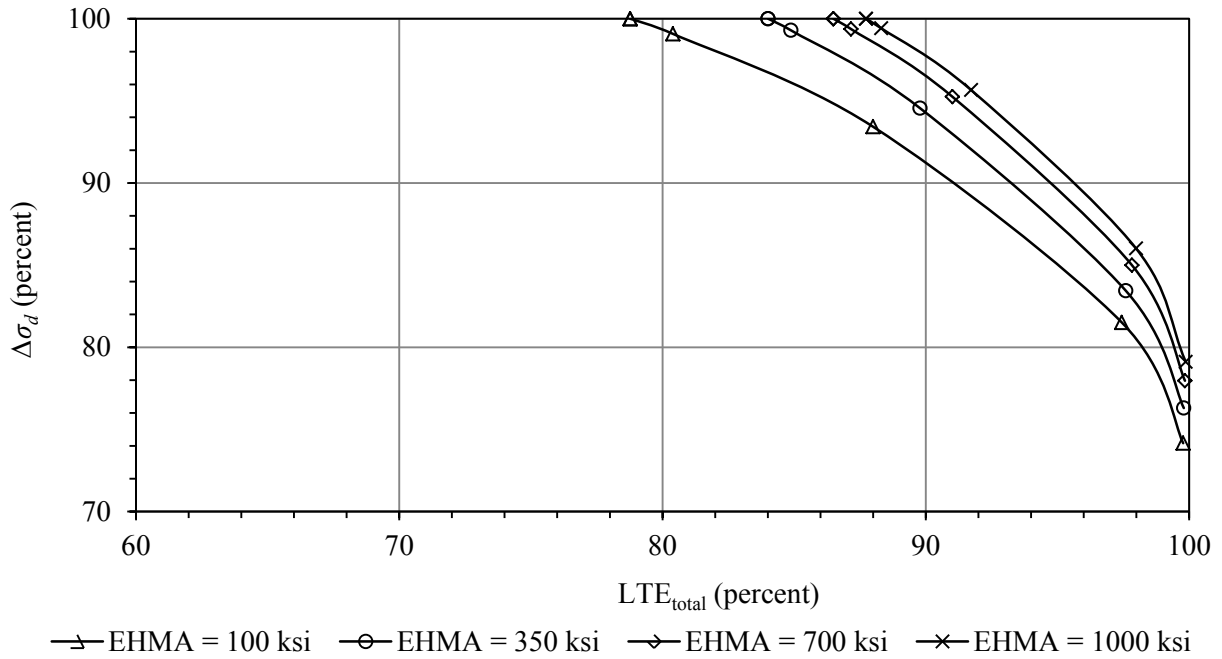
Figure 6.31. LTE$_{total}$ vs $\Delta\sigma_d$ for a 6-in whitetopping over a 4-in HMA with 5-ft x 6-ft slabs.
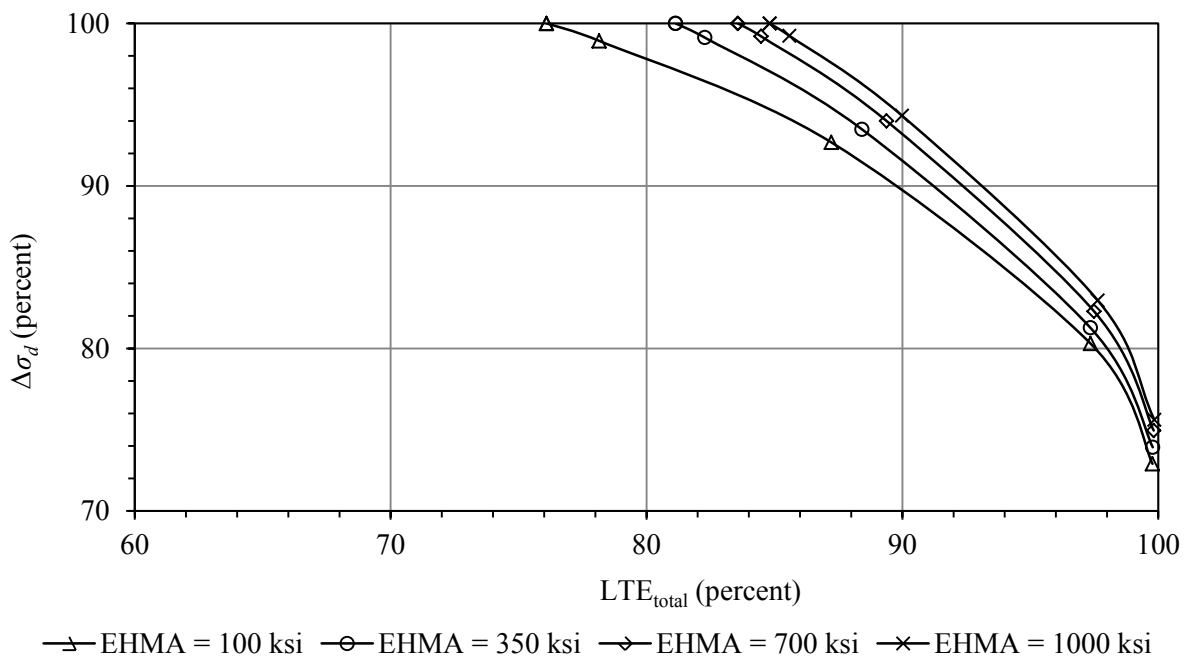
Figure 6.32. LTE$_{total}$ vs $\Delta\sigma_d$ for a 6-in whitetopping over a 3-in HMA with 5-ft x 6-ft slabs.

317
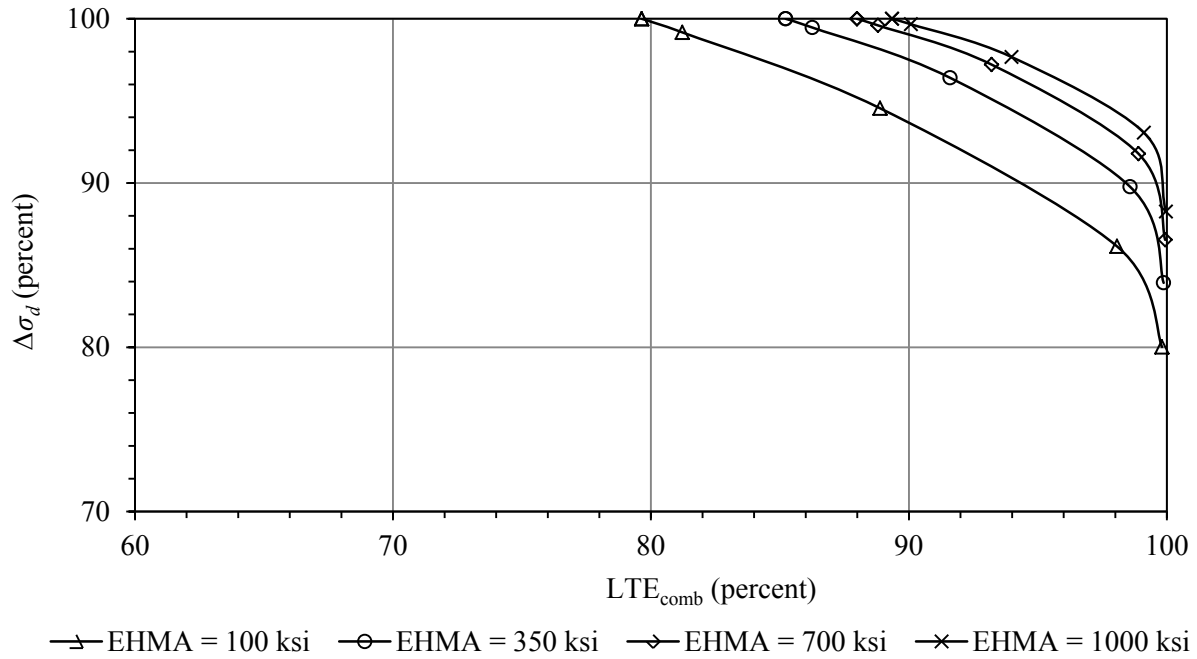
Figure 6.33. LTE$_{total}$ vs $\Delta\sigma_d$ for a 3-in whitetopping over a 4-in HMA with 5-ft x 6-ft slabs.
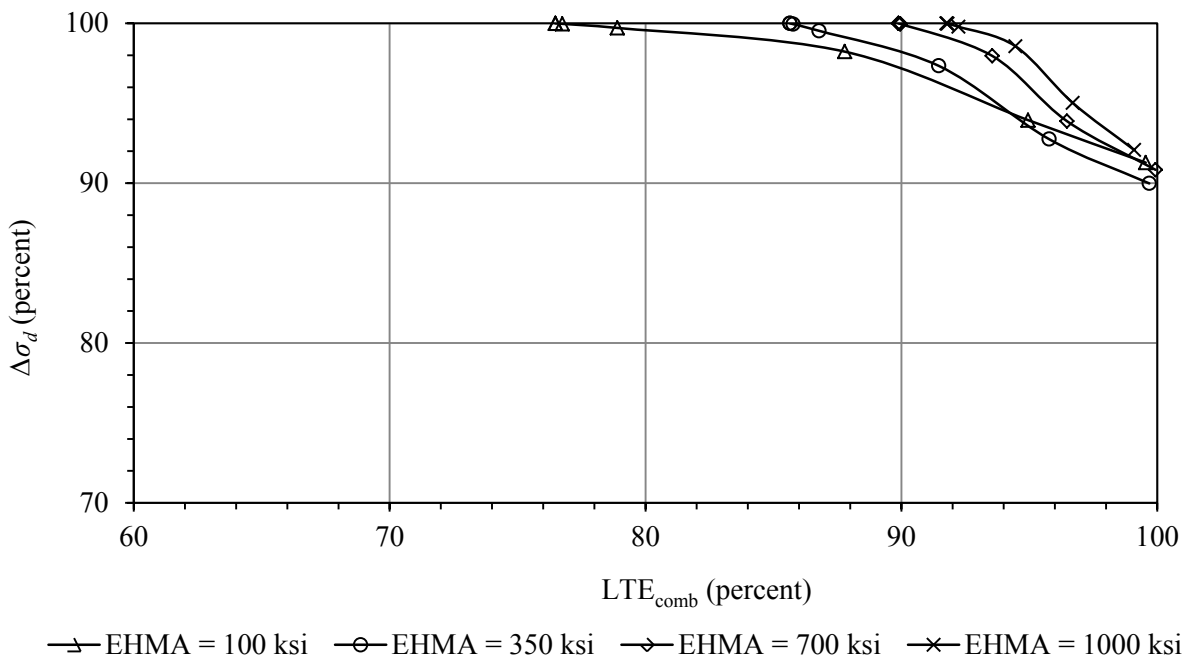
Figure 6.34. LTE$_{total}$ vs $\Delta\sigma_d$ for a 3-in whitetopping over a 4-in HMA in 4-ft x 4-ft slabs.

6.4   INFLUENCE OF INTERFACE BONDING ON THE DESIGN STRESS

The importance of the bond could be more when the total structure of the whitetopping and HMA layers are relatively weak. An investigation was carried out to verify the importance of interface bonding in regards to different whitetopping structures and flexural stiffnesses for HMA layer. The design stress computed for bonded and unbonded whitetopping overlays are compared. In addition to the previously presented FEM runs (Table 6.1), additional runs were performed considering no interface bonding between the whitetopping and HMA layers. The range of variables considered for these additional (unbounded) cases are presented in Table 6.3.

Table 6.3. Range of variables considered within the parametric study.

Slab size (ft x ft)	5 x 6
Whitetopping thickness (in)	3, 4 and 6
HMA thickness (in)	4, 6, 8
Modulus of elasticity of concrete (ksi)	4,000
Modulus of elasticity of HMA (ksi)	100, 350, 700 and 1,000
Poisson's ratio of concrete	0.15
Poisson's ratio of HMA	0.35
Modulus of subgrade reaction (psi/in)	150
Non-dimensional joint stiffness, AGG^*	1.0, 10.0

Figure 6.35, Figure 6.36 and Figure 6.37 present the design stresses computed for 3-, 4- and 6-in thick whitetoppings, respectively. The design stresses for the unbonded and bonded whitetopping structures are presented as a function of the flexural stiffness of the HMA layer, FS_{HMA} (Equation (6.3)). For each unbonded and bonded whitetopping, design stresses were computed considering two different AGG^* values, 1.0 and 10.0. In whitetopping, the LTE_{total} was found to be varying mostly when the AGG* values were varied between 1.0 and 10.0 (Figure 6.7 to Figure 6.18). In all three figures, it can be seen that the influence of AGG^* is

319

similar for bonded and unbonded whitetopping structures.   Also, in all three figures, the importance of bond is quite clear.

UB (AGG*= 1): y = -116.8ln(x) + 2241.3
R² = 0.98

UB (AGG*= 10): y = -101.7ln(x) + 1976.7
R² = 0.98

B (AGG*= 1): y = -89.94ln(x) + 1724.2
R² = 0.96

B (AGG*= 10): y = -80.38ln(x) + 1554.7
R² = 0.96

▲ UB (AGG*= 1)   ᐃ UB (AGG*= 10)   ● B (AGG*= 1)

○ B (AGG*= 10)   —— Log. (UB (AGG*= 1))   ········ Log. (UB (AGG*= 10))

—— Log. (B (AGG*= 1))   -------- Log. (B (AGG*= 10))

Note: UB- Unbonded and B- bonded
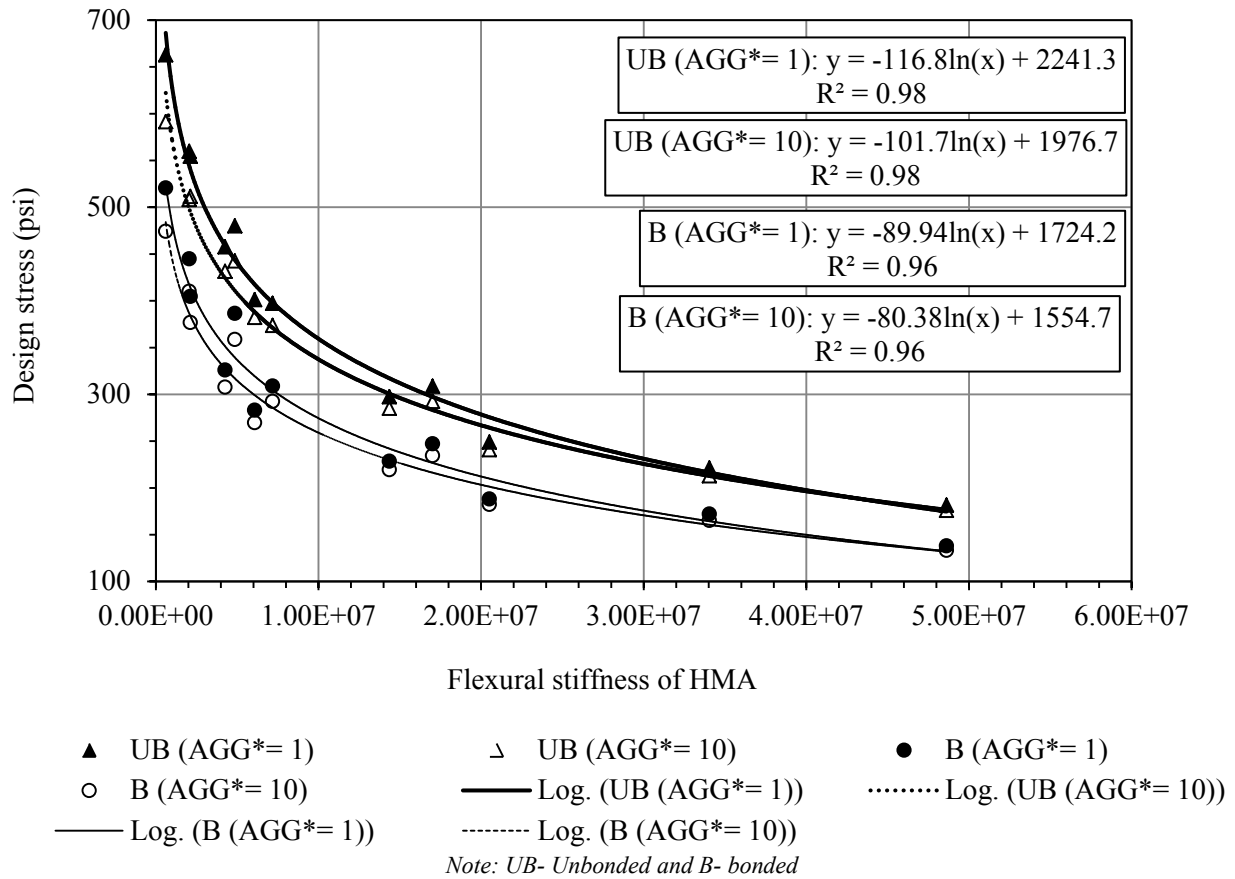
Figure 6.35. Comparison of design stresses between unbonded and bonded 3-in thick whitetopping with 5-ft x 6-ft slabs.
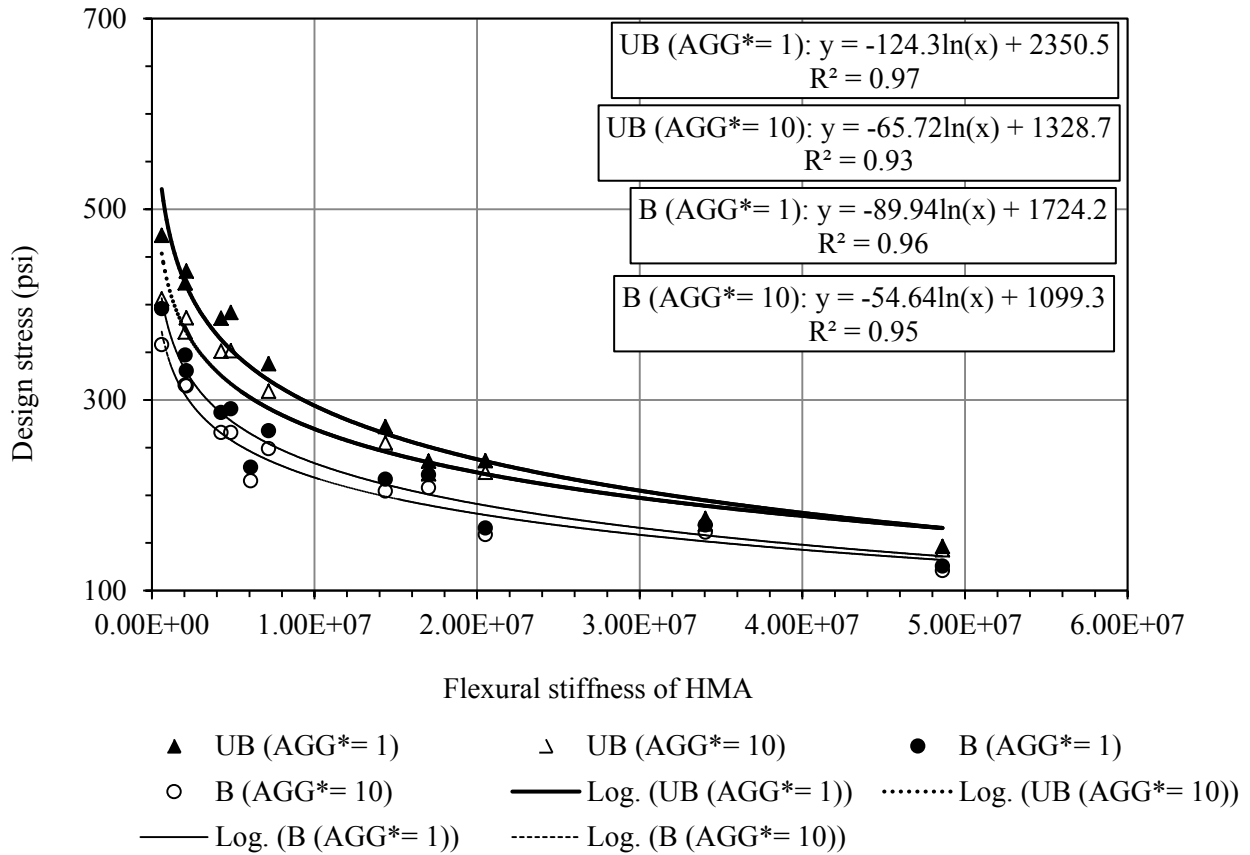
Figure 6.36: Comparison of design stresses between unbonded and bonded 4-in thick whitetopping with 5-ft x 6-ft slabs.

.

UB (AGG*= 1): y = -116.8ln(x) + 2241.3
R² = 0.98

UB (AGG*= 10): y = -17.72ln(x) + 471.39
R² = 0.78

B (AGG*= 1): y = -89.94ln(x) + 1724.2
R² = 0.96

B (AGG*= 10): y = -22.57ln(x) + 499.53
R² = 0.93

▲   UB (AGG*= 1)   △   UB (AGG*= 10)   ●   B (AGG*= 1)

○   B (AGG*= 10)   ——— Log. (UB (AGG*= 1))   ········ Log. (UB (AGG*= 10))

——— Log. (B (AGG*= 1))   -------- Log. (B (AGG*= 10))
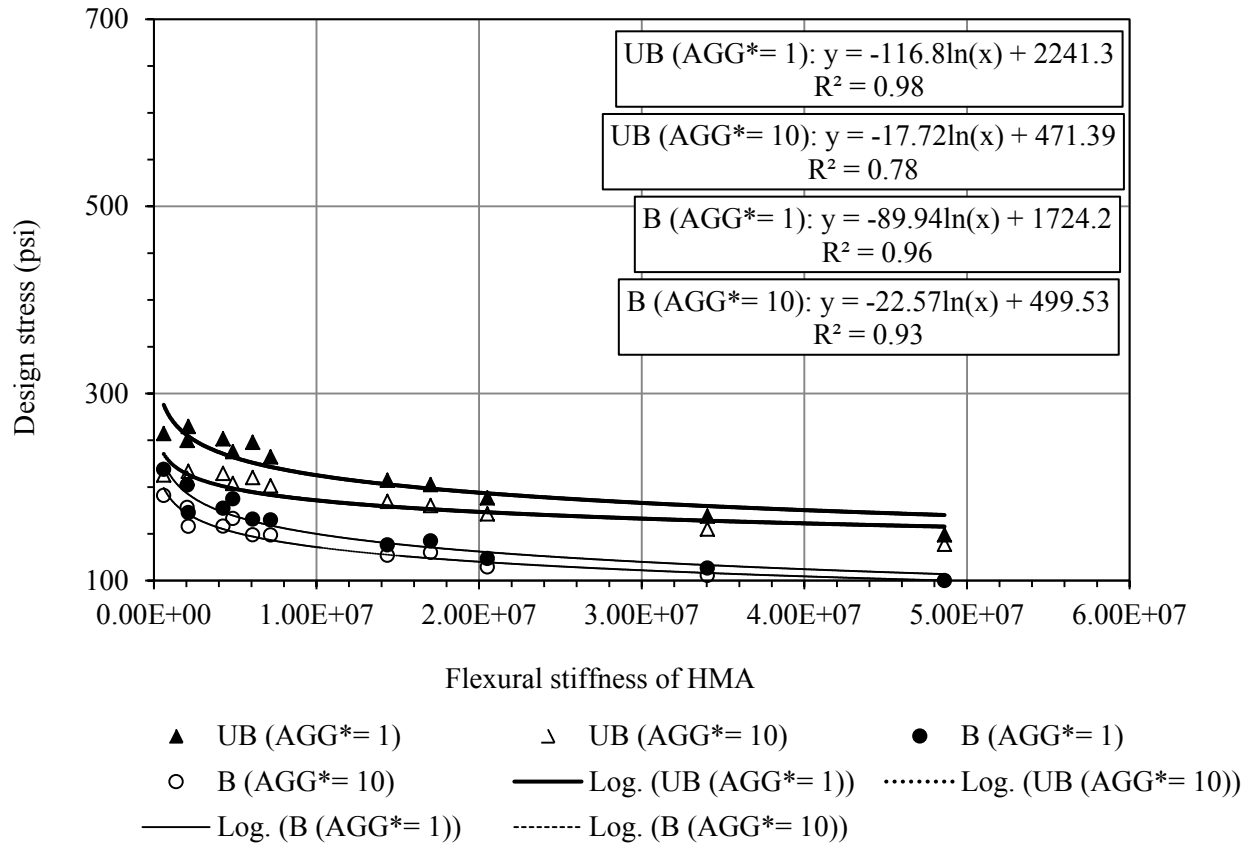
Figure 6.37. Comparison of design stresses between unbonded and bonded 6-in thick whitetopping with 5-ft x 6-ft slabs.

A comparison of the design stresses among the 3-, 4- and 6-in whitetopping thicknesses is presented in Figure 6.37.   Since, the influence of *AGG** in bonded and unbonded whitetoppings were found to be quite similar (Figure 6.35 through Figure 6.37), the design stress results computed for only *AGG** = 1.0 are in used in the comparison. It is very interesting to see that the thickness of the whitetopping can be decreased by ensuring bond at the interface. For example, the design stresses computed for a 3-in bonded and 4-in unbonded whitetopping are comparable. Also, for the case of a UTW, when the flexural stiffness of HMA layer is low (weak HMA layer structure) the interface bond helps in reducing the design stress by a significant amount. In 6-in whitetopping, since the contribution from the whitetopping overlay is

322

large, the influence of interface bond is found to be consistent regardless of the flexural stiffness of the HMA layer.
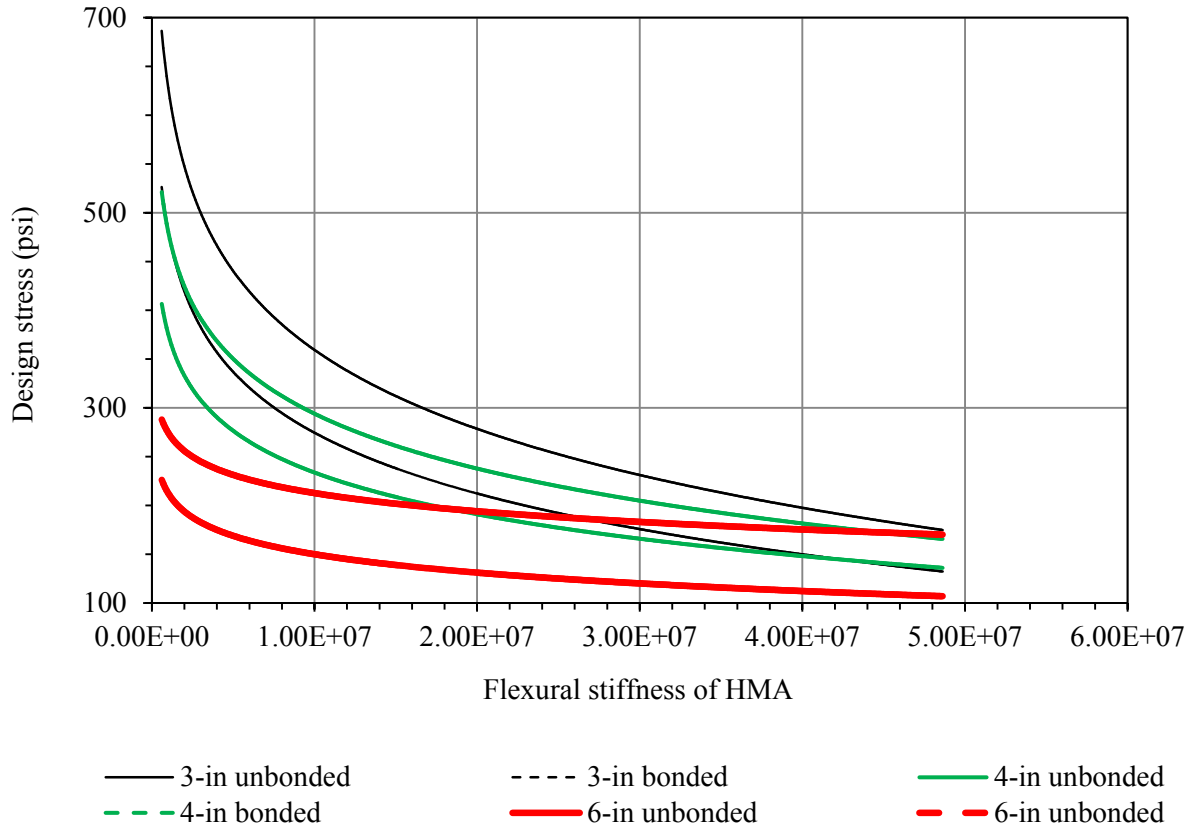
Figure 6.38. Comparison of the design stresses among 3-, 4- and 6-in whitetoppings for 5-ft x 6-ft slabs.

6.5 JOINT PERFORMANCE VS INTERFACE DEBONDING STRESS

Probably the most important contribution of the increased joint performance in whitetopping is the reduction in the potential for debonding. Debonding between the whitetopping and HMA layer at the interface is one of the primary causes for distress in the whitetopping. When a load is applied, the bottom surface of the whitetopping and the top surface of the HMA layer undergo

an equal deflection on the loaded slab. On the unloaded side, both the whitetopping and the HMA layer deflect as a result of load transfer. However, in addition to that, the HMA layer alone exhibits some downward force due to the existing continuity in the HMA layer under both sides. This downward force creates a normal tensile stress at the interface, known as the debonding stress (σ_{db}).

In the FEM modeling, as mentioned earlier, the interface bonding was simulated by assigning translational springs connecting the nodes at the bottom surface of the whitetopping and the top surface of the HMA layer. Since these springs are linearly elastic, applying a force results in some displacement. Theoretically, this displacement is equal to the difference in the deflections between the bottom of the whitetopping and the top of the HMA layer. However, this displacement is only a theoretical value and does not represent the actual differential deflection between the bottom of the whitetopping and the top of the HMA layer. In a real case, a threshold value for σ_{db} which will be referred to as the "peeling stress" is required to peel the HMA layer from the whitetopping. The debonding stress varies with joint performance.

To investigate whether an improved joint performance could reduce the σ_{db} that is responsible for interface debonding, the relationship between the σ_{db} and LTE$_{total}$ was studied. Figure 6.39 shows an example of the deflections generated using the FEM at the bottom of the whitetopping and the top of the HMA layer at the transverse joint for a 4-in whitetopping over a 4-in HMA layer, E_{HMA} = 100 ksi, and slab size = 5-ft x 6-ft. It can be seen that the difference between the deflections, which is equal to the spring displacement (d), is zero when the LTE$_{total}$ is 100 percent, and increases as the LTE$_{total}$ decreases. Ideally, when LTE$_{total}$ is equal to 100 percent, the two slabs respond as one continuous slab, so σ_{db} = 0. The product of d (in) and the

324

assigned interface spring stiffness (lb/in) provides the linear tensile stress (lb) in the spring and can provide as an estimate of the debonding stress.
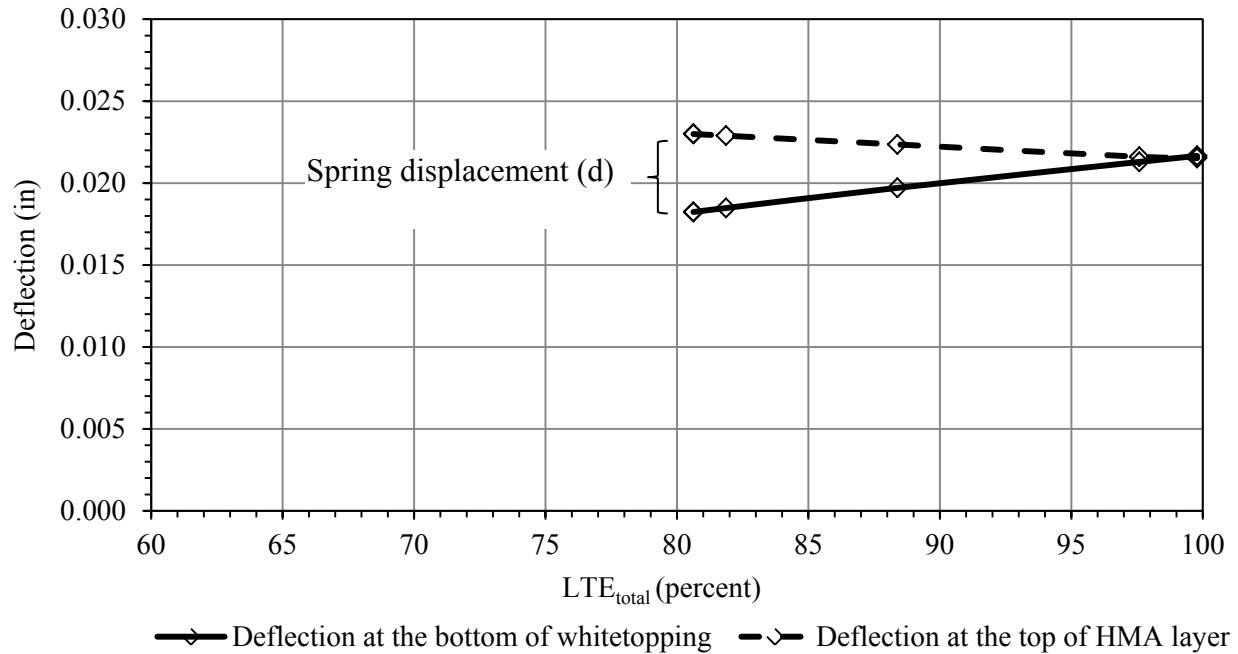
Figure 6.39. Deflections at the bottom of whitetopping and top of the HMA layer as a function of LTE$_{total}$ for a 4-in whitetopping over a 4-in HMA layer when E$_{HMA}$ = 100 ksi.

An initial scanning of the debonding stresses computed for different design variables for both the slab sizes revealed that the σ_{db} is insensitive to h_{HMA} and E_{HMA} and if it is insensitive to h$_{HMA}$ and E$_{HMA}$ then it will be insensitive to FS_{HMA}. However, it was moderately sensitive to the h_{wt}. Figure 6.41 depicts σ_{db} vs LTE$_{total}$ for four whitetopping thicknesses (3-, 4-, 5- and 6-in) for 5-ft x 6-ft slabs and Figure 6.41 depicts this relationship for two whitetopping thicknesses (3- and 4-in) for 4-ft x 4-ft slabs. For both slab sizes, it can be seen that the σ_{db} is higher for thinner whitetoppings.

In 5-ft x 6-ft slabs, for all the whitetopping thicknesses, a bi-linear relationship provided the best fit. The value of σ_{db} above and below 85% LTE$_{total}$ follows two separate trend lines.

325

Equations (6.10) to (6.17) provide the regression relationships for the σ_{db} as function of h_{wt} and LTE$_{\text{total}}$.

3-in UTW: LTE$_{\text{total}} \geq 85\%$

$$\sigma_{db} = -5.1216 LTE_{total} + 509.78; R^2 = 0.98 \tag{6.10}$$

3-in UTW: LTE$_{\text{total}} \leq 85\%$

$$\sigma_{db} = -9.1745 LTE_{total} + 859.68, R^2 = 0.99 \tag{6.11}$$

4-in UTW: LTE$_{\text{total}} \geq 85\%$

$$\sigma_{db} = -4.1689 LTE_{total} + 414.17; R^2 = 0.98 \tag{6.12}$$

4-in UTW: LTE$_{\text{total}} \leq 85\%$

$$\sigma_{db} = -7.0056 LTE_{total} + 660.55, R^2 = 0.99 \tag{6.13}$$

5-in UTW: LTE$_{\text{total}} \geq 85\%$

$$\sigma_{db} = -3.6444 LTE_{total} + 363.41; R^2 = 0.99 \tag{6.14}$$

5-in UTW: LTE$_{\text{total}} \leq 85\%$

$$\sigma_{db} = -5.8971 LTE_{total} + 557.48, R^2 = 0.99 \tag{6.15}$$

6-in UTW: LTE$_{\text{total}} \geq 85\%$

$$\sigma_{db} = -3.4544 LTE_{total} + 343.89; R^2 = 0.99$$

326

6-in UTW: LTE_{total} ≤ 85%

$$\sigma_{db} = -5.2872 LTE_{total} + 499.62, R^2 = 0.99$$

(6.17)
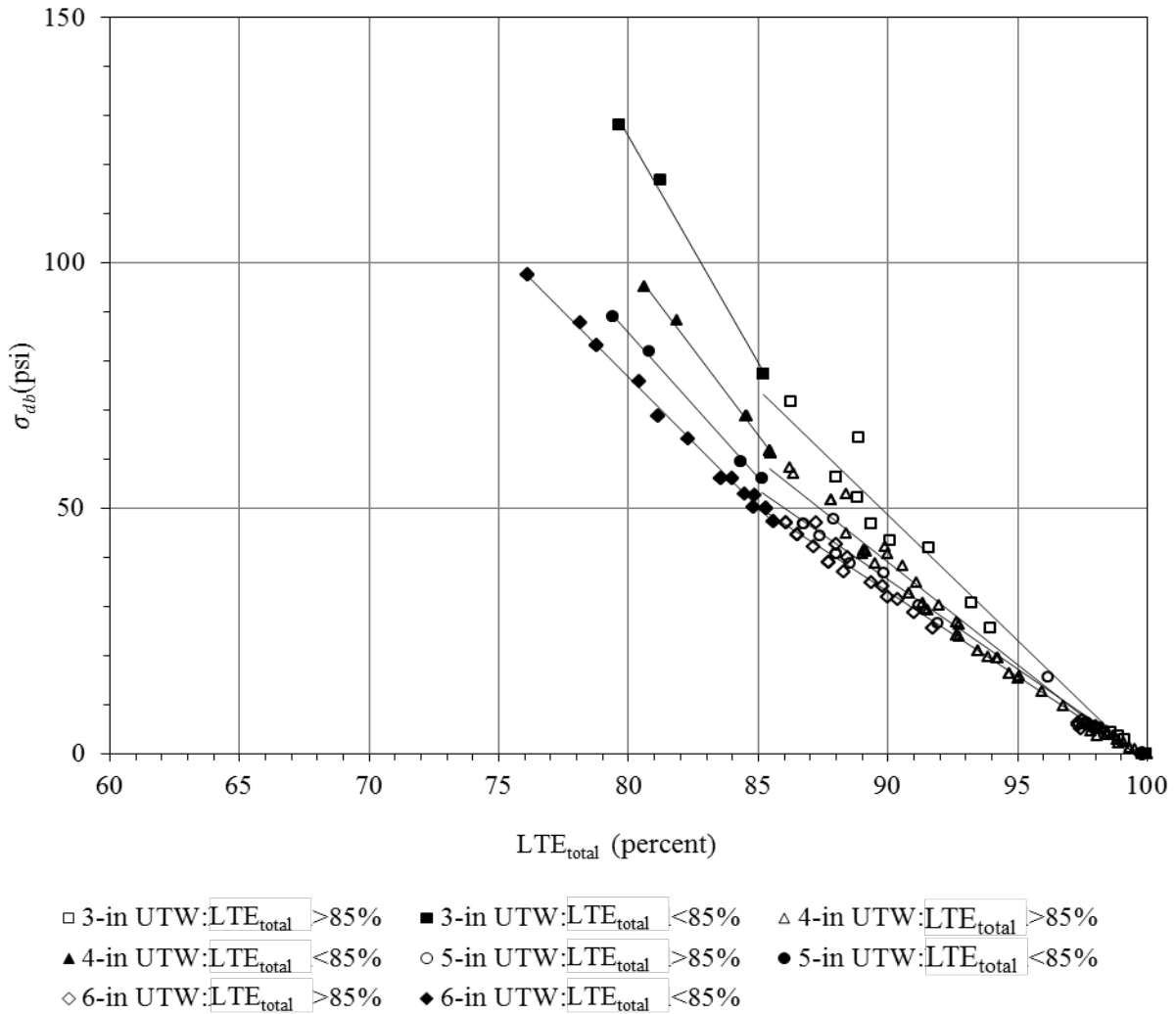
Figure 6.40. Debonding stress as a function of LTE_{total} for 3-, 4-, 5- and 6-in whitetoppings for 5-ft x 6-ft slabs.

327

In the 4-ft x 4-ft slabs, an exponential relationship provided the best fit for both 3- and 4-in thick UTWs. Equations (6.11) to (6.16) provide the regression relationships for the σ_{db} as function of h_{wt} and LTE_{total}.

3-in UTW:

$$\sigma_{db} = 1000000e^{-0.117LTE_{total}}, R^2 = 0.82 \qquad (6.18)$$

4-in UTW:

$$\sigma_{db} = 106211e^{-0.94LTE_{total}}, R^2 = 0.89 \qquad (6.19)$$
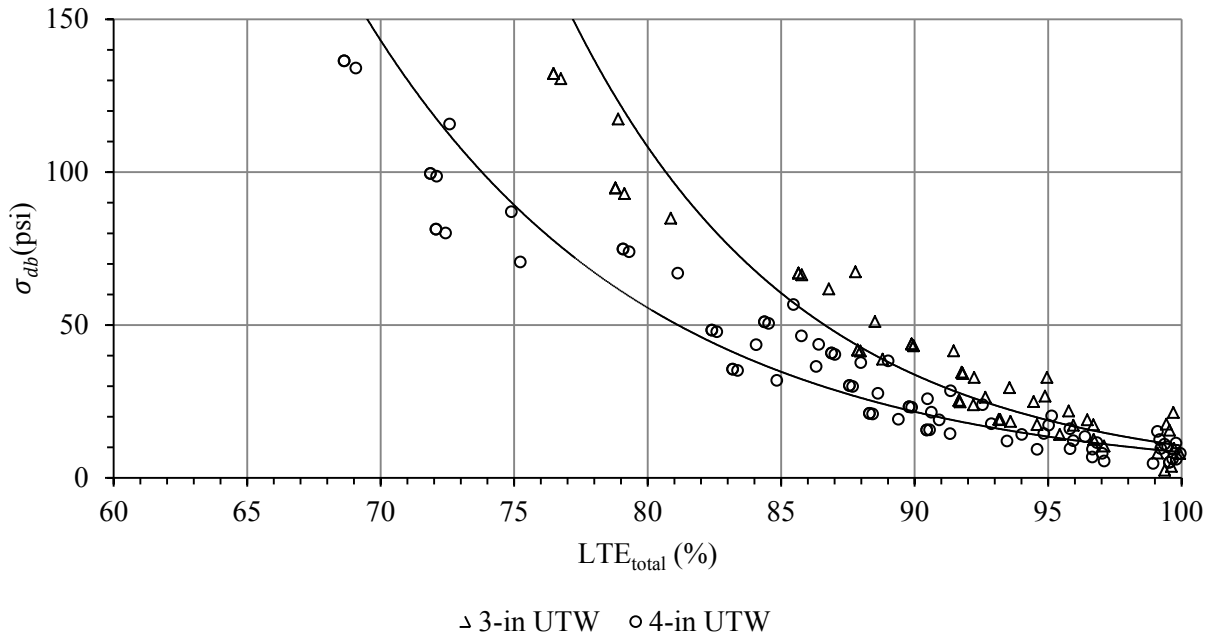
Figure 6.41. Debonding stress as a function of LTE_{total} for 3- and 4-in whitetoppings with 4-ft x 4-ft slabs.

6.6 ADVANTAGES OF FRC MIXTURES OVER PC MIXTURE

It was established from the laboratory results that both the FRC1 and FRC2 mixtures compared to the PC mixture exhibit a better joint performance for a given crack width. When the original LTE values were compared between PC and FRC mixtures, it was found that FRC mixture provides a higher load transfer. In this chapter, it was observed that the increased joint performance influences the *AGG**, design stress and debonding stress. Table 6.4 and Table 6.5 present example comparisons for these three parameters. One overlay thickness (h_{wt} =4 in), two HMA layer thicknesses (h_{HMA} = 4 and 6 in) and two HMA elastic moduli (E_{HMA} = 100,000 and 700,000 psi) along with four different crack widths were considered in the comparative study. The elastic modulus for the whitetopping was assumed to be 4 million psi. This comparison was only performed for the 5-ft x 6-ft slabs.

It can be seen that the non-dimensional joint stiffness, *AGG**, for both the FRC1 and FRC2 mixtures is higher than that of the PC mixture for all four crack widths in both of the tables. However, the increased *AGG** in the FRC mixtures did not decrease the design stress by a significant amount (2 to 6 percent). But the most significant contribution of the FRC is in the reduction of the interface debonding stress. In Table 6.4, it can be seen that when the E_{HMA} is 100,000 psi, debonding stress can be reduced by 50 and 69 percent using FRC1 and FRC2 mixtures, respectively. In Table 6.5, it can be seen that when the E_{HMA} is 700,000 psi, debonding stress can be reduced by 53 and 72 percent using FRC1 and FRC2 mixtures, respectively. It appears that the contribution of fibers in terms of reducing debonding stress is not significantly influenced by the magnitude of E_{HMA}. In all the designs presented in both the tables, it can be seen that the debonding stress increases with the increase in crack width. Also, similar benefits of fibers could be seen for different crack widths.

Table 6.4. Comparison of AGG*, σ_d and σ_{db} between the PC, FRC1 and FRC2 mixtures, E_{HMA} = 100,000 psi.

PC										
h_{wt} (in)	h_{HMA} (in)	FSR	LTE_{HMA} (percent)	cw (in)	LTE_{conc} (percent)	LTE_{wt} (percent)	LTE_{total} (percent)	AGG*	σ_d (psi)	σ_{db} (psi)
4	4	35.60	81	0.025	63	12	93	3.00	377	26
4	6	10.64	85	0.025	63	10	94	2.50	332	21
4	4	35.60	81	0.05	22	4	85	0.35	410	59
4	6	10.64	85	0.05	22	3	88	0.25	360	47
4	4	35.60	81	0.075	9	2	83	0.25	412	69
4	6	10.64	85	0.075	9	1	86	0.15	358	55
4	4	35.60	81	0.10	6	1	82	0.13	418	72
4	6	10.64	85	0.10	6	1	86	0.13	362	57
FRC1										
h_{wt} (in)	h_{HMA} (in)	FSR	LTE_{HMA} (percent)	cw (in)	LTE_{conc} (percent)	LTE_{wt} (percent)	LTE_{total} (percent)	AGG*	σ_d (psi)	σ_{db} (psi)
4	4	35.60	81	0.025	86	16	97	10.0	355	8
4	6	10.64	85	0.025	86	13	98	10.0	315	6
4	4	35.60	81	0.05	61	12	93	2.5	380	28
4	6	10.64	85	0.05	61	9	94	2.5	350	22
4	4	35.60	81	0.075	36	7	88	1.0	395	48
4	6	10.64	85	0.075	36	6	90	0.7	350	38
4	4	35.60	81	0.10	11	2	83	0.2	410	68
4	6	10.64	85	0.10	11	2	87	0.2	355	53
Average design stress reduction compared to PC = 4 percent										
Average debonding stress reduction compared to PC = 50 percent										
FRC2										
h_{wt} (in)	h_{HMA} (in)	FSR	LTE_{HMA} (percent)	cw (in)	LTE_{conc} (percent)	LTE_{wt} (percent)	LTE_{total} (percent)	AGG*	σ_d (psi)	σ_{db} (psi)
4	4	35.60	81	0.025	78	15	96	7.0	363	14
4	6	10.64	85	0.025	78	12	97	6.0	320	11
4	4	35.60	81	0.05	62	12	93	3.5	375	27
4	6	10.64	85	0.05	62	9	94	2.5	335	21
4	4	35.60	81	0.075	46	9	90	1.8	375	40
4	6	10.64	85	0.075	46	7	92	1.1	340	32
4	4	35.60	81	0.10	30	6	87	0.6	395	53
4	6	10.64	85	0.10	30	5	89	0.5	350	42
Average design stress reduction compared to PC = 6 percent										
Average debonding stress reduction compared to PC = 69 percent										

Table 6.5. Comparison of AGG*, σ_d and σ_{db} between the PC, FRC1 and FRC2 mixtures, E_{HMA} = 700,000 psi.

PC										
h_{wt} (in)	h_{HMA} (in)	FSR	LTE_{HMA} (percent)	cw (in)	LTE_{conc} (percent)	LTE_{wt} (percent)	LTE_{total} (percent)	AGG*	σ_d (psi)	σ_{db} (psi)
4	4	5.13	87	0.025	63	8	95	2.5	280	17
4	6	1.52	91	0.025	63	6	97	3.5	211	11
4	4	5.13	87	0.05	22	3	90	0.5	290	39
4	6	1.52	91	0.05	22	2	93	0.4	219	27
4	4	5.13	87	0.075	9	1	88	0.3	293	46
4	6	1.52	91	0.075	9	1	92	0.2	222	32
4	4	5.13	87	0.10	6	1	88	0.3	293	48
4	6	1.52	91	0.10	6	1	91	0.1	222	33
FRC1										
h_{wt} (in)	h_{HMA} (in)	FSR	LTE_{HMA} (percent)	cw (in)	LTE_{conc} (percent)	LTE_{wt} (percent)	LTE_{total} (percent)	AGG*	σ_d (psi)	σ_{db} (psi)
4	4	5.13	87	0.025	86	11	98	10.0	266	5
4	6	1.52	91	0.025	86	8	99	10.0	204	2
4	4	5.13	87	0.05	61	8	95	2.5	280	18
4	6	1.52	91	0.05	61	6	96	2.5	214	12
4	4	5.13	87	0.075	36	5	92	1.0	286	32
4	6	1.52	91	0.075	36	3	94	1.1	217	21
4	4	5.13	87	0.10	11	1	89	0.4	292	45
4	6	1.52	91	0.10	11	1	92	0.1	222	31
Average design stress reduction compared to PC = 2 percent										
Average debonding stress reduction compared to PC = 53 percent										
FRC2										
h_{wt} (in)	h_{HMA} (in)	FSR	LTE_{HMA} (percent)	cw (in)	LTE_{conc} (percent)	LTE_{wt} (percent)	LTE_{total} (percent)	AGG*	σ_d (psi)	σ_{db} (psi)
4	4	5.13	87	0.025	78	10	97	8.0	268	9
4	6	1.52	91	0.025	78	7	98	4.0	209	5
4	4	5.13	87	0.05	62	8	95	9.0	268	18
4	6	1.52	91	0.05	62	6	97	4.0	209	12
4	4	5.13	87	0.075	46	6	93	1.0	286	26
4	6	1.52	91	0.075	46	4	95	1.0	218	18
4	4	5.13	87	0.10	30	4	91	0.8	288	35
4	6	1.52	91	0.10	30	3	94	0.7	218	24
Average design stress reduction compared to PC = 3 percent										
Average debonding stress reduction compared to PC = 72 percent										

6.7   CONCLUSIONS

This chapter presented an analysis of the finite element modeling of the whitetopping joint. The modeling work was performed with the following objectives (i) establish the relationship between the LTE and *AGG**, (ii) investigate the influence of the joint performance on the design stress at the critical location on the loaded slab and (iii) investigate the influence of joint performance on the debonding stress. Two separate whitetopping models were developed, one for 5-ft x 6-ft slabs and another for 4-ft x 4-ft slabs. In both models, the location of the loading area was selected based on the actual wheelpath location for an in-service whitetopping, which is a function of the slab size. To account for the different bonding conditions in each model, both the full and partial interface bonding condition were considered.

It was observed that in the fully bonded condition, the influence of the joint performance is insignificant. But a considerable influence of the joint performance was noticed when the whitetopping and HMA layer were partially bonded. For the partially bonded case, a relationship between the LTE and *AGG** was established. This relationship is a function of the slab size, whitetopping design features, and whitetopping and HMA moduli. It was found that the LTE vs *AGG** relationship can be correlated with the ratio between the flexural stiffnesses of the whitetopping and HMA layers. A method for determining the load transfer contribution through the HMA layer was presented. Load transfer data from MnROAD was used to verify the applicability of the proposed procedure. Using the LTE vs *AGG** relationship developed in this chapter coupled with the joint performance vs the crack width relationship established in the previous chapter, the *AGG** at any crack width can be determined for different concrete mixtures. It may be reminded here that LTE vs crack width relationships were established for both (i) original or measured LTEs and (ii) non-fatigued LTEs. The first one represents the LTE

332

vs crack width relationship for a whitetopping where the joints are relatively stabilized or have experienced some level of fatiguing. Use of this relationship provides a better representation of the field condition. The second relationship was developed discarding the fatiguing effect in the joints. So, this relationship basically represents the joints of a newly constructed whitetopping.

An influence of joint performance on the design stress was observed. However, with the inclusion of the fiber, the load related stress is found to decrease only by approximately 6 percent at a given crack width. Part of this is the result of considering the effects of fiber only on the LTE. In reality, the application of fiber in the concrete mixture results in a redistribution of the stress within the slab. During the winter when slabs contract, the crack tends to widen and the fiber offers resistance against the opening of the crack. This phenomenon increases the area of the slab that effectively participates in distributing the wheel load which results in a reduction of the stress in the loaded slab. Also, the use of fiber can increase residual strength of the concrete. This improves the post-crack performance of the overlay.

The greatest contribution of the increased joint performance was in the reduction of the debonding stresses at the interface. A relationship was established to determine the debonding stress as a function of whitetopping thickness and joint performance. In a comparative study, it was shown that if fiber reinforced concrete is used, the debonding stress can be significantly reduced, by 50 to 72 percent. And when the flexural stiffness of HMA layer structure is relatively low, the interface bonding is very important in order to limit the stress at the critical location.

However, the benefit of fibers in increasing the load transfer or reducing the debonding stress can be varied with the season, based on the crack width. The crack width changes with the

333

ambient temperature. The limitation in using the synthetic structural fiber is that fiber becomes partially ineffective when the existing crack width is below the maximum crack opening that the joint has experienced in its life.

7.0   CONCLUSIONS AND RECOMMENDATIONS FOR FUTURE STUDY

7.1   INTRODUCTION

The joint performance is one of the main contributors for a longer design life of a bonded whitetopping overlay. The joint performance influences the integrity of the entire overlay system and contributes to the initiation of distresses as the performance declines. In whitetopping, a poor joint performance increases the potential for interlayer debonding and the magnitude of the stress in the loaded slab. However, no bonded whitetopping design procedure currently accounts for the joint stiffness or joint performance in predicting performance. Part of the reason behind the aversion to incorporating the joint performance into the design process is that the joint performance characterization itself is a challenging task. Most of the previous joint characterization studies were conducted using large size slabs, which require a considerable amount of time and monetary resources. Therefore, testing with large size slabs is typically cost-prohibitive when evaluating the joint performance with respect to a large number of variables. Also, no research work was previously conducted to characterize the joint performance of bonded whitetopping overlays or to study its influence on the different mechanisms responsible for distress development in the whitetopping.

Under the scope of this study, a new, economical, small-scale, and robust joint performance characterization technique was developed. The result from this small-scale test

335

method, B_{ALT}, was correlated with the result from a large scale joint performance test, S_{ALT}. Both PC and FRC mixtures were considered in the study. The benefits of FRC mixtures over the PC mixture were quantified in terms of LTE and DER. Regression relationships were developed to determine LTE and DER as a function of crack width and mixture type. Also, LTEs and DERs obtained by B_{ALT} and S_{ALT} procedures were correlated with the regression relationships. Subsequently, the best estimator of the LTE_S as well as DER_S were determined.

Using the FEM, LTE was then correlated to joint stiffness, $AGG*$, which can be used to determine the design stress. The influence of joint performance on the design stress and interface debonding stress was studied.

7.2 FINDINGS

(i) *Design and fabrication of the B_{ALT} setup*

The B_{ALT} procedure was developed with a vision to make the joint performance evaluation task very simple and economical so that the test can be conducted using readily available laboratory resources or with a marginal investment. In the B_{ALT} procedure, joint performance can be characterized by using the conventional 24-in x 6-in x 6-in beams. The test setup was designed to replicate the abrasive action that occurs on the joints of an in-service concrete pavement loaded with an 18-kip single axle load.

336

(ii)   *Investigate the joint performance of the PC and FRC concrete mixtures at different crack widths and load repetitions using both the procedures*

- The specimens fatigued at a 0.050-in crack width, as compared to a 0.035-in crack width, exhibited larger drop in LTE and DER.

- The decreasing rate in joint performance was larger between 0 to 500,000 load cycles when compared to the decreasing rate of joint performance that was observed after the application of the first 500,000 load cycles regardless of the mixture design.

- Overall, the drop in joint performance due to fatigue in the PC beams (an average of an 11 percent drop in the LTE and a 13 percent drop in the DER) were comparatively more than the FRC beams (An average of a percent drop in LTE and 6.5 percent drop in DER).

- The Enduro 600 fiber did not fatigue even after 10 million load cycles. So, it can be concluded that fibers probably do not degrade due to fatigue in the field during the design life of the whitetopping.

- A comparison of the LTE vs crack width and DER vs crack width relationships between the three mixtures reveals that the FRC mixtures provide a higher LTE and DER than that of PC mixture. In general it was found that the contribution of fiber is not very significant when the crack with is small and aggregate interlock is playing a significant role in load transfer. However, when the crack width is greater than approximately 0.02 in, the contribution of aggregate interlock decreases and the fibers play a larger role in transferring the load. The LTE and DER of the FRC mixtures is considerably higher than the PC mixture when the crack width is greater than 0.02 in.

- When the non-fatigued LTE_S were compared between the mixtures, it was found that the LTE_S declining rate as a function of crack width for the Enduro 600 mixture was lower than the PC and Strux 90/40 mixtures. The slope of the LTE_S vs crack width relationship

for PC and Strux 90/40 mixtures were found to be similar for up to a 0.05-in crack width. Both the Strux 90/40 and Enduro 600 mixtures show a linear relationship with the crack width for up to a 0.1-in crack width. Whereas, the PC mixture exhibited the linear relationship up to a0.05-in crack width.

- Regression relationships were developed for LTE and DER as a function of crack widths, mixture design and test procedure. Separate relationships were developed with the original and non-fatigued LTE and DER results for the procedure.

- It was observed that the effectiveness of fibers in transferring the load decreases when the crack width is reduced from a larger crack width that a beam or a slab has already experienced. Plastic deformation in the fiber could be responsible for this. When the joint closes, the fiber is no longer taut and becomes less effective in transferring load.

- It was found that FRC1 (Strux 90/40) and FRC2 (Enduro 600) slabs exhibited somewhat similar LTE vs crack and DER vs crack width relationships. The Strux 90/40 mix performed slightly better when the crack width was below 0.05 in, whereas, Enduro 600 mix performed slightly better when the crack width was greater than 0.05 in. The decreasing rate in LTE and DER with respect to crack width is higher for Strux 90/40 mix as compared to that of the Enduro 600 mix.

(iii)   *Correlating the results between the B_{ALT} and S_{ALT} procedures*

Correlations have been developed between joint performance parameters, such as LTE_S vs LTE_B, LTE_S vs DER_B, DER_S vs LTE_B, DER_S vs DER_B. It was found that the LTE_B is the best predictor of the LTE_S and also DER_B provides a good estimate for DER_S. The strongest correlation was between DER_B and DER_S. Therefore, when comparing the joint performance between mixtures,

338

the DER$_S$ vs DER$_B$ relationship is recommended. Also, since a considerable variation in the B$_{ALT}$ test results were noticed, so it is highly recommended that a minimum of 5 beams are tested.

(iv)   Establish a relationship between the LTE and AGG* for bonded whitetopping

It was found that for the fully bonded condition, the influence of the joint performance on the predicted stress is insignificant. It is significant when the whitetopping and HMA layer are only partially bonded. A method for determining the load transfer contribution of the HMA layer was presented. Load transfer data from the in-service pavements at MnROAD verified the applicability of the proposed procedure. Using a LTE vs *AGG** relationship coupled with the joint performance vs the crack width relationship, joint stiffness at any crack width can be determined for different concrete mixtures.

(v)   Quantify the benefits of the inclusion of fibers in terms of reducing the critical design stress

The influence of joint performance on the critical design stress was observed. However, with the inclusion of fiber, the load-related stress is found to not decrease significantly (approximately 6 percent). Part of this is the result of considering the contribution of fiber only with respect to joint performance. In reality, the use of fiber in the concrete mixture most likely results in a redistribution of the stress within the slab. This phenomenon would increase the area of the slab that effectively participates in distributing the wheel load resulting in a reduction of the magnitude of stress.

(vi) *Quantify the benefits of the inclusion of fibers in terms of reducing debonding stress.*

The greatest contribution of the increased joint performance was in the reduction of the debonding stress at the interface. A relationship was established to determine the debonding stress as a function of whitetopping thickness and joint performance. It was shown that the debonding stress can be significantly reduced (50 to 72 percent).

7.3 RECOMMENDATION FOR FUTURE STUDIES

Although an in-depth research study was conducted in characterizing the joint performance of whitetopping overlays, there are many more issues still left for further research. The following are areas needing further investigation.

1) The contribution of fibers in maintaining a narrower crack width in bonded whitetopping.

2) A broader range of fiber types and fiber dosages.

3) Verify the finding that the residual strength ratio can be used to establish equivalent joint performance enhancement between fiber types.

4) Incorporate the developed LTE vs $AGG*$ relationship in the stress predicting models.

5) Determine if findings related to the interface debonding can be extended to correlate with the erosion or delamination of the asphalt materials and the influence of fibers on their reduction.

6) Verify the field application of determining DER (in addition to LTE) using FWD testing.

7) Verify the feasibility of using DER in estimating the joint stiffness, $AGG*$.

APPENDIX A

APPENDIX A: SENSITIVITY ANALYSIS FOR DER$_S$

Figure A. 1. Approach and leave slabs DER$_S$ vs crack width for cut-off load = 500 lbs for PC slab.

Figure A. 2. Approach and leave slabs DER_S vs crack width for cut-off load = 750 lbs for PC slab.

Figure A. 3. Approach and leave slabs DER_S vs crack width for cut-off load = 1000 lbs for PC slab.
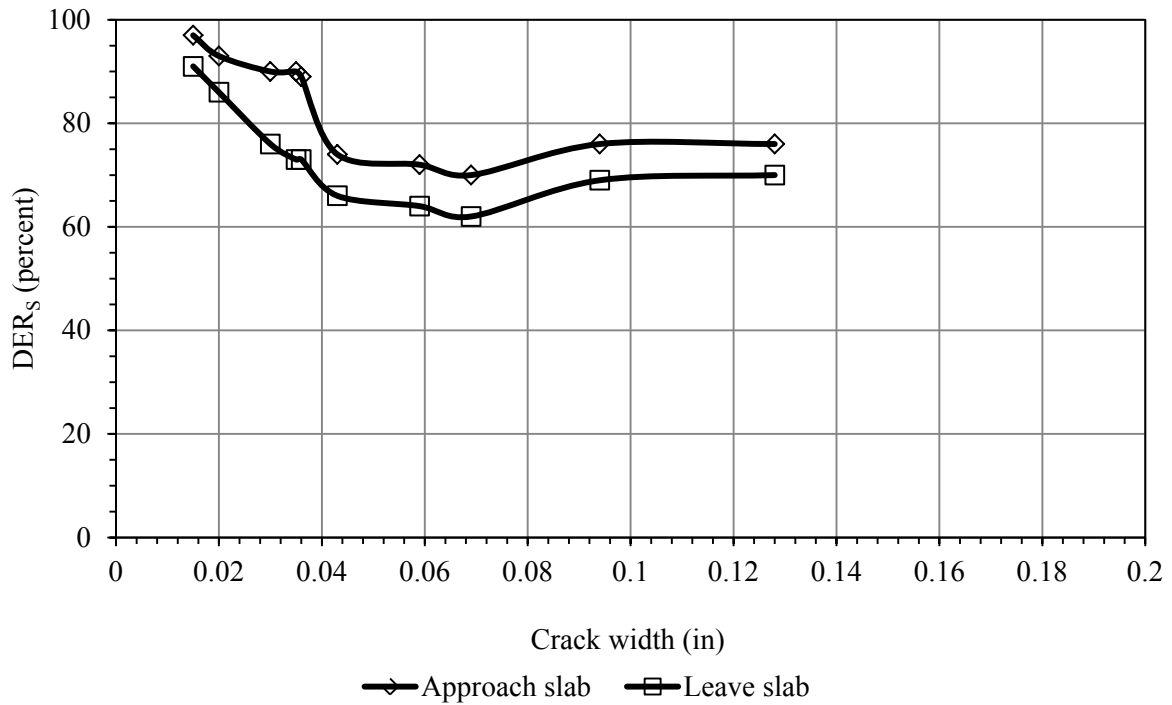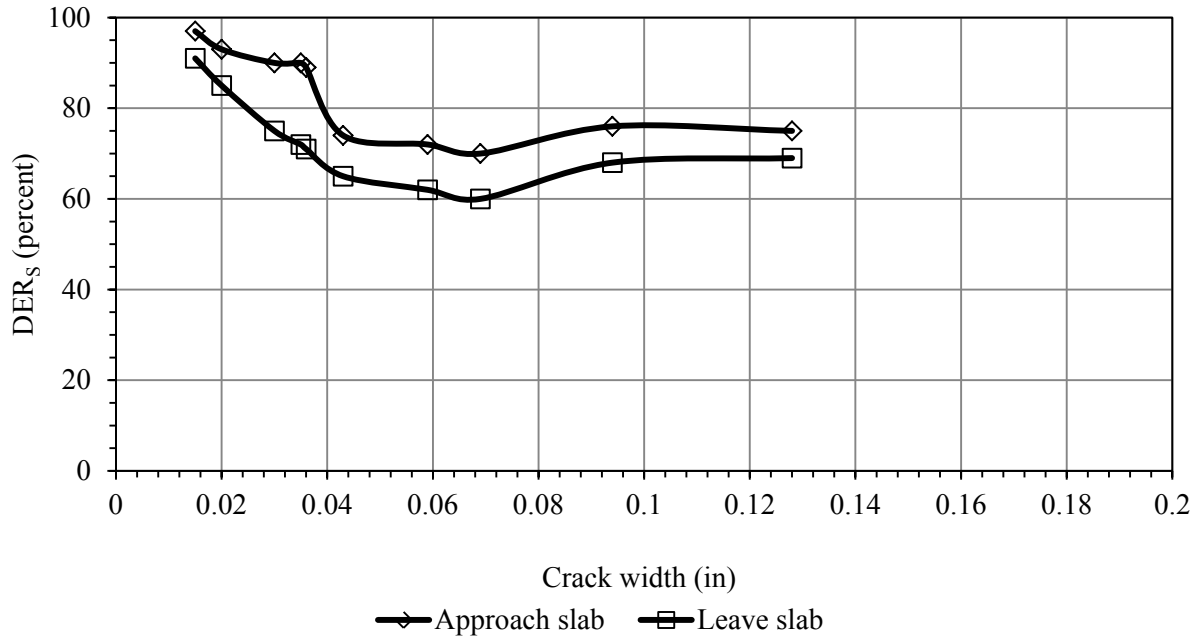
342

Figure A. 4. Approach and leave slabs DER$_S$ vs crack width for cut-off load = 1500 lbs for PC slab.

Figure A. 5. Approach and leave slabs DER$_S$ vs crack width for cut-off load = 2000 lbs for PC slab.

343

Figure A. 6. Approach and leave slabs DER_S vs crack width for cut-off load = 2500 lbs for PC slab.

Figure A. 7. Approach and leave slabs DER_S vs crack width considering differential load for PC slab.

344

Figure A. 8. Approach and leave slabs DER_S vs crack width for cut-off load = 500 lbs for FRC1 slab.

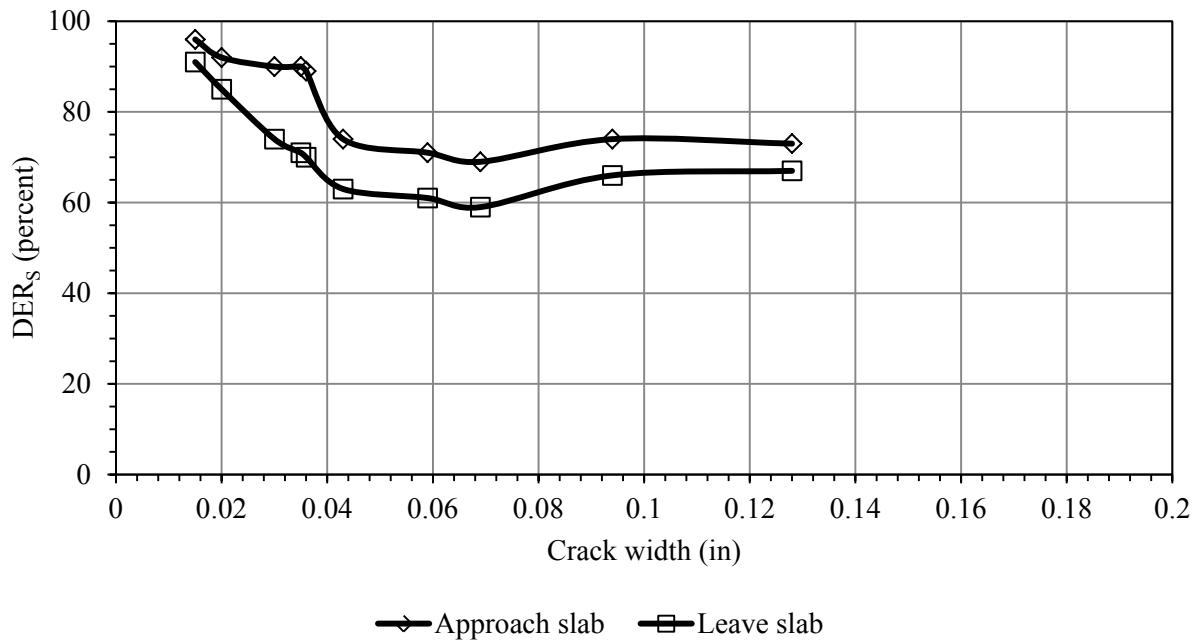Figure A. 9. Approach and leave slabs DER_S vs crack width for cut-off load = 750 lbs for FRC1 slab.

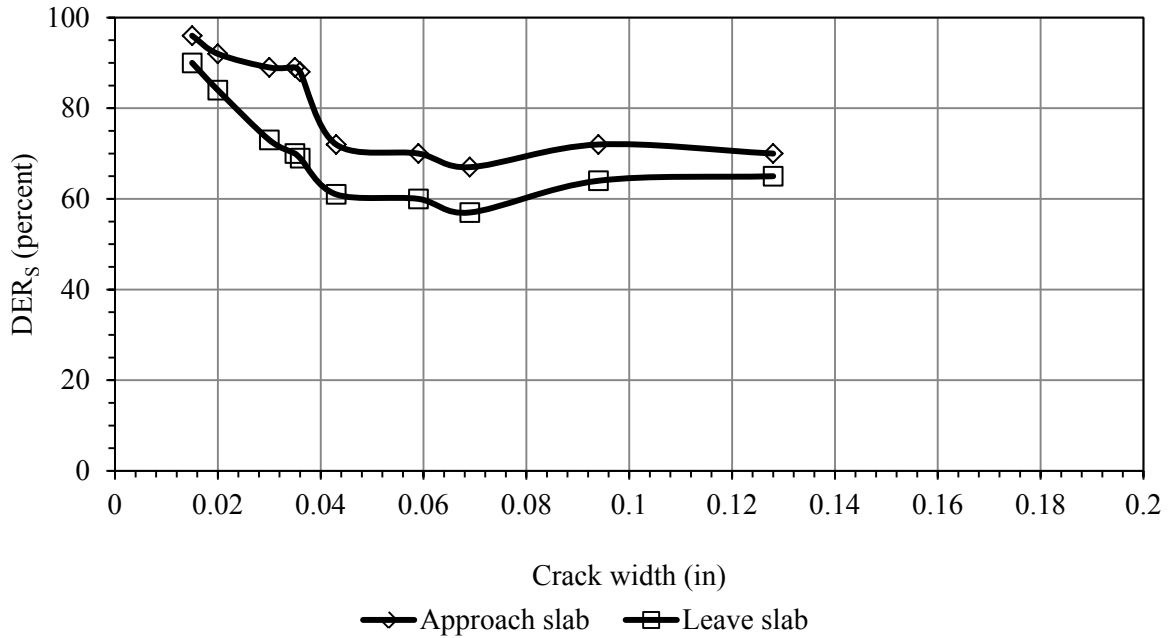Figure A. 10. Approach and leave slabs DER_S vs crack width for cut-off load = 1000 lbs for FRC1 slab.

Figure A. 11. Approach and leave slabs DER_S vs crack width for cut-off load = 1500 lbs for FRC1 slab.
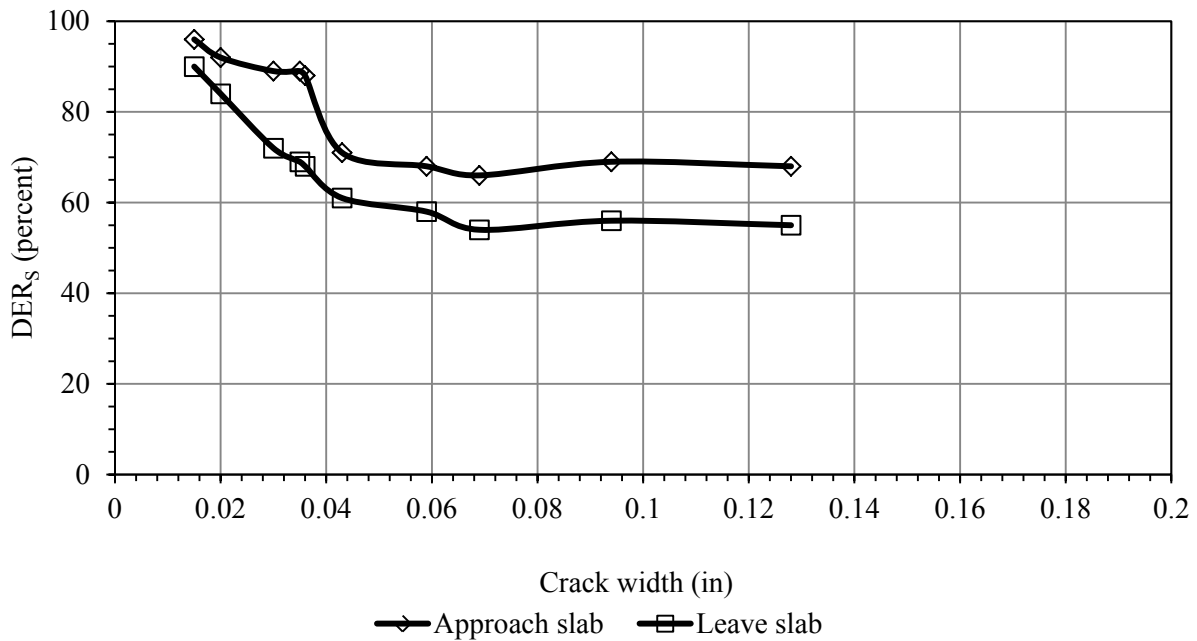
346

Figure A. 12. Approach and leave slabs DER$_S$ vs crack width for cut-off load = 2000 lbs for FRC1 slab.

Figure A. 13. Approach and leave slabs DER$_S$ vs crack width considering differential for FRC1 slab.
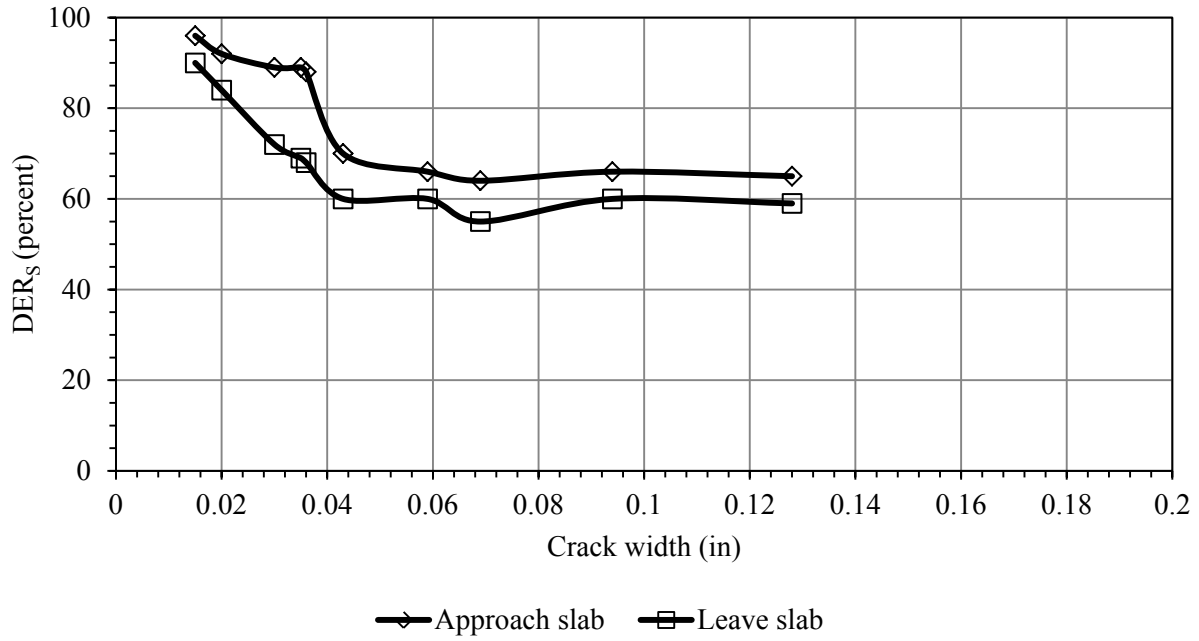
347

Figure A. 14. Approach and leave slabs DER_S vs crack width for cut-off load = 500 lbs for FRC2 slab.
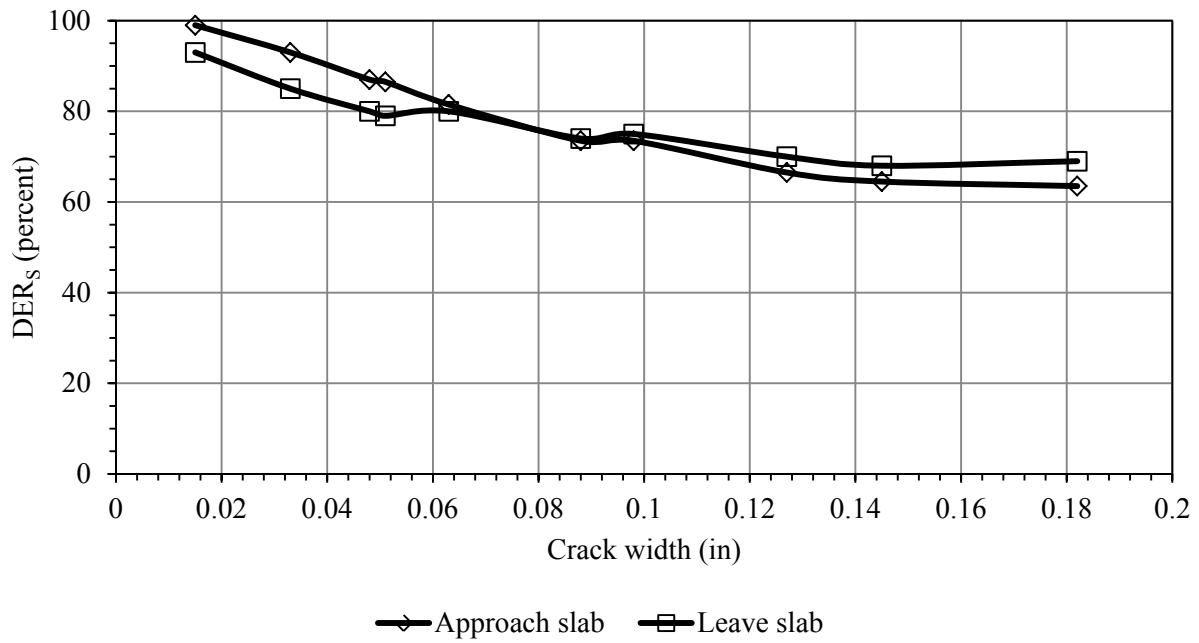
Figure A. 15. Approach and leave slabs DER_S vs crack width for cut-off load = 750 lbs for FRC2 slab.

348
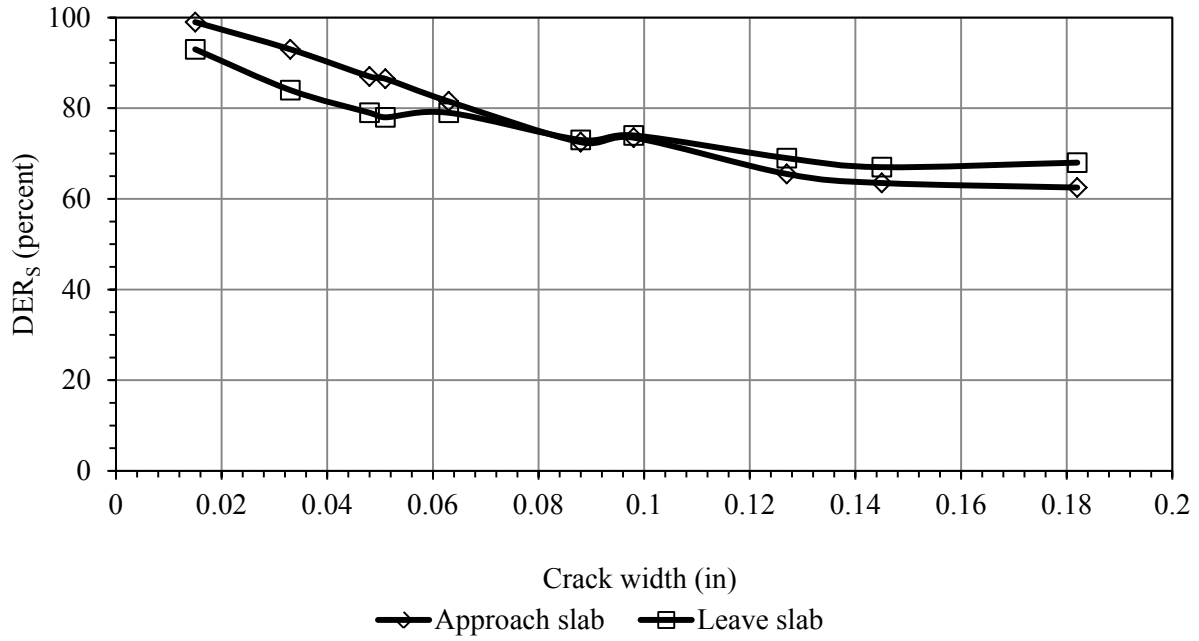
Figure A. 16. Approach and leave slabs DER_S vs crack width for cut-off load = 1000 lbs for FRC2 slab.
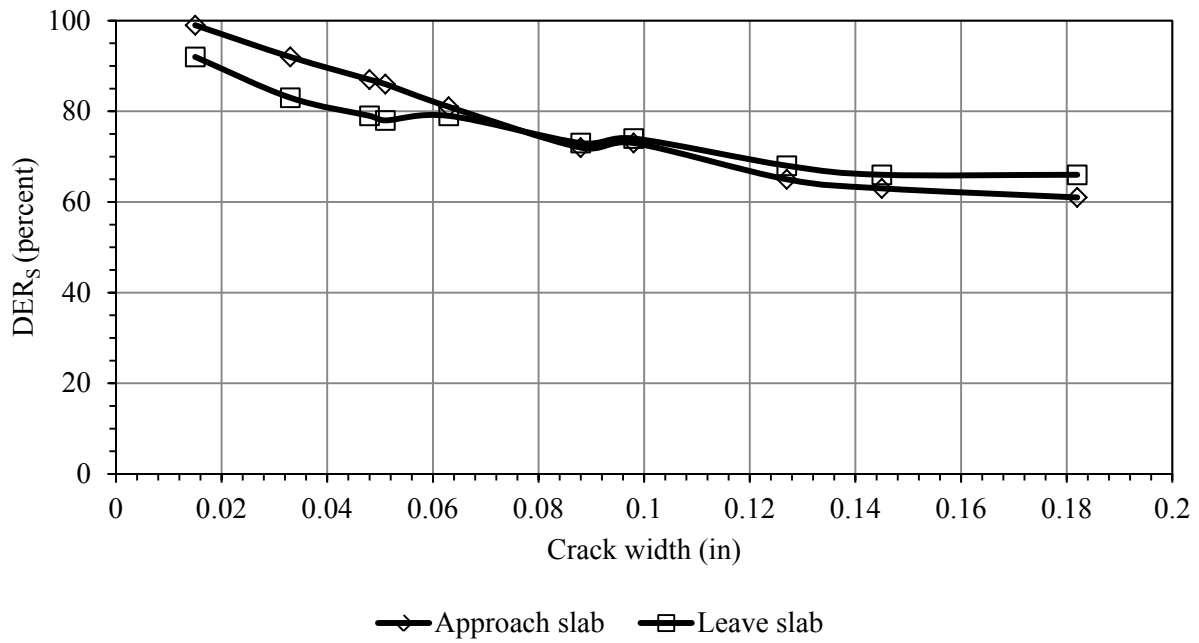
Figure A. 17. Approach and leave slabs DER_S vs crack width for cut-off load = 1500 lbs for FRC2 slab.
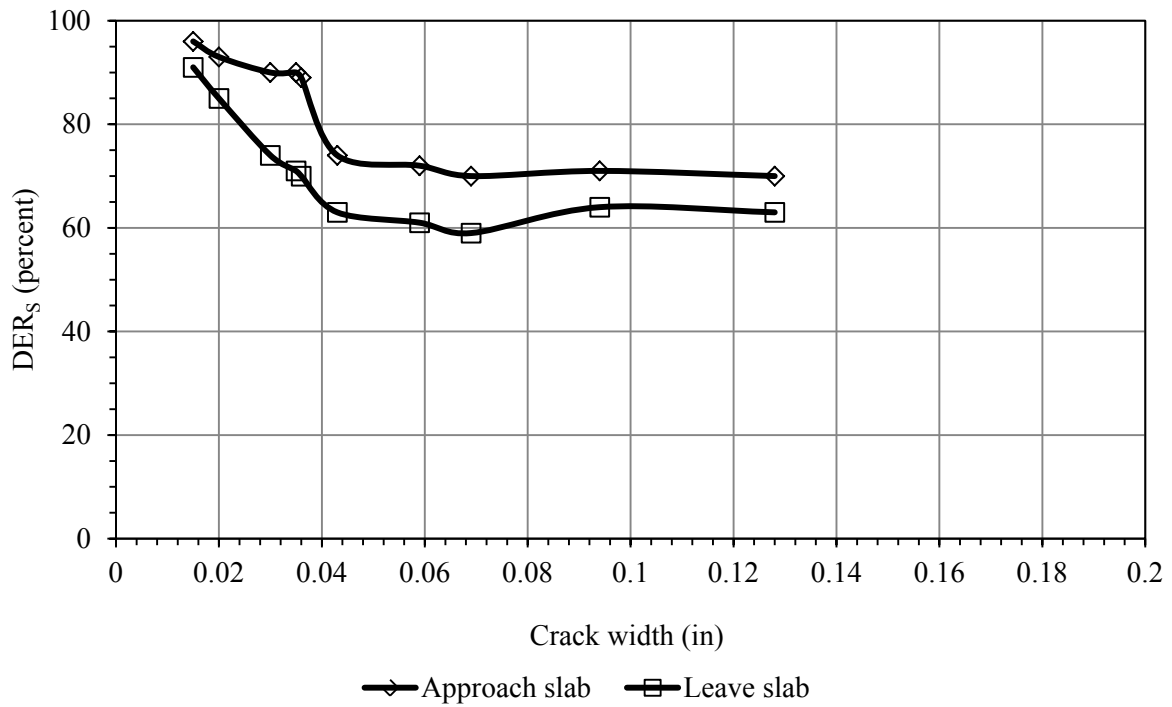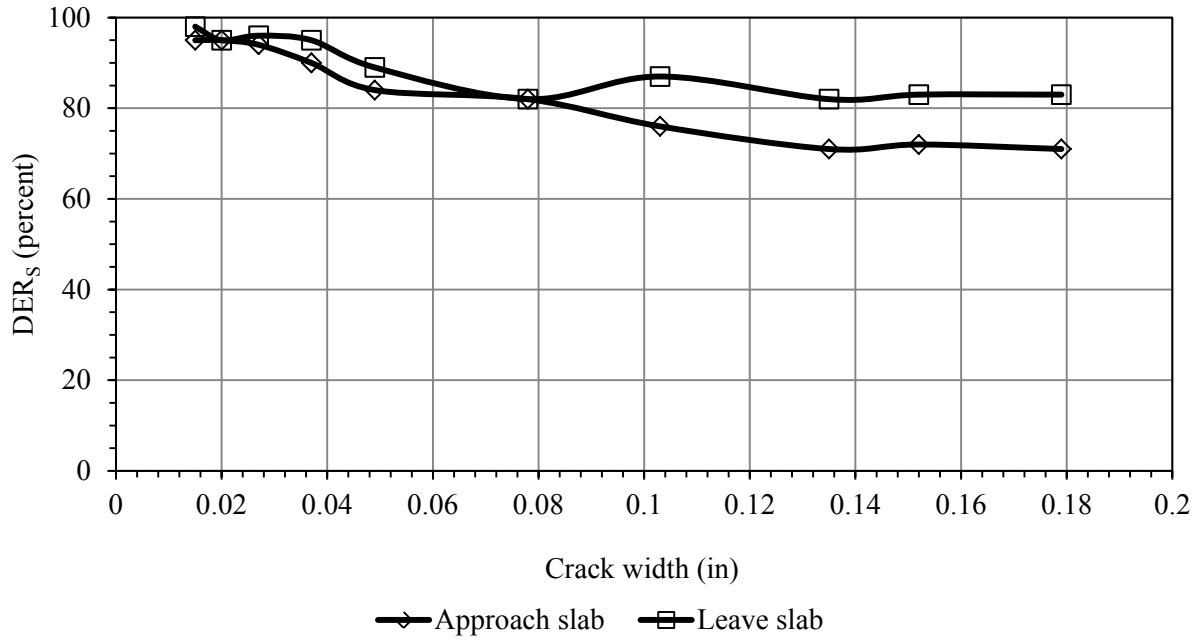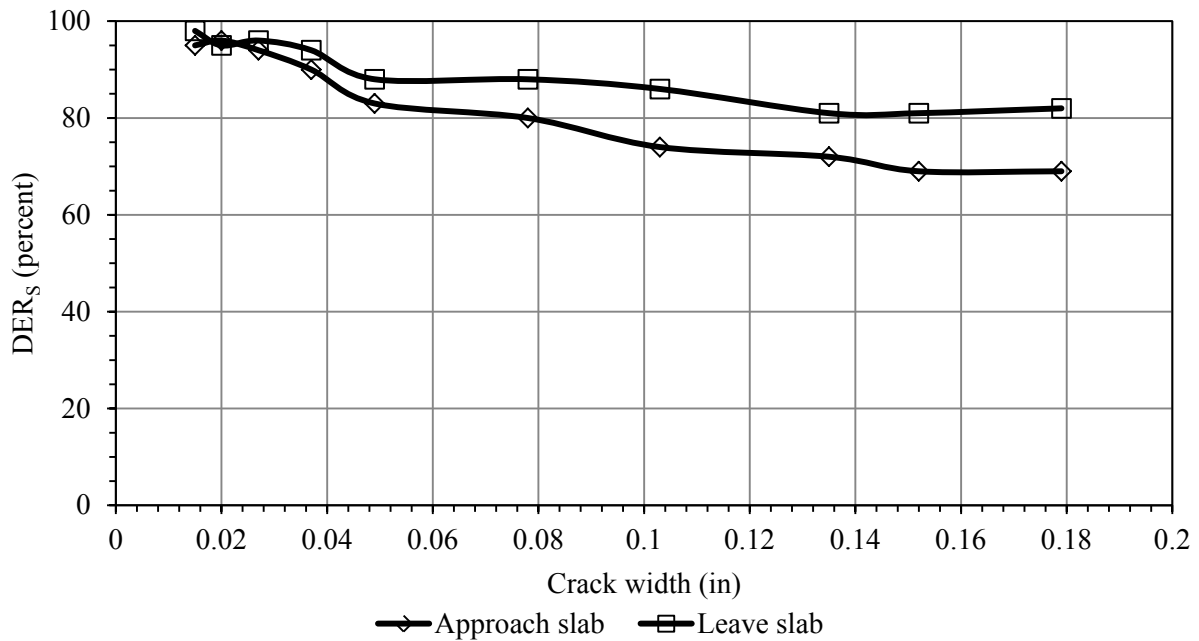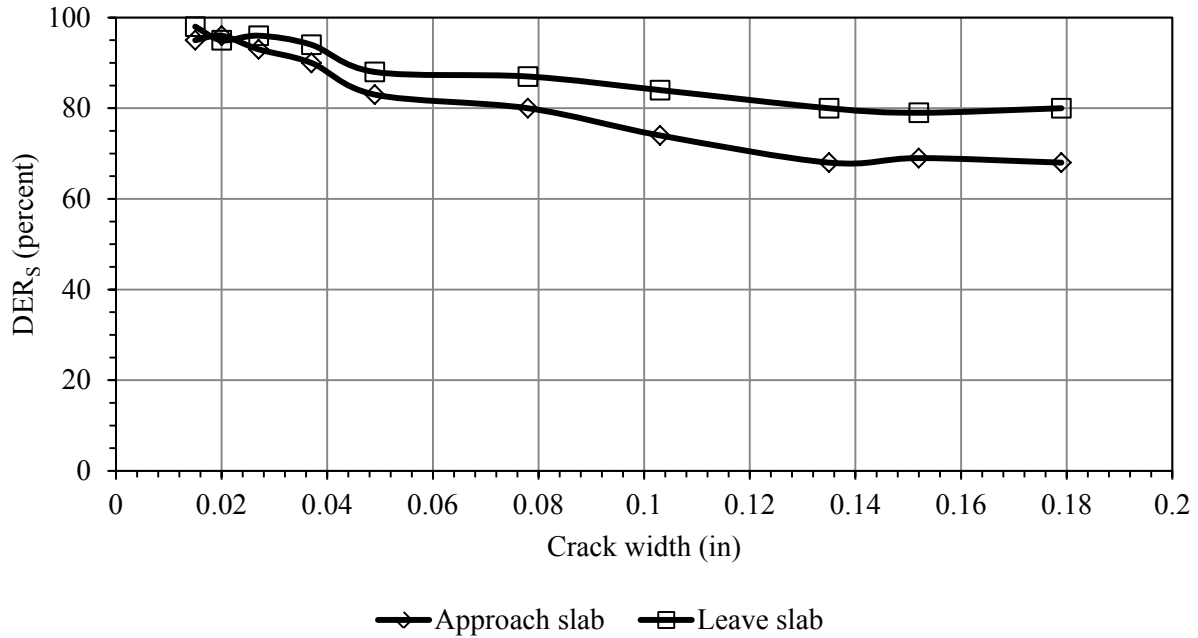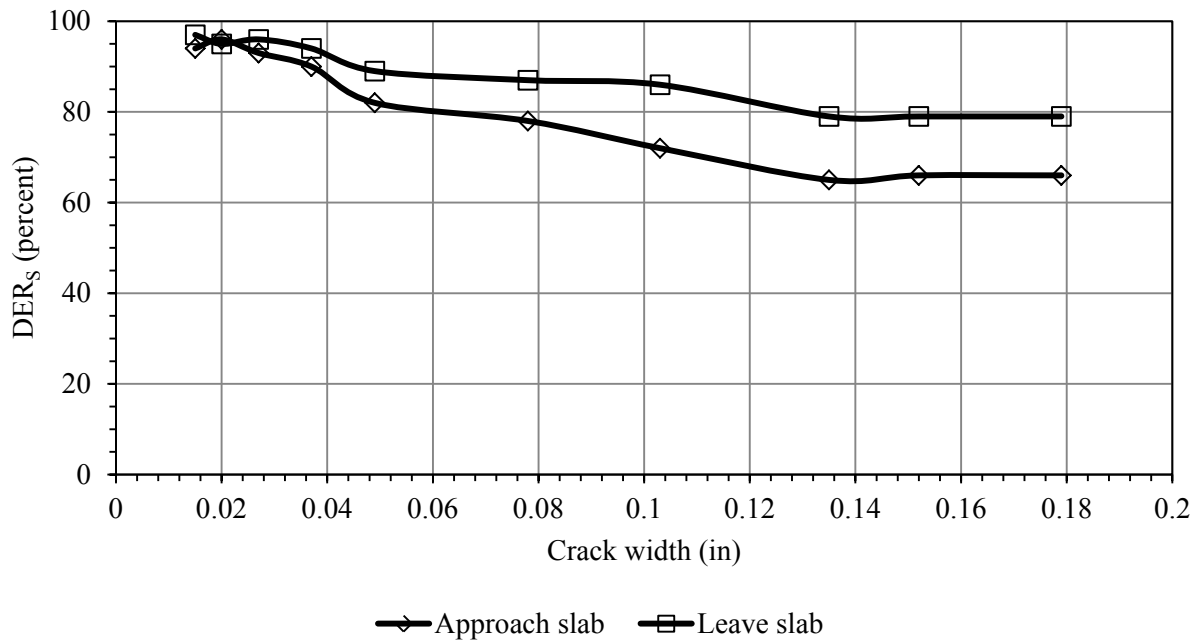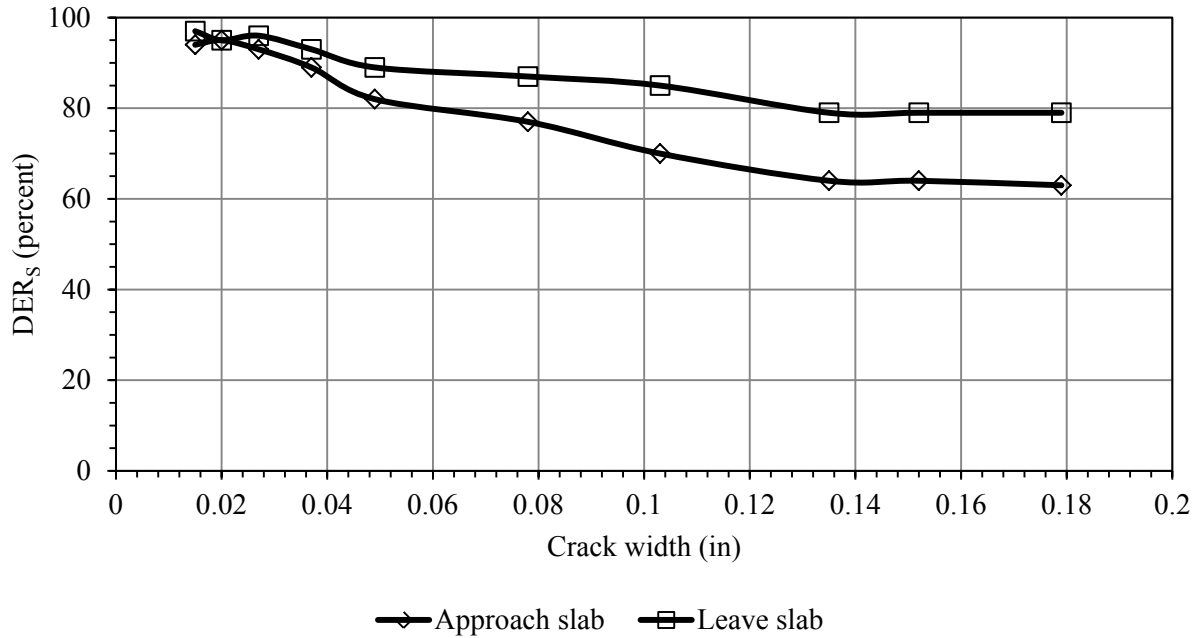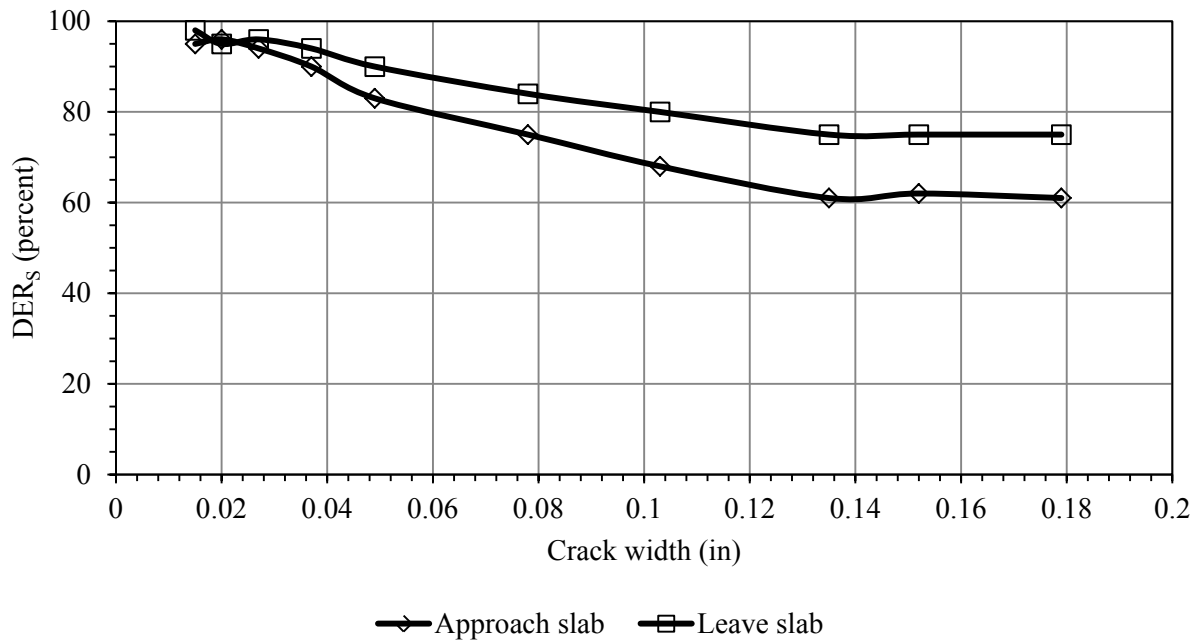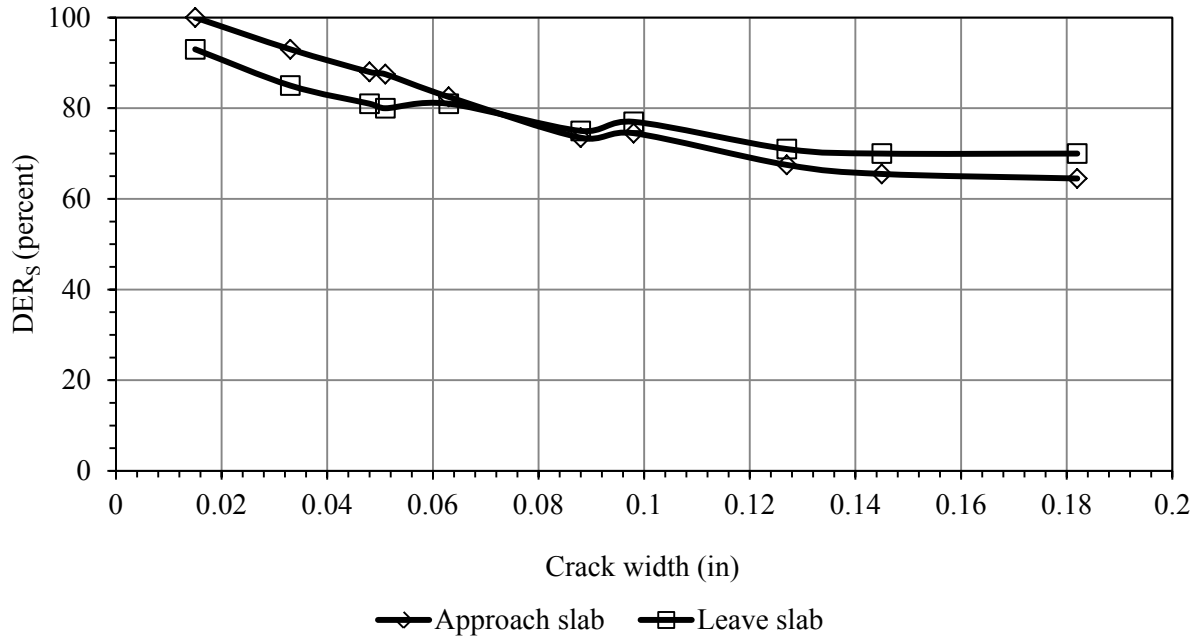
349
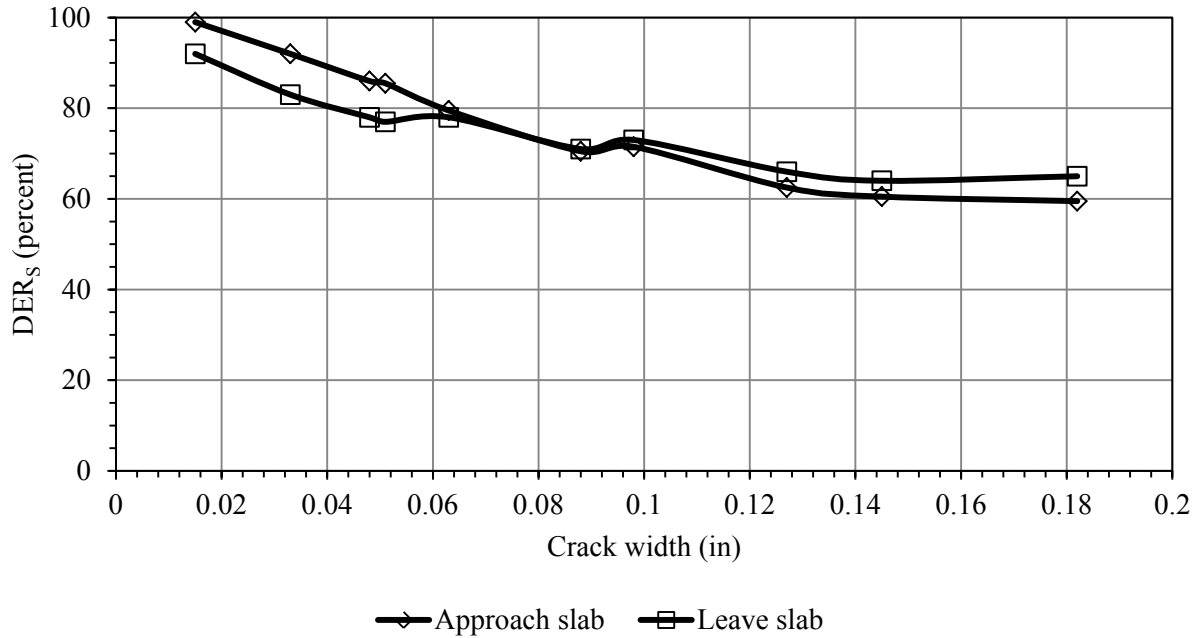
Figure A. 18. Approach and leave slabs DER$_S$ vs crack width for cut-off load = 2000 lbs for FRC2 slab.
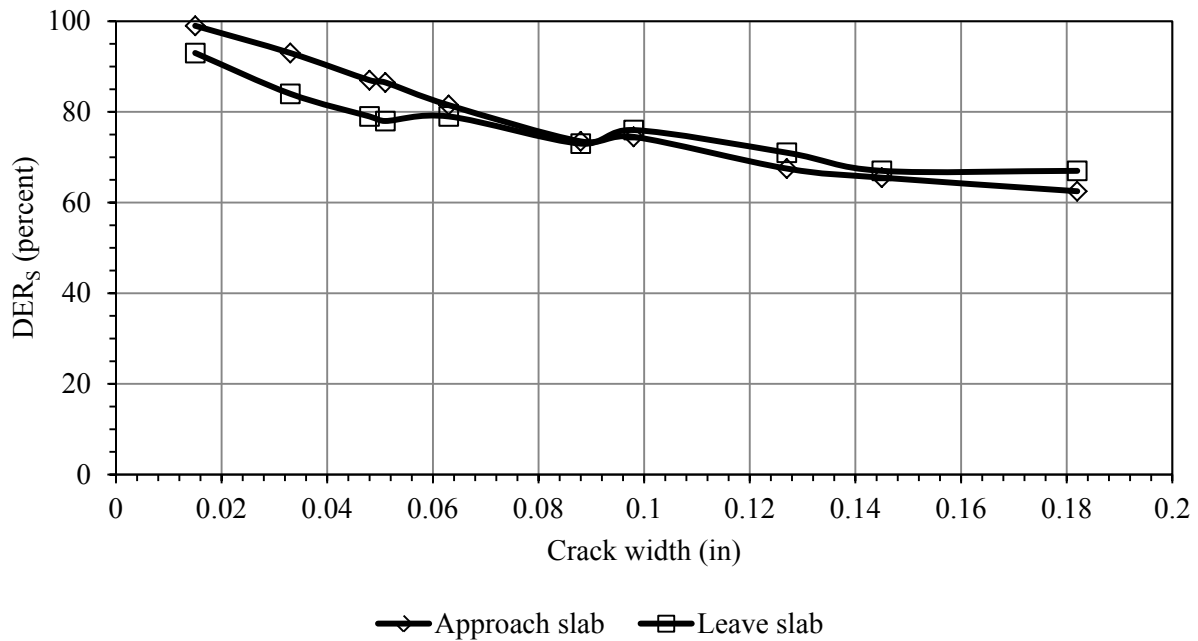
Figure A. 19. Approach and leave slabs DER$_S$ vs crack width considering differential load for FRC2 slab.

APPENDIX B

APPENDIX B: CORRECTION IN JOINT PERFORMANCE FOR FATIGUE

ADJUSTMENT

In order to adjust the drops in LTE and DER due to crack width increase during fatiguing, a correction was required to be made to the measured LTE or DER so that the drops in LTE and DER only due to fatiguing could be recognized. This section presents the correction procedure for the above mentioned problem. Even though the crack width increased in all the specimens during fatiguing, a few of them experienced a considerable increase. Correction was performed for all the specimens. This section includes the specimens which experienced a substantial amount of crack width increase (> 4 mil); a similar procedure was adopted for all other specimens. The correction procedure is described below.

The slope of the LTE or DER vs crack width relationship before the fatiguing (line 1) is drawn in each plot (Figure B1 to B6, Figure B1 can be referred to understand the procedure). It was assumed that this slope would have been continued if there was no fatiguing, at least up to the crack width immediately after the fatiguing. This assumption may not be exactly true, but for above mentioned correction purpose, this assumption might not influence the result by a significant amount. Then, a line matching with slope of line 1 was drawn intersecting the point

representing the crack width right after the fatiguing (line 2). One vertical line was drawn intersecting the crack width at which fatiguing was started (line 3). Three horizontal lines were drawn, (i) First one intersecting the point representing crack width before fatiguing (line 4), (ii) second one intersecting the point representing crack width after fatiguing (line 5), and (iii) A third horizontal line between the lines 4 and 5, passing through the intersection of lines 2 and 3.

From each of the plots, LTE or DER drop due to fatiguing and crack width increase together (a), LTE or DER drop due to crack width increase alone (b), and Magnitude of increase in LTE or DER to adjust for fatiguing (c) were determined. The increase in crack width is denoted as (d).

B.1   ADJUSTMENT IN LTE
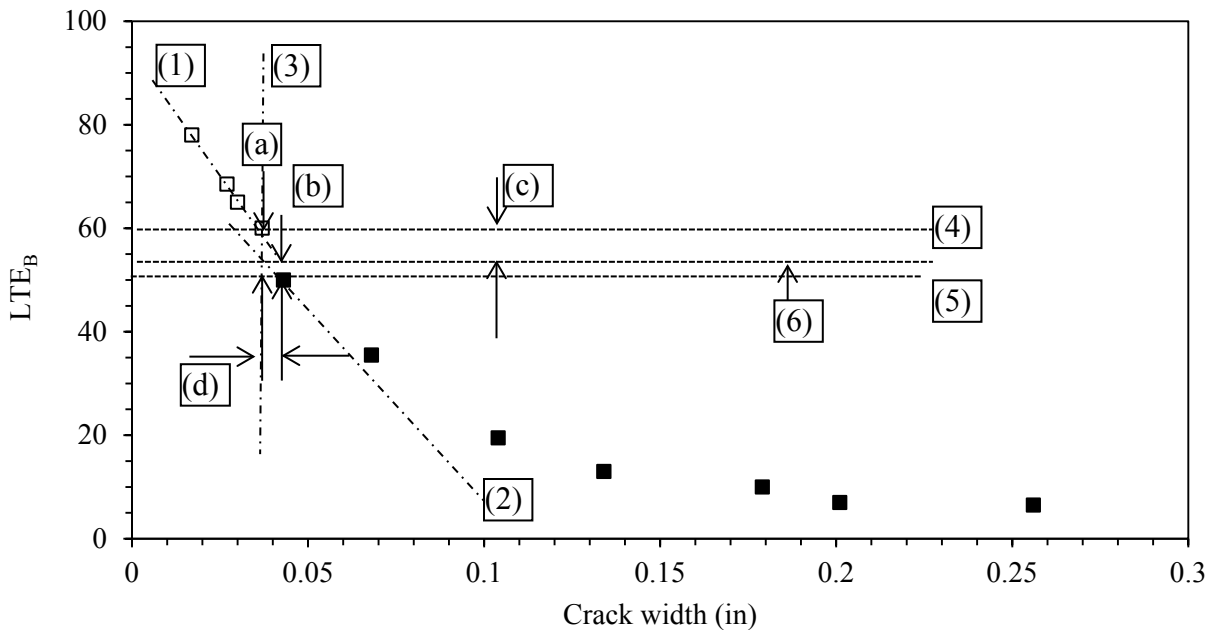
Note: a = 10 percent, b = 3 percent, c = 7 percent, and d = 6 mil.

Figure B.1. Adjustment for determining non-fatigued LTE$_B$ for beam, F1-3, 0.037-0.043, 0.1614.

352
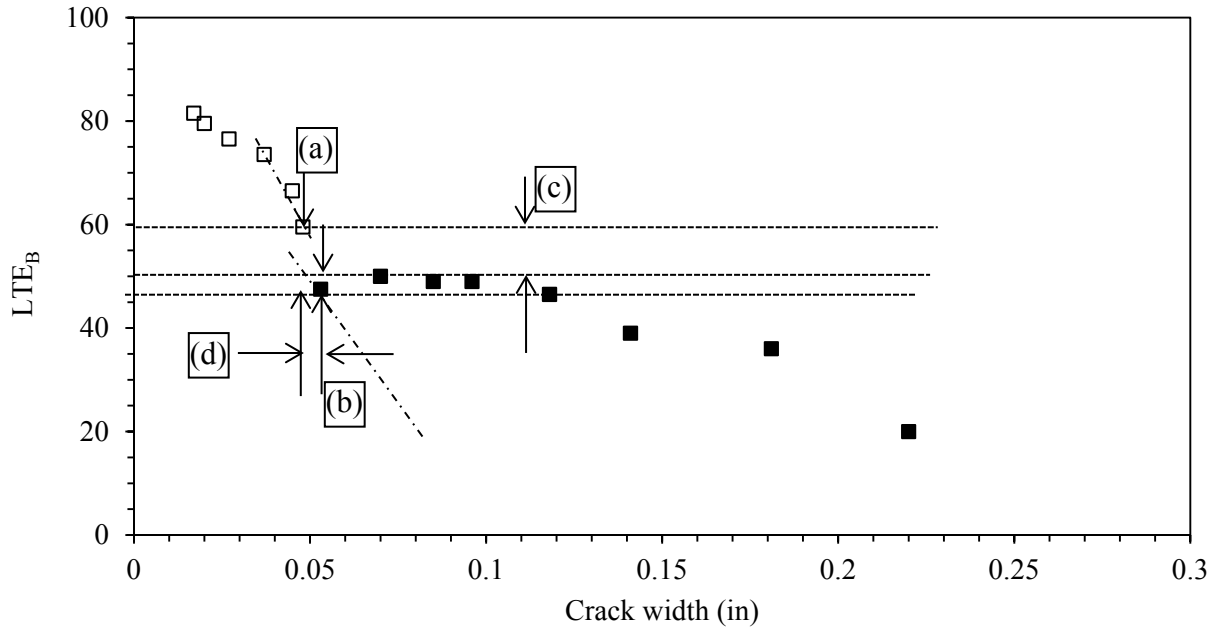
Note: a = 12 percent, b = 3 percent, c = 9 percent, and d = 5 mil.

Figure B. 2. Adjustment for determining non-fatigued LTE$_B$ for beam, F2-1, 0.048-0.053, 0.1771.

353
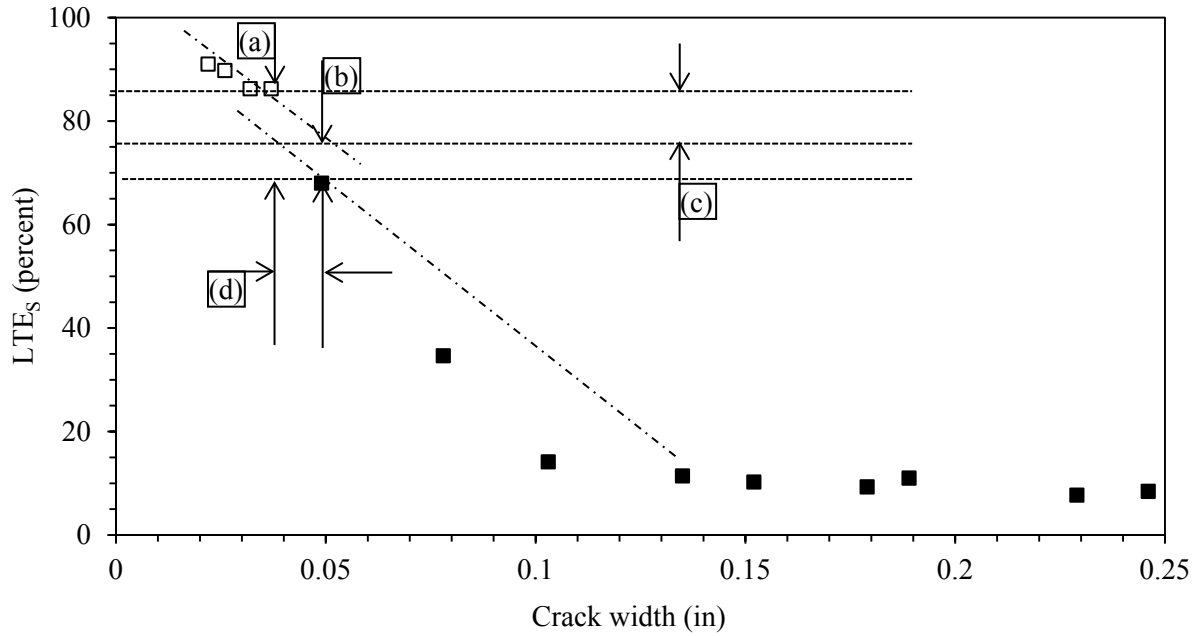
Note: a = 18 percent, b = 8 percent, c = 10 percent, and d = 12 mil.

Figure B. 3. Adjustment for determining non-fatigued LTE$_S$ for FRC1 slab.

B.2   ADJUSTMENT IN DER

Note: a = 14 percent, b = 4 percent, c = 10 percent, and d = 6 mil.

Figure B. 4. Adjustment for determining non-fatigued DER$_B$ for beam, F1-3, 0.037-0.043, 0.1614.
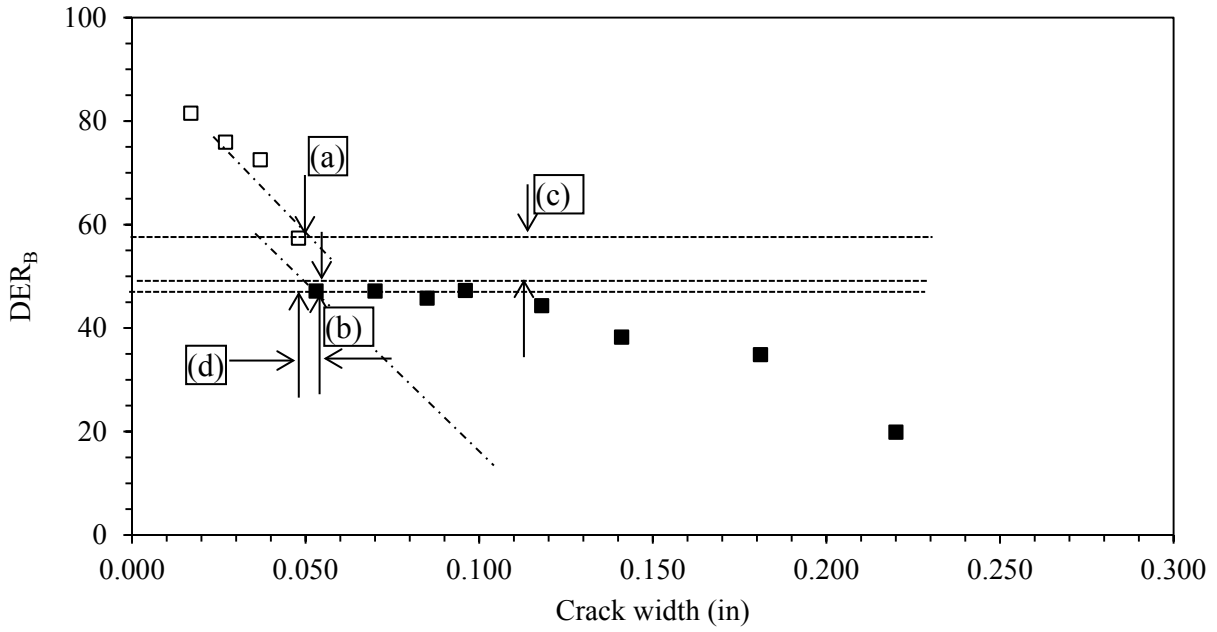
Note: a = 12 percent, b = 2 percent, c = 10 percent, and d = 5 mil.

Figure B. 5. Adjustment for determining non-fatigued DER_B for beam, F2-1, 0.048-0.053, 0.1771.
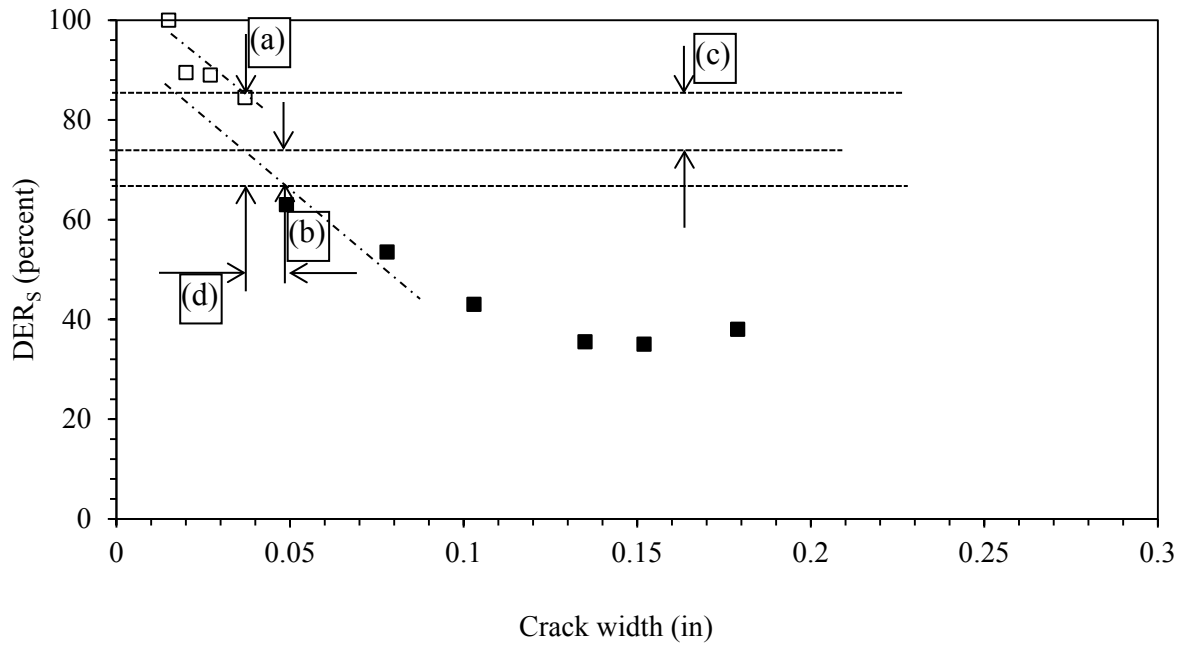
Note: a = 22 percent, b = 9 percent, c = 13 percent, and d = 12 mil.

Figure B. 6. Adjustment for determining non-fatigued DER$_S$ for FRC1 slab.

357

BIBLIOGRAPHY

ACPA, 1998. *Whitetopping—State of the Practice,* Skokie, IL: ACPA Publication EB210P, American Concrete Pavement Association.

Aldea, C. M., Ghandehari, M. & Shah, S. P. k. A., 2000. Estimation of Water flow through Cracked Concrete under Load. *ACI Materials Journal,* 97(M65), pp. 567-575.

ARA, 2004. *Guide for Mechanistic-Empirical Design of New and Rehabilitated Pavement Structures,* s.l.: ARA.

Arnold, S., Fleming, P., Austin, S. & and Robins, P. A., 2005. Test Method and Deterioration Model for Joints and Cracks. *Cement and Concrete Research,* Volume 35, pp. 2371-2383.

ASTM-C1609/D1609M, 2010. *Standard Test Method for Flexural Performance of Fiber-Reinforced Concrete (Using Beam With Third-Point Loading).* West Conshohocken, PA, American Society for Testing and Materials.

ASTM-C39/C39M-12a, 2010. *Standard Test Method for Compressive Strength of Cylindrical Concrete Specimens.* West Conshohocken, PA, ASTM International.

ASTM-C469/C469M, 2010. *Standard Test Method for Static Modulus of Elasticity and Poisson's Ratio of Concrete in Compression.* West Conshohocken, PA, ASTM International.

ASTM-C78/C78M, 2010. *Standard Test Method for Flexural Strength of Concrete (Using Simple Beam with Third-Point Loading).* West Conshohocken, American Society for Testing and Materials.

ASTM-D1195/D1195M, 2009. *Standard Test Method for Repetitive Static Plate Load Tests of Soils and Flexible Pavement Components, for Use in Evaluation and Design of Airport and Highway Pavements.* West Conshohocken, PA, American Society for Testing and Materials.

Barman, M., Mu, F. & Vandenbossche, J. M., 2011. *Development of a Rational Mechanistic-Empirical Based Design Guide for Thin and Ultra-Thin Whitetopping. Task 4 Report:Climatic Considerations.* Pittsburgh: University of Pittsburgh.

Barman, M., Vandenbossche, J. M., Mu, F. & Gatti, K., 2010. *Development of a Rational Mechanistic-Empirical Based Design Guide for Thin and Ultra-Thin Whitetopping. Task 1 Report: Compilation and Review of Existing Data and Information,* Pittsburgh, PA: Department

of Civil and Environmental Engineering Swanson School of Engineering, University of Pittsburgh.

Benkelman, A. C., 1933. Tests of Aggregate Interlock at Joints and Cracks. *Engineering News Record,* August, 111(NO.8), pp. 227-232.

Bentur, D. & Mindness, S., 1990. *Fiber Reinforced Cementiticious composites,* London: Spon Press, Taylor and Francis Group.

Bordelon, A. C., 2011. *Flowable Fibrous Concrete for Thin Pavement Inlays,* Urbana-Champaign, IL: University of Illinois at Urbana- Champaign.

Boredelon, A. C., 2005. *Fracture Behavior of Concrete Materials for Rigid Pavement Systems,* Champaign: University of Illinois at Urbana.

Brink, A. C. et al., 2004. *Improvement of Aggregate Interlock Equation used in CNCPAVE.* Pretoria, South Africa, Document Transformation Technologies CC, pp. 100-115.

Bruinsma, J. E., Raja, Z. I., Synder, M. B. & Vandenbossche, J. M., 1995. *Factors affecting the Deterioration of Transverse Cracks in JRCP.,* Lansing: Department of Transportation and Great Lakes center for Transportation Research.

Burnham, T. R., 2006. *Mn/ROAD Lessons learned: Thin and Ultra Thin Concrete Overlay.,* St. Paul, MN: Minnesota Department of Transportation.

Byrum, C. H. et al., 2011. *Joint load transfer in concret airfield pavements: Appendix B: Literature review, summary, Airport Pavement,* Rosemont, IL: s.n.

Chupanit, P. & Roesler, J. R., 2008. Fracture Energy Approach to Characterize Concrete Crack. *Journal of Materials in Civil Engineering,* pp. 275-282.

Chupanit, P. & Roesler, J. R., 2008. Fracture Energy Approach to Characterize Concrete Crack Surface Roughness and Shear Stiffness. *Journal of Materials in Civil Engineering, American Society of Civil Engineering (ASCE),* 20(4), pp. 275-282.

Colley, B. E. & Humphrey, H. A., 1967. Aggregate Interlock at Joints in Concrete Pavements. *Highway Research Record,* Issue 198, pp. 1-18.

Feng, Z. Z. & Ming, L. J., 2009. Finite Element Model of Airport Rigid Pavement Structure based on ABAQUS. *Journal of Traffic and Transportation Engineering,* 3(3).

Grzybowski, M. & Shah, S. P., 1990. Shrinkage Cracking of Fiber Reinforced Concrete. *ACI Materials Journal,* 87(2), pp. 138-148.

Gucunski, N., 1998. *Development of a Design Guide for Ultra-Thin Whitetopping (UTW),* Princeton, NJ: SWK Pavement Engineering.

Hammons, M., 1998. *Advanced Pavement Design: Finite Element Modeling for Rigid Pavement Joints, Report II: Model Development,* Washington: U.S. Department of Transportation Federal Aviation Administration.

Hammons, M. I., 1998. *Advance Pavement Design: Finite Element Modeling for Rigid Pavement Joints Report II: Model Development,* Springfield, Virginia: U.S. Department of Federal Administration, Federal Aviation Administration .

Hannant, D. J., 1978. *Fiber Cements and Fiber concrete.* Wiley, New York: John Wiley and Sons.

Hansen, W. et al., 1998. *Investigation of Transverse Cracking on Michigan PCC Pavements over Open-Graded Drainage Course,* s.l.: Michigan Department of Transportation.

Ioannides, A. & Korovesis, G., 1990. Aggregate Interlock: A Pure-Shear Load Transfer Mechanism. *Transportation Research Record: Journal of the Transportation Research Board,* Volume No. 1286, pp. 14-23.

Ioannides, A. M. & Korovesis, G. T., 1990. Aggregate Interlock: A Pure-Shear Load Transfer Mechanism. *Transportation Research Record: Journal of the Transportation Research Board,* Volume No. 1286, pp. 14-23.

Jensen, E. A. & Hansen, W., 2001. Mechanisms of Load Transfer-Crack width relation in JPCP: Influence of CA properties. *Procedures 7th Int. Conf. on Concrete Pavements, International Society of Concrete Pavement.*

Kanda, T. & Li, V. C., 1999. Effect of Fiber Strength and Fiber- Matrix Interface on Crack Bridging in Cement Composites. *Journal of Engineering Mechanics, ASCE,* 125(3), pp. 290 - 299.

Khazanovich, L., 1994. *Structural Analysis of Multi-Layered Concrete Pavement Systems,* Urbana, Illinois: University of Illinois.

Kou, C. M., 1994. *Three-dimensional finite element analysis of concrete pavement,* Urbana: University of Illinois at Urbana-Champaign.

Lepech, M. & Li, V. C., 2005. *Water Permeability of Cracked Cementitious Composites.* Turin, Italy, Paper 4539 of Compendium of Papers CD ROM, Eleventh International Conference on Fracture.

Lev, K. & Gotlif, A., 2002. *EVALUATION OF JOINT AND CRACK LOAD TRANSFER FINAL REPORT,* McLean, Virginia: U.S. Department of Transportation, Federal Highway Administration McLean, Virginia.

Li, Z., Duffala, N., Mu, F. & Vandenbossche, J. M., 2013. *Bonded Concrete Overlay of Asphalt Pavements Mechanistic- Empirical Design Guide (BCOA-ME)- Theory Manual,* Pittsburgh: University of Pittsburgh.

Mindess, S., Young, J. F. & Darwin, D., 2002. *Concrete.* 2nd ed. New Jersey: Prentice Hall.

Mitra, S. R., Reddy, K. S. & Ramchandra, L. S., 2010. Load Transfer Characteristics of Aggregates Interlocking in Concrete Pavement. *Journal of Transportation Engineering,* 136(3), pp. 190-195.

Mu, F. & Vandenbossche, J. M., 2010. *Development of a Rational Mechanistic-Empirical Based Design Guide for Thin and Ultra-Thin Whitetopping. Task 2 Report:Review and Selection of Structural Response Models.* Pittsburgh: University of Pittsburgh.

Naaman, A. E., Shah, S. P. & L., T. J., 1984. *Some Developments in Polypropylene Fibers for Concrete,* Farmington Hills, MI: Fiber Reinforced Concrete, SP-81, G.C. Hoff, Ed., American Concrete Institute.

Nishiyama, T., Lee, H. & Bhatti, A., 2005. Investigation of Bonding Condition in Concrete Overlay by Laboratory Testing, Finite Element Modeling, and Field Evaluation.. *Transportation Research Reccord, Journal of the Transportation Research Board,* Volume 1933, pp. 15-23.

Nishizawa, T., Murata, Y. & Kokubo, Y., 2003. Mechanical Behavior of Ultra-Thin Whitetopping Structure Under Stationary and Moving Loads. *Transportation Research Record, Journal of Transportation Research Board,* pp. 102-110.

Nowlen, W. J., 1968. Influence of Aggregate Properties on Effectiveness of Interlock Joints in Concrete Pavements. *Journal of the PCA, Research and Development Laboratories,* May , 10(No.2), pp. 2-8.

Rajabipour, F. & Akhavan, A., 2010. *Effect of Cracking on Concrete Permeability as a Function of Crack Width and Tortuosity.* Chicago, IL, Presented at ACI Spring Convention.

Raja, Z. I. & Snyder, M. B., 1995. *Factors Affecting the Deterioration of Transverse Cracks in JRCP,* East Lansing, MI: Michigan State University, Department of Civil and Environmental Engineering, Michigan Department of Transportation and Great Lakes Center for Truck Transportation Research University of Michigan..

Raja, Z. I. & Snyder, M. B., 1995. *Factors Affecting the Deterioration of Transverse Cracks in JRCP,* East Lansing, Michigan: Michigan Department of Transportation and Great Lakes Center for Truck Transportation Research University of Michigan.

Ramirez, L. C., 2010. *Concrete Mixer Properties affecting the Aggregate Interlock Mechanism of Joints and Cracks for Rigid Pavement Systems,* Pittsburgh: University of Pittsburgh.

Rapoport, J. et al., 2002. Permeability of Cracked Steel Fiber - Reinforced Concrete.. *Journal of Materials in Civil Engineering,ASCE,* 14(4), pp. 355-358.

Rasmussen, A. O. et al., 2002. *Identification of Pavement Failure Mechanisms at FHWA Accelerated Loading Facility Ultrathin Whitetopping Project,* Washington, Dc.: Transportation Research Record: Journal of the Transportation Research Board.

Rasmussen, R. O. & Rozycki, D. K., 2004. *Thin and Untra-Thin Whitetopping,* s.l.: NCHRP Synthesis of Highway Practice 338, National Cooperative Highway Research Program, National Research Council,Washington, DC..

Rasmussen, R. & Rozycki, D., 2004. *Thin and Untra-Thin Whitetopping. NCHRP Synthesis of Highway Practice 338 ,* Washington, DC: National Cooperative Highway Research Program.

Riley, R. et al., 2005. *Incorporation of Probabilistic Concepts Into Fatigue Analysis of Ultrathin Whitetopping as Developed for the American Concrete Pavement Association.* Denver, CO., Proceedings from the Best Practices in Ultra Thin and Thin Whitetopping, pp. 288-317.

Rodezno, M. C. & Kaloush, K. E., 2010. Effect of Different Dosages of Polypropylene Fibers in Thin Whitetopping Concrete Pavements. *ACI Materials Journal,* 107(1), pp. 42-47.

Roesler, J. & Cervantes, V., 2008. *Accelerated Pavement Testing and Design of Thin Concrete Pavements (TCP): Construction Report,* Urbana, IL: Department of Civil and Environmental Engineering University of Illinois, Urbana, IL (UIUC).

Roesler, J. R. et al., 2006. Effect of Synthetic Fibers on Structural Behavior of Concrete Slabs-on-Ground. *ACI Materials Journal,* 103(1), pp. 3-10.

Roesler, J. R. et al., 2008. *Design and Concrete Material Requirements for Ultra-Thin Whitetopping,* IL: Publication FHWA-ICT-08-016. Illinois Center for Transportation.

Roesler, J. & Wang, D., 2009. *Thermal stress analysis in ultra-thin whitetopping pavement.* Champaign, IL., Proceedings of the 8th International conference on the Bearing Capacity of Roads, Railways, and Airfields, Taylor & Francis Group (CRC Press).

Shah, S. P., Sharigaphuti, M. & E, K. M., 1994. *Comparison of Shrinkage Cracking Performance of Different Types of Fibers and Wire-Mesh.,* Farmington Hills, MI: Fiber Reinforced Concrete: Development and Innovations, SP- 142. J. Daniel and S. P. Shah, eds., American Concrete Institute.

Sheehan, M., Tarr, S. & Tayabji, S., 2004. *Instrumentation and Field Testing of Thin Whitetopping Pavement in Colorado and Revision of the Existing Colorado Thin Whitetopping Procedure.* Denver, CO, Colorado Department of Transportation Report No. CDOT-DTD-R-2004-12.

Tarr, S. M., Sheehan, M. J. & Okamoto, P. A., 1998. *Guidelines for the Thickness Design of Bonded Whitetopping Pavement in the State of Colorado. Report No. CDOTDTD- R-98-10,,* Denver, CO: Colorado Department of Transportation.

Thomas, J. & Ramaswamy, A., 2007. Mechanical Properties of Steel Fiber- Reinforced Concrete. *Journal of Materials in Civil Engineering, ASCE,* 19(5), pp. 385-392.

Vandenbossche, J. M., 1999. Estimating Potential Aggregate Interlock Load Transfer Based on Measurements of Volumetric Surface Texture of the Fracture Plane. *Transportation Research Record: Journal of the Transportation Research Board No.1673,* pp. 59-63.

Vandenbossche, J. M., 2003. Performance Analysis of Ultrathin Whitetopping Intersections on US-169, Elk River, Minnesota. *Transportation Research Record: Journal of the Transportation Research Board,* Volume 1853, pp. 18-27.

Vandenbossche, J. M. & Barman, M., 2010. Bonded Whitetopping Overlay DesignConsiderations for Prevention of Reflection Cracking, Joint Sealing,and the Use of Dowel Bars. *Transportation Research Record,* Volume No. 2155, pp. 3-11.

Vandenbossche, J. M., Barman, M. & Kremm, J. N., 2013. Using Surface Texture Measurements of Crack Surface to Establish Joint Spring Stiffness Representing Shear Transfer Capacity. *Transportation Research Record,* p. Accepted for publication.

Vandenbossche, J. M. & Li, Z., 2013. Redefining the Failure Mode for Thin and Ultra-thin Whitetopping with a 1.8- x 1.8-m (6- x 6-ft) Joint Spacing.

Won, J. P., Lin, D. H. & Park, C. G., 2006. Bond behavior and flexural performance of structural ynthetic fibre-reinforced concrete. *Magazine of Concrete Research,* 58(6), pp. 401-410.

Wu, C. et al., 1998. *Development of Ultra-Thin Whitetopping Design Procedure. Report RD 2124.,* Skokie, IL: Portland Cement Association.

Zhang, J., Stang, H. & Li, V. C., 2000. Experimental Study on Crack Bridging in FRC Under Uniaxial Fatigue Tension. *Journal of Materials in Civil Engineering, ASCE,* 12(1), pp. 66 -73.

Zhang, J., Stang, H. & Li, V. C., 2001. Crack Bridging Model or Fiber Reinforced Concrete Under Fatigue Tension. *International Journal of Fatigue,* Volume 23, pp. 55-670.

Zollo, R. F. & Ilter, J. A., 1986. *Plastic and Drying Shrinkage in Concrete Containing Collated Fibrillated Polypropylene Fiber.* Sheffiled, Developments in Fiber Reinforced Cement and Concrete, R. N. Swamy, R. L. wagstaffe, and D. R. Oakley. eds., Proceedings, RILEM Symposium.